Durham University

Durham E-Theses

Crustal accretionary processes at mid-ocean ridges - Valu Fa Ridge, Lau Basin

Ian mark Turner

How to cite:

Turner, Ian mark (1998) Crustal accretionary processes at mid-ocean ridges - Valu Fa Ridge, Lau Basin. Doctoral thesis, Durham University.

Use policy

The full-text may be used and/or reproduced, and given to third parties in any format or medium, without prior permission or charge, for personal research or study, educational, or not-for-profit purposes provided that:

- a full bibliographic reference is made to the original source
- a https://etheses.durham.ac.uk/id/eprint/5002/ is made to the metadata record in Durham E-Theses
- the full-text is not changed in any way

The full-text must not be sold in any format or medium without the formal permission of the copyright holders.

Please consult the full Durham E-Theses policy for further details.

Academic Support Office, The Palatine Centre, Durham University, Stockton Road, Durham, DH1 3LE
e-mail: e-theses.admin@durham.ac.uk Tel: +44 0191 334 6107
https://etheses.durham.ac.uk

Crustal accretionary processes at mid-ocean ridges – Valu Fa Ridge, Lau Basin

Ian Mark Turner

The copyright of this thesis rests with the author. No quotation from it should be published without the written consent of the author and information derived from it should be acknowledged.

A thesis submitted for the degree of Doctor of Philosophy at the University of Durham

Department of Geological Sciences

October 1998

24 FEB 1999

Declaration

This dissertation describes my own work, except where acknowledgement is made in the text, and is not substantially the same as any work that has been, or is being, submitted to any other university for any degree, diploma or other qualification.

Ian M. Turner October 1998

It's not the taking part that counts.....

.....it's the finishing!

Crustal accretionary processes at mid-ocean ridges – Valu Fa Ridge, Lau Basin

Ian Mark Turner

Abstract

The structure of oceanic crust is surprisingly uniform, which suggests that crustal accretionary processes at mid-ocean ridges must be broadly similar, despite their different spreading rates and seafloor morphologies. Seismic studies have revealed the presence of sub-axial magma chambers at fast, slow and intermediate spreading ridges, but constraints on their shape and size are generally restricted to the fast spreading East Pacific Rise. The aim of this study is to compare the processes of crustal accretion at fast, slow and intermediate ridges by investigating the detailed crustal structure and magma chamber geometry of a magmatically active intermediate spreading ridge, the Valu Fa Ridge.

A multidisciplinary geophysical experiment was conducted over the Central Valu Fa Ridge and its overlap with the Northern Valu Fa Ridge during *R/V Maurice Ewing* Cruise EW9512, and wide-angle seismic data, recorded on a set of digital ocean bottom seismometers, were used to generate velocity-depth models on two across-axis, two along-axis and two axis-parallel profiles. These models were further constrained by modelling of the normal incidence seismic and gravity data and the resulting combined models of crustal structure were interpreted to reveal that a composite magma chamber exists beneath the Valu Fa Ridge crest. The magma chamber consists of a thin, narrow (1-1.5 km) melt lens, with an interconnected melt fraction, overlying a wider (~4 km) region of hot rock or low melt fraction. A reflection from the top of the melt lens is identified on both the normal incidence seismic and wide-angle seismic data and delay-time modelling indicates that velocities as high as 5.5 km s^{-1} are achieved ~250 m below the top of the melt lens. The main body of the magma chamber corresponds to the region of hot rock below the melt lens and is delineated by anomalously low velocities, extending down through seismic layer 3 to within 1.5-2 km of the Moho.

Moho reflections from beneath the overlapping spreading centre and a low on the mantle Bouguer anomaly map implies that this region is currently, or has recently been, the site of enhanced magmatism. This observation is contrary to popular models of ridge segmentation and melt delivery.

The transition from pre-rift crust (both island arc and back-arc crust) to post-rift material, marked by considerable thinning of seismic layer 2, has also been uniquely identified in this study and describes the limit of VFR-generated crust.

The size and temporal stability of magma chambers are largely dependent on their magma budget and the Valu Fa Ridge magma chamber model, developed as part of this study, may bridge the gap between the large, long-lived magma chambers identified at the East Pacific Rise and the more transitory magma chambers proposed at slow spreading ridges. Melt ascends as small isolated pockets through the main body of the magma chamber at the Valu Fa Ridge and resides in the melt lens until eruption. Seismic layer 2 is constructed solely from material 'erupted' from the melt lens, with the main body of the magma chamber cooling to form seismic layer 3. Convection currents, induced by large thermal gradients at the sides of the magma chamber, both accelerate the cooling process, thus limiting its size, and helps to generate the thick layered sequences as observed in ophiolite studies. The entire crust is emplaced within the axial region and a distinct Moho is formed at ~0 Ma.

Acknowledgements

I have particularly enjoyed my time in Durham and this would not have been possible without the help of a considerable number of people.

First and foremost I wish to thank my supervisor, Chris Peirce. Over the past three years, Chris has tirelessly answered all of my incessant questions, provided invaluable comments on drafts of my thesis and given me the opportunity to participate in two unforgettable cruises, particularly the cruise to the Lau Basin.

I would also like to thank the officers and crew of the *R/V Maurice Ewing* and members of the EW9512 Scientific Party without whom data collection would not have been possible. Special thanks must also go to 'Team DOBS' - you know who you are!!

In my first year, Debbie Navin guided me through the intricacies of wide-angle seismic processing and modelling and answered many of my niggling questions, thus saving me the walk down the corridor to ask Chris. Thanks Debs.

Anthony Day, working on a 3-D tomography inversion of the EW9512 dataset has kindly persuaded his code to come up with inversions that agree favourably with my 2-D velocity-depth models. No mean feat and a big boost to the confidence.

Thanks to Martin Sinha and Lucy MacGregor for reading though my thesis and for valuable comments on the gravity and CSEM data.

I am particularly grateful to all those who solved my problems with computers and several computer programs, including Chris, Martin, Dave, Debs, Tony, George, Matt, Toby, Ziad, Simon, etc....

Stefan Calvert, Alison Offer and Ian Rushforth also deserve a mention for modelling various parts of the EW9512 dataset.

I have been financed by NERC throughout my Ph.D. and the research cruise to the Lau Basin was also NERC funded.

Thanks must also go to my parents, for doing what they do best and giving support when needed.

For making my time at Durham far more interesting I wish to thank all the Ph.D. and M.Sc. students I've met at the department (the list is too long and I would probably leave someone out!); my past office mates; Carol Carr, Alan Pearson and Robert Irvine at Hild Bede; and the guys from the squash club.

Last but not least thanks to Vanessa, for always being there.

Contents

1 Introduction
1.1 Tectonic setting 1
1.2 The Valu Fa Ridge 5
1.3 Oceanic crust 9
1.4 Crustal structure and magma chamber geometry at mid-ocean ridges 10
1.4.1 Fast spreading ridges 13
1.4.2 Slow spreading ridges 16
1.4.3 Intermediate spreading ridges 19
1.5 Aim of this study 22
1.6 Summary and structure of this dissertation 23
2 Data acquisition and processing
2.1 Introduction 25
2.2 Experimental configuration 26
2.3 Data acquisition 28
2.3.1 Wide-angle seismic data 29
2.3.2 Normal incidence seismic data 30
2.3.3 Additional datasets 30
2.4 Wide-angle seismic data processing 32
2.4.1 Data replay 32
2.4.2 Corrections applied to wide-angle seismic data 34
2.4.3 Generation of final record sections 34
2.4.4 Errors 34
2.5 Normal incidence seismic data processing 36
2.6 Sonobuoy data processing 37
2.7 Free-air gravity data processing 39
2.8 Summary 39
3 The Valu Fa Ridge wide-angle seismic dataset
3.1 Introduction 40
3.2 The wide-angle seismic dataset 40
3.2.1 Phase identification 41
3.2.2 Frequency analysis and filtering 41
3.3 Across-axis data sections 50
3.4 Along-axis data sections 54
3.5 Axis-parallel data sections 57
3.6 Summary 58
4 Modelling of the wide-angle seismic dataset
4.1 Introduction 59
4.2 *Seismic South* across-axis profile - Line 1 59
4.2.1 Initial model 59
4.2.2 Ray-trace modelling 62
4.2.3 Best fitting wide-angle seismic model 67
4.3 *Seismic North* across-axis profile - Line 6 76
4.3.1 Initial model 76
4.3.2 Best fitting wide-angle seismic model 81
4.4 Along-axis profiles - Line 4 (CVFR) and Line 9 (NVFR) 89
4.4.1 Initial models 89
4.4.2 Best fitting wide-angle seismic model - Line 4 96
4.4.3 Best fitting wide-angle seismic model - Line 9 101
4.5 Axis-parallel profiles - Line 5 and Line 11 105

4.5.1 Initial models 105
4.5.2 Best fitting wide-angle seismic model - Line 5 111
4.5.2 Best fitting wide-angle seismic model - Line 11 115
4.6 Further modelling of the wide-angle seismic dataset 118
4.6.1 *Rayinvr* 118
4.6.2 *Reflectivity* 121
4.7 Summary 124
5 Modelling of the normal incidence seismic and gravity datasets
5.1 Introduction 125
5.2 Normal incidence seismic data 125
5.2.1 Modelling strategy 128
5.2.2 *Seismic South* across-axis profile - Line 1 129
5.2.3 *Seismic South* along-axis profile - Line 4 132
5.2.4 *Seismic North* across-axis profile - Line 6 134
5.2.5 Summary 137
5.3 Gravity data 137
5.3.1 2-D gravity modelling 137
5.3.2 Residual mantle Bouguer anomaly 149
5.4 Summary 160
6 Crustal structure of the Valu Fa Ridge
6.1 Introduction 161
6.2 Upper crustal structure 164
6.2.1 Layer 2A 164
6.2.2 Layer 2B/C 167
6.3 Lower crustal structure 167
6.3.1 Layer 3 (off-axis) 168
6.3.2 Crustal thickness 168
6.4 Transition zones 170
6.5 Magma chamber geometry 174
6.5.1 Axial low velocity block 174
6.5.2 Low velocity zone 178
6.5.3 Magma chamber structure of the OSC at 22° 12′ S 179
6.5.4 Integrated magma chamber model 181
6.6 Summary 183
7 Conclusions and further work
7.1 Introduction 184
7.2 Results and conclusions from this study 184
7.2.1 Summary of results 184
7.2.2 Implications for understanding the processes of crustal accretion 187
7.3 Further study 189
7.3.1 Additional work of the existing VFR dataset 189
7.3.2 Suggestions for future surveys 190
7.4 Conclusions 193

References 194

Appendix A 204
Appendix B 236
Appendix C 254
Appendix D 260

List of figures

1.1	Tectonic and morphological features of the plate boundary between the Pacific and Indo-Australian Plates	2
1.2	Location map of the Central Lau Spreading Centre and Eastern Lau Spreading Centre	4
1.3	Seismic reflection profile *11*, cruise L5-82-LP (Morton and Sleep, 1985)	5
1.4	Structural map of the Southern Lau Basin	6
1.5	Map of the location of the magma chamber identified from across-axis reflection profiles	8
1.6	Axial morphology at fast, intermediate and slow spreading ridges	10
1.7	Across-axis magma chamber models	12
1.8	The East Pacific Rise: a fast spreading ridge	13
1.9	The Mid-Atlantic Ridge: a slow spreading ridge	17
1.10	Interpretative model of a magma chamber beneath a slow spreading ridge	18
1.11	The Juan de Fuca Ridge: an intermediate spreading ridge	20
2.1	The Valu Fa Ridge seismic study	27
2.2	The main specifications of the airgun array used during EW9512	29
2.3	Free-air gravity track lines	31
2.4	The main processing routines required to create SEG-Y_i from raw DOBS data	33
2.5	The main processing stages required to generate the final wide-angle seismic record sections	35
2.6	Normal incidence seismic data collected during EW9512	36
2.7	Correction for sonobuoy drift	38
3.1	Wide-angle seismic data from SDOBS3	42
3.2	A comparison of the frequency spectra of two traces from SDOBS3	44
3.3	Frequency analysis of trace 195 from SDOBS3	45
3.4	Vertical component geophone data from SDOBS4	47
3.5	Hydrophone data from SDOBS4	48
3.6	Filtered horizontal component geophone data from SDOBS4	49
3.7	Filtered vertical component geophone data from SDOBS2 showing the main phases of interest	51
3.8	Filtered vertical component geophone data from NDOBS1 showing the main phases of interest	52
3.9	Detail from the unfiltered hydrophone data on the two across-axis profiles	53
3.10	Filtered vertical component data from SDOBS4 (Line 4)	54
3.11	Along-axis record sections from SDOBS4	56
3.12	Filtered vertical component geophone data from NDOBS6 (axis-parallel record section)	57
4.1	Line 1, across-axis initial model	61
4.2	Ray-trace modelling of the initial across-axis seismic model for SDOBS2 on Line 1	64
4.3	Ray-trace modelling of the initial across-axis seismic model for SDOBS5 on Line 1	65
4.4	Line 1, across-axis final model	68
4.5	Ray-trace modelling of the final across-axis seismic model for SDOBS4 on Line 1	69
4.6	Ray-trace modelling of the final across-axis seismic model for SDOBS2 on Line 1	71
4.7	Ray-trace modelling of the final across-axis seismic model for SDOBS5 on Line 1	72
4.8	P-wave velocity anomaly plot for Line 1, *Seismic South*	75
4.9	Line 6, across-axis initial model	77
4.10	Ray-trace modelling of the initial across-axis seismic model for NDOBS5 on Line 6	79
4.11	Ray-trace modelling of the initial across-axis seismic model for NDOBS1 on Line 6	80
4.12	Line 6, across-axis final model	82

4.13	Ray-trace modelling of the final across-axis seismic model for NDOBS3 on Line 6	83
4.14	Ray-trace modelling of the final across-axis seismic model for NDOBS5 on Line 6	85
4.15	Ray-trace modelling of the final across-axis seismic model for NDOBS1 on Line 6	86
4.16	P-wave velocity anomaly plot for Line 6, *Seismic North*	88
4.17	Ray-trace modelling of the initial CVFR along-axis seismic model for SDOBS4 on Line 4	92
4.18	Ray-trace modelling of the initial CVFR along-axis seismic model for NDOBS2 on Line 4	93
4.19	Ray-trace modelling of the initial NVFR along-axis seismic model for NDOBS3 on Line 9	95
4.20	Line 4, along-axis final model	96
4.21	Ray-trace modelling of the final CVFR along-axis seismic model for SDOBS4 on Line 4	98
4.22	Ray-trace modelling of the final CVFR along-axis seismic model for NDOBS2 on Line 4	99
4.23	Line 9, along-axis final model	101
4.24	Ray-trace modelling of the final NVFR along-axis seismic model for NDOBS3 on Line 9	103
4.25	Ray-trace modelling of the final NVFR along-axis (Line 9) seismic model for two sonobuoys	104
4.26	Ray-trace modelling of the initial axis-parallel seismic model for SDOBS1 on Line 5	107
4.27	Ray-trace modelling of the initial axis-parallel seismic model for NDOBS6 on Line 5	108
4.28	Ray-trace modelling of the initial axis-parallel seismic model for NDOBS5 on Line 11	110
4.29	Line 5, axis-parallel final model	111
4.30	Ray-trace modelling of the final axis-parallel seismic model for SDOBS1 on Line 5	113
4.31	Ray-trace modelling of the final axis-parallel seismic model for NDOBS6 on Line 5	114
4.32	Line 11, axis-parallel final model	115
4.33	Ray-trace modelling of the final axis-parallel seismic model for NDOBS5 on Line 11	117
4.34	A comparison of the results of ray-trace modelling of the final across-axis (Line 1) seismic model for SDOBS2 using two different programs, *maslov* and *rayinvr*	119
4.35	A comparison of the results of ray-trace modelling of the final CVFR along-axis seismic model for SDOBS4 using two different programs, *maslov* and *rayinvr*	120
4.36	Synthetic data generated from a 1-D approximation to the final CVFR along-axis seismic model	122
5.1	Across-axis normal incidence seismic data showing the main features of interest	126
5.2	Along-axis normal incidence seismic data showing the main features of interest	127
5.3	Forward modelling of the normal incidence seismic data	129
5.4	Across-axis velocity-depth model used to generate the synthetic normal incidence seismic data	130
5.5	Across-axis normal incidence seismic forward modelling (Line 1)	131
5.6	Along-axis normal incidence seismic forward modelling (Line 4)	133
5.7	Along-axis normal incidence seismic data over the OSC	134
5.8	Across-axis velocity-depth model used to generate the synthetic normal incidence seismic data	135
5.9	Across-axis normal incidence seismic forward modelling (Line 6)	136
5.10	Velocity-density relationship of Nafe and Drake (1957)	138
5.11	Final across-axis 2-D free-air gravity model of Line 1	141
5.12	Final across-axis 2-D free-air gravity model of Line 6	142
5.13	Map showing the major topographic features surrounding Line 6	143
5.14	Final across-axis 2¾-D free-air gravity model of Line 6	145
5.15	Final across-axis 2¾-D free-air gravity model of Line 4	148
5.16	The main stages in the calculation of the residual mantle Bouguer anomaly	149
5.17	Free-air gravity map calculated from the EW9512 data	151
5.18	Model used as input to *grav2*	152
5.19	Calculation of the gravitational effect of a layered crust of constant thickness and density	153
5.20	Mantle Bouguer anomaly	155

5.21 Calculation of the thermal effect of a north-south ridge-transform-ridge system 158
5.22 Residual mantle Bouguer anomaly 159

6.1 Location map of the main seismic (and gravity) lines 161
6.2 Fence diagram showing the final velocity-depth models 162
6.3 Velocity-depth profiles of the VFR compared with the 'standard' velocity envelopes for EPR and MAR crust 163
6.4 Comparison between the emplacement of layer 2A at the EPR and VFR 166
6.5 Tectono-magmatic evolution of the VFR at 22° 26′ S 171
6.6 Structural map of the Southern Lau Basin 173
6.7 A comparison of low velocity zones observed at fast, slow and intermediate spreading ridges 180
6.8 Schematic diagram of the VFR lower crustal magma chamber 182

7.1 Crustal accretion at the VFR 187
7.2 The EW9512 3-D seismic tomography study 190
7.3 Experimental configuration for proposed future surveys 192

List of tables

1.1 The composition and physical properties of the oceanic crust 9
1.2 Summary of the observations of magma chamber geometry at the East Pacific Rise 15
1.3 Summary of the observations of possible magma chambers at intermediate spreading ridges 21

4.1 1-D velocity-depth model for the CVFR along-axis profile, Line 4 121

5.1 Initial layer densities for Line 1 139

Glossary of terms and abbreviations

The following terms and abbreviations are used throughout this dissertation:

R/V	Research Vessel
LHT	Lau-Havre-Taupo
CLSC	Central Lau Spreading Centre
NLSR	Northern Lau Spreading Centre
ELSC	Eastern Lau Spreading Centre
GLORIA	Geological LOng Range Inclined Asidic (sidescan sonar)
TWTT	Two-Way Travel Time
VFR	Valu Fa Ridge
SVFR	Southern Valu Fa Ridge
CVFR	Central Valu Fa Ridge
NVFR	Northern Valu Fa Ridge
ODP	Ocean Drilling Program
DSDP	Deep Sea Drilling Program
OSC	Overlapping Spreading Centre
MCS	Multi-Channel Seismic
RRS	Royal Research Ship
MCR	Magma Chamber Reflector
LVZ	Low Velocity Zone
EPR	East Pacific Rise
NEPR	Northern East Pacific Rise
SEPR	Southern East Pacific Rise
CSEM	Controlled Source ElectroMagnetic
ASC	Axial Summit Caldera
ESP	Expanding Spread Profile
MAR	Mid-Atlantic Ridge
AVR	Axial Volcanic Ridge
JDFR	Juan De Fuca Ridge
DOBS	Digital Ocean Bottom Seismometer
PDAS	Portable Data Acquisition System
SEG-Y	Multi-channel seismic recording standard (Barry *et al.*, 1975)
SEG-Y_i	Version of SEG-Y used for in-house processing
XBT	Expendable Bathymetric Thermographs
RAM	Random Access Memory
SNR	Signal-to-Noise Ratio
DWW	Direct Water Wave
P_g	P-wave Crustal Diving Ray
P_n	P-wave Mantle Diving Ray
P_mP	P-wave Moho Reflection
P_cP	P-wave Intracrustal Reflection
P_cS	P-wave Intracrustal Reflection (with P-S mode conversion)
P_s	P-wave Sediment Diving Ray
SV dip	Sound Velocity Dip
MBA	Mantle Bouguer Anomaly
RMBA	Residual Mantle Bouguer Anomaly
FFT	Fast Fourier Transform
AVO	Amplitude Versus Offset
TOBI	Towed Ocean Bottom Instrument

Chapter 1
Introduction

Geophysical constraints on the dimensions and properties of ridge crest magma chambers are largely derived from observations at the fast spreading East Pacific Rise. To understand the general processes of crustal accretion at mid-ocean ridges, further study must also be carried out on ridges with different spreading rates. Seismic studies have revealed the presence of magma chambers at both intermediate and slow spreading ridges, but constraints on their shape and size are relatively scarce. This dissertation contains the modelling and interpretation of parts of a multidisciplinary geophysical dataset acquired on the *R/V Maurice Ewing* (EW9512) in November-December 1995 at the intermediate spreading Valu Fa Ridge, Lau Basin.

This chapter begins with a general introduction to the study area followed by a summary of the current models of magma chambers and crustal structure at mid-ocean ridges.

1.1 Tectonic setting

Karig (1970, 1971) identified a series of marginal (or back-arc) basins behind island arc systems in the Western Pacific and suggested that they had an extensional origin. The Lau Basin, identified as one such back-arc basin, is associated with the plate convergence of the Pacific and Indo-Australian Plates and separates the volcanically active Tofua Arc (part of the Tonga Ridge) from the now inactive Lau Ridge (figure 1.1). The northern part of the plate boundary is discontinuous, jumping from westward subduction at Northern Tonga (Tonga-Kermadec Trench) to eastward subduction at the Southern New Hebrides (New Hebrides Trench). A broad and complex zone of Cenozoic tectonism separates the active trenches (Hamburger and Isacks, 1988). The divergence of the two trenches and subsequent eastward migration of the Tonga-Kermadec subduction hinge occurs largely by extensional deformation in the North Fiji and Lau Basins (Hamburger and Isacks, 1988).

Though one of the best studied back-arc basins in the Southwest Pacific, there has been considerable debate over the formation of the Lau Basin, ranging from a single spreading event initiated between 3 and 5 Ma by arc splitting to a more diffuse system

of back-arc extension (Karig, 1970 and 1971; Hawkins and Melchior 1985; Jenner *et al.*, 1987; Hamburger and Isacks, 1988; Parson *et al.*, 1990; Vallier *et al.*, 1991; Ocean Drilling Program Leg 135 Shipboard Scientific Party, 1992; Hilton *et al.*, 1993; Bevis *et al.*, 1995; Parson and Wright, 1996).

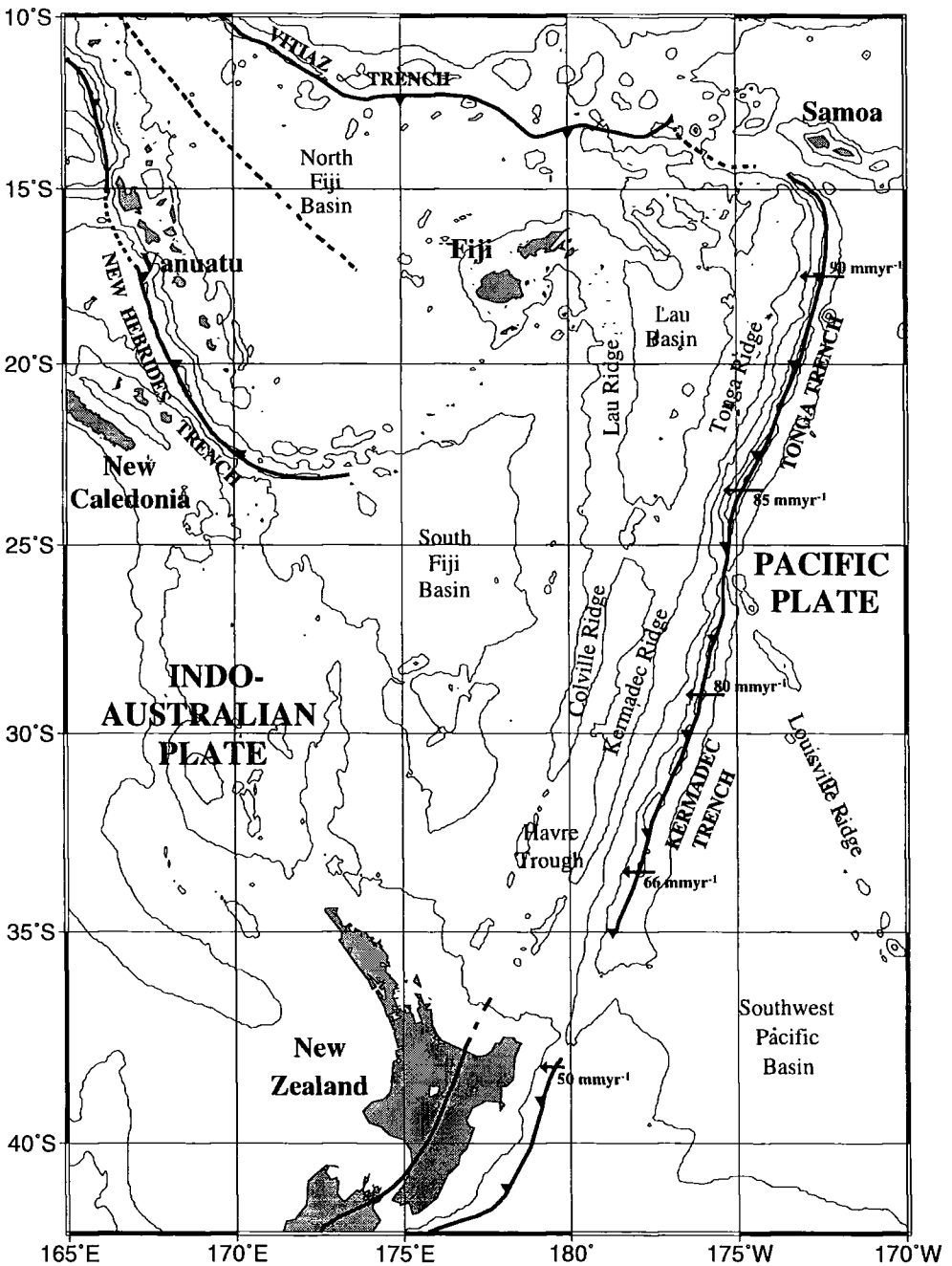

Figure 1.1: Tectonic and morphological features of the plate boundary between the Pacific and Indo-Australian Plates. Plate boundaries are identified (solid and dashed lines) and the major trenches, ridges and basins annotated. The triangular-shaped Lau Basin is centred on 20° S, 177° W and separates the Lau and Tonga ridges. Pacific plate subduction rates at the Tonga-Kermadec trench are also shown (after Parson and Wright, 1996). Note that the present subduction point of the Louisville Ridge coincides with the southern extension of the Lau Basin. Bathymetric contours are plotted at 2000 m intervals.

Parson and Wright (1996) used the enhanced spatial and temporal resolution of observed tectonic and magmatic processes along the strike of the Lau-Havre-Taupo (LHT) back-arc system, which extends over 2000 km between Tonga and New Zealand (see figure 1.1), to constrain a model for the evolution of back-arc rifting to seafloor spreading. A sequence of five stages is identified:

1) incipient simple and pure shear;
2) early, distributed and spatially heterogeneous half-graben rifting;
3) later half-graben rifting, confined to a contiguous axial zone;
4) initial oceanic spreading; and
5) reconfiguration of ridge geometry ⇒ ridge propagation.

The LHT system is observed to increase in 'maturity' northwards and the Lau Basin is currently in the process of initial oceanic spreading (stage 4) in the south and additional ridge propagation (stage 5) in the north.

Petrological data confirm the 'evolutionary' history of the Lau Basin and suggest that organised seafloor spreading accounts for only half of the crust with continued rifting in the west (Ocean Drilling Program Leg 135 Shipboard Scientific Party, 1992). Parson and Hawkins (1994) suggested that original estimates of seafloor spreading in the Lau Basin, of the order of 40-60 mm yr^{-1}, wrongly assumed that all the basin floor was oceanic crust. The revised magnetic anomaly interpretation indicates a late Pliocene and Quaternary spreading history at a full rate of 91 mm yr^{-1} between 20° and 22° S. However, Taylor *et al.* (1996) state that there is no evidence for present day rifting and significant off-axis extension in the west and calculate the Brunhes-Chron seafloor spreading rate at 21° S to be 65 mm yr^{-1}. Present day geodetic observations (Bevis *et al.*, 1995) reveal much higher spreading rates (e.g. ~90 mm yr^{-1} at 21° S), increasing northwards to a maximum of 160 mm yr^{-1} at ~16° S, which implies a recent increase in opening rates.

The two major spreading centres in the Lau Basin are the Central Lau Spreading Centre (CLSC) [also known as the Northern Lau Spreading Ridge (NLSR)] and the Eastern Lau Spreading Centre (ELSC). The southward-propagating CLSC is doing so at the expense of the northern tip of the ELSC (stage 5 - Parson and Wright, 1996) and the two ridges are separated by a complex relay zone (Wiedicke and Habler, 1993). The ELSC is located at the eastern edge of the Lau Basin between 19° and 23° S close to the inner escarpment of the Tonga Ridge (see figure 1.2) and is propagating southwards into rifted back-arc crust.

Since the early 1980s, several research cruises have focused on the Lau Basin and detailed surveys led to the discovery of a N-S trending magmatically active spreading segment, subsequently named the Valu Fa Ridge (VFR), which forms the southern extension of the ELSC (Hawkins and Melchior, 1985; Morton and Sleep, 1985; Foucher *et al.*, 1988; von Stackleberg *et al.*, 1988; Parson *et al.*, 1990).

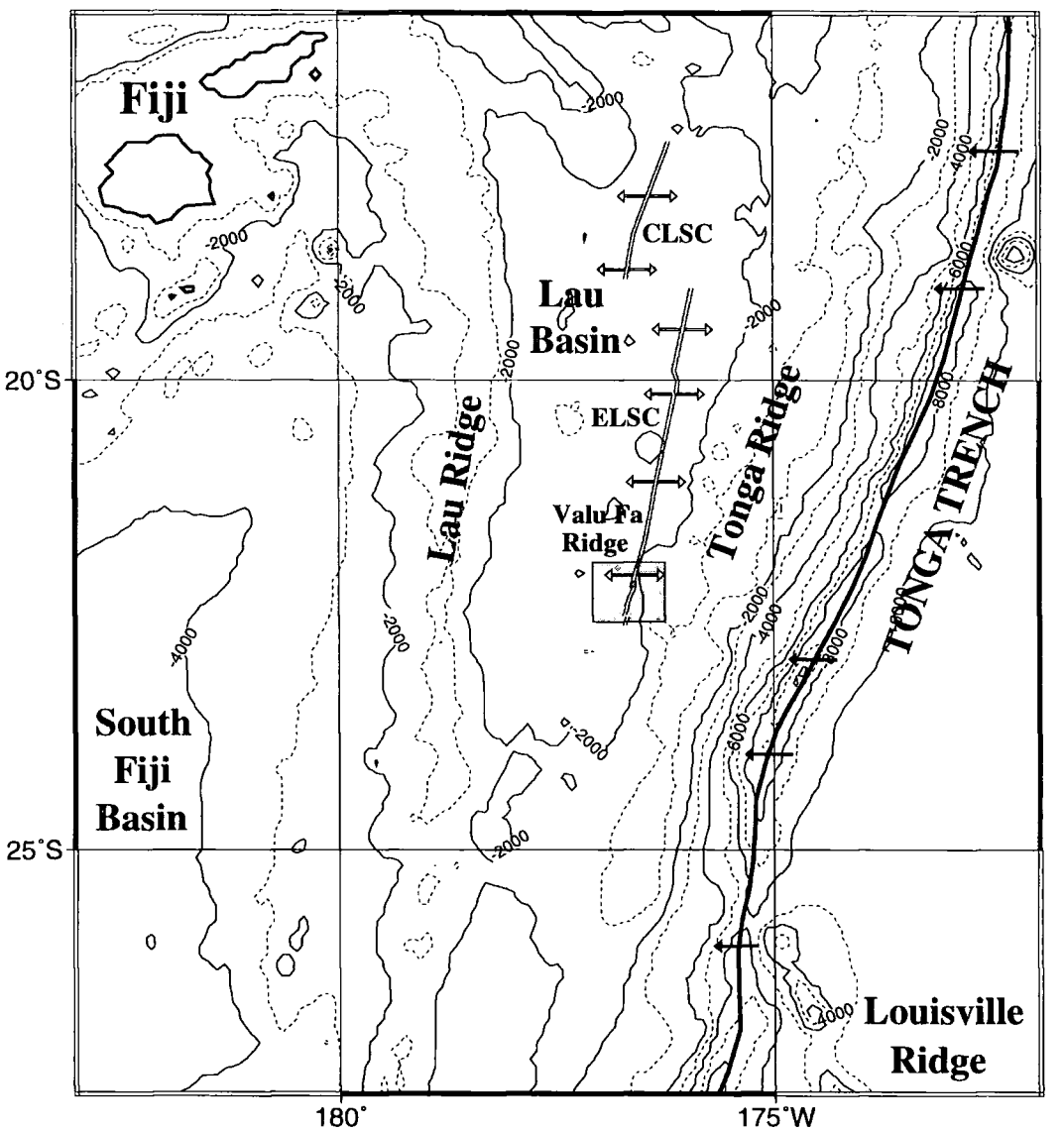

Figure 1.2: Location map of the Central Lau Spreading Centre (CLSC) and Eastern Lau Spreading Centre (ELSC) within the Lau Basin. The two spreading axes are delineated by parallel lines and divergent arrows, based on magnetic anomaly identification, GLORIA sidescan sonar and Sea Beam bathymetry (see text for details). Note the asymmetric position of the ELSC within the Lau Basin, extremely close to the active Tofua Arc (Tonga Ridge). The Valu Fa Ridge marks the southern extension of the ELSC and is also annotated. The main tectonic and morphological features are identified (cf. figure 1.1) and the location of EW9512 survey area is marked by the shaded box. Bathymetric contours are plotted at 1000 m (dashed line) and 2000 m (solid and annotated line) intervals.

1.2 The Valu Fa Ridge

Since the discovery of a large amplitude, sub-crustal reflector on reconnaissance multi-channel reflection profiles conducted by the US Geological Survey in 1982 (see figure 1.3), the Valu Fa Ridge has been the subject of several multidisciplinary cruises. The reflector, between 2 and 3 km wide and located at ~1.5 s two-way travel time (TWTT) below the seafloor, was also observed on further profiles obtained in 1984 and interpreted as the top of a crustal magma chamber (Morton and Sleep, 1985).

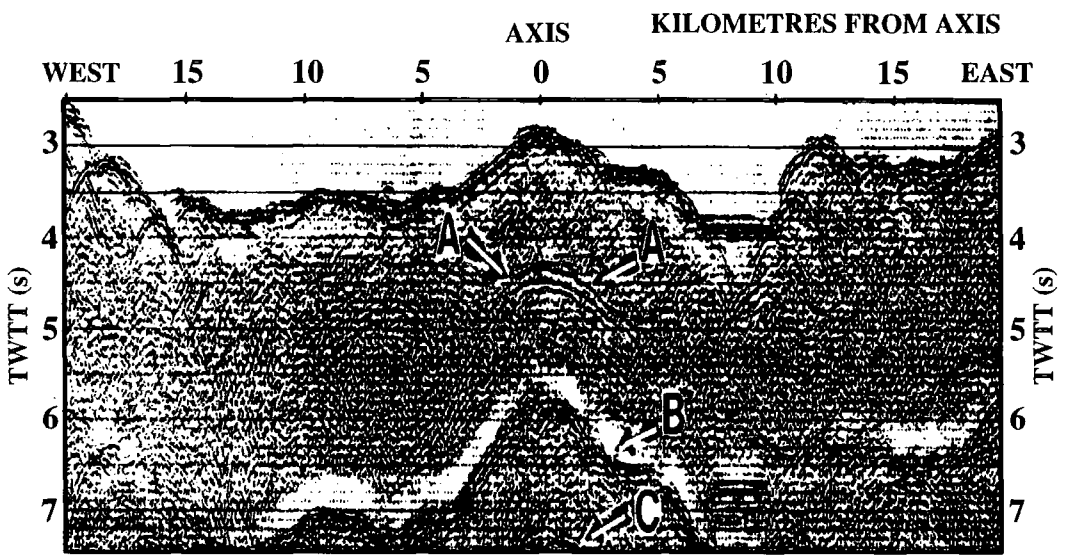

Figure 1.3: Seismic reflection profile *11*, cruise L5-82-LP (Morton and Sleep, 1985), showing the magma chamber reflector (A) and multiples (B of the seafloor and C of the magma chamber reflector). The vertical axis is displayed in seconds (two-way travel time) and the water depth to the top of the Valu Fa Ridge axis is less than 2000 m (after Vallier *et al.*, 1991).

The main conclusions drawn from previous studies at the Valu Fa Ridge are detailed below:

- Sea Beam swath bathymetry data, collected during three cruises by *R/V Sonne* in the 1980s, have shown that the VFR consists of three morphological segments (the Northern, Central and Southern segments) separated by short, non-transform offsets (von Stackleberg *et al.*, 1988; Sinha, 1995). More detailed investigations of ridge segmentation (see figure 1.4) are discussed in Collier and Sinha (1992a) and Wiedicke and Collier (1993), who compare this segmentation with the 'third-order' and 'fourth-order' segmentation observed at the East Pacific Rise (Macdonald *et al.*, 1988).

- Volcanic samples obtained by dredging consist of highly vesicular (30-50% porosity) fragments of flows (Jenner *et al.*, 1987; Davis *et al.*, 1990; Frenzel *et al.*, 1990). The petrologies of the rocks range from tholeiitic basalt to rhyolite but are predominantly highly evolved basaltic andesites and dacites at the VFR (Vallier *et al.*, 1991; Hilton *et al.*, 1993).

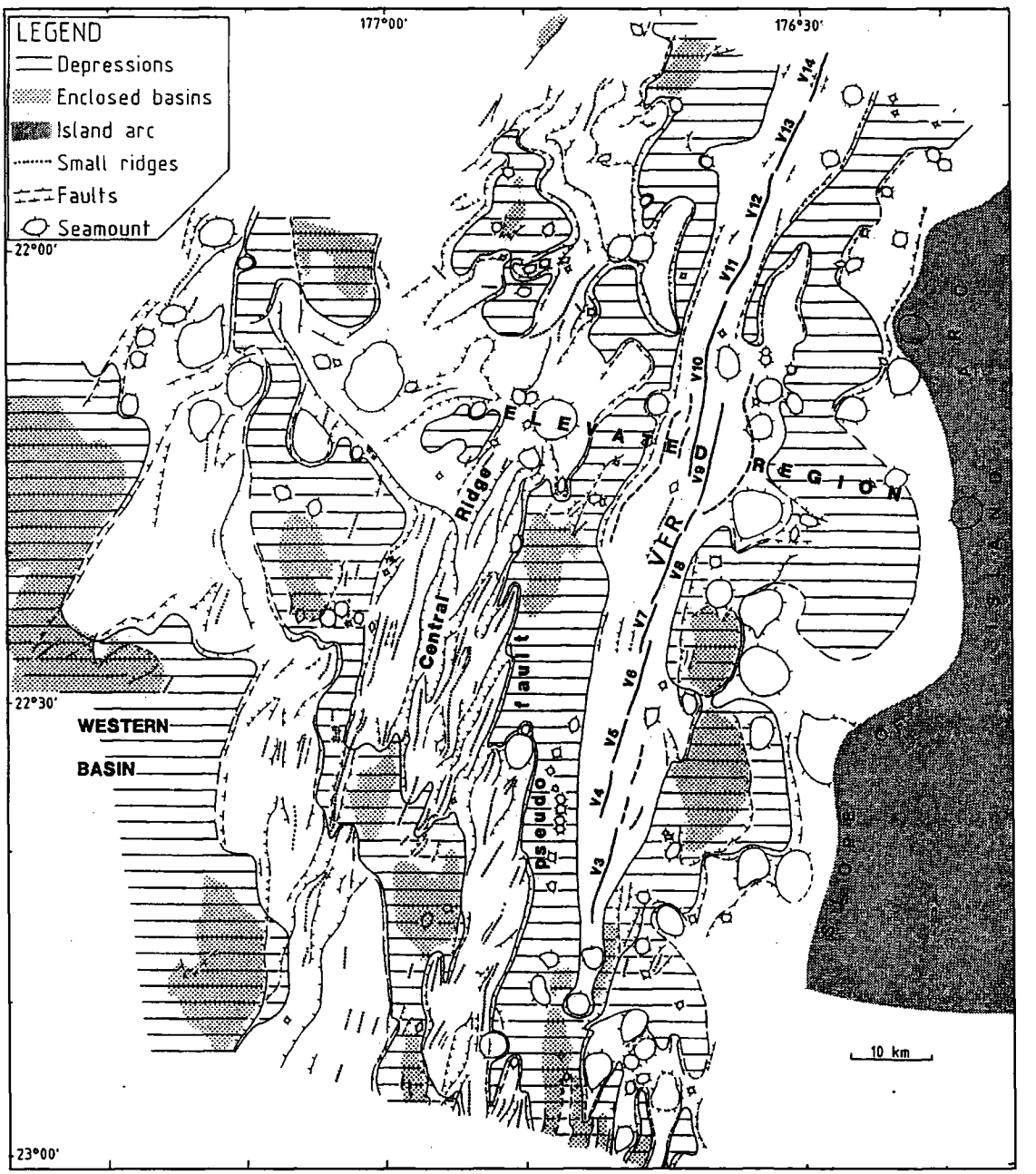

Figure 1.4: Structural map of the Southern Lau Basin (after Wiedicke and Collier, 1993). Large-scale features to the west of the VFR show a 170° trend (alternating regions of horizontal stripes and white background), while their fine-scale structural grain trends 20° (dotted lines, trend of small ridges). Note the fine-scale segmentation of the NVFR (segments V10-V14), CVFR (segments V7-V9) and SVFR (segments V3-V6) and that the southern tip of the SVFR terminates at 22° 45′ S. The seamounts located south of the ridge tip and localised graben formation may indicate an initial stage of southward ridge propagation. Note the position of the 'pseudofault' at 176° 50′ W, which intersects the southern tip and may mark the outer limit of crust generated at the Valu Fa Ridge.

- GLORIA sidescan imagery collected in 1988 detailed several areas of high backscatter, interpreted to be neovolcanic zones with little or no sediment cover providing evidence of recent activity at the VFR (Parson *et al.*, 1990).
- The Lau Basin was also the site of ODP Leg 135 - the main objective of which was to determine the evolution of the basin (Ocean Drilling Program Leg 135 Shipboard Scientific Party, 1992). Of particular interest here are the four sites located west of the ELSC (sites 836-839), together with the earlier DSDP site 203 (Deep Sea Drilling Project Leg XXI Shipboard Scientific Party, 1973) and site 840 located on the Tonga Ridge, east of the VFR.
- Hydrothermal activity has been widely observed over the whole of the Valu Fa Ridge system. Geological investigations with the submersible *Nautile* identified three major hydrothermal fields in the areas of the greatest differentiation of volcanic rocks (NAUTILAU Group, 1990; Fouquet *et al.*, 1991 and 1993). One field (the 'Vai Lili' field at 22° 13′ S), located near the overlapping spreading centre (OSC) of the Central Valu Fa Ridge (CVFR) and Northern Valu Fa Ridge (NVFR), is one of the most active hydrothermal fields known, discharging fluids up to ~350°C.
- Seismic tomography, waveform inversion and 3-D ray-tracing have been performed on seismological data collected in the SW Pacific, in an attempt to calculate the velocity structure of the subducting slab and overlying mantle wedge and determine the depth extent of the back-arc spreading centre (Bock *et al.*, 1991; Xu and Wiens, 1997; Zhao *et al.*, 1997). Slow anomalies are observed in the mantle beneath the Tonga Ridge and Lau back-arc basin. One of the main conclusions arising from this work is that although the two low velocity regions seem to be separated at shallow levels, where most of the magma is generated, there may be some interchange between the magma systems at depths greater than 100 km. This interchange with slab-derived volatiles may help to explain some of the unique features in the petrology of the back-arc magmas, including excess volatiles and large ion lithophile enrichment (Zhao *et al.*, 1997).
- In 1988, a dense grid of multi-channel seismic (MCS) profiles were collected over the CVFR and its overlap with the NVFR during *RRS Charles Darwin* cruise CD34/88 (Collier and Sinha, 1990 and 1992b). A magma chamber reflector (MCR) similar to the reflection observed by Morton and Sleep (1985) was identified on most profiles, including those over the OSC at 22° 12′ S

showing this area to be magmatically active (see figure 1.5). Gravity data collected during CD34/88 also suggest that the OSC is the site of enhanced magmatism, with either increased crustal thickness or a density reduction in the crust and/or mantle (Sinha, 1995). The significance of the seismic and gravity data collected during CD34/88 will be discussed in greater detail in the following chapters.

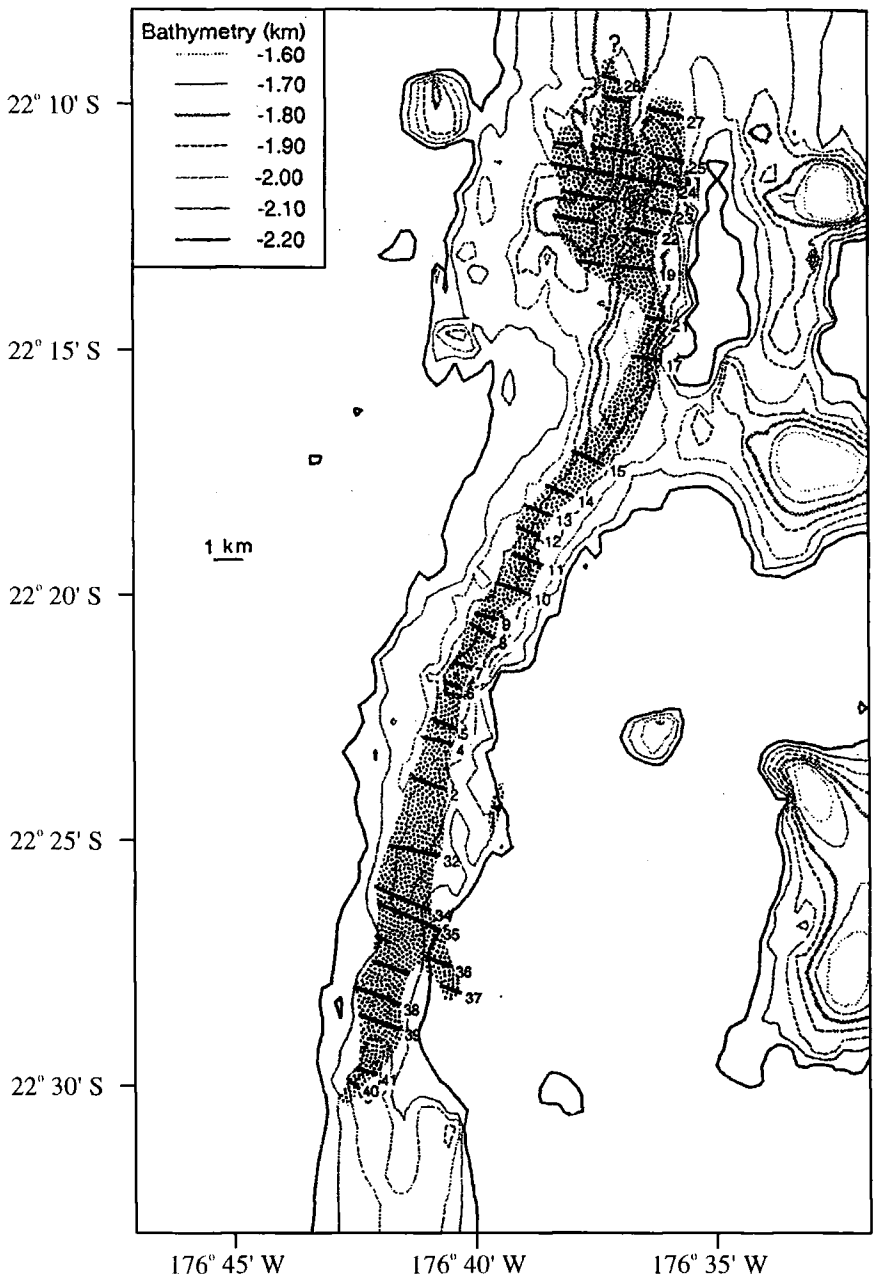

Figure 1.5: Map of the location of the magma chamber (shown by solid bars) identified from across-axis reflection profiles (as numbered) plotted on a basemap of ridge bathymetry (after Collier and Sinha, 1992b). The stippled shading shows the inferred geometry of the reflector between across-axis profiles. This map was constructed from the migrated images of the reflector and from forward modelling (ray-tracing) of the unmigrated data (see Collier and Sinha, 1992b for details). Forward modelling of the unmigrated data also enabled the determination of the magma chamber reflector width beneath the northern tip of the CVFR where the steep seafloor morphology results in unrealistic migrated images.

1.3 Oceanic crust

This section introduces the main components of 'normal' oceanic crust. The oceanic crust is surprisingly uniform and was initially modelled to consist of three main layers of constant seismic velocity and density (Hill, 1957; Raitt, 1963). The majority of the seabed is sedimented and this upper layer (layer 1) overlies an extrusive and intrusive 'volcanic' section (layer 2), which in turn overlies an 'oceanic' layer (layer 3).

Detailed geophysical investigations of the oceanic crust have since subdivided layer 2 and layer 3 and the original constant velocity layers with first-order boundaries (discrete velocity steps) have been replaced by layers of constant vertical velocity gradient separated by first or second-order (changes in the vertical velocity gradient) boundaries (Houtz and Ewing, 1976; Spudich and Orcutt, 1980; Bratt and Purdy, 1984; Solomon and Toomey, 1992). A summary of the layered structure of the oceanic crust is shown in table 1.1 and this layered scheme will be used throughout this dissertation. However, there is still considerable debate as to the exact position and nature of the layering scheme including the layer 2/3 boundary (e.g. Detrick *et al.*, 1994) and in particular the layer 2A/2B boundary (e.g. Christenson *et al.*, 1996; Hooft *et al.*, 1996).

<table>
<tr><th></th><th></th><th colspan="2">typical ophiolite</th><th colspan="3">oceanic crust</th></tr>
<tr><th></th><th></th><th>thickness (km)</th><th>velocity (km s^{-1})</th><th>thickness (km)</th><th>velocity (km s^{-1})</th><th>velocity gradient (s^{-1})</th></tr>
<tr><td>deep sea sediments</td><td>layer 1</td><td>~0.3</td><td>-</td><td>0.5</td><td>~2.0</td><td>-</td></tr>
<tr><td>highly fractured pillow lavas</td><td>layer 2A</td><td rowspan="2">0.3-0.7</td><td rowspan="2">3.3</td><td>0.5</td><td>2.5-4.5</td><td>5</td></tr>
<tr><td>less porous extrusives with interfingering dykes</td><td>layer 2B</td><td>0.5</td><td>4.5</td><td>0</td></tr>
<tr><td>sheeted dykes</td><td>layer 2C</td><td>1.0-1.5</td><td>4.1</td><td>1.0</td><td>4.5-6.5</td><td>1</td></tr>
<tr><td rowspan="2">gabbro</td><td>layer 3A</td><td rowspan="2">2.0-5.0</td><td rowspan="2">5.1</td><td>1.0</td><td>6.5-6.8</td><td rowspan="2">0.1</td></tr>
<tr><td>layer 3B</td><td>2.0</td><td>6.8-7.0</td></tr>
<tr><td>layered peridotite</td><td rowspan="2">layer 4</td><td rowspan="2"></td><td rowspan="2">2.5-4.2</td><td rowspan="2"></td><td rowspan="2">8.0+</td><td rowspan="2">0.03</td></tr>
<tr><td>peridotite/dunite unlayered</td></tr>
</table>

Table 1.1: The composition and physical properties of the oceanic crust based on ophiolite studies and seismic data (after Brown and Musset, 1981; Bratt and Purdy, 1984; Navin, 1996). The seismic Moho is located at the base of layer 3, whereas the petrological Moho is located between the layered and unlayered peridotite. Note the decrease in vertical velocity gradient with depth.

1.4 Crustal structure and magma chamber geometry at mid-ocean ridges

Mid-ocean ridges are now widely recognised as the sites of crustal accretion and fit neatly into theories of plate tectonics and seafloor spreading (Vine, 1966; Cann, 1974; East Pacific Rise Study Group, 1981; Macdonald, 1982; Sempere and Macdonald, 1987; Fowler, 1990; Solomon and Toomey, 1992). However, the general processes of crustal accretion are not fully understood and present theories are based largely on evidence from the fast spreading East Pacific Rise. Primary evidence for the hypothesis that the crustal structure and crustal accretionary processes may vary with spreading rate can be found in their differing seafloor morphologies (see figure 1.6). Thus, data from mid-ocean ridges with a broad range of spreading rates must be incorporated into present models to improve our understanding of the processes of crustal accretion.

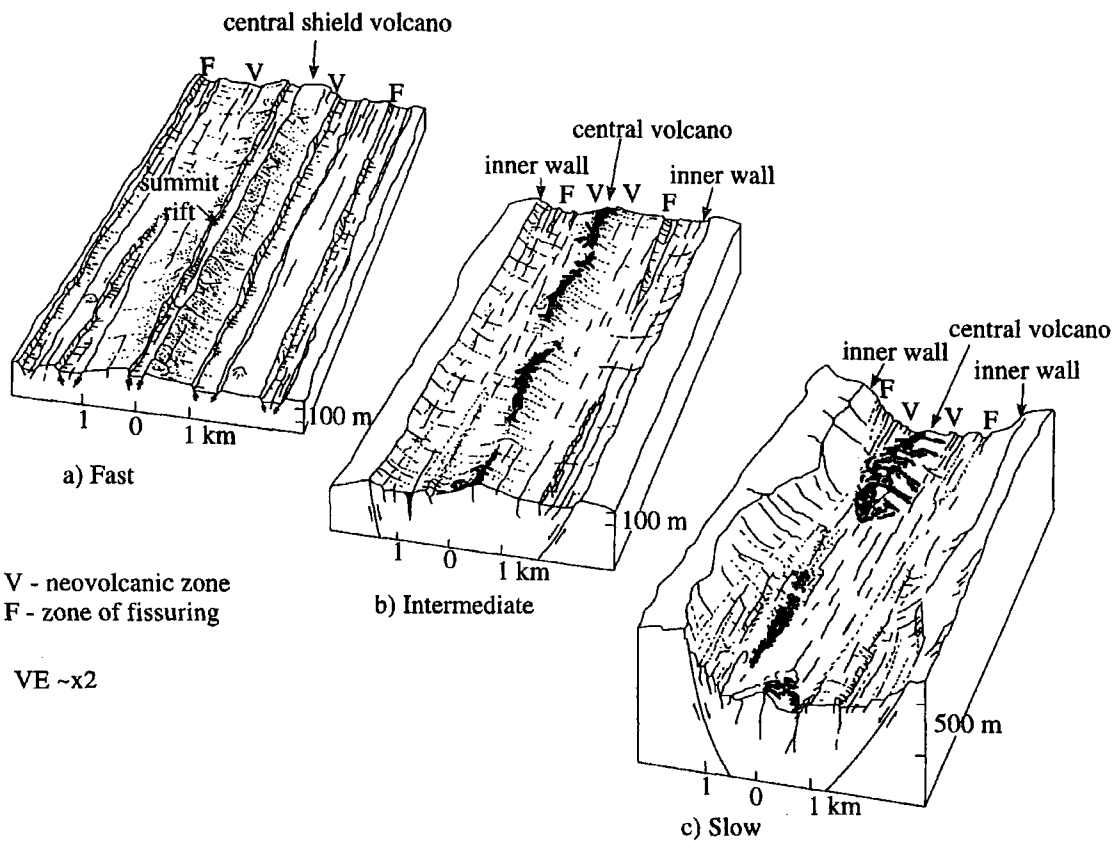

Figure 1.6: Schematic illustrations of the axial morphology at fast, intermediate and slow spreading mid-ocean ridges (after Macdonald, 1982; Navin, 1996). The central volcano is continuous at fast rates (a), moderately continuous with *en echelon* offsets at intermediate rates (b) and highly discontinuous at slow rates (c). Note the different vertical scales.

The presence of a sub-crustal magma chamber is a critical component of models of the crustal structure at mid-ocean ridges (Cann, 1974; Sinton and Detrick, 1992). The petrology, structure and stratigraphy of the oceanic crust depend largely on the width, shape and depth of the magma chamber, determined primarily from geophysical observations. Comparisons with ancient mid-ocean ridge analogues (i.e. ophiolite studies) have revealed many similarities, but there is still considerable conflict over the actual size of the magma chamber. Magma chamber models based on ophiolite studies, thermal models of the processes of crustal accretion and recent geophysical observations are shown in figure 1.7.

The traditional model of a large, essentially molten reservoir (see figure 1.7a) in which melt accumulates and undergoes magmatic differentiation prior to its eruption or emplacement in the crust provides a relatively simple explanation for the stratigraphy of oceanic crust inferred from seismic investigations and ophiolite studies (Sinton and Detrick, 1992). The lavas and dykes of layer 2 can be produced directly from eruptions from the chamber and the isotropic and layered gabbros of layer 3 can be formed from cooling of the chamber at its sides and base. The concept of a large, essentially molten reservoir can also explain the formation of the cumulate layer at the base of layer 3 by crystal settling. However, geophysical observations have revealed evidence of small, sill-like melt bodies, overlying sub-circular low velocity zones (LVZ) of hot rock or very low percentage partial melt within layer 3 (base of the LVZ within layer 3, not at the Moho - Toomey *et al.*, 1990 and 1994) and evidence for complex 3-D melt migration (Dunn and Toomey, 1997). A summary of the geophysical studies of crustal structure and magma chamber geometry at mid-ocean ridges of differing spreading rates can be found in the following sections.

(a) Geological models

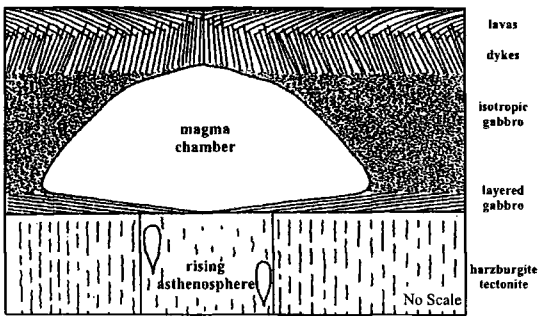

Cann (1974)

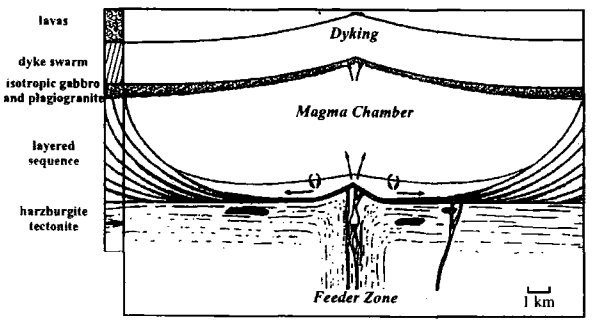

Smewing (1981)

(b) Thermal models

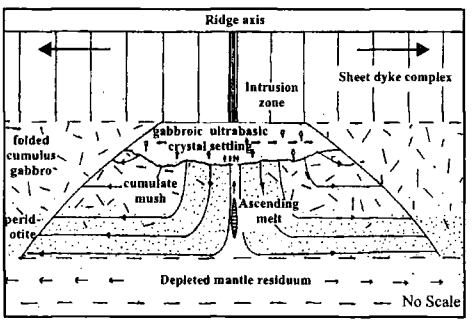

Sleep (1975)

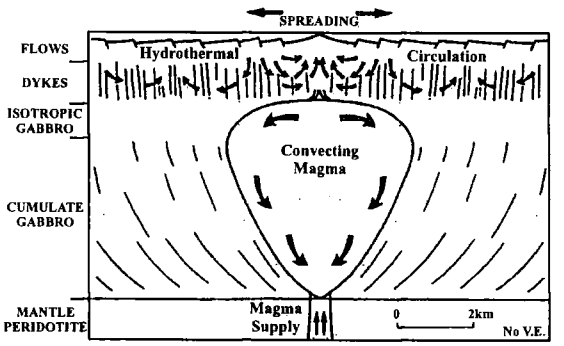

Wilson *et al.* (1988)

(c) Integrated geophysical models

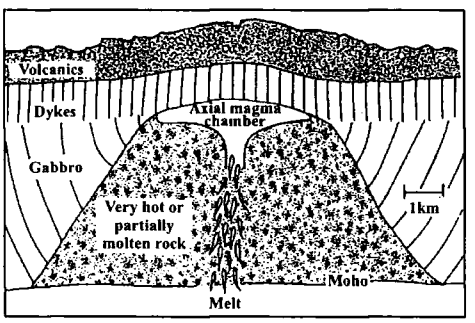

Macdonald (1989)

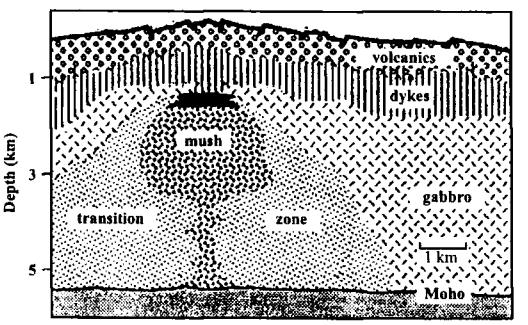

Sinton and Detrick (1992)

Figure 1.7: Across-axis magma chamber models.
(a) Geological models based on theoretical models of the processes taking place at mid-ocean ridges (after Cann, 1974 - 'infinite onion' model) and the interpretation of gabbro layering and genesis of the Oman Ophiolite (after Smewing, 1981; Phipps Morgan and Chen, 1993). Note the relatively large width of the proposed magma chamber.
(b) Thermal models based on energy conservation and conductive cooling (Sleep, 1975) and additional convective cooling (Wilson *et al.*, 1988). Note the difference in the magma chamber geometry with the addition of convective cooling.
(c) Integrated geophysical models combining recent seismic observations of the geometry of the melt and underlying low velocity zone at the East Pacific Rise (Detrick *et al.*, 1987; Vera *et al.*, 1990) with previous geological and thermal models.

1.4.1 Fast spreading ridges

Fast spreading ridges, defined as those having a full spreading rate of greater than 90 mm yr^{-1}, are characterised by a broad, low relief axial high and a small axial summit caldera (ASC) (see figure 1.6; Macdonald, 1982; Fornari *et al.*, 1998) and are typified by the East Pacific Rise (see figure 1.8 for EPR location).

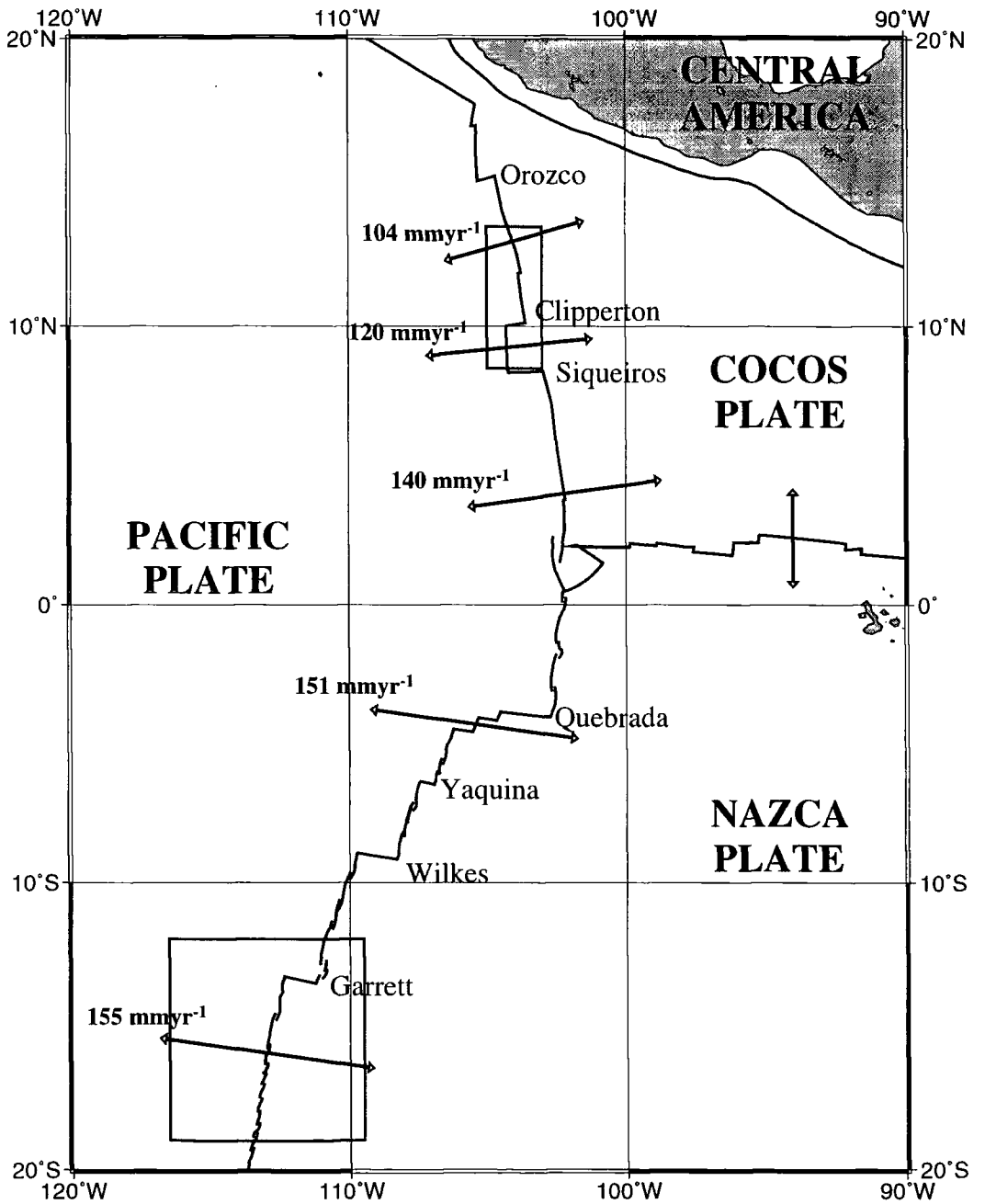

Figure 1.8: The East Pacific Rise: a fast spreading mid-ocean ridge.
The EPR runs approximately north-south and separates the Pacific Plate from the Cocos and Nazca Plates. Major transform faults and fracture zones are annotated and mid-ocean ridge full spreading rates are shown (after Sempere and Macdonald, 1987). Note the general increase in spreading rate to the south. The two main sites of geophysical study (9°-13° N and 12°-19° S) are highlighted. The Galapagos ridge, separating the Cocos and Nazca Plates, meets the EPR at a complex triple junction (2° N, 102° W) and splits the EPR into the Northern East Pacific Rise (NEPR) and Southern East Pacific Rise (SEPR).

The East Pacific Rise has been the target of several multidisciplinary geophysical studies, in particular sites near 9° N, 13° N and 17° S (e.g. Detrick *et al.*, 1987; Vera *et al.*, 1990; Christenson *et al.*, 1994; The MELT Seismic Team, 1998) and the crustal structure observed at the EPR is summarised below.

- Studies of the upper crust at the EPR have revealed that layer 2A has a laterally varying thickness across the ridge axis and consists of highly attenuating (i.e. low Q ~10-20), high porosity (>20 %), low velocity (~2.5 km s^{-1}) extrusive material (Wilkens *et al.*, 1991; Moos and Marion, 1994; Vera and Diebold, 1994; Wilcock *et al.*, 1995; Goldberg and Sun, 1997). The layer 2A/2B boundary is characterised by a sharp increase in velocity from 2.5 to 5.0 km s^{-1} in ~250 m corresponding to the transition zone between pillow lavas/sheet flows and sheeted dykes. This interface can be imaged as a strong retrograde reflection-like arrival on MCS data (Vera *et al.*, 1990; Vera and Diebold, 1994). Detailed mapping of this reflector has shown that layer 2A is emplaced as a thin surficial layer (thickness ~100 m) within the ASC and doubles in thickness within 2-4 km of the ridge crest by off-axis conduits and sheet flows overflowing the ASC (Christenson *et al.*, 1992, 1994 and 1996; Harding *et al.*, 1993; Carbotte and Macdonald, 1994; Toomey *et al.*, 1994; Vera and Diebold, 1994; Kappus *et al.*, 1995; Hooft *et al.*, 1996 and 1997; Carbotte *et al.*, 1997). The final thickness of layer 2A is thus attained before large-scale tectonic faulting occurs.
- Layer 2, with a P-wave velocity of 5.0-6.0 km s^{-1}, has essentially constant thickness (~1 km) beneath the transitional layer 2A/2B boundary and is thus fully emplaced within the neovolcanic zone (Vera *et al.*, 1990; Solomon and Toomey, 1992; Harding *et al.*, 1993).
- The layer 2/3 boundary off-axis is marked by a decrease in the vertical velocity gradient (see table 1.1; Spudich and Orcutt, 1980; Bratt and Purdy, 1984) and probably marks the transition from sheeted dykes to gabbros (cf. Detrick *et al.*, 1994).
- Crustal thicknesses at the EPR are ~6-7 km (White *et al.*, 1992). Moho reflections have been observed as horizontal events on MCS data (Herron *et al.*, 1980; Detrick *et al.*, 1987) and P_mP arrivals on expanding spread profile (ESP) data (Harding *et al.*, 1989; Vera *et al.*, 1990) to within 2-3 km of the ridge axis, thus layer 3 and a distinct Moho are also formed within the axial region.

Evidence for the existence of magma chambers at the EPR comes largely from MCS and ESP data. A large amplitude, reversed polarity, sub-horizontal reflector (MCR) imaged beneath the axial region on MCS profiles marks the roof of a partially to fully molten layer. Refraction data suggest that a wider region of slightly reduced velocities (LVZ) exists beneath this molten layer corresponding to a region of much lower percentage melt fraction. A summary of the results to date are shown in table 1.2.

	Location	MCR	LVZ	Geometry
Orcutt *et al.*, 1975 (refraction profile)	9°-10° N		X	Unreversed refraction profile LVZ 'channel' 4.8 km s^{-1} 2 km depth, 1.4 km thick
Herron *et al.*, 1980 (MCS profiles)	9°-10° N	X		MCR 2-8 km wide, 1.5-2.0 km depth Weak Moho reflections beneath axis
Detrick *et al.*, 1987 (MCS profiles)	9° N 13° N	X	X	MCR 4-6 km wide, 1.2-2.4 km depth Reversed polarity, good along-strike continuity LVZ narrow (4-6 km) - Moho observed off-axis
Harding *et al.*, 1989 (ESP data)	13° N	X	X	Reduced P-wave velocities -0.5 to -1.0 km s^{-1} Bell-shaped LVZ - width >6 km
Kent *et al.*, 1990 (MCS profiles)	9° 30′ N	X		Forward modelling of Detrick *et al.* (1987) MCS MCR width 0.8-1.2 km No basal reflection - gradient or very thin body
Toomey *et al.*, 1990 (3-D Tomography)	9° 30′ N		X	Axial low velocity anomaly Sub-circular LVZ 4-6 km wide Base of LVZ above the Moho
Vera *et al.*, 1990 (ESP data)	9° N	X	X	LVZ 1.6 km depth, 3 km s^{-1} - molten material ? Bell-shaped LVZ - observed on all profiles ? Off-axis smoother transition - no 'pure' melt
Caress *et al.*, 1992 (Tomography)	12° 50′ N		X	LVZ 7 km wide, extends down to the Moho Anomaly -0.4 to -0.7 km s^{-1} - 3 % partial melt Slight asymmetry to the east
Wilcock *et al.*, 1992 (P-wave attenuation)	9° 30′ N		X	High attenuation depth 2 km to base of crust Need only small % of partial melt
Detrick *et al.*, 1993 (MCS & ESP data)	14° 15′ S 17° 20′ S	X	X	Ultra-fast spreading (>150 mm yr^{-1}) MCR ~1 km wide - spreading rate independent MCR depth ~1.3 km - underlying LVZ
Harding *et al.*, 1993 (MCS profiles)	9° N	X		Reprocessed Detrick *et al.* (1987) MCS MCR constant delay behind layer 2A reflection
Kent *et al.*, 1994 (MCS profiles)	14° 15′ S	X	X	Narrow (1 km) melt lens, along-strike continuity Moho observed within 1 km of MCR edge Therefore narrow LVZ
Collier & Singh, 1997 (waveform inversion)	9° 40′ N	X		No basal reflector ? 30 m thick molten sill (2.6 km s^{-1}) 50 m thick gradient zone (2.6-3.5 km s^{-1})

Table 1.2: Summary of the observations of magma chamber geometry at the East Pacific Rise. Note the bias of results towards the area between 9° and 10° N. Several of the more recent studies, with the exception of Collier and Singh (1997), have concentrated more on the systematic occurrence of LVZs and melt bodies at the EPR rather than trying to further constrain their geometries (see text for details).

Geophysical investigations have constrained the geometry of the axial magma chamber at both the NEPR and SEPR (see table 1.2). Improved seismic techniques have imaged the region of high percentage melt as a thin (10-100 m), narrow (1-2 km) lens. The geometry of the underlying LVZ is poorly constrained and inconsistent across datasets. Most studies identify a 4-6 km wide LVZ with velocity anomalies between -0.5 and -1.0 km s^{-1} corresponding to a region of low percentage melt which feeds the overlying melt lens. However, discrepancies in the shape of the LVZ (bell-shaped vs. sub-circular) and the depth extent of the LVZ (observed down to the Moho or not) still exist (cf. figure 1.7c).

Recent studies, concentrating on the systematic occurrence of magma chambers and processes of crustal accretion at the EPR, have suggested that the width of the melt lens is invariant with spreading rate (Kent *et al.*, 1994), although the depth to this body seems to decrease with increasing spreading rate (Purdy *et al.*, 1992; Kent *et al.*, 1994). Other studies have also suggested that anomalous axial morphology (e.g. a shallower and broader ridge crest) is perhaps an indication of an enhanced magmatic budget (Mutter *et al.*, 1995; Hooft *et al.*, 1997). Melt upwelling and migration, once thought to be 2-D at fast spreading rates, are now modelled as 3-D diapiric flow within the upper mantle, but with a continuous distribution of melt near the crust/mantle interface (Wang and Cochran, 1993; Dunn and Toomey, 1997; The MELT Seismic Team, 1998).

Although the breadth of knowledge concerning the processes of crustal accretion and geometry of magma chambers at the EPR is large, it is important to realise that these observations are typical of just a few selected sections of a single mid-ocean ridge. To formulate a general hypothesis for the processes of crustal accretion at mid-ocean ridges, data from other ridges with differing spreading rates and seabed morphology must be incorporated.

1.4.2 Slow spreading ridges

Slow spreading ridges, defined as those having a full spreading rate of less than 50 mm yr^{-1}, are typified by the Mid-Atlantic Ridge (see figure 1.9 for MAR location) and consist of a wide (5-15 km) median valley bounded by a series of large normal faults (see figure 1.6). Within the 1-3 km deep median valley a discontinuous chain of axial volcanic ridges (AVRs) are interpreted to be the sites of local extrusion (Macdonald, 1982; Sempere *et al.*, 1993).

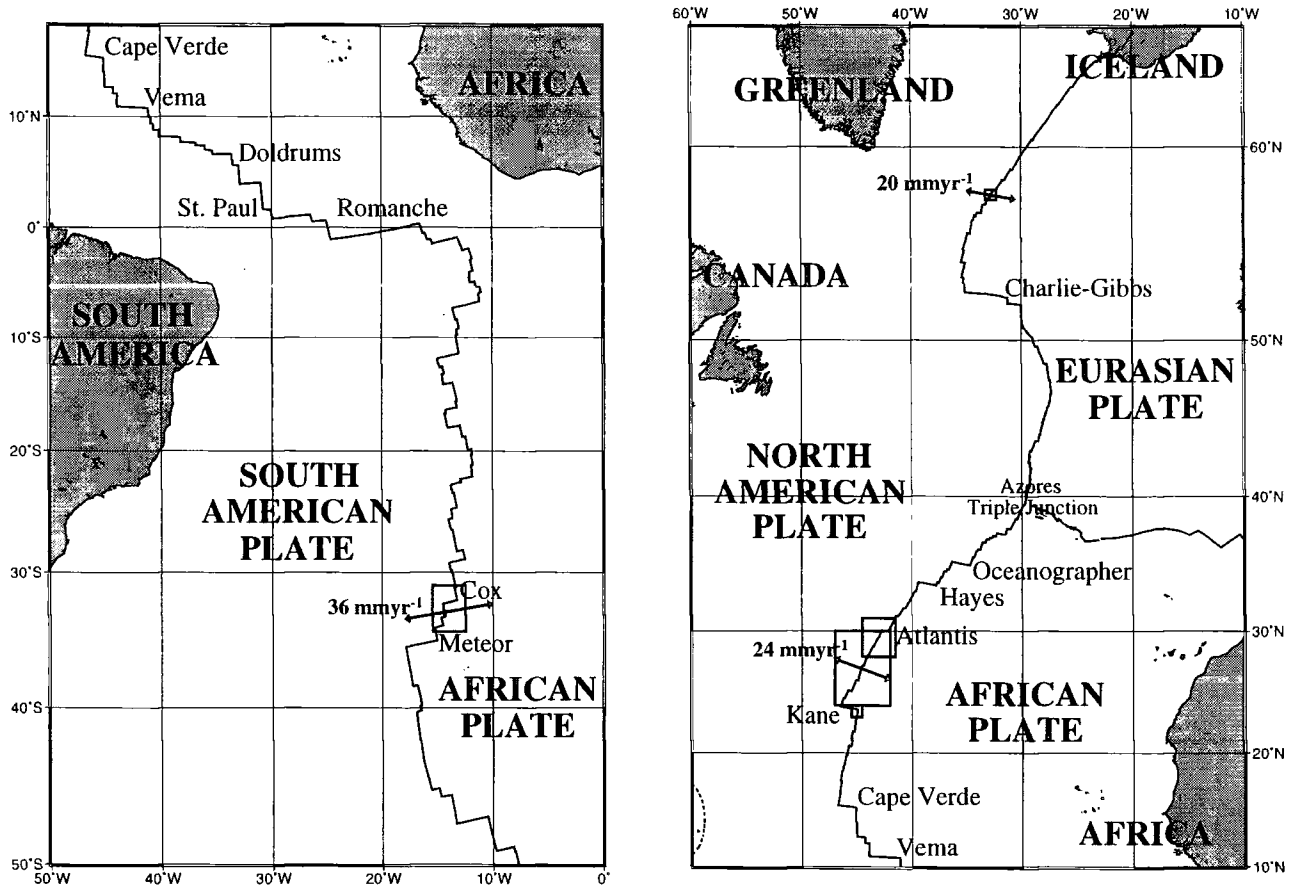

Figure 1.9: The Mid-Atlantic Ridge: a slow spreading mid-ocean ridge.
The MAR runs approximately north-south and separates the North Atlantic Plate from the Eurasian and African Plates. Major transform faults and fracture zones are annotated and mid-ocean ridge full spreading rates are shown (after Kuo and Forsyth, 1988; Sempere *et al.*, 1993; Navin, 1996). Note the general increase in spreading rate to the south, as observed on the EPR. Several sites of geophysical study (31°-35° S, 24°-30° N and 56°-57° N) are highlighted. The African and Eurasian Plates are split by Azores-Gibraltar Fracture Zone, which meets the MAR at the Azores Triple Junction (40° N, 30° W). Note that Iceland is located on the MAR and thus provides a unique opportunity to observe the processes of crustal accretion at the surface.

At slow spreading ridges the axial crust is significantly cooler than along faster spreading ridges (Sleep, 1975), which leads to a stronger, thicker lithosphere and a large proportion of plate divergence (>20%) is actually accommodated by normal faulting and lithospheric stretching (Solomon and Toomey, 1992). As previously mentioned, the oceanic crust is surprisingly uniform with similar crustal thicknesses (~6.5-7.5 km at the MAR - White *et al.*, 1992), independent of spreading rate. Despite this uniformity of crust >1 Ma, there are subtle differences in the processes of crustal accretion at slow spreading rates compared with fast spreading rates (see section 1.4.1) and the crustal structure is described below.

- Recent studies suggest that layer 2A (predominantly pillow lavas) thins off-axis (Smallwood *et al.*, 1995; Navin, 1996), which implies that this layer is completely emplaced within the axial region and is thinned by faulting as it moves off-axis (cf. EPR - off-axis thickening). However, the debate concerning the nature of the seismic layer 2A/2B boundary (lithology vs. porosity) is seemingly unresolved at slow spreading ridges and the observed thinning of layer 2A may simply be the result of a loss of porosity with age.
- Navin (1996) identified a low velocity anomaly within layer 2B within the axial region at the Reykjanes Ridge (57° 45′ N) which was interpreted to be the result of fracturing of the upper crust. Higher crustal temperatures would explain the absence of this zone at faster spreading ridges.
- Mantle Bouguer anomalies calculated at the MAR show considerable along-axis variation in crustal thickness and/or crustal and mantle densities. 'Bull's-eye' gravity lows suggest that magmatic accretion is a 3-D process, focused near the segment centre (Kuo and Forsyth, 1988; Lin *et al.*, 1990; Sempere *et al.*, 1993; Ballu *et al.*, 1998).

Detailed refraction studies preclude the existence of large, steady-state magma chambers at many locations along the MAR. However, Sinton and Detrick (1992) suggest that smaller localised crustal magma bodies may be present, at least intermittently (see figure 1.10).

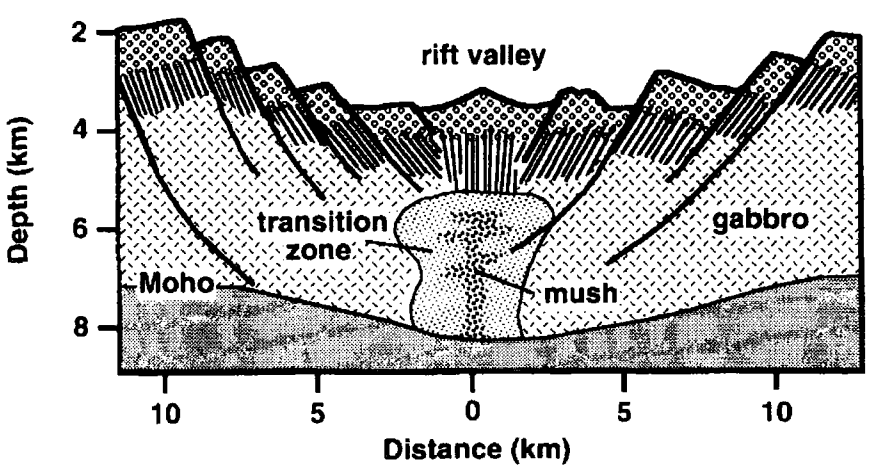

Figure 1.10: Interpretative model of a magma chamber beneath a slow spreading ridge (low magma supply) like the Mid-Atlantic Ridge (after Sinton and Detrick, 1992). Such ridges are unlikely to be underlain by an eruptable magma lens in any steady-state sense. A dyke-like mush zone is envisaged beneath the rift valley forming small sill-like intrusive bodies which progressively crystallise to form oceanic crust. Eruptions will be closely coupled in time to injection events of new magma from the mantle.

Low velocity zones, observed on several refraction profiles over the MAR (e.g. 23° N - Purdy and Detrick, 1986) do not necessarily provide evidence of the existence of magma chambers and MCS profiles had shown no evidence for a MCR (Detrick *et al.*, 1990). However, subsequent reprocessing of the Detrick *et al.* (1990) dataset by Calvert (1995) suggests that a low amplitude reflector observed at a depth of 1.2 km (not observed in the original processing due to large amplitude coherent noise - diffractions possessing high stacking velocities) may correspond to the roof of a small magma chamber.

The most conclusive proof to date of a magma chamber at any slow spreading ridge is that of Sinha *et al.* (1998) following a detailed geophysical study of the Reykjanes Ridge at 57° 45′ N (see also Navin, 1996; Sinha *et al.*, 1997; Navin *et al.*, 1998). Ray-trace modelling of along-axis and across-axis wide-angle seismic data located an axial LVZ in layer 3 beneath the AVR, which extends to a depth of 8 km (1 km above the Moho) and has a width of ~8 km. This LVZ, interpreted to be the main body of the magma chamber containing a low percentage melt, was in turn modelled to be overlain by an axial low velocity block at a depth of 2.5 km beneath the seafloor, with a nominal thickness of 100 m and a P-wave velocity of 3.0 km s^{-1}. Forward modelling of coincident CSEM (Controlled Source ElectroMagnetic) data suggests that a wide low resistivity layer (~1 Ωm) exists within layer 3 (MacGregor *et al.*, 1998), which compares favourably with the LVZ described by Navin *et al.* (1998).

These recent observations of EPR-like MCRs and LVZs suggest that the crustal structure and processes of crustal accretion at slow spreading ridges are broadly similar to those at fast spreading ridges. However, differences in the temporal stability of magma chambers, emplacement of the upper crust and the process of melt migration still exist.

1.4.3 Intermediate spreading ridges

Intermediate spreading ridges, defined as those having a full spreading rate of between 50 mm yr^{-1} and 90 mm yr^{-1}, are characterised by a moderately continuous axial high of volcanic construction with *en echelon* offsets (Macdonald, 1982) and are typified by the Valu Fa and Juan de Fuca Ridges (see figures 1.2 and 1.11 for the locations of the VFR and JDFR respectively). The crustal structure of intermediate spreading ridges may provide the key to the transition from crustal accretionary processes observed at slow spreading ridges to those at fast spreading ridges.

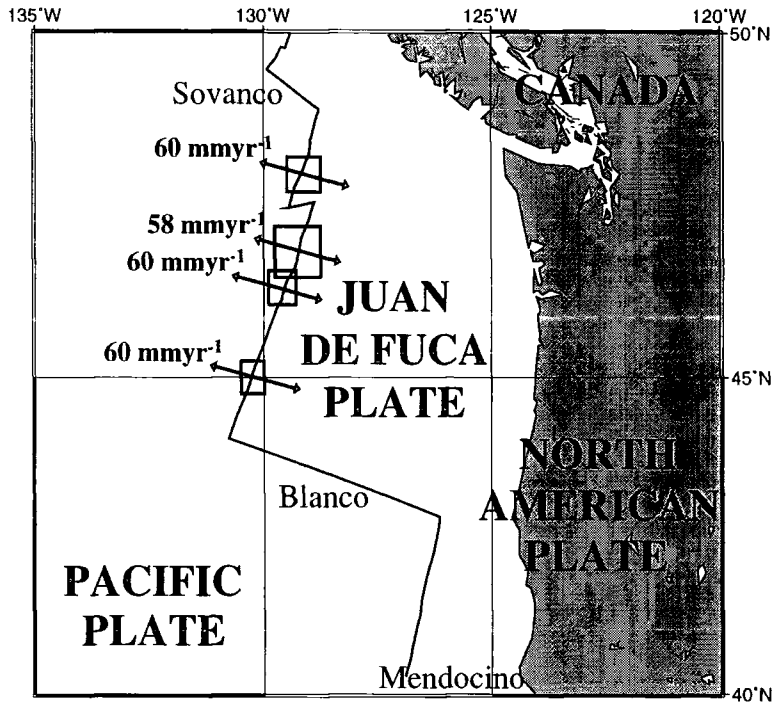

Figure 1.11: The Juan de Fuca Ridge: an intermediate spreading mid-ocean ridge.
The JDFR runs approximately north-northeast – south-southwest and is located between the Sovanco and Blanco transforms (after Davis and Currie, 1993). The JDFR system, including the Gorda Ridge to the south and Explorer Ridge to the north, separates the Pacific Plate from the Juan de Fuca Plate. A result of the fragmentation of the ancient Farallon Plate, the Juan de Fuca Plate is separated from the North American Plate by the Cascadia Subduction Zone (not shown here), which approximately follows the North American coastline. Four sites of geophysical study are highlighted. Major transform faults are annotated and mid-ocean ridge full spreading rates are shown.

The crustal structure of the JDFR is well documented and shows similar features to the crust modelled at fast spreading ridges (see section 1.4.1). However, like the slow spreading MAR the main difference seems to be the emplacement of the upper crust, which attains its full thickness within the axial region (cf. EPR). The crustal structure is summarised below.

- Layer 2A is modelled with considerable lateral thickness variation (0.2-0.6 km) and low P-wave velocities (<3.0 km s^{-1}), indicating a layer of high porosity extrusives (Rohr *et al.*, 1988; Cudrak and Clowes, 1993; McDonald *et al.*, 1994). The layer 2A/2B boundary corresponds to the transition from volcanic extrusives to sheeted dykes and is identified by a sudden increase in P-wave velocity to ~5.0 km s^{-1} (velocity gradient of 10 s^{-1}).
- The remainder of the crust is similar to that observed at fast spreading ridges (see section 1.4.1), however a small positive velocity anomaly is modelled within the

axial region in the upper crust beneath layer 2A (Cudrak and Clowes, 1993). Toomey *et al.* (1990) suggested that a similar positive anomaly at the EPR was the result of a decrease in depth to the sheeted dyke complex within the axial region. However, substantial evidence suggests that there is no decrease in depth of the sheeted dykes at the JDFR and the positive anomaly is probably the result of a lack of pervasive cracking of the fresher, axial material (Cudrak and Clowes, 1993).

- There is considerable variation in crustal thicknesses at the JDFR (Hasselgren and Clowes, 1995) and thicknesses (~6-8 km) are generally greater than at the EPR, mainly a result of a thicker upper crust (e.g. Sohn *et al.*, 1997). This hypothesis is further substantiated by the observations of a thicker layer 2 in DSDP Hole 504B and at the intermediate spreading Costa Rica Rift (Buck *et al.*, 1997) and VFR (Collier, 1990; Collier and Sinha, 1992b).

Detailed geophysical studies suggest that magma chambers with similar features to those observed at the EPR may exist beneath intermediate spreading ridges, but few have actually been found. A summary of some of the results to date is shown below.

	Location	MCR	LVZ	Geometry
Morton and Sleep, 1985 (MCS profiles)	Valu Fa Ridge	X		Large amplitude, axial reflector - 2-3 km wide Top of magma chamber - depth of ~3 km Spreading rate ~60 mm yr^{-1}
Morton *et al.*, 1987 (MCS profiles)	45° N JDFR	X		Weak axial reflector - 1-2 km wide Top of magma chamber - 2.3-2.5 km depth MCR shallowest where ridge crest is shallowest
Rohr *et al.*, 1988 (MCS profiles)	48° N JDFR	X	X	Axial reflector - 1 km wide, 2.5 km depth Magma chamber? - not erupted recently No evidence for LVZ beneath reflector
Collier and Sinha, 1992b (MCS profiles)	Valu Fa Ridge	X		MCR depth 3.2 ± 0.2 km, 0.6-2.5 km wide Large % melt - 2.7 km s^{-1} if a planar interface MCR observed beneath OSC
Christeson *et al.*, 1993 (refraction survey)	47° N JDFR		X	No evidence for LVZ Crust comparable with 40-70 ka EPR crust N. Symmetrical Segment - presently inactive
Cudrak and Clowes, 1993 (refraction survey)	48° N JDFR		X	Minor LVZ (-0.1 to -0.2 km s^{-1}) - hot rock? Depth >2 km Endeavour Ridge - diminished magma supply
Mutter *et al.*, 1995 (MCS profiles)	Costa Rica Rift	X		Large amplitude axial reflector Depth of 2.7 ± 0.25 km Spreading rate of 67 mm yr^{-1}
Livermore *et al.*, 1997 (MCS profiles)	E. Scotia Ridge	X		Axial reflector - top of magma chamber Depth of ~3 km, <1 km wide Spreading rate of 65-70 mm yr^{-1}

Table 1.3: Summary of the observations of possible magma chambers at intermediate spreading ridges. Note that although MCRs have been imaged at several ridges, constraints on the shape and size of the underlying LVZ are scarce.

Large amplitude, sub-crustal reflectors (MCRs) have revealed the presence of axial magma chambers at several intermediate spreading ridges (see table 1.3) and the observation of a narrow (<2 km wide) melt lens compares favourably with those observed at the fast spreading EPR. The upper crust is generally thicker at intermediate spreading ridges and the depth to the melt lens (top of the magma chamber) is modelled between 2 and 3 km.

The main gap in our knowledge of magma chambers at intermediate spreading ridges is concerned with the underlying LVZ, which corresponds to the region of low percentage melt feeding the melt lens. Its existence has been proposed at the JDFR (Endeavour Ridge), but the small velocity anomalies suggest that this part of the ridge system has a diminished magma supply at this present time. Studies on other parts of the JDFR system have failed to image a LVZ, even in the presence of a supposed MCR (Rohr *et al.*, 1988). Modelling of sonobuoy data collected along the VFR and on several axis-parallel seismic lines suggests that a LVZ exists beneath the axial region (Collier, 1990; Collier and Sinha, 1992b) although there is little constraint on the shape and size of this region (width <8 km - Collier, 1990).

A quantitative study of the geometry of a magma chamber at an intermediate spreading ridge must be carried out and the shape and size of the LVZ must be determined. Measurements such as the depth extent of the LVZ (down to the Moho or not), variations in the width of the LVZ and the along-axis continuity of both the melt lens and underlying LVZ will provide comparisons with the EPR and help determine the processes of crustal accretion at intermediate spreading rates.

1.5 Aim of this study

The aim of this study is to compare the processes of crustal accretion at fast, slow and intermediate spreading ridges, by investigating the detailed crustal structure and magma chamber geometry of a magmatically active intermediate spreading ridge, the Valu Fa Ridge (see Chapter 2 for experimental configuration). The following aspects of the crustal structure will be addressed.

- The velocity and density structure of the Valu Fa Ridge will be determined down to upper mantle depths and compared with features observed elsewhere on the mid-ocean ridge system.

- The influence of the island arc (Tofua arc) and back-arc environment on the overall crustal structure will be considered.
- The transition from pre-rift crust (both island arc and back-arc crust) to post-rift VFR-generated material, identified on the seafloor as a 'pseudofault' (Wiedicke and Collier, 1993) will be investigated.
- The existence of a magma chamber beneath the CVFR, and its overlap with the NVFR will be determined. The relationship between the melt body, capable of producing the reflection observed in previous studies, and a possible underlying LVZ will be identified. These features will then be compared with observations from other mid-ocean ridges to consider the differences in the crustal accretionary processes at fast, intermediate and slow spreading ridges.
- The spatial continuity and physical properties of the melt body and underlying LVZ will also be determined.

1.6 Summary and structure of this dissertation

Mid-ocean ridges are now widely recognised as the sites of crustal accretion. Mature oceanic crust is surprisingly uniform, however different seafloor morphologies observed at fast, intermediate and slow spreading ridges imply that crustal accretionary processes vary with spreading rate. Large amplitude reflections corresponding to the roof of a sub-crustal magma chamber have now been observed at all spreading rates, although constraints on the geometry of the underlying LVZ are mainly restricted to the EPR. The aim of this study is to investigate the detailed crustal structure of a magmatically active intermediate spreading ridge, determine the magma chamber geometry and compare this with existing models from the EPR. The VFR was chosen as the site of the multidisciplinary geophysical experiment as it had previously been shown to be underlain by a melt body, characterised by a strong, reversed polarity, sub-crustal reflection event.

In this chapter the tectonic setting of the study area has been described and existing data from the VFR summarised. Current models of mid-ocean ridge crustal structure, including a summary of the geophysical observations of magma chambers at fast, intermediate and slow spreading ridges, have also been introduced.

Chapter 2 describes the experimental configuration and data acquisition. The processing required to generate interpretable record sections is also briefly outlined.

The main features of the wide-angle seismic dataset are described in Chapter 3.

Chapter 4 contains a detailed description of the modelling of the wide-angle seismic dataset. The generation of the initial velocity-depth models is discussed and the ray-trace modelling method is defined, together with a comparison with other forward modelling techniques. Best fitting velocity-depth models are described for the main 2-D seismic lines, consisting of two across-axis, two along-axis and two axis-parallel profiles.

Forward modelling of the normal incidence seismic and gravity datasets is described in Chapter 5. These datasets were used to further constrain the crustal models generated from ray-trace modelling of the wide-angle seismic data and the final models are described in detail.

Chapter 6 contains an interpretation of the velocity and density models and compares them with existing data from the VFR and other mid-ocean ridges to determine the processes of crustal accretion.

The main conclusions drawn from this study are highlighted in Chapter 7. Further work on the existing EW9512 dataset is discussed and suggestions for future surveys are also proposed.

Appendix A contains a complete set of the 2-D wide-angle seismic record sections. Ray-trace modelled wide-angle seismic record sections for all DOBSs and forward modelled gravity profiles can also be found in Appendices B and C respectively. Example *GMT* scripts used to calculate the residual mantle Bouguer anomaly are listed in Appendix D.

Chapter 2

Data acquisition and processing

2.1 Introduction

The dataset described in this dissertation was acquired on the *R/V Maurice Ewing* (EW9512) in November-December 1995. A multidisciplinary geophysical experiment conducted during EW9512 was centred on 22° 20′ S, 176° 40′ W and targeted the intermediate spreading (full rate of 60 mm yr^{-1}) Valu Fa Ridge in the Lau Basin. The VFR was chosen for this study as it was already one of the most intensely studied sections of the global ridge system and large amplitude reflections from the top of a magma chamber had been previously observed.

Wide-angle seismic and controlled source electromagnetic data were collected over this ridge system in an attempt to understand the processes of crustal accretion at this constructive margin and compare and contrast these processes with ridges of different spreading rates. Although the VFR is situated in a back-arc environment, many of its characteristics are similar to those observed at mid-ocean ridges and therefore direct comparisons are feasible. The Central Valu Fa Ridge and its overlap with the Northern Valu Fa Ridge were chosen as the study area for several reasons:

- Previous seismic studies have shown that the VFR is underlain by a magma chamber. A dense grid of normal incidence seismic profiles collected over the CVFR and its overlap with the NVFR, during *RRS Charles Darwin* cruise CD34/88 (Collier and Sinha, 1990 and 1992b), showed this area to be magmatically active with a magma chamber reflector observed on most profiles.
- Overlapping spreading centres (OSCs) have been previously suggested to be regions of low magmatic budget, based primarily on the fact that no MCRs have been observed beneath OSCs at the East Pacific Rise. However, a wide MCR, extending beneath both the CVFR and NVFR, was identified on several of the normal incidence seismic profiles collected over the OSC at 22° 12′ S during CD34/88, which implies an apparently high magmatic budget and contrasts with the EPR observations. Gravity studies conducted over the VFR (Sinha, 1995) have also suggested that this OSC is the site of enhanced magmatism, with either

increased crustal thickness (cf. thinner crust observed beneath OSCs at the EPR) or a density reduction in the mantle accounting for the observed gravity low.

- Previous Sea Beam bathymetry data (von Stackleberg *et al.*, 1988) showed that the seabed topography was relatively smooth, thus minimising the scattering of seismic energy at the seabed, which is a considerable problem at mid-ocean ridges when surveying with seismic methods.
- A water depth of greater than 1000 m was required to conduct the CSEM experiment to minimise the effect of atmospheric electromagnetic signals, which swamp crustal CSEM signals.

In this chapter the methodology and instrumentation used for the seismic component of the experiment are described and details of the additional datasets collected throughout the cruise are summarised. The data replay and processing routines are as described in detail in Navin (1996).

2.2 Experimental configuration

A perpendicular network of seismic profiles was collected over the VFR during EW9512 using two DOBS (Digital Ocean Bottom Seismometer) deployments – *Seismic South* and *Seismic North* - so called due to their relative locations within the work area (see figure 2.1).

The survey was primarily designed to investigate the crustal structure both parallel and perpendicular to the main spreading direction and the bulk of this dissertation presents the results of modelling the main 2-D seismic profiles (Lines 1, 4 and 6). Profiles were collected both along-axis and across-axis with further reference lines collected to the west, parallel to the spreading axes. The seismic profiles located to the west of the spreading axes were situated on possible pre-rift back-arc crust, based on evidence derived from an interpretation of the seabed topography by Wiedicke and Collier (1993), to provide a direct comparison with the VFR-generated crust. The locations of the main 2-D seismic profiles are shown in figure 2.1.

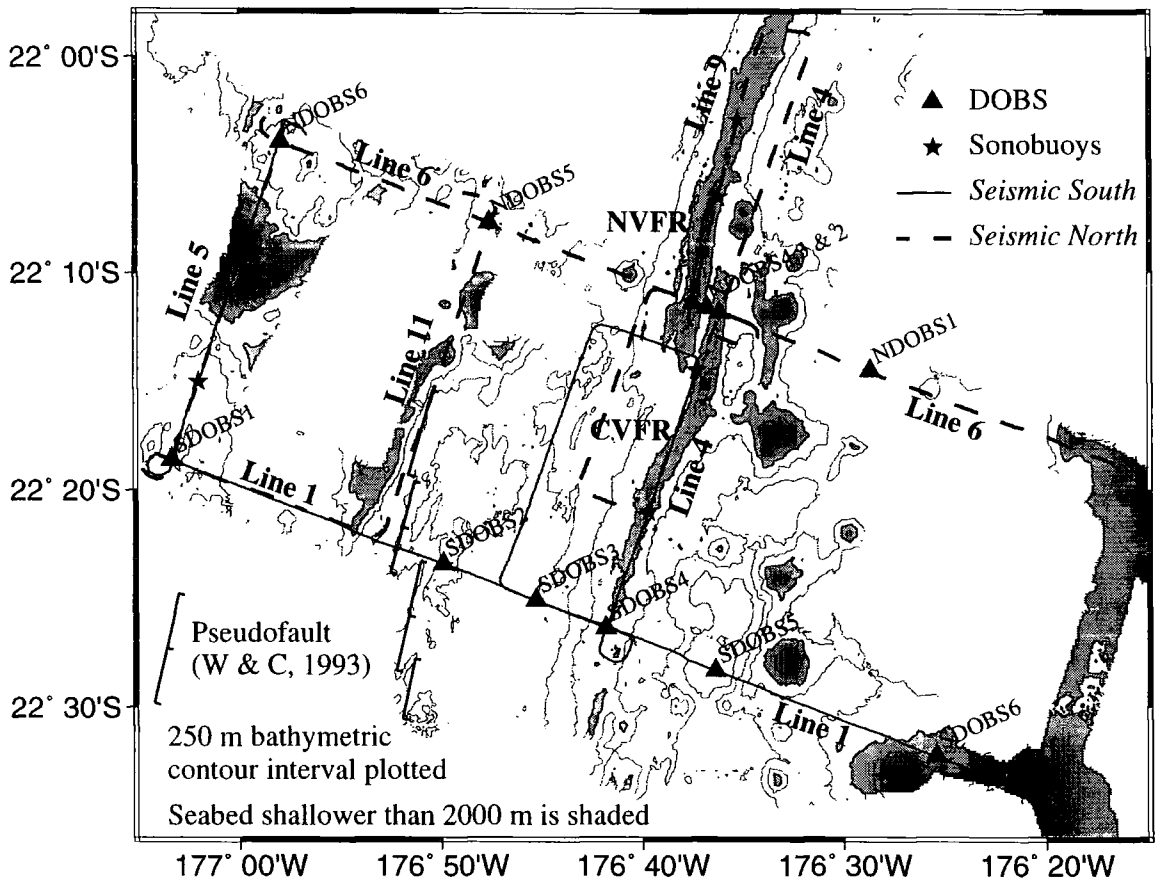

Figure 2.1: The Valu Fa Ridge seismic study (after Peirce *et al.*, 1996).
Seismic experimental configuration overlying the bathymetry of the study area. Profile lines are shown by solid (*Seismic South*) and dashed (*Seismic North*) lines and the main 2-D seismic profiles modelled in this dissertation are annotated. Seabed depths shallower than 2000 m have been shaded to show the location of the CVFR and NVFR and DOBS and sonobuoy locations are marked by triangles and stars respectively. The pseudofault identified by Wiedicke and Collier (1993), possibly representing the boundary between pre-rift and post-rift, VFR-generated crust is also shown (~176° 52′ W).

- Line 1, oriented parallel to the spreading direction (approximately west-northwest – east-southeast), crosses the CVFR at 22° 26.5′ S, 176° 42′ W and extends 40 km off-axis both to the east and west. The profile was designed to cross the CVFR at approximately the same location as one of the normal incidence profiles collected during CD34/88, which showed a wide, bright MCR beneath the axis (Line 35 - Collier and Sinha, 1992b).
- Line 6 runs parallel to, and 30 km to the north of, Line 1 crossing the northern tip of the CVFR and the southern tip of the NVFR at 22° 12′ S, 176° 36′ W and 22° 11.5′ S, 176° 37.5′ W respectively. Line 6 was also 80 km in length and was centred on the overlap basin. Line 6 was designed to investigate the processes of

crustal accretion at an 'active' OSC, as Collier and Sinha (1990) observed a MCR beneath both overlapping ridge tips at this location and directly beneath the overlap basin.

- The along-axis profile Line 4, oriented north-northeast – south-southwest, linearly follows the shallowest bathymetric expression of the CVFR and intersects both Line 1 and Line 6 at 22° 26.5′ S, 176° 42′ W and 22° 12′ S, 176° 36′ W respectively. The profile was designed to investigate the variation in crustal structure along the entire CVFR spreading segment and extends a further 20 km north-northeast from its intersection with Line 6, running approximately parallel to the NVFR, to determine the lateral extent of the magma chamber beneath the CVFR ridge tip.
- Line 9, also oriented north-northeast – south-southwest follows the shallowest bathymetric expression of the NVFR extending 20 km north-northeast from its intersection with Line 6 at 22° 12′ S, 176° 36′ W. The NVFR, with the exception of the southern tip, was not surveyed during CD34/88 and Line 9 was designed to investigate its upper crustal axial structure for comparison with the CVFR.
- Lines 5 and 11 were oriented parallel to the CVFR along-axis profile Line 4 and were located 40 km and 21 km west of the ridge axis respectively. Wiedicke and Collier (1993) observed a 'pseudofault' west of the Valu Fa Ridge, running north-south at 176° 50′ W and interpreted this to be the transition between pre-rift and post-rift (VFR-generated) crust (see figures 1.4 and 2.1). Line 5 was located west of this 'transition' and was therefore shot as a reference line sampling pre-rift crust. However, Line 11 was shot as the final section of *Seismic North* and crosses the bathymetric expression of the pseudofault at 22° 15′ S (figure 2.1).

2.3 Data acquisition

All seismic profiles were shot using a 20-gun (8510 in^3) airgun array as source (figure 2.2). The array was specifically designed and tuned to produce the large amplitude, low frequency (dominant frequency of ~8 Hz) source signature required for lower crustal investigation. Shots were fired at 40 s intervals resulting in a trace spacing of 100 m.

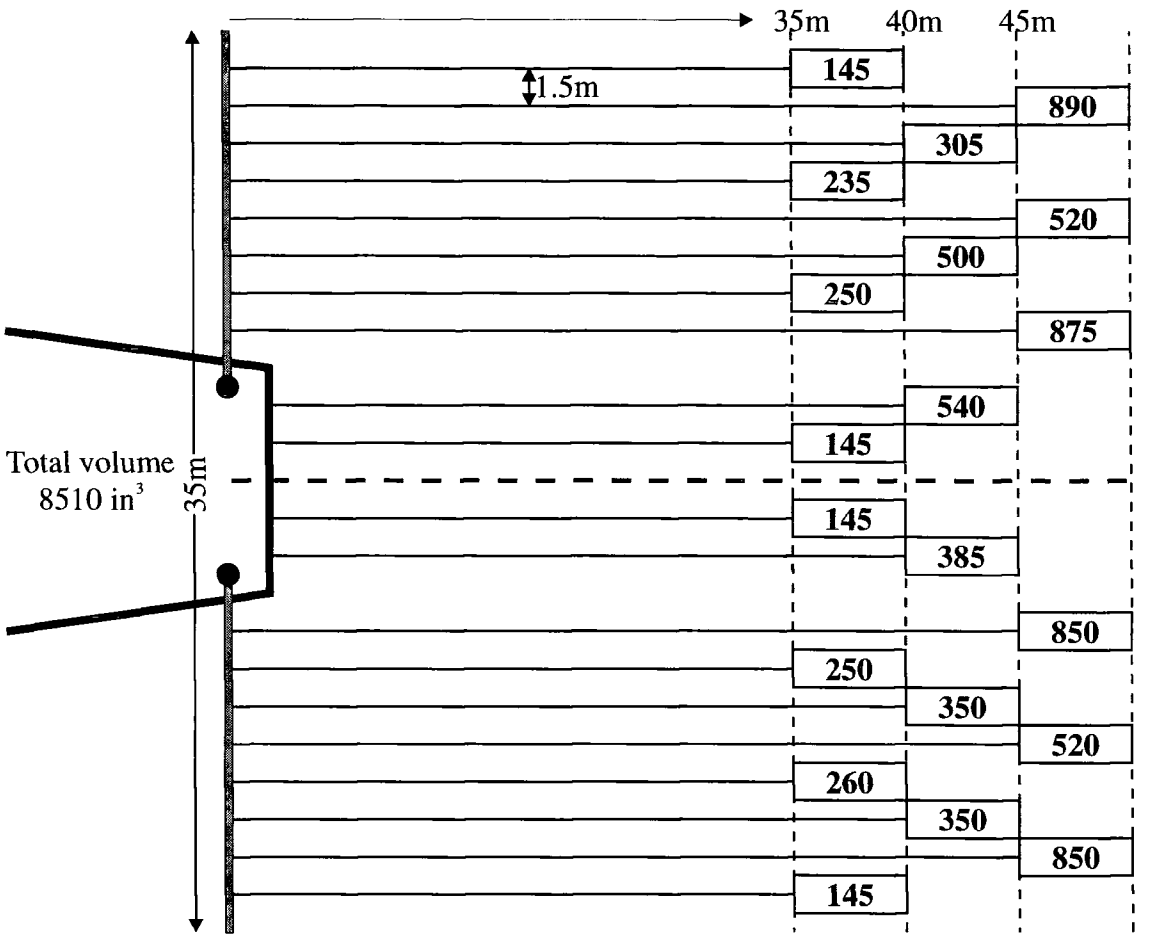

Figure 2.2: Schematic diagram showing the main specifications of the airgun array used during EW9512.

2.3.1 Wide-angle seismic data

The wide-angle seismic data were recorded using six DOBSs during two separate deployments - *Seismic South* and *Seismic North*. Each DOBS was fitted with a hydrophone and gimballed three-component geophone package as sensors. The DOBSs were programmed to record in a 19 s long scheduled, windowed mode (see Teledyne Geotech, 1988) with an 80 s repeat interval at 200 sps (i.e. alternate shots were recorded resulting in a 200 m trace spacing). A detailed description of the DOBS instrumentation can be found in Chapter 2 (pp.37-41) of Navin (1996).

In addition disposable sonobuoys were deployed at specific locations during both experiments to supplement data coverage and reverse a number of the off-axis wide-angle seismic profiles. Sonobuoy signals were received using an aerial on the main mast and an ICOM radio located in the main laboratory. The analogue signal was then digitised and recorded using a spare DOBS (Teledyne Geotech PDAS-100) datalogger, which was programmed to record in a 19 s long scheduled, windowed mode with a 40 s

repeat interval at 200 sps (i.e. every shot was recorded resulting in a 100 m trace spacing (cf. DOBS data). Paper playouts were also generated using an EPC graphic recorder.

2.3.2 Normal incidence seismic data

Normal incidence seismic data were recorded opportunistically in a piggy-back fashion during the wide-angle experiment, again using a PDAS datalogger and a single-channel streamer. There had been no intention to collect normal incidence seismic data until a spare single-channel streamer was found on board.

The majority of the survey area had been previously mapped with a detailed grid of four-fold normal incidence profiles (Collier, 1990), thus the EW9512 normal incidence seismic data were collected as an additional dataset to aid construction of the initial wide-angle seismic models and to further constrain the shallow sub-seabed structure.

2.3.3 Additional datasets

Free-air gravity data

In addition to the seismic data, free-air gravity data were collected throughout the cruise using a Bell Aerospace BGM-3 marine gravimeter (figure 2.3). The free-air gravity data coincident with the modelled 2-D seismic lines were extracted from this dataset and modelled independently to test the uniqueness of the best fitting crustal models generated. Several gravity profiles, oriented parallel to the spreading direction, were also collected south of the work area (see inset of figure 2.3). These gravity profiles have been subsequently modelled and interpreted by Calvert (1996).

Swath bathymetry data

Swath bathymetry data were collected using a Krupp Atlas Hydrosweep system. This provided a detailed bathymetry dataset to identify seabed structures and investigate problems of scattering of seismic energy and to extend previous coverage (von Stackleberg *et al.*, 1988 and Sinha, 1988). Centre beam depths were extracted from the dataset to help in the generation of 2-D crustal models. Bad pings were edited and the gridded bathymetry dataset provides coverage over an area of >3000 km^2 (Peirce *et al.*, 1996).

Water column data

A sound velocity dip meter and 12 expendable bathymetric thermographs (XBTs) were deployed during EW9512 to collect water column data. The sound

velocity dip, which measures the acoustic seismic velocity in the water column to generate a velocity-depth profile, was carried out using a Plessey sound velocity profiler at 22° 26′ S, 176° 36′ W (Peirce *et al.*, 1996). The velocity profile was supplemented by 12 XBT deployments, to measure the temperature and conductivity of the water column and determine whether the depth extent of the thermocline is consistent over the survey area. A good estimate of the water column structure was necessary to accurately locate instruments and faithfully reproduce the seismic ray-paths during the modelling stage.

Total intensity magnetic field data

Magnetic profiles were collected during airgun firing and swath bathymetry data collection using a Varian V75 magnetometer. The magnetic data were logged every 6 s, corrected using the International Geomagnetic Reference Field 1990 and the total intensity field interpolated every 60 s. This dataset does not form part of this dissertation.

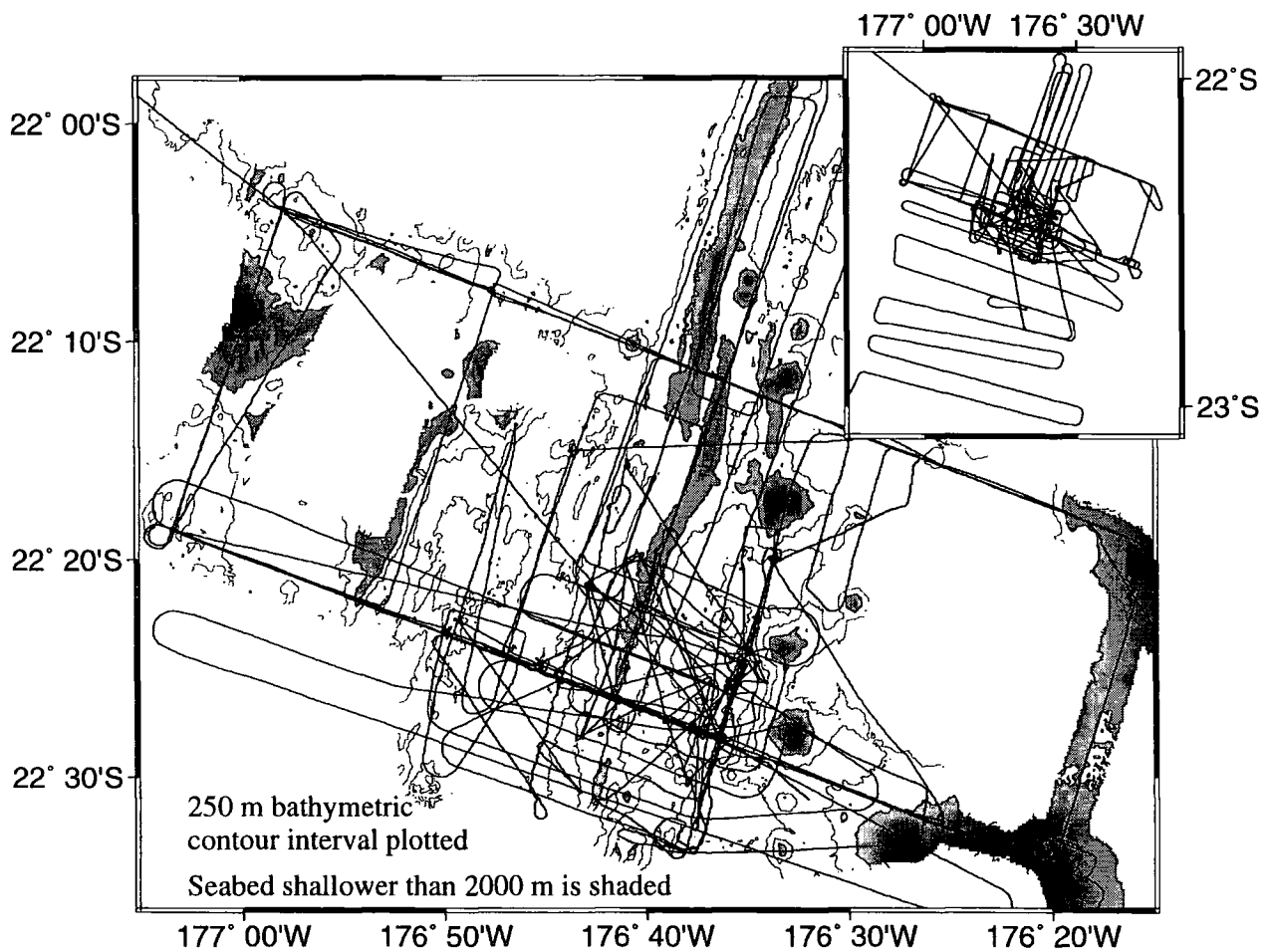

Figure 2.3: Free-air gravity track lines (after Peirce *et al.*, 1996). Seabed depths shallower than 2000 m have been shaded to show the location of the CVFR and NVFR. Seven further gravity profiles oriented west-northwest – east-southeast were also collected south of the main survey area (see inset and Calvert, 1996).

2.4 Wide-angle seismic data processing

2.4.1 Data replay

The processes involved in the conversion of DOS binary files recorded on the DOBS' PDAS datalogger to SEG-Y_i files are displayed in figure 2.4. However, the main stages of producing wide-angle seismic data sections from the raw PDAS output are described in detail in Chapter 2 (pp 53-70) of Navin (1996) and a full description of the Durham in-house variation of the standard SEG-Y format for seismic data storage (SEG-Y_i) can be found in Peirce (1990) and Matthews (1993).

Ten of the twelve DOBSs (six DOBSs on each deployment) encountered no problems and recorded 100% of the shots fired.

During quality control checking of the PDAS data (figure 2.4), it became apparent for NDOBS4 (situated on the NVFR tip - figure 2.1) that only a few shots, including the first 30 shots on each channel were recorded. A problem was also encountered with SDOBS5 (located in the basin east of the CVFR - figure 2.1), where the first 520 shots of *Seismic South* were not recorded by the vertical geophone. The source of this problem appeared to be the lodging of the innards of the vertical geophone in its housing when the DOBS hit the seabed on deployment. The geophone innards gradually worked themselves free during *Seismic South*, resulting in only the first half of Line 1 not being recorded. However, this did not cause major difficulties during the data interpretation and modelling stages as the coincident hydrophone data were recorded without any problems.

Approximately 1800 shots were recorded on the sections of each of *Seismic South* and *Seismic North* modelled in this dissertation (see figure 2.1 for line locations) resulting in ~26 000 individual seismograms.

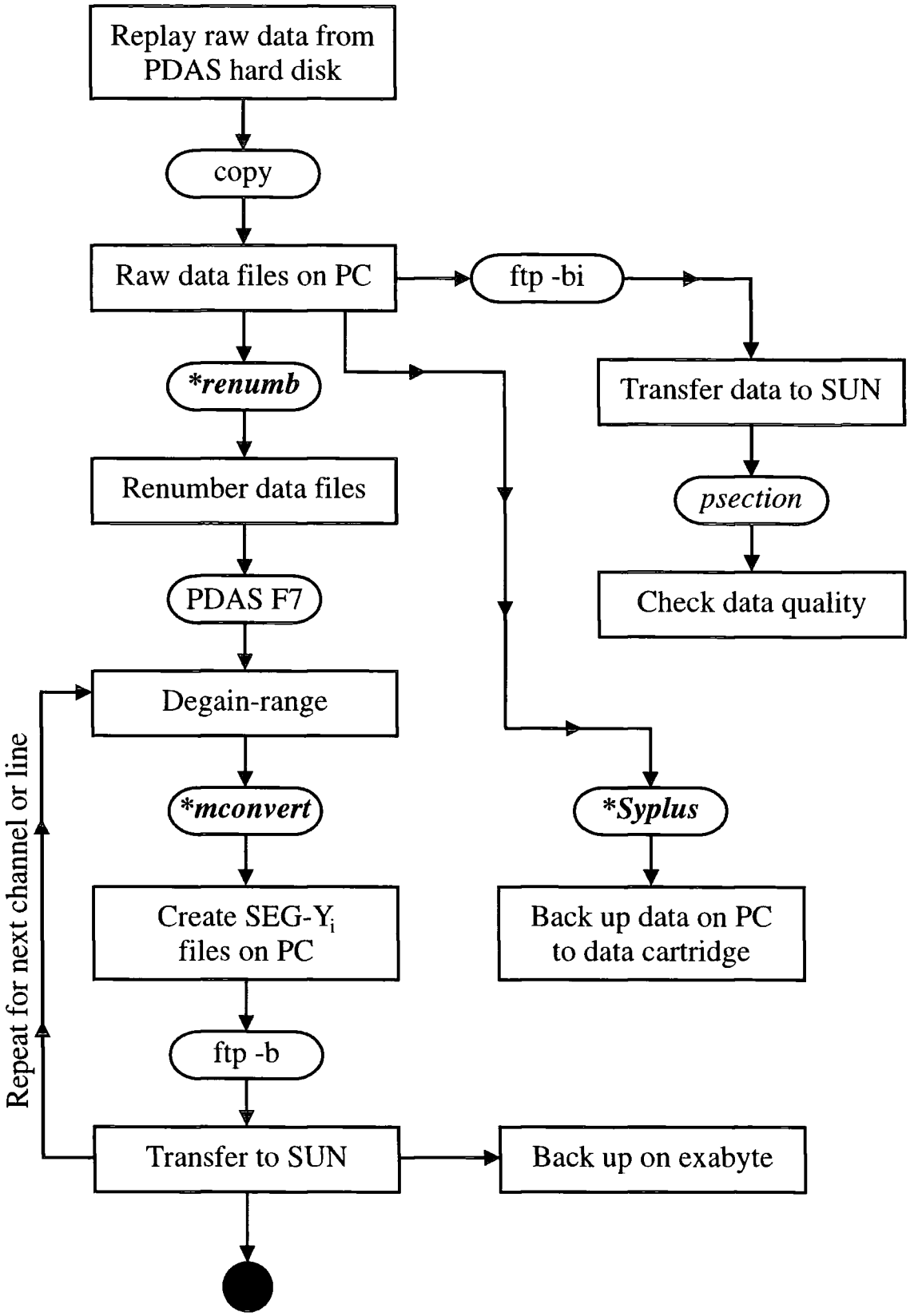

Figure 2.4: Flow diagram adapted from Navin (1996) showing the main processing routines required to create SEG-Y_i from the raw DOBS data. Processes, described in detail in Navin (1996), are surrounded by rectangles and programs (given in italics) or system commands are enclosed by lozenges. Stars indicate where programs differ from those used in Navin (1996). The programs *renumb* and *mconvert* accommodate more than 999 files on one day and *Syplus* is a proprietary backup software product. The filled circle at the end of the flow marks the continuation point on figure 2.5.

2.4.2 Corrections applied to wide-angle seismic data

All DOBS' internal clocks were synchronised to the *Ewing's* TrueTime master clock prior to deployment and were checked for drift on recovery (Peirce *et al.*, 1996). Clock drifts, assumed to be linear between deployment and recovery, were applied during the processing stage of *mconvert* (see figure 2.4 - conversion of raw PDAS data to SEG-Y_i). Corrected shot instants were also incorporated into the processing routine using *mconvert*.

2.4.3 Generation of final record sections

The main processing stages required to generate the final wide-angle record sections are summarised in figure 2.5. These stages are described in detail in Navin (1996) from which this figure has been adapted.

The only significant difference in the processing routines compared with Navin (1996) concerns the calculation of the shot-receiver ranges. The shot instant file (obtained from the Ewing's computerised shot firing system) contained the latitude and longitude of each shot and shot-receiver separations were thus easily calculated. Shot separations were checked for consistency across all instruments and to provide an initial estimate of how far off-line, if at all, each instrument was located.

2.4.4 Errors

An estimate of the error in the travel time picks is essential before any forward modelling can proceed. The errors associated with the wide-angle seismic data are described below.

The shot-receiver range is controlled by several factors. The errors associated with shot position (±1 m), depth of the airgun array (±1 m), water column velocity structure (±5 ms^{-1}) and corrected receiver position (±25 m) combine to generate a total error for shot-receiver ranges of approximately ±20 ms.

The data sampling rate was 5 ms and a travel time picking error (with 80% confidence interval) was calculated to be four samples (±20 ms).

Thus the maximum possible error for picks from a DOBS was estimated to be approximately ±40 ms.

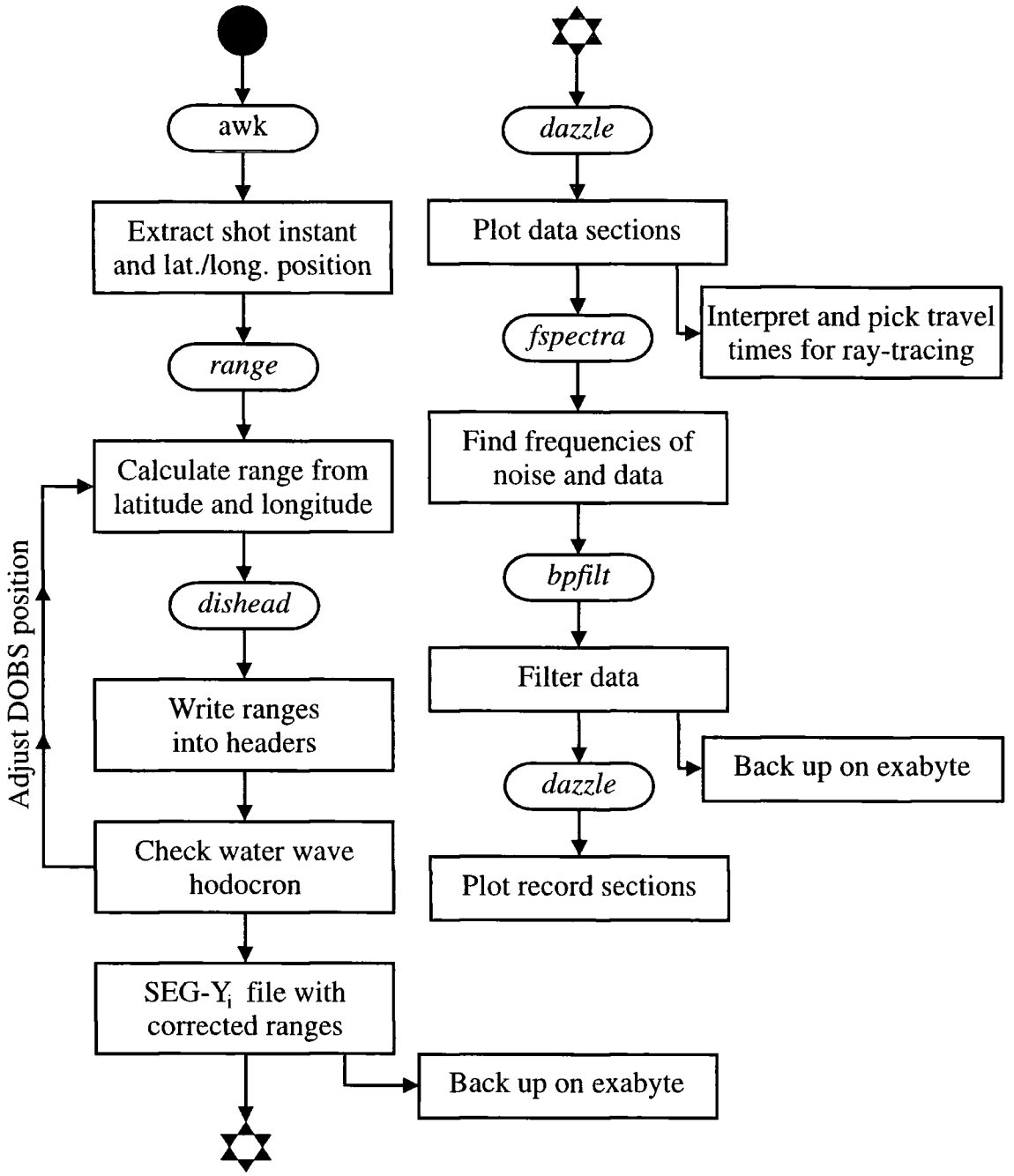

Figure 2.5: Flow diagram adapted from Navin (1996) showing the main processing stages required to generate the final wide-angle seismic record sections. The filled circle at the beginning of the flow marks the continuation point from figure 2.4. The connection between the left and right flow on this figure is marked by a star. Display parameters are described in figure 2.4.

2.5 Normal incidence seismic data processing

As previously described, the normal incidence seismic data were recorded opportunistically using a PDAS datalogger and a spare single-channel streamer. During the recording process data stored in the PDAS datalogger random access memory (RAM) had to be regularly downloaded to its hard disk due to the rapid acquisition rate. During this process datalogging had to cease and some data was unavoidably lost. Downloading was carried out on *Seismic South* every two hours and ~10 shots (~1 km of data) were not recorded each time. Unfortunately a problem occurred on *Seismic North* during downloading and the first thirteen hours of data were lost. After the source of this problem was identified and rectified, downloading was carried out every three to four hours and ~20 shots (~2 km of data) were not recorded during each operation. A summary of normal incidence seismic data collected is shown in figure 2.6.

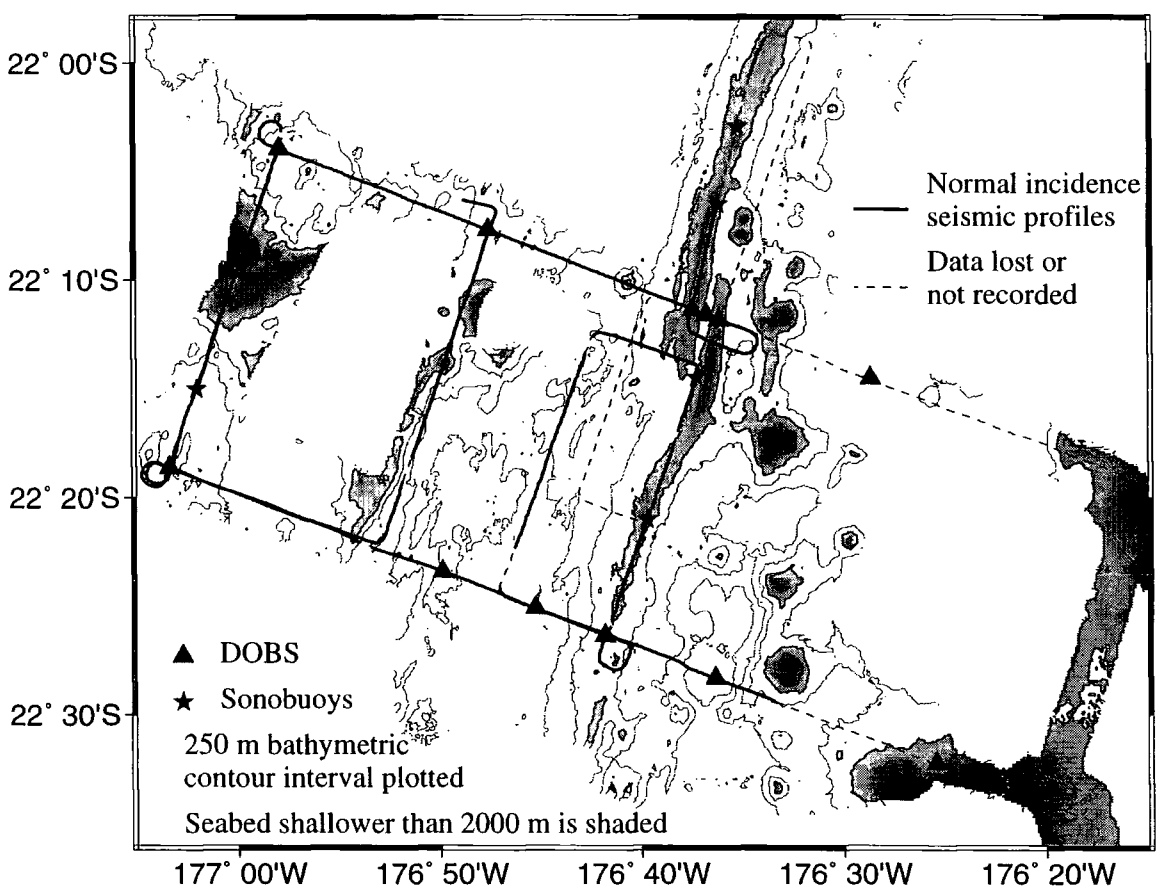

Figure 2.6: Normal incidence seismic data collected during EW9512 (after Peirce *et al.*, 1996). Seismic profiles are shown by a thick solid line. The thinner dashed line represents data lost or not recorded during the downloading procedure. Display parameters are described in figure 2.1.

Normal incidence seismic data were processed from DOS binary files, recorded on the PDAS datalogger, to SEG-Y_i files using the wide-angle processing scheme described in figure 2.4. The SEG-Y_i files were then converted to standard SEG-Y (Barry *et al.*, 1975) using *segy write* and *tget* (written by D.L. Stevenson) for input into Advance Geophysical Corporation's *ProMAX* (version 6.0). Further signal processing (e.g. filtering, deconvolution and migration) was carried out using *ProMAX*, but did not significantly enhance the dataset.

2.6 Sonobuoy data processing

Sonobuoy data were collected continuously using the PDAS datalogger described in section 2.3.1 and data coverage was essentially the same as the normal incidence seismic data coverage (figure 2.6), except that the shots fired on Line 9 into the two sonobuoys were also recorded. Thus data from six sonobuoys (two each on Lines 4, 5 and 9) were converted into SEG-Y_i using the processing routines described in figure 2.4.

Shot-receiver ranges

Shot-receiver ranges were calculated using the routines as shown in the left flow of figure 2.5. However, inspection of the travel times of the direct water waves on each sonobuoy showed a systematic error (see figure 2.7). This was attributed to the fact that the receiver position (i.e. sonobuoy) was not fixed in the water column and drifted with the water column currents as a function of time. Sonobuoy shot-receiver ranges were thus corrected for drift by an average of approximately 10 m per shot.

Errors

Due to the lower signal-to-noise ratio (SNR) and uncertainties in shot-receiver ranges, the errors on travel time picks for the sonobuoy data are far greater than those of the DOBSs. The problem of receiver drift, combined with the errors associated with shot position, depth of airgun array and water column velocity (see section 2.4.4) generate a total error for shot-receiver ranges of approximately ±50 ms.

The sample rate of the sonobuoy data was 5 ms and a travel time picking error (with 80% confidence interval) was calculated to be approximately ±30 ms.

Thus the maximum possible error for picks on a sonobuoy data section was estimated to be approximately ±80 ms.

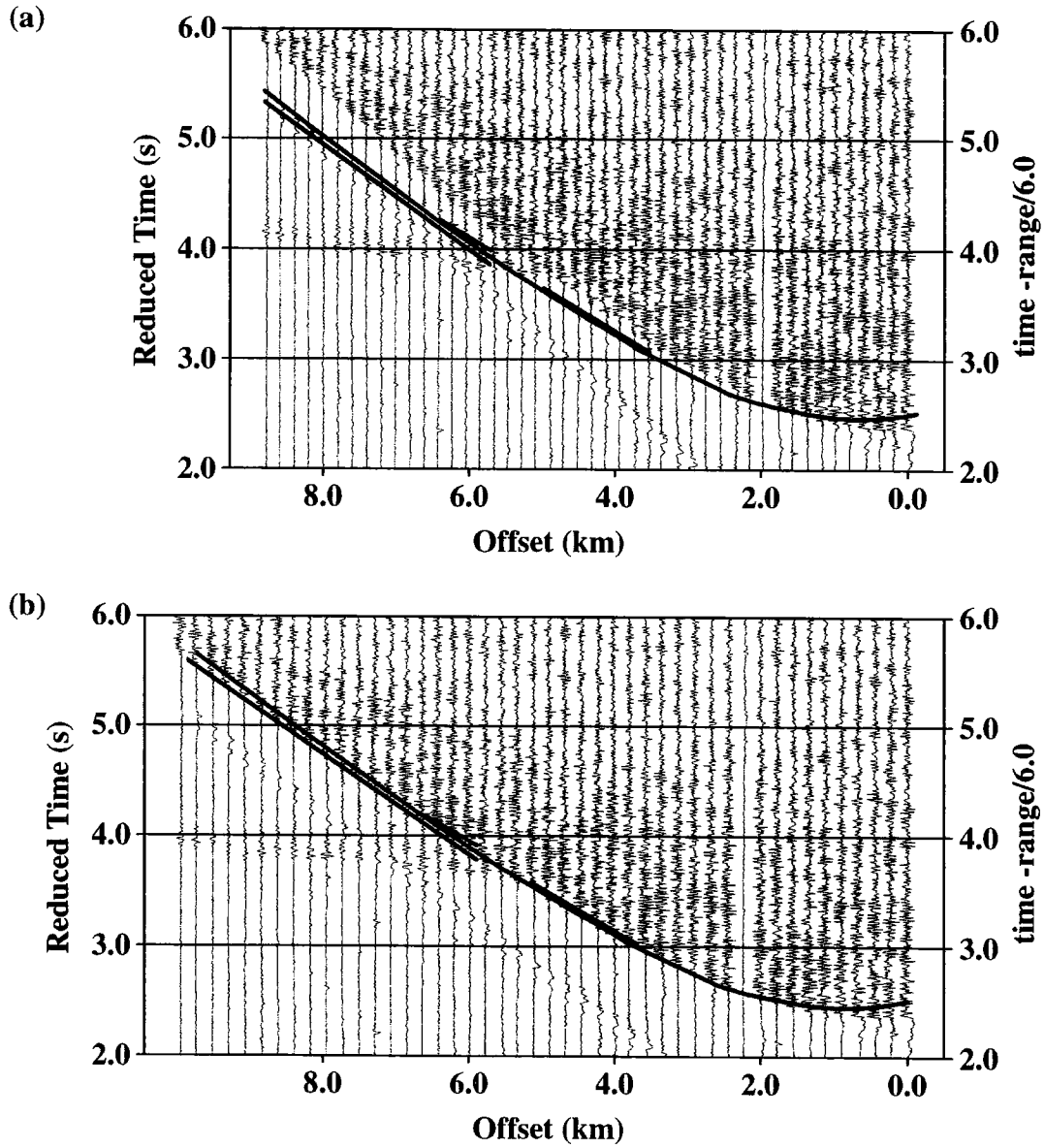

Figure 2.7: Correction for sonobuoy drift.
(a) Example sonobuoy record section showing a high-amplitude water wave arrival. The water wave arrival hodocron calculated from forward modelling is shown by a thick solid line and the systematic error is clearly visible. Note that the hodocron is composed of multiple segments due to the uneven nature of the seabed and variable angles of incidence and reflection. Alternate shots are plotted for clarity.
(b) The same sonobuoy record section corrected for a drift of, in this case, 12 m per shot. Note the improved alignment of the observed and calculated water wave arrival.

2.7 Free-air gravity data processing

The observed gravity data were logged every 1 s, filtered and Eötvös corrected onboard ship and the output interpolated to every 60 s. A Potsdam correction was then applied to the data to generate the free-air gravity anomaly. Calculation of the Eötvös correction around turns is unreliable and this data was discarded.

2.8 Summary

A description of the data acquisition and processing of some of the EW9512 dataset has been presented in this chapter. An estimate of the error on travel time picks in the wide-angle seismic data (both DOBSs and sonobuoys) has been calculated and a significant bias towards the data from the DOBSs must be included when combining results from both the DOBSs and sonobuoys. This bias should take into consideration the lower SNR observed on the sonobuoy record sections and uncertainty in sonobuoy position.

Chapter 3

The Valu Fa Ridge wide-angle seismic dataset

3.1 Introduction

The main features of the wide-angle seismic dataset are described in this chapter. The frequency content of the wide-angle seismic data will be analysed and the main phases of interest identified and their relevance to the study highlighted.

3.2 The wide-angle seismic dataset

The main features observed on the wide-angle seismic data sections are summarised below and in figure 3.1 (SDOBS3 was chosen as all the main phases could be identified on a single record section). All data sections described in this chapter are plotted at true amplitude with a reduction velocity of 6.0 km s^{-1}. Data quality is extremely good with a high signal-to-noise ratio. However, the data sections described in this chapter are by no means the best sections and were chosen solely to exhibit all the features of interest from instruments located on and at both sides of the ridge axes. A complete set of data sections can be found in Appendix A.

Large amplitude arrivals (e.g. direct water waves) have been clipped to enable plotting of seismic sections at a suitable scale for identifying lower crustal phases, and alternate shots are plotted for clarity. The darker bands (~10 km wide) in the centre of the across-axis record sections indicate where the profiles pass over the same axial regions twice (i.e. double the density of traces). The horizontal axes of all record sections are labelled by model offset, with the exception of figure 3.1 which is labelled by shot-receiver range. SDOBS4 located at the intersection of Line 1 and Line 4, at 22° 26.5′ S, 176° 42′ W (see figure 2.1) was chosen to be the point of origin in the work area and model offsets were calculated relative to this location. Line 1 (across-axis) and Line 4 (along-axis)were thus zero-reference lines and shots north of Line 1 were given a positive 'y' model offset and shots east of Line 4 were given a positive 'x' model offset.

3.2.1 Phase identification

Direct water waves (DWW) and crustal (P_g) and mantle (P_n) diving rays are observed as first arrivals with considerable variation in amplitude with offset. Many of the amplitude variations are associated with scattering on severe seabed topography, but some may be related to sub-surface features encountered during their ray-path. The relative positions of these first arrivals are shown in figure 3.1 (Boxes II, III, IV). Many of these first arrivals can also be traced as second arrivals at certain ranges:

- Boxes II & III: Large amplitude direct water waves are clearly observed behind crustal diving rays (>4 km range).
- Box IV: Crustal diving rays can be identified behind the mantle diving ray beyond the Moho triplication point (between 25 and 30 km range).

Moho reflections (P_mP) are also observed as large amplitude, secondary arrivals (e.g. figure 3.1 - Box I). Moho reflections are observed on all sections and include reflections from directly beneath the ridge axis.

Seabed multiples and P-S mode conversions can also be identified on the wide-angle seismic record sections, but were not used in ray-trace modelling of the dataset and are thus not described in detail here.

3.2.2 Frequency analysis and filtering

The seismic section displayed in figure 3.1 is unfiltered and a feint, high frequency banding can be observed (e.g. Box 1: range -32 to -27 km). On inspection, this was found to be temporally related to periods of data transfer to the PDAS hard disk during recording (i.e. it is representative of the PDAS hard disk spinning during the data write process). The program *fspectra* (originated by D. Graham and modified by C. Peirce) was used to determine the frequency of this banding and any additional background noise and to investigate the frequency of the main observed seismic phases. The results of frequency analysis of the vertical component geophone data are described below and summarised in figures 3.2 and 3.3. The hydrophone is more sensitive to higher frequencies than the vertical component geophone and is referred to when appropriate. Note that the main observations from frequency analysis of the vertical component geophone data also apply to the horizontal component geophone data.

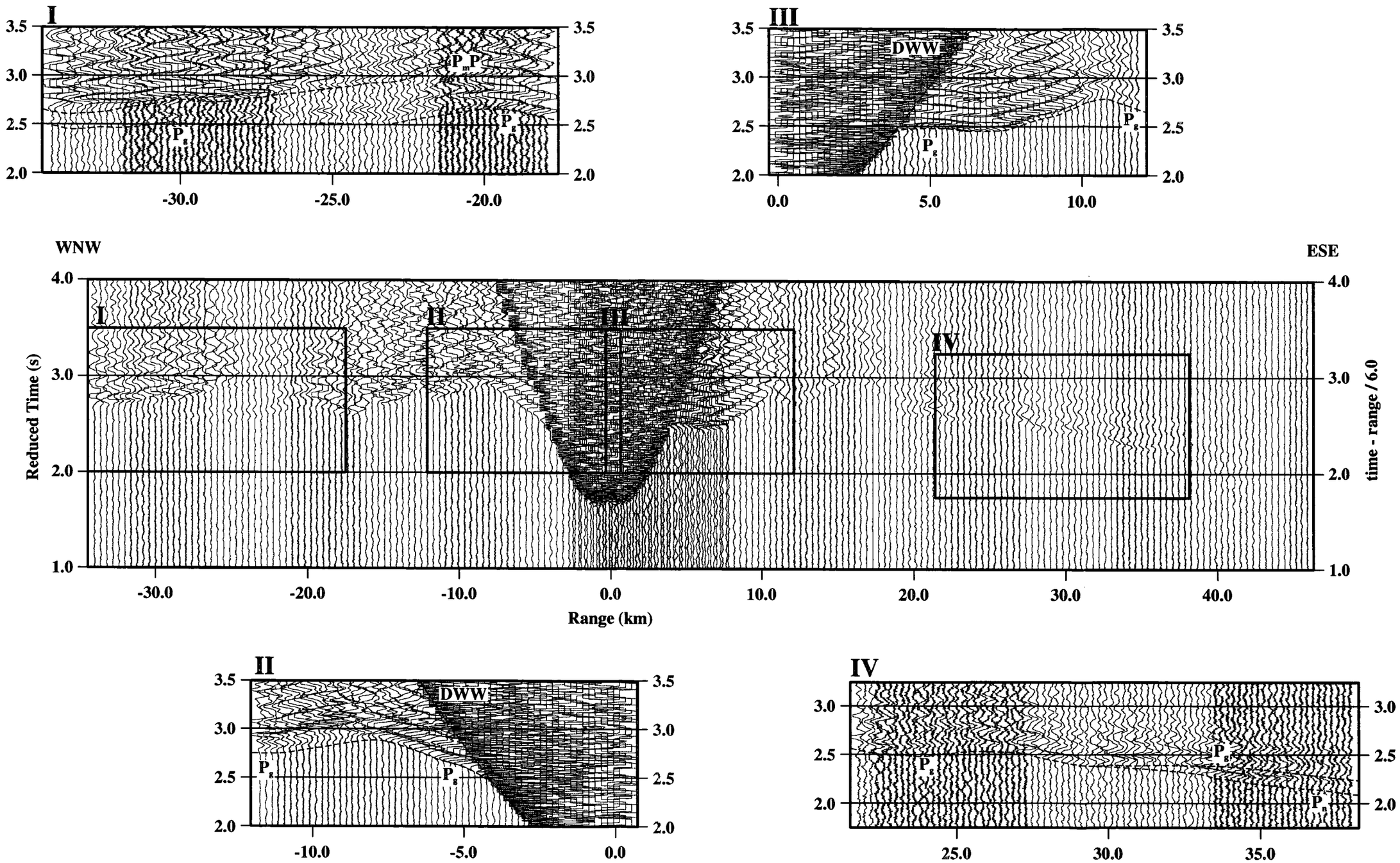

Figure 3.1: Wide-angle seismic data from SDOBS3, located 8 km west of the CVFR on Line 1 (see figure 2.1). Seismograms are plotted at true amplitude with a reduction velocity of 6 km s^{-1}. The vertical component geophone record section is plotted at a suitable scale to show the variation in amplitude with offset of the first arrivals, and alternate traces are displayed. Insets I-IV show expanded regions of the record section (with every trace plotted), to clearly identify the different phases observed. Insets I and IV are plotted at a scale factor equivalent to five times that of the main record section (insets II and III are plotted at a scale factor x2). Note the interaction between the crustal (P_g) and mantle (P_n) diving rays in inset IV and the large amplitude Moho reflection (P_mP) observed as a secondary arrival behind the lower amplitude crustal diving ray in inset I.

- The dominant source frequency is ~7-8 Hz.
- The banding observed on the vertical geophone record section in figure 3.1 has a dominant frequency of 60-62 Hz (see figure 3.2a). However, the noise on the hydrophone resulting from the data transfer to disk is identified by two broad peaks in the frequency spectra at ~40 Hz (range 32-48 Hz) and ~80 Hz (range 75-85 Hz). Instrument generated noise is thus well above the signal band of interest and can be filtered out when necessary.
- The background noise frequency spectrum is dominated by coherent noise, attributed to reverberations of previous airgun shots in the water column (figure 3.3c: Box I).
- Low frequency noise below ~7-8 Hz is minimal, however the geophones (Mark L15-B) have a natural frequency of 4.5 Hz and the amplitude response of frequencies below 4.5 Hz is therefore unreliable. Secondary peaks in the background noise occur at frequencies of 12 Hz, 15 Hz and 22 Hz, but are approximately a quarter of the amplitude of the coherent noise. Background noise is thus considered to be insignificant at frequencies other than the dominant source frequency. However, an additional high frequency peak at ~74 Hz is observed on the hydrophone frequency spectrum (figure 3.2b - solid line), but this is also well above the signal band of interest.
- Crustal diving rays have a dominant frequency ~8 Hz (range 6.5-13.5 Hz), with a secondary peak at ~15 Hz. The signal has negligible amplitude above a frequency of ~19 Hz (figure 3.3c: Box II).
- The frequency spectrum for the direct water wave is dominated by the double peak at ~8 Hz and ~15 Hz and a broad peak at frequencies centred on 60 Hz (range 40-80 Hz). The hydrophone frequency spectrum shows similar features to the vertical component, with an additional double peak at ~22 Hz and ~28 Hz (figure 3.3c: Box III).

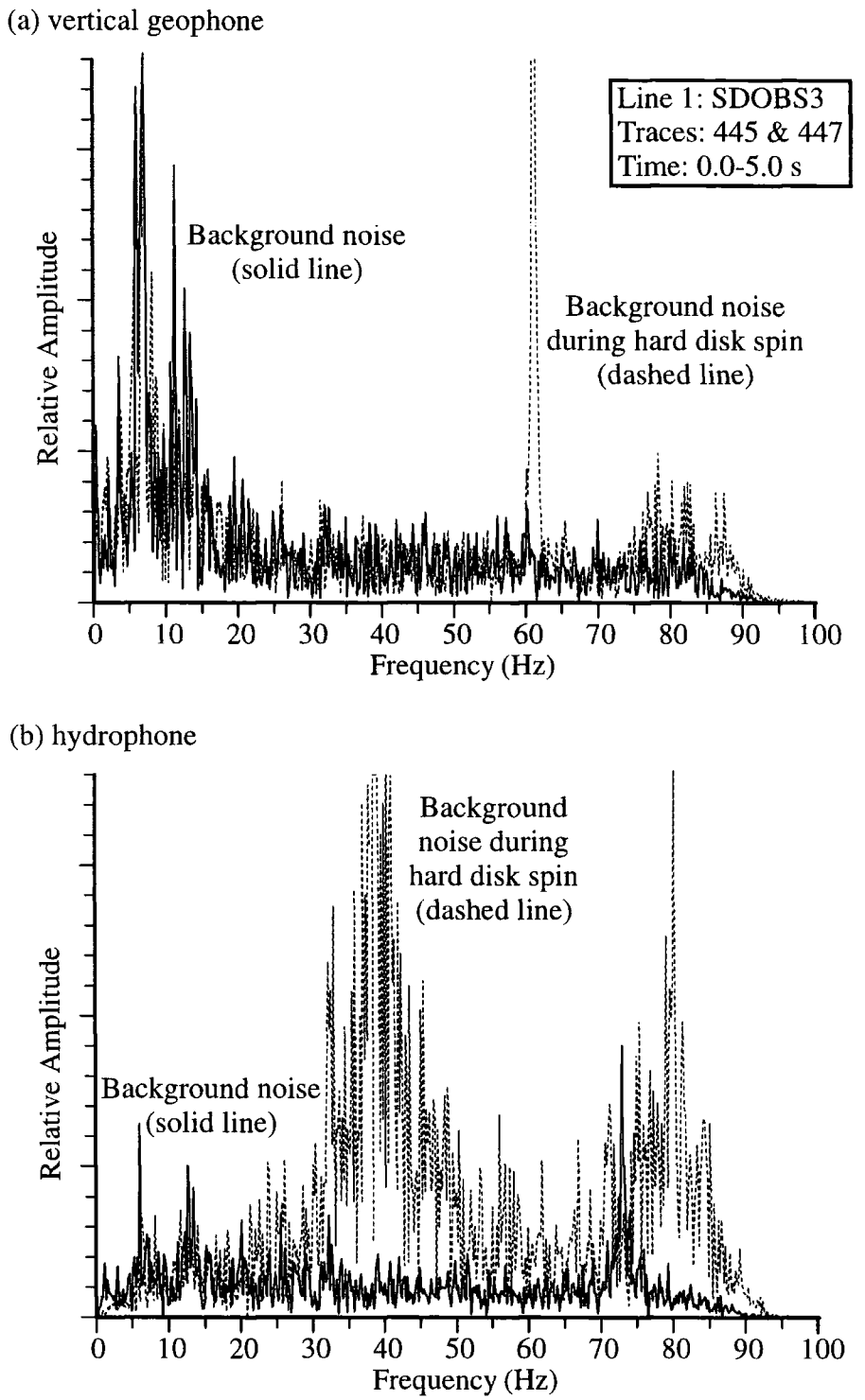

Figure 3.2: A comparison of the frequency spectra of two traces from SDOBS3. Frequency spectra are calculated on the first five seconds of each trace (i.e. before the onset of the first arrival).
(a) Vertical component geophone: Trace 445 (dashed line) was recorded whilst the hard disk was spinning during data transfer and clearly shows the 60-62 Hz frequency of the disk spin.
(b) Hydrophone: Note the noise due to data transfer and disk spin is less distinct and forms two broad peaks centred on ~40 Hz (range 32-48 Hz) and ~80 Hz (range 75-85 Hz). The peak centred on ~40 Hz is the more dominant.

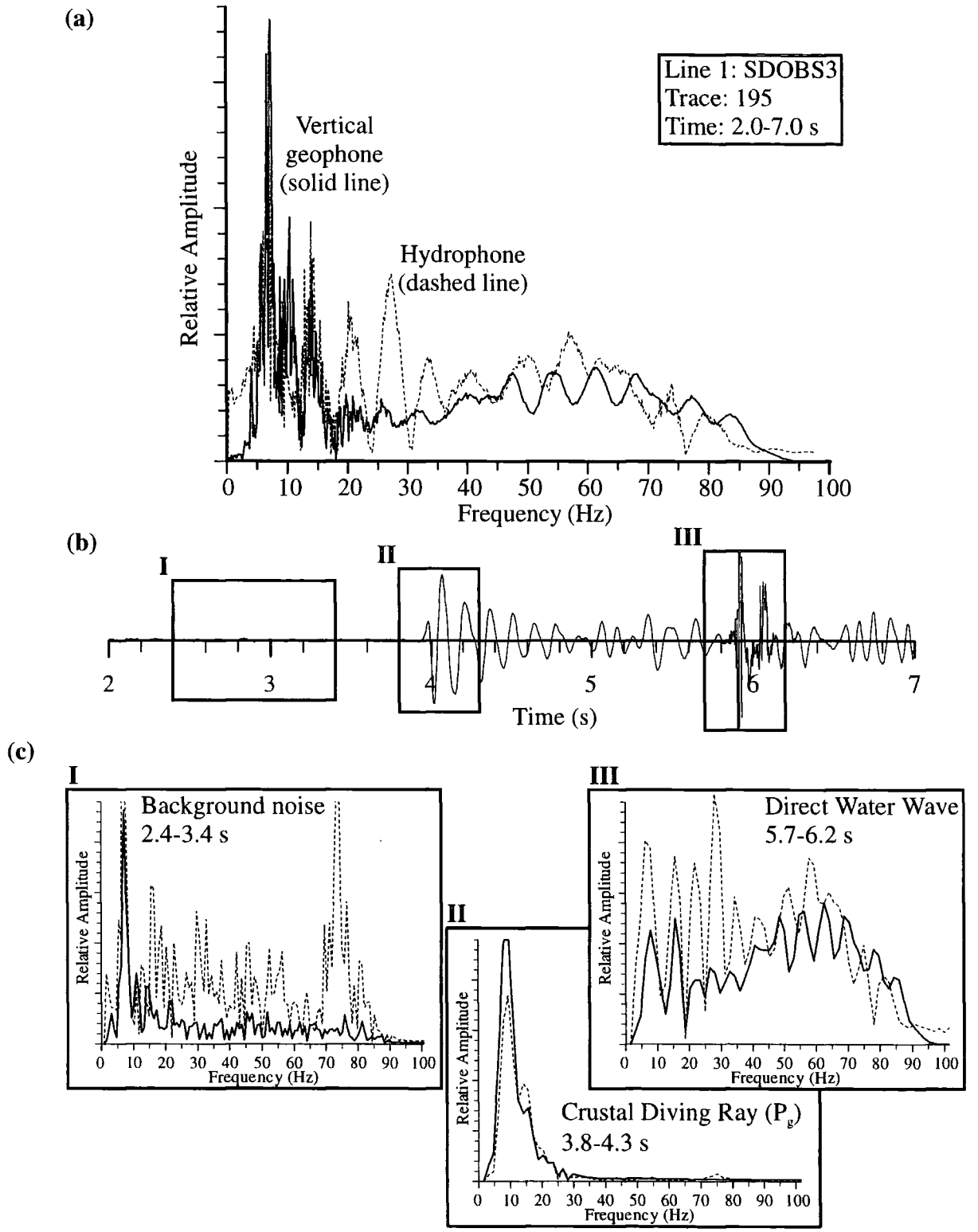

Figure 3.3: Frequency analysis of trace 195 from SDOBS3.

(a) Frequency spectra of five seconds of data from trace 195, for both the vertical component geophone (solid line) and hydrophone (dashed line), are shown with the dominant source frequency identified at ~7-8 Hz.

(b) Seismogram plotted between 2.0 and 7.0 s. First arrival (P_g ~4 s) and direct water wave arrival (the higher frequency arrival at ~5.8 s) can be clearly identified.

(c) Frequency spectra from specific portions of the seismogram are also generated and displayed in Boxes I, II and III. Display parameters in each inset are described in part (a).

The frequency spectra of all instruments were investigated to determine suitable corner frequencies for the filtering of the wide-angle seismic data. Filtering was performed for display purposes only and travel time picks, for use in the modelling process, were made on unfiltered record sections. The vertical component geophone data were filtered with a Hanning window, low-pass (high cut) filter with corner frequencies of 40 and 50 Hz (figure 3.4) and the hydrophone data were filtered with a tighter low-pass filter with corner frequencies of 15 and 20 Hz (figure 3.5), in an attempt to remove some of the high frequency noise observed. All filtering processes were carried out using the program *bpfilt*.

In addition to the vertical component geophone and hydrophone seismic data, data were collected using two horizontal component geophones. An example of the results obtained from these components are shown here, but detailed analysis is beyond the scope of this dissertation. On initial inspection, the main phase of interest, which differs from the vertical component geophone and hydrophone data, concerns the arrival between 3.5 and 4.0 s at model offsets greater than 10 km (figure 3.6: note the different time scale). This arrival has a constant delay of ~0.8 s behind the first arrival and is interpreted to be a P-S mode conversion. Due to the general form of the arrival (a constant delay behind the first arrival), the P-S mode conversion is interpreted to have been generated at mid-crustal levels, directly beneath the instrument. There is no evidence of this arrival on the hydrophone data (an upgoing S-wave incident with the seabed would have to convert again to a P-wave to be observed on the hydrophone), but it can be identified as a lower amplitude arrival on the vertical geophone component data (see figure 3.4b: model offset >10 km, between 3.6 and 4.0 s).

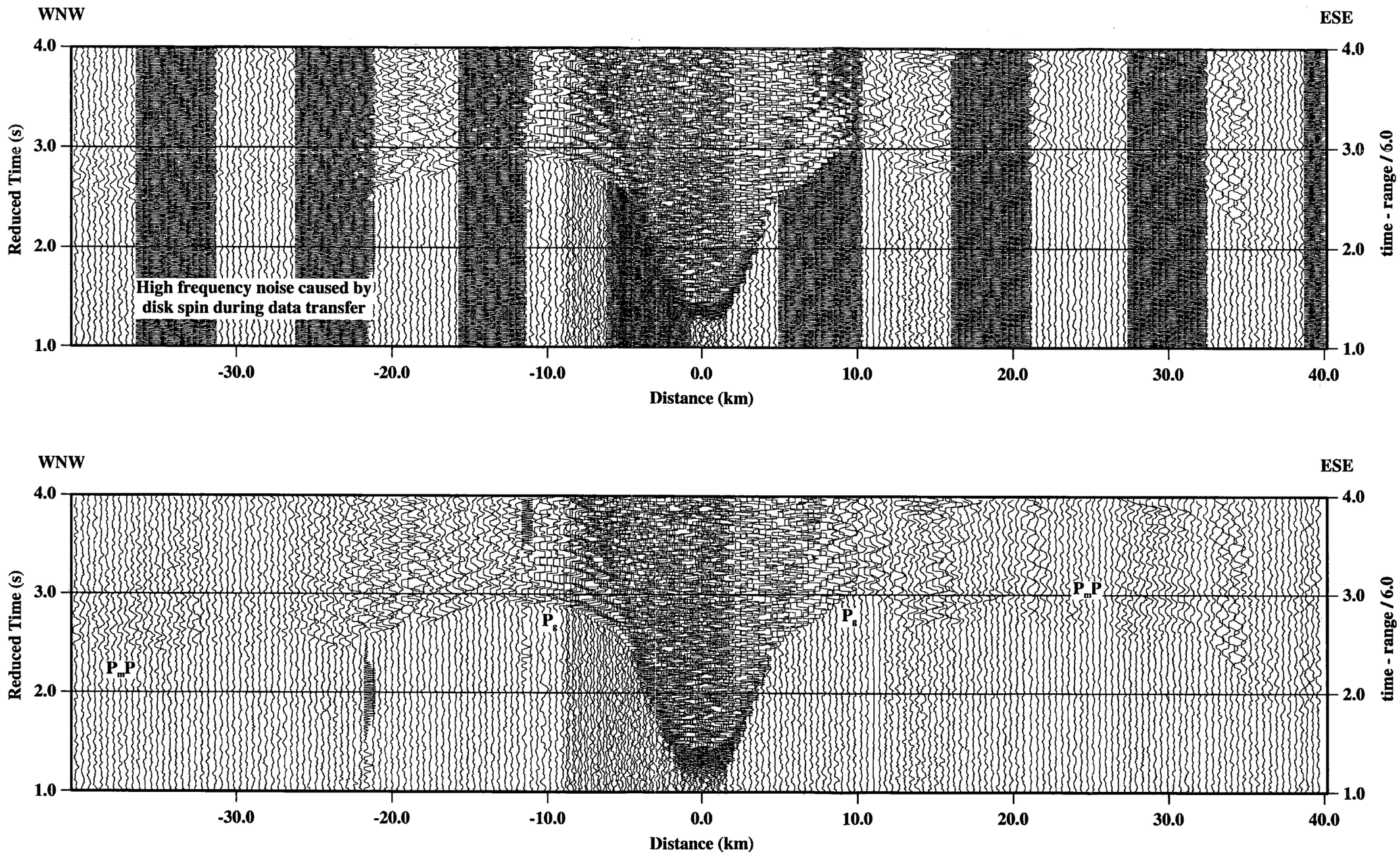

Figure 3.4: Vertical component geophone data from SDOBS4, situated on the CVFR on Line 1 (see figure 2.1). Seismograms are plotted at true amplitude with a reduction velocity of 6.0 km s^{-1}. The darker band between -8 and 2 km model offset shows where the same axial region was crossed over twice (i.e. double the density of traces).
(a) Unfiltered record section clearly showing the high frequency noise generated from the hard disk spin during data transfer.
(b) Record section filtered using a Hanning window low-pass filter with corner frequencies of 40 and 50 Hz. The main phases of interest are highlighted. Note the noise burst at -21 km model of fset. These noise burst are generated during the initial stages of data transfer, whilst the hard disk is 'getting up to speed' and has a lower frequency content than the main disk spin. However, the low-pass filter was not tightened to encompass the additional noise bursts as they do not significantly affect the data quality.

(a)

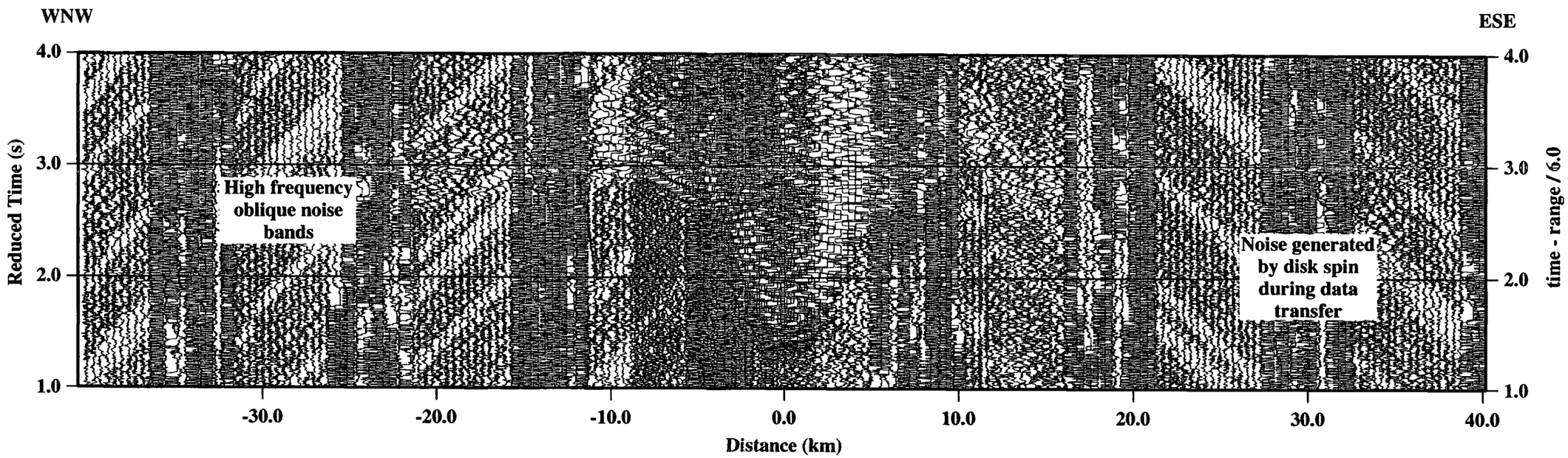

(b)

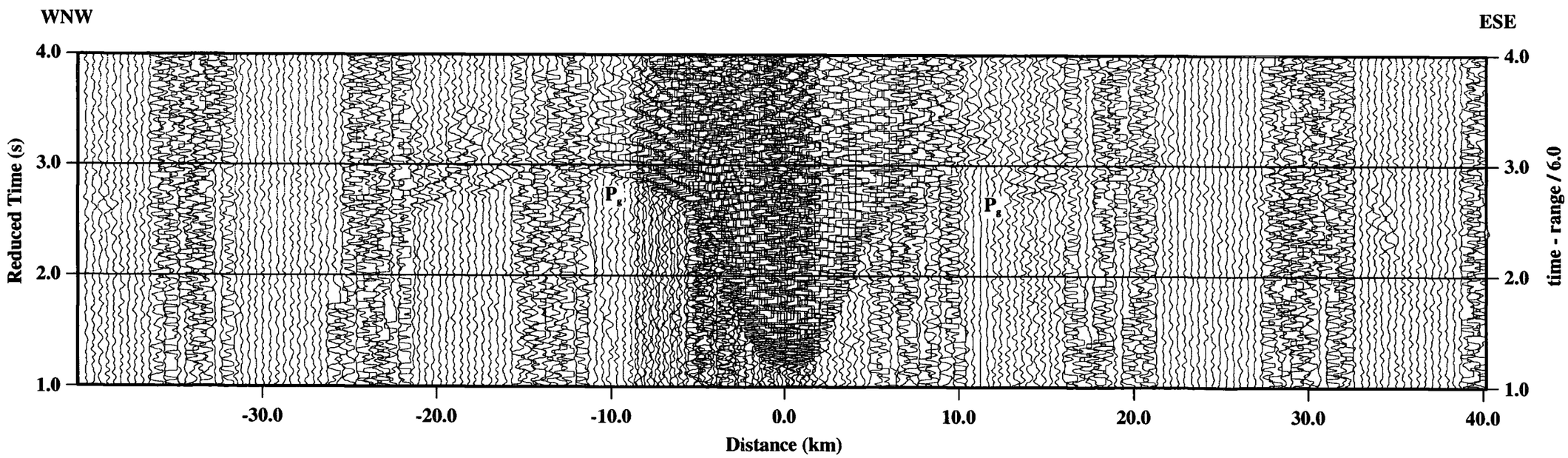

Figure 3.5: Hydrophone data from SDOBS4. Plotting parameters are described in figure 3.4. The SNR is poor compared with the vertical component geophone (cf. figure 3.4).
(a) Unfiltered record section clearly showing the noise generated from the hard disk spin during data transfer and an additional high frequency oblique banding (electrical interference?). Note that the obliqueness of the latter is artificial and is simply a function of the reduction velocity (i.e. horizontal banding on an unreduced record section).
(b) Record section filtered using a Hanning window low-pass filter with corner frequencies of 15 and 20 Hz. The large amplitude direct water wave (~0 km model offset) and upper crustal phases can be identified, but arrivals at greater offsets (cf. figure 3.4b) are less evident. The high frequency oblique banding has been filtered out, however the noise generated during data transfer has a frequency spectrum which extends into the frequency spectrum of the signal and thus has not been completely removed.

(a)

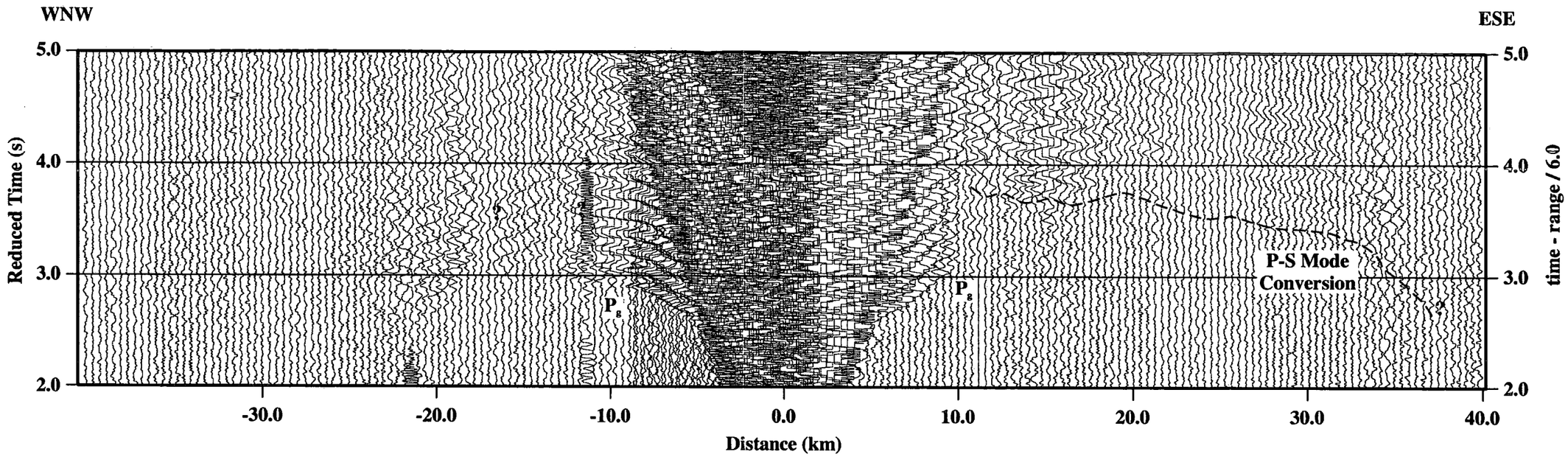

(b)

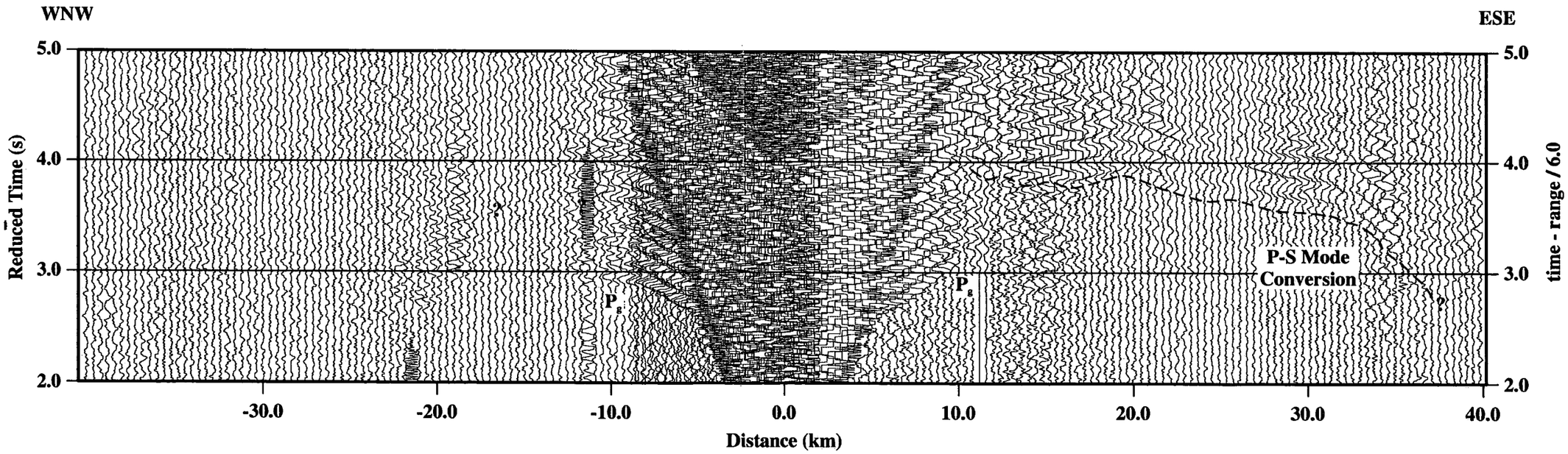

Figure 3.6: Filtered horizontal component geophone data from SDOBS4. Plotting and filtering parameters are described in figure 3.4. Note the different time scale (cf. figures 3.4 and 3.5).
(a) X-component record section. Direct water waves and upper crustal diving rays (at near offset) are observed as first arrivals. However, the most significant arrival is the P-S mode conversion (dashed line) at delay of ~0.8 s behind the first arrival (cf. figure 3.4b). Note that a similar mode conversion is not easily identified to the west of the instrument (i.e. west of the CVFR axis).
(b) Y-component record section. Direct water waves, upper crustal diving rays and a P-S mode conversion (dashed line) are observed as in part (a). Note that there is no significant delay in time between the P-S mode conversions identified on the X and Y-component geophone record sections.

3.3 Across-axis data sections

The main features of interest observed on the across-axis data sections (Line 1 and Line 6 - figure 2.1) are described below:

- The largest amplitude first arrivals, with the exception of the direct water wave, are the crustal diving rays (P_g) observed at near offset. At greater ranges mantle diving rays (P_n) are observed as low amplitude first arrivals (figure 3.7). The verification of this P_n phase was only possible after extensive ray-trace modelling and all observed first arrivals were thus assumed to be P_g phases until proven otherwise. First arrivals are observed up to a range of ~40 km and ~50 km on the across-axis profiles, Line 1 and Line 6 respectively.
- Large amplitude Moho reflections (P_mP) are observed as secondary arrivals on most instruments and include reflections from directly beneath the axial region (e.g. figure 3.8).
- There is considerable variation in the amplitude of the crustal diving rays with offset. Most of this amplitude variation is related to scattering of seismic energy at the seabed, although seabed topography does not account for all of the amplitude variations and some may be related to sub-surface features (see section 3.2.1). Many of these amplitude variations are spatially related to the ridge axis and this can be seen in figure 3.7 which shows considerable variation in P_g amplitude between 0 and 10 km model offset. This feature is described as a shadow zone and is one of the primary pieces of evidence for the existence of a low velocity zone at depth beneath the axis. There is a large reduction in amplitude of the first arrival between 2 and 3 km model offset and it is difficult to identify the P_g phase at model offsets greater than 3 km, due to the low SNR. A large amplitude arrival observed at >8 km model offset is identified, following detailed ray-trace modelling, as a reflection from the Moho beneath the axis (see figure 3.8 also). The significance of this arrival and the shadow zone will be discussed in detail later.

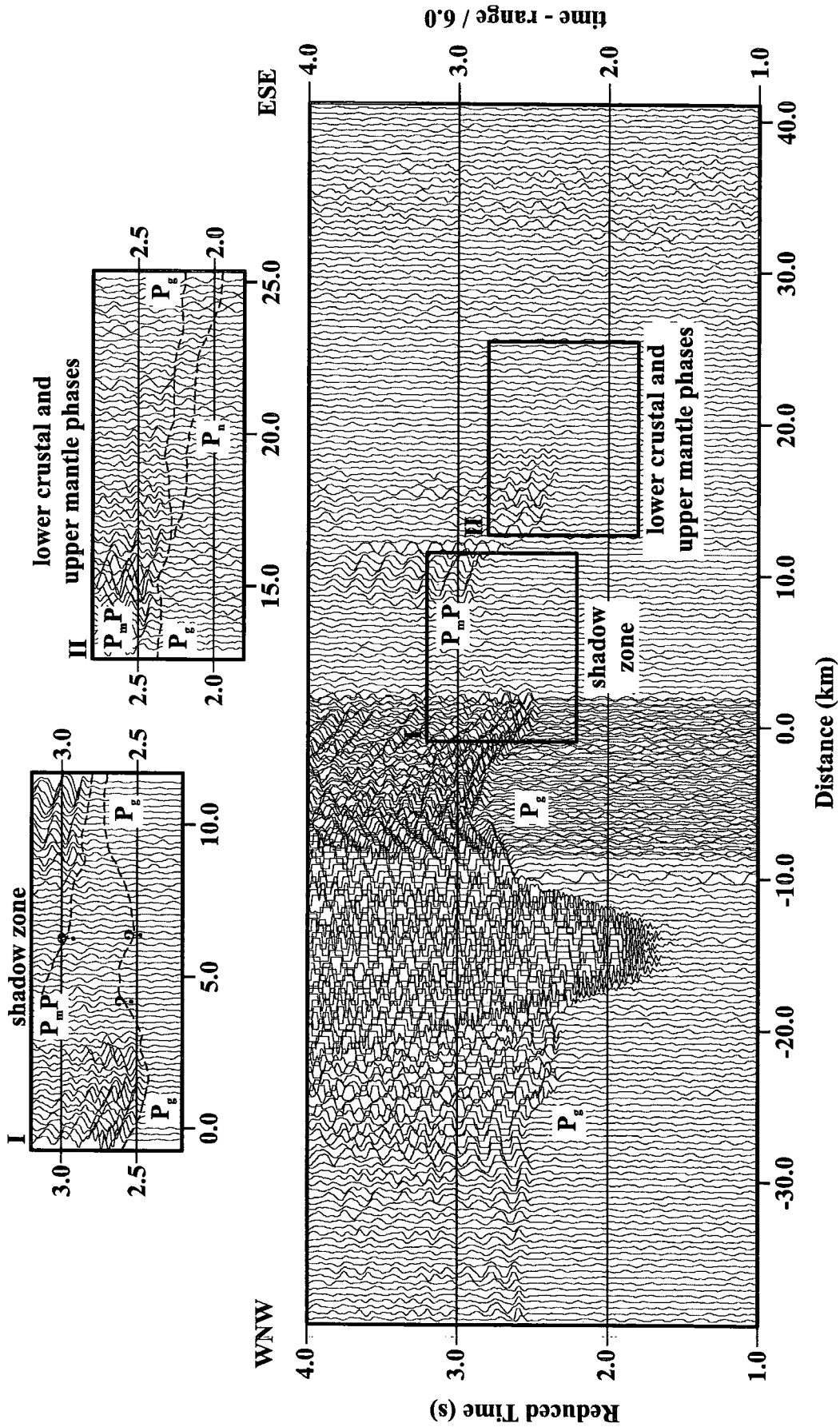

Figure 3.7: Filtered vertical component geophone data from SDOBS2 showing the main phases of interest. Plotting parameters are described in figure 3.4 and alternate traces are plotted. Insets I and II highlight regions of specific interest and every trace is plotted within these regions for greater trace-to-trace coherence.

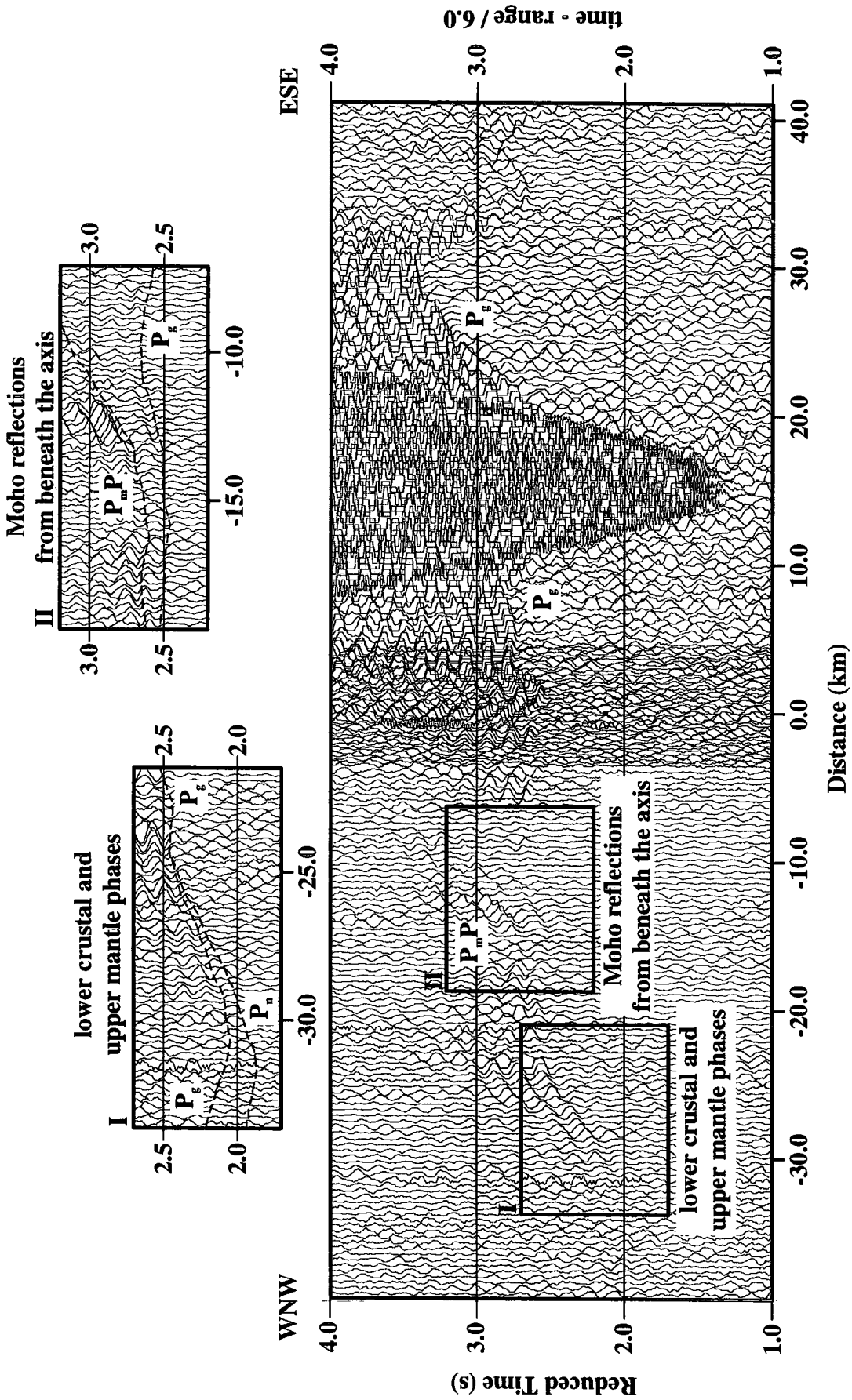

Figure 3.8: Filtered vertical component geophone data from NDOBS1 showing the main phases of interest. Plotting parameters are described in figures 3.4 and 3.7.

On closer inspection of the across-axis hydrophone data from SDOBS4 (figure 3.4), when displayed at a much lower gain, one further arrival can be observed. This arrival is a high amplitude, reversed polarity, intracrustal P-wave reflection (P_cP) observed directly beneath the instrument, with a delay of ~1.4 s behind the direct water wave (figure 3.9a). The source of this reflection is interpreted to be the top of an axial magma chamber. A similar, less distinct reflection can also be observed on Line 6 on the instruments situated in the overlap basin (figure 3.9b) and on the northern tip of the CVFR. The importance of this arrival will also be discussed in detail later.

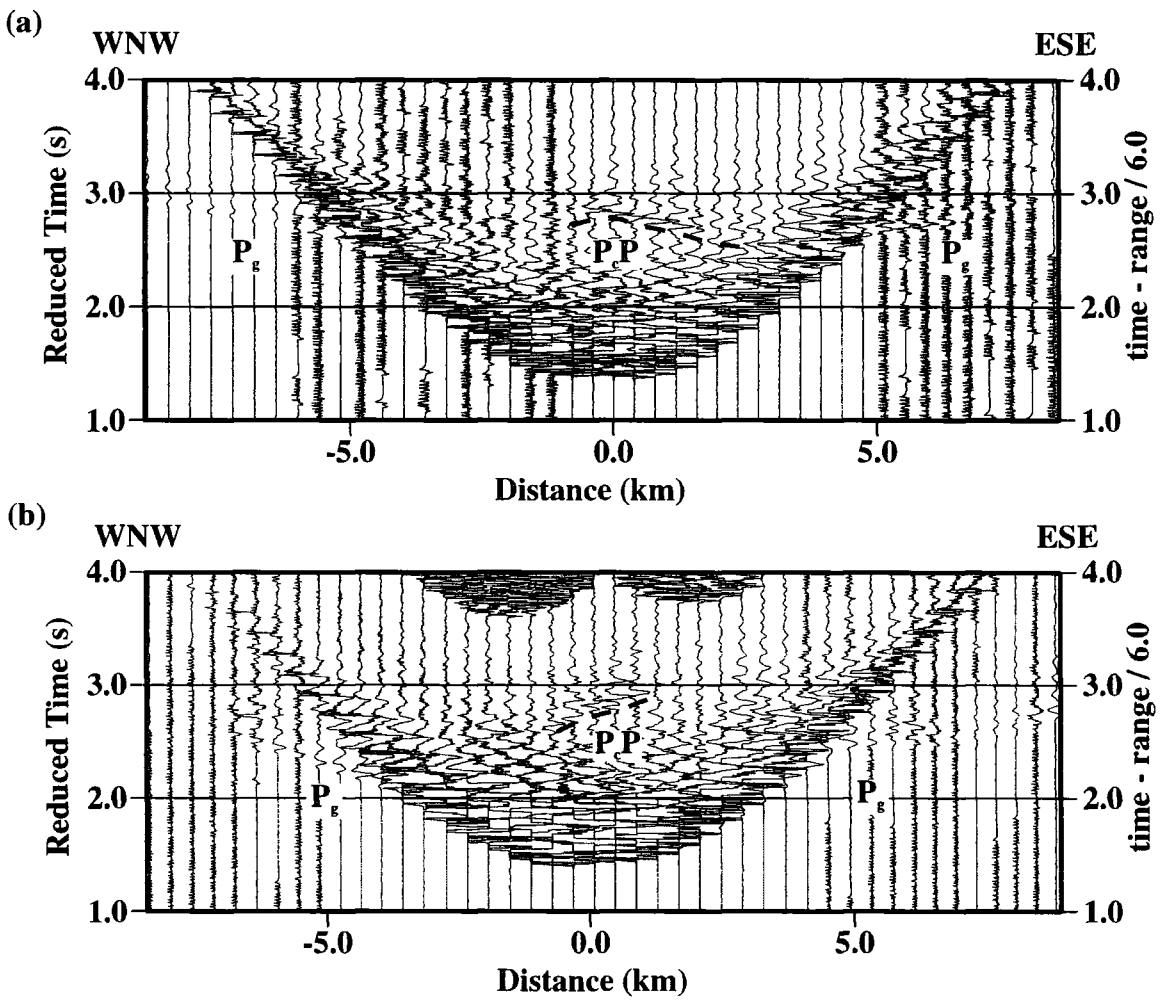

Figure 3.9: Detail from the unfiltered hydrophone data on the two across-axis profiles (Line 1 and Line 6). Plotting parameters are described in figure 3.4.
(a) Record section from SDOBS4 situated on the CVFR axis (see figure 2.1 for instrument location). The reversed polarity arrival located behind the direct water wave at ~2.5-2.8 s is generated by a P-wave reflection off the top of the magma chamber.
(b) Record section from NDOBS3 situated in the overlap basin at 22° 12′ S (see figure 2.1 for instrument location). A similar arrival to the one identified in part (a) is observed behind the direct water wave at ~2.6-2.9 s.

3.4 Along-axis data sections

The main features of interest observed on the along-axis data sections (Line 4 and Line 9 - figure 2.1) are described below:

- Dominant first arrivals on the along-axis data sections are the crustal diving rays (P_g), which are observed at ranges of >3 km (at ranges of <3 km the direct water wave is the first arrival and swamps the P_g phase). However, a large reduction in amplitude of the P_g phase is observed at ~15 km (e.g. figure 3.10) and this phase cannot be identified, above the level of noise, on any of the along-axis profiles at greater ranges.
- No mantle diving rays or Moho reflections are observed on the along-axis data sections.

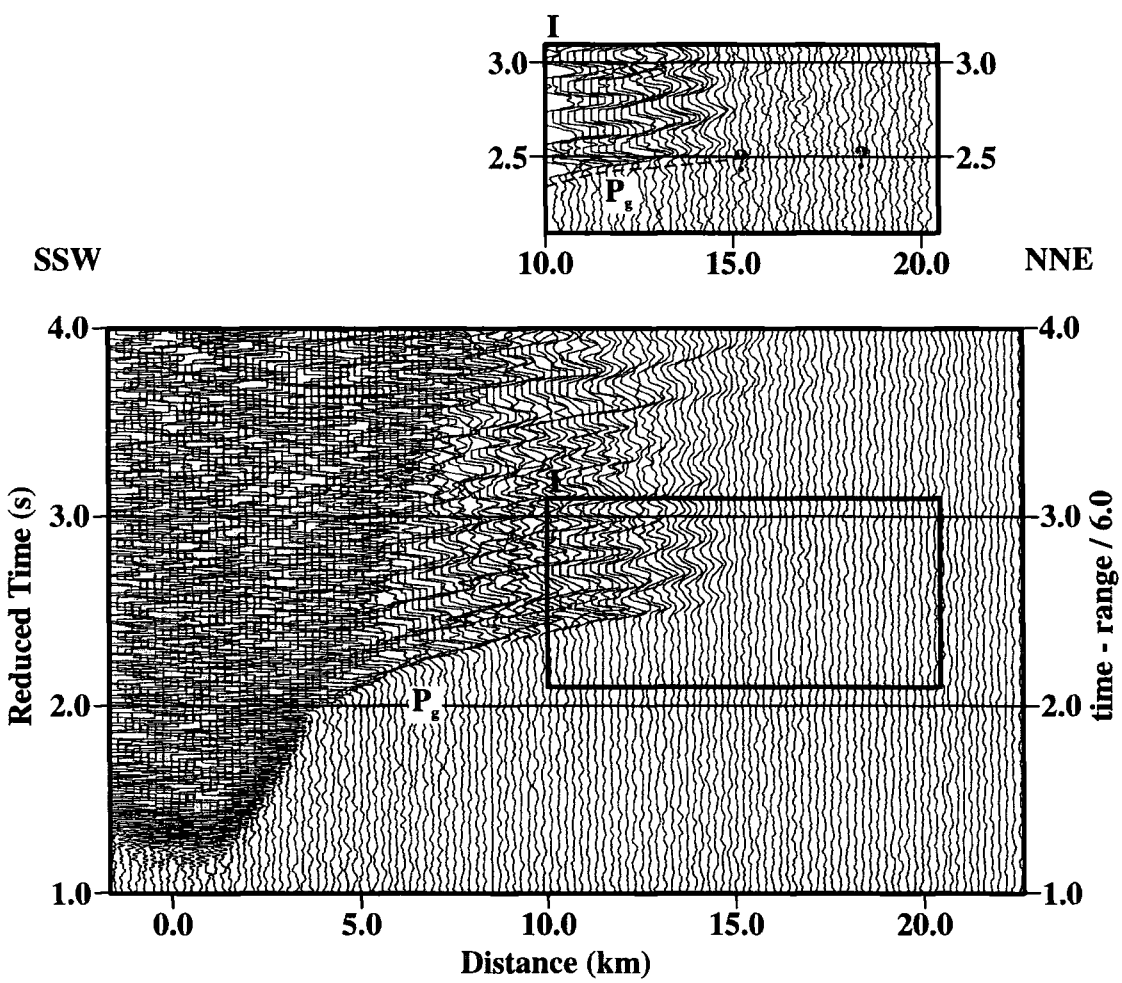

Figure 3.10: Filtered vertical component geophone data from SDOBS4 (Line 4 - along-axis record section). Plotting parameters are described in figure 3.4. Note the significant reduction in amplitude of arrivals at a range of ~15 km. No arrivals are observed, above the level of noise, at ranges greater than 15 km. Inset I shows the dramatic reduction in amplitude at ~15 km. A continuation of the P_g arrival cannot be identified above the noise level even at a higher gain.

- Along-axis data from instrument SDOBS4, situated at the southern end of the CVFR (see figure 2.1), are shown in figure 3.11 and a unique pair of phases are identified. A reversed polarity P_cP phase observed on several of the across-axis record sections (e.g. figure 3.9), interpreted to be a reflection from the top of a magma chamber, is again clearly observed on the along-axis hydrophone data (figure 3.11a). However, the amplitude of the trailing edge of the direct water wave is too large on the vertical component geophone data for the P_cP phase to be observed, but a lower frequency phase is identified at ~3.5 s (figure 3.11b). This phase is also clearly observed on the two horizontal geophone component record sections (figure 3.11c), but is not observed on the hydrophone data. Ray-trace modelling suggests that this arrival is the result of a P-S mode conversion on reflection at the top of a magma chamber (P_cS), which would explain the clear observation of this phase on the horizontal component geophone data, but absence from the hydrophone data. The significance of the P_cP phase and the P_cS phase will be discussed in detail later.
- The P_cP phase is observed out to a range of ~2 km, whereas the P_cS phase is observed out to a range of ~5 km. However, there is a distinct reduction in amplitude of the P_cS phase at near offset (ranges of <1 km).

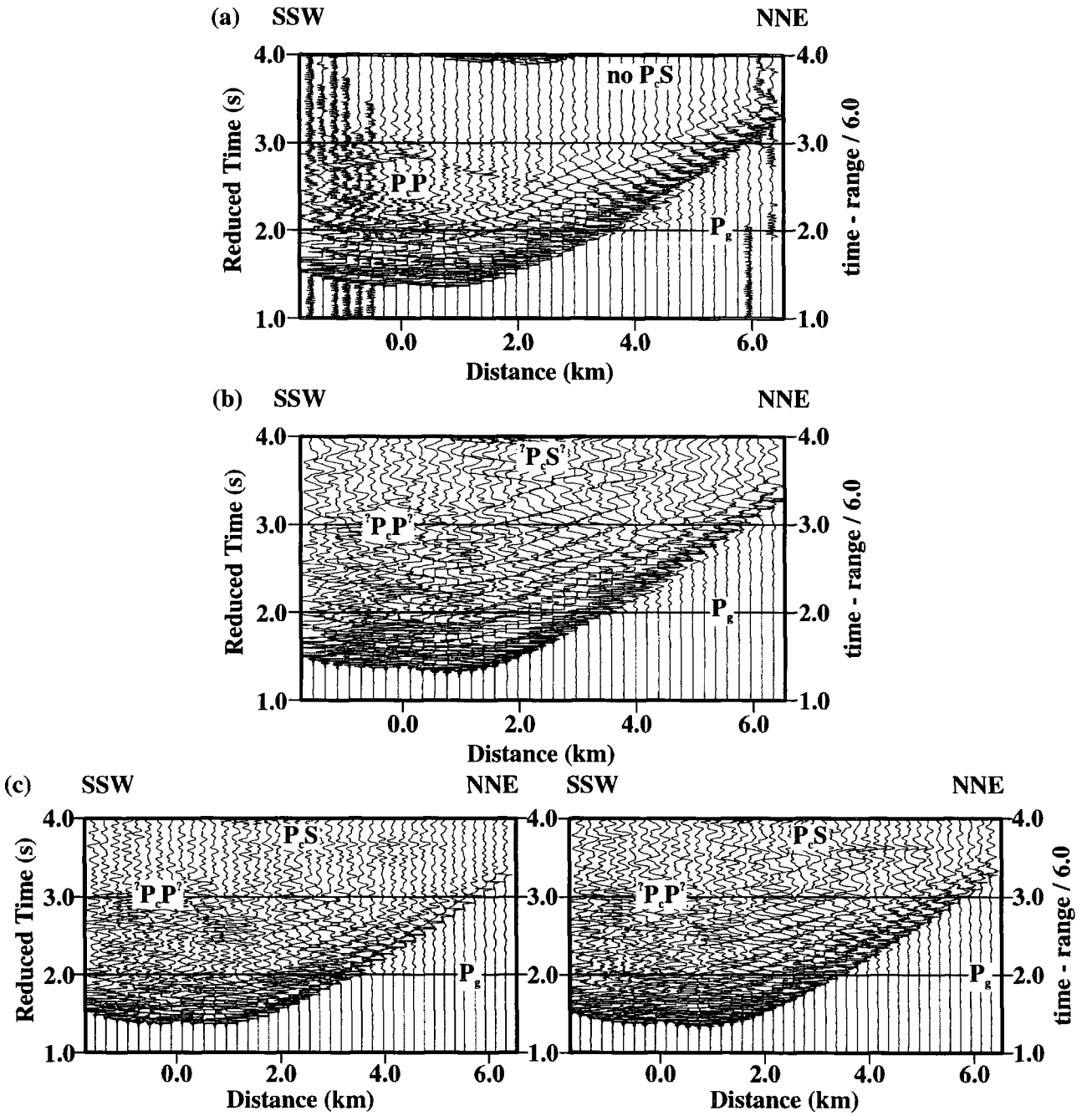

Figure 3.11: Along-axis record sections from SDOBS4, situated at the southern end of the CVFR axis (see figure 2.1) showing the crustal diving ray (P_g) and two further phases observed behind the high amplitude direct water wave. The reversed polarity P_cP phase is interpreted to be a P-wave reflection from the top of an axial magma chamber and the P_cS phase is interpreted to be a P-S mode conversion on reflection at the same interface. Plotting parameters are described in figure 3.4.

(a) Unfiltered hydrophone data. Note the reversed polarity P_cP phase at ~2.8 s, observed out to a range of ~2 km, and the absence of the second P_cS phase.

(b) Unfiltered vertical component geophone data. The P_cP phase is swamped by the high amplitude trailing edge of the direct water wave, but a lower frequency P_cS phase is observed at ~3.5 s.

(c) Unfiltered horizontal component geophone data. The P_cS phase can be clearly identified at ~3.5 s on both orthogonal components. Note the reduction in amplitude of this phase at ranges of <1 km.

3.5 Axis-parallel data sections

The main features of interest observed on the axis-parallel data sections (Line 5 and Line 11 - figure 2.1) are described below:

- Crustal diving rays (P_g) are again observed as the dominant first arrival up to a range of ~30 km (the maximum offset of any of the axis-parallel lines), with considerable variation in amplitude with offset (figure 3.12). However, the majority of the reductions in amplitude are caused by scattering of seismic energy on severe seabed topography (e.g. figure 3.12: between 13 and 19 km model offset with the position of the seamount on Line 5 - figure 2.1). The maximum shot-receiver range of the axis-parallel lines of ~30 km is too short (cf. figure 3.7) to observe mantle diving rays (P_n).
- Moho reflections (P_mP) are observed as large amplitude secondary arrivals at ranges of >20 km (e.g. figure 3.12: between 0 and 10 km model offset).

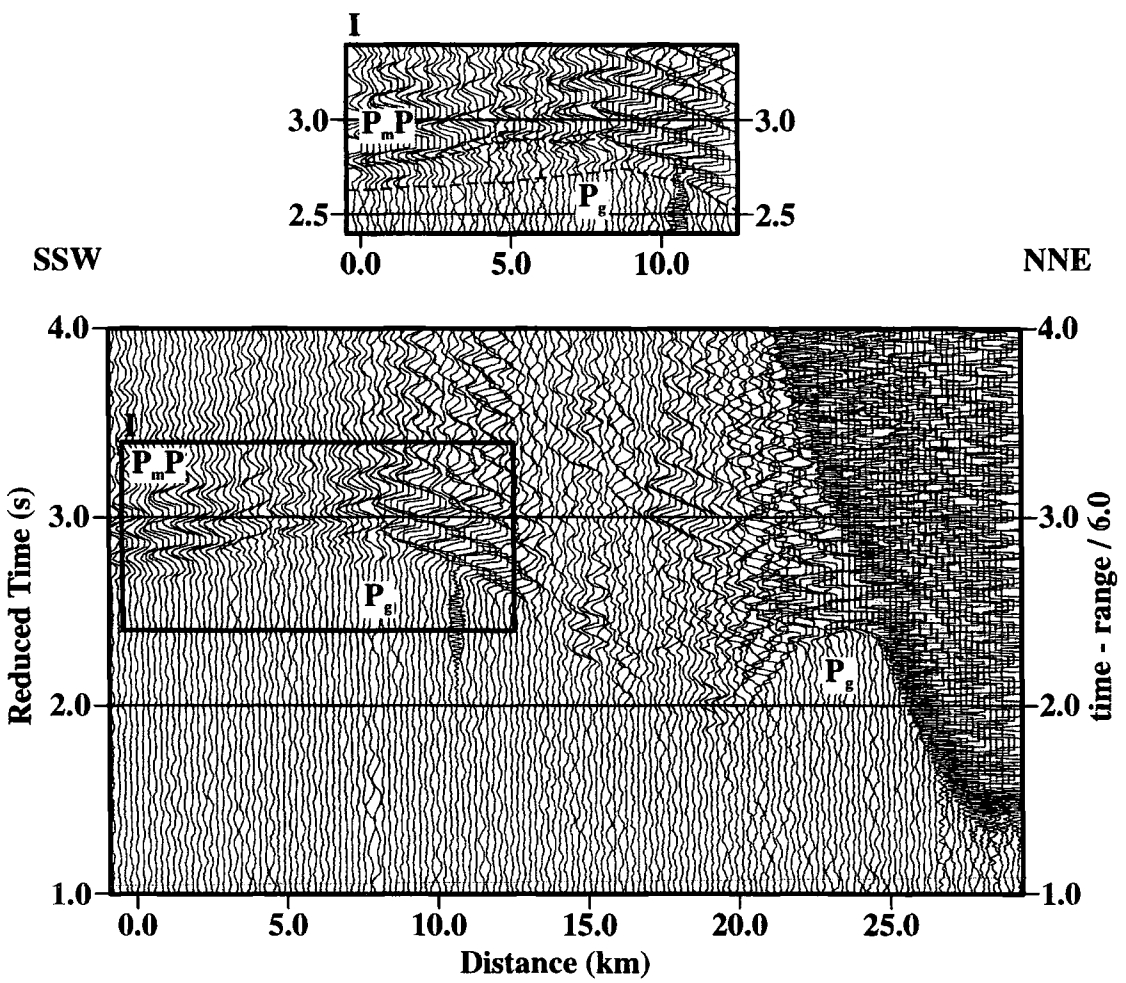

Figure 3.12: Filtered vertical component geophone data from NDOBS6 (axis-parallel record section) showing the main phases of interest. Plotting parameters are described in figure 3.4. Inset I shows the high amplitude Moho reflection (P_mP) as a secondary arrival behind the crustal diving ray (P_g).

3.6 Summary

In this chapter example 2-D profiles from the EW9512 wide-angle seismic dataset and a description of the main phases of interest have been presented. Details of the frequency content of these phases of interest and the background noise have also been described to determine suitable corner frequencies for the filtering of the wide-angle seismic data. However, filtering was only performed for display purposes and travel time picks, for use in the modelling process, were made on unfiltered hydrophone and geophone data. The travel time and amplitude modelling of this dataset is presented in Chapter 4.

Chapter 4

Modelling of the wide-angle seismic dataset

4.1 Introduction

The results of modelling of the wide-angle seismic dataset are described in this chapter. The wide-angle seismic dataset consists of two across-axis, two along-axis and two axis-parallel profiles (see figure 2.1), and initial models and best fitting velocity-depth models, with a description of the modelling method, are presented in this chapter. The results generated from alternative modelling programs are also discussed.

4.2 *Seismic South* across-axis profile - Line 1

Line 1 is the southernmost across-axis profile, which crosses the CVFR at 22° 26′ S, 176° 42′ W. This profile was chosen first for modelling as complete datasets from all six DOBSs were available to help constrain the crustal model and it potentially had the simplest axial structure (i.e. no OSC).

4.2.1 Initial model

An initial seismic model was constructed along the entire 80 km length of Line 1 and projected down to 20 km below the sea surface. The initial model consisted of a water column, an upper and lower crust and part of the upper mantle.

Sound velocity dip (SV dip) data (see section 2.3.3) were used to provide an estimate of the velocity and hence velocity gradient of the water column over the entire work area. The seabed depths were extracted from the centre beam depths of the underway Hydrosweep data and combined with the SV dip data to generate the seawater layer of the initial model. To decrease the number of nodes in the model and optimise computation time of the ray-tracing, the seabed depths, originally at ~150 m intervals, were downsampled into 250 m, 500 m and 1 km data files. The files were then merged to provide a dataset containing the minimum number of points that faithfully reproduced

the seafloor topography without significantly affecting the propagation paths of the traced rays.

The VFR is a relatively unsedimented ridge and thus a sedimentary layer was not incorporated into the initial model. However, it was evident from the coincident normal incidence seismic data that a small, isolated sediment pond was located in the basin east of the ridge (~10 km model offset) and this was incorporated into the model during the early stages of ray-trace modelling. Estimates of sediment velocities were extracted from previous DSDP and ODP results in the Lau Basin (site 203 at 22° 09′ 13″ S, 177° 32′ 46″ W - Shipboard Scientific Party leg 21, 1973; site 840 at 22° 13′ 15″ S, 175° 44′ 55″ W - Shipboard Scientific Party leg 135, 1992). The normal incidence seismic data provided an initial estimate of the sediment thickness.

One-dimensional, slope intercept, travel time inversions of the data recorded by each DOBS were carried out to obtain an initial estimate of the crustal structure adjacent to each instrument. The results of these inversions were then combined with previous studies of the oceanic crust (e.g. Spudich and Orcutt, 1980; Bratt and Purdy, 1984; Solomon and Toomey, 1992; White *et al.*, 1992; Kappus *et al.*, 1995) to generate a 2-D velocity-depth model of the crust and upper mantle.

The complete initial model for Line 1 (figure 4.1) consisted of five layers with 126 nodes on each layer and is described below. All velocities described are P-wave seismic velocities and model depths are indicated as the depth below the sea surface.

The water column is split by two second-order boundaries (i.e. a change in the velocity gradient, but no velocity step across the boundary) to reproduce the large thermocline observed in the sound velocity dip data. The seismic velocity at the sea surface is 1.533 km s^{-1}. Second-order boundaries are incorporated into the model at 0.6 km (velocity of 1.49 km s^{-1}) and 1.1 km (1.481 km s^{-1}) and the velocity directly above the seabed is modelled to be 1.50 km s^{-1} (independent of the depth to the seabed). The seabed is represented by a first-order boundary between the water column and layer 2.

The remainder of the initial model represents the top 10 km of the crust and mantle. Four layers, each with differing velocity gradients were assigned to the crustal layers 2A, 2B/C and 3 and the upper mantle, as described in Bratt and Purdy (1984) and Solomon and Toomey (1992). Due to the lack of any off-axis, intracrustal reflections layer interfaces were modelled as second-order boundaries, with the exception of the boundary between the crust and the upper mantle.

- The 4.5, 6.5 and 6.9 km s^{-1} isovelocity contours divide the initial model into the four layers described above.
- The velocity at the top of layer 2A is 2.5 km s^{-1} (i.e. a velocity step of 1.0 km s^{-1} across the seabed) and the second-order boundary between layer 2A and layer 2B (4.5 km s^{-1} isovelocity contour) is situated at a constant depth of 3.8 km off-axis. Beneath the axial region, the layer 2A/2B boundary gradually increases in depth to a maximum of 4.05 km (figure 4.1: 0 km model offset). The vertical velocity gradient within layer 2A is influenced by the considerable range in depths to the seabed (i.e. top of layer 2A), but is on average 1.45 s^{-1}.

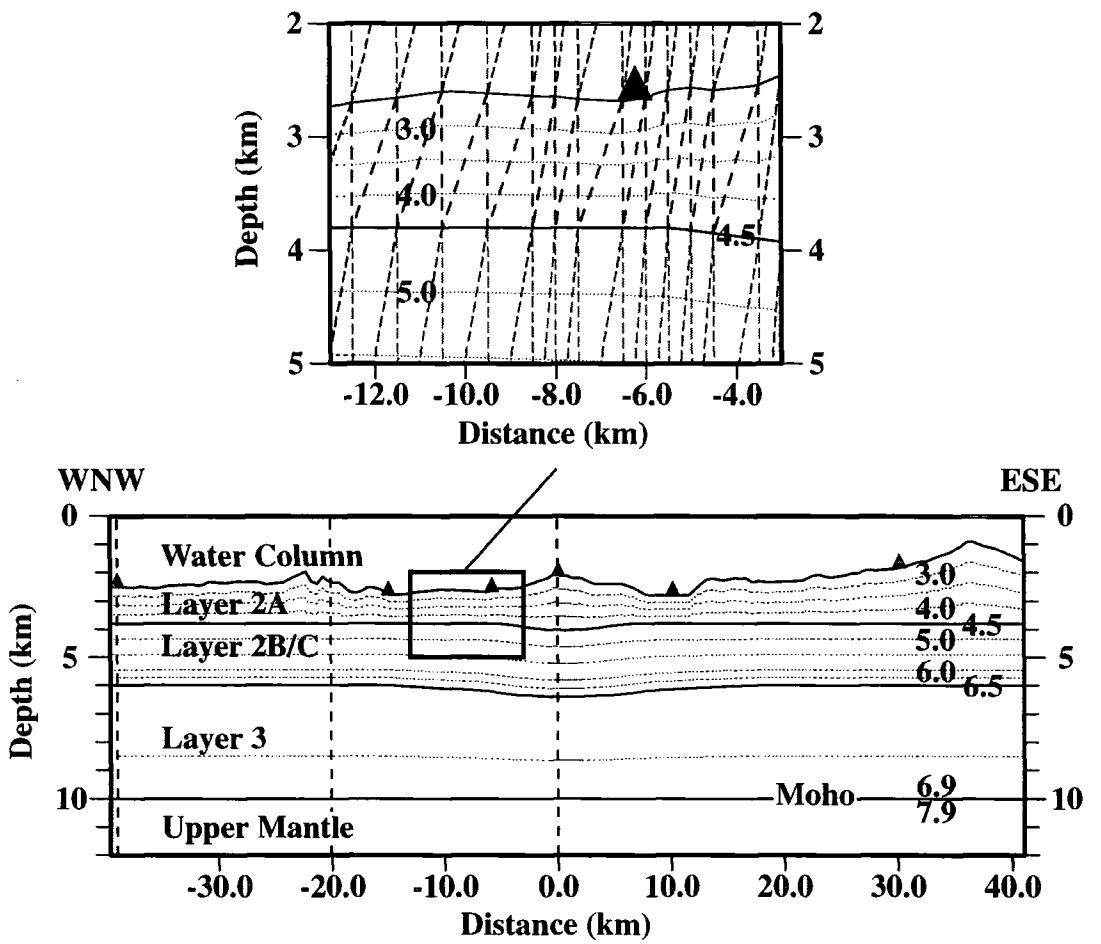

Figure 4.1: Line 1, across-axis initial model. Inset shows the construction of the initial model in the vicinity of one of the DOBS with triangle corners representing the velocity nodes of the initial model. The velocities are linearly interpolated between the nodes to create a 2-D model. Solid lines indicate the location and geometry of the seabed, layer 2A/2B boundary, layer 2/3 boundary and the seismic Moho. Dotted lines represent the 3.0, 3.5, 4.0, 4.5 (layer 2A/2B boundary), 5.0, 5.5, 6.0, 6.25, 6.5 (layer 2/3 boundary) and 6.75 km s^{-1} isovelocity contours. DOBS locations are indicated by triangles and intersection points with along-axis and axis-parallel profiles (cf. figure 2.1) are marked by vertical dashed lines. Vertical exaggeration x2.5.

Asymptotic ray theory is based on an approximation to the wave equation and is widely used to describe body waves in homogeneous media, in which lateral and vertical variations are smooth on the scale of a seismic wavelength. ART fails at caustics, shadows, critical points, etc. where the media is not smooth (Navin, 1996), hence ART is generally combined with transform methods (e.g. WKBJ, Gaussian beams, Kirchoff integrals, etc.) to investigate waves at these singular points

***Maslov* modelling technique (after Chapman and Drummond, 1982)**

The program *maslov* (originally written by R. Drummond op. cit., and rewritten by D.G. Lyness, in a modular form, and S. Horsefield, to run under UNIX using the UNIRAS graphics package) is based on *Maslov* ray theory. *Maslov* ray-tracing technique combines ART with WKBJ seismograms to obtain a uniform solution. Normal ART calculates the wave solution in just the spatial domain, however the WKBJ transform solution determines the amplitude in the spatial domain and in the mixed (position and slowness) domain. Singularities in the spatial and mixed domains are known as x-caustics and y-caustics respectively (Navin, 1996) and occur at different locations, hence by combining the solutions many singularities are overcome. A user-defined weighting between the ART and WKBJ solutions is designed to test for y-caustics (i.e. WKBJ solution breaks down) and the ART solution is thus used where these are likely to occur.

The model, used as input for *maslov*, is divided into triangles with linear velocity gradients along each side to facilitate the modelling of complex structures. The linear gradients within these triangles cause the ray to follow a circular ray path which is computationally efficient (Navin, 1996).

***Rayinvr* modelling technique (after Zelt and Smith, 1992)**

Rayinvr consists of a series of programs written by C.A. Zelt, which solve the ART equations numerically (Zelt and Smith, 1992) and is used here as an independent test on the synthetic seismograms calculated by *maslov*. The model is divided into a series of trapezoids with vertical left and right boundaries and linear velocity gradients along each side (cf. *maslov*). The program *vmodel* identifies crossing boundaries, velocity inversions and extremes of velocity and gradient. A smoothing option, using a three-point averaging filter, is available to reduce geometrical shadows due to steep gradients and smooth layer boundaries (cf. using transform methods [e.g. WKBJ] for these aspects of the model).

- Layer 2B/C, delineated by the 4.5 and 6.5 km s^{-1} isovelocity contours, is described with an average vertical velocity gradient of 0.91 s^{-1}. The second-order layer 2/3 boundary is located at a depth of 6.0 km, with a gradual increase in depth of 0.4 km into the axial region.
- The seismic Moho, located at a constant depth of 10.0 km below sea level at the base of layer 3, is marked by a first-order boundary with a velocity step of 1.0 km s^{-1} (representing the 'transition' between the lower crust and upper mantle). Layer 3 has a thickness of 4 km and a vertical velocity gradient of 0.10 s^{-1}.
- The velocity directly beneath the Moho is assigned as 7.9 km s^{-1} and the upper mantle has a constant vertical velocity gradient of 0.03 s^{-1} (White *et al.*, 1992). The model, though only shown down to a depth of 12.0 km in figure 4.1, extends down to 20.0 km.

4.2.2 Ray-trace modelling

Modelling of the wide-angle dataset was mainly carried out using the program *maslov* (based on the Maslov asymptotic ray theory of Chapman and Drummond, 1982). During the early stages of modelling the suitability of this approach was assessed, by comparing the resulting synthetic seismograms with those generated by *rayinvr* (Zelt and Smith, 1992). A summary of the results generated by *rayinvr* are described in section 4.6.1. There appeared to be no significant difference in the synthetic seismograms generated from both approaches, but *maslov* provided greater flexibility with the density of rays and their ray-paths and was more accommodating to the need for small distinct bodies, thus *maslov* was chosen as the primary modelling tool. Problems with ray-tracing artefacts often generated by *maslov*, when tracing through layers of complex geometry (e.g. end-point contributions; Thomson and Chapman, 1986) were minimised by the careful choice of ray-packet parameters. A detailed description of the *maslov* ray-tracing technique can be found in Chapter 4 (pp.146-148) of Navin (1996).

The results and conclusions drawn from ray-trace modelling of the initial model are described below and shown in figures 4.2 and 4.3. SDOBS2 (figure 4.2) and SDOBS5 (figure 4.3) were chosen to display the results of ray-trace modelling solely to show the maximum number of arrivals, including those whose ray-paths have turned beneath the ridge axis originating from shots located on both sides of the CVFR. Both observed and synthetic seismograms are plotted at true amplitude with a reduction

velocity of 6.0 km s^{-1}. Travel time picks, extracted from both the unfiltered hydrophone and geophone data sections are plotted as circles on the synthetic sections, with a radius equal to the minimum error observed on each data point (~40 ms), and plotted as crosses on the observed data section for reference. A small subset of the rays traced to generate the synthetic seismograms is also displayed.

- A significant time delay on observed arrivals at ~10 km model offset (e.g. figure 4.2b) suggests the need for an isolated region of low velocity in this basin, thus ray-trace modelling of the initial model provides additional evidence of the small sediment pond identified on the normal incidence seismic data (see section 4.2.1). SDOBS5 is located in this sediment basin and the calculated upper crustal diving rays (P_g) from this instrument arrive too early (~200 ms) confirming the existence of a zone of low velocities at this location.
- The travel time fits of near-offset crustal diving rays are markedly different on either side of the DOBSs (e.g. figure 4.2: -20 to -10 km model offset), implying that the depth to the layer 2A/2B boundary varies considerably with model offset.
- Rays travelling beneath the axial region at mid-crustal depths have significantly shorter travel times than those observed, which indicates that the seismic velocities in the initial model are too high (e.g. figure 4.3: -10 km model offset).
- The amplitude fit of the first arrivals is poor, in particular the amplitude of the synthetic lower crustal phases, which are too low. The relatively low modelled amplitude of the lower crustal phases suggests that the velocity gradient in layer 2 of the initial model is too high and/or the velocity gradient in layer 3 is too low.
- The 'shadow zone' observed between 3 and 8 km model offset in figure 4.2a (see also figure 3.8) is not reproduced in the synthetic data. However, the inclusion of lower velocities beneath the axial region at mid-crustal depths would help decrease the amplitude of the rays travelling through this region. The attenuation structure of this lower velocity region may also be different.
- Large amplitude arrivals observed at far offset (e.g. figure 4.3: -20 to -10 km model offset) may indicate the presence of different phases (e.g. Moho reflections) not traced during the initial stages of modelling.

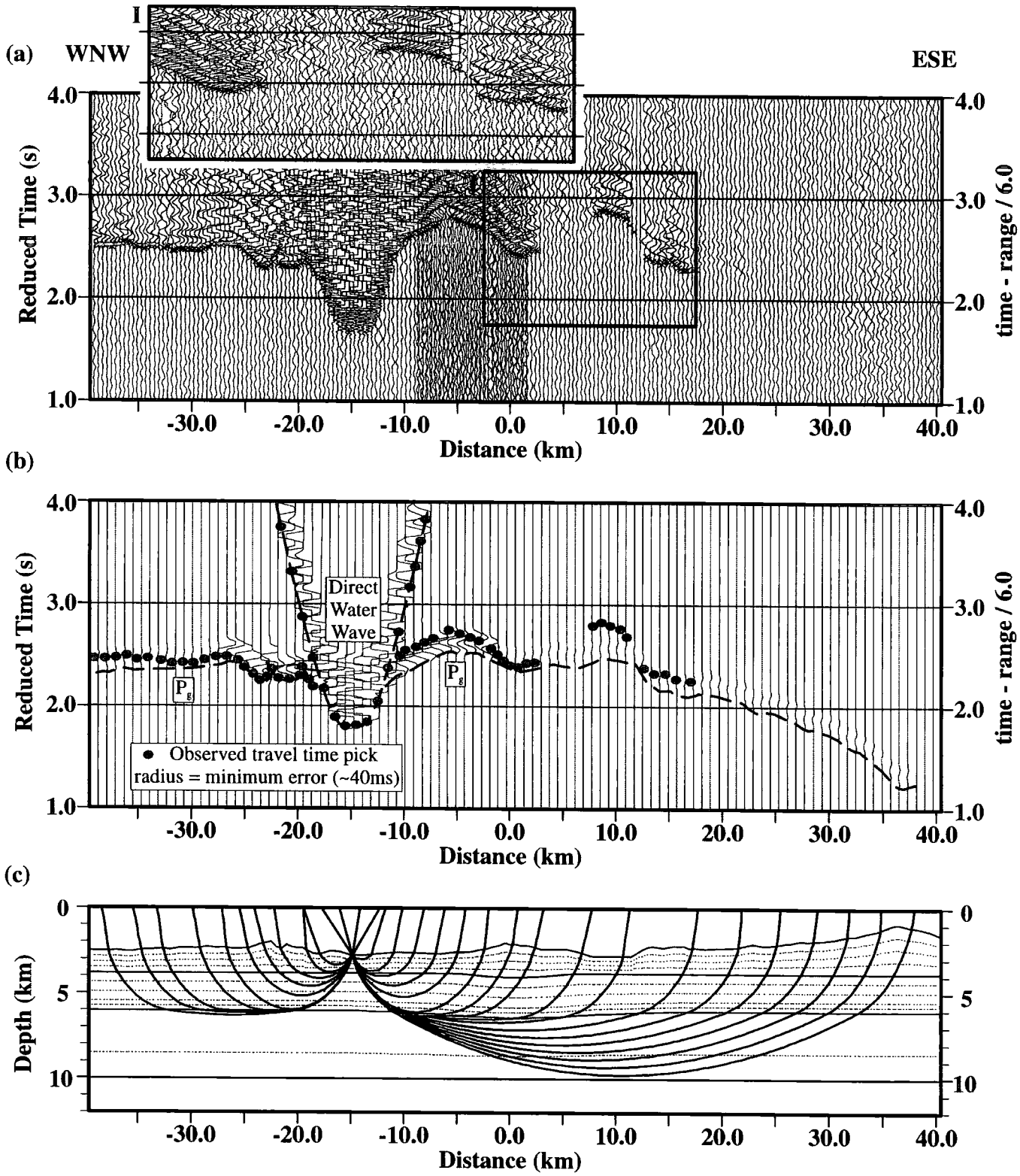

Figure 4.2: Ray-trace modelling of the initial across-axis seismic model for SDOBS2 on Line 1 (see figure 2.1 for instrument location).

(a) Filtered vertical component record section plotted at true amplitude to show the amplitude variations of the first arrivals. Plotting parameters are described in figure 3.4 and travel time picks are represented by crosses. Inset I displays the lower crustal and upper mantle phases in greater detail.

(b) Synthetic seismograms calculated from the initial model. The geometrical ray-traced solution is shown by a long-dashed line and crustal diving rays (P_g) and direct water waves are annotated. Travel time picks from the observed data are shown by solid dots [cf. crosses in (a)], where the dot size is equivalent to the travel time error.

(c) Initial model with, for clarity, a subset of the rays used to calculate the synthetic seismograms shown in (b). Display parameters are described in figure 4.1.

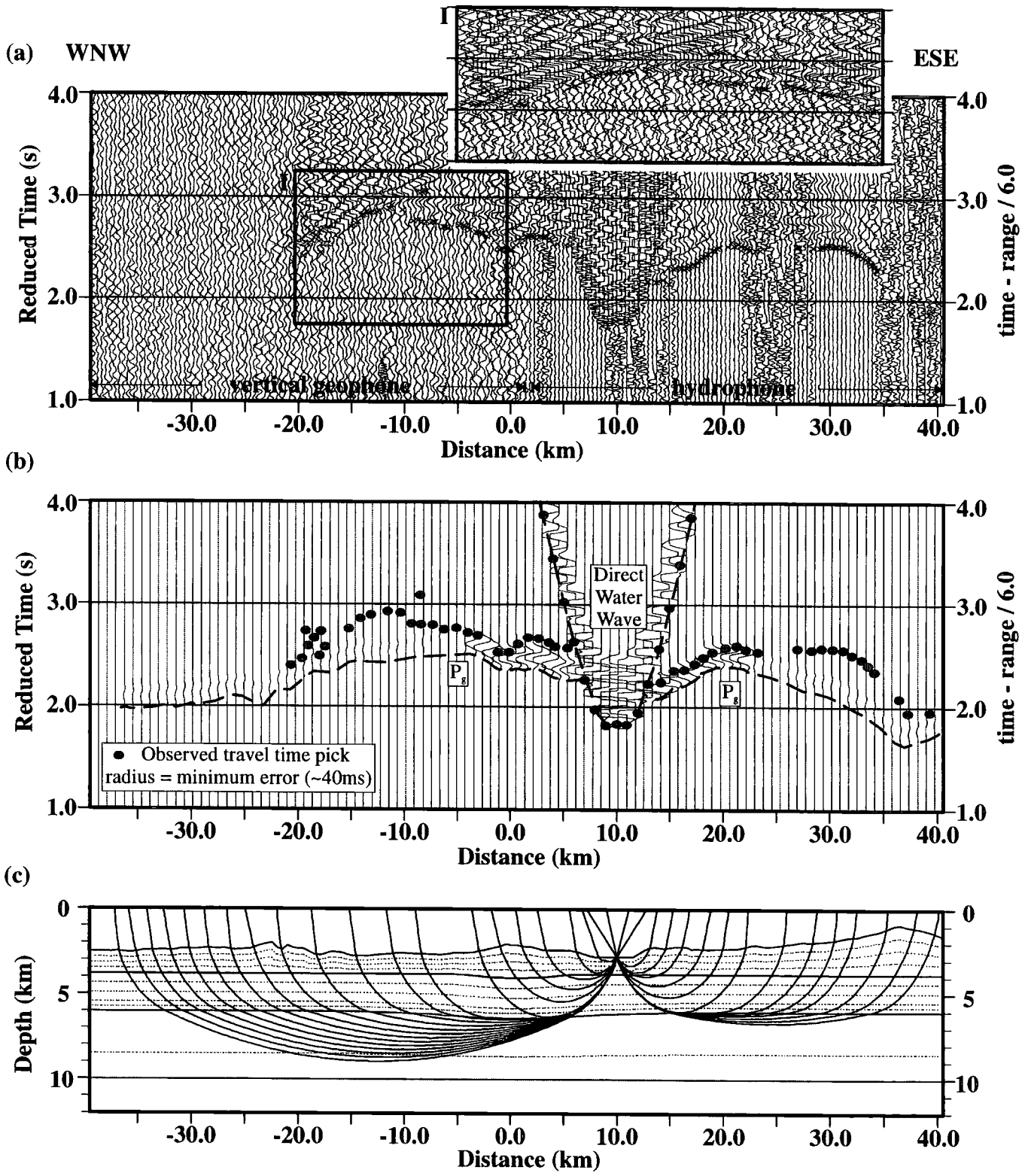

Figure 4.3: Ray-trace modelling of the initial across-axis seismic model for SDOBS5 on Line 1 (see figure 2.1 for instrument location).

(a) Filtered vertical component (-39 to 2 km model offset) and hydrophone (2 to 41 km model offset) record section plotted at true amplitude to show the amplitude variations of the first arrivals. The two components are shown here on one 'hybrid' record section as data were not recorded on the vertical geophone for the eastern end of Line 1 (see section 2.4). Display parameters are described in figure 4.2a. Inset I shows the larger amplitude Moho reflection as a secondary arrival behind the lower crustal phase.

(b) Synthetic seismograms calculated from the initial model. Display parameters are described in figure 4.2b.

(c) Initial model with, for clarity, a subset of the rays used to calculate the synthetic seismograms shown in (b). Display parameters are described in figure 4.1.

Modelling proceeded using a trial and error approach by ray-tracing the model, evaluating the travel time and amplitude fit of the synthetics with the observed data, adjusting the model accordingly and re-ray-tracing (Peirce, 1990). To prevent bias towards any one DOBS all instruments were modelled simultaneously, working down through the crust and into the upper mantle layer by layer. The modelling strategy is outlined below:

1) The direct water waves and their water column multiples were modelled to check that the locations of each instrument were correct (see figure 2.5). The initial locations (estimated from the deployment position) were adjusted when necessary until they were consistent with the seismic data.
2) Near-offset upper crustal phases were then modelled to constrain the upper crustal structure.
3) Once the upper crust, generally the most variable feature of a constructive ridge, had been modelled, the lower crustal and upper mantle phases were modelled.

At every stage of the modelling process both the travel time and amplitude fit of the synthetic and observed data were assessed. All arrivals were assumed to be crustal diving rays (P_g) until proven otherwise. However, detailed ray-trace modelling identified the existence of Moho reflections (P_mP) as large amplitude secondary arrivals (e.g. figure 4.3a: 10 km model offset) and mantle diving rays (P_n) on several instruments.

The model resolution outlined below was calculated by changing the velocity and depth of different interfaces within the model and determining whether the change in travel time (and amplitude) was significant. Variations in the velocity and the depth of crustal boundaries of 0.05-0.1 km s^{-1} and 50-150 m were considered sufficient to cause a reduction in the quality of the synthetic fit. The vertical resolution at the depth of the Moho was estimated to be ~250 m and the velocity directly beneath the Moho was constrained to ±0.1 km s^{-1}, but 'local' velocity variations within the upper mantle (e.g. lower velocities below the axis) cannot be resolved due to the limited number of observed mantle diving rays. The model resolution for the other profiles described in this chapter is similar to that described above, although the resolution in the lower crust is poor on the along-axis and axis-parallel lines as a consequence of the lack of turning rays at lower crustal depths (profile length <30 km).

4.2.3 Best fitting wide-angle seismic model

The final wide-angle seismic model for Line 1 is shown in figure 4.4. The layering described in the initial model (section 4.2.1) remains in the final model, with the addition of sediment where appropriate, and is thus divided into six layers (water column, sediment, layer 2A, layer 2B/C, layer 3 and upper mantle).

The profile may also be split into five distinct lateral regions:

1) pre-rift back-arc crust (WNW end of the model to -21 km model offset)
2) pre-rift island arc crust (22 km to ESE end of model)
3) post-rift VFR-generated material (-14 to 14 km)
4) post-rift material: axial region (-2 to 3 km)
5) transition zones (-21 to -14 km and 14 to 22 km)

Note that the lateral extents of these regions are entirely subjective and are predominantly based on where layer 2 thins considerably into the transition zones (region 5). The division of the model into the five regions described above and their geological implications will be discussed in greater detail in Chapter 6.

Previous normal incidence studies of the VFR (Morton and Sleep, 1985; Collier, 1990; Collier and Sinha, 1990 and 1992b) observed a high amplitude intracrustal reflection, which was interpreted to be a reflection off the top of a magma chamber (MCR). Careful investigation of travel times and amplitudes against offset in the EW9512 wide-angle seismic data suggested the presence of a zone of depressed seismic velocity within layer 3 beneath the axial region. A large amplitude, reversed polarity reflection was also observed approximately 1.4 s behind the direct water wave on SDOBS4 (figure 4.5a: 2.7 s reduced time, -1 to 2 km model offset), which confirmed the need for a small, isolated low velocity block beneath the axial region. Travel time modelling showed that this low velocity block must coincide with the top of the low velocity zone (i.e. a broad low velocity zone within layer 3 is overlain by a small isolated low velocity block, coincident with the layer 2/3 boundary). The wider implications of this feature will be discussed in Chapter 6.

The depth and geometry of the Moho were constrained by ray-trace modelling of the Moho reflection and upper mantle phases. The Moho is defined as a first-order boundary and could be constrained across the majority of the model. Synthetic and observed P_mP amplitudes match each other well and thus the Moho is interpreted as a sharp boundary, within the order of the vertical resolution at this depth (~250 m).

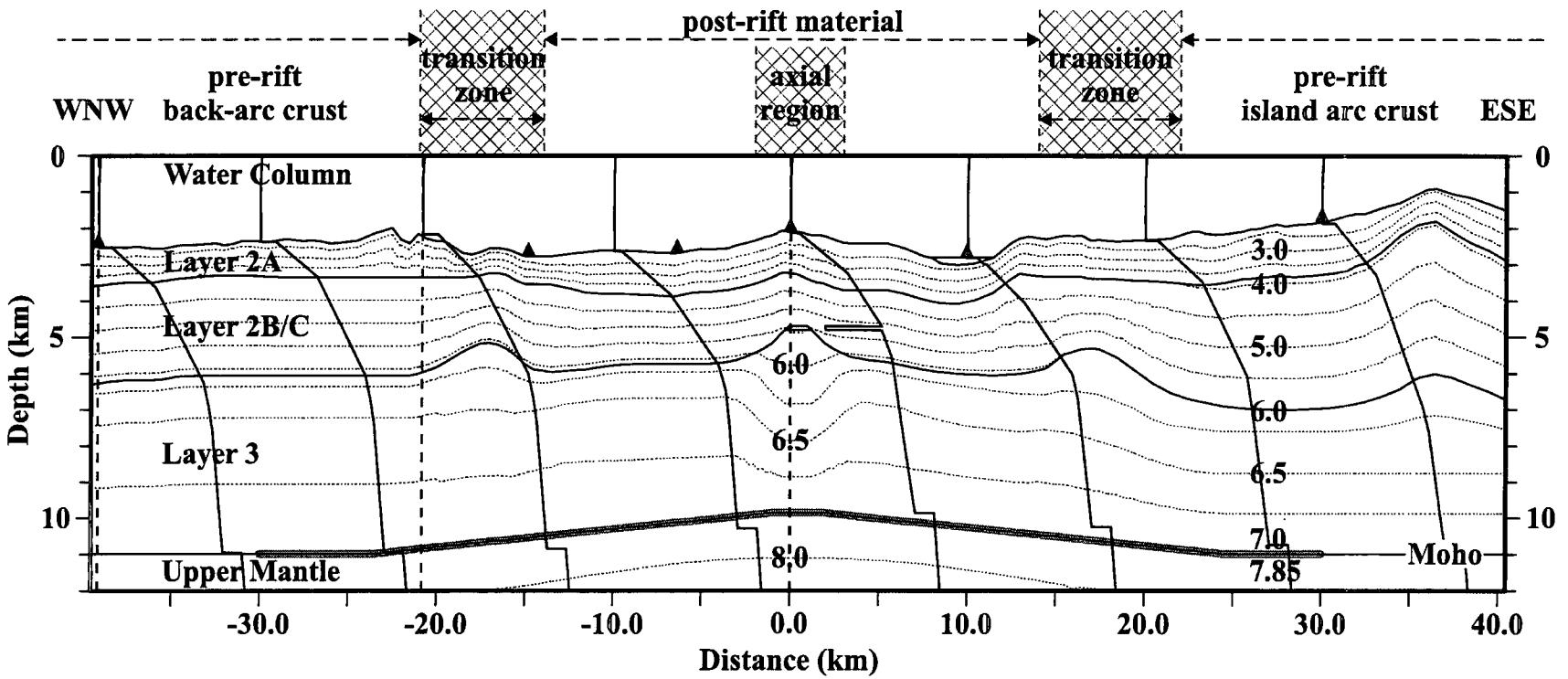

Figure 4.4: Line 1, across-axis final model. Solid lines indicate the location and geometry of the seabed, layer 2A/2B boundary, layer 2/3 boundary and the seismic Moho (constrained between -30 and 30 km model offset - thicker grey line). Note the sediment pond located at 10 km model offset. The model is also divided into five lateral regions (see text for details). Dotted lines represent the 2.5, 3.0, 3.5, 4.0 (layer 2A/2B boundary), 4.5, 5.0, 5.5, 6.0, 6.25, 6.5, 6.75, 7.0 (Moho) and 8.0 km s^{-1} isovelocity contours. DOBS locations are indicated by triangles and the intersection points with the along-axis profile (Line 4) and axis-parallel profiles (Line 5 and Line 11) are marked by vertical dashed lines (cf. figure 2.1). Velocity-depth profiles are calculated at ~10 km intervals. Vertical exaggeration x2. Note the lower velocities within layer 3 beneath the axial region and the low velocity block at a depth of ~5 km (c.f. notch in the velocity-depth profile at 0 km model offset). Note also the thinning of layer 2 into the transition zones and decrease in depth of the Moho in the post-rift region.

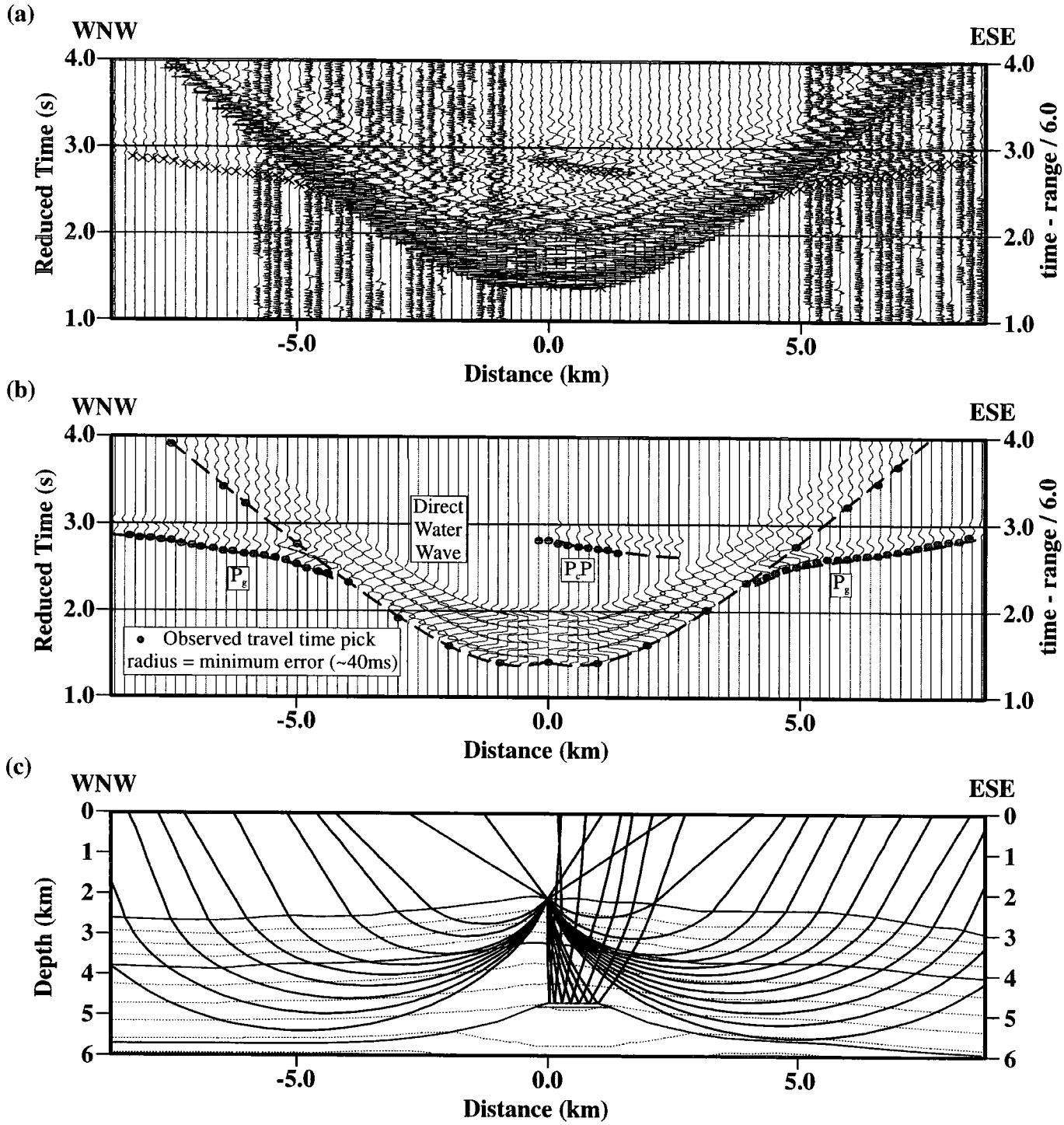

Figure 4.5: Ray-trace modelling of the final across-axis seismic model for SDOBS4 on Line 1 (see figure 2.1 for instrument location) showing a large amplitude, reversed polarity intracrustal reflection (P_cP) generated from the top of layer 3.

(a) Filtered vertical component record section plotted at true amplitude to show the amplitude variations of the first arrivals. Display parameters are described in figure 4.2a. Note the large amplitude P_cP arrival at 2.7 s (-1 to 2 km model offset).

(b) Synthetic seismograms calculated from the final model. Display parameters are described in figure 4.2b.

(c) Final model with, for clarity, a subset of the rays used to calculate the synthetic seismograms shown in (b). Display parameters are described in figure 4.1.

The final ray-trace modelled sections for SDOBS2 and SDOBS5 (see figure 2.1 for instrument locations) are shown in figures 4.6-4.7 and a complete set of final ray-trace modelled sections for Line 1 can be found in Appendix B. Display parameters are described in section 4.2.2 and summarised at the front of Appendix B.

The travel times of synthetic arrivals fit the observed data well within the error bounds (~40-50 ms) and amplitude variations with offset are also well matched. The main aim of the modelling process was to generate the simplest velocity model that would faithfully reproduce the observed arrivals, thus velocity gradients within layers are assigned simple linear functions. Minor differences in the amplitude of observed and synthetic phases coincide with rays that have travelled close to the second-order crustal boundaries of layer 2A/2B and layer 2/3. A good fit between the synthetic and observed arrivals could be achieved using sharp boundaries and the addition of transitional layer boundaries did not significantly improve the fit. However, the sharp change in gradient modelled at these interfaces may, in reality, be a more complex transition (e.g. layer 2A/2B boundary: interfingering of dykes and pillow lavas). Scattering effects generated from severe out-of-plane topography are not considered to be a major problem on Line 1, due to the approximate 2-D nature of the surrounding seabed (see figure 2.1).

The model is described here layer-by-layer for consistency, although layering of this nature does not strictly apply to the pre-rift island arc crust (region 2). All velocities described in the model are P-wave velocities and depths are described in km below the sea surface.

- The basin located at ~10 km model offset (see figure 4.4) is the only significant accumulation of sediment along this profile. SDOBS5 sits neatly above this sediment pond, but the lack of turning rays within the sediment (P_s) prevents the determination of sediment velocities with data from this instrument. Delay times of rays tracing through the basin from other instruments and data from other sources (normal incidence seismic and previous DSDP and ODP results) were used to estimate sediment properties. The basin, modelled with a maximum thickness of 200 m and an average velocity of 2.0 km s^{-1}, is thought to have originated from the north-south seamount chain at 176° 33′ W (figure 2.1) and this origin would also explain the lack of sediment to the west of the ridge.

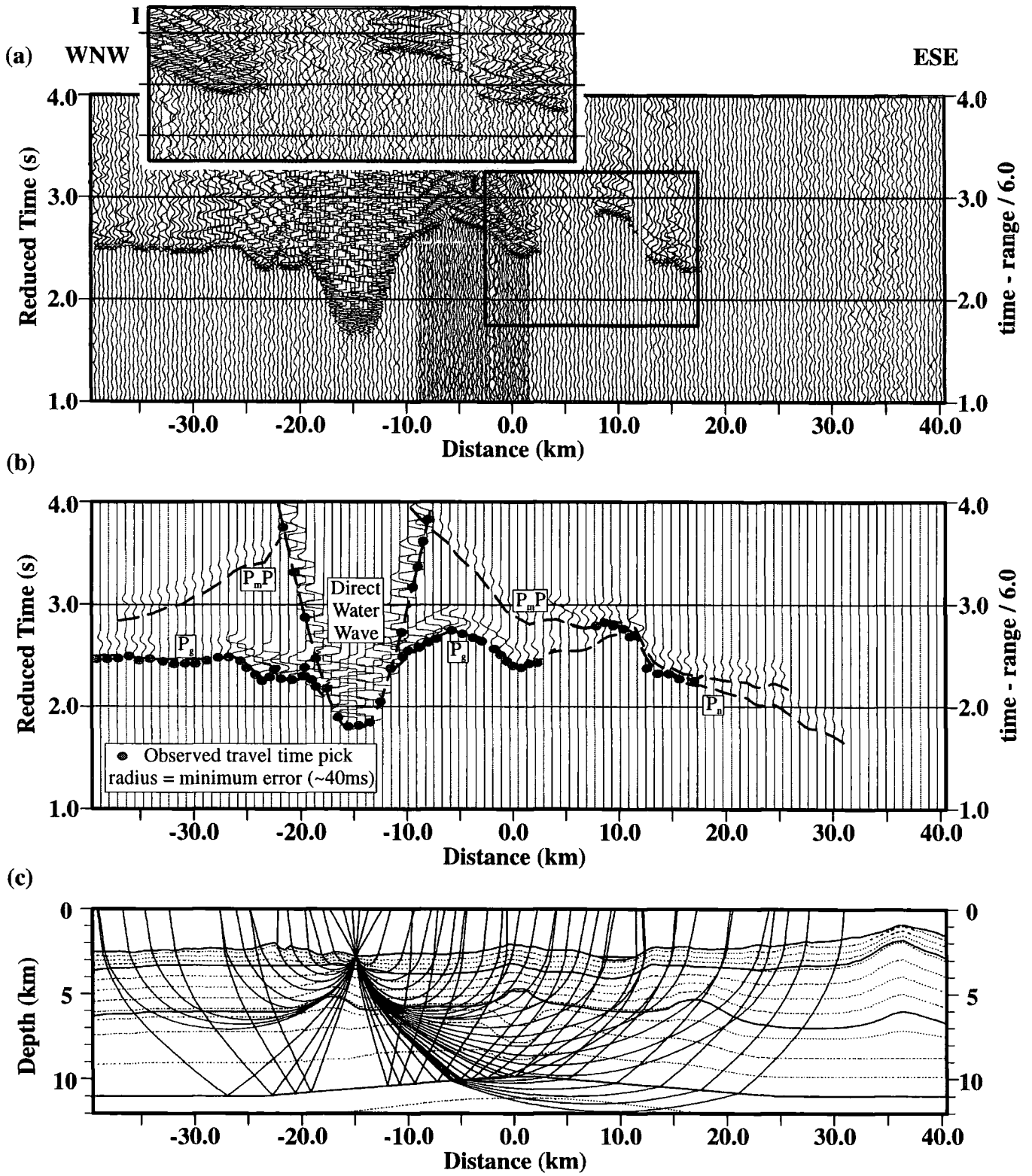

Figure 4.6: Ray-trace modelling of the final across-axis seismic model for SDOBS2 on Line 1 (see figure 2.1 for instrument location) showing the main phases of interest.

(a) Filtered vertical component record section plotted at true amplitude to show the amplitude variations of the first arrivals. Display parameters are described in figure 4.2a. Inset I displays the lower crustal and upper mantle phases in greater detail.

(b) Synthetic seismograms calculated from the final model. Display parameters are described in figure 4.2b. Note the faithful reproduction of the loss of amplitude of the first arrival between 3 and 7 km model offset, which corresponds to rays turning in layer 3 beneath the axial region.

(c) Final model with, for clarity, a subset of the rays used to calculate the synthetic seismograms shown in (b). Display parameters are described in figure 4.1.

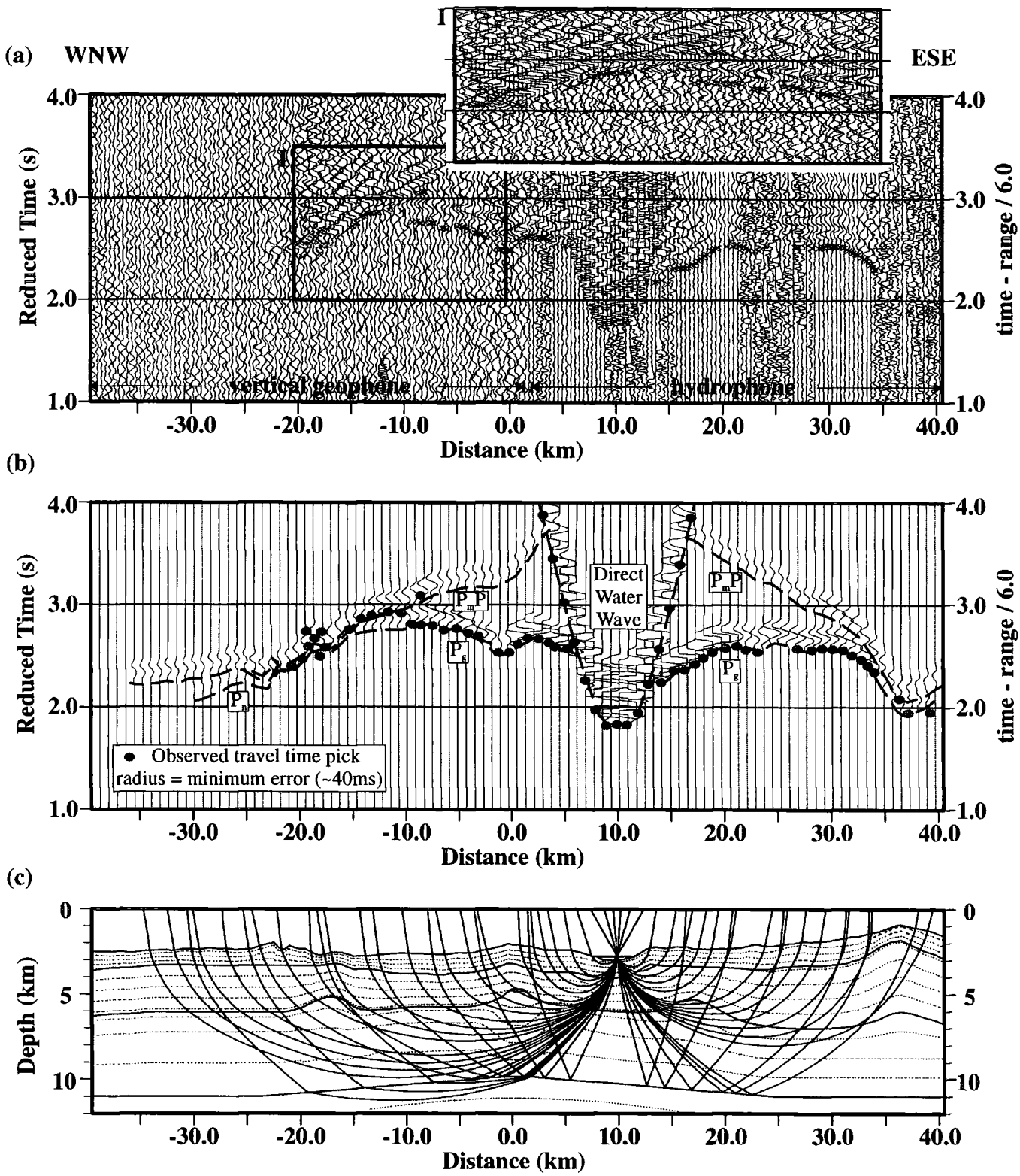

Figure 4.7: Ray-trace modelling of the final across-axis seismic model for SDOBS5 on Line 1 (see figure 2.1 for instrument location) showing the main phases of interest.

(a) Filtered vertical component (-39 to 2 km model offset) and hydrophone (2 to 41 km model offset) record section plotted at true amplitude to show the amplitude variations of the first arrivals. Display parameters are described in figure 4.2a. The two components are shown here on one 'hybrid' record section as data were not recorded on the vertical geophone for the eastern end of Line 1 (see section 2.3). Inset I shows the larger amplitude Moho reflection as a secondary arrival behind the lower crustal phase.

(b) Synthetic seismograms calculated from the final model. Display parameters are described in figure 4.2b. Note the good travel time of the P_mP phase as a secondary arrival (-15 to -9 km model offset).

(c) Final model with, for clarity, a subset of the rays used to calculate the synthetic seismograms shown in (b). Display parameters are described in figure 4.1.

- The top of oceanic layer 2A (the first sub-seabed layer in the final model) has a velocity of 1.9-2.3 km s^{-1} and a lower boundary coincident with the 4.0 km s^{-1} isovelocity contour. Layer thickness is variable with an average thickness of 1.0, 1.25, 1.2, 1.1 and 1.0 km in regions 1, 2, 3, 4, and 5 respectively.
- A second-order boundary between layer 2A and layer 2B/C marks a reduction in the average vertical velocity gradient from ~1.85 to ~1.05 s^{-1} and essentially follows the long wavelength variations in seabed topography.
- Layer 2B/C is modelled with an upper boundary coincident with the 4.0 km s^{-1} isovelocity contour and a lower boundary with velocities ranging from 6.0 to 6.15 km s^{-1}, with the exception of the axial region where velocities at the base of layer 2 are modelled as 5.5 km s^{-1}. Layer 2B/C displays large lateral thickness variations, but these variations are systematic across the profile. The thickness of layer 2B/C in the post-rift region (region 3) is ~1.75 km, significantly less than the thickness of this layer in the pre-rift back-arc crust (~2.5 km), but similar to that observed in the transition zones. The abnormally large thickness of this layer (4 km) in the pre-rift island arc region (>22 km model offset) demonstrates the inherent problems of trying to assign 'oceanic' layering to crust generated in an island arc environment.
- Layer 2 (i.e. layer 2A and layer 2B/C combined), or the volcanic layer as it is often referred to, has a constant thickness of 3.5 km in the pre-rift back-arc crust, which thins into the transition zone (see figure 4.4) to a minimum thickness of 2.5 km. The thickness of layer 2 remains constant within the post-rift crust at ~3 km, with minor thinning on-axis, before thinning again into the eastern transition zone (~17 km model offset). The thinning of layer 2 into the transition zones proved to be the only viable way of modelling the upper crustal arrivals seen on SDOBS2 (figure 4.6: -25 to -20 km model offset) and SDOBS5 (figure 4.7: 12 to 17 km model offset). The depth to the 6.0 km s^{-1} isovelocity contour in the island arc region (coincident with the layer 2/3 boundary in the model) is greater than 5.0 km.
- The second-order boundary between layer 2 and layer 3 (off-axis) marks a further shallowing of the vertical velocity gradient from ~1.05 to ~0.35 s^{-1}. The topography of this boundary is relatively smooth with a reduction in depth occurring within the axial region and two transition zones.

- One of the most prominent features of the model is the low velocity block between layer 2 and layer 3 within the axial region, offset slightly to the east of the shallowest bathymetric point. The location and dimensions of this body are well constrained by refracted arrivals from four DOBSs positioned near the ridge and the unique reflection event observed on the axial instrument, SDOBS4 (figure 4.5: 2.7 s reduced time, -1 to 2 km model offset). The body is located 2.7 km below the seabed, with a modelled width of 1-1.5 km (cf. Collier and Sinha, 1992b: 3.2 ± 0.2 km depth, 2 km width). A seismic velocity of 3.0 km s^{-1} was initially assigned to the block, a value derived from laboratory experiments on molten rocks (Murase and McBirney, 1973), to provide a large reversed polarity reflection (velocity step of -2.5 km s^{-1}) similar to that observed on SDOBS4 (figure 4.5a). Detailed analysis of the physical properties of the low velocity block will be discussed in Chapter 6. No significant time delay was observed for phases travelling through this region and thus a nominal thickness of 100 m was initially assigned to the low velocity block.
- Layer 3 (the oceanic layer) has upper and lower boundary velocities of 6.0-6.15 km s^{-1} and 7.0 km s^{-1} respectively and a thickness of ~5 km in the pre-rift crust and ~4 km in the post-rift crust. The thickening of layer 3 in the transition zones is the result of a reduction in the depth of its upper boundary. Layer 3 is also split by two second-order boundaries. The lower boundary, ~1.25 km below the base of layer 2, marks a change in the vertical velocity gradient from 0.35 to 0.1 s^{-1}, whereas the upper boundary is only included across the entire model to accommodate the anomalous velocity structure beneath the axial region and transition zones due to the constraints of the modelling package. Within the transition zones, the vertical velocity gradient in layer 3 increases from 0.25 to 0.3 s^{-1} occurring at the first second-order boundary, with a reduction from 0.3 to 0.1 s^{-1} at the lower boundary before 'normal' seismic velocities (i.e. velocities similar to those observed in the adjacent regions) are attained ~2 km into layer 3. The velocity anomaly within the axial region was calculated by subtracting a constant thickness layered crust (equivalent to the average velocity-depth profile of post-rift VFR-generated material - see figure 4.4) from the velocity-depth model. A zone of depressed seismic velocity (anomaly greater than -0.2 km s^{-1}) within the axial region is centred on ~0.5 km model offset, has a width of 4 km and extends down in layer 3 to within 2 km of the Moho (see figure 4.8).

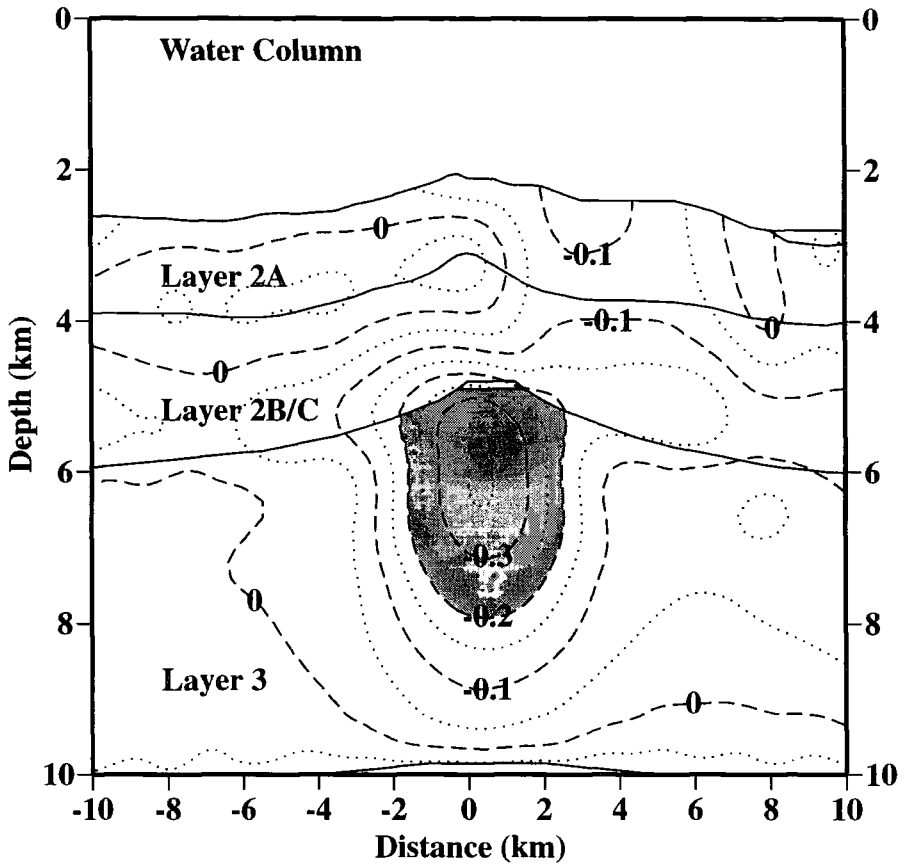

Figure 4.8: P-wave velocity anomaly plot for Line 1, *Seismic South* showing a zone of depressed seismic velocity (shaded region: anomaly greater than -0.2 km s^{-1}) within the axial region. Contours of velocity anomaly are shown by dotted and dashed lines. Vertical exaggeration x2. Anomalies are calculated relative to a constant thickness layered crust equivalent to the average post-rift crustal structure (cf. figure 4.4).

- The Moho is constrained between -30 and 30 km model offset by at least two sets of ray-paths. There is no evidence for the reduction in depth of this boundary in the transition zones, as seen on the layer 2/3 boundary, but there is a gradual reduction in the depth (1.25 km - significantly greater than the vertical resolution [~250 m] at this depth) in the post-rift regions, which is centred on the axial region. A first-order boundary at the Moho marks a velocity step from 7.0 to 7.85 km s^{-1}, yet there is no significant change in gradient across this boundary. Crustal thicknesses vary between 7 and 10 km, with post-rift crust being considerably thinner (~1-1.5 km) than pre-rift crust.
- The upper mantle is assigned a velocity of 7.85 km s^{-1} at its upper boundary, constrained by upper mantle diving rays, with a second-order boundary located 1 km below the Moho which decreases the vertical velocity gradient from 0.15 to 0.02 s^{-1}. The model is not constrained below 12 km by the available data.

The significance of the main features of the final velocity-depth model for the across-axis profile, Line 1, in relation to the general crustal structure and their implications for the processes of crustal accretion at the VFR will be discussed in Chapter 6.

4.3 *Seismic North* across-axis profile - Line 6

The second across-axis profile, Line 6, runs parallel to and 30 km to the north of Line 1 and is centred on 22° 12′ S, 176° 36′ W, which corresponds to the location of NDOBS2 (see figure 2.1) and the intersection with the along-axis profile, Line 4. Wide-angle seismic data from five DOBSs were used to constrain the crustal model.

4.3.1 Initial model

An initial seismic model for Line 6 was generated in a similar way to that described for Line 1 in section 4.2.1. However, a thin layer of sediment was observed over the majority of the seabed to the east of the CVFR on this profile and sediment was thus incorporated into the initial model (figure 4.9). Travel time inversions of the data recorded by each DOBS were again calculated and combined with an estimate of the general crustal structure obtained on Line 1, in addition to the results of previous studies of oceanic crust.

The initial model for Line 6 comprised six layers, each containing 127 nodes and the main features of the model are described below.

- The water column structure is the same as Line 1, with second-order boundaries located at a depth of 0.6 km and 1.1 km and a velocity of 1.50 km s^{-1} at the seabed.
- The five remaining layers represent the sediment, the crustal layers 2A, 2B/C and 3 and the upper mantle (cf. Bratt and Purdy, 1984 and Solomon and Toomey, 1992). The boundaries between these layers in the model are coincident with the 2.0 (layer 1/2), 4.0 (layer 2A/2B), 6.2 (layer 2/3) and 7.0 km s^{-1} (layer 3/upper mantle boundary) isovelocity contours. All layer interfaces are again modelled as second-order boundaries, with the exception of the boundary between layer 3 and the upper mantle.
- The velocity at the top of the sedimentary layer is 1.8 km s^{-1}, indicating a velocity step of 0.3 km s^{-1} across the seabed, increasing to 2.0 km s^{-1} at its base.

- Layer 2A, bounded by the 2.0 km s^{-1} isovelocity contour (i.e. a velocity step of 0.5 km s^{-1} across the seabed in unsedimented regions) and the 4.0 km s^{-1} isovelocity contour, has an average vertical velocity gradient of 1.37 s^{-1}.
- Layer 2B/C, with upper and lower boundaries located at depths of 3.6 km (4.0 km s^{-1}) and 6.0 km (6.2 km s^{-1} isovelocity contour) respectively has a constant vertical velocity gradient of 0.92 s^{-1}.
- Layer 3 is modelled with a thickness of 4.0 km and increases in velocity with depth from 6.2 to 7.0 km s^{-1} at its base (i.e. a vertical velocity gradient of 0.2 s^{-1}). The base of layer 3 is defined by the seismic Moho, situated at a depth of 10.0 km and represents a velocity step of 0.9 km s^{-1}.
- A second-order boundary, coincident with the 8.0 km s^{-1} isovelocity contour located 1.0 km beneath the Moho (model depth of 11.0 km) marks a change in gradient from 0.1 s^{-1} to 0.02 s^{-1}. The initial model extends down to a depth of 20.0 km, coincident with the 8.2 km s^{-1} isovelocity contour.

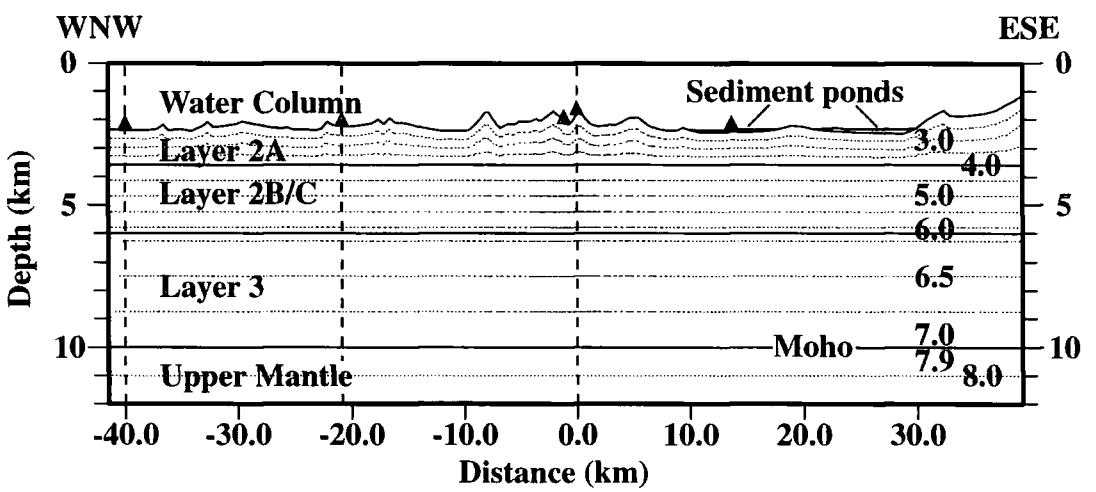

Figure 4.9: Line 6, across-axis initial model. Display parameters are described in figure 4.1. Note the sediment ponds centred on 14 km and 26 km model offset.

Ray-trace modelling of Line 6 followed a similar strategy to Line 1 (see section 4.2.2) and the results of, and conclusions drawn from, ray-trace modelling of the initial model are described below and in figures 4.10 and 4.11. NDOBS5 (figure 4.10) and NDOBS1 (figure 4.11) were chosen to display the results of ray-trace modelling for the same reason as SDOBS2 and SDOBS5 on Line 1 (section 4.2.2). Both instruments display a large number of arrivals whose ray-paths have turned at depth beneath the axial region. The error on each data point is ~40 ms, but out-of-plane effects are of

greater concern on Line 6 due to the problems associated with the 3-D nature of the OSC and the numerous off-axis seamounts and ridges (see figure 2.1).

- The travel time fit of arrivals west of the OSC is remarkably good (e.g. figure 4.10), which implies that the upper crustal structure of Line 6 away from the influence of the island arc is broadly similar to that modelled on Line 1.
- The poor travel time fit (modelled arrival is 600 ms early) of the P_g phase, which turns in the upper crust east of the OSC (e.g. figure 4.11: 25 to 30 km model offset) suggests that layer 2 is considerably thicker at model offsets greater than 5 km.
- Errors in the travel time fit of rays tracing beneath the OSC indicate that a more complex upper crustal structure must be incorporated into the model beneath both spreading axes.
- The general amplitude fit of first arrivals is good and the relative amplitude of the lower crustal phases (in relation to the upper crustal phases) is faithfully reproduced (e.g. figure 4.11).
- The observed data cannot be modelled with P_g phases alone and large amplitude secondary arrivals indicate the presence of different phases (e.g. Moho reflections).

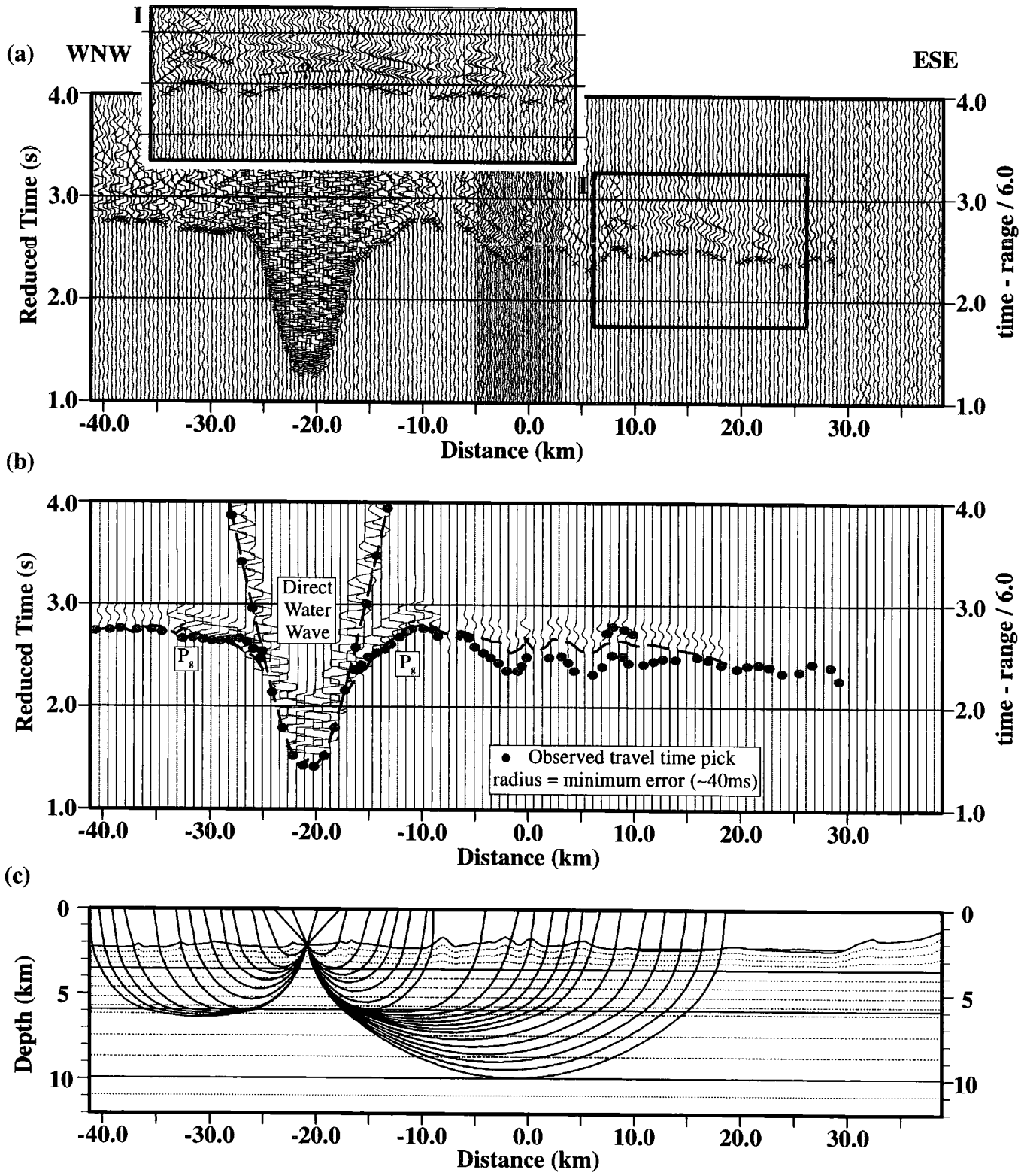

Figure 4.10: Ray-trace modelling of the initial across-axis seismic model for NDOBS5 on Line 6 (see figure 2.1 for instrument location).

(a) Filtered vertical component record section plotted at true amplitude to show the amplitude variations of the first arrivals. Display parameters are described in figure 4.2a. Inset I shows the travel time picks of the lower crustal and upper mantle phases in greater detail.

(b) Synthetic seismograms calculated from the initial model. Display parameters are described in figure 4.2b. Note the good fit (within error) of the calculated and observed data except at model offsets greater than -5 km. The 'early' observed arrivals suggest that the crust thins or has higher velocities within this region

(c) Initial model with, for clarity, a subset of the rays used to calculate the synthetic seismograms shown in (b). Display parameters are described in figure 4.1.

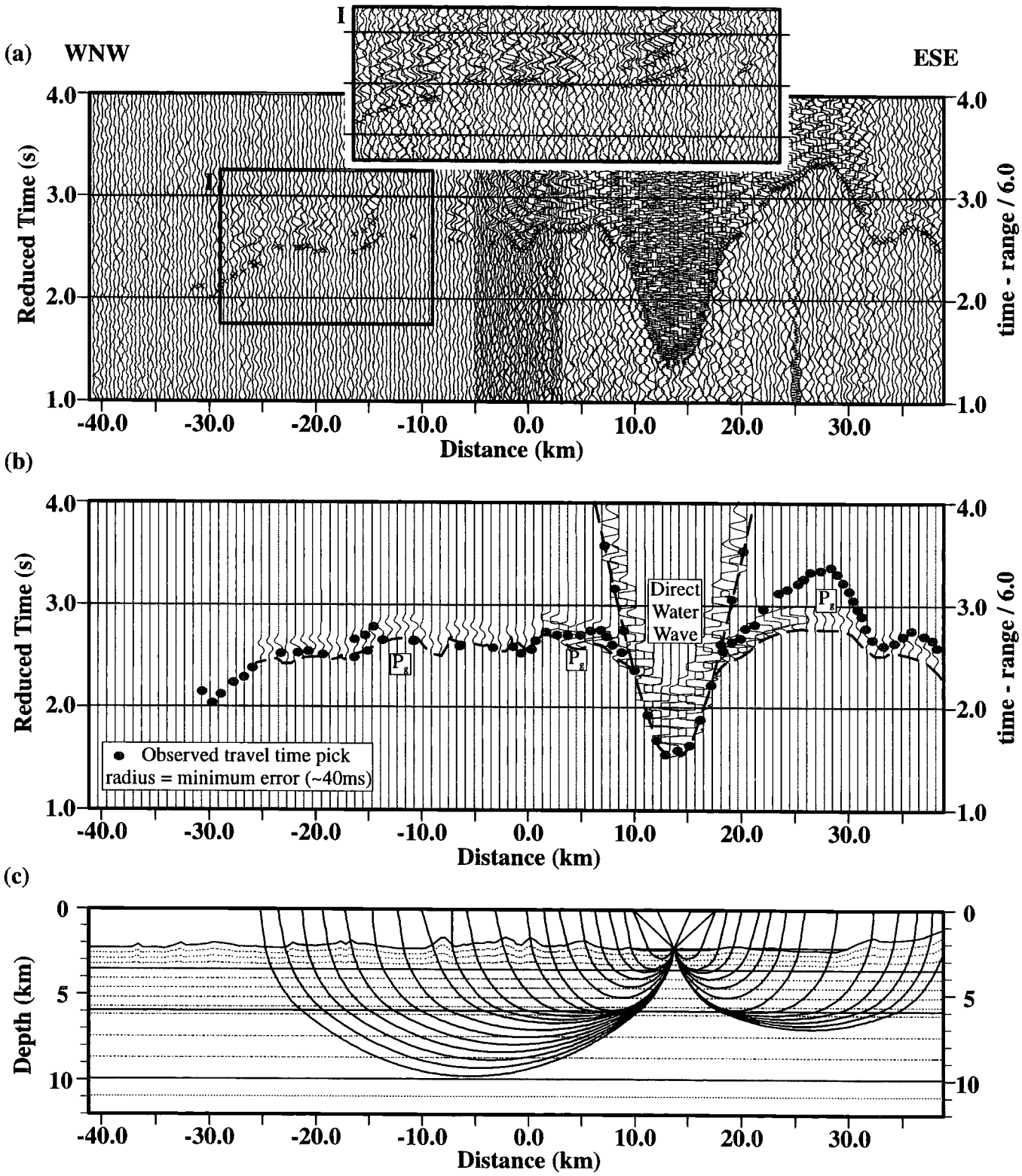

Figure 4.11: Ray-trace modelling of the initial across-axis seismic model for NDOBS1 on Line 6 (see figure 2.1 for instrument location).

(a) Filtered vertical component record section plotted at true amplitude to show the amplitude variations of the first arrivals. Display parameters are described in figure 4.2a. Inset I shows the travel time picks of the lower crustal and upper mantle phases in greater detail.

(b) Synthetic seismograms calculated from the initial model. Display parameters are described in figure 4.2b. The large misfit between 20 and 30 km model offset (modelled first arrivals up to 600 ms early relative to the observed data) implies a considerably thicker layer 2 east of the OSC.

(c) Initial model with, for clarity, a subset of the rays used to calculate the synthetic seismograms shown in (b). Display parameters are described in figure 4.1.

4.3.2 Best fitting wide-angle seismic model

The final wide-angle seismic model for Line 6 is shown in figure 4.12. The model is divided into the same six layers described in the initial model and an additional low velocity block, similar to the one modelled on Line 1 (figure 4.5c: ~0.5 km model offset) has also been incorporated.

The low velocity block, added to the model to generate the large amplitude reflection observed behind the water wave on NDOBS3 (figure 4.13a: 2.6 s reduced time, -2 to 0 km model offset), coincides with the top of a zone of depressed seismic velocity within layer 3 below the OSC. A similar reflection observed on NDOBS2, situated on the CVFR axis, is only identified to the west of the instrument, which suggests that the low velocity block does not extend under the entire width of the CVFR axis at this location.

The depth and geometry of the Moho were again constrained by ray-trace modelling of the Moho reflection and upper mantle phases.

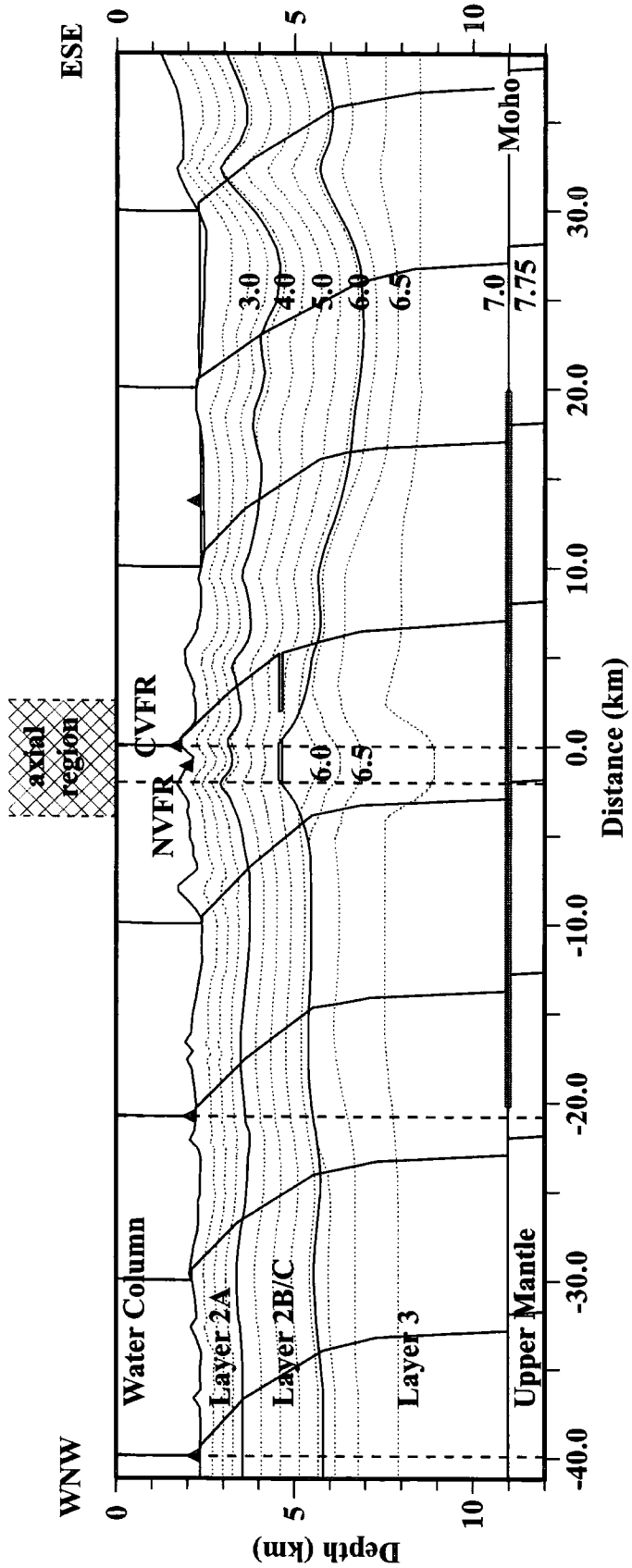

Figure 4.12: Line 6, across-axis final model. Display parameters are described in figure 4.4. Vertical exaggeration x2. The seismic Moho is constrained between -20 and 20 km model offset (thicker grey line) and is modelled at a constant depth across the entire profile. Note the low velocities beneath the axial region (cf. figure 4.4) and the low velocity block between -2 and 0 km model offset (cf. notch in the velocity-depth profile at 0 km model offset).

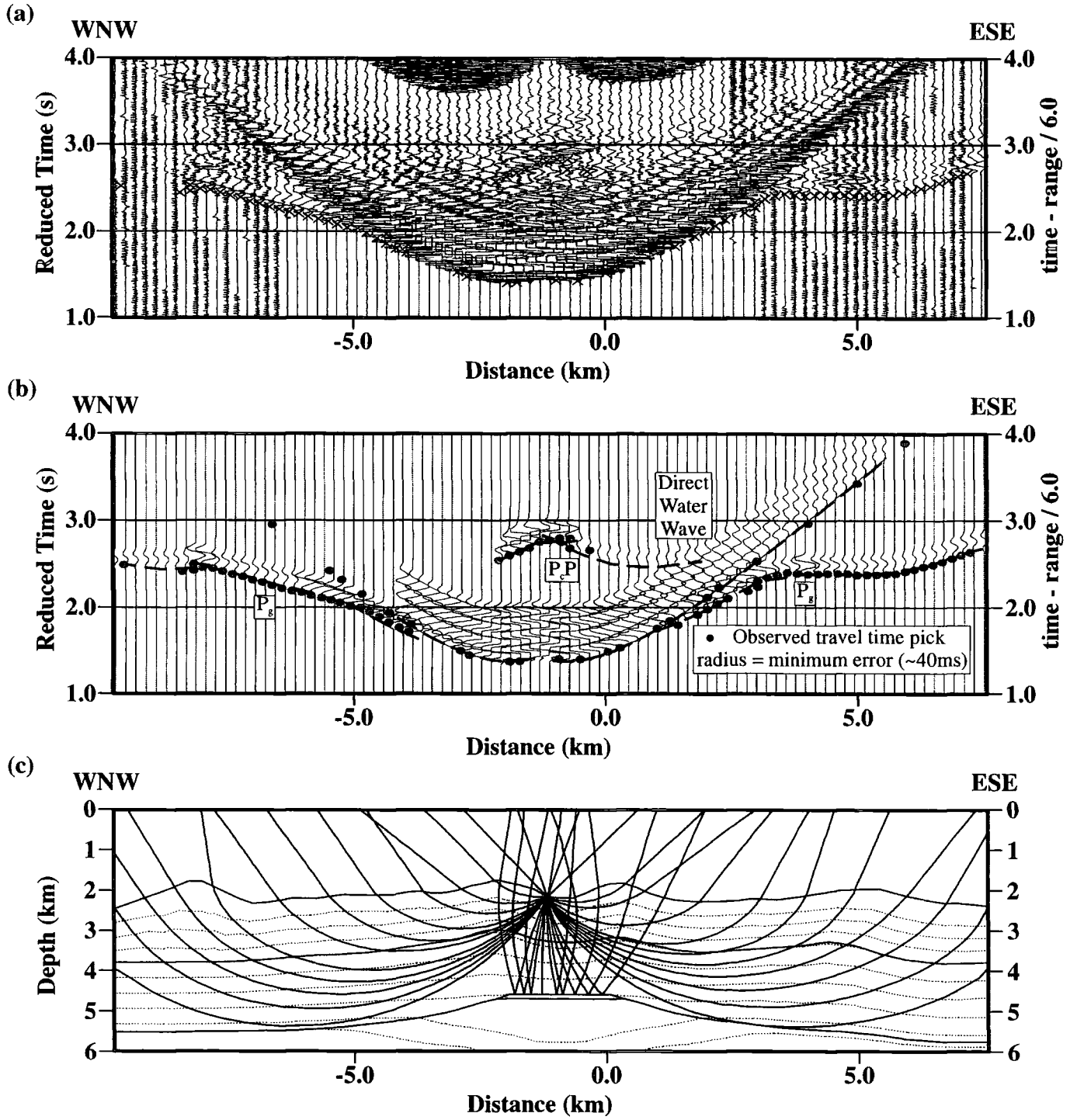

Figure 4.13: Ray-trace modelling of the final across-axis seismic model for NDOBS3 on Line 6 (see figure 2.1 for instrument location) showing a large amplitude intracrustal reflection (P_cP) generated from the top of layer 3.

(a) Filtered vertical component record section plotted at true amplitude to show the amplitude variations of the first arrivals. Display parameters are described in figure 4.2a. Note the large amplitude P_cP arrival between 2.6 s and 2.9 s reduced time (-2 to 0 km model offset).

(b) Synthetic seismograms calculated from the final model. Display parameters are described in figure 4.2b. Direct water waves cannot be traced beyond -4 km model offset due to the general shape of the seabed topography.

(c) Final model with, for clarity, a subset of the rays used to calculate the synthetic seismograms shown in (b). Display parameters are described in figure 4.1.

The final ray-trace modelled sections for NDOBS5 and NDOBS1 (see figure 2.1 for instrument locations) are shown in figures 4.14 and 4.15 and a complete set of ray-trace modelled sections for Line 6 can be found in Appendix B. Display parameters are described in section 4.2.2.

The errors and limitations of the dataset are the same as described at the end of section 2.4 for Line 1 and a good travel time and amplitude fit was achieved within the error bounds for all instruments. The model is described layer-by-layer, starting at the seabed and working down through the crust and into the upper mantle. All velocities described in the model are P-wave seismic velocities and depths are described in km below the sea surface.

- Sediment accumulation is restricted to two areas centred on 14 and 26 km model offset. NDOBS1 is located above one of these sediment ponds (14 km model offset), but no intrasediment turning rays (P_s) are observed and thus sediment velocities cannot be determined directly from this instrument. Delay times of rays travelling through the sediment and recorded by more distant instruments, the normal incidence seismic data and previous drilling results (in particular ODP site 840 to the east of the survey area at 22° 13′ 15″ S, 175° 44′ 55″ W) were used to constrain sediment thickness and velocity. The two sediment ponds are modelled with a maximum thickness of 75 m (11 km model offset) and 150 m (28 km model offset) and with an average velocity of 1.70 km s^{-1}. The restricted location of these sediment ponds suggests the western edge of the island arc as their possible source.
- The velocity at the top of layer 2A varies between 1.75 and 2.15 km s^{-1} and has a lower boundary coincident with the 4.0 km s^{-1} isovelocity contour over the majority of the profile. Lower velocities are modelled at this boundary within the axial region (a minimum of 3.7 km s^{-1}) and to the east of 20 km model offset (3.9 km s^{-1}). The average layer thickness over the majority of the profile is 1.3 km, which thins by ~150 m west of -25 km model offset. The depth to the 4.0 km s^{-1} isovelocity contour increases to more than 1.8 km at model offsets greater than 10 km, perhaps an influence of the proximity of the island arc.

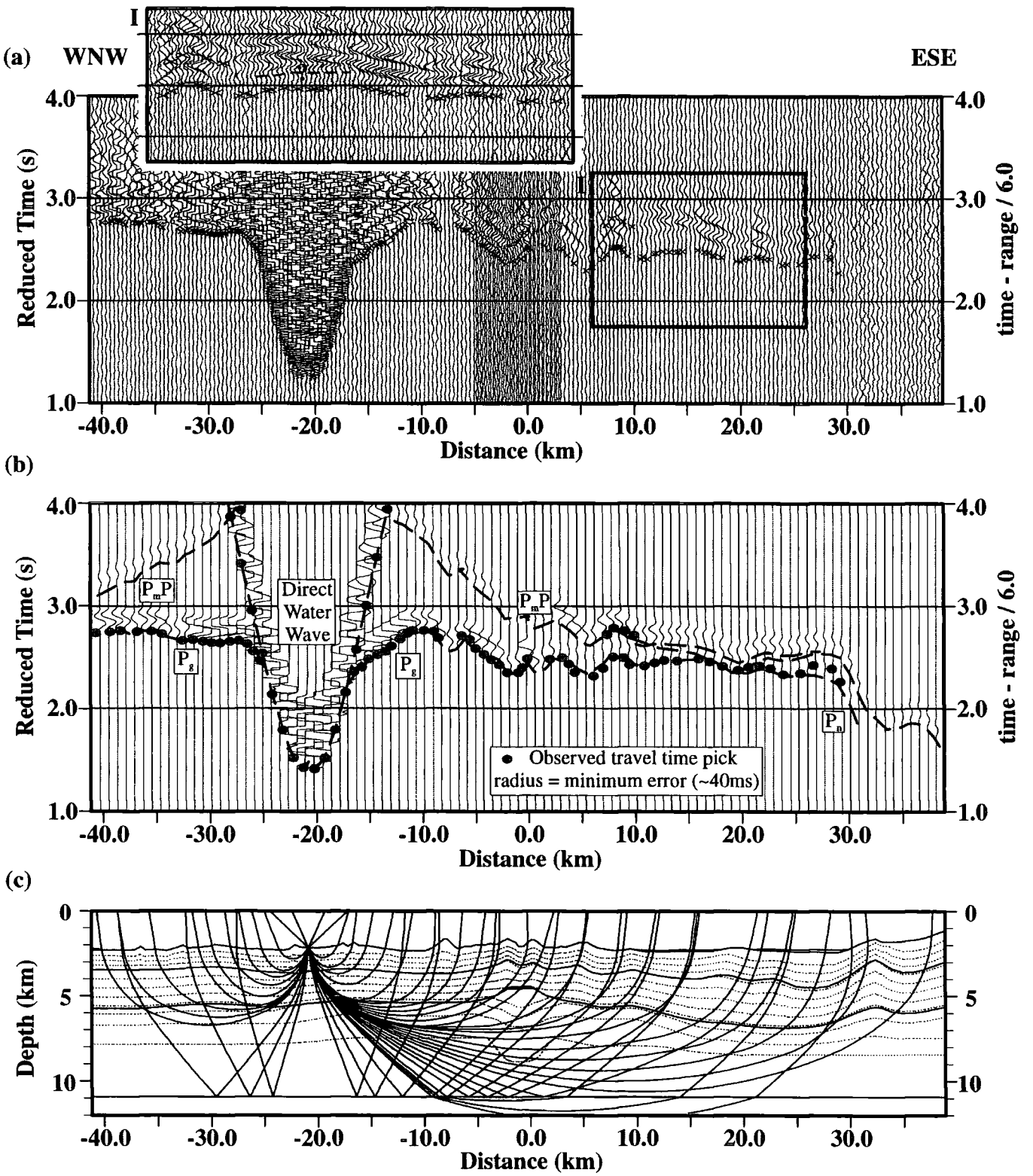

Figure 4.14: Ray-trace modelling of the final across-axis seismic model for NDOBS5 on Line 6 (see figure 2.1 for instrument location) showing the main phases of interest.

(a) Filtered vertical component record section plotted at true amplitude to show the amplitude variations of the first arrivals. Display parameters are described in figure 4.2a. Inset I shows the travel time picks of the lower crustal and upper mantle phases in greater detail.

(b) Synthetic seismograms calculated from the final model. Display parameters are described in figure 4.2b. Note that the relative amplitude of the P_mP and P_g phase between 5 and 20 km model offset (inset of part a) is faithfully reproduced in the synthetic data.

(c) Final model with, for clarity, a subset of the rays used to calculate the synthetic seismograms shown in (b). Display parameters are described in figure 4.1.

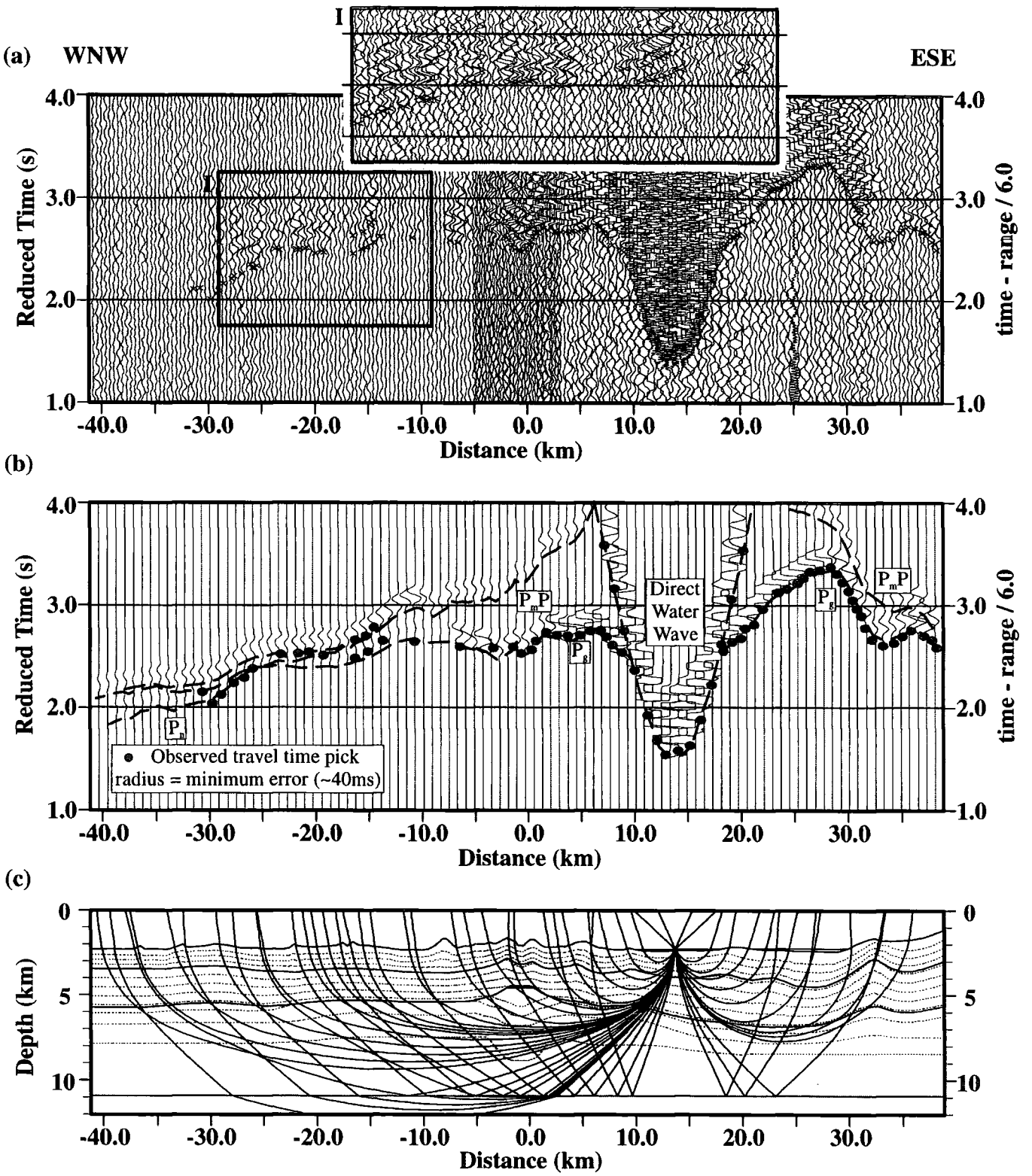

Figure 4.15: Ray-trace modelling of the final across-axis seismic model for NDOBS1 on Line 6 (see figure 2.1 for instrument location) showing the main phases of interest.

(a) Filtered vertical component record section plotted at true amplitude to show the amplitude variations of the first arrivals. Display parameters are described in figure 4.2a. Inset I shows the travel time picks of the lower crustal and upper mantle phases in greater detail.

(b) Synthetic seismograms calculated from the final model. Display parameters are described in figure 4.2b. Note the faithful reproduction of the relative amplitudes of the lower crustal and upper mantle phases between -25 and -5 km model offset (cf. figure 4.14).

(c) Final model with, for clarity, a subset of the rays used to calculate the synthetic seismograms shown in (b). Display parameters are described in figure 4.1.

- A second-order boundary interpreted to be the base of layer 2A follows the long wavelength variations in seabed topography and marks a reduction in the vertical velocity gradient from 1.70 to 1.05 s^{-1}, with the exception of the island arc influenced crust to the east where the change in gradient is minimal.
- Layer 2B/C has a relatively constant thickness of 1.9 km, but thickens towards the western (~2.1 km thick) and eastern (~2.5 km) ends of the profile. The upper and lower boundaries are generally coincident with the 4.0 and 6.2 km s^{-1} isovelocity contours respectively across the majority of the model, although the velocity at the lower boundary is modelled to decrease to 5.5 km s^{-1} in the axial region.
- The thickness of the volcanic layer (layer 2) between -40 and 10 km model offset is ~3.25 km. However, the ratio between the thickness of layer 2A and layer 2B/C is lower west of -25 km model offset (i.e. a thinner layer 2A) than elsewhere which may mark the transition from VFR-generated crust to pre-rift back-arc crust (cf. figure 4.4). East of 10 km model offset layer 2 is thickened considerably, due to the inferred influence of the island arc.
- The second-order boundary between layer 2 and layer 3 denotes a further reduction in the velocity gradient from 1.05 to 0.20 s^{-1} and generally follows the seabed topography.
- A low velocity block located at a constant depth of 4.6 km between layer 2 and layer 3 (cf. Line 1: figure 4.5), is centred on -1 km model offset and corresponds to a depth of 2.8 km beneath the seabed at the ridge axes. The observation of a less distinct, but still identifiable reflection at near normal incidence on instrument NDOBS3 (figure 4.13) provides compelling evidence of the existence of a low velocity block beneath the OSC and the absence of delay times associated with rays travelling through the block limits its thickness to a maximum of ~100 m. The low velocity block is modelled with a velocity of 3.0 km s^{-1} (i.e. a velocity step of -2.5 km s^{-1} occurs at the upper and lower boundary) and is constrained to a width of 2 km, extending beneath the inside flanks of both ridges and the overlap basin.
- Layer 3 has an average thickness of 4.25 km, with upper and lower boundary velocities of 6.1-6.25 and 7.0 km s^{-1} respectively. At model offsets greater than 15 km layer 3 is observed to thin considerably (figure 4.12), but the depth to the lower boundary here is poorly constrained. The velocity at the top of layer 3 on-

axis (i.e. the base of the low velocity block) is modelled as 5.5 km s^{-1} for convenience as the constraints on an exact value are limited. Two second-order boundaries at a depth below the low velocity block of 0.85 and 2.25 km change the vertical velocity gradient from 0.5 to 0.175 s^{-1} and 0.175 to 0.15 s^{-1} respectively. A zone of depressed seismic velocity relative to a constant thickness layered crust (cf. Line 1), with an anomaly greater than -0.2 km s^{-1} extends ~3 km down into layer 3, has a width of 4 km and is centred on the overlap basin (figure 4.16). The heart-shaped top of -0.2 km s^{-1} velocity anomaly contour is a function of the method of calculating the velocity anomaly, (the final model is compared with seafloor conformable layers and an average off-axis velocity profile away from arc-influenced crust to the east), therefore short wavelength variations in topography are often reproduced in the velocity anomaly. Beyond the axial region the lower second-order boundary decreases the vertical velocity gradient from 0.2 to 0.05 s^{-1}.

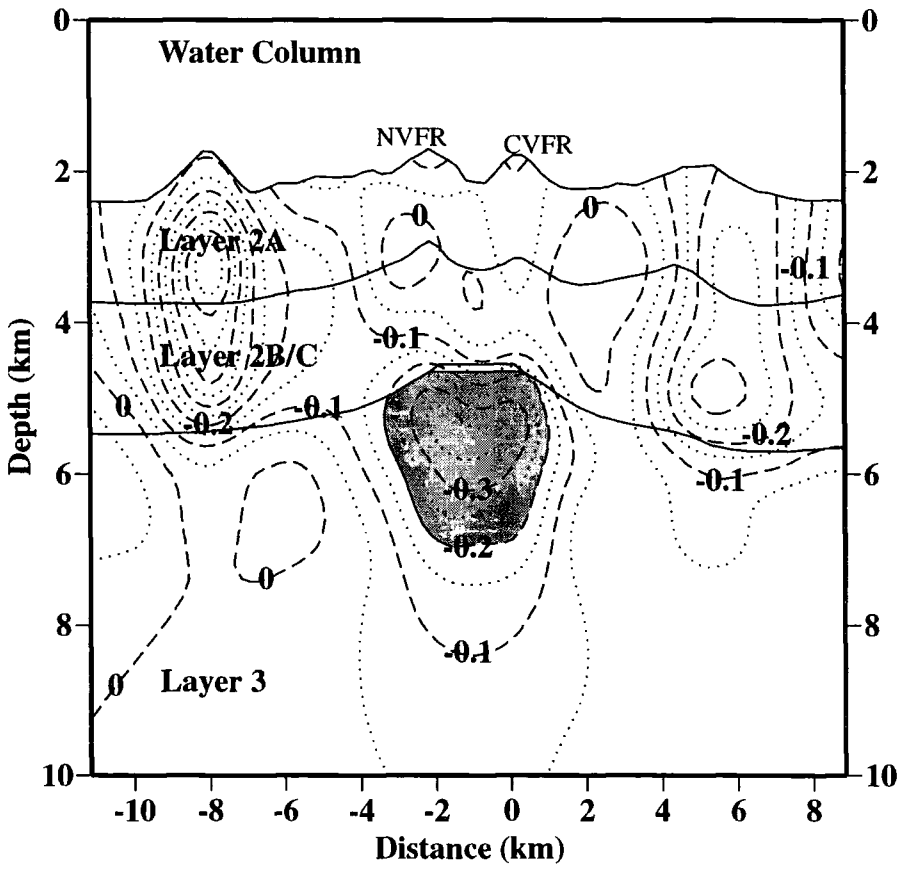

Figure 4.16: P-wave velocity anomaly plot for Line 6, *Seismic North* showing a zone of depressed seismic velocity beneath the OSC (shaded region: anomaly greater than -0.2 km s^{-1}). Contours of velocity anomaly are shown by dotted and dashed lines. Vertical exaggeration x2. Note that the velocity anomalies are calculated relative to a constant thickness layered crust (cf. figure 4.8).

- The Moho, at an average depth of 8.5 km below the seabed, is constrained between -21 and 19 km model offset. The velocity increases from 7.0 to 7.75 km s^{-1} across this boundary and coincides with an increase in vertical velocity gradient from 0.05 to 0.1 s^{-1}. Note the slightly reduced upper mantle velocity compared with Line 1 (7.85 km s^{-1}).
- The upper mantle velocity structure is split into two regions by a second-order boundary located at a depth of 1.5 km below the Moho which dramatically decreases the velocity gradient from 0.1 to 0.02 s^{-1}. Again, there is no further constraint on the model below 12 km.

Many of the features of the final velocity-depth model for the across-axis profile, Line 6, have wider implications for the general crustal structures and the processes of crustal accretion at the VFR and will be discussed in Chapter 6.

4.4 Along-axis profiles - Line 4 (CVFR) and Line 9 (NVFR)

Line 4 and Line 9 correspond to the two along-axis profiles over the CVFR and NVFR respectively. SDOBS4 and NDOBS2 are located on the CVFR along-axis profile at 0 km and 28.5 km model offset respectively and correspond to the intersections with the two across-axis profiles, Line 1 and Line 6. Two disposable sonobuoys were also deployed along Line 4 during *Seismic South* (see figure 2.1 for sonobuoy locations) and data collected on these instruments were used to improve the constraint on the along-axis crustal structure.

NDOBS4, located at the intersection of Line 9 and the across-axis profile, Line 6 unfortunately failed to record any useful data (see section 2.4.1). However, NDOBS3 situated in the overlap basin was used to model Line 9 together with two disposable sonobuoys (see figure 2.1 for sonobuoy locations). Although NDOBS3 was located 1.4 km off-line, it was still considered suitable for 2-D modelling of this profile, as long-range data would not be significantly affected by the slight difference in travel path.

4.4.1 Initial models

Initial seismic models for both along-axis profiles were generated by extrapolating the seismic structure identified at the intersection points on the across-axis profiles along each profile in a one-dimensional sense.

Line 4

The initial model for Line 4 was constructed prior to the completion of the modelling of Line 6 and was thus created solely from the velocity structure extracted and extrapolated from the intersection point on Line 1 (see figure 4.4). The main features of the initial model are described below.

- The model is divided into six layers by the seabed, the layer 2A/2B boundary, the upper and lower boundary of a low velocity block (cf. figure 4.13c) and the Moho. All layer interfaces are first-order boundaries with the exception of the layer 2A/2B boundary.
- The water column structure is essentially the same as Line 1.
- The first layer beneath the seabed, described as layer 2A, has upper and lower boundary seismic velocities of 1.9 km s^{-1} (i.e. a velocity step of 0.4 km s^{-1} across the seabed) and 4.0 km s^{-1} respectively and an average vertical velocity gradient of 2.0 s^{-1}. The layer 2A/2B boundary is located at a depth of 3.0 km.
- Layer 2B/C has a thickness of 1.8 km and a velocity of 4.0 and 5.5 km s^{-1} at its upper and lower boundary and therefore a vertical velocity gradient of 0.83 s^{-1}.
- A low velocity block located at a depth of 4.8 km between layer 2 and layer 3 has a thickness of 100 m and is assigned a velocity of 3.0 km s^{-1}. A velocity step is identified at the upper (-2.5 km s^{-1}) and lower (+2.5 km s^{-1}) boundaries.
- Two second-order boundaries coincident with the 5.8 km s^{-1} (5.5 km depth) and 6.2 km s^{-1} (7.1 km depth) isovelocity contours change the vertical velocity gradient in layer 3 from 0.5 to 0.25 s^{-1} and 0.25 to 0.32 s^{-1} respectively. The Moho, located at the base of layer 3 at a depth of 9.6 km, denotes a velocity step of 0.85 km s^{-1} (from 7.0 to 7.85 km s^{-1}).
- The upper mantle, divided by the 8.0 km s^{-1} isovelocity contour at depth of 11.0 km is modelled down to a depth of 20.0 km where it is assigned a velocity of 8.2 km s^{-1}.

The initial model was ray-traced using the modelling program *maslov* and the travel time and amplitude fit assessed. The results of ray-trace modelling are described below and in figures 4.17 and 4.18, however out-of-plane effects are a considerable problem on the along-axis profiles, especially near the OSC.

- The initial model provides a good travel time fit for upper crustal phases identified on SDOBS4 (figure 4.17b: 3 to 8 km model offset), which implies that there is not a significant amount of P-wave seismic anisotropy within the axial region.
- All crustal phases observed on NDOBS2 arrive too early, especially rays turning below layer 2A (e.g. figure 4.18b: <22 km model offset).
- The travel time fit of the P_cP reflection from the top of the low velocity block on SDOBS4 is also good. However, lower crustal phases arrive too early (>9 km model offset) which suggests that the upper crust is thicker at greater model offsets and/or the velocity in layer 3 below the low velocity block is much lower.
- The onset of the dramatic reduction in amplitude observed in the SDOBS4 data (figure 4.17a: 14 km model offset) is faithfully reproduced on the synthetic section, but occurs at a shorter offset (figure 4.17b: 11 km model offset). This reduction in amplitude is interpreted to coincide with rays travelling through the low velocity block and into layer 3 and the error in its modelled position suggests that the depth to the low velocity block increases and/or the upper crustal structure is different at greater offsets. However, a similar amplitude reduction modelled on NDOBS2 (figure 4.18b: 17 km model offset) matches the observed data well.

Line 9

The main features of the initial model for Line 9, constructed from the velocity profile observed at the intersection point on Line 6 (figure 4.12), are described below.

- The intersection point on Line 6 lies beyond the extent of the low velocity block modelled between layer 2 and layer 3 on that profile, therefore the initial model is divided into just five layers (water column, layers 2A, 2B/C and 3 and the upper mantle).
- The water column structure is consistent with other profiles.
- The velocity at the upper boundary of layer 2A (i.e. directly beneath the seabed) is modelled as 1.75 km s^{-1}. The lower boundary (coincident with the 3.95 km s^{-1} isovelocity contour) is located at a depth of 3.05 km and the average vertical velocity gradient in layer 2A is 1.75 s^{-1}.

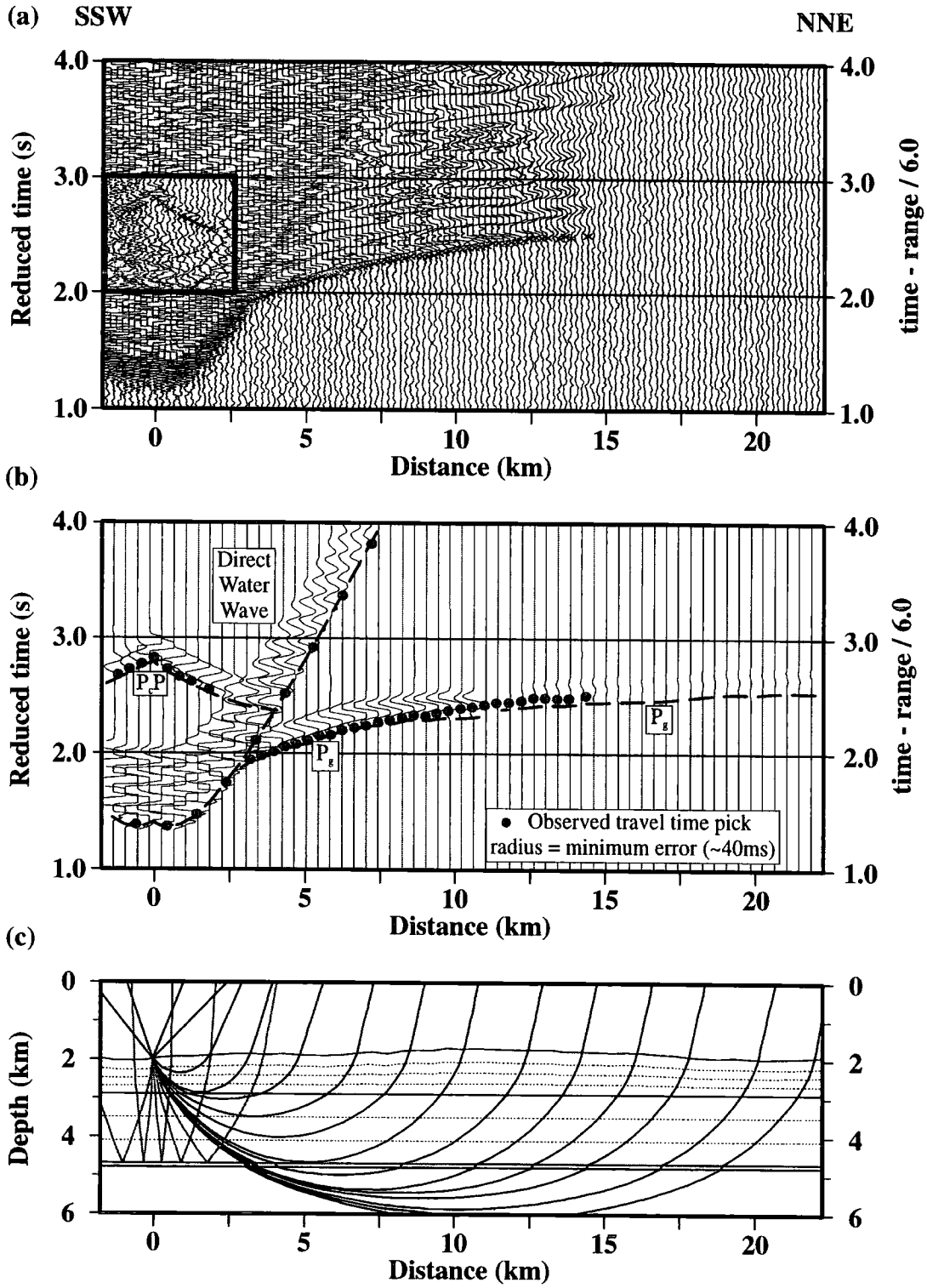

Figure 4.17: Ray-trace modelling of the initial CVFR along-axis seismic model for SDOBS4 on Line 4 (see figure 2.1 for instrument location).

(a) Filtered vertical component record section plotted at true amplitude to show the amplitude variations of the first arrivals. Note the absence of arrivals above the noise level at model offsets greater than 14 km. Display parameters are described in figure 4.2a. Inset shows a large amplitude, reversed polarity intracrustal reflection (P_cP) generated from the top of layer 3 (~0 km model offset).

(b) Synthetic seismograms calculated from the initial model. Display parameters are described in figure 4.2b.

(c) Initial model with, for clarity, a subset of the rays used to calculate the synthetic seismograms shown in (b). Display parameters are described in figure 4.1.

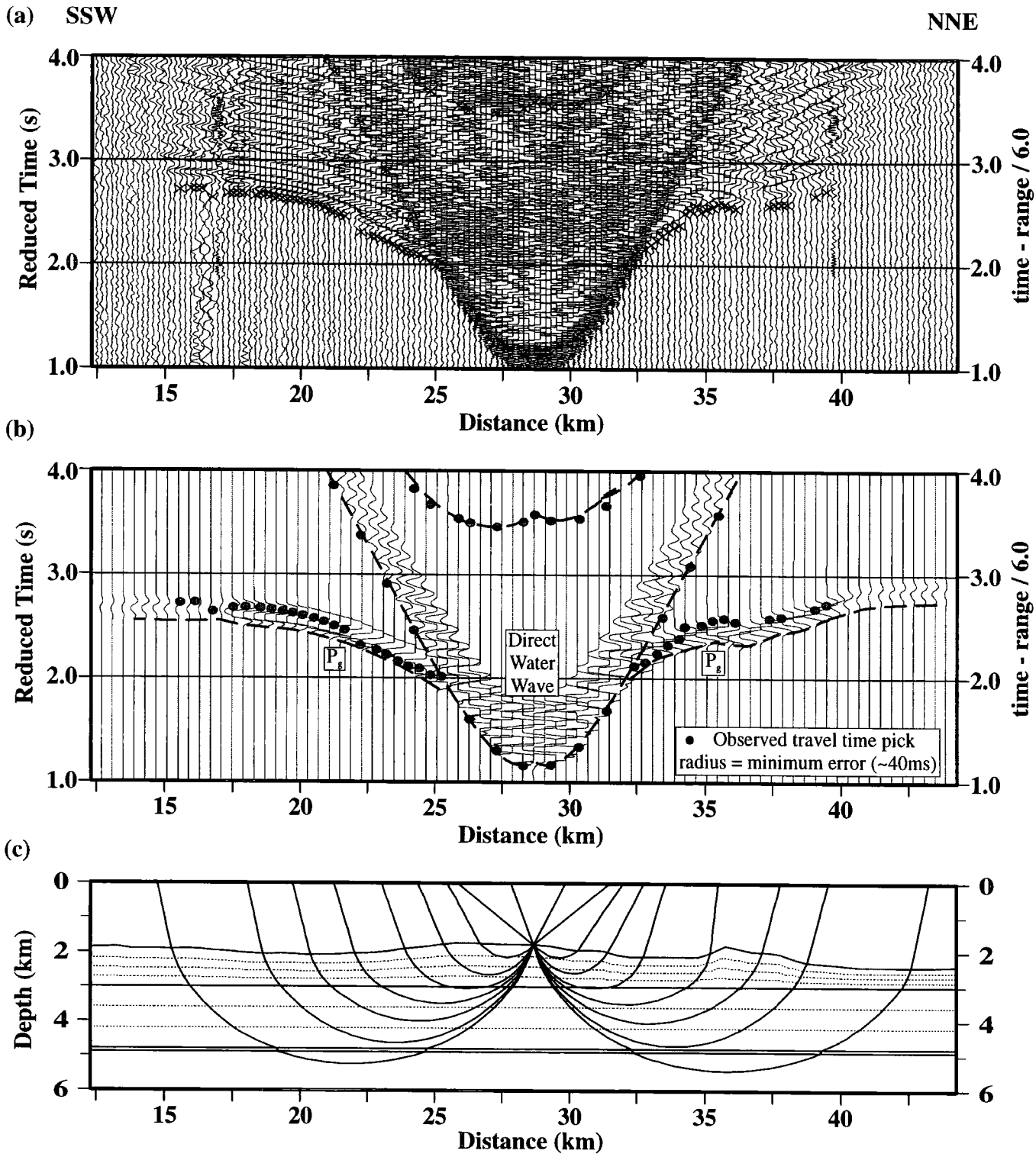

Figure 4.18: Ray-trace modelling of the initial CVFR along-axis seismic model for NDOBS2 on Line 4 (see figure 2.1 for instrument location).

(a) Filtered vertical component record section plotted at true amplitude to show the amplitude variations of the first arrivals. Note the large reduction in amplitude at 17 km model offset (cf. figure 4.17: 14 km model offset). Display parameters are described in figure 4.2a.

(b) Synthetic seismograms calculated from the initial model. Display parameters are described in figure 4.2b.

(c) Initial model with, for clarity, a subset of the rays used to calculate the synthetic seismograms shown in (b). Display parameters are described in figure 4.1.

- Layer 2B/C, bounded by the 3.95 and 5.70 km s^{-1} isovelocity contours has a thickness of 1.7 km and therefore a vertical velocity gradient of ~1.0 s^{-1}.
- Layer 3 is modelled with a thickness of 6.25 km and velocities of 5.70 and 7.0 km s^{-1} at its upper and lower boundaries respectively. Two second-order boundaries located at a depth of 5.85 km (6.2 km s^{-1} contour) and 6.85 km (6.55 km s^{-1} contour) decrease the vertical velocity gradient in layer 3 from 0.45 to 0.35 s^{-1} and 0.35 to 0.11 s^{-1} respectively.
- The upper mantle, included in the model for completeness, has a velocity of 7.75 km s^{-1} directly beneath the Moho (i.e. a velocity step of 0.75 km s^{-1}) and extends down to a depth of 20.0 km.

NDOBS3, used in the 2-D modelling of Line 9, was located slightly off-line and shot-receiver ranges were corrected for this prior to ray-trace modelling (compare the crosses and dots [corrected picks] in figure 4.19b). NDOBS3, situated in the overlap basin, is also located at a depth of 2.15 km (~350 m greater than the NVFR crest) and this must also be taken into account when determining the significance of the travel time fit of the synthetic data. The results of ray-trace modelling of the initial seismic model are described below and in figure 4.19.

- The travel time fit of the first arrivals is good with a slight delay, which increases with offset, observed mainly on phases turning below layer 2A (figure 4.19b: 5 to 11 km model offset.
- The amplitudes of rays turning in layer 3 are generally too high (figure 4.19: >11 km model offset). Note the amplitude cut off at 11 km model offset.

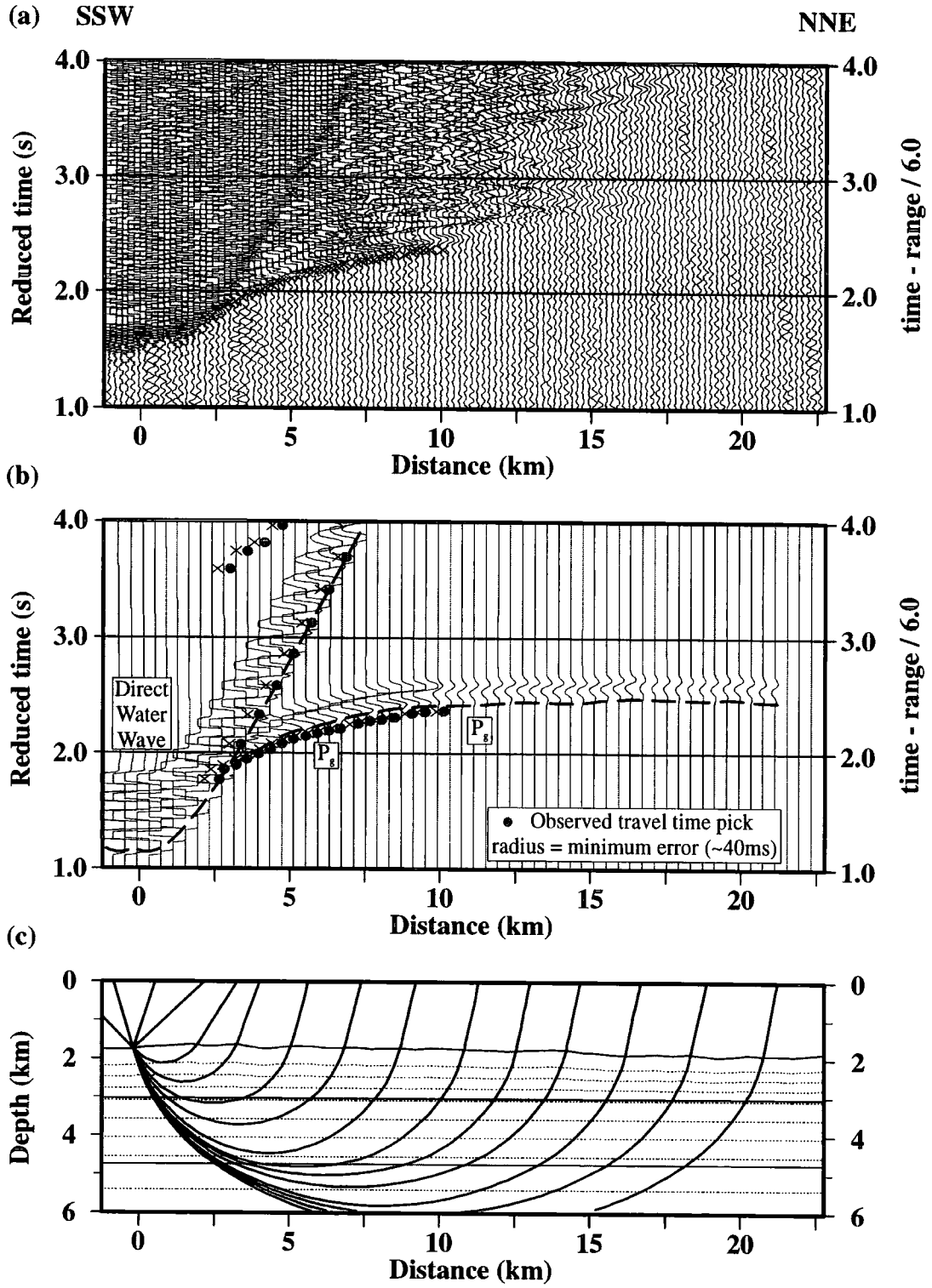

Figure 4.19: Ray-trace modelling of the initial NVFR along-axis seismic model for NDOBS3 on Line 9 (see figure 2.1 for instrument location - 1.3 km off-line to the east).
(a) Filtered vertical component record section plotted at true amplitude to show the amplitude variations of the first arrivals. Display parameters are described in figure 4.2a.
(b) Synthetic seismograms calculated from the initial model. Display parameters are described in figure 4.2b. Note that the crosses and dots represent travel time picks before and after the adjustment for the range to NDOBS3 respectively.
(c) Initial model with, for clarity, a subset of the rays used to calculate the synthetic seismograms shown in (b). Display parameters are described in figure 4.1.

4.4.2 Best fitting wide-angle seismic model - Line 4

The final velocity-depth model for Line 4 is shown in figure 4.20. The layering previously described in the initial model remains, however the seismic structure of layer 2B/C is defined in greater detail.

In addition to the P_cP reflection observed on SDOBS4 (figure 4.17a: highlighted region between 2.0 and 3.0 s reduced time), a further arrival is observed on both horizontal component record sections which corresponds to a P-S mode conversion on reflection (P_cS) at the top of the low velocity block (see figure 3.11). The modelling and significance of this arrival will be discussed in section 4.6.2.

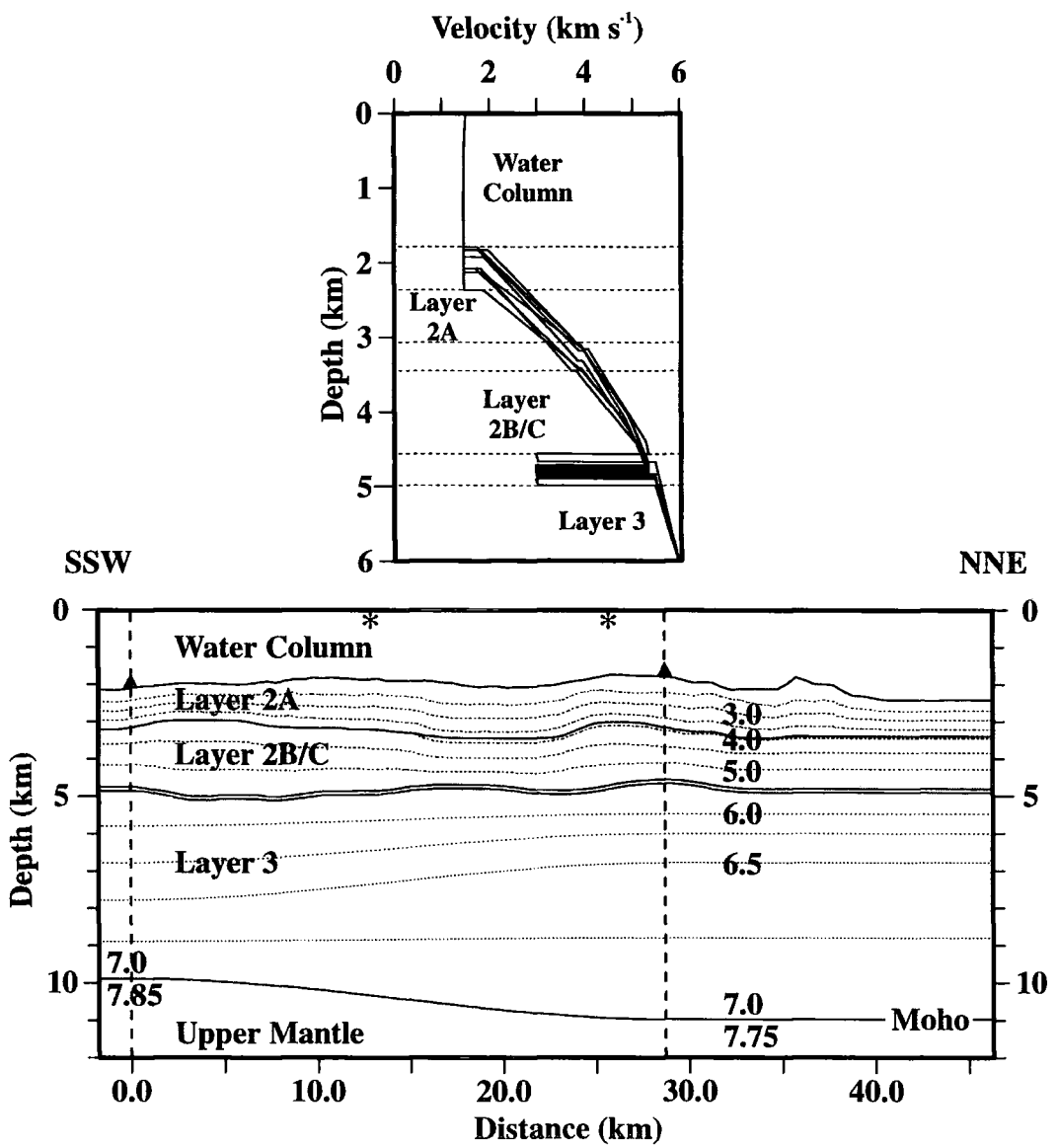

Figure 4.20: Line 4, along-axis final model. Display parameters are described in figure 4.4. Sonobuoy locations are denoted by stars. Vertical exaggeration x2. Inset shows velocity-depth profiles calculated at ~5 km intervals.

Final ray-trace modelled sections for SDOBS4 and NDOBS2 (see figure 2.1 for instrument locations) are shown in figures 4.21 and 4.22. A complete set of ray-trace modelled sections, which include synthetic seismograms generated for two sonobuoys deployed on this line can be found in the Appendix B.

A good travel time and amplitude fit within the error bounds was achieved for all instruments and the main features of the final velocity-depth model are described below. All velocities described in the model are P-wave seismic velocities and depths are described in km below the sea surface.

- Layer 2A, with upper and lower boundary velocities of 1.75-2.15 km s^{-1} and 3.75-4.0 km s^{-1}, has an average thickness of 1.3 km. The thickness of this layer is not uniform across the section and thickens by 250-500 m towards the centre of the CVFR segment (10-30 km model offset).
- The first-order boundary between layer 2A and layer 2B/C marks the position of a velocity step of 0.1 km s^{-1}. Although modelled as a second-order boundary on the across-axis profiles, a small velocity step improved the synthetic fit and was thus included. The layer 2A/2B boundary follows the general topography of the seabed and marks a change in the velocity gradient from ~1.5 to ~1.2 s^{-1}.
- Layer 2B/C is split by two second-order boundaries to enable accurate modelling of both travel time and especially amplitudes of the along-axis data. The subdivision of layer 2B/C was possible due to the relative simplicity of the along-axis structure and the small number of nodes in the model. Although the subdivision of layer 2B/C is not extended into the seismic models of the across-axis profiles, the main layer boundaries are coincident and the travel times of rays travelling through this layer at near normal incidence on both across and along-axis profiles are identical. The upper boundary, coincident with the 4.9 km s^{-1} isovelocity contour at a depth of 0.75-1 km beneath the base of layer 2A, denotes a change in the vertical velocity gradient from ~1.2 to ~0.65 s^{-1}. The lower boundary, incorporated into the model to simulate the gradual reduction in amplitude of the first arrivals observed on the DOBS data (e.g. figure 4.21a: 12 to 14 km model offset and figure 4.22a: 15 to 18 km model offset), is located along the 5.3 km s^{-1} isovelocity contour (150 m above the base of layer 2) and reduces the vertical velocity gradient to 0.33 s^{-1}. The velocity at the base of layer 2 is 5.35 km s^{-1}.

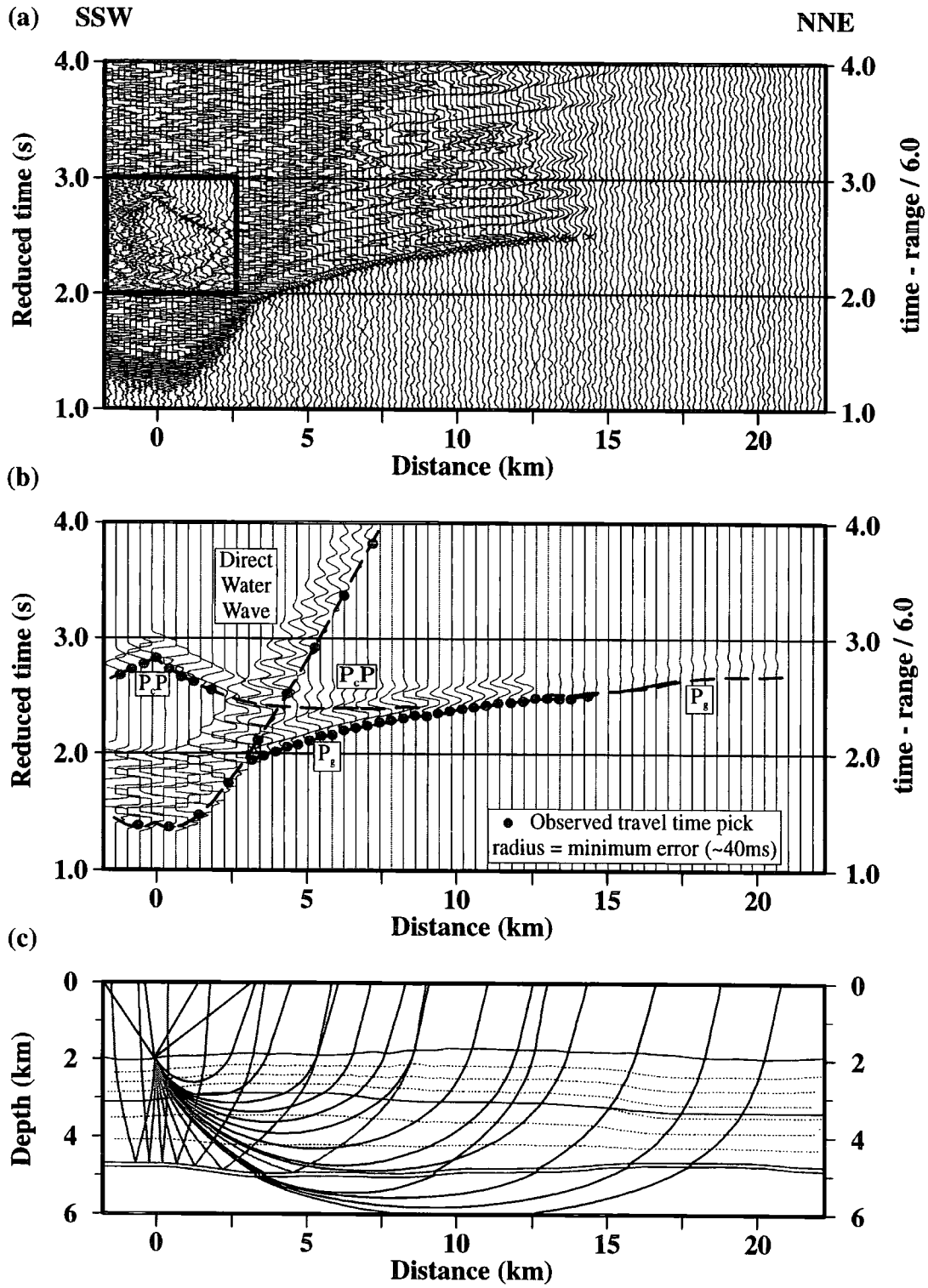

Figure 4.21: Ray-trace modelling of the final CVFR along-axis seismic model for SDOBS4 on Line 4 (see figure 2.1 for instrument location).

(a) Filtered vertical component record section plotted at true amplitude to show the amplitude variations of the first arrivals. Display parameters are described in figure 4.2a. Inset shows a large amplitude, reversed polarity intracrustal reflection (P_cP) generated from the top of layer 3 (~0 km model offset).

(b) Synthetic seismograms calculated from the final model. Display parameters are described in figure 4.2b. Note that the onset of the amplitude reduction in the observed data (~12 km model offset) is faithfully reproduced in the synthetic data.

(c) Final model with, for clarity, a subset of the rays used to calculate the synthetic seismograms shown in (b). Display parameters are described in figure 4.1.

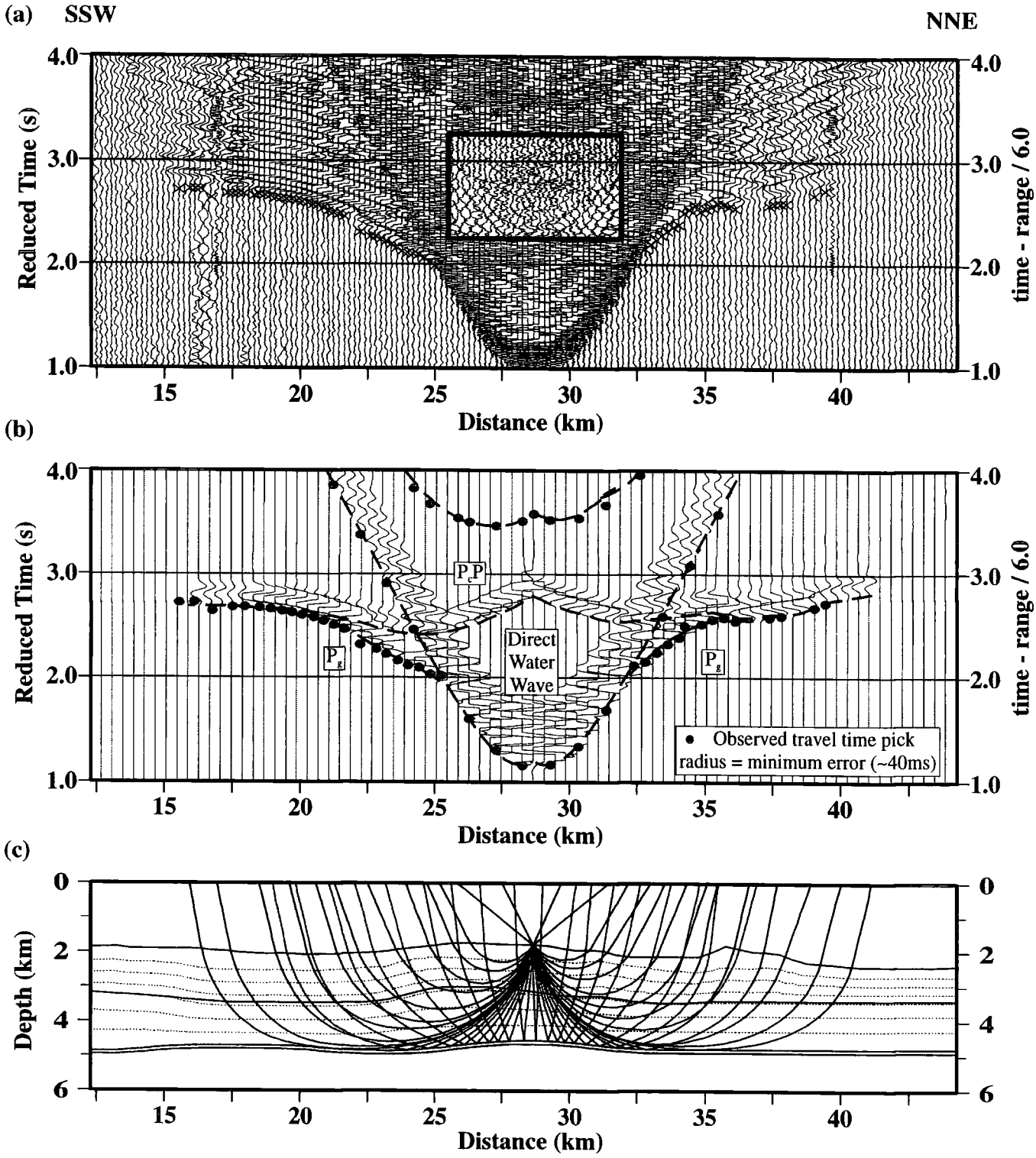

Figure 4.22: Ray-trace modelling of the final CVFR along-axis seismic model for NDOBS2 on Line 4 (see figure 2.1 for instrument location).

(a) Filtered vertical component record section plotted at true amplitude to show the amplitude variations of the first arrivals. Display parameters are described in figure 4.2a. Inset shows the region where an intracrustal reflection generated from the top of layer 3 (~28.5 km model offset) should be observed (cf. figure 4.21).

(b) Synthetic seismograms calculated from the final model. Display parameters are described in figure 4.2b.

(c) Final model with, for clarity, a subset of the rays used to calculate the synthetic seismograms shown in (b). Display parameters are described in figure 4.1.

- The first-order boundary at the base of layer 2 denotes a velocity step of -2.35 km s^{-1} and is located at a depth of 2.9 ± 0.3 km below the seabed. The smaller velocity contrast across this boundary (cf. the across-axis profiles) is purely a function of more detailed modelling of layer 2B/C on the along-axis profile, which generates a slightly lower velocity at the base of layer 2 and is not due to any kind of anisotropy. Below this boundary a low velocity block, nominally assigned a seismic velocity of 3.0 km s^{-1}, is included across the entire length of the profile. In the absence of the low velocity block, rays turning beneath layer 2 arrive at too large an amplitude compared with the observed data, though the prime evidence for its existence is the P_cP reflection observed behind the direct water wave on SDOBS4 (figure 4.21: highlighted region between 2.0 and 3.0 s reduced time). Due to the absence of arrivals with amplitudes significantly above the noise level travelling through the low velocity block, an estimation of its thickness cannot be determined from the along-axis data alone, thus a thickness of 100 m, taken from the across-axis profiles, was assigned to the layer.
- A P_cP reflection is not easily observed on NDOBS2 (figure 4.22: highlighted region between 2.25 and 3.25 s reduced time), although this may be due to the severe seabed topography at the OSC. A similar reduction in amplitude of rays travelling through the low velocity block and into layer 3 to that observed on SDOBS4 (>12 km model offset) provides evidence of the possible existence of the low velocity block at this location.
- The intersection points with the across-axis profiles provide the only constraint on the seismic structure below the low velocity block, as a result of a lack of any lower crustal arrivals identified on the axial instruments. Layer velocities have been simply interpolated between the two intersection points (see figure 4.20).

The significance of the final velocity-depth model for the along-axis profile, Line 4, in relation to the general crustal structure at the VFR will be discussed in Chapter 6. The variation in the upper crustal thickness and depth to the low velocity block have important implications when comparing the processes of crustal accretion at the VFR with other mid-ocean ridges.

4.4.3 Best fitting wide-angle seismic model - Line 9

The final velocity-depth model for Line 9 is shown in figure 4.23. The layering previously described in the initial model remains, however a low velocity block equivalent to the one modelled on Line 4 is also incorporated into the model.

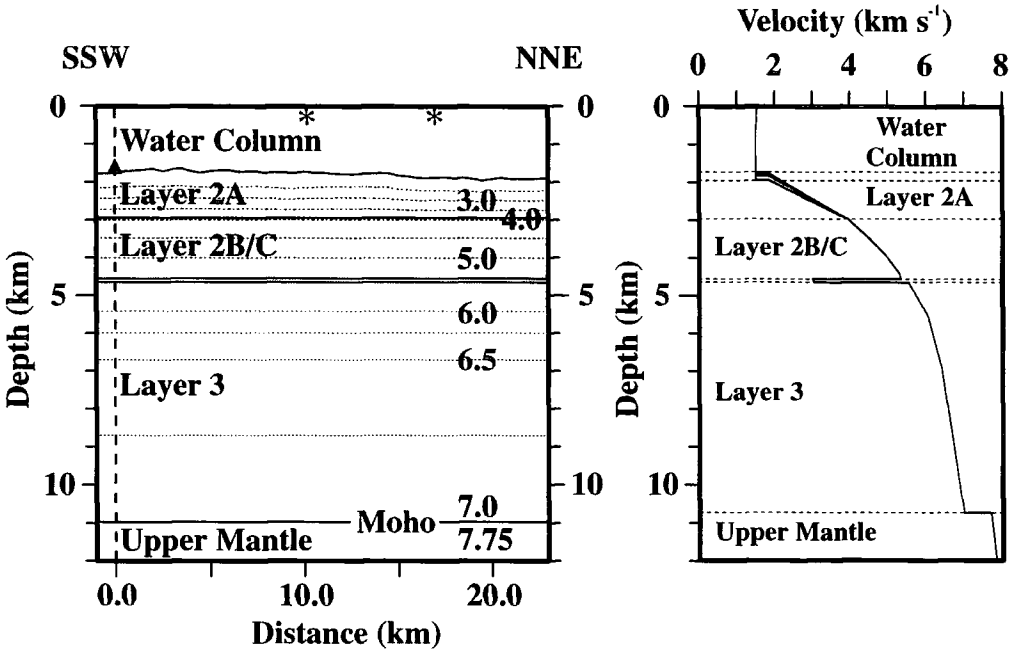

Figure 4.23: Line 9, along-axis final model. Display parameters are described in figure 4.4. Sonobuoy locations are denoted by stars. Velocity-depth profiles are calculated at ~5 km intervals. Vertical exaggeration x2.

Final ray-trace modelled sections for NDOBS3 and the two sonobuoys deployed along Line 9 are shown in figures 4.24 and 4.25. The off-axis location of NDOBS3 and the drift observed on the sonobuoys provide relatively poor constraint on the seismic structure of this line in comparison with the other profiles. Horizontal layer boundaries below the seabed provide a good fit to the majority of the data while the poor fit of the sonobuoy data on figure 4.25 (sonobuoy located at 9.25 km) is most likely due to drift off-line during shot firing (the predominant drift direction is to the northeast). All velocities described in the model are P-wave seismic velocities and depths are described in km below the sea surface.

- Layer 2A is modelled with an average thickness of 1.15 km and upper boundary (directly beneath the seabed) and lower boundary velocities of 1.75-1.95 km s^{-1} and 3.9 km s^{-1} respectively. The layer 2A/2B boundary, located at a depth of 2.95

km marks a velocity step of 0.05 km s^{-1} and a reduction in the vertical velocity gradient from an average of 1.78 s^{-1} to 1.03 s^{-1}.

- The division of layer 2B/C by two second-order boundaries (coincident with the 4.9 and 5.3 km s^{-1} isovelocity contours) modelled on Line 4 is also incorporated into the model of Line 9 to simulate the gradual reduction in amplitude of the first arrivals travelling near the base of layer 2 (figure 4.24: 8 to 11 km model offset). These two second-order boundaries are located at a depth of 3.9 and 4.4 km on Line 9 and thus decrease the vertical velocity gradient from 1.0 to 0.8 s^{-1} at the first boundary and from 0.8 to 0.33 s^{-1} at the deeper boundary. The velocity at the base of layer 2 is 5.35 km s^{-1}.
- A low velocity block similar to those observed on the across-axis profiles and Line 4 is included in the model at a depth of 4.55 km with a thickness of 100 m to faithfully reproduce the low amplitudes of rays turning in layer 3 (figure 4.24: >11 km model offset). However, the low velocity block may in fact lie off-line to the east as NDOBS3 (used to model this profile) is actually located in the overlap basin and the low velocity block modelled on Line 6 does not extend as far as the intersection point with Line 9. The minimum shot-receiver offset on NDOBS3 is 1.4 km as a consequence of its off-axis location, which limits the possibility of identifying a P_cP reflection on this instrument as the amplitude of the tail-end of the direct water wave is large compared with the reflection at offsets greater than 2.0 km (cf. inset on figure 4.21a: ~0 km model offset). The noise on the sonobuoy data also prevents the identification of any possible phases behind the seabed reflection at near offsets.
- There is no constraint on the velocity structure below layer 2. The velocity structure in layer 3 and the upper mantle are coincident with the intersection point on Line 6 and are as described for the initial model for this line.

The significance of the final velocity-depth model of the NVFR along-axis profile, Line 9, in relation to the general crustal structure at the VFR will also be discussed in Chapter 6.

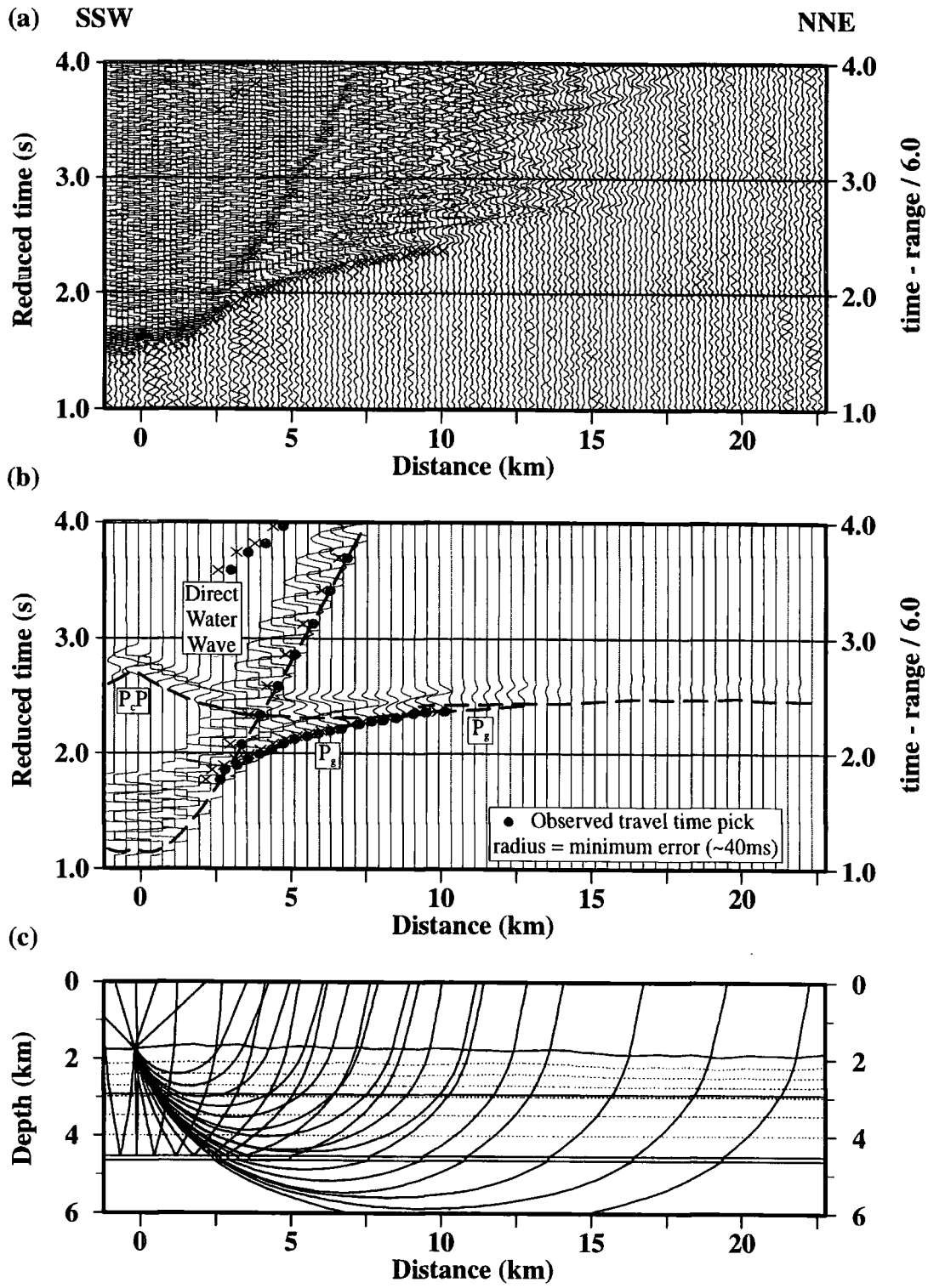

Figure 4.24: Ray-trace modelling of the final NVFR along-axis seismic model for NDOBS3 on Line 9 (see figure 2.1 for instrument location).

(a) Filtered vertical component record section plotted at true amplitude to show the amplitude variations of the first arrivals. Display parameters are described in figure 4.2a.

(b) Synthetic seismograms calculated from the final model. Display parameters are described in figure 4.2b. Note that the crosses and dots represent travel time picks before and after the adjustment for the range to NDOBS3 respectively.

(c) Final model with, for clarity, a subset of the rays used to calculate the synthetic seismograms shown in (b). Display parameters are described in figure 4.1.

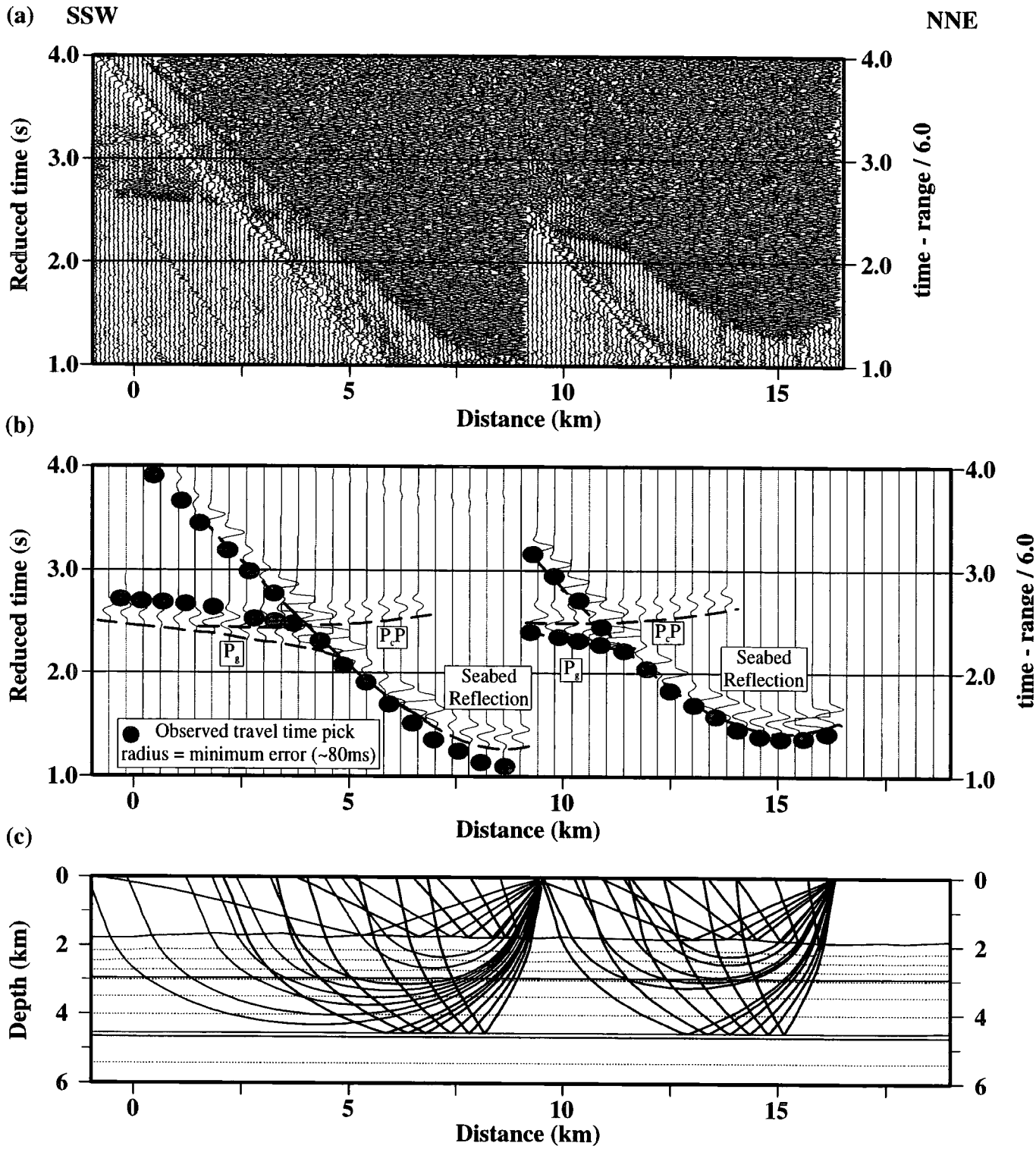

Figure 4.25: Ray-trace modelling of the final NVFR along-axis (Line 9) seismic model for two sonobuoys (see figure 2.1 for sonobuoy locations).

(a) Sonobuoy record sections corrected for instrument drift. Display parameters are described in figure 4.2a.

(b) Synthetic seismograms calculated from the final model. Display parameters are described in figure 4.2b. Note that the minimum error on the sonobuoy travel time picks is ~80 ms. Note the misfit of the upper crustal phases (P_g) on the SSW sonobuoy, possibly due to drift off-line and away from the ridge crest after deployment.

(c) Final model with, for clarity, a subset of the rays used to calculate the synthetic seismograms shown in (b). Display parameters are described in figure 4.1.

4.5 Axis-parallel profiles - Line 5 and Line 11

Two axis-parallel profiles, situated 40 km (Line 5) and 21 km (Line 11) west of the CVFR axis were modelled to provide further constraint on the off-axis velocity structure. SDOBS1 and NDOBS6 (see figure 2.1 for instrument locations) were located at the extreme ends of Line 5 (0 and 28.5 km model offset respectively) and correspond to the intersections with Line 1 and Line 6. Data recorded by disposable sonobuoys, deployed during *Seismic South* were also used to help constrain upper crustal velocities.

Line 11 was shot as an additional line on *Seismic North* (see section 2.2) and the model is constrained solely by NDOBS5 (see figure 2.1 for instrument location), in other words it is not reversed.

4.5.1 Initial models

Both axis-parallel profiles were analysed during the final stages of modelling of the wide-angle seismic dataset and initial models were generated from the intersection points with the two across-axis profiles. The velocity structure across the entire profile is thus a result of simple interpolation between the two intersection points (see figures 4.4 and 4.12).

Line 5

The main features of the initial model for Line 5 are described below.

- The model is divided by four layer boundaries, which extend across the entire model and mark a change in the vertical velocity gradient and, in the case of the seabed and Moho, a distinct velocity step.
- The water column structure is the same as Line 1.
- The velocity at the top of layer 2A decreases from 2.1 km s^{-1} at the southern end of the profile to 1.9 km s^{-1} at the northern end. The layer 2A/2B boundary (coincident with the 4.0 km s^{-1} isovelocity contour) is located at a depth of 3.55-3.6 km (i.e. the average thickness of layer 2A is ~1.5 km) and denotes a decrease in the vertical velocity gradient from 1.33 to 0.81-0.94 s^{-1}.
- Layer 2B/C is modelled with a velocity of 4.0 and 6.15 km s^{-1} at its upper and lower boundaries respectively and an average thickness of 2.5 km.
- The thickness of layer 3, delimited by the layer 2/3 boundary and the Moho, is ~3.6 km and is further subdivided by two second-order boundaries which reduce

the vertical velocity gradient from ~0.36 to ~0.31 s^{-1} and ~0.31 to ~0.11 s^{-1}. The Moho is modelled at a depth of 11.0 km and marks a velocity step of 0.85 and 0.75 km s^{-1} at the southern and northern ends of the profile respectively.

- The upper mantle, modelled down to a depth of 20.0 km (8.2 km s^{-1} isovelocity contour) is split by a second-order boundary which reduces the vertical velocity gradient from ~0.1 to ~0.02 s^{-1}.

The results of ray-trace modelling of the initial model (described above) and the travel time and amplitude fit of the main phases are described below and in figures 4.26 and 4.27. The main topographic feature observed on Line 5 is the large seamount centred on 19 km model offset (see figure 2.1 and figure 4.26) and out-of-plane effects arising from this feature must be considered when determining the significance of the travel time misfit.

- The velocity structure constructed from the two intersection points on the across-axis profiles provides a remarkably good fit to the observed travel times of first arrivals on both DOBSs.
- The only significant travel time misfits of the synthetic first arrivals are associated with rays that turn beneath the large seamount centred on 19 km model offset (figure 4.26: 17 to 25 km model offset and figure 4.27: 12 to 22 km model offset). First arrivals tracing through this region arrive at a considerable delay (up to 500 ms) which implies that the upper crust beneath the seamount must be thinner compared with the initial model and/or higher velocities exist within this region.
- Knowledge and experience gained from modelling the other profiles in the VFR dataset tends to suggest that the larger amplitude secondary arrivals observed on figure 4.27 (<6 km model offset, ~2.8 s reduced time) are generated by a reflection from the Moho (P_mP).
- The amplitude fit of the synthetic data generated from the initial model is very good, with the exception of the region close to the seamount where the amplitude of phases are generally too large. This variation in amplitude may be due to a different velocity and attenuation structure beneath the seamount or may simply be a function of the increased scattering of seismic energy at the rougher seabed.

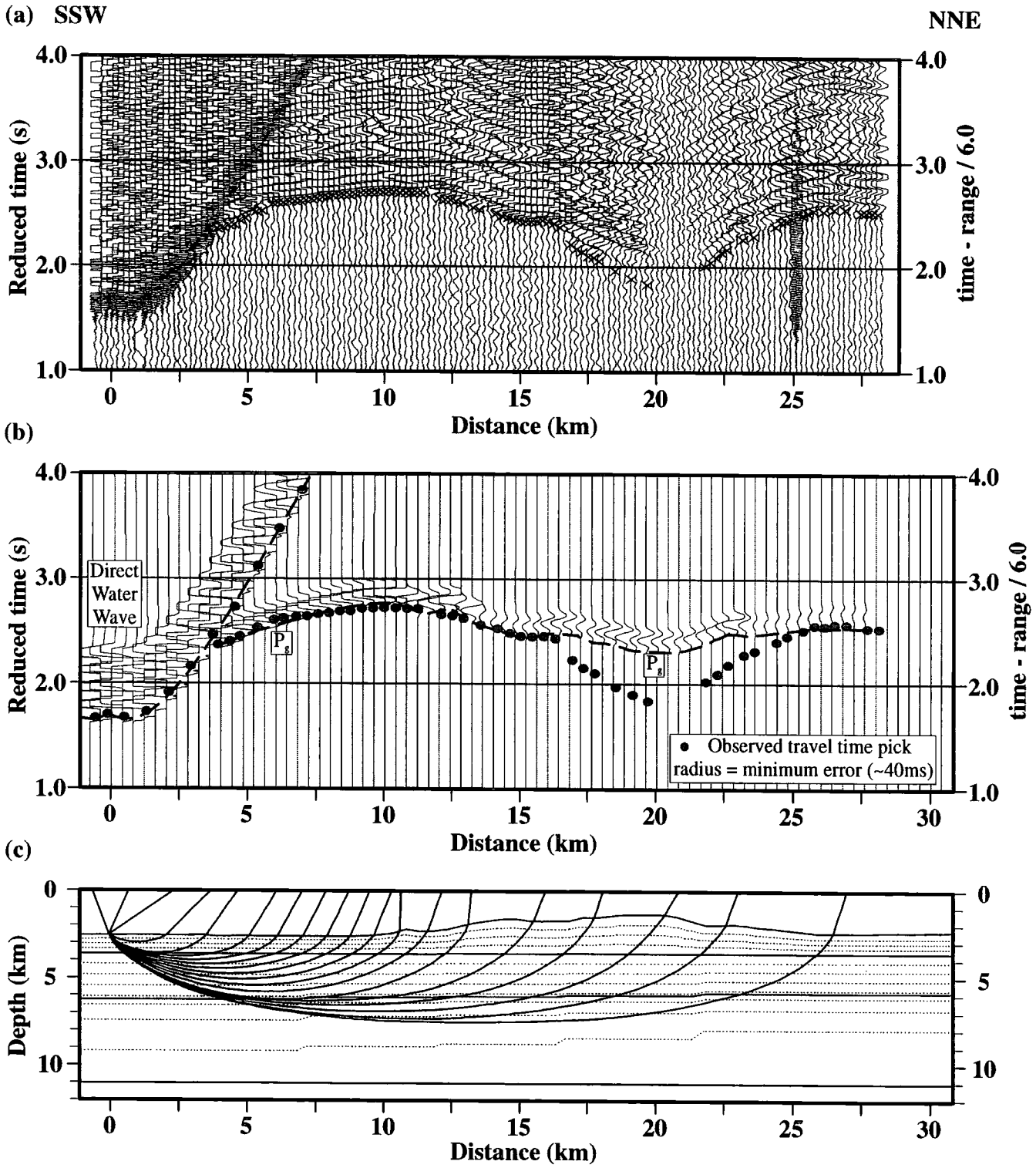

Figure 4.26: Ray-trace modelling of the initial axis-parallel seismic model for SDOBS1 on Line 5 (see figure 2.1 for instrument location).

(a) Filtered vertical component record section plotted at true amplitude to show the amplitude variations of the first arrivals. Display parameters are described in figure 4.2a. Note the reduction in amplitude between 17 km and 25 km model offset and the larger amplitude secondary arrival between 17 and 20 km model offset.

(b) Synthetic seismograms calculated from the initial model. Display parameters are described in figure 4.2b.

(c) Initial model with, for clarity, a subset of the rays used to calculate the synthetic seismograms shown in (b). Display parameters are described in figure 4.1.

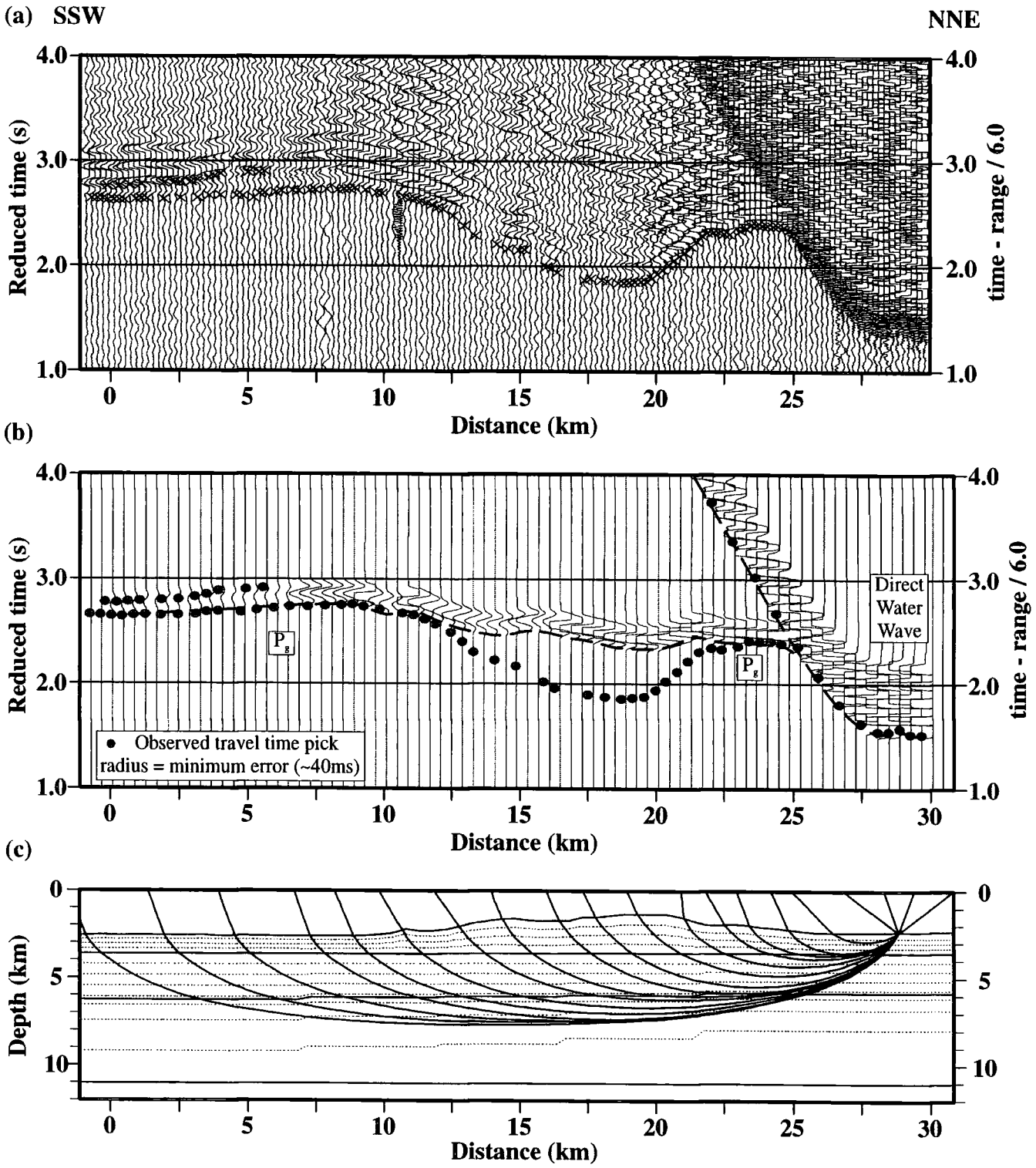

Figure 4.27: Ray-trace modelling of the initial axis-parallel seismic model for NDOBS6 on Line 5 (see figure 2.1 for instrument location).

(a) Filtered vertical component record section plotted at true amplitude to show the amplitude variations of the first arrivals. Display parameters are described in figure 4.2a. Note the loss of amplitude of first arrivals between 13 and 20 km model offset and the large amplitude secondary arrivals observed at model offsets less than 6 km.

(b) Synthetic seismograms calculated from the initial model. Display parameters are described in figure 4.2b.

(c) Initial model with, for clarity, a subset of the rays used to calculate the synthetic seismograms shown in (b). Display parameters are described in figure 4.1.

Line 11

The main features of the initial model for Line 11 are described below.

- The initial model is divided into a water column (see Line 1 for details of its velocity structure), three crustal layers (layer 2A, layer 2B/C and layer 3) and an upper mantle.
- Layer 2A increases in velocity from 1.85-2.15 km s^{-1} at the seabed to 4.0 km s^{-1} at the layer 2A/2B boundary and is modelled with a thickness of 1.1-1.4 km and an average vertical velocity gradient of 1.6 s^{-1}.
- The thickness of layer 2B/C decreases from 2.65 km to 1.9 km between the intersections with Line 1 and Line 6 respectively (i.e. decreases in thickness to the north of the profile) and the velocity at the base of this layer also increases from 6.15 to 6.25 km s^{-1} in the same direction.
- Layer 3, with an average thickness of 4.25 km and upper and lower boundary velocities of ~6.2 and 7.0 km s^{-1} respectively, is divided by two second-order boundaries similar to those described for Line 5.
- The Moho, situated at the base of layer 3, denotes a velocity step of 0.75-0.85 km s^{-1}, however the vertical velocity gradient does not change significantly across this boundary.
- The upper mantle is divided by a second-order boundary ~1.5 km beneath the Moho which decreases the vertical velocity gradient from 0.1 to 0.02 s^{-1}.

The travel time and amplitude fit of the ray-trace modelled sections are described below and shown in figure 4.28. Out-of-plane effects are again a considerable problem on Line 11 due to the seamount located east of 20-25 km model offset (figure 2.1: 22° 12′ S) and the large off-axis ridge running parallel to and to the west of the profile (see figure 2.1 for ridge location).

- The travel time fit of upper crustal phases is generally good with a slight delay (~100 ms) observed between 13 and 23 km model offset, although the travel time fit at model offsets less than 13 km increases to ~250 ms and is perhaps due to the influence of the off-axis ridge located to the west.
- The relative amplitudes of the lower crustal phases are too high between 5 and 13 km model offset, which suggests that the velocity structure of the mid-lower crust is not accurately represented in the initial model.

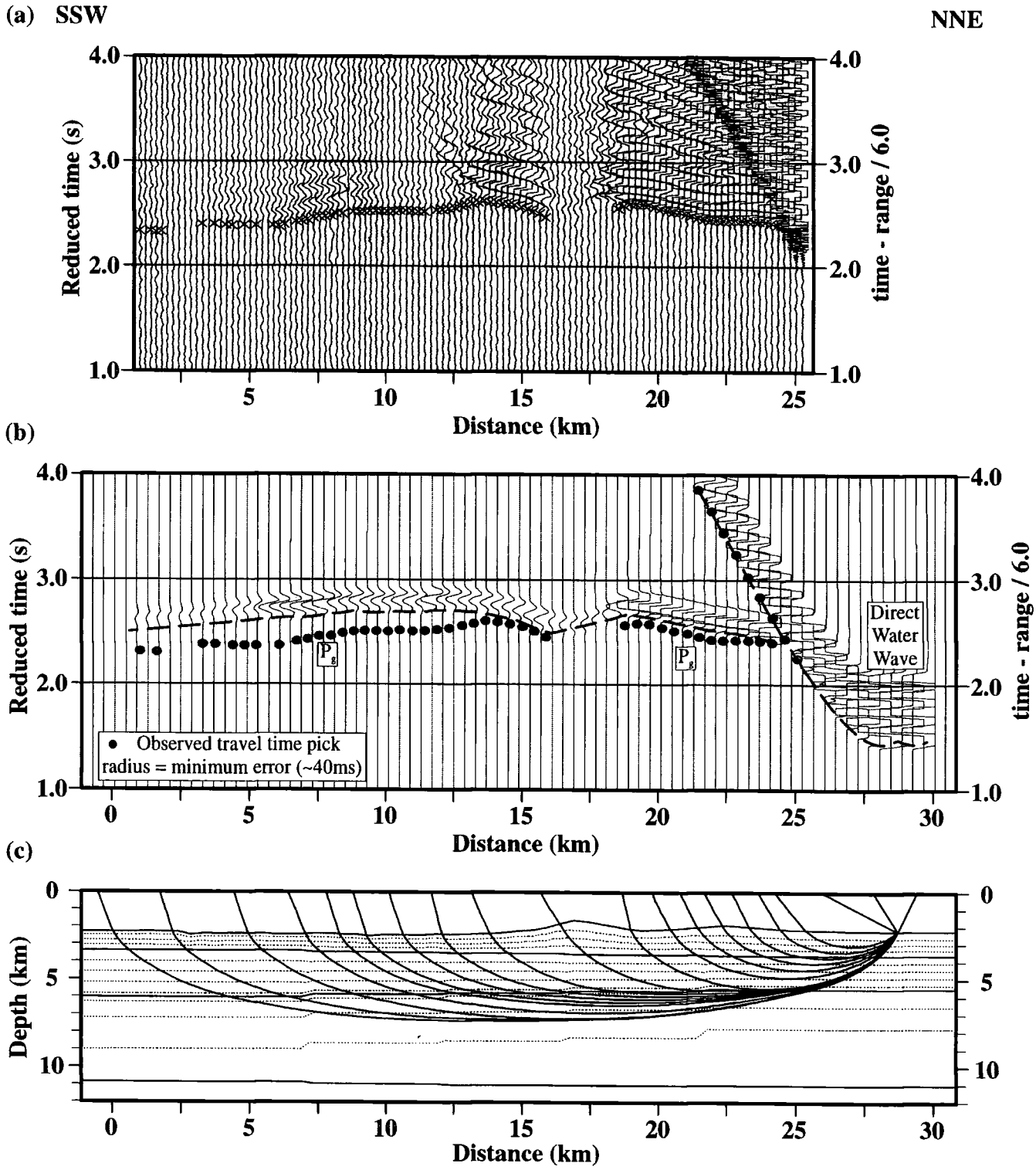

Figure 4.28: Ray-trace modelling of the initial axis-parallel seismic model for NDOBS5 on Line 11 (see figure 2.1 for instrument location).

(a) Filtered vertical component record section plotted at true amplitude to show the amplitude variations of the first arrivals. Display parameters are described in figure 4.2a. Note the general reduction in amplitude at model offsets less than 13 km.

(b) Synthetic seismograms calculated from the initial model. Display parameters are described in figure 4.2b.

(c) Initial model with, for clarity, a subset of the rays used to calculate the synthetic seismograms shown in (b). Display parameters are described in figure 4.1.

4.5.2 Best fitting wide-angle seismic model - Line 5

The final velocity-depth model for Line 5 is shown in figure 4.29 and the layering described in the initial model remains.

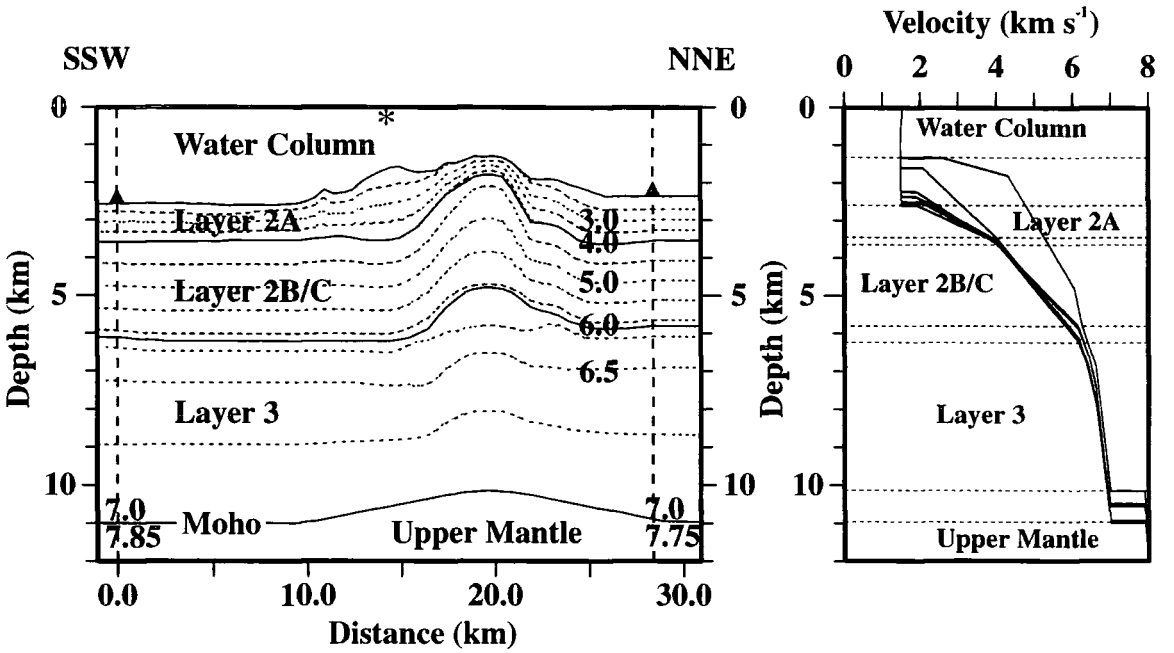

Figure 4.29: Line 5, axis-parallel final model. Display parameters are described in figure 4.4. Sonobuoy location is marked by a star. Velocity-depth profiles are calculated at ~5 km intervals. Vertical exaggeration x2.

The final ray-trace modelled sections for SDOBS1 and NDOBS6 (see figure 2.1 for instrument locations) are shown in figures 4.30 and 4.31. Data recorded on a sonobuoy, deployed during *Seismic South* and located at ~14 km model offset, was also used to constrain the final velocity model and a complete set of ray-trace modelled sections can be found in Appendix B.

A good travel time and amplitude fit was achieved for all data and the main features of the final velocity-depth model are described below. All velocities described in the model are P-wave seismic velocities and depths are described in km below the sea surface.

- The majority of the velocity structure described in the initial model is still present in the best fitting velocity-depth model (see section 4.5.1 of details of this velocity structure), with the exception of the region surrounding the large seamount centred on 19 km model offset.

- Layer 2A thins considerably beneath the seamount to ~500 m and the upper boundary velocity increases to 2.6 km s^{-1}, although early first arrivals observed on both DOBS (e.g. figure 4.30: ~20 km model offset) may be out-of-plane arrivals generated from the sides of the seamount. The ridge running northeast-southwest just to the south of the seamount (see figure 2.1) and crossing Line 5 between 14 and 15 km model offset marks a local thickening of layer 2A (~1.9 km), however the velocity structure of this ridge below layer 2A is concordant with the initial model.
- The layer 2A/2B boundary (modelled with a velocity of 4.3 km s^{-1} beneath the seamount) marks a decrease in vertical velocity gradient from ~3.5 to ~0.6 s^{-1} and the thickness of layer 2B/C increases by ~500 m beneath the seamount (total thickness of 3 km).
- The depth to the layer 2/3 boundary (coincident with the 6.15 km s^{-1} contour) decreases by ~1 km beneath the seamount and marks a further decrease in the vertical velocity gradient from ~0.6 to 0.2 s^{-1}.
- Layer 3 is divided by the two second-order boundaries described in the initial model, but the Moho gradually decreases in depth and is ~800 m shallower than elsewhere beneath the seamount.

The final velocity-depth model for Line 5 provides detailed information on the crustal structure of possible pre-rift material and the significance of this in relation to the general crustal structure at the VFR will be discussed in Chapter 6.

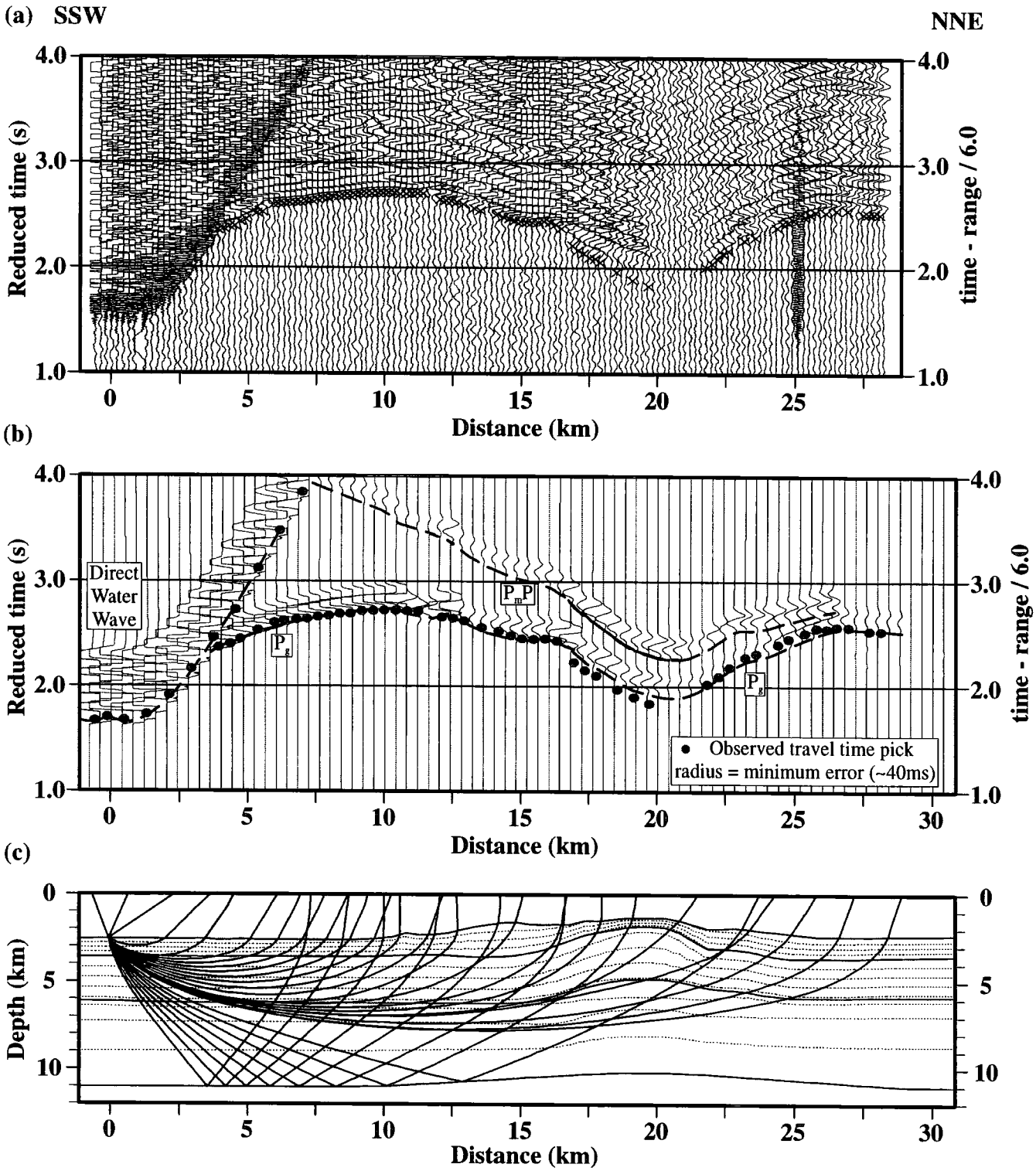

Figure 4.30: Ray-trace modelling of the final axis-parallel seismic model for SDOBS1 on Line 5 (see figure 2.1 for instrument location).

(a) Filtered vertical component record section plotted at true amplitude to show the amplitude variations of the first arrivals. Display parameters are described in figure 4.2a.

(b) Synthetic seismograms calculated from the final model. Display parameters are described in figure 4.2b. Note the slight misfit in travel time and amplitude of the arrivals between 17 and 21 km model offset, possibly caused by the off-axis extent of the seamount located 20 km model offset.

(c) Final model with, for clarity, a subset of the rays used to calculate the synthetic seismograms shown in (b). Display parameters are described in figure 4.1.

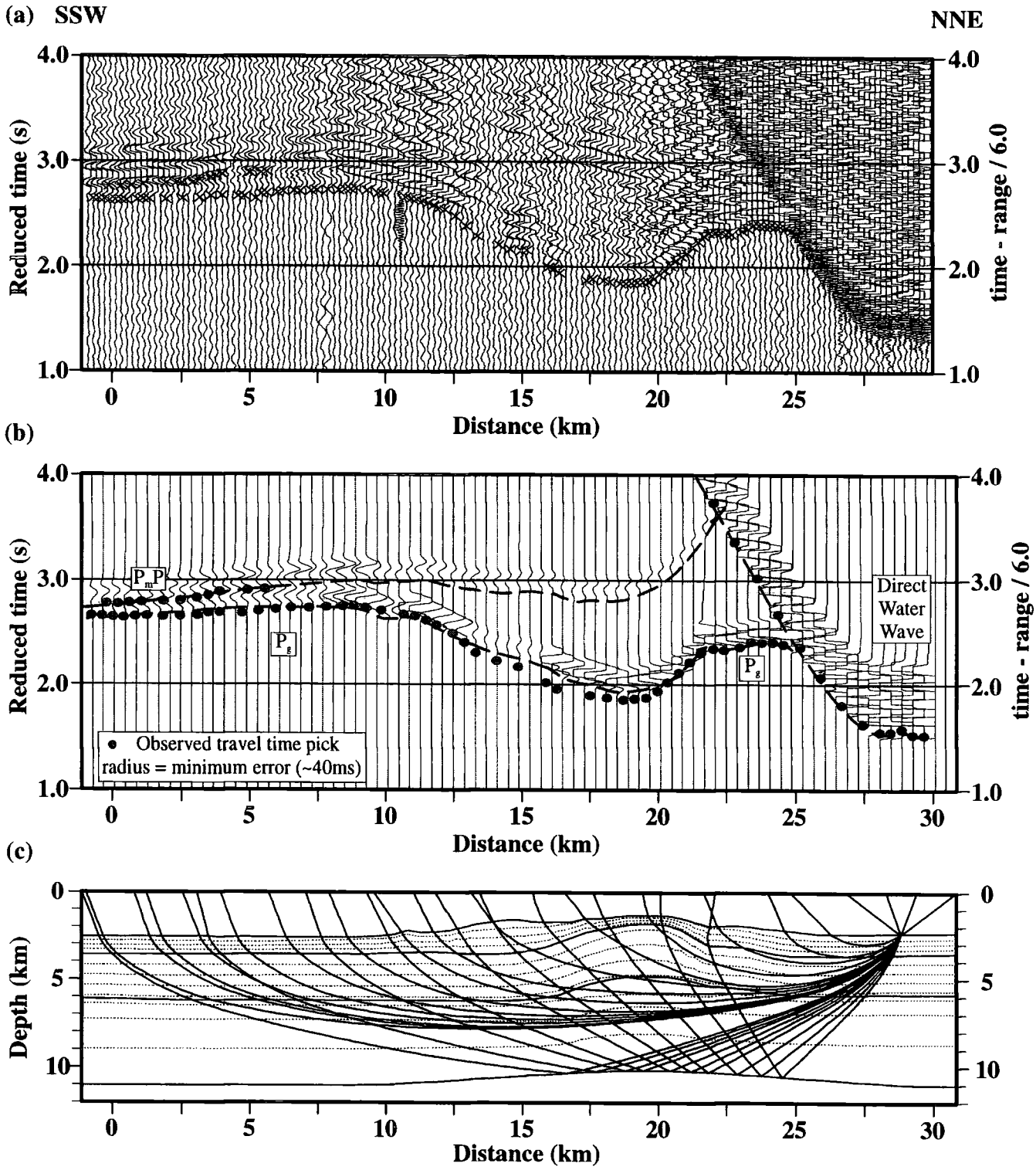

Figure 4.31: Ray-trace modelling of the final axis-parallel seismic model for NDOBS6 on Line 5 (see figure 2.1 for instrument location).

(a) Filtered vertical component record section plotted at true amplitude to show the amplitude variations of the first arrivals. Display parameters are described in figure 4.2a.

(b) Synthetic seismograms calculated from the final model. Display parameters are described in figure 4.2b. Note the general amplitude and travel time fit of the primary (P_g) and secondary (P_mP) phase between 0 and 7 km model offset.

(c) Final model with, for clarity, a subset of the rays used to calculate the synthetic seismograms shown in (b). Display parameters are described in figure 4.1.

4.5.2 Best fitting wide-angle seismic model - Line 11

The final velocity-depth model for Line 11 is shown in figure 4.32 and the layering described in the initial model remains.

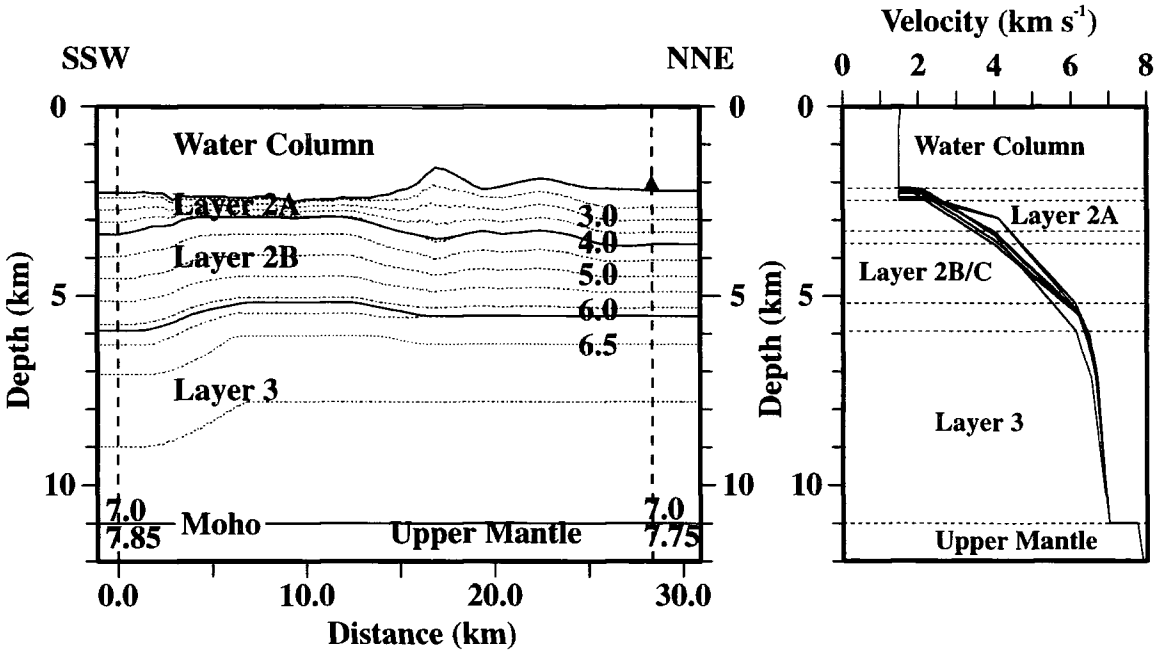

Figure 4.32: Line 11, axis-parallel final model. Display parameters are described in figure 4.4. Velocity-depth profiles are calculated at ~5 km intervals. Vertical exaggeration x2.

The final ray-trace modelled section for NDOBS5 (see figure 2.1 for instrument location) is shown in figure 4.33. The synthetic travel time fit of the final velocity-depth model is good and the main features of this final model are described below. All velocities described in the model are P-wave seismic velocities and depths are described in km below the sea surface.

The relative amplitude of the lower crustal phases (figure 4.33: <13 km model offset) could not be faithfully reproduced during ray-trace modelling and the low amplitudes observed in the NDOBS5 dataset are interpreted to be the result of out-of-plane effects originating from the off-axis ridge located to the west of Line 11.

- The top of layer 2A has a velocity of 1.85 km s^{-1} at the northern end of Line 11, which increases to 2.3 km s^{-1} to the south (<13 km model offset) and a lower boundary velocity of 4.0 km s^{-1}. The thickness of layer 2A is ~1 km and ~1.4 km at the southern and northern ends of line 11 respectively and locally thickens beneath the seamount located at 17 km model offset. The 'early' first arrivals observed between 3 and 13 km model offset have been modelled as the result of

significant thinning of layer 2A to ~500 m, however they may also be due, in part, to rays travelling off-line through shallower crust to the west (i.e. shallower crust ⇒ shorter path through the lower velocity water column ⇒ earlier travel time), which is substantiated by the associated low amplitudes described above.

- Beneath layer 2A the final model does not differ significantly from the initial model for Line 11 described in section 4.5.1 and layer 2B/C and layer 3 are modelled with thicknesses of 2.45 ± 0.2 km and 4.9 ± 0.3 km respectively.
- There is no constraint on the model below ~7 km with this dataset, with the exception of the intersection points on the across-axis profiles.

Line 11, as previously mentioned, crosses the 'pseudofault' described by Wiedicke and Collier (1993) and interpreted as the transition between pre-rift and post-rift crust. The final velocity-depth model for Line 11 thus provides an opportunity to look at this 'transition' beneath the seabed and its significance in relation to the general crustal structure at the VFR will be discussed in Chapter 6.

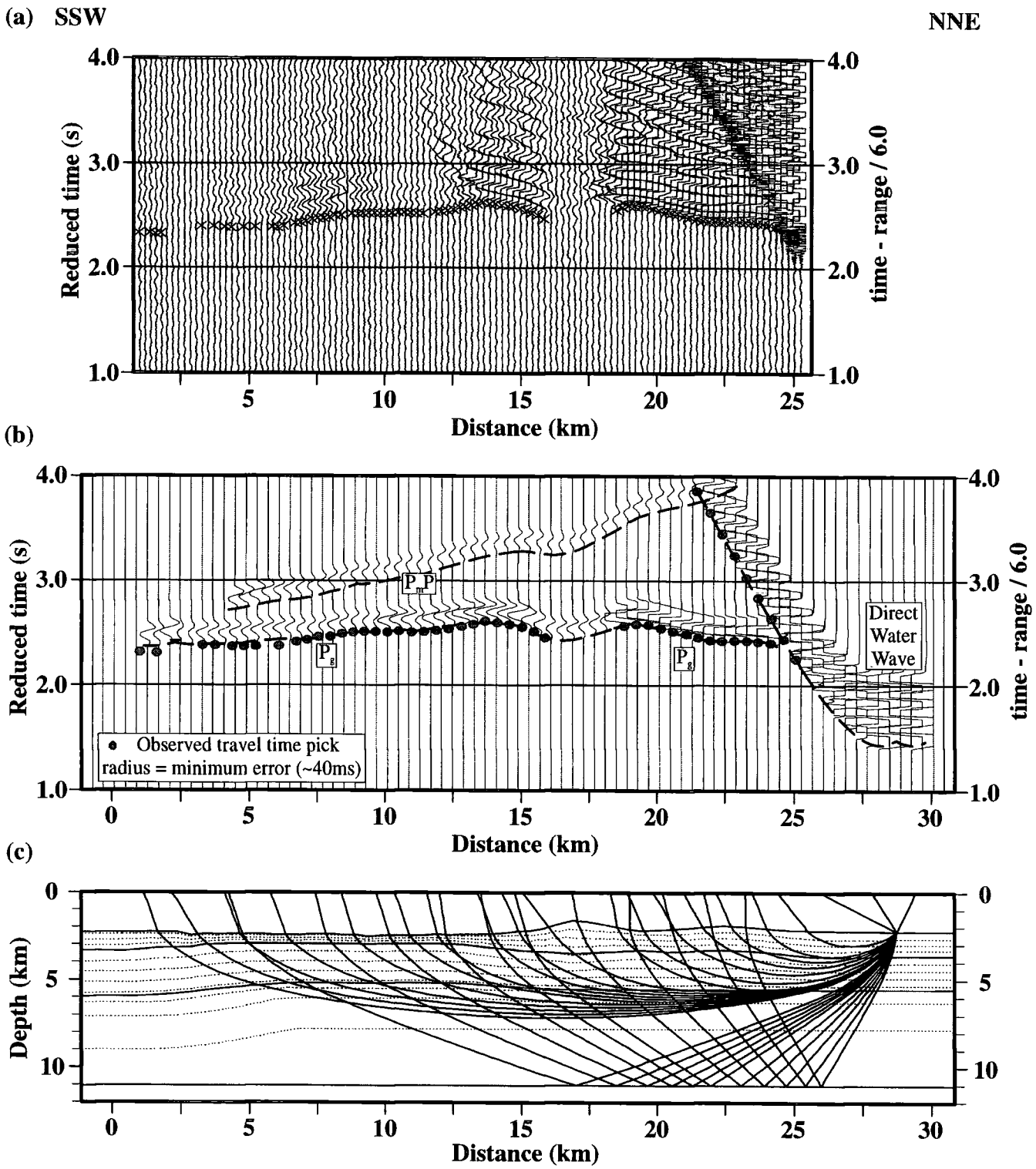

Figure 4.33: Ray-trace modelling of the final axis-parallel seismic model for NDOBS5 on Line 11 (see figure 2.1 for instrument location).
(a) Filtered vertical component record section plotted at true amplitude to show the amplitude variations of the first arrivals. Display parameters are described in figure 4.2a.
(b) Synthetic seismograms calculated from the final model. Display parameters are described in figure 4.2b. Note the misfit in the relative amplitude of the first arrivals at model offsets less than 13 km, perhaps the influence of out-of-plane features (see main body of text for details).
(c) Final model with, for clarity, a subset of the rays used to calculate the synthetic seismograms shown in (b). Display parameters are described in figure 4.1.

4.6 Further modelling of the wide-angle seismic dataset

A detailed description of the modelling of the wide-angle dataset using *maslov* (based on Maslov asymptotic ray theory [ART]) can be found in section 4.2.2. This section also introduced the program *rayinvr* (based on the numerical solution of ART), which was used to check the synthetics generated from *maslov*.

The CVFR along-axis data (Line 4) was also modelled using the reflectivity method of Fuchs and Müller (1971) in an attempt to faithfully reproduce the P_cP and P_cS reflections generated from the top of the low velocity block (see section 4.4.2).

4.6.1 *Rayinvr*

A detailed description of *rayinvr* and all other programs involved in the ray-trace modelling process can be found in Chapter 4 (pp.146-151) of Navin (1996). The final velocity-depth models were converted into the format required for *rayinvr* and ray-trace modelled for direct comparison with the results generated by *maslov*. The main disadvantages of modelling this dataset using *rayinvr* were:

- All layers defined in the model must extend across the entire model, which created particular problems when reproducing the low velocity block and the sediment ponds. Although not an ideal solution, this problem could be overcome by modelling these layers with zero thickness over the majority of the model.
- The input model must be parameterised by fewer nodes on each layer, thus decreasing the complexity of the layer geometries, which is of particular importance when trying to faithfully reproduce the seabed.
- Second-order boundaries (i.e. a simple change in the vertical velocity gradient) must be parameterised as pseudo 'first-order' boundaries for input into *rayinvr*.
- The ray-tracer has less control on the ray packets traced through the model and a separate ray packet must be described for each layer, which may result in gaps in the ray coverage and create artificial shadow zones.

The results of ray-trace modelling of Line 1 and Line 4 using both *maslov* and *rayinvr* are shown in figures 4.34 and 4.35. Note that the synthetic seismograms calculated by *rayinvr* are in general agreement with those calculated by *maslov*, which increases the confidence placed in the final velocity-depth models.

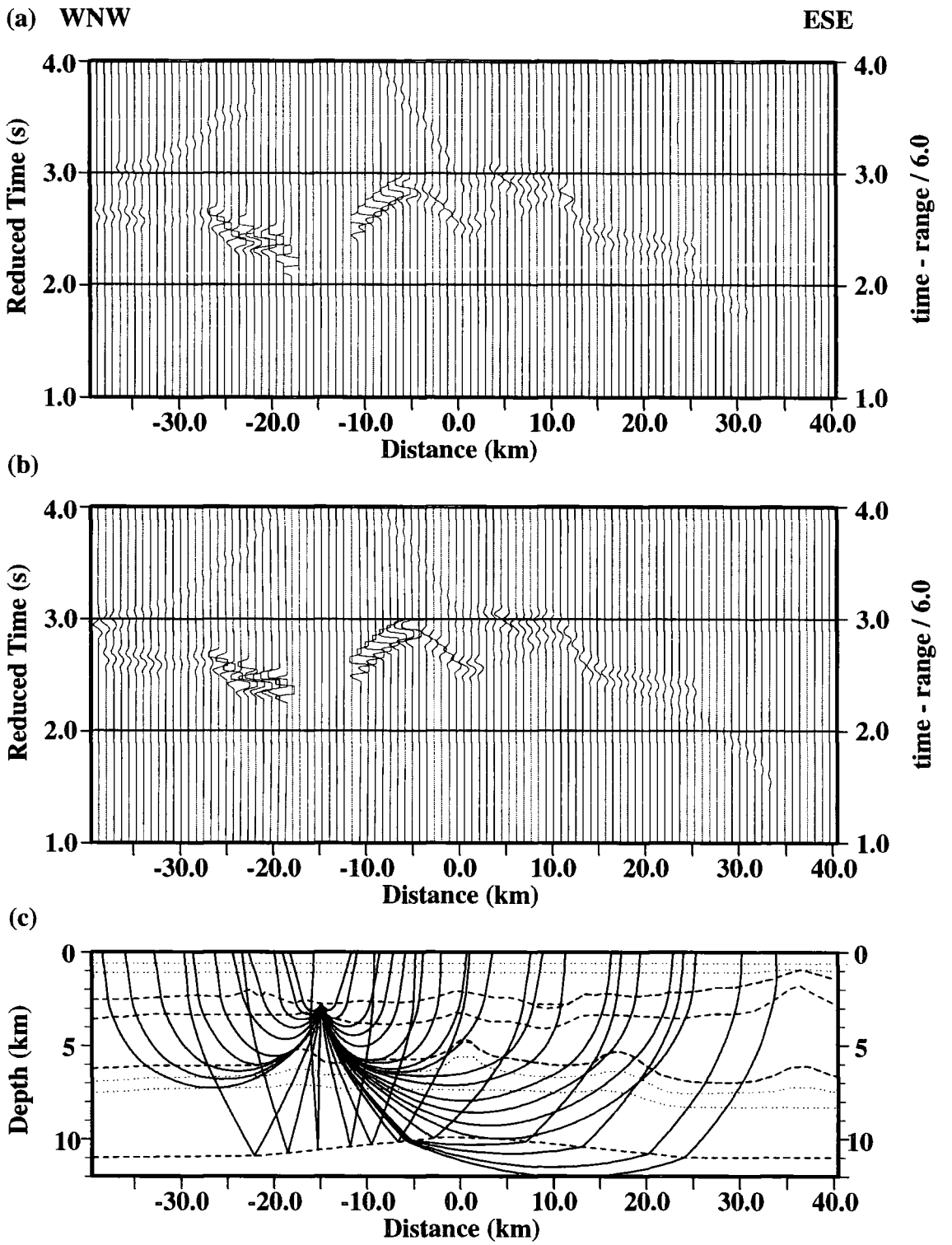

Figure 4.34: A comparison of the results of ray-trace modelling of the final across-axis (Line 1) seismic model for SDOBS2 (see figure 2.1 for instrument location) using two different programs, *maslov* and *rayinvr* (cf. figure 4.6).

(a) Synthetic seismograms calculated from the final model using the ray-trace modelling program *maslov*. Display parameters are described in figure 4.2b.

(b) Synthetic seismograms calculated from the final model using the ray-trace modelling program *rayinvr*. Display parameters are also described in figure 4.2b.

(c) Final model input for *rayinvr* with, for clarity, a subset of the rays used to calculate the synthetic seismograms shown in (b). Display parameters are described in figure 4.1.

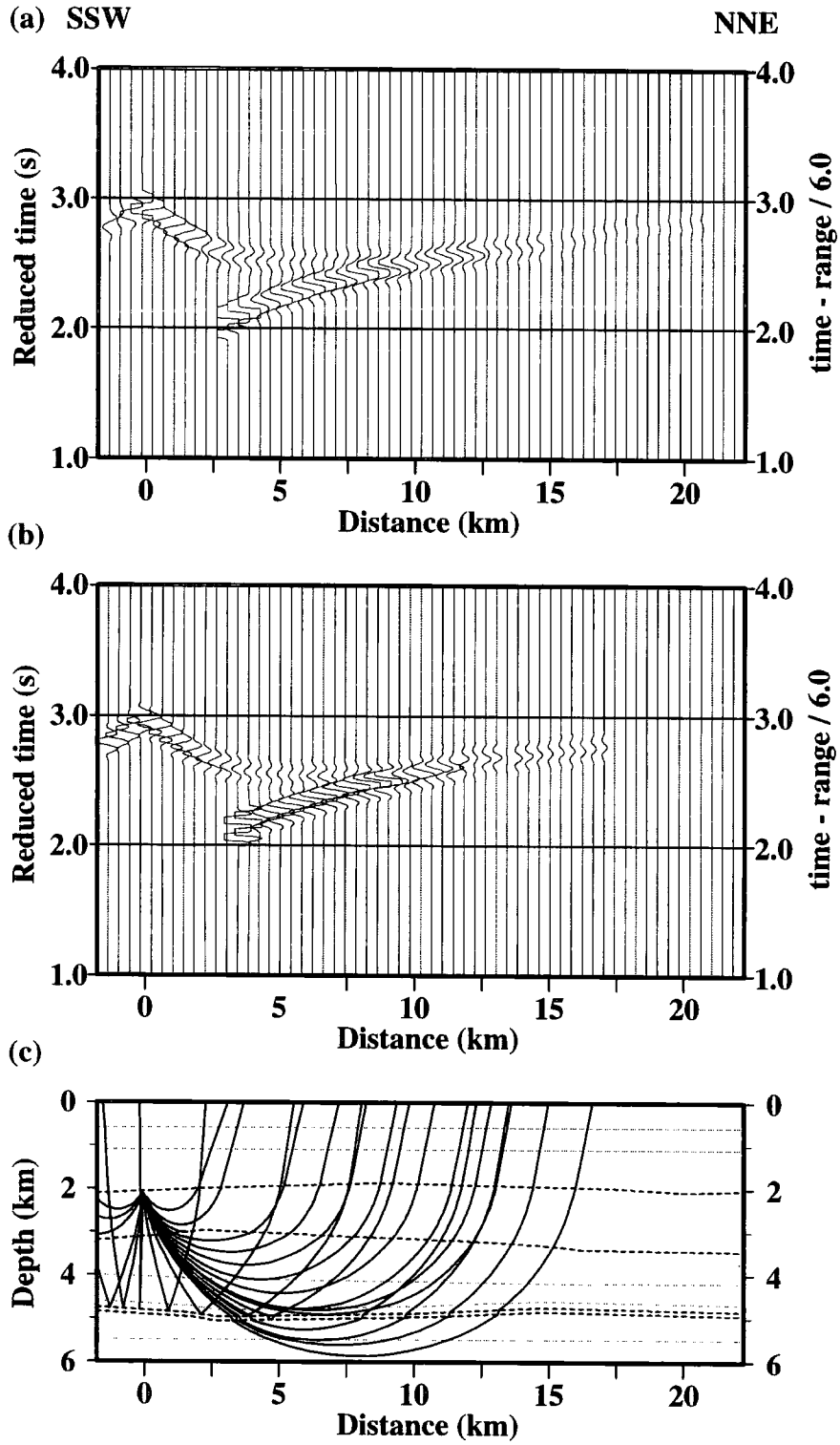

Figure 4.35: A comparison of the results of ray-trace modelling of the final CVFR along-axis (Line 4) seismic model for SDOBS4 (see figure 2.1 for instrument location) using two different programs, *maslov* and *rayinvr* (cf. figure 4.21).

(a) Synthetic seismograms calculated from the final model using the ray-trace modelling program *maslov*. Display parameters are described in figure 4.2b.

(b) Synthetic seismograms calculated from the final model using the ray-trace modelling program *rayinvr*. Display parameters are also described in figure 4.2b.

(c) Final model input for *rayinvr* with, for clarity, a subset of the rays used to calculate the synthetic seismograms shown in (b). Display parameters are described in figure 4.1.

4.6.2 *Reflectivity*

Wide-angle seismic data cannot be directly interpreted as knowledge of the velocity and density variations along the entire ray-path is required and the only exact solution is that given by the reflectivity method of Fuchs and Müller (1971), which is limited to one-dimension (Navin, 1996).

A one-dimensional approximation to the final CVFR along-axis velocity model (see figure 4.20) was used to compare the results generated from the *reflectivity* program with those calculated by *maslov*. The 1-D velocity-depth model used as input for the *reflectivity* program is shown in table 4.1. The velocity/density model is divided into 225 homogeneous layers of thickness 10-50 m, which faithfully reproduce the velocity gradients observed in the *maslov* model. Poisson's ratio (σ) decreases from ~0.40 directly beneath the seabed to ~0.35 at the base of layer 2 (just above the low velocity block) and is assigned a value of 0.3 in layer 3 (taken from Fowler, 1990). The S-wave velocity of the low velocity block is modelled as 0 km s^{-1}. One of the input parameters for the *reflectivity* program is the attenuation (Q) factor and the significance of these values (table 4.1: final column) will be discussed in detail later.

	depth (km)	V_p (km s^{-1})	no. of layers	thickness (m)	Q_p
water column	0.000	1.53	0	0	-
	0.600	1.49	12	50	-
	1.100	1.48	10	50	-
	2.120	1.50	28	40	-
layer 2A	2.120	1.90	1	0	22.5
	3.050	3.95	31	30	37.5
layer 2B/C	3.050	4.05	1	0	37.5
	4.050	4.90	50	20	80
	4.750	5.30	35	20	160
	4.900	5.35	15	10	175
low velocity block	4.900	3.00	1	0	20
	5.000	3.05	10	10	20
layer 3	5.000	5.50	1	0	50
	7.000	6.50	80	25	50

Table 4.1: 1-D velocity-depth model for the CVFR along-axis profile, Line 4, used as input for *reflectivity* modelling. The final column displays the Q values, calculated from amplitude modelling of the crustal diving ray which is discussed in greater detail in Chapter 6.

Synthetic seismograms calculated from both *maslov* and *reflectivity* are compared in figure 4.36 and the major upper crustal phases (crustal diving rays (P_g) and P_cP and P_cS reflections from the top of the low velocity block) are identified. The travel times of upper crustal phases and the large amplitude direct water waves are identical and the arrival observed at ~2.0 s on both sets of seismograms (figure 4.36: 0 to 2 km model offset) is identified as a reflection from the layer 2A/2B boundary. The additional arrivals located on the *reflectivity* synthetics (figure 4.36b: 4.0-7.0 km model offset, between 2.5 and 3.0s reduced time) are the result of diving rays that have travelled through layer 2A twice after reflection of the upgoing ray at the seabed (i.e. a peg-leg multiple - see figure 4.36b).

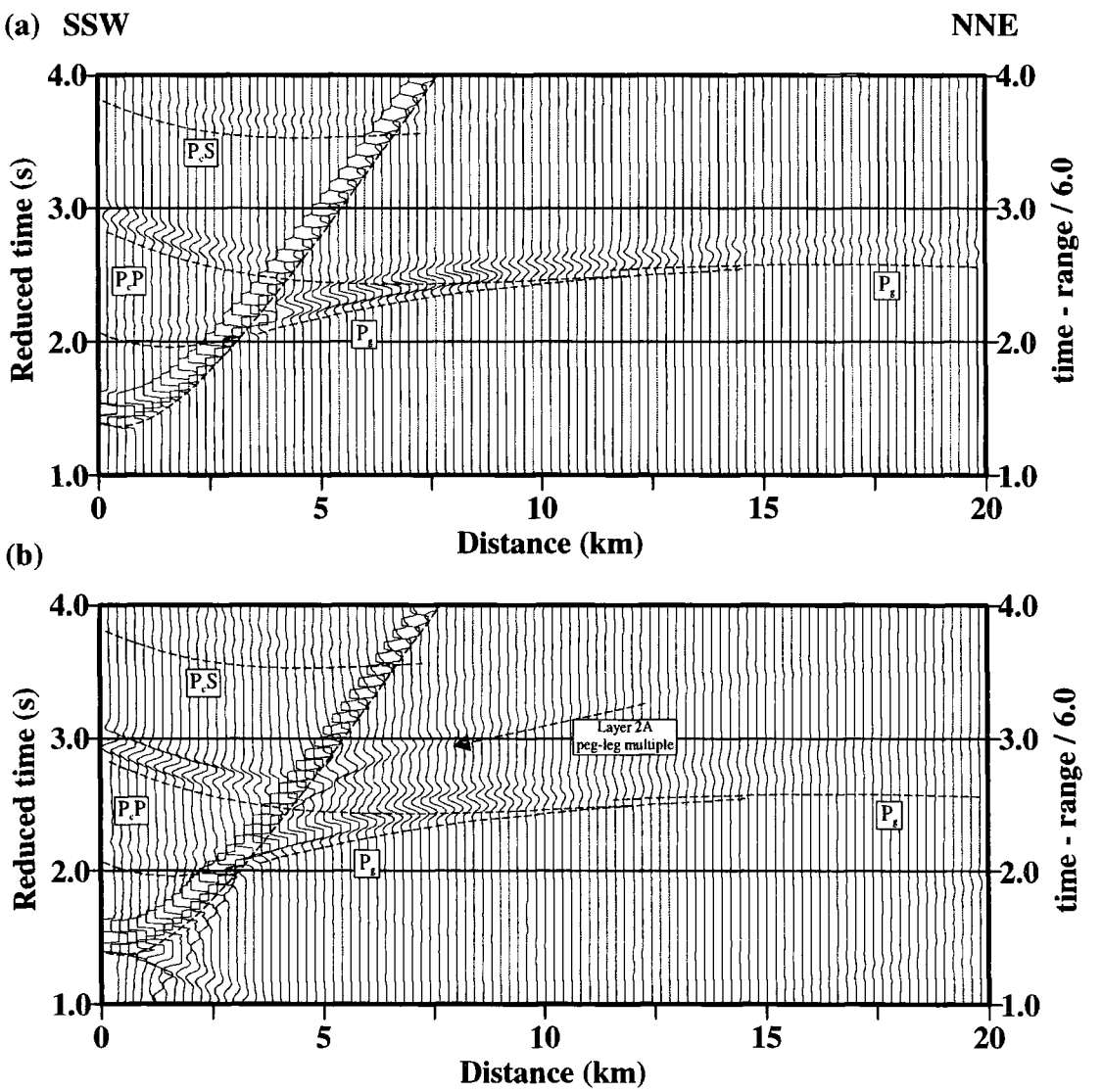

Figure 4.36: Synthetic data generated from a 1-D approximation to the final CVFR along-axis, Line 4, seismic model. Display parameters are described in figure 4.2b.
(a) Synthetic seismograms generated by the ray-trace modelling program *maslov*.
(b) Synthetic seismograms generated by the ray-trace modelling program *reflectivity*. Note the slight difference in amplitude with offset of the crustal diving ray (P_g), perhaps due to the low Q factors used in the *reflectivity* input.

After closer inspection of the synthetic seismograms generated by *reflectivity* and *maslov*, small differences in the amplitude of phases are observed.

- The reduction in amplitude with offset of the crustal diving ray (P_g) is more prominent on the *reflectivity* synthetics (figure 4.36: 8 to 14 km model offset), which is perhaps due to additional constraint of operator-controlled Q factors. The Q-factors input in the final model are the result of detailed amplitude modelling of the crustal diving ray and the direct water wave, which is discussed in Chapter 6.
- The relative amplitude of the P_cP reflection is much larger on the *reflectivity* synthetics than those generated by *maslov*. Modelling of the wide-angle seismic data provided no evidence of the depth to the base of the low velocity block and the nature of its lower boundary, except for an initial estimate on its thickness (100 m), thus a reflection from the base of the block is not included in the *maslov* synthetic data (figure 4.36a). However, *reflectivity* calculates the total response of reflections from all layers, which includes a reflection from the base of the low velocity block and any peg-leg multiples thereafter and this may be the cause of the larger amplitude observed in the synthetics.
- A P-S mode conversion on reflection at the top of the low velocity block (P_cS) is identified on both sets of synthetic seismograms as a small amplitude arrival at ~3.6 s reduced time (figure 4.36: 2 to 7 km model offset). The travel time and variation in amplitude with offset (i.e. lower amplitudes at zero offset) compare favourably with the observed data (e.g. figure 3.11c: 1 to 5 km model offset), although the measured amplitude is generally too small. The DOBS cannot be located exactly on a layer boundary with either modelling package and is thus modelled just above the seabed, which means that rays must transmit through an additional layer in the synthetic data. In the case of the P_cS phase this transmission through the seabed involves an additional mode conversion back to a P-wave, which could explain the difference in amplitude between the synthetic and observed data. The suggestion that the arrival could be the result of a downgoing S-wave and S-P mode conversion on reflection at top of the low velocity block (S_cP) was also investigated, but the amplitude of this phase was very small as the S-wave velocity at the base of layer 2 is similar to the P-wave

velocity modelled in the low velocity block, thus resulting in a small reflection coefficient.

4.7 Summary

Ray-trace modelling of the VFR wide-angle dataset has been described in detail in this chapter. The majority of the modelling process was carried out using the program *maslov* and the modelling strategy and resolution were outlined in section 4.2. The results generated from alternative modelling programs have also been summarised and their similarity to the synthetic data calculated by *maslov* greatly increases the overall confidence in the final models.

Final velocity-depth models for two across-axis, two along-axis (CVFR and NVFR) and two axis-parallel profiles have been presented and these models were independently modelled as a test of uniqueness by both gravity and normal incidence seismic data. A description of the modelling of the gravity and normal incidence seismic data can be found in the following chapter and Chapter 6 includes an interpretation of the combined VFR crustal models.

Chapter 5

Modelling of the normal incidence seismic and gravity datasets

5.1 Introduction

Normal incidence seismic and gravity data were used to further constrain the crustal models determined from ray-trace modelling of the wide-angle seismic data and provide some control on the uniqueness of each model. Modelling of these additional datasets was carried out during the latter stages of ray-trace modelling, although changes in the crustal structure as a result of normal incidence seismic modelling of the reflection from the top of the low velocity block were incorporated into the final wide-angle seismic models. More detailed normal incidence seismic and gravity data were collected during CD34/88 (Collier and Sinha, 1992b; Sinha, 1995) and the results, broadly consistent with the EW9512 data, are briefly discussed here and in Chapter 6.

5.2 Normal incidence seismic data

Normal incidence seismic data were collected contemporaneously and coincidentally with both *Seismic South* and *Seismic North* and a summary of the data acquisition and processing can be found in Chapter 2 (section 2.5). Example across and along-axis record sections are shown in figures 5.1 and 5.2. Times indicated on the record sections are two-way travel times (TWTT).

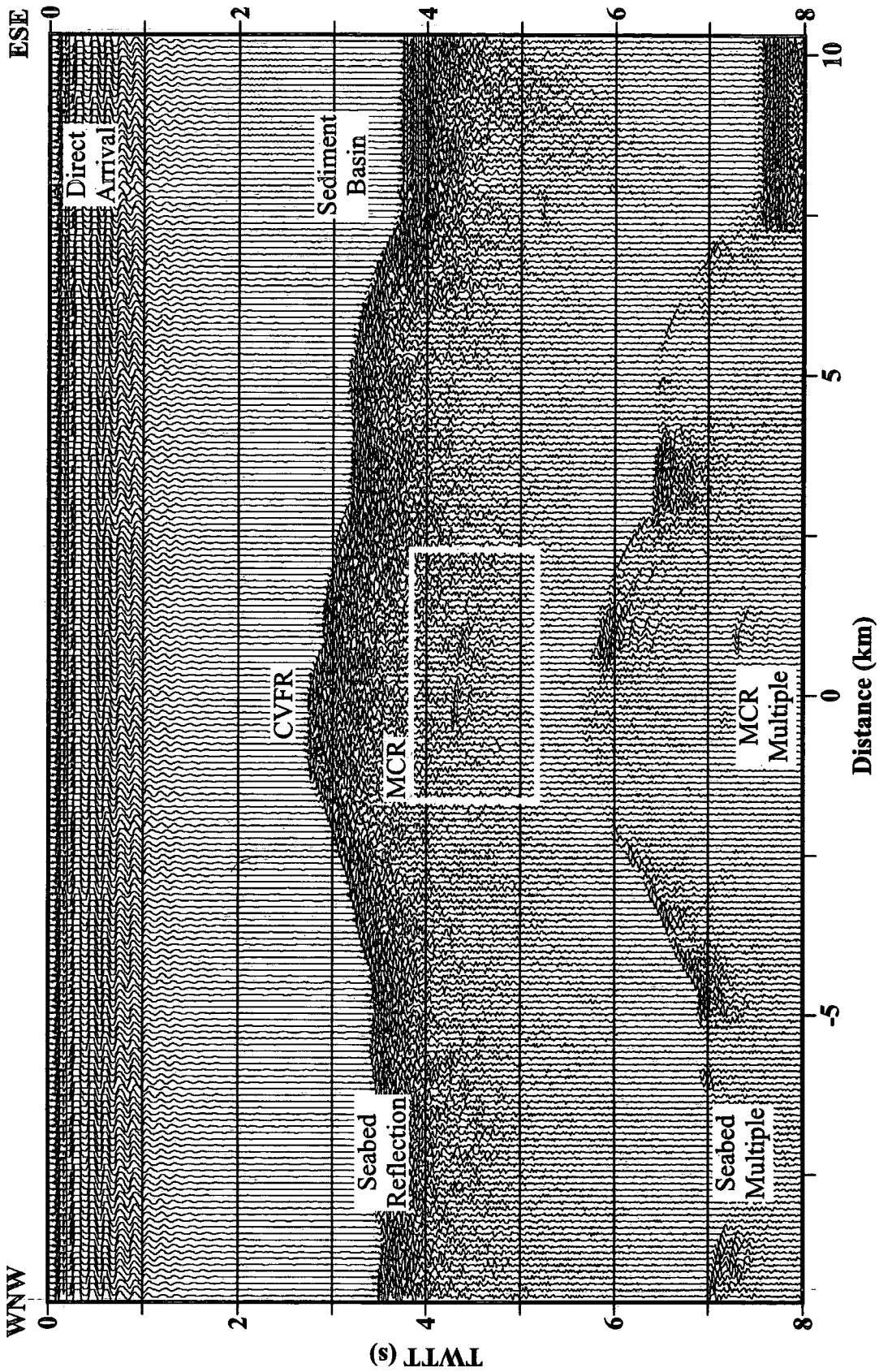

Figure 5.1: Across-axis normal incidence seismic data showing the main features of interest. The horizontal axis is annotated by model offset, as described for the wide-angle seismic models (i.e. the CVFR along-axis profile, Line 4 is located at 0 km). There are no obvious intracrustal reflections with the exception of the arrival highlighted beneath the CVFR axis, which corresponds to the MCR identified in Collier and Sinha (1992). Note the seabed multiple of the MCR observed at ~7.2 s TWTT.

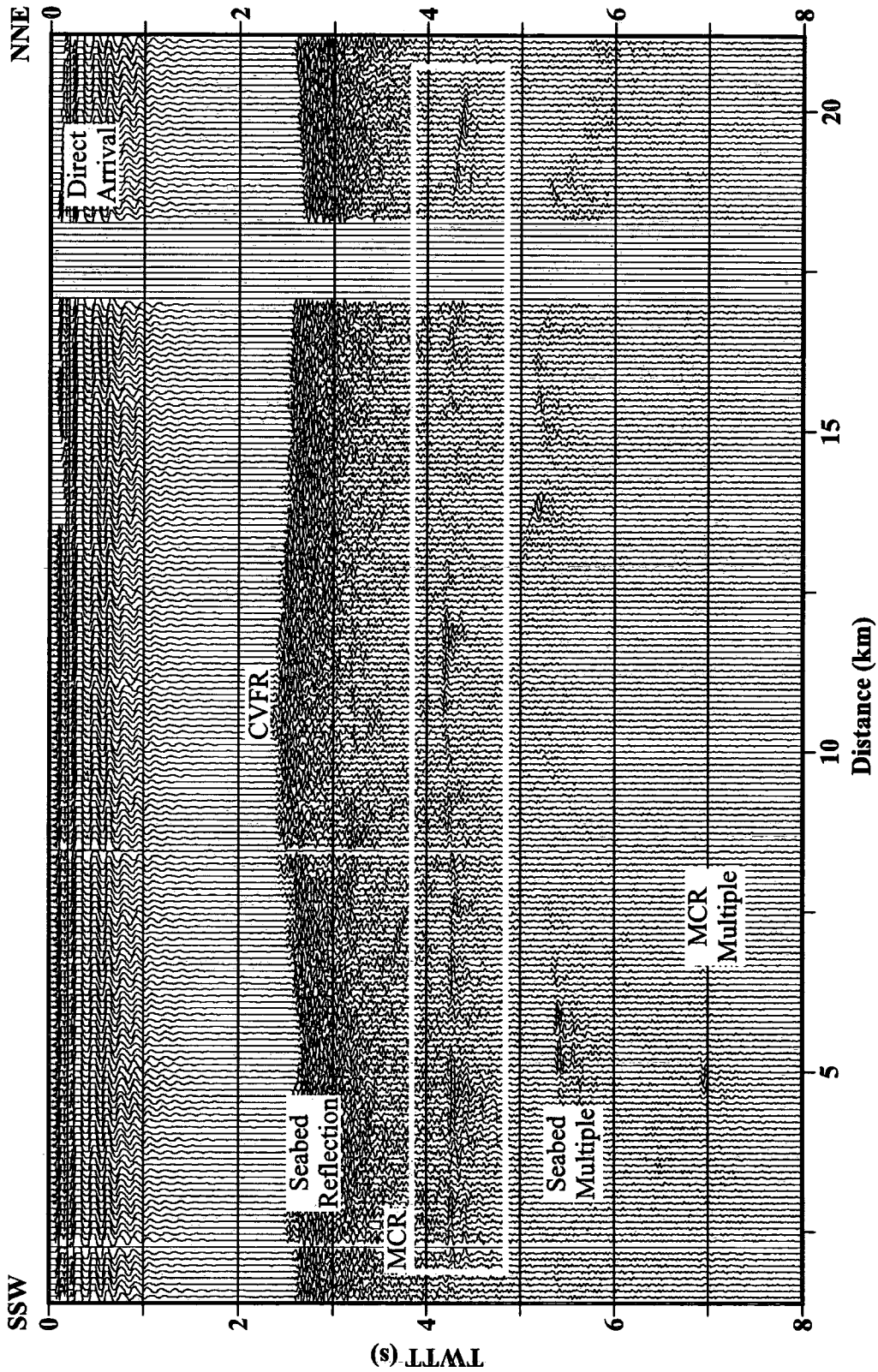

Figure 5.2: Along-axis normal incidence seismic data showing the main features of interest. The horizontal axis is also annotated by model offset (cf. figure 5.1), as described for the wide-angle seismic models (i.e. *Seismic South* across-axis profile, Line 1 is located at 0 km). In addition to the direct arrival and seabed reflections, the record section is dominated by the large amplitude reflection located at ~4.2-4.4 s TWTT. Note the seabed multiple of this reflection observed at ~6.9 s TWTT. The dead traces observed between 17 and 18 km are the result of shots not recorded during the data transfer process.

The single-channel normal incidence seismic data are presented here as raw, unprocessed sections to show the exceptional quality and strength of the intracrustal reflection on-axis. Profiles have been reversed with respect to the shooting direction when appropriate to provide a direct comparison with the wide-angle velocity models, but no data enhancement techniques have been used. The low frequency source (~7-8 Hz), tailored to the requirements of the refraction survey, was not an ideal source for the collection of normal incidence seismic data. However, it must be stressed that this dataset was collected opportunistically to provide additional information on near-surface crustal structure and sediment thickness only. The lack of upper-crustal reflections off-axis confirms the observations from ray-trace modelling of the wide-angle seismic data that gradational boundaries exist within the extrusive layer.

5.2.1 Modelling strategy

Forward modelling of the normal incidence seismic dataset was carried out using *GXII* version 2.1 (GX Technology Corporation) to further constrain the location of the low velocity block (see Chapter 4). The velocity structure calculated from ray-trace modelling of the wide-angle dataset was used as an initial model since the determination of seismic velocities from the normal incidence data alone was not possible as it is single-channel data. Synthetic seismograms were calculated and compared with the observed data to investigate the travel time and amplitude fit of the major reflections. The model was adjusted, re-modelled and again compared with the observed data until a consistent model fitting both seismic datasets was achieved. Seabed reflections were modelled first to check the location of each profile. The source signature used in generating the synthetic seismograms was derived from summing the first 300 ms of the seabed reflection from several adjacent traces in an area of flat seabed (see figure 5.3a for an example of the source signature - note the small negative polarity first breaks at the seabed).

The most obvious sub-crustal feature on the normal incidence data is the large amplitude, reversed polarity reflection identified at ~4.2 s TWTT, which is observed whenever the profile crosses, or travels along, either the CVFR or the NVFR. The reflection event (also observed in the wide-angle seismic data - e.g. figure 4.5) was modelled as a reflection from the top of the low velocity block and the reversed polarity of this arrival can be clearly seen in figure 5.3. White noise was added to the synthetic seismograms below the seabed to provide a closer resemblance to the observed data and

to display the inherent problems of trying to pick the first break (small positive kick) above the noise (e.g. figure 5.3b).

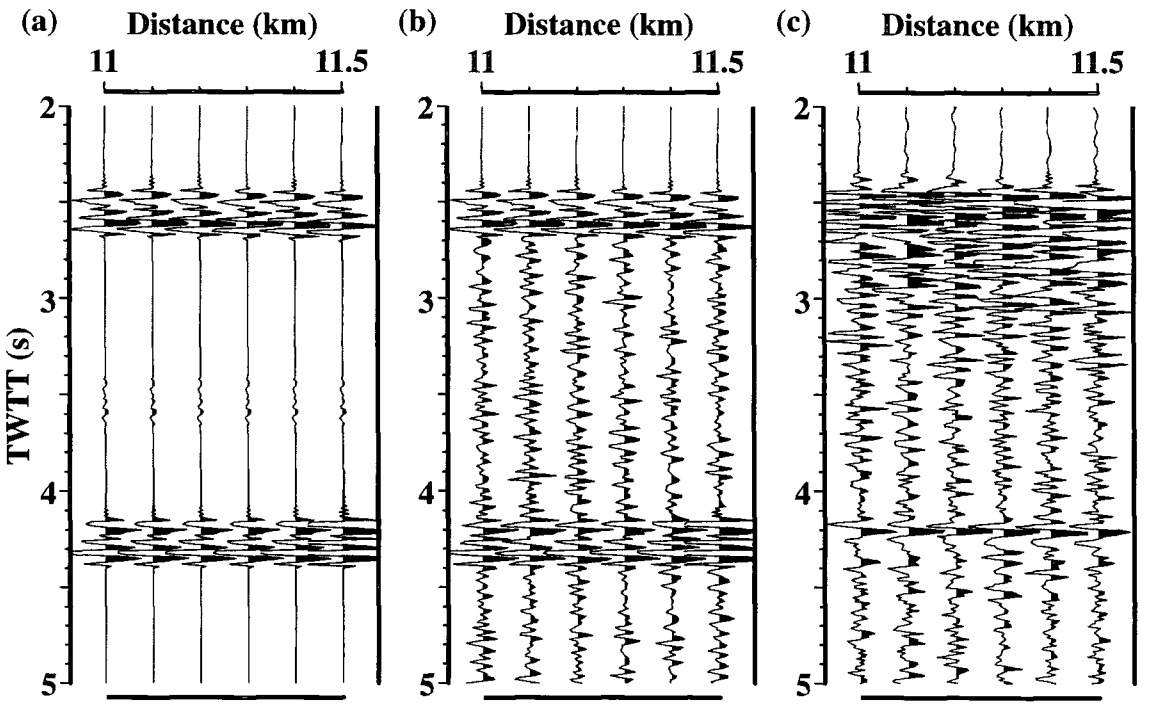

Figure 5.3: Forward modelling of the normal incidence seismic data.
(a) Synthetic seismograms generated using *GXII* showing the seabed reflection (~2.4 s) and the reflection from the top of the low velocity block (~4.2 s). Note the small negative and corresponding positive first break of the seabed and sub-crustal reflection.
(b) As (a), but with white noise added in the frequency range 8-30 Hz beneath the seabed reflection in an attempt to more faithfully reproduce the observed data. Note that the positive first break at ~4.2 s is now partially obscured by the added noise.
(c) Raw, unprocessed normal incidence seismic data from Line 4 (cf. figure 5.2). The amplitude of the positive first break of the intracrustal reflection is close to the level of noise at this depth, however subsequent peaks provide a good fit with the synthetic data. Note that the main seabed reflection is observed at ~2.4 s, although lower amplitude arrivals often precede this main event - a result of reflected energy from shallower off-line features (sideswipe).

5.2.2 *Seismic South* across-axis profile - Line 1

Line 1 crosses the southern tip of the CVFR and the arrival corresponding to a reflection from the top of the low velocity block is observed as a coherent event over several traces with low amplitude diffraction tails (figure 5.1). The results of normal incidence seismic forward modelling of Line 1 (see figure 5.4) are shown in figure 5.5.

The lateral extent of the reflector was modelled to be 1.25 km (note that this modelled width is consistent with the wide-angle seismic data (1-1.5 km) and was determined in two ways. Firstly, reflection amplitudes are observed to fall off

dramatically in the observed data (figure 5.5b: -0.5 and 1 km model offset) and *GXII* modelling simulates this variation on a trace-to-trace scale. Further constraint on the location of this reflector (i.e. top of the low velocity block) was possible by travel time modelling of the diffraction tails. To generate the large amplitude, reversed polarity reflection observed in figure 5.5 a considerable velocity step was required and a velocity step of 2.5 km s^{-1}, as modelled in the wide-angle data, adequately reproduced this reflection amplitude. A reflection from the base of the low velocity block was also modelled, but detailed waveform analysis was not possible with this single-channel dataset alone (see section 5.2.3 for further details).

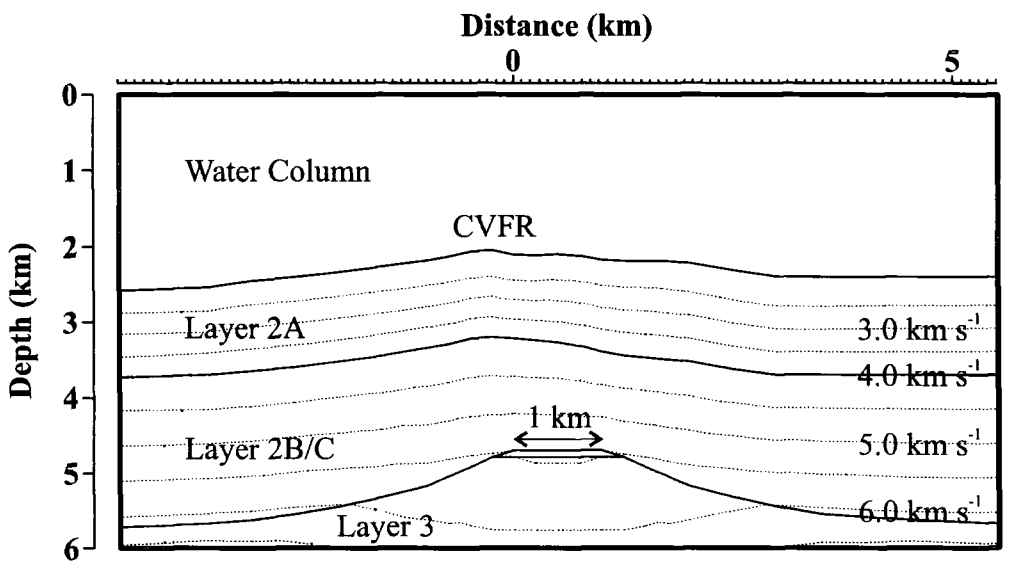

Figure 5.4: Across-axis velocity-depth model used to generate the synthetic normal incidence seismic data shown in figure 5.5. The low velocity block (~4.8 km depth) has a minimum width of 1 km and was modelled to be coincident with the layer 2/3 boundary. Note that the low velocity block was not modelled directly beneath the CVFR crest and is offset ~1 km to the east. No reflections were observed below layer 2, however the velocity structure below the layer 2/3 boundary was included for completeness.

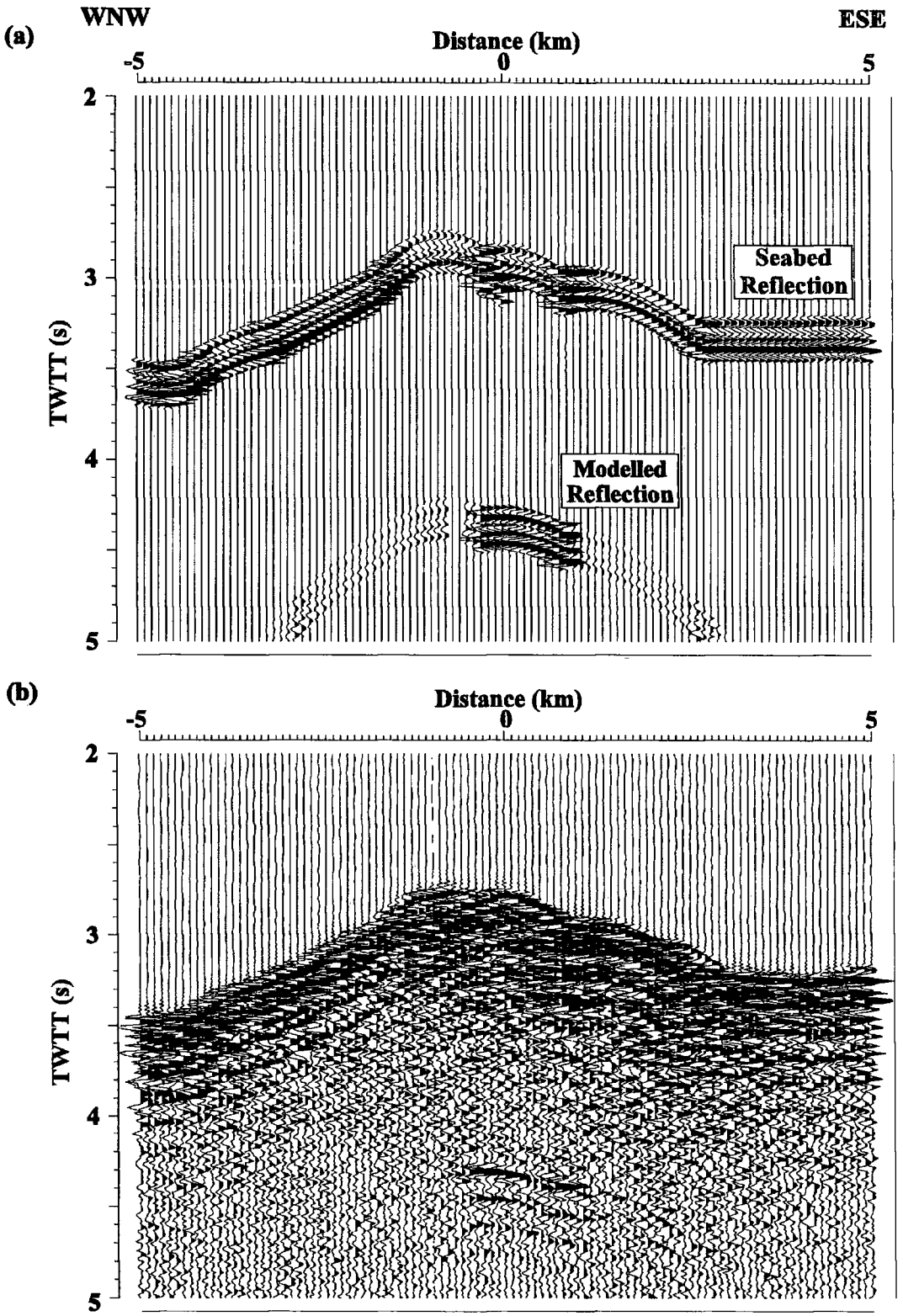

Figure 5.5: Across-axis normal incidence seismic forward modelling of the wide-angle final model for Line 1 between -5 and 5 km model offset (cf. figure 4.5).

(a) Synthetic seismograms generated using *GXII* showing the seabed reflection and the reflection from the top of the low velocity block. Note the low amplitude diffraction tails at either side of the main reflection.

(b) Raw, unprocessed normal incidence seismic data from Line 1 (cf. figure 5.1). The modelled first break of the reflection from the top of the low velocity block is close to the noise level, but waveform analysis showed the reflection to be of reversed polarity.

5.2.3 *Seismic South* along-axis profile - Line 4

A large amplitude reflection from the top of the low velocity block, identified at a TWTT of 4.2 ± 0.2 s on the along-axis profile, is continuous along the majority of the CVFR spreading segment (see figure 5.2). Forward modelling of the normal incidence seismic data recorded on a 10 km long section of the CVFR is shown in figure 5.6. The low velocity block was modelled as a continuous feature along the entire length of Line 4, but the radius of the Fresnel zone at the depth of this reflector is ~1 km and truncations in the reflector of up to 2 km would be difficult to resolve with this dataset. Hence, the variations in amplitude of the reflection event (figure 5.6c) are either the result of variations in the degree of seabed scattering of the down-going wavefield or actual breaks in the lateral continuity of the body.

The reversed polarity of the reflection can be clearly seen in the observed data and although the positive first break is close to the noise level it can be picked from its trace-to-trace continuity (e.g. figure 5.6: 11 to 12 km model offset).

As previously mentioned for Line 1 (section 5.2.2), a reflection from the base of the low velocity block was also modelled. The thickness of the low velocity block was varied to model the difference in the resultant signals generated from the interaction of reflections from both the upper and lower boundaries of the low velocity block. Detailed waveform analysis proved difficult due to the generally high level of noise on the section (the data is only single-channel and hence unstackable to improve SNR). The major peaks in the observed data could be faithfully reproduced with a single reflection from the top of the low velocity block (e.g. figure 5.6: ~4.4 s TWTT), hence a reflection from the base of the low velocity block was not included in the final model and this interface was interpreted to have a more gradational nature.

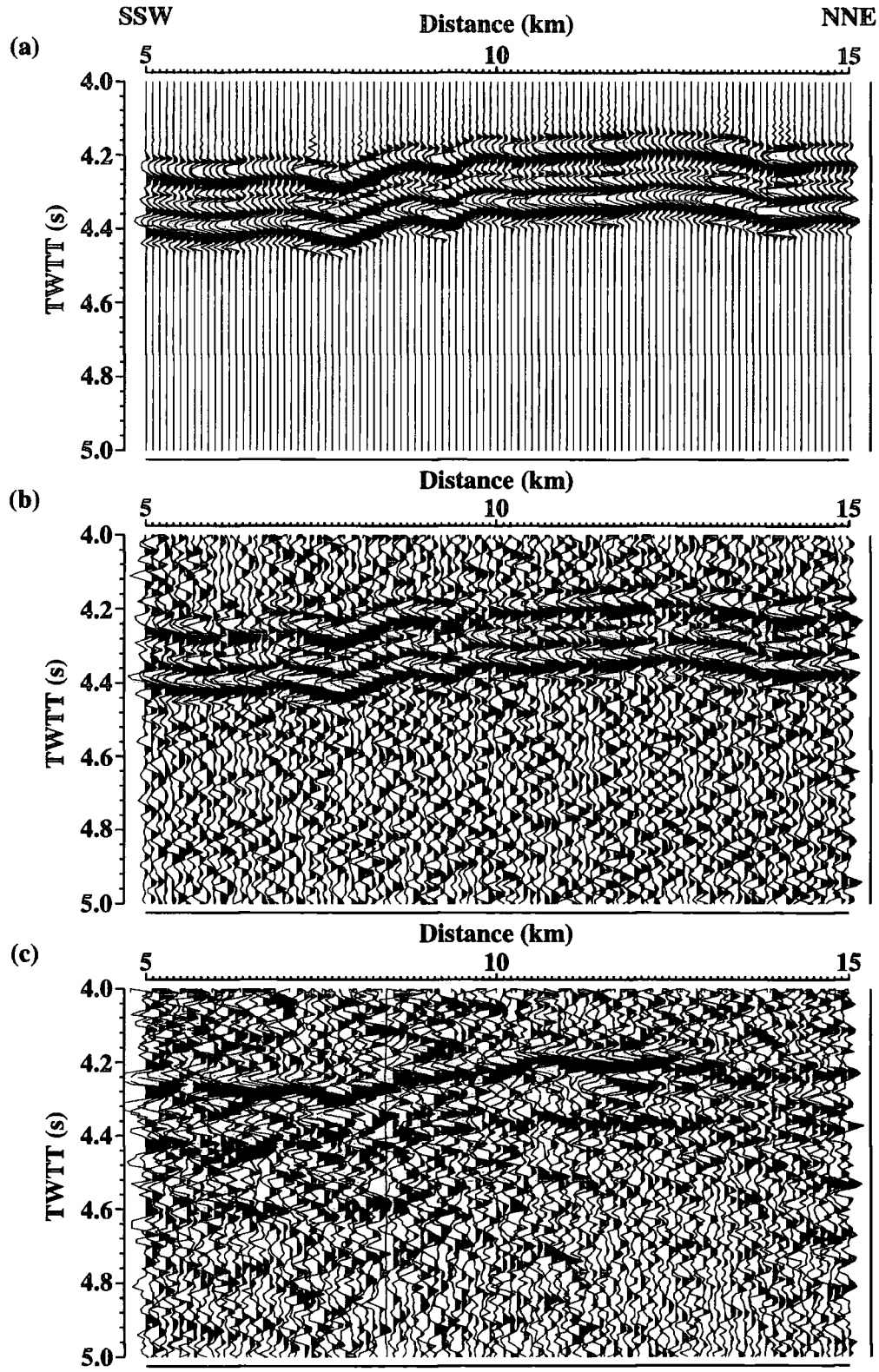

Figure 5.6: Along-axis normal incidence seismic forward modelling of the wide-angle final model for Line 4 between 5 and 15 km model offset (cf. figure 4.20).

(a) Synthetic seismograms generated using *GXII* of the reflection event from the top of the low velocity block.

(b) As (a) with additional white noise in the frequency range 8-30 Hz, which partially obscures the small positive first break.

(c) Raw, unprocessed normal incidence seismic data from Line 4 (cf. figure 5.2). Note the good fit of the secondary peak at ~4.4 s TWTT.

5.2.4 *Seismic North* across-axis profile - Line 6

A reflection generated from the top of the low velocity block is also identified on Line 6 over the OSC (figure 5.7) and has a distinctive 'bow-tie' shape, a function of the steep synclinal nature of the overlap region. The severe topography causes difficulties when trying to forward model the data as synthetic rays reflecting off the low velocity block are focused by the two ridges producing an overestimate of the reflection amplitude in the overlap basin.

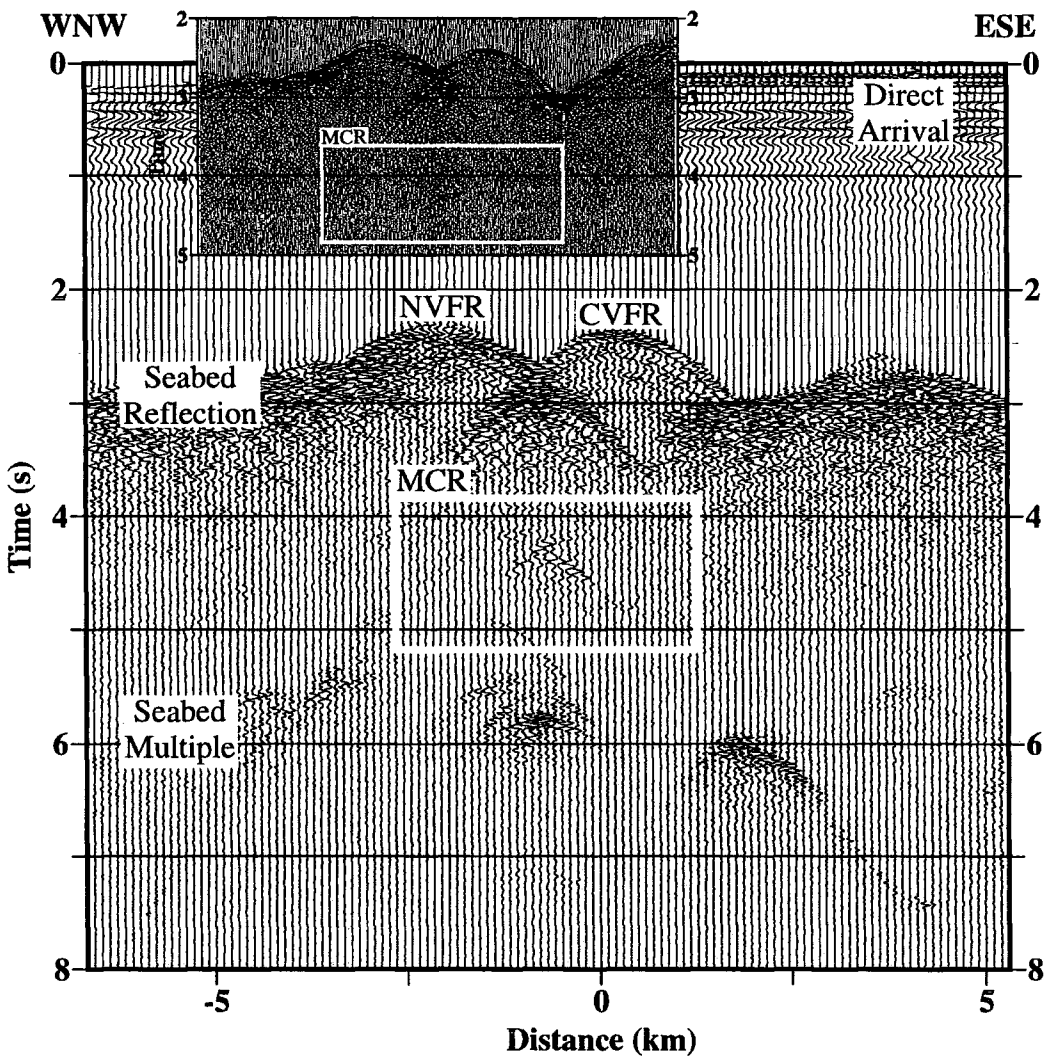

Figure 5.7: Across-axis normal incidence seismic data over the OSC (-3 to 2 km model offset). Note the 'bow-tie' shaped reflection between 4.1 and 4.6 s TWTT beneath the overlap basin corresponding to a reflection off the low velocity block and is equivalent to the MCR observed in the CD34/88 dataset (Collier and Sinha, 1992b; Day, 1997 and inset). A low amplitude seabed multiple of this arrival can also be observed at ~7 s TWTT.

The low velocity block was modelled as a single body with a lateral extent of 2 km, centred on the overlap basin and extending beneath both ridges, although the width of the Fresnel zone at this depth (~1 km) creates significant problems when determining the lateral continuity of the reflector. The observed reflection can also be modelled to a satisfactory degree by two bodies of 0.5 km width, located beneath the inner flanks (i.e. the slopes that dip into the overlap basin) of both ridges with a 1 km gap (cf. Fresnel zone) between them (see figure 5.8: hashed region). The outer edges of the low velocity block are well constrained by the relative positions of the reflections and diffractions and do not extend beneath the outer flanks of either ridge. The final models used for input into *GXII* are shown in figure 5.8. The discrepancy between the two models (i.e. one continuous low velocity block or two separate bodies) cannot be constrained with the available data, although the existence of a reflection on the wide-angle seismic data from NDOBS3, located at -1 km model offset in the overlap basin (see figure 4.13), suggests that a low velocity block does in fact exist as a continuous body beneath both ridges. Previous studies of more detailed normal incidence seismic data over this OSC have also resulted in several possible models for the position of the low velocity block(s) and these will be discussed in detail in Chapter 6.

The results of forward modelling of the normal incidence seismic data over the OSC with a single low velocity block (see figure 5.8) are shown in figure 5.9.

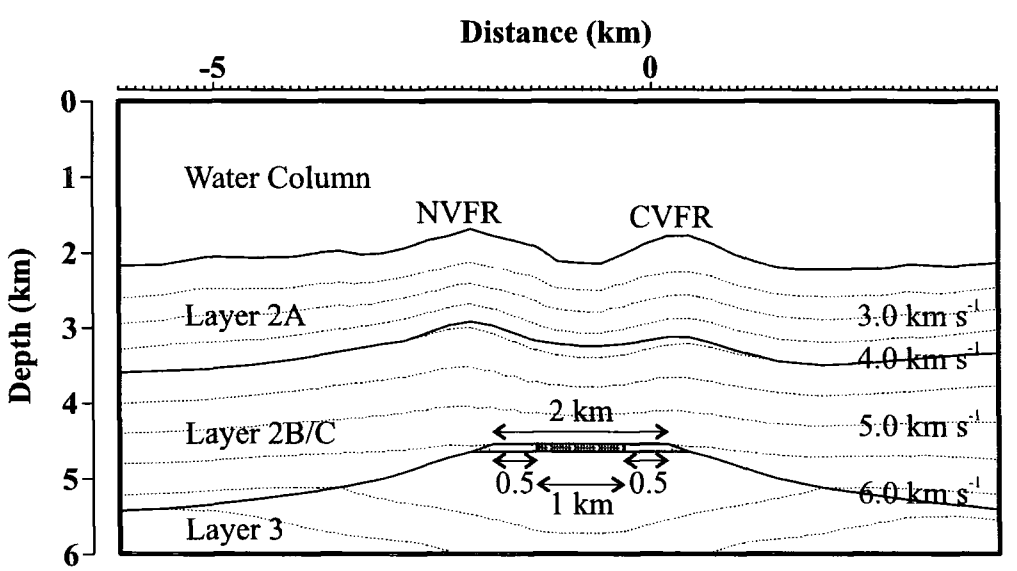

Figure 5.8: Across-axis velocity-depth model used to generate the synthetic normal incidence seismic data shown in figure 5.9. The low velocity block (~4.6 km depth) is centred on the overlap basin and has a width of 2 km, extending beneath both ridges. Note that the low velocity block does not extend beneath the whole of the ridge and is modelled beneath the inside flanks only. The observed normal incidence seismic data can also be faithfully reproduced with two separate bodies beneath each ridge and the hashed region within the low velocity block denotes the gap between these two bodies.

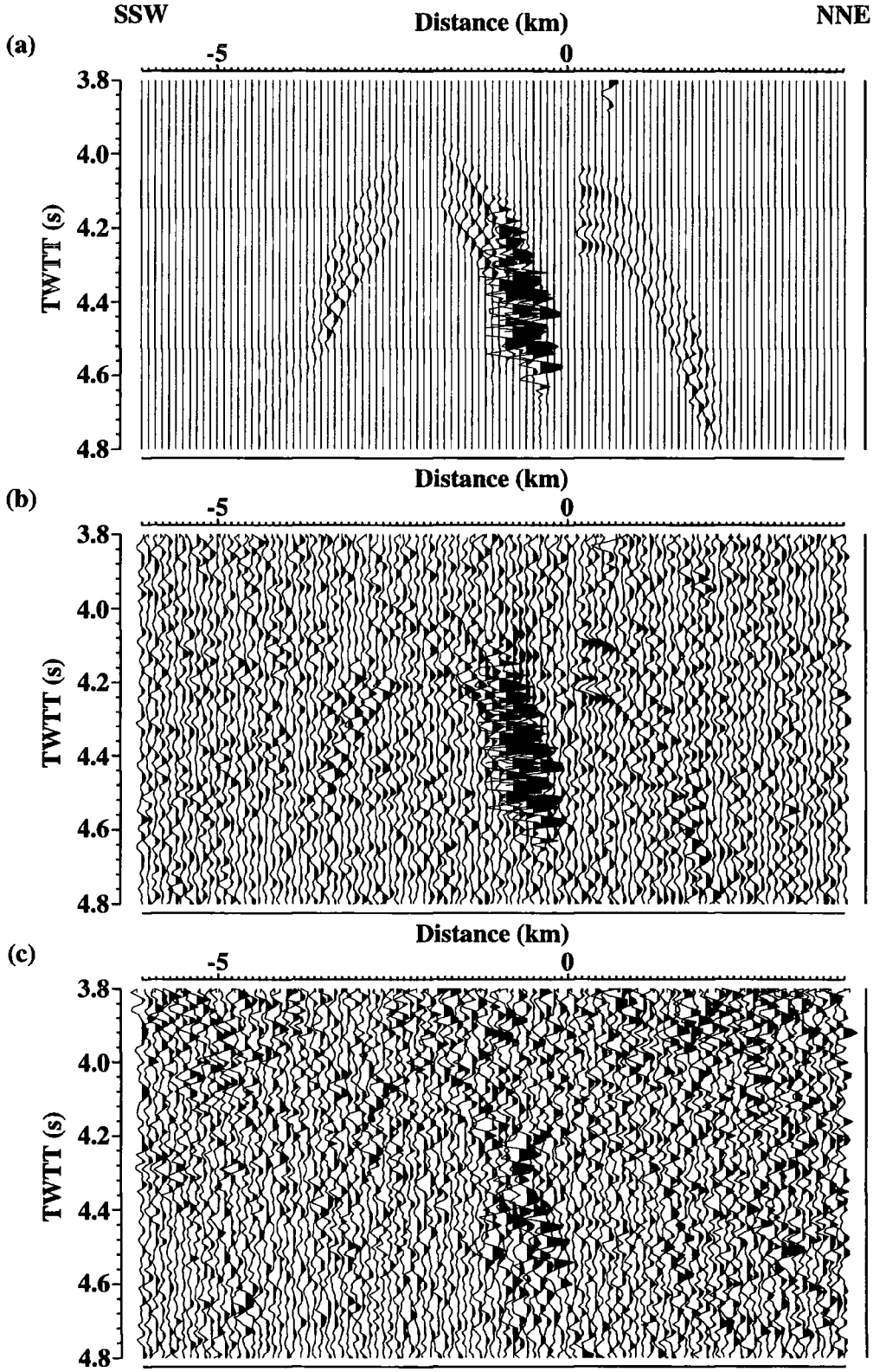

Figure 5.9: Across-axis normal incidence seismic forward modelling of the wide-angle final model for Line 6 over the OSC (cf. figure 4.13).

(a) Synthetic seismograms generated using *GXII* of the reflection event from the top of the low velocity block. Note the large amplitude arrivals between -1 and 0 km model offset as a result of focusing of the ray-paths by the ridge topography.

(b) As (a) with additional white noise in the frequency range 8-30 Hz.

(c) Raw, unprocessed normal incidence seismic data from Line 6 (cf. figure 5.2). Note the good fit of the diffraction tails with the synthetic data in (b).

5.2.5 Summary

Forward modelling of the normal incidence seismic dataset was carried out on both across-axis profiles (Line 1 - CVFR axis and Line 6 - OSC) and the *Seismic South* along-axis profile (Line 4 - CVFR). However, the low velocity block identified using the wide-angle seismic dataset on the *Seismic North* along-axis profile (Line 9 - NVFR) could not be modelled as there was insufficient data. The large amplitude intracrustal reflection observed between 4.2 and 4.4 s TWTT was faithfully reproduced on all profiles by a reflection from the upper boundary of the low velocity block and the lateral extent of this body was determined from the relative positions of the observed reflections and diffractions. A reflection from the base of the low velocity block, to provide an estimate of the thickness of the low velocity block, could not be modelled due to the high noise level on the single-channel data and relative strength of the preceding reflection from the upper boundary.

The vertical resolution at the top of the low velocity block is ~150 m and the horizontal resolution, determined by modelling the diffraction tails, is 100-150 m on all profiles.

5.3 Gravity data

Free-air gravity data were collected throughout the cruise and the track chart is shown on figure 2.3. The gravity data coincident with the main seismic profiles were used to confirm the positions of the main layer boundaries and obtain estimates of layer densities to further constrain the seismically derived 2-D crustal models. In addition to the 2-D modelling, a subset of the EW9512 gravity dataset was used to calculate the mantle Bouguer anomaly over the CVFR and NVFR.

5.3.1 2-D gravity modelling

The 2-D velocity-depth models calculated from ray-trace modelling of the wide-angle seismic data were converted to crustal density models and compared with the free-air gravity anomaly as a test of uniqueness. The P-wave velocity-depth models were converted to crustal density models using the mean velocity-density envelope of Nafe and Drake (1957), together with methods 2 and 3 of Carlson and Raskin (1984) and the method of Christenson and Salisbury (1975). The numerous relationships between P-wave velocity and density are summarised in figure 5.10.

Modelling of the gravity data was carried out using the program *grav2d* (written by J.H. Leutgart of the USGS, based on the Talwani *et al.*, 1959 algorithm), which is based on the assumption that the structure is infinite perpendicular to the model. This assumption is more than satisfactory for Line 1 (*Seismic South*), where topographic features are relatively 2-D (see figure 2.1) and this profile was modelled first. However, the 3-D nature of the OSC and the numerous large seamounts close to many of the other profiles have a significant effect on the gravity signal and these features cannot be accommodated in *grav2d*. The along-axis and axis-parallel profiles were also modelled in 2¾-D using the program *GMSYS* (Northwest Geophysical Associates Inc., 1995) in an attempt to faithfully reproduce the major off-line seabed topography.

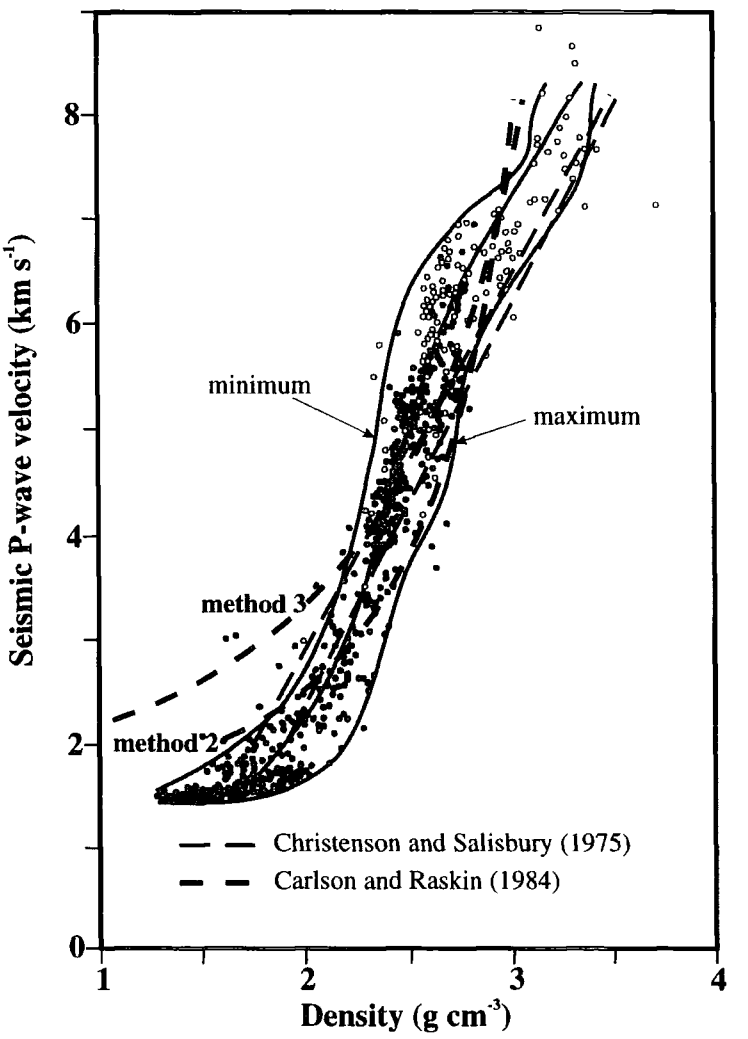

Figure 5.10: Velocity-density relationship of Nafe and Drake (1957) (after Barton, 1986; Peirce, 1990; Navin, 1996) used to estimate densities for the initial gravity models. The velocity-density relationships of Christenson and Salisbury (1975) and the curves of method 2 and 3 of Carlson and Raskin (1984) are also displayed for comparison.

Gravity modelling of the two across-axis profiles (Line 1 and Line 6) and the CVFR along-axis profile (Line 4) are described here and a complete set of gravity modelled sections can be found in Appendix C.

Line 1 - *Seismic South*

Average P-wave seismic velocities for the six main layers of the wide-angle seismic model for Line 1 (i.e. water column, sediment, layer 2A, layer 2B/C, layer 3 and upper mantle) were converted to crustal densities using the velocity-density relationships described in figure 5.10 and are shown in table 5.1. Densities calculated from the mean velocity-density envelope of Nafe and Drake (1957) and methods 2 and 3 of Carlson and Raskin (1984) were averaged to provide initial estimates of layer densities. However, method 3 of Carlson and Raskin (1984) attempts to take into account the large-scale porosity of the extrusive layer, hence a density derived using this method only was used for layer 2A and the Nafe-Drake relationship, determined from measurements of sediment density, was thus used for the sediment pond at 10 km model offset. A density of 1.03 g cm^{-3} was assigned to the water column (Kuo and Forsyth, 1988) and the mantle was assigned a density of 3.30 g cm^{-3} - used in most gravity studies of mid-ocean ridges (e.g. Kuo and Forsyth, 1988; Solomon and Toomey, 1992; Cormier *et al.*, 1995). The velocity-density relationships of Christenson and Salisbury (1975) were used as a final check on the calculated layer densities (table 5.1 - last column).

		Nafe-Drake	Carlson and Raskin			
	Velocity (km s^{-1})	ρ_{nd} (g cm^{-3})	ρ_{m2} (g cm^{-3})	ρ_{m3} (g cm^{-3})	Av_{ρ} (g cm^{-3})	$\rho_{c\&s}$ (g cm^{-3})
water column	1.49	-	-	-	**1.03**	-
sediment	2.15	**1.98**	1.02	1.74	1.58	1.80
layer 2A	3.02	2.20	1.83	**2.25**	2.09	2.04
layer 2B/C	5.01	2.51	2.61	2.74	**2.62**	2.60
layer 3	6.58	2.83	2.90	2.92	**2.88**	3.04
mantle	8.08	3.33	3.07	3.03	***3.30***	3.47

Table 5.1: Initial layer densities for Line 1 calculated from the velocity-depth relationships described in figure 5.9. Densities from the Nafe and Drake (1957) relationship (ρ_{nd}) and methods 2 and 3 (ρ_{m2} & ρ_{m3}) of Carlson and Raskin (1984) are displayed and the penultimate column represents the average of these three methods, in addition to the generally accepted mantle density (denoted by *). Initial density estimates used in the gravity modelling process are shown in bold. The final column shows densities calculated from the relationship of Christenson and Salisbury (1975).

Layer boundaries were left unaltered throughout modelling and layer densities required only minor adjustments from the initial estimates (±0.04 g cm^{-3}) to generate a free-air anomaly that fitted the observed data to within ±1-2 mGal (see figure 5.11).

The results of gravity modelling Line 1 using the program *grav2d* are shown in figure 5.11 and are described below. The only significant misfit to the observed free-air gravity anomaly is centred on ~14 km model offset and is attributed to the gravity effect of the large seamount located to the north of the profile (figure 2.1 - 176° 33′ W).

- The uppermost layer of the model represents the water column with an average density of 1.03 g cm^{-3}.
- The sediment layer, restricted to the basin centred on 10 km model offset, was modelled with a density of 1.98 g cm^{-3}.
- The density of layer 2A, calculated as 2.25 g cm^{-3} using method 3 of Carlson and Raskin (1984), was kept constant across the entire model as there is little variation in the seismic velocity of this layer.
- Layer 2B/C has a laterally varying thickness of the order ±1 km and this layer can therefore have a significant effect on the overall free-air anomaly. The density of this layer is modelled as 2.62 g cm^{-3}, although east of ~31 km model offset the density is reduced to 2.60 g cm^{-3} to simulate the lower P-wave seismic velocities observed beneath the island arc.
- The free-air gravity anomaly could not be faithfully reproduced with a constant density in layer 3. Layer 3 was thus divided into five distinct regions, which coincide with the two pre-rift regions, the two transition zones and the post-rift region postulated in section 4.2.3. The density of layer 3 was modelled as 2.89 g cm^{-3} and a reduced density of 2.86 g cm^{-3} was necessary within the interpreted transition zones. Densities of 2.86 g cm^{-3} and 2.84 g cm^{-3} (within the 'envelope' of possibilities for the modelled velocities) are modelled beneath the pre-rift back-arc and island arc crust respectively, although part of the observed anomaly may be the result of an increase in the depth of the Moho, which is only constrained between -30 and 30 km model offset by the wide-angle seismic data (see figure 4.4).
- A density of 3.30 g cm^{-3} is generally acknowledged to be a reasonable estimate for the upper mantle and due to the lack of any evidence to the contrary this density was assigned across the entire profile.

- The low velocity block modelled at a depth of ~3 km beneath the axis using the wide-angle seismic data was incorporated into the model for completeness. This block has no noticeable effect on the free-air gravity and was assigned a density of 2.50 g cm^{-3}, the density of molten andesite (Murase and McBirney, 1973).

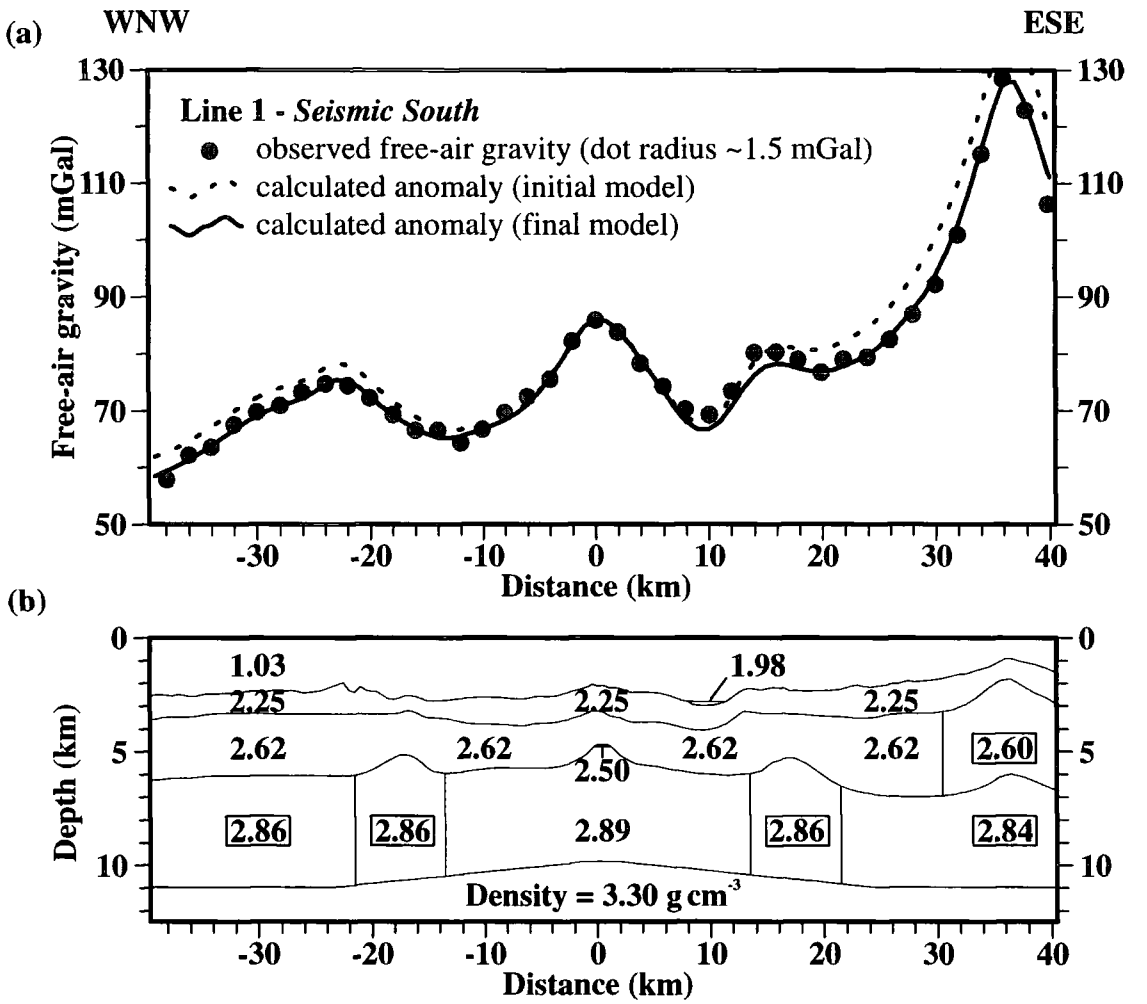

Figure 5.11: Final across-axis 2-D free-air gravity model of Line 1, *Seismic South*, using average P-wave seismic velocities, extracted from the wide-angle seismic model described in figure 4.4, to estimate initial densities. All layer boundaries remain unchanged from the best fitting velocity-depth model for this line.
(a) Comparison of the observed (dots) and calculated (solid line) free-air gravity anomalies. Dot size gives an indication of the error bars (±1.5 mGal). The calculated gravity anomaly of the initial model (dashed line) consisting of constant layer densities is also shown for reference and shows the need for the inclusion of reduced densities at either end of the profile. Note the general good fit of the main anomaly peaks and the slight misfit centred on 14 km model offset is attributed to the large seamount north of the profile (see figure 2.1).
(b) Best fitting density model with layer densities shown in g cm^{-3}. The model extends down to a depth of 15 km and has a semi-infinite half space at either end of the profile. Note the presence of lower densities beneath the island arc region towards the eastern end of the model and higher densities in layer 3 within the post-rift region. Vertical exaggeration x2.

Line 6 - *Seismic North*

Gravity modelling of the more northerly across-axis profile (Line 6) proved more problematic, mostly caused by the numerous off-line seamounts in the vicinity of this profile. The results of 2-D modelling of the free-air gravity data from Line 6 using the program *grav2d* are shown in figure 5.12. The addition of lower densities at each end of the profile, consistent with those modelled on Line 1 (see figure 5.11b), improved the fit of the observed and calculated gravity anomaly (figure 5.12), although a considerable misfit (up to 7 mGal) is apparent between -40 to -5 km model offset.

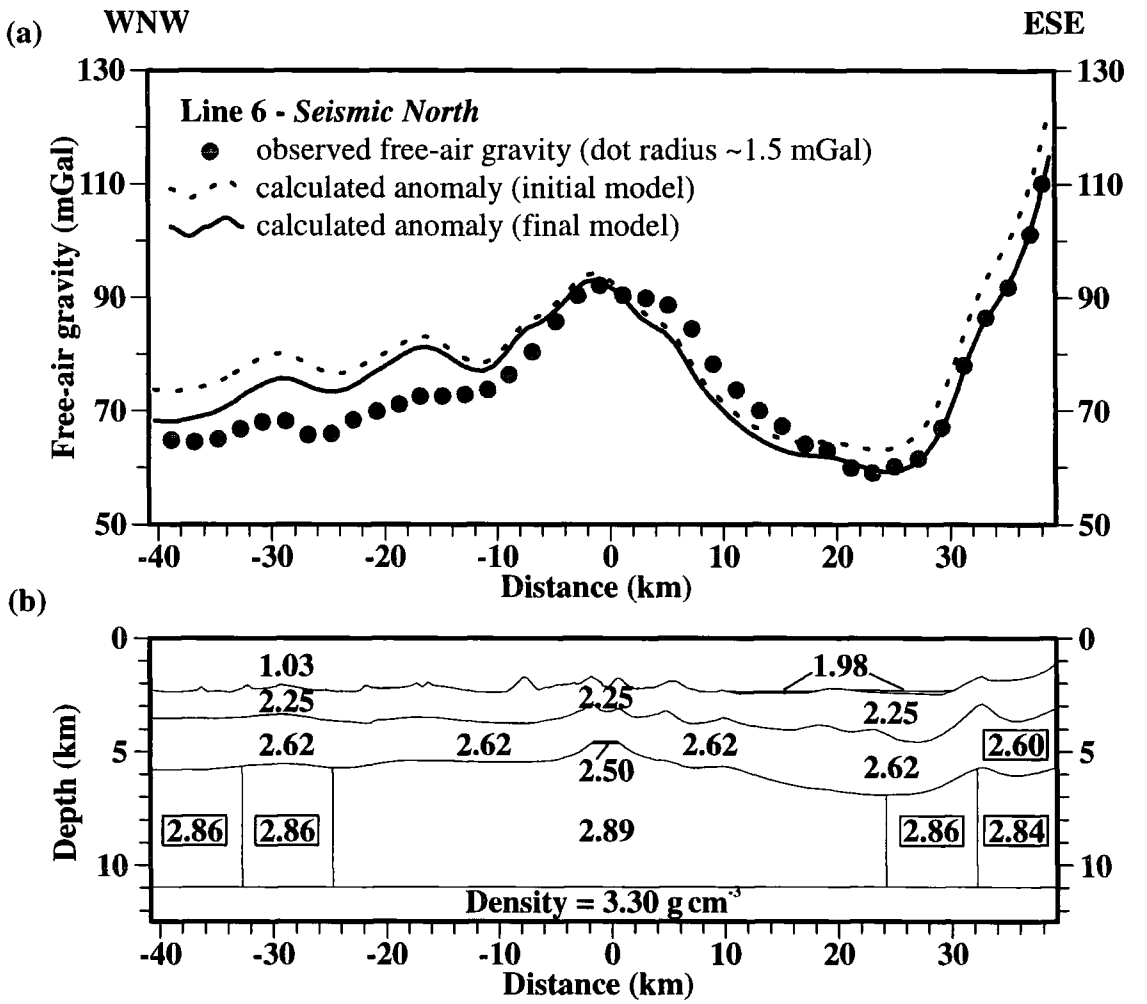

Figure 5.12: Final across-axis 2-D free-air gravity model of Line 6, *Seismic North*, using average P-wave seismic velocities (extracted from the wide-angle seismic model described in figure 4.12) to estimate initial densities. All layer boundaries remain unchanged from the best fitting velocity-depth model for this line. Display parameters are described in figure 5.11

(a) Comparison of the observed (dots) and calculated (solid line) free-air gravity anomalies. Note the poor fit to the west of -5 km model offset.

(b) Best fitting density model with layer densities shown in g cm^{-3}. Note the density of 2.60 g cm^{-3} in layer 2B/C is actually located in the semi-infinite half-space at model offsets greater than 40 km.

Following detailed modelling with the program *grav2d* it was concluded that the observed gravity anomaly on Line 6 could not be faithfully reproduced by a 2-D crustal structure, without the addition of a regional gradient. However, there was no evidence of a regional gravity gradient from additional datasets (e.g. 2′x 2′ gravity grid - Sandwell and Smith, 1986) and the profile was thus modelled in 2¾-D using *GMSYS*, in an attempt to reproduce the 3-D nature of the seafloor topography. The main topographic features surrounding Line 6 are highlighted in figure 5.13 and their input parameters for modelling with *GMSYS* are described below. The advantage of 2¾-D modelling is that 'out-of-plane' features can be incorporated into the model, in addition to being able to restrict the perpendicular extents of structures along the profile itself (2½-D). Note that 2¾-D input parameters are described here as a minimum and maximum y-length, which corresponds to the lateral extent of structures perpendicular to Line 6 (positive values denote the extent south of the profile and negative to the north).

The final gravity model is shown in figure 5.14 and the calculated anomaly from *grav2d* modelling is shown for comparison.

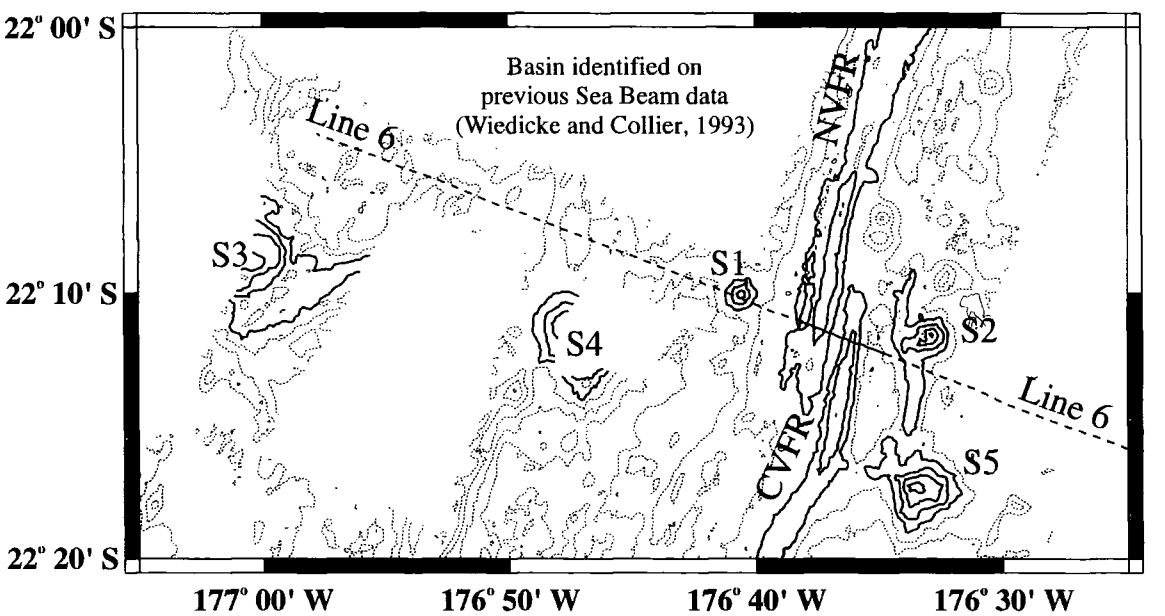

Figure 5.13: Map showing the major topographic features surrounding Line 6 (dashed line). Five seamounts (S1-S5) are highlighted in addition to the CVFR and NVFR and a large basin to the west of the NVFR, and north of Line 6, is identified on previous Sea Beam data (Wiedicke and Collier, 1993). Bathymetric contours are plotted at 200 m intervals.

- For modelling purposes the CVFR (or NVFR) was described as having an infinite extent south (or north) of the profile. The CVFR was modelled with a minimum y-length of -5 km (i.e. extending 5 km north of Line 6) and the NVFR was modelled with a maximum y-length of 5 km (i.e. extending 5 km south of Line 6).
- Five large seamounts (S1-S5) are highlighted in figure 5.13, although the three seamounts south of Line 6 (S3-S5) were not incorporated into the final *GMSYS* density model, due to their greater perpendicular distance from the profile.
- Seamount S1 lies on Line 6 at -7 km model offset and extends to a height of >400 m above the surrounding seafloor. It is clear from the conical shape of this topographic feature that it does not have infinite extent north and south of Line 6 and was thus modelled with minimum and maximum y-lengths of -0.5 and 1 km for the top 200 m of the seamount and -1 and 1.5 km for the bottom 200 m (see figure 5.14b).
- To the north of Line 6 at 6 km model offset seamount S2, with a height of 500 m is modelled with minimum and maximum y-lengths of -4 and -1 km.
- No bathymetry data to the north of Line 6 between -40 km and -10 km model offset was collected during EW9512. However previous Sea Beam data from three R/V *Sonne* cruises (SO-35, SO-48 and SO-67), as described in Wiedicke and Collier (1993), identify a large basin north of 22° 05′ S and this feature was also incorporated into the *GMSYS* model. The average depth to the seabed north of Line 6 is ~2.5 km and therefore any crust above this depth on Line 6 was modelled in 2¾-D with a minimum y-length of -2 km (i.e. extending only 2 km north of the profile) to simulate the basin described above, and infinite extent south of the profile as the seabed is effectively 2-D in that direction (see figure 5.14b). Similar parameters were used to describe the layer 2A/2B boundary to maintain a constant thickness of layer 2A off-axis.

The main layer densities used in the *grav2d* modelling remain in the final *GMSYS* density model and the lower densities at each end of the profile are also included. Although the average density of layer 2A is modelled as 2.25 g cm^{-3}, the seamounts and ridges modelled in 2¾-D with *GMSYS* are given lower densities (2.15 and 2.20 g cm^{-3}) as they represent only the uppermost part of this layer. A density of

2.52 g cm^{-3} is assigned to the top of layer 2B/C west of -10 km model offset for a similar reason (see figure 5.14b).

The final 2¾-D across-axis density model provides a far better fit to the observed anomaly and the maximum misfit is ~3 mGal.

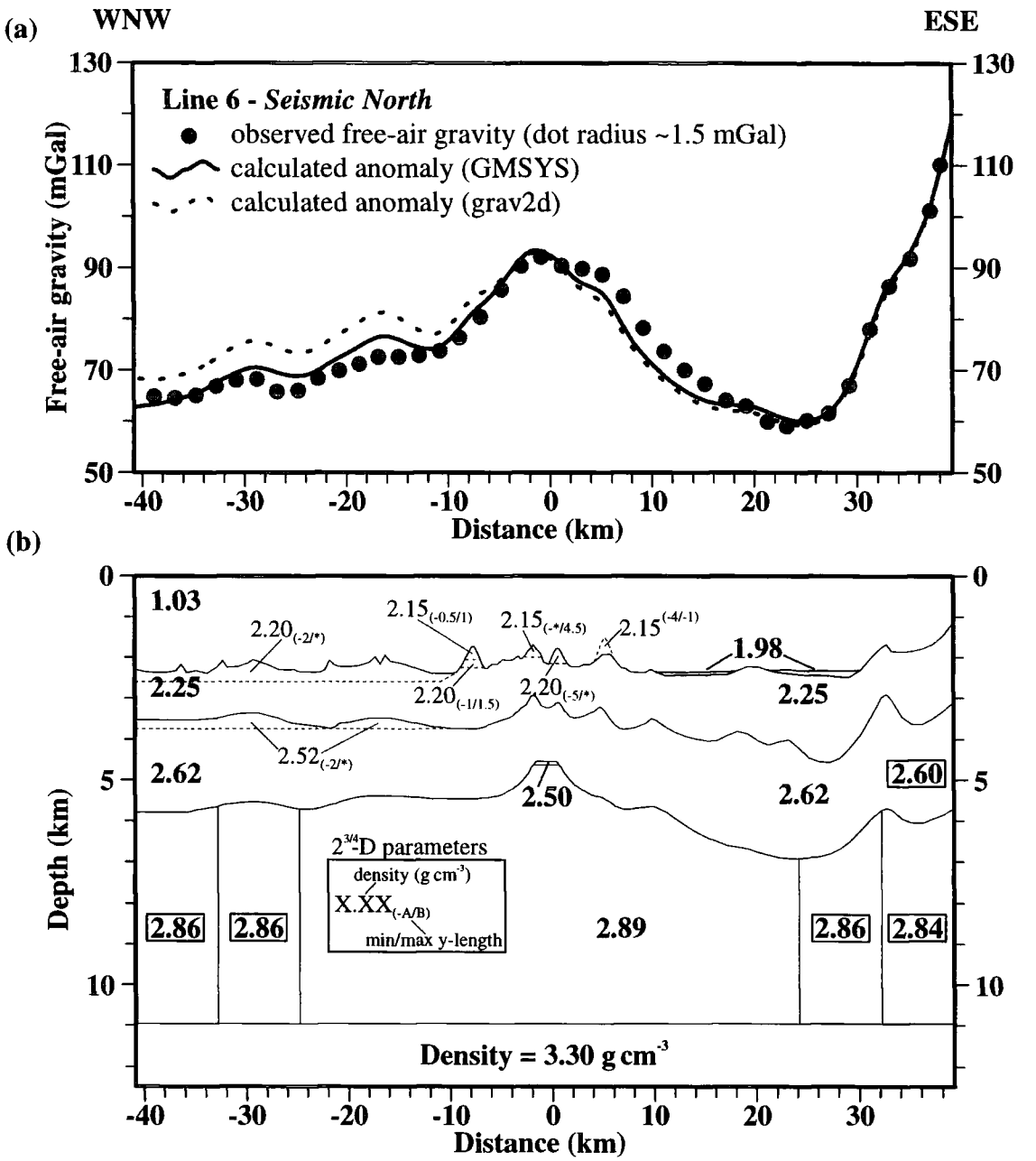

Figure 5.14: Final across-axis 2¾-D free-air gravity model of Line 6. Display parameters are described in figure 11.
(a) Comparison of the observed (dots) and calculated (solid line) free-air gravity anomalies. The calculated anomaly from *grav2d* gravity modelling (dashed line) is included for comparison. Note the better fit of the calculated anomaly generated by *GMSYS* west of -5 km model offset.
(b) Best fitting density model with layer densities shown in g cm^{-3}. 2¾-D input parameters are also shown with densities and minimum and maximum y-lengths shown as subscripts (on-line structures) and superscripts (off-line structures). Stars (-*/*) denote infinite lateral extents.

Line 4 - along-axis (CVFR)

Densities for the CVFR along-axis profile (Line 4) were extracted from the intersections with the two across-axis profiles, Line 1 and Line 6 and extrapolated across the entire model. The five main layer densities (there is no sediment on the along-axis profile) - the water column, layer 2A, layer 2B/C, layer 3 and upper mantle were thus modelled as 1.03, 2.25, 2.62, 2.89 and 3.30 g cm^{-3} respectively.

The perpendicular extent of the crustal structure of Line 4 is clearly not 2-D (see figure 2.1) and was thus modelled in 2¾-D using *GMSYS* in an attempt to simulate the off-line topographic features and the limited extent of the CVFR perpendicular to the profile. The final 2¾-D gravity model is shown in figure 5.15, with input parameters similar to those described for Line 6 (cf. figure 5.14b) and the main features incorporated into the *GMSYS* model are described below. Note that for 2¾-D modelling on Line 4 a positive y-length corresponds to a structure that extends east of the profile and negative to the west. The maximum error in the fit of the calculated and observed free-air gravity data is ~3 mGal.

- The NVFR, situated west of Line 4 at model offsets greater than 30 km, was reproduced using three separate blocks located at different depths (1.9 to 2.1 km; 2.1-2.3 km and >2.3 km depth). The shallowest block was modelled with a density of 2.15 g cm^{-3} and minimum and maximum y-lengths of -6 and -3 km centred on 34 km model offset and -7 and -4 km at model offsets greater than 37 km. Below this block lies a body of density 2.20 g cm^{-3}, with minimum and maximum y-lengths of -9 and -2.5 km and is modelled at >39 km model offset. The deepest block is modelled with a density of 2.25 g cm^{-3} and a width of 10 km and its eastern limit is 1 km to the west of Line 4.
- Line 4 linearly follows the shallowest bathymetric expression of the CVFR, which has limited extent perpendicular to the profile. In an attempt to reproduce this feature, blocks of different density (2.15-2.25 g cm^{-3}) were incorporated into the model with differing minimum and maximum y-lengths (e.g. figure 5.15b: block centred on 11 km model offset with a density of 2.20 g cm^{-3} extending 2 km west and 1 km east of Line 4).
- In maintaining a linear north-northeast – south-southwest profile, Line 4 did not follow the shallowest bathymetric expression of the CVFR along the entire length of the profile as the ridge orientation is altered by the two devals at 22°

21′ S and 22° 16′ S. Between 17 and 24 km model offset, the ridge crest is located 2 km east of the profile and was thus modelled in 2¾-D with an additional block of density 2.20 g cm^{-3}, a width of 2 km and a height of ~200 m.

- Topographical variations in the layer 2A/2B boundary were also modelled perpendicular to the profile with additional blocks centred on 5 km (density of 2.52 g cm^{-3} - top of layer 2B/C) and 20 km model offset (density of 2.35 g cm^{-3} - base of layer 2A).
- The depth of the Moho on Line 4 is constrained solely from the two intersection points with the across-axis profiles (0 and 28.5 km model offset), thus there is more scope for changing the depth of the Moho away from these two points in order to fit the observed gravity. The Moho on Line 1 decreases in depth away from axial region (cf. figure 4.4) and thus the upper mantle between 0 and 30 km model offset, at depths less than 11 km, is modelled with a lateral extent of 10 km east and west of Line 4. The slight decrease in depth of the Moho (~0.7 km) at model offsets greater than 30 km (dashed line) provides a much better fit to the observed data and is thus included as an additional constraint in the final model. However, the inclusion of a regional gradient can also faithfully reproduce the observed free-air gravity data and cannot be discounted.

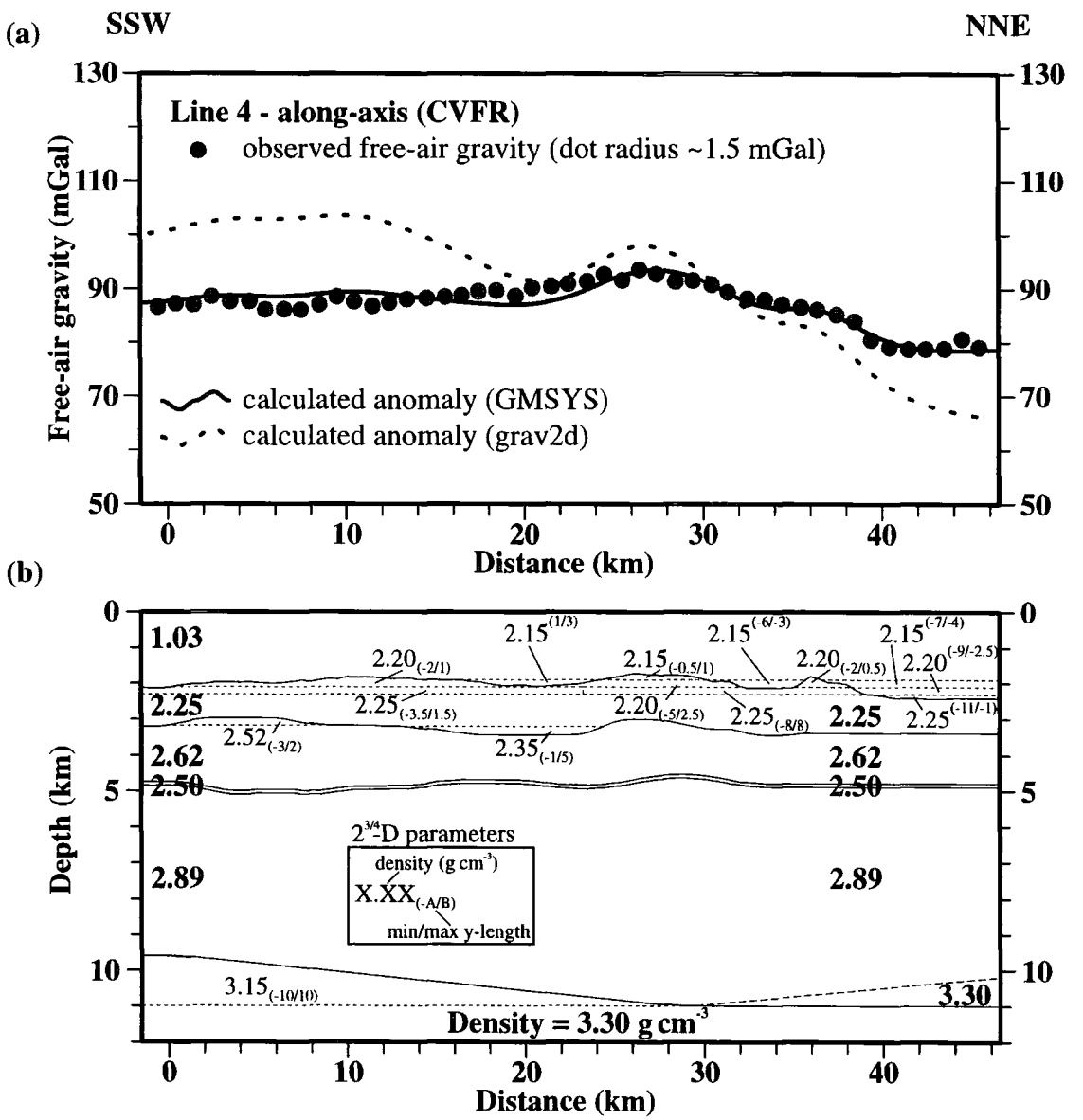

Figure 5.15: Final across-axis 2¾-D free-air gravity model of Line 4. Display parameters are described in figures 5.11 and 5.14.

(a) Comparison of the observed (dots) and calculated (solid line) free-air gravity anomaly. Note the greatly improved fit of the calculated anomaly generated by *GMSYS*.

(b) Best fitting density model with layer densities shown in g cm^{-3}.

5.3.2 Residual mantle Bouguer anomaly

The main stages involved in the calculation of the mantle Bouguer anomaly (MBA) and subsequent residual mantle Bouguer anomaly (RMBA) are described in detail in Chapter 5 (pp.172-188) of Navin (1996) and are summarised in figure 5.16. Graphical representation and manipulation of the data was carried out using *GMT* version 3.1 (Wessel and Smith, 1995) and example scripts can be found in Appendix D.

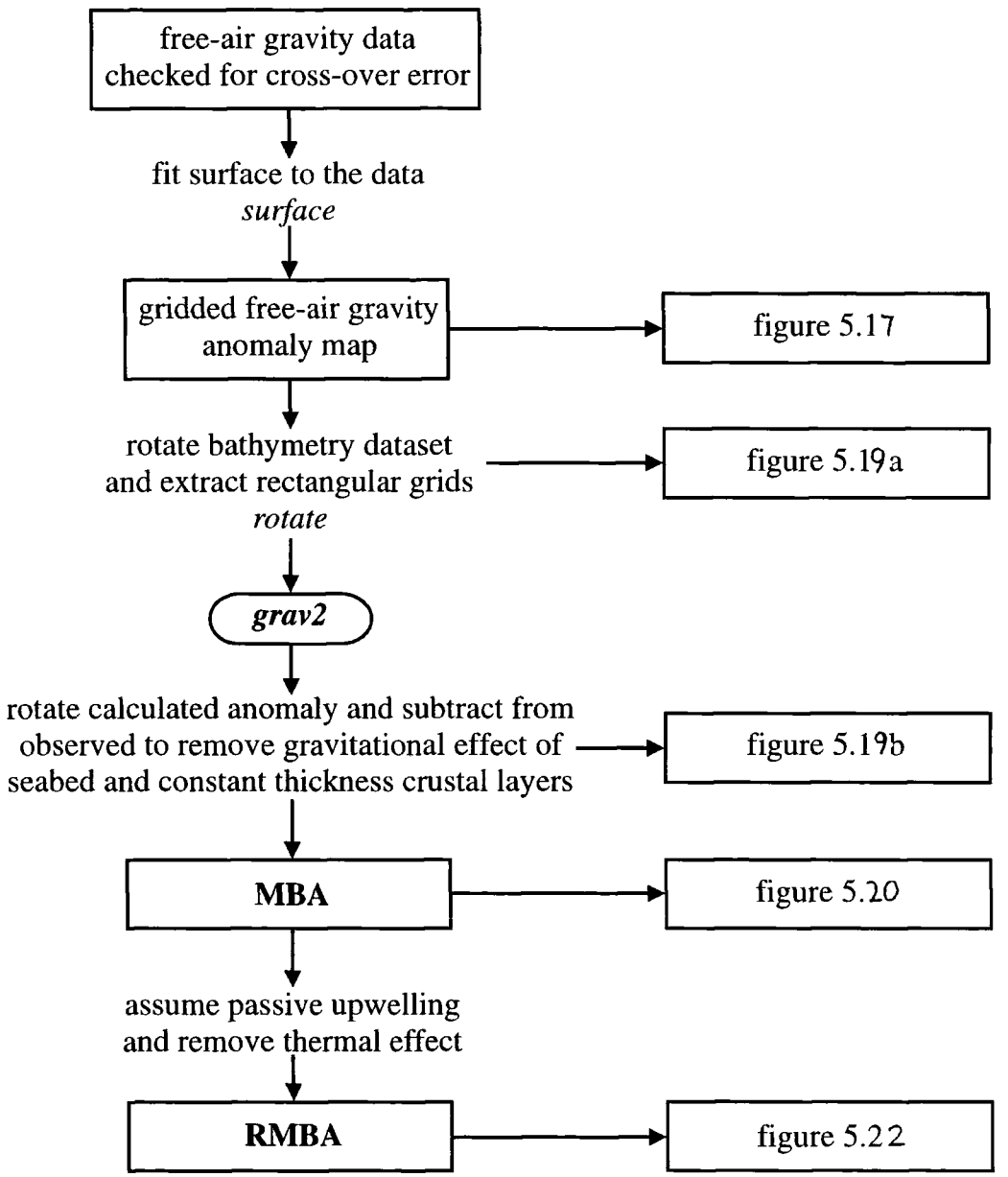

Figure 5.16: Flow diagram showing the main stages in the calculation of the residual mantle Bouguer anomaly. Intermediate stages in the flow and their corresponding figures in this chapter are also displayed. *GMT* scripts (version 3.1 - Wessel and Smith, 1995) are shown in italics.

Calculation of the mantle Bouguer anomaly

The MBA represents the gravity field arising from lateral variations in the crustal thickness and lateral and vertical variations in crustal and/or mantle densities. The MBA is calculated by subtracting the gravitational attraction of layers of constant crustal thickness and density and their corresponding first-order interfaces (e.g. seabed and Moho) from the free-air gravity anomaly (Prince and Forsyth, 1988; Lin *et* al., 1990).

The EW9512 free-air gravity dataset was edited to remove data collected during ship turns (i.e. poor data quality due to inaccurate Eötvös correction) and checked for cross-over errors (i.e. values are the same at line intersections within error). A surface was then fit to the observed gravity data using *surface* (*GMT* version 3.1) and the final gridded free-air gravity anomaly map shown in figure 5.17 created. Free-air gravity anomaly data were also compared with regional data from the Sandwell and Smith (1986) 2′x2′ gravity grid to check the relative base levels of the two datasets.

The calculation of the MBA was carried out using the program *grav2* [written by B.Y. Kuo and based on the method of Parker (1972)], which calculates the gravitational effect of topography and a constant density contrast at user-defined boundaries (Kuo and Forsyth, 1988). This method requires a *rectangular* grid of regularly spaced bathymetry data points with the grid spacing set to less than the water depth to avoid aliasing (Navin, 1996).

The VFR bathymetry dataset is elongate parallel and perpendicular to the spreading axes, hence in its geographical co-ordinate system a suitable *rectangular* grid cannot be extracted for input into *grav2*. The 'geographic' dataset was thus rotated to align the horizontal axis parallel to the spreading direction (i.e. parallel to the two across-axis seismic profiles, Line 1 and Line 6) and resampled to a new x-y co-ordinate system using *rotate* (*GMT* version 3.1). Two rectangular grids of 256 samples square, encompassing both the CVFR and NVFR and up to 16 km off-axis, were then extracted from the new dataset and used as input for *grav2* (see figure 5.18). The location of the two grids with respect to the geographical co-ordinate system is also shown in figure 5.17 and described below.

1. 32 km x 32 km square grid centred on the CVFR.
2. 16 km x 64 km rectangular grid centred horizontally on the along-axis seismic profile, Line 4 and extending from beyond the southern tip of the CVFR to the northern tip of the NVFR.

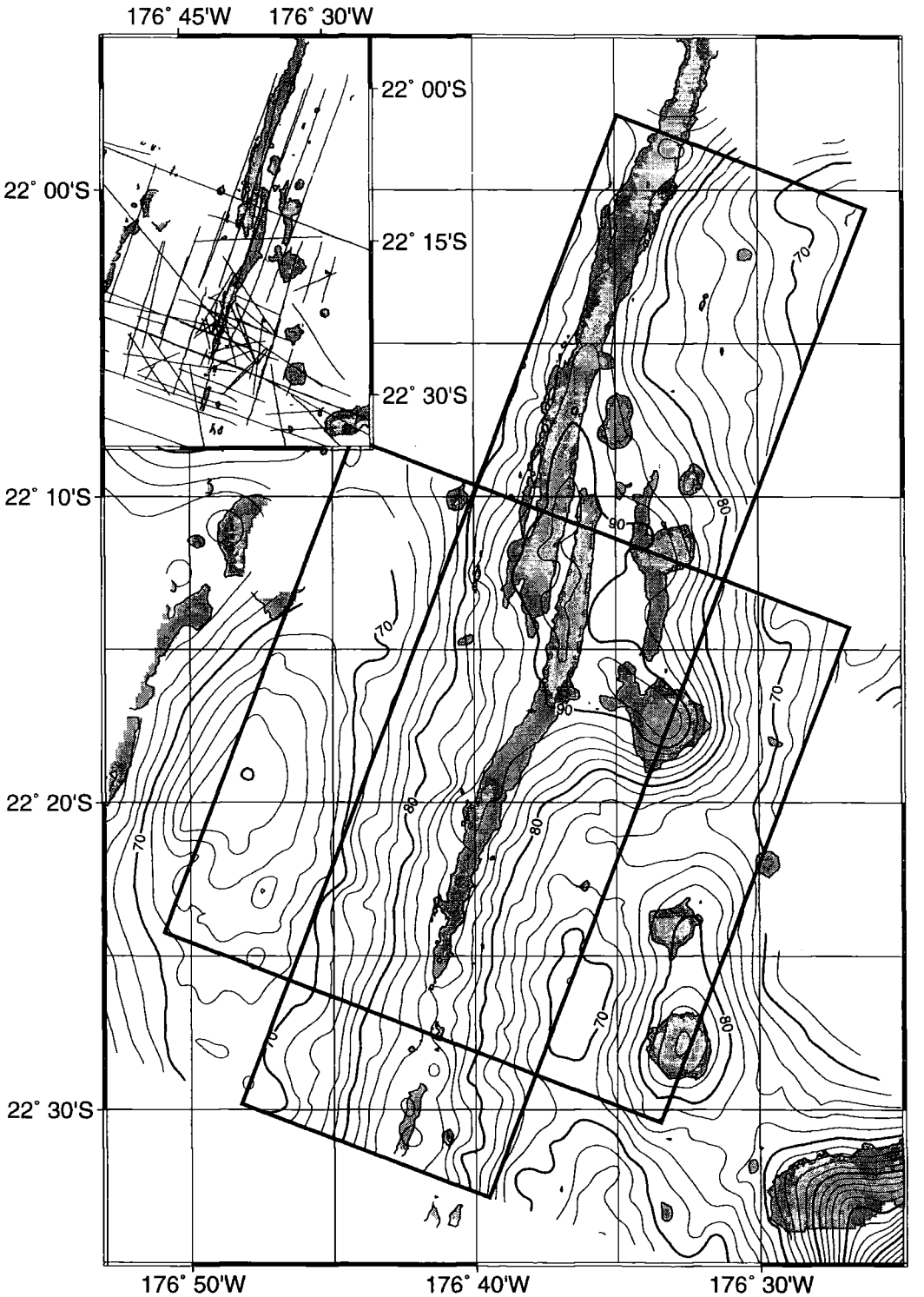

Figure 5.17: Free-air gravity anomaly map calculated from the EW9512 data overlying seabed bathymetry with depths shallower than 2000 m shaded to show the location of the CVFR and NVFR. Contour interval is 2 mGal. Note the general agreement between the topography and observed free-air anomaly. Inset shows the location of the gravity data used to create the free-air gravity grid.

Within these two grids the free-air anomalies associated with the predictable components of the gravity field (water column depth and layers of constant thickness and density) are removed from the observed free-air gravity anomaly (figure 5.17). Detailed modelling of the crustal structure at the VFR using wide-angle seismic data (Chapter 4) and 2-D gravity modelling (section 5.3.1) produced a reliable estimate of layer thicknesses and densities and the data input to *grav2* consists of a density contrast at each layer boundary and the depths of these boundaries below the zero datum - the seabed, as defined by the topography grid (see Appendix D - run_grav2). Previous calculations of the MBA (e.g. Kuo and Forsyth, 1988; Lin *et al.*, 1990) assume a constant density for the entire crust and Kuo and Forsyth (1988) state that a stratified crust (a gradual density increase from 2.4 g cm^{-3} at the seabed to 2.95 g cm^{-3} at the base of the crust) changes the predicted anomaly by less than 1 mGal. However, the density stratification of the crust was readily available from 2-D seismic and gravity modelling and it was thus included in the calculation and is described in figure 5.18.

The predicted gravitational effect of the seabed with a density contrast of 1.22 g cm^{-3} and the associated relief of the layer 2A/2B boundary (density contrast of 0.37 g cm^{-3}), layer 2/3 boundary (0.26 g cm^{-3}) and Moho (0.42 g cm^{-3}) is shown in figure 5.19b. The seabed topography (figure 5.19a) contributes ~70% of the total calculated anomaly (peak-to-peak amplitude of 34 mGal), thus the density contrast across the seabed is an important factor when determining the gravitational effect of the crust (layered vs. uniform crust) especially in regions of severe topography.

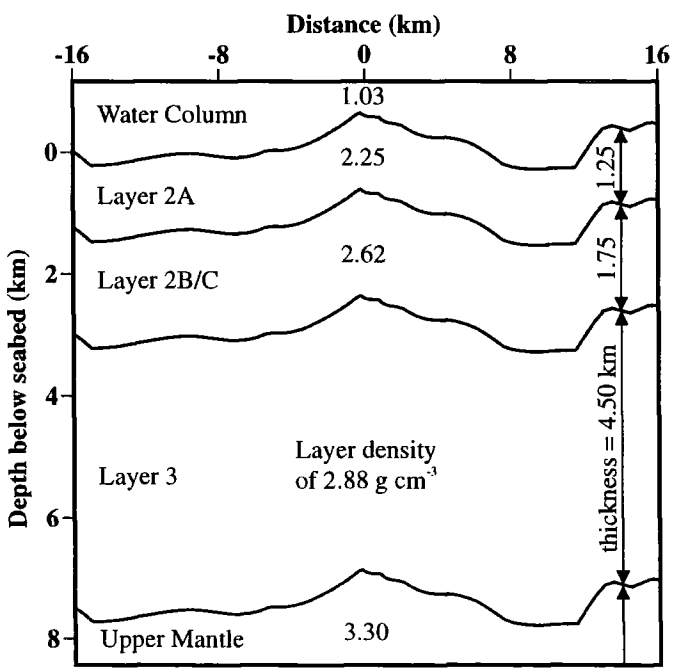

Figure 5.18: Model used as input for *grav2* to calculate the gravitational attraction of a layered crust of constant density and thickness.

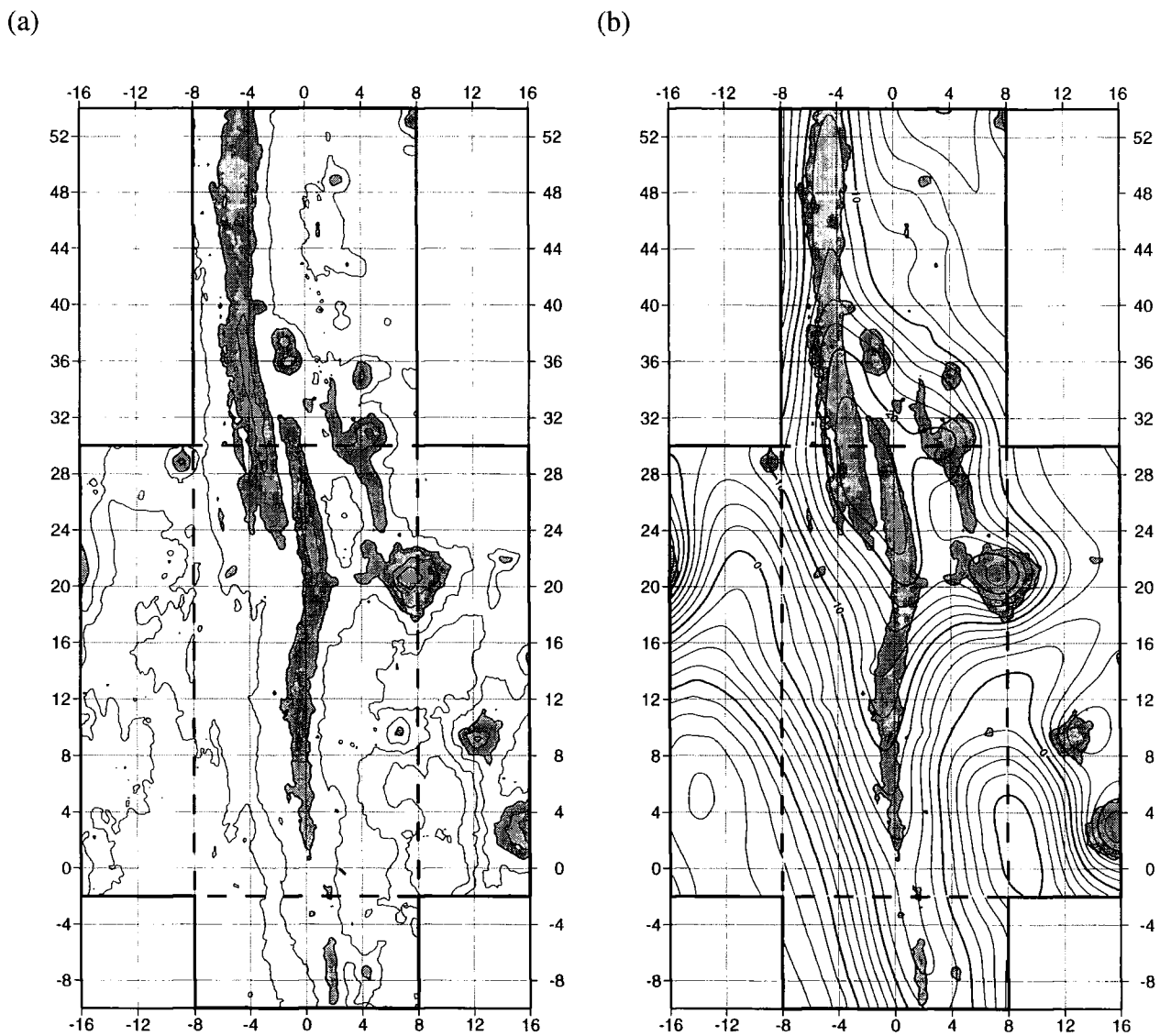

Figure 5.19: Calculation of the gravitational effect of a layered crust of constant layer thickness and density. The axes of the rotated x-y co-ordinate system are annotated in kilometres and seabed depths shallower than 2000 m have been shaded to show the location of the CVFR and NVFR. Thick solid lines denote the extent of the combined rectangular grids used in the calculation of the MBA.

(a) Bathymetry data from EW9512 used as the zero horizon for input into *grav2*. Bathymetric contours are plotted at 250 m intervals.

(b) Gravitational attraction due to the seabed, layer 2A/2B and layer 2/3 boundaries and the Moho. The gravitational attraction due to the seabed contributes to ~70% of the total calculated field. Contour interval is 2 mGal. Note the large gravitational effect of the 'inflated' OSC centred on (-2, 28).

The predicted gravity anomaly shown in figure 5.18 was then rotated back to geographical co-ordinates and subtracted from the observed free-air gravity anomaly to generate the MBA (figure 5.20). The MBA has a peak-to-peak amplitude of 18 mGal, except for the region at the eastern edge of the seamount centred on 22° 12′ S, 176° 47′ W (figure 5.13: seamount S4) - the result of poor data coverage and 'oversmoothing' of the free-air anomaly when fitting a surface to the observed data. The slight decrease in anomaly to the east (east of 176° 32′ W) is perhaps due to the proximity of the Tofua island arc (see figure 1.2 - Tonga Ridge). Contours are deviated, mirroring the topography, around large seamounts (e.g. 22° 18′ S, 176° 33′ W), which implies a locally thickened upper crust, probably due to an increase in the volume of intrusive and extrusive material.

The major feature of interest on the MBA plot is the general decrease in anomaly amplitude from the southern tip of the CVFR (~85 mGal) to the OSC at 22° 12′ S (~69 mGal), which implies thicker crust and/or lower crustal/mantle densities beneath the OSC. An MBA plot of the CD34/88 gravity dataset, calculated using the forward modelling algorithm of Talwani and Ewing (1960), is described in Sinha (1995). The general decrease in anomaly towards the OSC shown in figure 5.20 is also observed in the CD34/88 data (inset - figure 5.20).

Sinha (1995) also notes that areas of relatively low MBA correlate with the areas of shallowest seafloor topography, in particular the ridge crest, suggesting a remarkable degree of isostasy. This correlation is not observed in the EW9512 dataset and may be due to the more extensive bathymetry dataset used here to calculated the gravitational attraction due to a layered crust of constant thickness and density (see figure 5.19). The enclosed basins to the west and east of the CVFR crest are bounded by the central ridge at 176° 52′ W (Wiedicke and Collier, 1993) and the large north-south seamount chain at 176° 34′ W respectively (see figure 5.1). However, these shallow bathymetric features lie outside the topographic grid used by Sinha (1995) and are thus not included in the CD34/88 MBA calculation. The gravitational attraction of the shallower seafloor external to the CD34/88 grid and hence more negative MBA either side of the ridge crest may explain the difference between the two MBA plots (see figure 5.20 and inset).

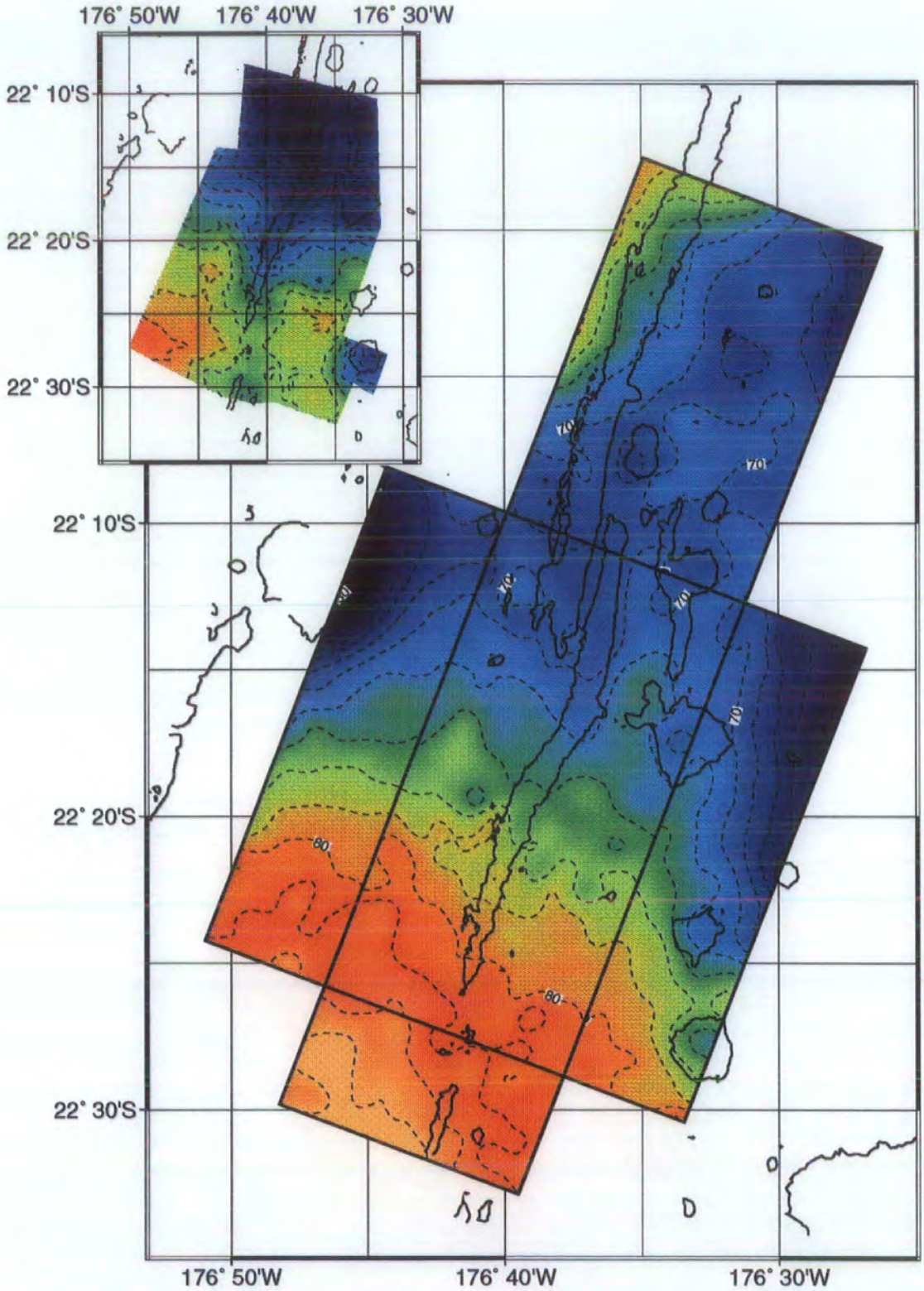

Figure 5.20: Mantle Bouguer anomaly calculated by subtracting the gravitational effect of a layered crust of constant layer thickness and density (figure 5.19) from the observed free-air gravity anomaly (figure 5.17). Contour interval (dashed line) is 2 mGal. The 2000 m bathymetric contour (solid line) is also plotted for reference. Note the general decrease in anomaly towards the OSC (22° 12′ S). Inset shows the MBA calculated using the forward modelling algorithm of Talwani and Ewing (1960) on the CD34/88 free-air gravity dataset (Sinha, 1995) for comparison. Note that the Sinha (1995) MBA still contains a large topographic component which is not apparent in the EW9512 data.

Calculation of the residual mantle Bouguer anomaly

A series of programs written and developed by Forsyth (Forsyth and Wilson, 1984) calculate the thermal effect of a north-south trending ridge-transform-ridge system (Navin, 1996). Passive upwelling occurs within a triangular region whose apex lies beneath the ridge crest and flow is horizontal elsewhere, parallel to the direction of plate motion (Forsyth and Wilson, 1984; Prince and Forsyth, 1988). A steady-state thermal model of the ridge-transform-ridge system can thus be converted into a model of density variation by multiplying by an appropriate thermal expansion coefficient (Prince and Forsyth, 1988). This thermal anomaly is then subtracted from the MBA to generate a RMBA. The main input parameters are described in figure 5.21a and a more detailed description of calculation of the residual mantle Bouguer anomaly can be found in Forsyth and Wilson (1984), Prince and Forsyth (1988) and Navin (1996).

The VFR is not however a simple north-south ridge-transform-ridge system in geographical co-ordinates, although a reasonable approximation can be obtained using the rotated dataset, as shown in figure 5.19a. The CVFR and NVFR were located on a 128 km x 128 km grid (see figure 5.21a) and additional ridges were added on the basis of GLORIA sidescan imagery and other geophysical data (Parson *et al.*, 1990; Cann, 1994; Parson and Wright, 1996) to complete the grid (inset of figure 5.21a). A large grid was used in an attempt to minimise the effect of periodicity of the FFT calculations involved in the Forsyth programs and a 32 km 'buffer zone' was therefore incorporated around the highlighted work area. The spreading direction was assumed to be east-west with a constant half-spreading rate of 30 mm yr^{-1} over the entire grid and the resulting calculated thermal gravity anomaly is shown in figure 5.21b.

The thermal gravity anomaly was then rotated back to geographical co-ordinates and subtracted from the MBA to generate a residual mantle Bouguer anomaly (figure 5.22). The RMBA shows similar features to those observed on the MBA (figure 5.20) and is dominated by the general decrease in anomaly towards the OSC at 22° 12′ S. The anomaly decreases from ~92 mGal beyond the southern tip of the CVFR to ~76 mGal, centred on the OSC (a range of 16 mGal). The significance of this, in relation to the results of wide-angle seismic modelling, will be discussed in detail in Chapter 6. When considering the implications of the general decrease in anomaly towards the OSC it should be noted that the ridge-transform-ridge system, used to calculate the thermal anomaly, breaks down at this location because the CVFR and NVFR are not separated by a 'simple' transform fault and overlap by at least 10 km (figure 5.20a). The proximity

of the active Tofua island arc and the presence of the subducting former Pacific plate at a depth of 200 km beneath the VFR axis (Sinha, 1995) should also be factors in the calculation of the thermal anomaly, but this is beyond the scope of this dissertation.

The main observation of the negative anomaly beneath the OSC at 22° 12′ S on both the MBA and RMBA contrasts with the 'Bull's-eye' negative anomalies identified at the centre of spreading segments on both the MAR and EPR. It should be noted that the observed anomalies may be alternatively interpreted as a general increase in anomaly towards the younger crust to the south and the implications of both interpretations will be discussed in Chapter 6. The other feature of note is the complete absence of any topographic component in the MBA and RMBA, implying that the VFR is not isostatically compensated.

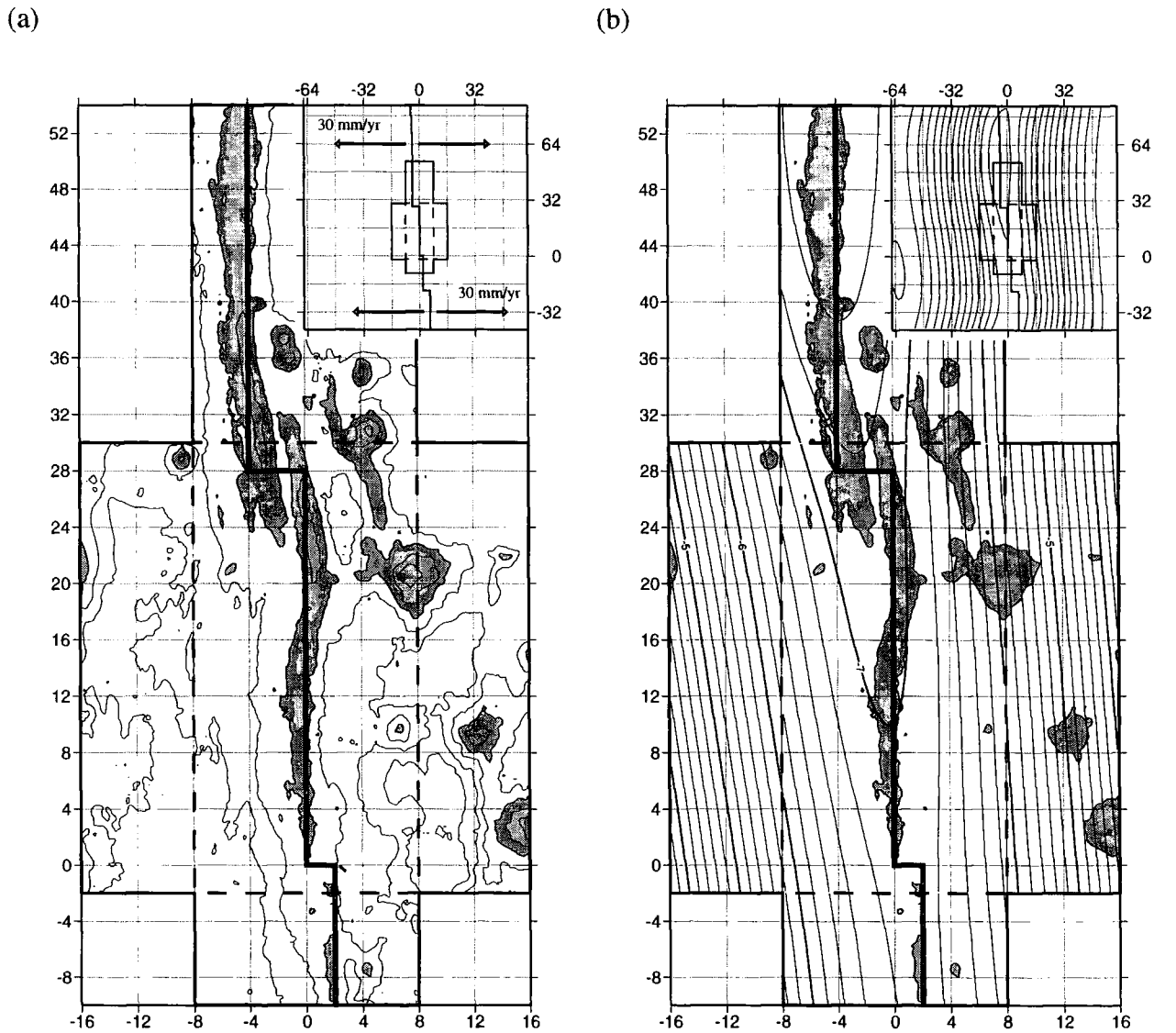

Figure 5.21: Calculation of the thermal effect of a north-south ridge-transform-ridge system assuming passive upwelling. Display parameters are described in figure 5.18. Insets show the location of the survey area with respect to the complete 128 km x 128 km grid.

(a) Location of the ridge-transform-ridge system (thick solid lines) used to calculate the thermal anomaly overlying the bathymetry. Ridges are modelled with an east-west half-spreading rate of 30 mm yr^{-1} and the inset shows the position of additional ridges derived from previous GLORIA sidescan imagery (Parson *et al.*, 1990).

(b) Thermal anomaly due to passive upwelling calculated using a series of programs written by Forsyth (see text). Note that the largest anomaly is associated with the longest spreading segment. Contour interval is 0.2 mGal. Inset shows the inherent problems of the periodicity of the thermal anomaly (general s-shape of the anomaly) and the contour interval here is 1 mGal.

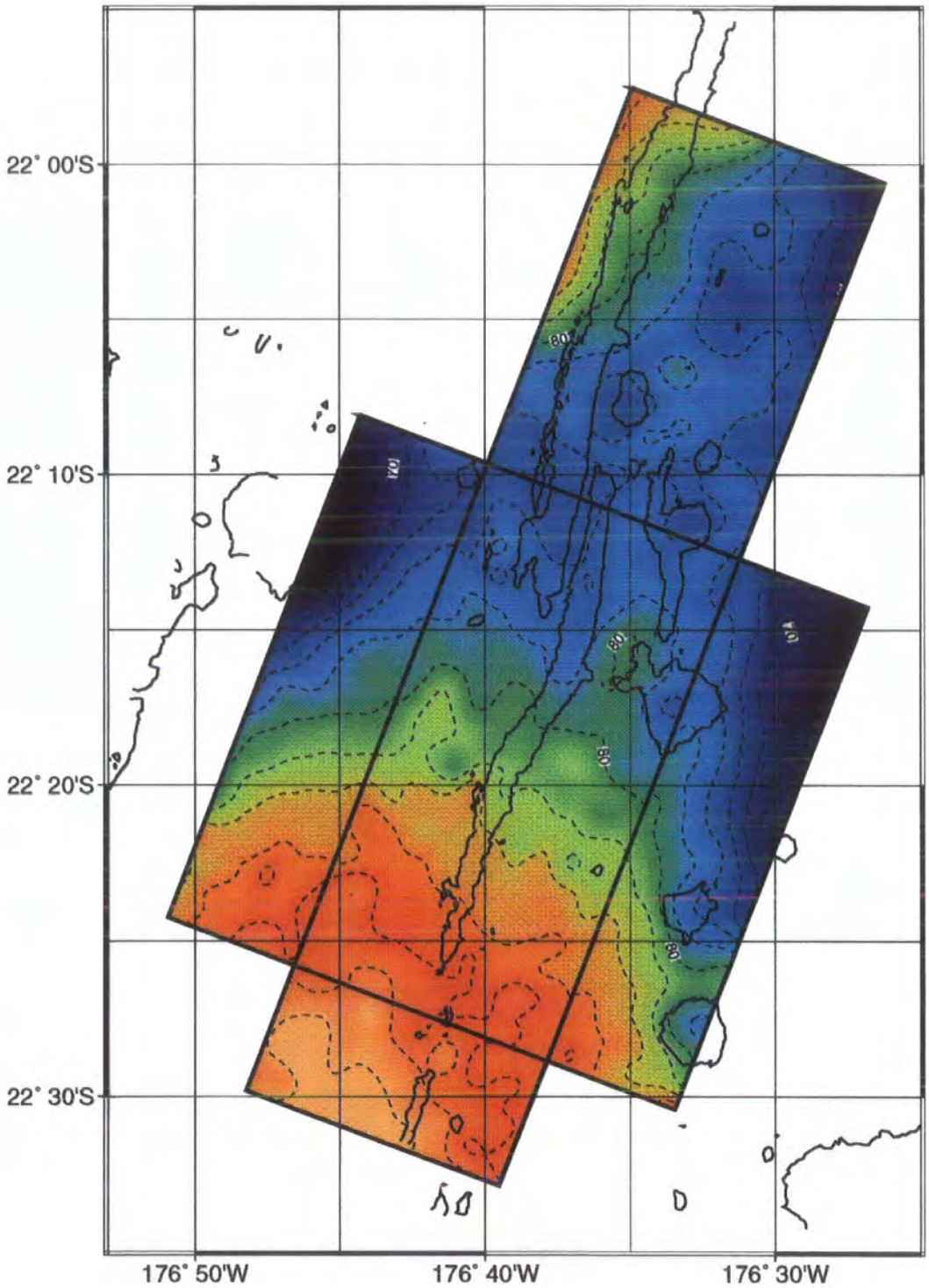

Figure 5.22: Residual mantle Bouguer anomaly calculated by subtracting the thermal effect of passive upwelling at a ridge-transform-ridge system (figure 5.21b) from the mantle Bouguer anomaly (figure 5.20). Contour interval (dashed line) is 2 mGal. The 2000 m bathymetric contour (solid line) is also plotted for reference. Note that the removal of the thermal component does not remove the general decrease in anomaly towards the OSC (22° 12′ S), observed in the MBA (figure 5.20).

5.4 Summary

Modelling of the normal incidence seismic data and gravity data have been presented in this chapter to provide an additional constraint on the crustal structure at the VFR. The normal incidence seismic data provide further constraint on the low velocity block modelled between layer 2 and layer 3, characterised by a large amplitude, reversed polarity reflection from its upper boundary, and the 2-D gravity data was used to test the uniqueness of the final wide-angle seismic models and provide an estimate of the layer densities. A subset of the entire free-air gravity dataset was also used to calculate a MBA and RMBA over the CVFR and NVFR to independently test variations in crustal thickness and investigate possible variations in crustal/mantle density. A synthesis of the VFR crustal models, calculated from the wide-angle and normal incidence seismic data and gravity data, is presented in the following chapter and the correlation with pre-existing data from the VFR is discussed.

Chapter 6

Crustal structure of the Valu Fa Ridge

6.1 Introduction

The velocity and density structure of the VFR have been modelled in Chapters 4 and 5. The complete dataset consists of two 80 km long across-axis profiles, two along-axis profiles (CVFR - 50 km long, NVFR - 20 km long) and two 30 km long axis-parallel profiles. This network of profiles (shown in figures 6.1 and 6.2) not only provides good constraint on the crustal structure of VFR-generated crust, but also on the transition into pre-rift back-arc and island arc crust (see also figure 4.4).

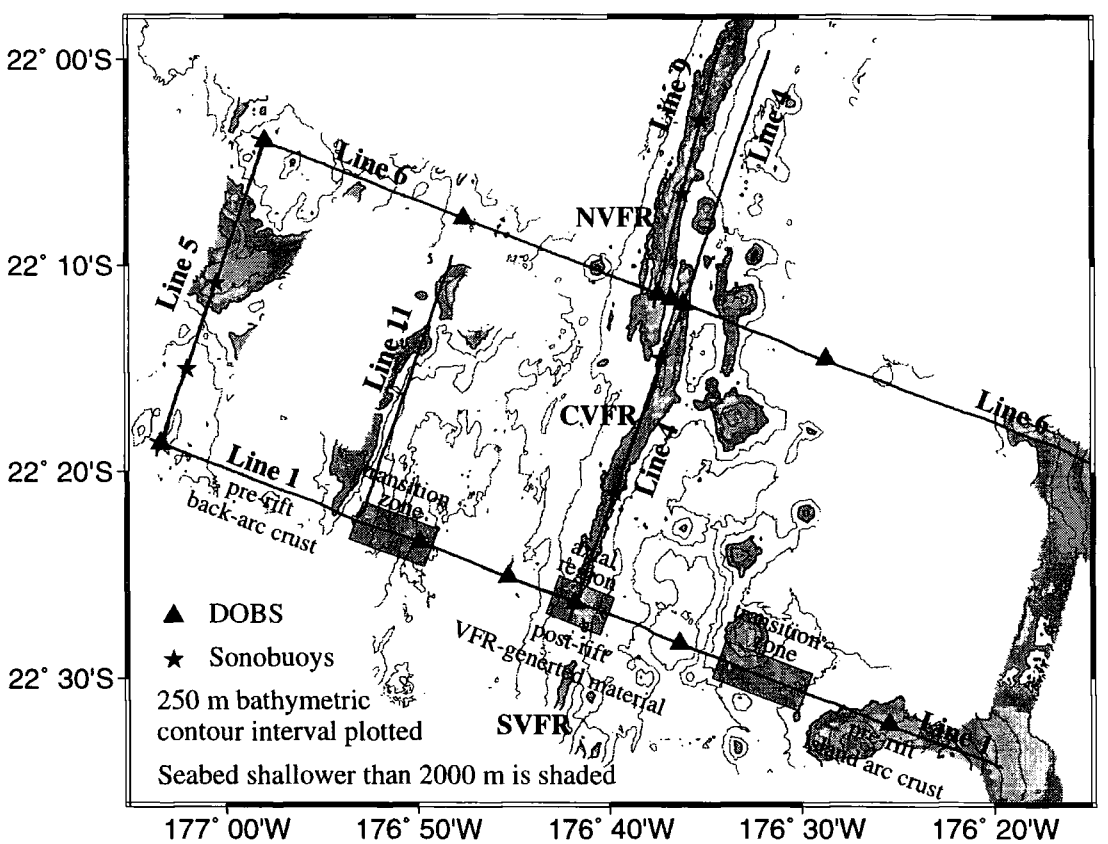

Figure 6.1: Location map of the main seismic (and gravity) lines modelled in this dissertation (after Peirce *et al.*, 1996). DOBS and sonobuoy locations are marked by triangles and stars respectively and bathymetric contours are plotted at 250 m intervals. Seabed depths shallower than 2000 m have been shaded to show the location of the NVFR, CVFR and SVFR. The five lateral regions identified on Line 1 (see figure 4.4) are also shown. The two transition zones (shaded boxes at 176° 52′ W and 176° 32′ W) separate post-rift VFR-generated material from pre-rift back-arc and island arc crust. The axial region containing the LVZ within layer 3 has also been annotated (shaded box at 176° 42′ W). A low velocity block was modelled beneath the entire length of the CVFR (Line 4) and at least the southern portion of the NVFR (Line 9).

Figure 6.2: Fence diagram showing the final velocity-depth models for each seismic line shown in figure 6.1. Solid lines indicate the location and geometry of the main layer boundaries and dotted lines represent isovelocity contours. DOBS and sonobuoy locations are marked by triangles and stars respectively. Intersection points with the along-axis and axis-parallel profiles are shown by vertical dashed lines. The across-axis profiles are oriented WNW-ESE and the along-axis and axis-parallel profiles are oriented SSW-NNE. Note that all intersection points are consistent with the across-axis profiles (e.g. Line 6: 0 km model offset). Note the lower velocities beneath the axial region on both across-axis profiles and the low velocity block at ~5 km depth. The thinning of the upper crust on Line 1 (+/- 17 km model offset) corresponds to the transition from pre-rift to post-rift VFR-generated material. Note how this thinning is also observed to a lesser degree on the southern half of the axis-parallel profile, Line 11.

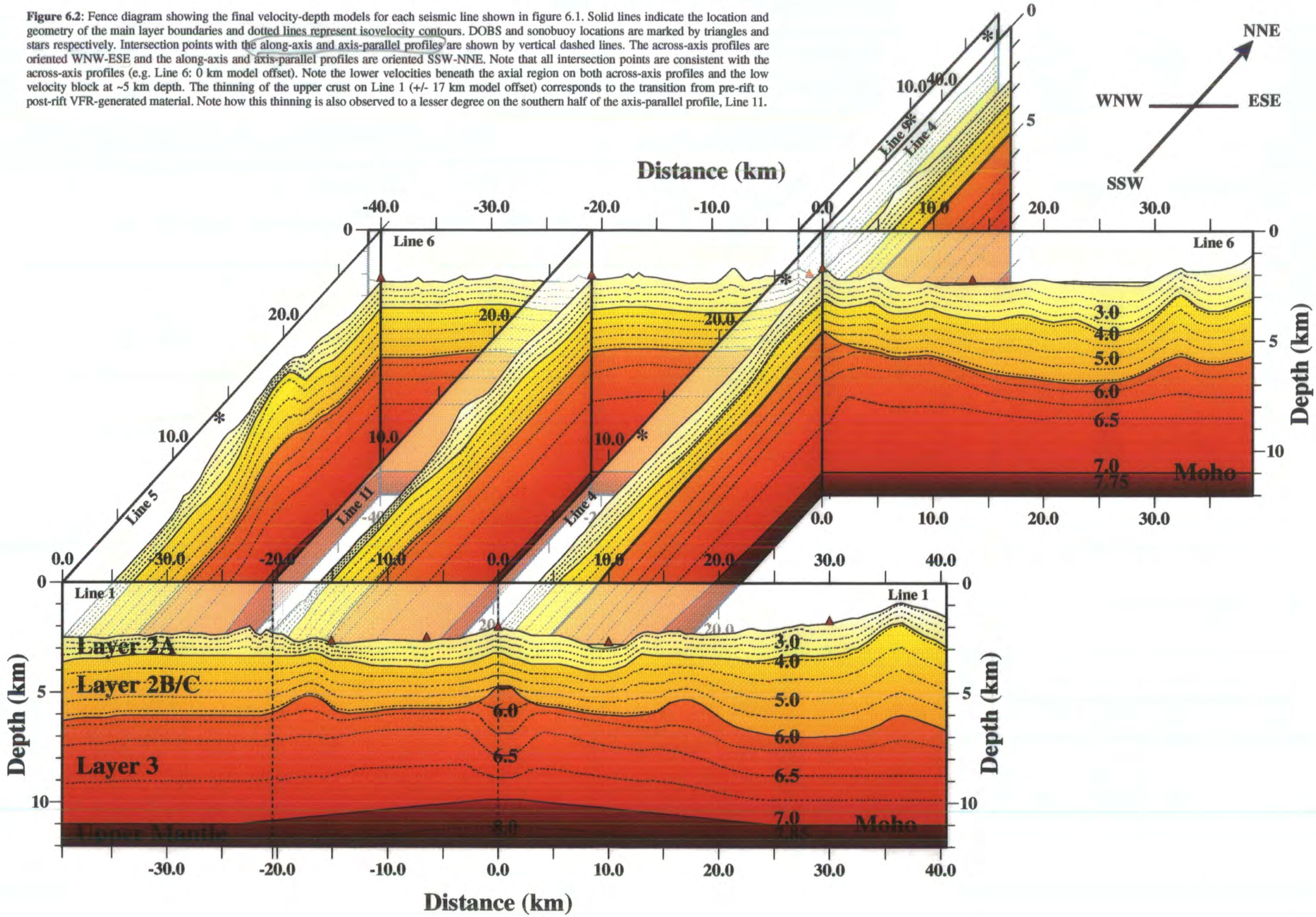

Velocity-depth profiles extracted from the wide-angle seismic models are compared with the results from both the fast spreading EPR and the slow spreading MAR (White *et al.*, 1992) and significant differences can be observed (figure 6.3). The seismic structure beneath the VFR clearly displays the influence of the island arc and back-arc regime, evidenced by lower velocities and a much thicker upper crust. Despite the profound influence of the back-arc environment, there are many similar features in VFR crust compared with 'normal' mid-ocean ridge crust. The velocity-depth profiles demonstrate a general decrease in the vertical velocity gradient with depth and can be split into oceanic layers 2A, 2B/C etc., according to the layering described in section 1.3. This oceanic layering nomenclature has been extended into the pre-rift island arc crust for model continuity, although the crustal structure in this region is significantly different.

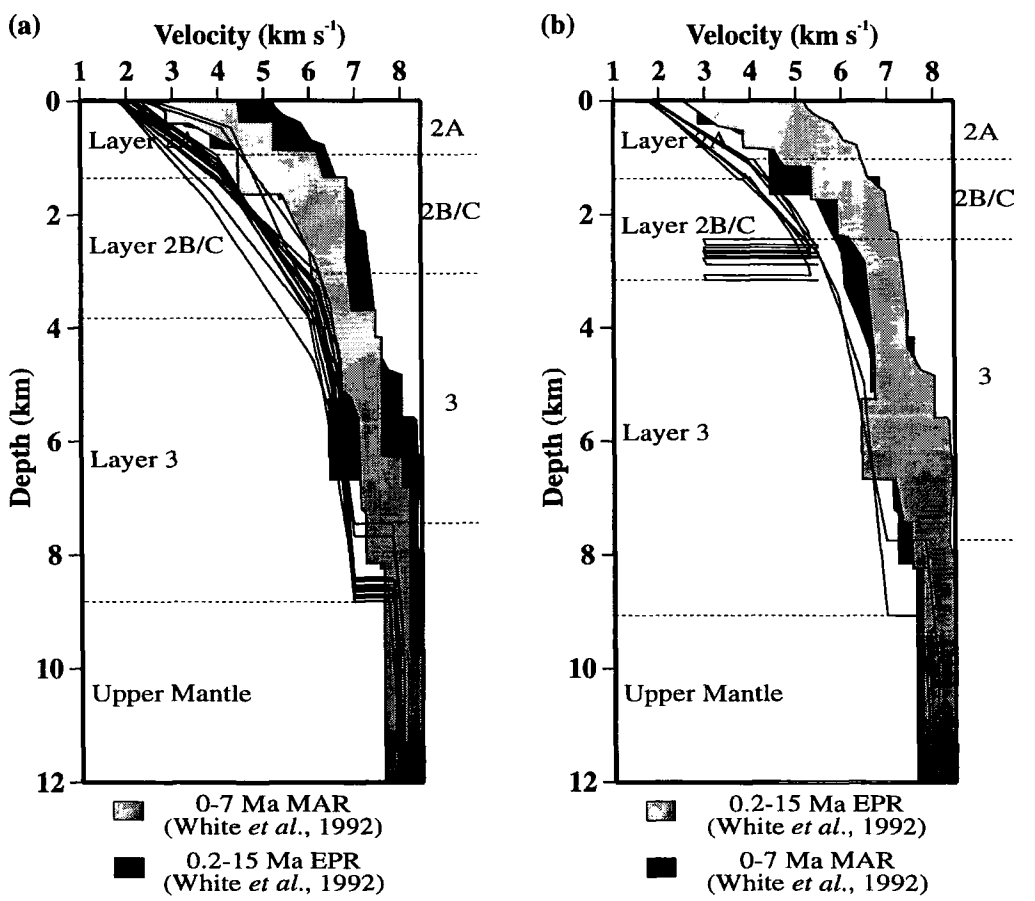

Figure 6.3: Velocity-depth profiles of the VFR compared with the 'standard' velocity envelopes of White *et al.* (1992) for EPR and MAR crust (modified from Navin *et al.*, 1996). Minimum and maximum depths to layer boundaries are annotated (horizontal dashed lines).
(a) Off-axis velocity-depth profiles from the two across-axis and two axis-parallel profiles. Note the shift of the profiles to the left of the MAR and EPR crust implying thicker crust and/or lower velocities.
(b) On-axis velocity-depth profiles. Note the position of the velocity inversion at the layer 2/3 boundary. Also note that the velocity structure beneath the layer 2/3 boundary is only constrained by the two across-axis profiles.

6.2 Upper crustal structure

The upper crustal structure described here consists of a 'volcanic' section (layer 2) overlain by small isolated sediment ponds (layer 1).

The VFR is a young (<1 Ma), relatively unsedimented ridge. Accumulations of sediment identified on the seismic profiles are confined to the east of the VFR, suggesting that the Tofua Arc and the north-south oriented seamount chain (176° 33′ W) are the probable sources. Analysis of sediment retrieved from ODP Drill Site 840 identified that more recent volcaniclastic sediments were sourced from Ata Island (situated at the eastern end of Line 6) and surrounding islands.

Layer 2 is further subdivided into layers 2A, 2B and 2C consistent with the nomenclature of Bratt and Purdy (1984) and is modelled here with low P-wave velocities and high vertical velocity gradients, which decrease with depth

6.2.1 Layer 2A

Layer 2A has been consistently identified as the most variable layer within the ocean crust. There have been many detailed investigations into the seismic properties of layer 2A at mid-ocean ridges (e.g. Cudrak and Clowes, 1993; Harding *et al.*, 1993; Vera and Diebold, 1994; Kappus *et al.*, 1995; Carbotte *et al.*, 1997). The results of these detailed studies, combined with observations from several ODP drill sites (e.g. Hole 504b) have identified the top of oceanic layer 2A as a zone of high porosity, high permeability, fractured extrusives (pillow lavas and sheet flows).

Upper boundary velocities are modelled between 2.0 km s^{-1} and 3.0 km s^{-1} at fast, slow and intermediate spreading ridges (e.g. Vera and Diebold, 1994; Navin *et al.*, 1998; Cudrak and Clowes, 1993). The velocities modelled at the VFR lie at the lower end of this scale and are sometimes modelled to be less than 2.0 km s^{-1}. These low velocities, and a modelled density of 2.25 g cm^{-3}, indicate the presence of highly fractured surficial material of an unusually high porosity and permeability, perhaps a consequence of the increased volatile content within the back-arc andesitic lavas. The highly fractured nature of this surficial material is confirmed by the dredging of "vesicular (occasionally scoriaceous) fragments of pillows" (Jenner *et al.*, 1987). Low resistivities modelled in the coincident EW9512 CSEM data also suggest an uppermost kilometre of highly fractured, permeable extrusive material with high, interconnected porosity and saturated with seawater (MacGregor *et al.*, 1997).

Layer 2A is modelled here as a layer of uniform vertical velocity gradient (1.8 ± 0.2 s^{-1}) and an average thickness of 1.25 km (cf. thickness of layer 2A at EPR and JDFR: 0.2-0.4 km and 0.2-0.6 km respectively). Several studies, predominantly at the EPR and also at the JDFR, have further subdivided layer 2A using a number of layers separated by second-order boundaries (e.g. Vera and Diebold, 1994) or a single layer of constantly changing vertical velocity gradient (e.g. Kappus *et al.*, 1995). The EW9512 experiment was specifically designed to investigate lower crustal structure and this dataset does not necessarily permit more detailed velocity-depth modelling of layer 2A. However, the single vertical velocity gradient modelled at the VFR from ~2.0 km s^{-1} to 4.0 km s^{-1} may potentially be an averaging of a more complex upper crustal structure.

Layer 2A is ~100-200 m thicker in post-rift VFR-generated crust than in pre-rift back-arc crust on both across-axis profiles (see figures 4.4, 4.12, 6.1 and 6.2). The axis-parallel profile, Line 5, located west of the 'pseudofault' described in Wiedicke and Collier (1993), also displays a slightly thinner layer 2A than post-rift material. The difference in the thickness of layer 2A between pre-rift and post-rift material could be the result of:

1) slightly different source magma compositions;
2) differing spreading rates at the time of emplacement; and/or
3) pre-rift tectonism as a consequence of renewed spreading.

There is no significant thickening of layer 2A outside the axial region, as seen at the EPR (see figure 6.4), which suggests complete emplacement of the extrusive layer within 1 km of the axis. However, the thickness of layer 2A does not remain constant on the CVFR along-axis profile, increasing in thickness towards the OSC at 22° 12′ S (see figure 4.20), which implies variations in melt delivery and crustal accretion along the CVFR spreading segment. Seismic data show an increase of both extrusive (layer 2A) and crustal thicknesses toward the OSC at 9° 03′ N on the EPR, as seen here at the VFR, however the process of focusing of this crustal accretion is unclear (Kent *et al.*, 1993).

The geological significance of the layer 2A/2B boundary has been the subject of contention over the past few years. The velocity transition has been interpreted either as the lithological boundary between extrusive pillow lavas/sheet flows and intrusive sheeted dykes or as a porosity boundary within the extrusive section associated with a fracture front or hydrothermal alteration (Carbotte *et al.*, 1997). There is no direct

evidence from the EW9512 dataset of a velocity discontinuity at the base of layer 2A, although weak upper crustal reflections (cf. the strong retrograde reflection-like arrival observed on EPR stacked MCS data - see section 1.4.1) have been observed in previous studies of the VFR (Collier and Sinha, 1992b). The boundary is thus modelled as a simple change in vertical velocity gradient from ~1.8 s^{-1} to ~1.0 s^{-1}, coincident with the 4.0 km s^{-1} isovelocity contour. The anomalous depth to this boundary (cf. EPR: figure 6.4a) seems more consistent with an increase in depth to the top of the sheeted dykes rather than a boundary controlled by porosity. Currently, there is little evidence for more extensive fracturing and/or deeper zones of hydrothermal alteration at the VFR, when compared with the EPR, although detailed modelling of the CSEM data may help to determine the depth extent of these processes.

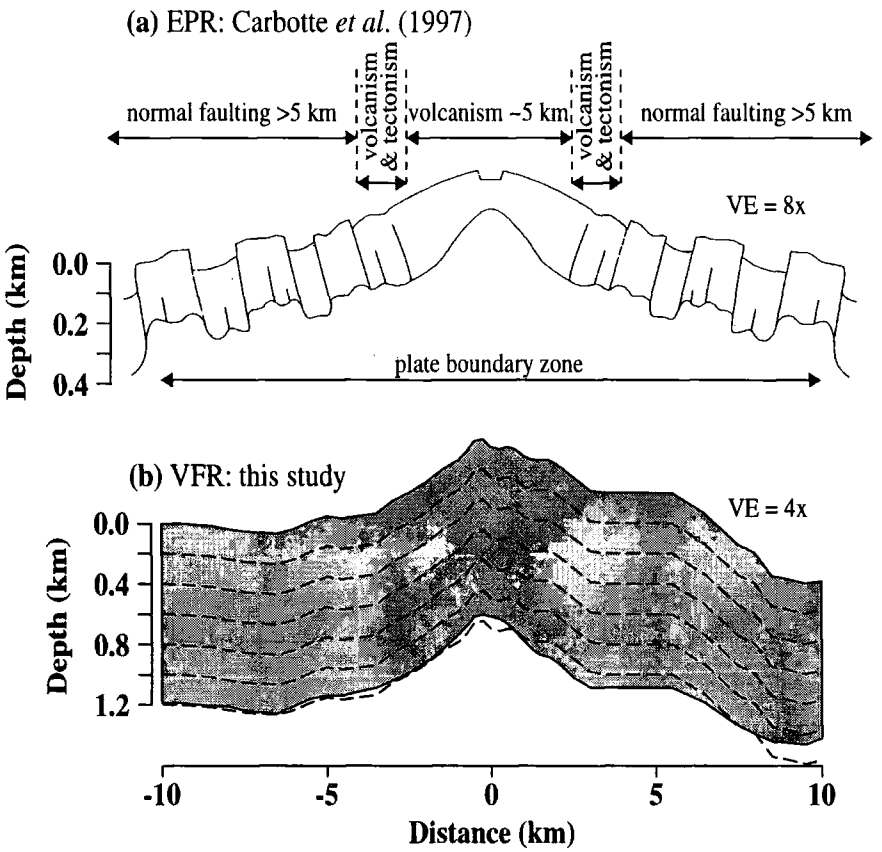

Figure 6.4: Comparison between the emplacement of layer 2A at the EPR and VFR.
(a) The structure of the plate boundary zone at the EPR (after Carbotte *et al.*, 1997). The extrusive layer accumulates within a region ~5 km wide about the ASC. Normal faults begin to develop at the edges of this zone but may be covered by minor periodic lava flows. Vertical exaggeration x8.
(b) Modelled thickness of layer 2A (shaded region) on the CVFR across-axis profile, Line 1 (see figure 6.1 for line location). The seabed topography is shifted down at 200 m intervals (long dashed lines) and the thickness of extrusive layer is shown to be relatively constant (~1.2 km) over a 20 km wide zone, centred on the ridge crest. A slight thickening of layer 2A between 1 and 6 km model offset is attributed to the northern extension of the SVFR (see figure 6.1 for SVFR location). Note the much thicker extrusive layer at the VFR. Vertical exaggeration x4.

6.2.2 Layer 2B/C

Oceanic layers 2B and 2C, as described in section 1.3, are combined into a single layer of constant vertical velocity gradient for all profiles in this study, with the exception of the CVFR along-axis profile (Line 4). The CVFR along-axis profile is modelled in greater detail to account for the observed amplitude variations with increasing offset. A change in gradient located ~0.75-1 km below the base of layer 2A possibly delineates the layer 2B/2C boundary, although the amplitude variations may simply be caused by a more gradual decreasing of the vertical velocity gradient. The difference between these two models cannot be resolved with the EW9512 dataset.

The modelled thickness of layer 2B/C (1.85 ± 0.15 km) at the VFR is thicker than observed at other mid-ocean ridges (<1.5 km), which is probably a function of its back-arc location. However, the thickness of this layer remains relatively constant off-axis at all mid-ocean ridges and this is also the case at the VFR (±0.1 km) with significant variations in thickness only observed within the transition zones on Line 1 (discussed in detail in section 6.4).

A density of 2.62 g cm^{-3} is modelled in layer 2B/C for all profiles at the VFR, although a slightly lower density of 2.60 g cm^{-3} is modelled beneath the island arc crust on Line 1 (>30 km model offset), consistent with the lower velocities observed in this region. Evidence from velocity and density modelling suggests that layer 2B/C is composed of sheeted dykes of basaltic andesite to andesite composition.

The velocity of the lower boundary of layer 2B/C increases from ~5.5 km s^{-1} beneath the ridge crest to greater than 6.0 km s^{-1} within 2-3 km off-axis. This pattern is also observed in the coincident EW9512 CSEM data centred on the intersection of Line 1 and Line 4, where the overall bulk resistivity of the top 2-3 km increases with distance from the ridge. There is no significant off-axis resistivity increase in the uppermost 1 km of the crust (layer 2A) and therefore the increase in bulk resistivity is attributed to variations in layer 2B/C (L.M. MacGregor, pers. comm.). The lower velocity, more conductive material implies that the sheeted dykes are still relatively hot within the axial region and may have hot brines circulating through them.

6.3 Lower crustal structure

The lower crust consists of 'oceanic' layer 3 and is distinguished from the upper crust (seismic layer 2) by a higher P-wave velocity and a shallower vertical velocity

gradient (<0.5 s^{-1}). The velocity structure of layer 3 within the axial region will be discussed in detail in section 6.5. The seismic Moho, identified on seismic reflection and refraction record sections at other mid-ocean ridges, separates the lower crust and upper mantle (characterised by velocities greater than 7.5-8.0 km s^{-1}).

6.3.1 Layer 3 (off-axis)

The majority of layer 3 consists of isotropic and layered igneous material (Bratt and Purdy, 1984) formed from the cooling of the magma chamber at its sides and base. The modelled thickness of 4-5 km for layer 3 in post-rift crust at the VFR is within the bounds described in the Raitt-Hill layering of the oceanic crust (4.86 ± 1.42 km - Fowler, 1990). There is minimal off-axis thickening of this layer, which implies that layer 3 is completely emplaced within the axial region.

Layer 3 is split by a decrease in vertical velocity gradient 1.0 ± 0.25 km below the base of layer 2. It is postulated that this second-order boundary marks the transition from material formed within the upper levels of an axial magma chamber to material accreted, at lower levels, to the sides and base of the axial magma chamber. Thus the boundary may delineate a petrological transition, which corresponds to a decrease in the degree of fractionation or a structural transition from isotropic to layered material. Primary field evidence for this transition comes from ophiolite studies (e.g. Smewing, 1981; Vine and Smith, 1990), which identify a transition from 'plagiogranites' and isotropic gabbros to the layered gabbro series (Gass, 1990).

6.3.2 Crustal thickness

Crustal thickness is determined in this study by the observed depth to the Moho. As previously mentioned, Moho reflections have often been observed on seismic reflection data at mid-ocean ridges (e.g. Herron *et al.*, 1980; Detrick *et al.*, 1987), but no similar reflections have been observed at the VFR, except for a weak discontinuous reflector observed in the CD34/88 normal incidence data (Collier, 1990). The depth to the Moho was thus determined from P_mP arrivals observed on the wide-angle seismic record sections (e.g. figure 3.1: inset I).

Crustal thicknesses at the VFR are generally 1-1.5 km greater than observed at other mid-ocean ridges (cf. EPR/MAR 7.1 ± 0.8 km - White *et al.*, 1992). This increased thickness is attributed to the location of the VFR within a back-arc basin, the influence and proximity of the Tofua Arc and the more intermediate composition of the primary

magma (cf. isotope studies of Jenner *et al.*, 1987 and Hilton *et al.*, 1993). The thickness of layer 3 at the VFR is similar to that observed elsewhere on the global mid-ocean ridge system and the increased crustal thickness modelled at the VFR is thus accommodated within the upper crust (layer 2). The increased thickness of layer 2 is observed in both the pre-rift and post-rift crust, strengthening the hypothesis that the main cause of the increased crustal thickness is the more intermediate primary magma composition.

A wide-angle reflection generated from the Moho is observed on the majority of the across-axis record sections and on one of the axis-parallel profiles (Line 5). As a consequence of the vertical resolution at Moho depths, the wide-angle seismic data cannot distinguish between a sharp velocity interface and a gradient zone over a distance of ~200-250 m (a quarter of the seismic wavelength at this depth). The lack of a similar reflection in the normal incidence seismic data may point to a Moho characterised by a steep gradient zone with reflections only observed at longer offsets (cf. layer 2A retrograde reflection-like arrival - Vera and Diebold, 1994). However, the exact nature of this transition could not be resolved and the boundary was modelled as a first-order velocity step of 0.75-0.85 km s^{-1}.

The most interesting feature concerning the Moho reflection is that it is observed beneath the ridge crest (e.g. SDOBS5 - figures 4.7: model offset of -10 km). A Moho reflection has been observed beneath the majority of the ridge-axis region at the EPR, although this reflection event is observed to be truncated within a 4-6 km zone immediately beneath the ridge crest (Detrick *et al.*, 1987). It is currently impossible, due to the resolution and quality of the EPR datasets to determine whether this apparent truncation is caused by a termination of the reflector, a consequence of highly attenuating crust on-axis or the scattering of seismic energy by the rough axial topography. The observation of a large amplitude P_mP arrival beneath the ridge crest at the VFR clearly demonstrates that a seismic Moho is formed here at ~0 Ma.

Along-axis crustal thickness variations are interpreted from the MBA map and the intersection points of the CVFR along-axis profile with the two across-axis profiles. The depth to the modelled Moho increases by ~1 km from the southern tip of the CVFR (Line 1) to the OSC at 22° 12′ S (Line 6). The MBA map shows a general decrease in anomaly in the same direction (figure 5.20), which also implies that thicker crust and possibly lower mantle densities exist beneath the OSC. This increased crustal thickness (and possible reduced mantle densities) suggests that the OSC at 22° 12′ S is presently or has been recently the focus of melt upwelling and enhanced magmatism. Additional

evidence for this hypothesis comes from modelling the P_mP and P_n arrivals in the wide-angle seismic data and the identification of a slightly lower upper mantle P-wave velocity on Line 6 (see figure 6.2). The general decrease in MBA from the southern tip of the CVFR to the OSC at 22° 12′ S may also be a function of the thinner crust observed within the axial region of Line 1 and on gravity profiles modelled by Calvert (1996) over the SVFR and propagating rift tip.

6.4 Transition zones

The transition zones, identified on the southern across-axis profile - Line 1 (see figure 6.1 for line location), correspond to a region separating pre-rift and post-rift crust (see figure 4.4). Post-rift VFR-generated crust has been modelled with a thicker layer 2A in relation to layer 2B/C than pre-rift back-arc crust, which suggests a different source (either in time or composition). The transition between pre-rift and post-rift crust is marked by a considerable thinning of layer 2 (~1 km), yet there is no crustal thinning observed at Moho depths (figure 6.2: -14 to -21 km model offset). The thinning of layer 2, required to faithfully reproduce the wide-angle seismic data, is the first observation of such a feature in a young, mid-ocean ridge environment, but it can be related to crustal thinning observed at continental margins. The absence of significant thinning at Moho depths could be due to thermal relaxation of this boundary through time and/or emplacement of material in the lower crust. The relative location of the transition zones on Line 1 implies that seafloor spreading in this part of the Lau Basin is symmetrical.

Reactivation of spreading at the VFR is interpreted to be a gradual process of back-arc rifting and thinning before true seafloor spreading is initiated (figure 6.5). Parson and Wright (1996) suggest that the Southern Lau Basin (VFR) is currently in the process of initial oceanic spreading (stage 4) after a period of late rifting (stage 3). Gravity models across the advancing tip of the SVFR show significant thinning of the crust and Calvert (1996) suggested that the SVFR is 'bulldozing' its way south and rifting the old back-arc crust. The thinning of layer 2 is interpreted to be the result of this rifting of old back-arc crust prior to seafloor spreading. During the early stages of seafloor spreading, layer 2 will be accreted onto cold pre-rift material, which may also result in an anomalously thin upper crust (figure 6.5b).

(a) Pre-rift

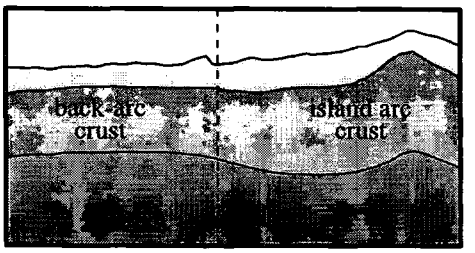

(b) Rifting and thinning of pre-rift crust (cf. Parson and Wright, 1996)

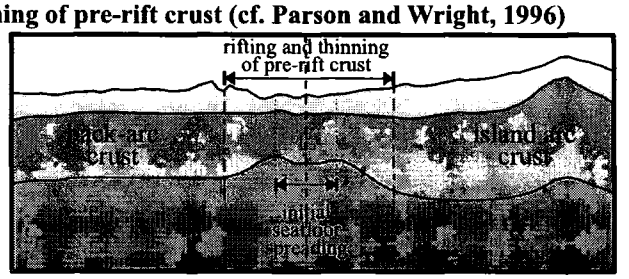

(c) Organised seafloor spreading

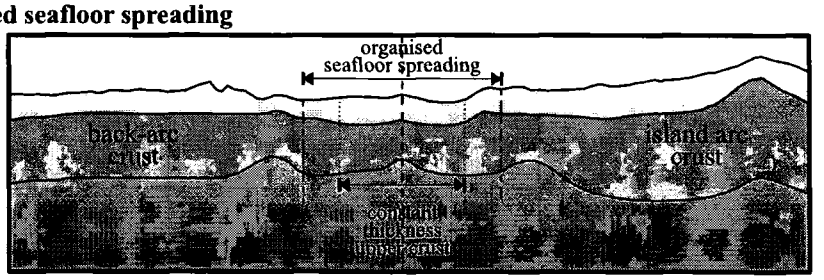

(d) Present day

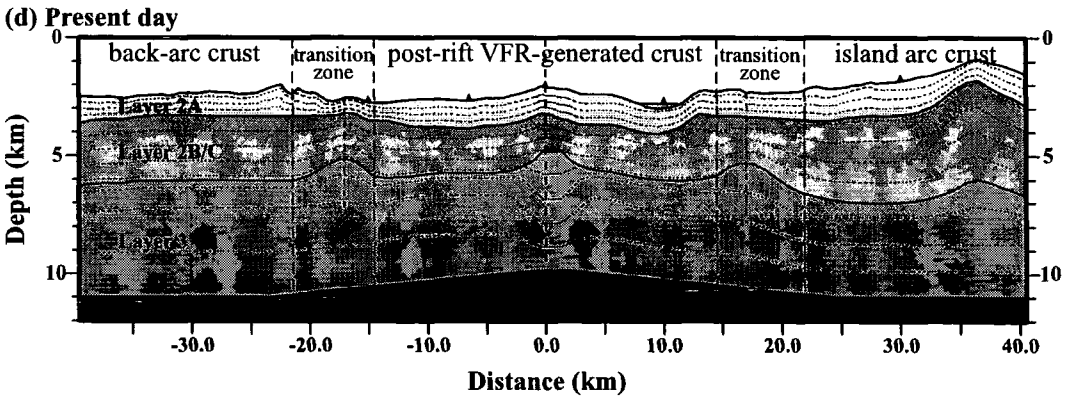

Figure 6.5: Tectono-magmatic evolution of the VFR at 22° 26′ S (Line 1: *Seismic South*). Models are divided into 5 layers: the water column, layer 2A, layer 2B/C, layer 3 and the upper mantle [only shown in part (d)]. Vertical exaggeration x2.

(a) Pre-rift back-arc and island arc crust (>725 ka - based on a spreading rate of 60 mm yr^{-1}).

(b) 'Focused' rifting of the back-arc crust due to the southward propagation of the VFR significantly thins the upper crust (layer 2A and layer 2B/C). Initial seafloor spreading accretes material onto cold pre-rift crust also resulting in a thinner layer 2.

(c) Organised seafloor spreading (<475 ka). Note the constant thickness of the VFR-generated upper crust within the central region (delineated by vertical dotted lines).

(d) Present day velocity-depth model for Line 1. The transitions from pre-rift crust to post-rift VFR-generated crust are denoted by long dashed lines. Short dashed lines within these transition zones mark the minimum depths to the layer 2/3 boundary and the possible onset of seafloor spreading. DOBS locations are marked by triangles and sub-horizontal dotted lines represent isovelocity contours (see figure 6.2).

Crustal thinning is not as dramatic on the northern across-axis profile - Line 6 (see figure 6.1 for line location), perhaps an indication of a different stress regime in the early stages of rifting and/or overprinting by the two large seamounts south of Line 6 (~22° 10′ S). Additional evidence for the former comes from morphological studies based on the geometry of active and abandoned ridge tips at the OSC on Line 6 by Wiedicke and Collier (1993), which suggest that the OSC has been in its present position for a considerable time (>220 ka). However, the ratio between the thickness of layer 2A and layer 2B/C is smaller (i.e. a thinner layer 2A) west of -25 km model offset (see figure 4.12) which may mark the transition from VFR-generated crust to pre-rift back-arc crust (cf. figure 4.4). A similar feature cannot be identified east of the ridge due to the overprint of the nearby island arc (e.g. Ata Island to the east). Significant thinning of the upper crust is also modelled on the most easterly axis-parallel profile - Line 11 (see figure 6.1 for line location), between 2 and 16 km model offset, thus providing a possible link between the two across-axis profiles (see figure 6.6).

Wiedicke and Collier (1993) observed a 'pseudofault' on swath bathymetry data from the Lau Basin spatially related to the VFR and forming the eastern escarpment of the Central Ridge (see figure 1.4). This 'pseudofault' may mark the western limit of oceanic crust generated at the VFR and is mapped southwards, converging on the propagating tip of SVFR (figure 6.6). The transition zones modelled in this study coincide with the northern extension of the 'pseudofault' (figure 6.6) and it is postulated that the 'pseudofault' is the seafloor expression of the thinning of the upper crust during rifting and early seafloor spreading (figure 6.5b).

As previously mentioned, significant thinning of the upper crust is also modelled to the east of the VFR on Line 1 (figure 4.4). There is no evidence of a 'pseudofault' in the bathymetry data, probably due to overprinting by seamounts and the proximity of the island arc (Wiedicke and Collier, 1993). However, Calvert (1996) modelled an anomalously thin upper crust on several gravity lines immediately to the south of Line 1 and thus identified the possible location of the eastern 'pseudofault'. The transition zone modelled on Line 1 in this study coincides with the proposed location of the 'pseudofault' and thus marks the eastern limit of crust generated at the VFR (figure 6.6).

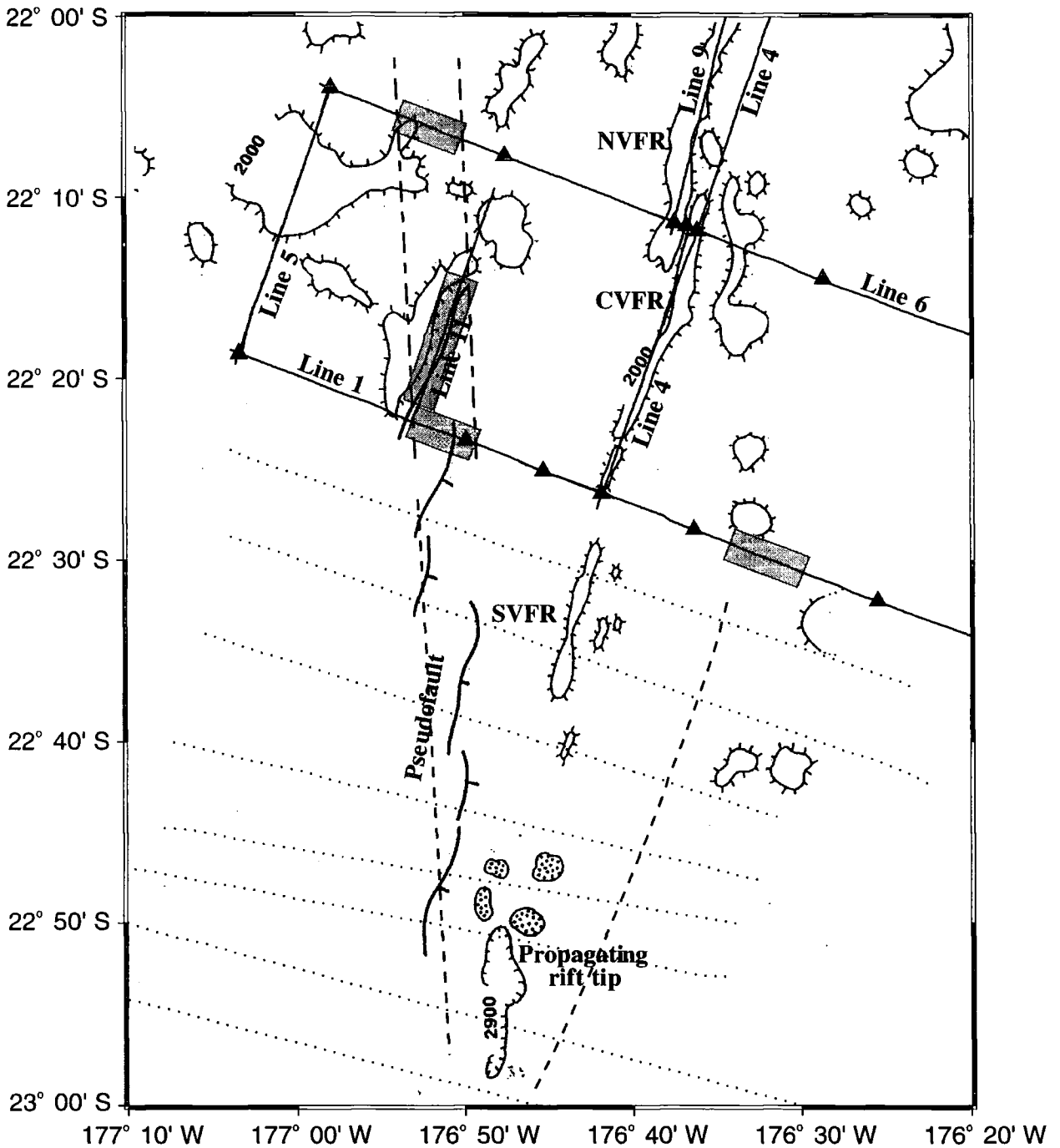

Figure 6.6: Structural map of the Southern Lau Basin overlain by the EW9512 wide-angle seismic lines (after Wiedicke and Collier, 1993; Sinha, 1995). DOBS locations are marked by triangles. The Valu Fa Ridge, major off-axis seamounts and other areas of shallower water are delineated by the 2000 m bathymetric contour. The NVFR, CVFR and SVFR are annotated and at its southern end the SVFR deepens and runs into a group of four closely spaced seamounts (stippled regions: 22° 48′ S). South of this again the propagating rift tip is marked by a bathymetric low, shown here by the closed 2900 m contour. West of the axis, the limit of crust formed by seafloor spreading can be identified by a series of bathymetric lineaments, identified by Wiedicke and Collier (1993) as a 'pseudofault' and shown here as a set of lines with ticks on the downslope sides. To the east of the axis, the location of the 'pseudofault' is unclear. A series of sub-parallel dotted lines south of 22° 24′ S mark the location of several gravity profiles collected during EW9512. Modelling of these profiles by Calvert (1996) identified considerable thinning of the crust and the proposed 'pseudofault' locations are shown by short dashed lines that converge on the propagating rift tip. Shaded boxes show the locations of the transition zones modelled on the wide-angle seismic lines in this study. Note the good correlation with the inferred location of the 'pseudofault' both east and west of the axis.

6.5 Magma chamber geometry

Geophysical constraints on the dimensions and properties of ridge crest magma chambers at fast, slow and intermediate spreading ridges are summarised in section 1.4. Figure 1.7 shows a selection of the previous across-axis magma chamber models based on geological and thermal constraints and integrated models which incorporate geophysical constraints into the aforementioned geological and thermal models. A magma chamber model for the VFR is presented here and compared and contrasted with existing models.

6.5.1 Axial low velocity block

An axial low velocity block (~3.0 km s^{-1}) is identified on both across-axis and along-axis profiles at a depth of 2.9 ± 0.3 km below the seafloor (see figure 6.3b). The low velocity block is modelled with a nominal thickness of 100 m, as there is no significant time delay on wide-angle seismic phases travelling through this region. The low velocity block is interpreted to be a melt lens at the roof of an axial magma chamber and agrees well with previous studies at the VFR (Morton and Sleep, 1985; Collier and Sinha, 1990 and 1992b). This is the first time that the existence of a low velocity block has been determined unequivocally by coincident wide-angle and normal incidence seismic data. All first arrivals observed in the wide-angle seismic data can be faithfully reproduced using a velocity-depth model with no discrete low velocity block. However, conclusive evidence for the existence of the low velocity block comes from the reflections generated from the upper boundary (coincident with the base of layer 2), which are observed in both the wide-angle (e.g. figure 4.17: P_cP arrivals) and normal incidence seismic data (e.g. figure 5.2: MCR). The reduction of transmitted energy at this interface also explains the lack of any identifiable arrivals below layer 2 on the along-axis profile.

The reflection (P_cP) event in the wide-angle seismic data is observed as a large amplitude, reversed polarity arrival on SDOBS4, located at the southern tip of the CVFR. However, this arrival is not only identified on the along-axis profile (figure 4.17), but for the first time it has also been observed on the across-axis profile (figure 4.5). Similar arrivals are also observed on DOBSs on the *Seismic North* across-axis profile, including NDOBS3 situated in the overlap basin (figure 4.13). Initial constraints on the lateral extent of the low velocity block were determined from modelling of this

reflection event in the wide-angle seismic data, prior to modelling in greater detail using the normal incidence seismic data.

The normal incidence seismic reflection is clearly of reversed polarity (see figure 5.3) and the across-axis extents of the low velocity block were determined by forward modelling of the reflection and associated diffraction tails. The width of the low velocity block was constrained to be 1.25 km, offset to the east of the ridge crest at the southern tip of the CVFR (Line 1) and 2 km, centred on the overlap basin at the OSC with the NVFR (Line 6). Similar reflection events have been previously observed on stacked MCS profiles at other mid-ocean ridges, which are summarised in Chapter 1. Modelled widths are generally <2 km, although earlier studies estimated widths up to 6-8 km (e.g. Herron *et al.*, 1980; Detrick *et al.*, 1987). Kent *et al.* (1990) argue that undermigration of diffraction energy from the edges of a smaller body could produce overestimates of the width in early studies and subsequent reprocessing of the Detrick *et al.* (1987) EPR dataset generated a lateral extent of the low velocity block of 0.8-1.2 km, compared with the previous estimates of 4-6 km. A comparison of recent constraints on the width of the low velocity block at the EPR by Kent *et al.* (1994) suggests that this parameter is invariant of spreading rate. This theory is further substantiated by observations at the JDFR and here at the VFR.

Although the lateral extent of the low velocity block can be determined to a satisfactory degree, there is less constraint on the vertical extent and nature of its boundaries. The low velocity block is modelled with this dataset as a 100 m thick discrete body. Preliminary analysis of the reflection amplitude suggests that the top boundary consists of a planar interface, with a velocity of 3.0 km s^{-1} (cf. Murase and McBirney, 1973) at the top of the low velocity block (i.e. a velocity step of ~2.5 km s^{-1}). Collier (1990) calculated the reflection coefficients of the seafloor and MCR at the VFR using the CD34/88 dataset and suggested that velocities of 2.7 and 3.8 km s^{-1}, for planar and layered interfaces respectively, were required to generate the observed reflection event. Subsequent remodelling of this MCR, using realistic estimates of attenuation in the upper crust, predicted a lower reflection amplitude than the observed data. Day (1997) suggested that the addition of water to the melt could cause a significant decrease in density, thus increasing the absolute value of the reflection coefficient. Vera *et al.* (1990) observed a high velocity lid above their magma chamber, but there is no evidence of such a feature at the VFR.

Amplitude versus offset (AVO) analysis was performed on the P_cP arrivals observed on SDOBS4 (figure 3.11) in an attempt to determine the properties of the low velocity block. Before AVO analysis could be performed a reasonable estimate of the attenuation (Q) factors of the upper crust had to be determined. Direct water waves and crustal diving rays (P_g) were forward modelled using the reflectivity method of Fuchs and Müller (1971) and values of Q were adjusted until a satisfactory amplitude fit was achieved. The final model (described in table 4.1) consists of Q values ranging from 22.5 at the top of layer 2A to 175 at the base of layer 2, however this final model consistently predicted lower reflection amplitudes than in the observed data, similar to the findings of Day (1997). To generate the large amplitude P_cP arrivals, there must be some form of amplitude enhancement at the VFR, perhaps due to seismic tuning within the upper crust and/or the low velocity block (cf. Collier, 1990). This enhancement of relative amplitudes is unfortunately unresolvable with this dataset.

Constraints on the exact nature of the lower boundary are more elusive. No reflection event from the base of the low velocity block is required to model the observed arrivals in both the wide-angle and normal incidence seismic data (e.g. figure 5.6: matching of the secondary peak at ~4.4 s). However, the relative strength of the observed reflection from the upper boundary, associated high reflection coefficient and more importantly low transmission coefficient creates problems when determining the nature of the lower boundary. A reflection from the base of the low velocity block would need to transmit through the upper boundary twice during its ray-path, resulting in a low amplitude signal swamped by the preceding upper boundary reflection. An alternative explanation for the absence of a basal reflection is that the lower boundary is characterised by a gradational boundary. The difference between the two models cannot be resolved with this dataset. The only constraint on a gradational boundary is that 'normal' P-wave velocities, in this case the velocity observed directly above the low velocity block (~5.5 km s^{-1}), must be achieved ~250 m below the upper boundary to prevent a significant time delay being observed on wide-angle rays travelling just beneath the low velocity block. The results of detailed modelling of the MCR signature in the CD34/88 dataset also suggests there is no direct evidence for a basal reflection (Day, 1997).

The search for a possible basal reflection is not restricted to the VFR and the Detrick *et al.* (1987) EPR dataset has been reprocessed several times to try to determine the nature of the lower boundary. Kent *et al.* (1990) used a reflectivity approach to

investigate the interference effects of reflections off the top and bottom of the melt body. They concluded that the lack of a distinct basal reflection could be explained by either a low velocity block of thickness ~10-50 m or a zone with a transitional lower boundary (i.e. melt to crystal mush). A recent interpretation using waveform inversion modelled a distinct upper boundary above a 30 m thick zone with less than 30% crystals (P and S-wave velocities of 2.6 km s^{-1} and 0 km s^{-1} respectively), which is underlain by a gradient zone (~18 s^{-1}) over a vertical distance of 50 m (Collier and Singh, 1997). The low velocity block at the VFR, although nominally assigned a discrete lower boundary due to the vertical resolution of the seismic data, is interpreted to have a gradational lower interface with high velocity gradient, corresponding to decreasing melt fraction.

A reflection from the top of the low velocity block can be identified along the entire length of the CVFR on the along-axis profile (Line 4) and in the axial region of the two across-axis profiles. Collier and Sinha (1992b) also observe a MCR on every one of the CD34/88 across-axis reflection profiles, including those crossing the OSC, suggesting a relatively continuous body. The northern extension of the melt lens beneath the CVFR is poorly constrained, although the dramatic loss of amplitude of lower crustal arrivals observed on NDOBS2 (see figure 4.22) implies that the melt lens must extend at least as far as the first of two seamounts located at 22° 08′ S (see figure 6.1).

The depth to the top of the low velocity block (2.9 ± 0.3 km) is significantly greater than observed at the EPR (1.5 ± 0.7 km). Several studies have tried to explain the different depths to the tops of these melt bodies. Purdy *et al.* (1992) described a strong spreading rate dependence on the depths to the top of the low velocity block, although recent results from the slow spreading MAR (e.g. Navin *et al.*, 1998) tend to refute this theory. Sinton and Detrick (1992) suggest that where the average crustal density is low (VFR-erupted lavas are mainly low-density, highly vesicular andesites) ascending magma encounters a horizon of neutral buoyancy at a greater depth (i.e. the low velocity block). However, the depth to the axial magma chamber is generally believed to reflect axial thermal structure, the lens forming at the shallowest depth where the magma does not freeze (Phipps Morgan and Chen, 1993). In conclusion the increased depth to the low velocity block observed in this study is probably a function of the intermediate spreading rate (cf. JDFR - Morton *et al.*, 1987; Rohr *et al.*, 1988), the more intermediate composition and viscous nature of the magma and/or the location of the VFR in a back-arc environment and its associated 'anomalous' thermal structure.

6.5.2 Low velocity zone

Previous studies at the VFR have observed a MCR, but due to the significant loss of transmitted energy at this interface the nature of the lower crust below this reflector (i.e. a low LVZ) could not be determined. One of the main objectives of collecting the wide-angle seismic dataset was to constrain the velocity structure beneath the low velocity block. Forward modelling of the data suggests the existence of a LVZ beneath the low velocity block, interpreted to be an axial magma chamber containing a very low melt fraction (~1%), beneath both the CVFR (on Line 1) and its overlap with the NVFR (on Line 6). The inclusion of these LVZs in the velocity-depth models faithfully reproduced the low amplitudes and 'late' travel times of rays passing through these regions (e.g. figure 4.6: 2 to 7 km model offset). There is no direct evidence in the VFR dataset for the along-axis continuity of the underlying LVZ, but the observation of a continuous low velocity block confidently suggests the existence of a continuous LVZ. The lack of observed phases travelling beneath the low velocity block on the along-axis profile prevents any determination of along-axis variation in the physical properties of the LVZ.

The LVZ (delimited by the -0.2 km s^{-1} velocity anomaly contour on the across-axis profiles) has a width of ~4 km and extends down through layer 3 to within 2-3 km of the Moho (figures 4.8 and 4.16). The velocity anomaly is more extensive across the southern tip of the CVFR (Line 1).

The velocity anomaly and dimensions of the LVZ are generally smaller than those observed at the EPR. Vera *et al.* (1990) identified a wide 'pear-shaped' LVZ, which extends down to the Moho and increases in width from 3 km below the low velocity block to a maximum of 10-12 km. Subsequent tomographic modelling (Toomey *et al.*, 1990 and 1994) suggests a narrower (~5 km wide), circular LVZ, more consistent with the observations in this study. The identification of Moho reflections close to the ridge axis (e.g. Detrick *et al.*, 1987) also shows evidence of a LVZ that does not widen considerably with depth, although the horizontal resolution at this depth is a controlling factor.

Recent studies on the slow spreading MAR, specifically the Reykjanes Ridge at 57° 45′ N, have also observed a LVZ in layer 3 beneath the ridge axis (Navin *et al.*, 1998). However, the shape of this LVZ differs from that modelled at the EPR and in this study. Navin *et al.* (1998) identified a wide (8-20 km) 'cone-shaped' LVZ, which narrows with depth in layer 3 before truncating ~1 km above the Moho. It is postulated

that the increased width of this LVZ beneath the layer 2/3 boundary is a consequence of a thicker upper crust in the axial region and the 'residual' LVZ (~6-10 km wide) closely resembles the sub-circular LVZs imaged at the EPR and in this study at the VFR.

The geometry of the LVZs, determined from detailed geophysical studies are shown to be similar at fast, slow and intermediate spreading ridges, which implies that crustal accretionary processes at all spreading rates must be closely related (figure 6.7). The small magma chambers (LVZs) imaged in these studies differ greatly from the large magma chambers suggested from ophiolite investigations and thermal modelling (figure 1.7). However, Wilson *et al.* (1988) resolved the discrepancy between the observations of narrow (~4 km) magma chambers at mid-ocean ridges and predictions based on thermal models of wide (~20 km) magma chambers with additional cooling of the lower crust by convection in the magma chamber. This convection cooling and subsequent crystal segregation may also explain the discrepancy between the thick layered sequences identified in ophiolite studies, suggested to have resulted from crystal settling in a large magma chamber, and the small magma chambers observed in seismic studies.

6.5.3 Magma chamber structure of the OSC at 22° 12′ S

Collier and Sinha (1992b) suggested that the complex MCR event observed beneath the OSC originates from small reflectors beneath both the CVFR and NVFR with an additional reflector beneath the overlap. Subsequent remodelling of the dataset suggested that there is no clear-cut evidence for the presence of melt beneath the overlap basin, but its presence could not be ruled out (Day, 1997). The low velocity block was modelled with the EW9512 dataset as a single body with a lateral extent of 2 km, centred on the overlap basin and extending beneath both ridges, but can be modelled to a satisfactory degree by two bodies of 0.5 km width, located beneath the inner flanks of both ridges. The discrepancy between the two models cannot be constrained with the available data, although the existence of a P_cP reflection on the wide-angle seismic data of NDOBS3, situated in the overlap basin favours the single body model.

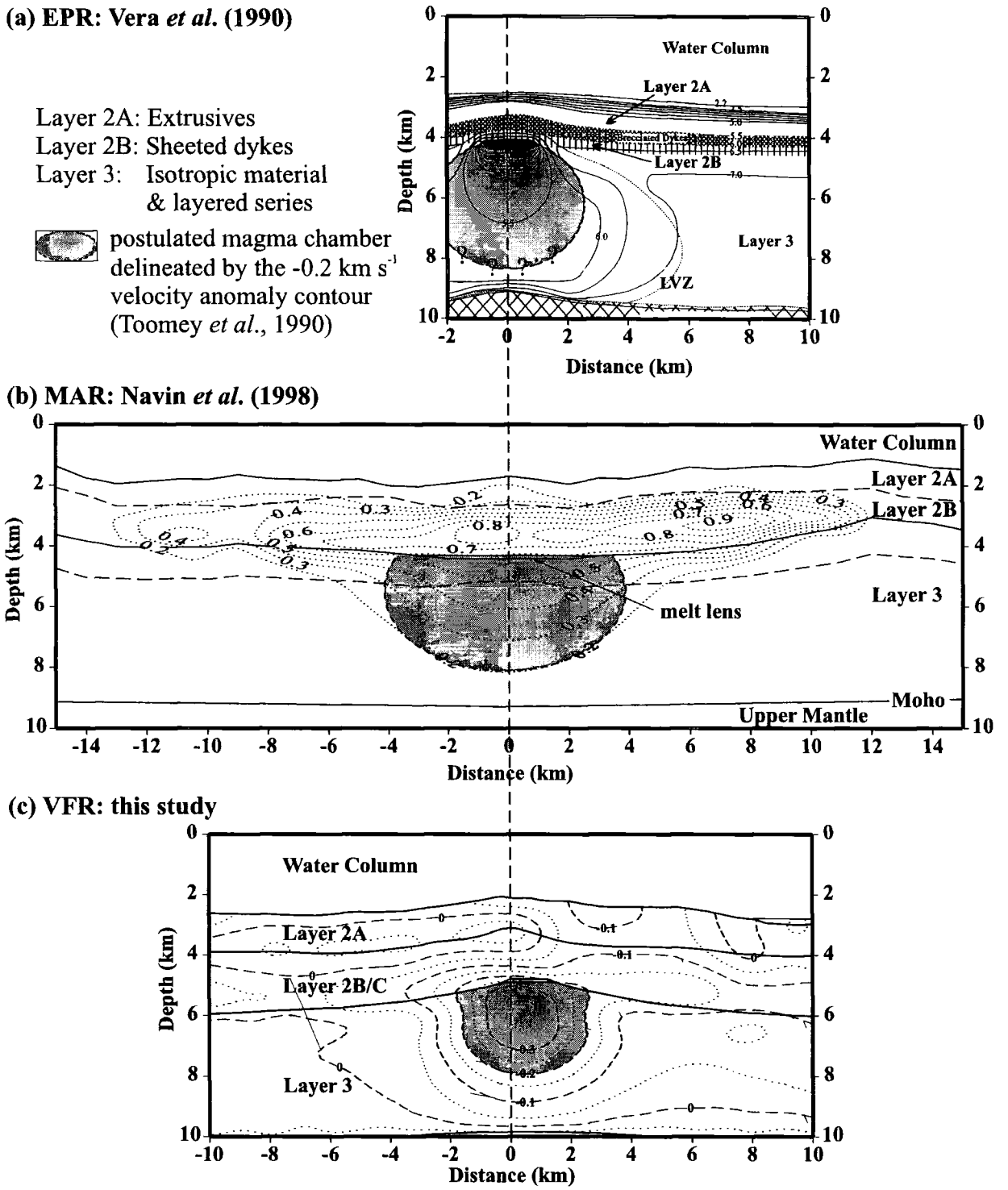

Figure 6.7: A comparison of low velocity zones observed at fast, slow and intermediate spreading ridges. The spreading axes are located at 0 km model offset and sub-crustal magma chambers are delineated by the -0.2 km s^{-1} velocity anomaly contour (i.e. isovelocity contours relative to an 'average' off-axis velocity-depth profile - see Chapter 4 for details). No vertical exaggeration.

(a) EPR crustal structure at 9° 30′ N (after Vera *et al.*, 1990). Isovelocity contours are labelled in km s^{-1}. A 10 km wide sub-circular magma chamber (shaded region) is identified and extends down to the Moho.

(b) Reykjanes Ridge crustal structure at 57° 45′ N (after Navin *et al.*, 1998). Velocity anomaly contours are labelled in km s^{-1}. Note the v-shaped tapering of the -0.2 km s^{-1} contour with depth, possibly due to a thicker layer 2 on-axis. A 8 km wide 'residual' magma chamber is postulated here (see text for details), which extends down to within 1 km of the Moho.

(c) VFR crustal structure at 22° 26′ S (this study). Velocity anomaly contours are labelled in km s^{-1}. A 4 km wide magma chamber is identified and extends down to within 2 km of the Moho. Note the smaller dimensions of the LVZ imaged at the VFR compared to the EPR and MAR.

The axial MCR observed at the EPR is interpreted to deepen towards the OSCs at 9° 03′ N and 11° 45′ N and disappears before reaching the overlapping ridge tips (Detrick *et al.*, 1987). This implication, together with the observation of a gap in the reflector across small offset OSCs, has been previously used to discuss the relative applicability of several OSC models (e.g. Lonsdale, 1983 and 1986; Macdonald *et al.*, 1984 and 1986; Langmuir *et al.*, 1986). However, Kim and Orcutt (1989) suggest that the observed gaps in the reflector are not conclusive evidence for real gaps in the sub-axial magma chamber and deviations in the ship tracks could also be used to explain the apparent dipping of this reflector in the OSCs.

Barth (1994) investigated the relative positions of the MCR and Moho in the vicinity of the OSC at 9° 03′ N on the EPR and determined the plate boundary geometry within this region. It was proposed that the northern propagating ridge has captured a portion of the deep crustal magma conduit connected with the southern ridge, thus establishing a single magma supply to the OSC. There is no direct evidence as to exact lower crustal structure beneath OSCs at other mid-ocean ridges, but the existence of a regular LVZ at the VFR (see figure 4.16) implies a single sub-crustal magma chamber beneath the OSC, independent of whether it feeds one, two or three low velocity blocks.

6.4.4 Integrated magma chamber model

Figure 6.8 shows a cartoon summarising the general magma chamber geometry and geological interpretation. This is by no means a general magma chamber model, but explains the main features identified in this study. However, there are many similarities between the crustal structure modelled here and that observed at other mid-ocean ridges and elements of the model can be extended elsewhere.

The lower crustal magma chamber model is composed of two parts:

1) a melt lens, consisting of an interconnected melt fraction.
2) an underlying region of hot rock or low melt fraction corresponding to the main body of the magma chamber.

The pillow lavas (layer 2A) and sheeted dykes (layer 2B/C) are formed solely from material within the melt lens. A considerable volume of material is required to accrete the entire thickness of layer 2 (~3-3.5 km), but the melt lens has been modelled as a narrow (~1-2 km) body of limited thickness (100 m). The space problem is resolved by replenishment of the melt lens material from the underlying magma chamber in layer 3 (LVZ).

Collier (1990) carried out a detailed study of the magmatic cycles at the VFR and concluded that the cycles may be driven by either the episodic delivery of material into the chamber (passive transport) or episodic mobilisation of material out of the chamber (active transport). The latter suggests that a significant melt fraction resides in the main magma chamber at any one time, however the LVZs modelled here have small velocity anomalies (cf. EPR: Vera *et al.*, 1990; Toomey *et al.*, 1994), which suggests a low melt fraction. It is proposed that melt ascends as small isolated pockets through the main body of the chamber (passive transport) and resides in the melt lens until eruption.

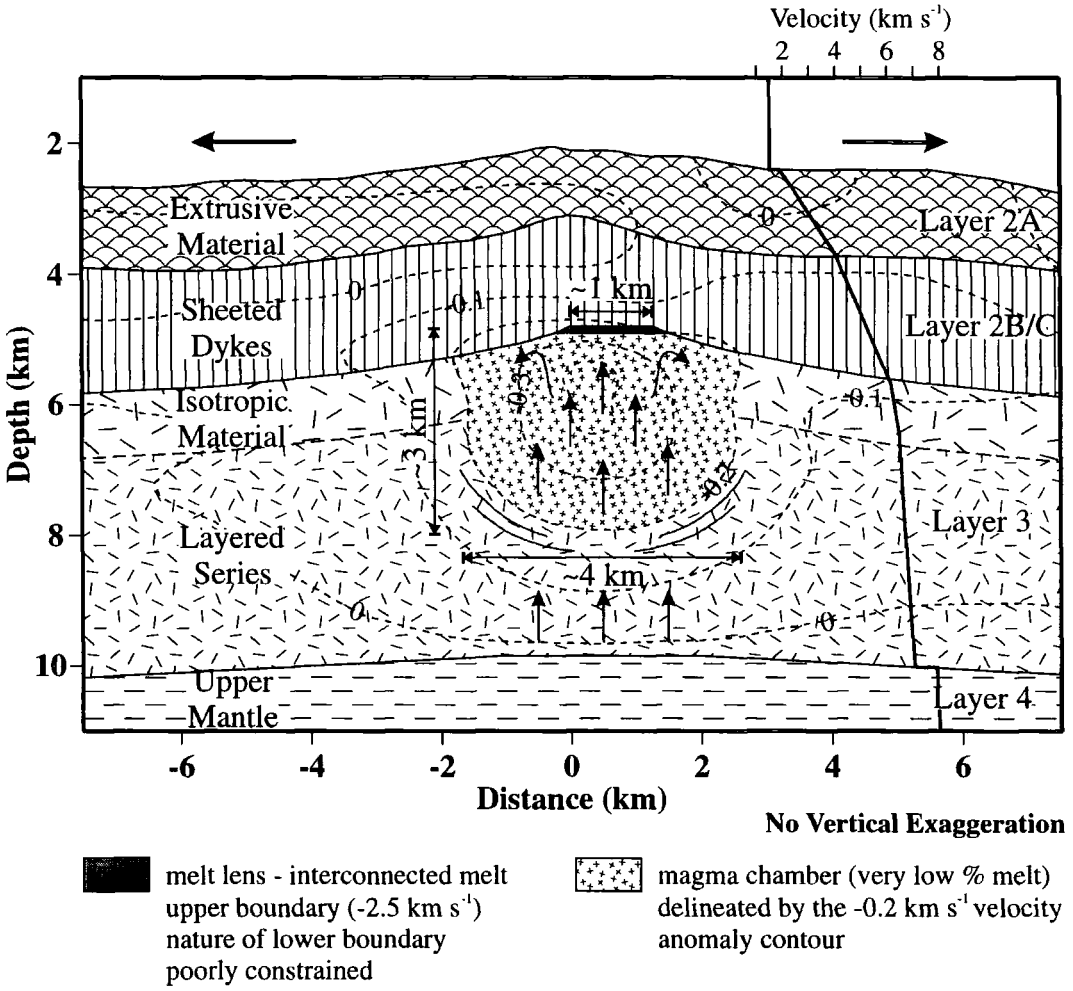

Figure 6.8: Schematic diagram of the VFR lower crustal magma chamber. No vertical exaggeration. Geological interpretations of the main seismic layers are annotated and velocity anomaly contours are shown by dashed lines (i.e. isovelocity contours relative to an 'average' off-axis velocity-depth profile - see Chapter 4 for details). The axial magma chamber is composed of a melt lens located at the layer 2/3 boundary and an underlying sub-circular magma chamber of hot rock (very low melt fraction), delineated by the -0.2 km s^{-1} velocity anomaly contour. A velocity-depth profile located at 5 km model offset shows the gradual decrease in vertical velocity gradient with depth. Melt ascends as isolated pockets within the magma chamber towards the melt lens, which explains the small axial velocity anomaly (<0.5 km s^{-1}). Convection currents originate from large lateral thermal gradients at the sides of the magma chamber, especially at the base of layer 2. Flow lines of melt fraction in the axial region are shown by arrows. The layered series is generated from cooling at the base and sides of the magma chamber and a change in vertical velocity gradient identified in the velocity-depth profile may coincide with the transition from isotropic material to this layered series. Note the relatively small dimensions of the magma chamber (cf. EPR: figure 6.7a) and the offset of the melt lens to the east of the ridge crest (0 km).

The main body of the magma chamber (LVZ) is essentially a region of hot rock that facilitates the ascension of melt into the melt lens. Large thermal gradients at the sides of the magma chamber, especially at the base of layer 2 may induce small-scale convection currents, thus accelerating the cooling process and restricting the size of the magma chamber (cf. Wilson *et al.*, 1988). The layered series (lower part of layer 3) is produced from cooling at the base and sides of this magma chamber. A slight decrease in gradient observed on off-axis velocity-depth profiles ~1 km below the layer 2/3 boundary may mark the transition from isotropic material to the layered series (see section 6.2.1 and figure 6.8).

6.6 Summary

The crustal structure of the VFR and implications for the processes of crustal accretion have been discussed in this chapter. The upper and lower crustal structure have been compared and contrasted with the crustal structure observed at other mid-ocean ridges and the influence of the back-arc location has been determined. The geometry of a lower crustal magma chamber at the VFR has also been defined and compares favourably with previous geophysical models at fast and slow spreading ridges. The transition from pre-rift crust to post-rift VFR-generated material has been identified and a tectono-magmatic evolution for the Southern Lau Basin has been proposed. The conclusions drawn from this study are summarised in Chapter 7.

Chapter 7

Conclusions and further work

7.1 Introduction

In this chapter the crustal structure of the VFR, modelled in this dissertation, is summarised and its contribution to the current understanding of the processes of crustal accretion at mid-ocean ridges is considered. Suggestions for further study both at the VFR and elsewhere on the global ridge system are also introduced.

7.2 Results and conclusions from this study

The aim of this study was to investigate the detailed crustal structure and magma chamber geometry of a magmatically active intermediate spreading ridge, the VFR; the results then being combined with existing data from other mid-ocean ridges to compare the processes of crustal accretion at all spreading rates.

7.2.1 Summary of results

Despite the profound influence of the back-arc environment, evidenced by lower velocities and a much thicker upper crust, there are many features observed at the VFR, which are similar when compared with 'normal' mid-ocean ridge crust, including the distinctive oceanic layering observed in 'mature' oceanic crust.

The low upper crustal velocities (~2.0 km s^{-1}) modelled at the VFR indicate the presence of highly fractured surficial material with an unusually high porosity and permeability. There is no significant thickening of layer 2A outside the axial region, which suggests complete emplacement of the extrusive layer within 1 km of the axis (cf. EPR), although changes in the along-axis thickness of layer 2A point to local variations in melt delivery and crustal accretion.

Velocity and density models suggest that layer 2B/C is composed of sheeted dykes of andesitic composition and the greater thickness of this layer compared with other mid-ocean ridges is again probably a function of the back-arc location. Lower axial velocities (and higher conductivities) indicate that the sheeted dykes are still relatively hot within the axial region and may have hot brines circulating through them.

The modelled thickness of 4-5 km for layer 3 at the VFR is within the bounds described in the Raitt-Hill layering of the oceanic crust. A decrease in vertical velocity gradient ~1 km below the base of layer 2 may represent a petrological transition, which corresponds to a decrease in the degree of fractionation or could identify a structural transition from isotropic to layered material.

The VFR is modelled with a thicker crust than observed at other mid-ocean ridges. This additional thickness is largely accommodated in layer 2 and is probably due to the more intermediate primary magma composition at the VFR. The thickest crust is modelled beneath the OSC, which contrary to popular models of ridge segmentation, implies that the OSC is the site of enhanced magmatism.

Wide-angle Moho reflections from beneath the CVFR clearly demonstrate that this crust-mantle transition is formed at ~0 Ma, as observed at the slow spreading Reykjanes Ridge (Navin *et al.*, 1998). There is no evidence for the formation of a distinct Moho at the EPR, although the observed 'gap' in the Moho reflection could simply be a consequence of the loss of seismic energy whilst travelling through highly attenuating lower crust within the axial region.

The transition from pre-rift crust (both island arc and back-arc crust) to post-rift material has been uniquely identified in this study. A 'pseudofault' had been previously described as the limit of VFR-generated crust by Wiedicke and Collier (1993), but there had been no evidence for a change in the sub-surface crustal structure within these transition zones. The transition zone is modelled here as the site of considerable thinning of layer 2 and can be related to the crustal thinning observed at continental margins. The thinning of layer 2 is thus interpreted to be the result of rifting of old back-arc crust prior to seafloor spreading. During the early stages of seafloor spreading, layer 2 is accreted onto cold pre-rift material, which may also result in an anomalously thin upper crust. The spatial relationship of the proposed transition zones west of the CVFR compares well with the inferred trend of the 'pseudofault' towards the propagating rift tip and the location of the eastern transition zone identified on Line 1 shows that seafloor spreading at the CVFR is approximately symmetrical.

An axial low velocity block (<3.0 km s^{-1}), interpreted to be a melt lens at the top of an axial magma chamber, has been identified along the entire length of the CVFR. Reflections from the top of the melt lens, observed in normal incidence seismic data and, for the first time, in DOBS data (P_cP arrivals) were used to locate the melt lens at a depth of 2.9 ± 0.3 km below the seafloor, significantly greater than observed at mid-

ocean ridges and to constrain its geometry. The width of the melt lens was thus constrained to be 1.25 km (offset to the east of the ridge crest) across the southern tip of the CVFR and 2 km (centred on the overlap basin) over the OSC at 22° 12′ S.

Forward modelling of the variations in amplitude with offset of the along-axis P_cP arrivals consistently predicted lower reflection amplitudes (assuming a lens of pure melt) than in the observed data, suggesting some form of amplitude enhancement within the upper crust. Constraints on the nature of the lower boundary are more elusive and have been modelled here as a first-order boundary for simplicity. The loss of seismic energy whilst travelling through the highly attenuating melt lens and interference caused by the preceding large amplitude upper boundary reflection would make it difficult to identify a basal reflection, should one exist. An alternative explanation is that the melt lens is characterised by a gradational lower boundary. The only constraint on a possible gradational boundary beneath the CVFR is that velocities as high as 5.5 km s^{-1} must be achieved ~250 m below the upper boundary, due to the absence of any significant delay on wide-angle rays travelling beneath the melt lens.

Forward modelling of the wide-angle seismic data points to the existence of a LVZ beneath the melt lens, interpreted to be an axial magma chamber containing a very low melt fraction (<1%), beneath both the CVFR and its overlap with the NVFR. The LVZ has a modelled width of ~4 km and extends down through layer 3 to within 2-3 km of the Moho. There is no primary evidence in this dataset for the along-axis continuity of the LVZ, but the observation of a continuous melt lens implies a relatively continuous LVZ.

The velocity anomaly within the LVZ is generally smaller than observed at the EPR, however the sub-circular geometry of the LVZ can be extended to existing seismic models from fast, slow and intermediate spreading ridges, which implies that crustal accretionary processes at all spreading rates are broadly similar. Additional cooling of the magma chamber by convection not only resolves the difference between narrow (~4 km) 'geophysical' magma chambers and wide (~20 km) 'thermal' magma chambers (Wilson *et al.*, 1988), but may also explain the thick layered sequences observed in ophiolites.

A single magma chamber is modelled beneath the OSC at 22° 12′ S, centred on the overlap basin, which feeds both the CVFR and NVFR. The overlying melt lens is modelled as a single body (~2 km wide) centred on the overlap basin, although the complex MCR event can be modelled to a satisfactory degree with two separate bodies

(0.5 km wide) located beneath the inner flanks of both ridges. The discrepancy between the two models cannot be constrained with either the EW9512 or CD34/88 datasets, although the existence of a P_cP reflection on NDOBS3, situated in the overlap basin favours the single body model.

7.2.2 Implications for understanding the processes of crustal accretion

The composite magma chamber model (see figure 7.1) identifies a melt lens, consisting of an interconnected melt fraction, overlying a region of hot rock or low melt fraction, which corresponds to the main body of the magma chamber. The model attempts to bridge the gap between the large, long-lived magma chambers identified at the EPR and the more transitory magma chambers proposed at slow spreading ridges. The model also provides new insight into the generation of the thick layered series identified in ophiolite studies, once thought to be the result of crystal settling in a large, molten reservoir.

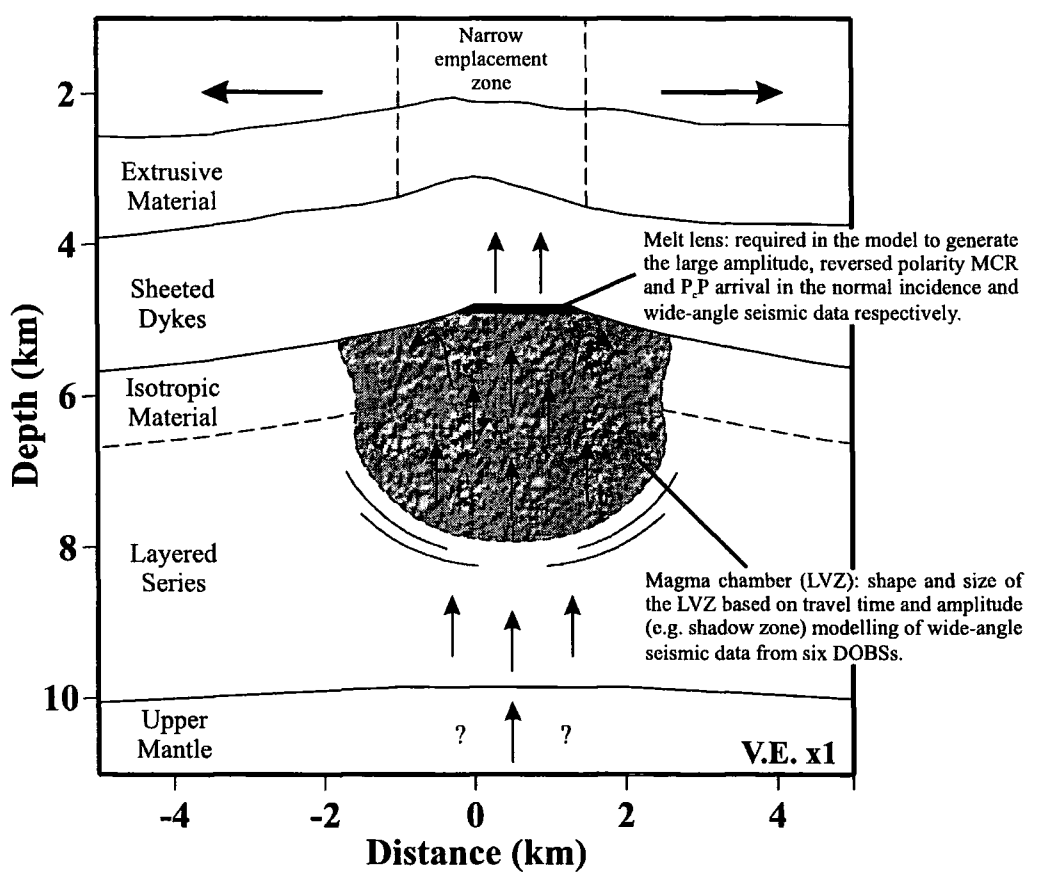

Figure 7.1: Crustal accretion at the VFR. The axial magma chamber is composed of thin, narrow melt lens overlying a sub-circular region of hot rock (stippled). Melt ascends into the main body of the magma chamber as isolated pockets and rises towards the melt lens (flow lines are shown by arrows). Layer 2 is constructed solely from material 'erupted' from the melt lens and the extrusive layer is thus completely emplaced within 1 km of the axis. Convection currents originate from large lateral thermal gradients at the sides of the magma chamber and the layered series is generated from cooling at the base and sides of the chamber. The slight offset of the magma chamber and melt lens east of the ridge crest (0 km) is due to the proximity of the northern tip of the SVFR.

The main body of the magma chamber is essentially a region of hot rock, which cools to form seismic layer 3 and facilitates the ascension of melt into the melt lens. Melt ascends as small isolated pockets through the main body of the magma chamber and resides in the melt lens until eruption (see figure 7.1). Convection currents, induced by large thermal gradients at the sides of the magma chamber, both accelerate the cooling process (cf. thermal models based solely on conduction) and provide the basis for more efficient crystal segregation, necessary to generate the thick layered sequences observed in ophiolites.

Layer 2 is proposed to be constructed solely from material 'erupted' from the melt lens, which is replenished from the underlying magma chamber (see figure 7.1). Complete emplacement of the extrusive layer within 1 km of the axis is identified at slow and intermediate spreading ridges, which also points to a focused intrusion zone. Furthermore, the off-axis thickening of layer 2A identified at fast-spreading ridges is not the result of off-axis intrusion and has been identified as the 'stacking' of less viscous sheet flows that have flowed out of the ASC (i.e. narrow intrusion zone).

The size and temporal stability of magma chambers are largely dependent on their magmatic budget. The low magmatic budget identified at most slow spreading ridges explains the transient nature and hence limited observations of magma chambers. However, the proposed high magmatic budget of fast spreading ridges implies that episodes of magmatic inactivity are short and although the size of the melt lens at the EPR is similar to those observed at intermediate spreading ridges, lower velocities within the main body of the magma chamber suggest a higher melt fraction.

The VFR is proposed to be an example of an intermediate spreading ridge with an anomalously high magmatic budget. The size of the magma chamber may wax and wane with time, but the observation of a continuous melt lens along the entire CVFR implies relative magma chamber stability.

The LVZ is observed to extend down to the Moho at the EPR (cf. figure 7.1), an indication of a higher and more continuous magmatic budget. Wide-angle reflections from the base of the crust, beneath the ridge crest clearly demonstrate that a seismic Moho is formed at ~0 Ma at the VFR. The deeper extent of the LVZ at the EPR may prevent the formation of a distinct Moho within the axial region (cf. EPR MCS data).

It can clearly be seen that the crustal structure modelled at the VFR compares favourably with that observed elsewhere on the global ridge system. Constraints on the

shape and size of magma chambers beneath the intermediate spreading VFR (this study) and the slow spreading Reykjanes Ridge (Navin *et al.*, 1998), in addition to constraints from the EPR, have shown that the processes of crustal accretion are broadly similar at all spreading rates.

7.3 Further study

The VFR has been the subject of a significant number of multidisciplinary cruises and is an important area for the global study of seafloor spreading. The crustal structure and magma chamber geometry modelled at the VFR compare favourably with other mid-ocean ridges and further work should be carried out on the EW9512 data to elucidate some of the conclusions proposed in this study.

The thinning of the upper crust in the transition from pre-rift crust to post-rift material and a comparison with the crustal thinning observed at continental margins raises some interesting points for further study. Detailed surveys south of the EW9512 work area towards the propagating rift tip may shed greater light on the processes involved in the reactivation of seafloor spreading in the Lau Basin.

7.3.1 Additional work on the existing VFR dataset

This dissertation describes the results of 2-D modelling of main across-axis, along-axis and axis-parallel seismic lines. However, the entire EW9512 dataset consists of a 3-D network of profiles with good coverage over both the CVFR and west of the ridge crest, up to 40 km off-axis (see figure 7.2).

A 3-D tomographic study over the CVFR and its overlap with the NVFR is currently being carried out by a A.J. Day at the University of Durham. Modelling of the 2-D seismic profiles, described in this dissertation, identifies many interesting crustal structures and a 3-D tomographic study should provide additional constraints on the lateral extent and continuity of some of these features. In particular, the geometry of the LVZ, identified here beneath both across-axis lines, could be modelled beneath the entire CVFR in the 3-D study. Furthermore, a detailed investigation of the off-axis crustal structure, west of the CVFR and the transition from pre-rift crust to post-rift VFR-generated material between the two across-axis lines could be carried out.

Further work should also be carried on the free-air gravity dataset. The VFR has been comprehensively mapped using multibeam echosounders (Wiedicke and Collier,

1993), although the majority of the data exist only on paper records. The digitisation of this dataset and combination with the EW9512 bathymetry dataset would provide a more extensive topographic grid for the calculation of the MBA. Gravity data collected during CD34/88, including a long (130 km) profile aligned parallel to the spreading direction, crossing the centre of the CVFR (i.e. between Lines 1 and 6 of this study) combined with the EW9512 data would also provide a more detailed free-air gravity grid to study the transition from pre-rift crust to post-rift VFR-generated material.

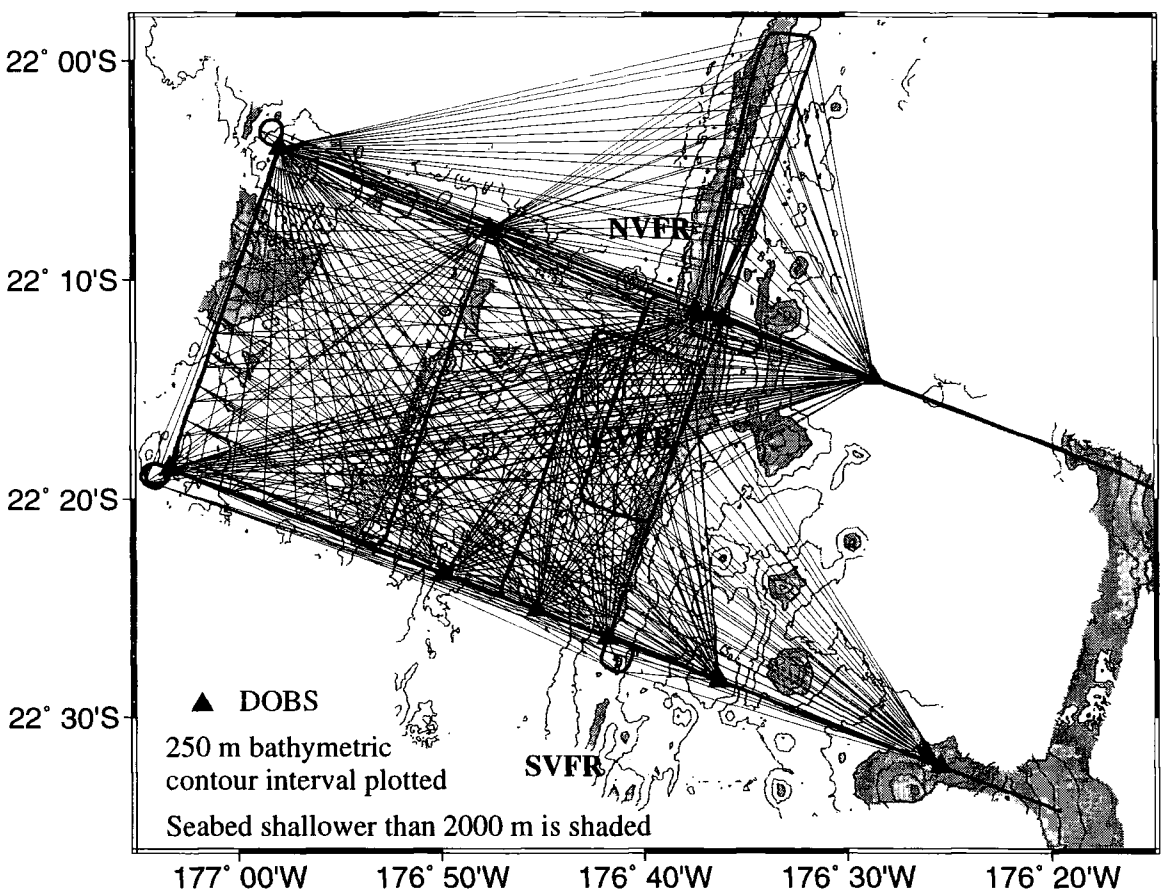

Figure 7.2: The EW9512 3-D seismic tomography study.
Seismic experimental configuration overlying the bathymetry of the study area. DOBS locations are marked by triangles and the 250 m bathymetric contour has been plotted. Seabed depths shallower than 2000 m have been shaded to show the location of the NVFR, CVFR and SVFR. Lines drawn from shot to receiver show the good 3-D coverage acquired over the CVFR and off-axis to the west. Note that only every fifteenth shot is shown for clarity.

7.3.2 Suggestions for future surveys

Multidisciplinary geophysical surveys have provided valuable insight into the processes of crustal accretion at the CVFR, which can be extended to other mid-ocean ridges. The VFR is an excellent example of a propagating ridge, where the transition

from pre-rift crust to post-rift material can be clearly identified as a significant thinning of the upper crust and its seafloor expression, a 'pseudofault'. The results of this study may have furthered our understanding of the crustal accretionary processes occurring at the VFR, but they have also pointed us towards some still unanswered questions:

1) Is there any evidence of a magma chamber beneath the SVFR?
2) What are the physical properties of the melt lens and what is the nature of its lower boundary?
3) Does the crustal structure within the transition zones change as you approach the propagating rift tip?
4) When does rifting give way to back-arc spreading?
5) What is the crustal structure within the propagating rift tip and what does it tell us about how ridges propagate?

In an attempt to answer some of these questions two additional surveys are proposed here and summarised in figure 7.3. Ultimately, a multidisciplinary experiment similar to the one described in this study should be carried out on other magmatically active, intermediate spreading ridges in 'normal' mid-ocean ridge environments and used to confirm (or dispute) the conclusions proposed in this dissertation.

Survey A: Wide-angle and MCS investigations of the crustal structure of the SVFR

The SVFR is so far the least studied portion of the VFR system, although it is the site of the Hine Hina hydrothermal field (Fouquet *et al.*, 1993). The main aim of this survey is to provide a detailed 3-D model of the crustal structure at the SVFR, which could be used in combination with results from studies over the CVFR to determine the evolution of the Southern Lau Basin. Due to the general southward propagation of the VFR, the crustal structure modelled within the axial region at the SVFR could be directly compared (and contrasted) with the off-axis crustal structure of similar age (relative to the onset of spreading) at the CVFR. The southern extension of upper crustal thinning, identified within the transition zones on Line 1 (this study) could also be modelled and used to determine the maximum extent of VFR-generated crust.

Shots fired along the proposed 3-D network of lines could be recorded on ten DOBSs, located on two of the axis-perpendicular lines (see figure 7.3). The regular spacing of the shots and receivers should provide an ideal dataset for both 2-D forward modelling (two across-axis and five axis-parallel lines, including one along-axis line)

and a 3-D tomographic study. The two DOBSs located on the SVFR ridge crest should also record P_cP and P_cS arrivals, similar to those observed on SDOBS4 in this study.

The acquisition of coincident MCS data would also provide an extension to the CD34/88 dataset, but the general non-reflective nature of the VFR crust limits the general effectiveness of this method, except for mapping the extent of the MCR. However, with a sufficiently long multi-channel streamer (>2.5 km) data could be used for AVO analysis to determine the physical properties of the melt lens.

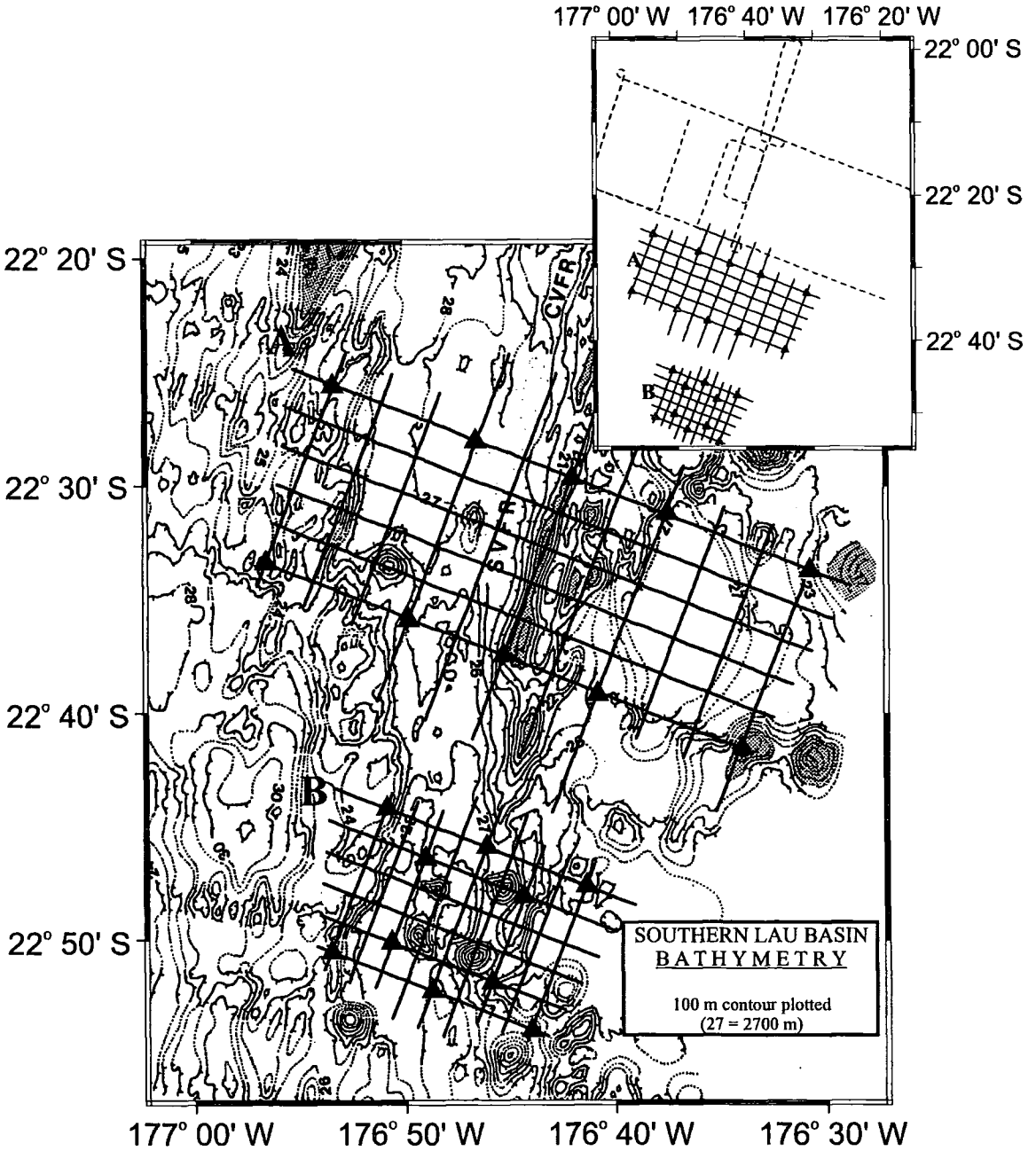

Figure 7.3: Experimental configuration for proposed future surveys.
Bathymetric map of the Southern Lau Basin (after Wiedicke and Collier, 1993) overlain by the proposed wide-angle seismic lines. DOBS locations are marked by triangles and bathymetric contours are plotted at 100 m intervals. Seabed depths shallower than 2000 m have been shaded to show the location of the CVFR, SVFR and four large seamounts surrounding the propagating ridge tip. Inset shows the location of Surveys A and B relative to the EW9512 seismic lines (dashed lines).

Further work - global context

The processes of crustal accretion at the VFR have been investigated here and the VFR is proposed to be an example of an intermediate spreading ridge with anomalously high magmatic budget. To investigate the global considerations of these findings, further related work must be carried out elsewhere.

To determine the influence of the back-arc environment, work must be carried out on magmatically active, intermediate spreading ridges in 'normal' mid-ocean ridge settings (e.g. Costa Rica Rift - Mutter *et al.*, 1995). Transitions in axial morphology have been previously identified along the intermediate spreading Southeast Indian Ridge, perhaps indicative of variations in magmatic budget along the ridge. Detailed investigations of the crustal structure near areas of possible enhanced magmatic budget may be used to compare and contrast with the crustal accretionary processes proposed at other intermediate spreading ridges (e.g. VFR and JDFR). Additional work on other magmatically active spreading ridges within back-arc basins (e.g. East Scotia Ridge - Livermore *et al.*, 1997) may also provide further insight into the accretionary processes occurring beneath the VFR.

This dissertation has also provided evidence of significant thinning of the upper crust at the transition between pre-rift crust and post-rift VFR-generated material, which is associated with the propagation of the ridge tip. The southward propagation of the rift tip at the VFR provides an excellent opportunity to investigate the transition from pre-rift to post-rift material throughout its 'evolution'. However, to fully understand the processes involved detailed investigation of the rift tip at the VFR (Survey B) and at other propagating ridges must be carried out.

ALVIN studies of the Galapagos active propagating rift system (Hey *et al.*, 1992) have previously defined the fine-scale structural and volcanic patterns produced by active rift and spreading centre propagation. An organised spreading centre has been clearly identified, which lies behind a triangular block of stretched and fractured pre-existing lithosphere (the proposed propagating rift is at the tip of this triangular block). A detailed refraction study over the propagating rift tip, and the transition into organised spreading, may greatly improve our understanding of the processes of crustal accretion at propagating rift tips and may further elucidate some of the features identified in this study.

Survey B: A 3-D tomographic study of the propagating rift tip

This detailed study consists of ten DOBSs located on a regular 20x20 km grid of seismic lines and is designed to sample the top 4 km of the crust. Again, the unreflective nature of the crust in the Lau Basin means that wide-angle refraction is the preferred method, although a short-offset streamer could be easily utilised to provide an additional dataset. The crustal structure of the propagating rift tip should provide additional information on the transition from rifting and thinning of the crust to 'true' seafloor spreading.

Further insight into the processes involved in ridge propagation could be determined from the collection of TOBI (Towed Ocean Bottom Instrument) data. Seafloor characteristics identified in the TOBI data could be used to determine the deformation resulting from the propagating rift tip, any associated fault patterns and locate any evidence of new magmatic material.

Coincident free-air gravity data collected during both surveys would add to the increasing volume of data collected over the entire VFR system. The gravity could then be combined with the CD34/88 and EW9512 datasets and used to calculate a MBA from the northern tip of the NVFR down to the propagating rift tip to determine which parts (if any) of the ridge system are in isostatic equilibrium.

7.4 Conclusion

In conclusion, detailed modelling of the wide-angle seismic, normal incidence seismic and free-air gravity datasets presented in this dissertation has greatly improved our understanding of the processes of crustal accretion at the VFR and has extended our knowledge of the transition from rifting to 'true' seafloor spreading in the Lau Basin. In a global context, the results from this study provide a link between the crustal structure of fast and slow spreading ridges and seismic evidence for the evolution of the VFR may stimulate further study of seafloor spreading in back-arc basins.

References

Ballu, V., J. Dubois, C. Deplus, M. Diament and S. Bonvalot, 1998, Crustal structure of the Mid-Atlantic Ridge south of the Kane Fracture Zone from seafloor and sea surface gravity data. *J. geophys. Res.*, vol. 103, no. B2, p.2615-2631.

Barry, K.M., D.A. Cavers and C.W. Kneale, 1975, Recommended standards for digital tape formats. *Geophysics*, vol. 40, no. 2, p.344-352.

Barth, G.A., 1994, Plate boundary geometry to Moho depths within the 9° 03′ N and 12° 54′ N overlapping spreading centres of the East Pacific Rise. *Earth Planet. Sci. Lett.*, vol. 128, p.99-112.

Barton, P.J., 1986, The relationship between seismic velocity and density in the continental crust – A useful constraint. *Geophys. J. R. astr. Soc.*, vol. 87, no. 1, p.195-208.

Bevis, M., F.W. Taylor, B.E. Schutz, J. Recy, B.L. Isacks, S. Helu, R. Singh, E. Kendrick, J. Stowell, B. Taylor and S. Calmant, 1995, Geodetic observations of very rapid convergence and back-arc extension at the Tonga arc. *Nature*, vol. 374, p.249-251.

Bock, G., T. Eguchi and Y. Fujinawa, 1991, P-wave velocity anomalies between the Tonga subducting slab and the overlying mantle beneath the Lau Basin. *J. geophys. Res.*, vol. 96, no. B11, p.18119-18128.

Bratt, S.R. and G.M. Purdy, 1984, Structure and variability of oceanic crust on the flanks of the East Pacific Rise between 11° and 13°N. *J. geophys. Res.*, vol. 89, no. B7, p.6111-6125.

Brown, G.C. and A.E. Musset, 1981, The inaccessible earth. George Allen and Unwin Ltd., pp.235.

Buck, W.R., S.M. Carbotte and C. Mutter, 1995, Controls on extrusion at mid-ocean ridges. *Geology*, vol. 25, p.935-938.

Calvert, A.J., 1995, Seismic evidence for a magma chamber beneath the slow-spreading Mid-Atlantic Ridge. *Nature*, vol. 377, p.410-414.

Calvert, S.E.E., 1996, Southern Valu Fa Ridge, The Lau Basin: A gravity and bathymetric investigation. unpublished MSc. thesis, University of Durham, pp.120.

Cann, J.R., 1974, A model for oceanic crustal structure developed. *Geophys. J. R. astr. Soc.*, vol. 39, p.169-187.

Cann, M., 1994, A magnetic interpretation of the Lau Basin, Southwest Pacific. unpublished MSc. thesis, University of Durham, pp.81.

Carbotte, S.M. and K.C. Macdonald, 1994, The axial topographic high at intermediate and fast spreading ridges. *Earth Planet. Sci. Lett.*, vol. 128, no. 3-4, p.85-97.

Carbotte, S.M., J.C. Mutter and L. Xu, 1997, Contribution of volcanism and tectonism to axial and flank morphology of the Southern East Pacific Rise 17° 10' S - 17° 40' S, from a study of layer 2A geometry. *J. geophys. Res.*, vol. 102, no. B5, p.10165-10184.

Caress, D.W., M.S. Burnett and J.A. Orcutt, 1992, Tomographic image of the axial low velocity zone at 12° 50' N on the East Pacific Rise. *J. geophys. Res.*, vol. 97, no. B6, p.9243-9264.

Carlson, R.L. and G.S. Raskin, 1984, Density of the oceanic crust. *Nature*, vol. 311, p.555-558.

Chapman, C.H. and R. Drummond, 1982, Body-wave seismograms in inhomogeneous media using Maslov asymptotic theory. *Bull. Seism. Soc. Am.*, vol. 72, no. 6, p.5277-5317.

Christensen, N.I. and M.H. Salisbury, 1975, Structure and constitution of the lower oceanic crust. *Rev. Geophys. Space Phys.*, vol. 13, p.57-86.

Christenson, G.L., G.M. Purdy and K.M.M. Rhor, 1993, Structure of the northern symmetrical segment of the Juan de Fuca Ridge. *Marine geophys. Res.*, vol. 15, p.219-240.

Christenson, G.L., G.M. Purdy and G.J. Fryer, 1992, Structure of young upper crust at the East Pacific Rise near 9° 30′ N. *Geophys. Res. Lett.*, vol. 19, no. 10, p.1045-1048.

Christenson, G.L., G.M. Purdy and G.J. Fryer, 1994, Seismic constraints on shallow crustal emplacement processes at the fast spreading East Pacific Rise. *J. geophys. Res.*, vol. 99, no. B9, p.17957-17973.

Christenson, G.L., G.M. Kent, G.M. Purdy and R.S. Detrick, 1996, Extrusive thickness variability at the East Pacific Rise, 9°-10°N: Constraints from seismic techniques. *J. geophys. Res.*, vol. 101, no. B2, p.2859-2873.

Collier, J.S., 1990, Seismic imaging of magma chambers and mud diapirs. unpublished Ph.D. thesis, University of Cambridge, pp.231.

Collier, J.S. and S.C. Singh, 1997, Detailed structure of the top of the melt body beneath the East Pacific Rise at 9° 40′ N from waveform inversion of seismic reflection data. *J. geophys. Res.*, vol. 102, no. B9, p.20287-20304.

Collier, J.S. and M.C. Sinha, 1990, Seismic images of a magma chamber beneath the Lau Basin back-arc spreading centre. *Nature*, vol. 346, p.646-648.

Collier, J.S. and M.C. Sinha, 1992a, The Valu Fa Ridge: The pattern of volcanic activity at a back-arc spreading centre. *Marine Geology*, vol. 104, p.243-263.

Collier, J.S. and M.C. Sinha, 1992b, Seismic mapping of a magma chamber beneath the Valu Fa Ridge, Lau Basin. *J. geophys. Res.*, vol. 97, no. B10, p.14031-14053.

Cormier, M.-H., K.C. Macdonald and D.S. Wilson, 1995, A three-dimensional gravity analysis of the East Pacific Rise from 18° to 21°30'S. *J. geophys. Res.*, vol. 100, no. B5, p.8063-8082.

Cudrak, C.F. and R.M. Clowes, 1993, Crustal structure of Endeavour Ridge segment, Juan de Fuca Ridge, from a detailed seismic refraction survey. *J. geophys. Res.*, vol. 98, no. B4, p.6 329-6349.

Davis, A.S., D.A. Clague and J.L. Morton, 1990, Volcanic glass compositions from two spreading centres in the Lau Basin, Southwest Pacific. *Geol. Jahrb., Reihe D*, vol. 72, p.481-501.

Davis, E.E. and R.G. Currie, 1993, Geophysical observations of the northern Juan de Fuca Ridge system: lessons in seafloor spreading. *Can. J. Earth Sci.*, vol. 30, p.278-300.

Day, A.J., 1997, Seismic reflection imaging and modelling of the melt lens beneath the Valu Fa Ridge. unpublished MSc. thesis, University of Durham, pp.67.

Detrick, R.S., P. Buhl, E.E. Vera, J.A. Mutter, J.A. Orcutt, J. Madsen and T. Brocher, 1987, Multichannel seismic imaging of a crustal magma chamber along the East Pacific Rise. *Nature*, vol. 326, p.35-41.

Detrick, R.S., J.C. Mutter, P. Buhl and I.I. Kim, 1990, No evidence from multichannel reflection data for a crustal magma chamber in the MARK area on the Mid-Atlantic Ridge. *Nature*, vol. 347, p.61-64.

Detrick, R.S., A.J. Harding, G.M. Kent, J.A. Orcutt, J.C. Mutter and P. Buhl, 1993, Seismic structure of the southern East Pacific Rise. *Science*, vol. 259, p.499-503.

Detrick, R.S., J. Collins, R. Stephen and S. Swift, 1994, In situ evidence of the nature of the seismic layer 2/3 boundary in oceanic crust. *Nature*, vol. 370, p.288-290.

Dunn, R.A. and D.R. Toomey, 1997, Seismological evidence for 3-D melt migration beneath the East Pacific Rise. *Nature*, vol. 388, p.259-262.

East Pacific Rise Study Group, 1981, Crustal processes of the mid-ocean ridge. *Science*, vol. 213, p.31-40.

Fornari, D.J., R.M. Haymon, M.R. Perfit, T.K.P. Gregg and M.H. Edwards, 1998, Axial summit trough of the East Pacific Rise 9°-10° N: Geological characteristics and evolution of the axial zone on fast spreading mid-ocean ridges. *J. geophys. Res.*, vol. 103, no. B5, p.9827-9855.

Forsyth, D.W. and B. Wilson, 1984, Three dimensional temperature structure of a ridge-transform-ridge system. *Earth Planet. Sci. Lett.*, vol. 70, p.355-362.

Foucher, J.P. and the Shipboard Scientific Party, 1988, La ride volcanique de Valu Fa dans le bassin de Lau méridional (Sud-ouest Pacifique). *C. R. Acad. Sci. Paris Série II*, vol. 307, p.609-616.

Fouquet, Y., U. von Stackelberg, J.L. Charlou, J. Erzinger, P. Herzig, R. Mühe and M. Wiedicke, 1993, Metallogenesis in back-arc environments. *Economic Geology*, vol. 88, p.2154-2181.

Fouquet, Y., U. von Stackelberg, J.L. Charlou, J.P. Donval, J.P. Foucher, J. Erzinger, P. Herzig, R. Mühe, M. Wiedicke, S. Soakai and H. Whitechurch, 1991, Hydrothermal activity in the Lau back-arc basin: Sulphides and water chemistry. *Geology*, vol. 19, p.303-306.

Fowler, C.M.R., 1990, The solid earth: An introduction to global geophysics. Cambridge University Press, pp.472.

Frenzel, G., R. Mühe and P. Stoffers, 1990, Petrology of the volcanic rocks from the Lau Basin, Southwest Pacific. *Geol. Jahrb., Reihe D*, vol. 72, p.395-479.

Fuchs, K. and G. Müller, 1971, Computation of synthetic seismograms with the reflectivity method and comparison of observations. *Geophys. J. R. astr. Soc.*, vol. 23, p.417-433.

Gass, I.G., 1990, Ophiolites and oceanic lithosphere. In: *J. Malpas, E.M. Moores, A. Panayiotou and C. Xenophontos (eds.), Ophiolites: Oceanic crustal analogues.* Cyprus Geological Survey Department, p.1-12.

Goldberg, D. and Y.F. Sun, 1997, Seismic structure of the upper oceanic crust revealed by in situ Q logs. *Geophys. Res. Lett.*, vol. 24, no. 3, p.333-336.

Hamburger, M.W. and B.L. Isacks, 1988, Diffuse back-arc deformation in the Southwest Pacific. *Nature*, vol. 332, p.599-604.

Harding, A.J., J.A. Orcutt, M.E. Kappus, E.E. Vera, J.C. Mutter, P. Buhl, R.S. Detrick and T.M. Brocher, 1989, Structure of young oceanic crust at 13°N on the East Pacific Rise from expanding spread profiles. *J. geophys. Res.*, vol. 94, no. B9, p.12163-12196.

Harding, A.J., G.M. Kent and J.A. Orcutt, 1993, A multichannel seismic investigation of upper crustal structure at 9°N on the East Pacific Rise: Implications for crustal accretion. *J. geophys. Res.*, vol. 98, no. B8, p.13925-13944.

Hasslegren, E.O. and R.M. Clowes, 1995, Crustal structure of the Northern Juan de Fuca plate from multichannel reflection data. *J. geophys. Res.*, vol. 100, no. B4, p.6469-6486.

Hawkins, J.W. and J.T. Melchior, 1985, Petrology of Mariana Trough and Lau Basin basalts. *J. geophys. Res.*, vol. 90, no. B13, p.11431-11468.

Herron, T.J., P.L. Stoff and P. Buhl, 1980, Magma chamber and mantle reflections - East Pacific Rise. *Geophys. Res. Lett.*, vol. 7, no. 11, p.989-992.

Hill, D.P., 1957, Recent geophysical exploration of the ocean floor. *Phys. Chem. Earth*, vol. 2, p.129-163.

Hilton, D.R., K. Hammerschmidt, G. Loock and H. Friedrichsen, 1993, Helium and argon isotope systematics of the Central Lau Basin and Valu Fa Ridge: Evidence of crust/mantle interactions in a back-arc basin. *Geochim. Cosmochim. Acta*, vol. 57, p.2819-2841.

Hooft, E.E.E., R.S. Detrick and G.M. Kent, 1997, Seismic structure and indicators of magma budget along the Southern East Pacific Rise. *J. geophys. Res.*, vol. 102, no. B12, p.27319-27340.

Hooft, E.E.E., H. Schouten and R.S. Detrick, 1996, Constraining crustal emplacement process from the variation in seismic layer 2A thickness at the East Pacific Rise. *Earth Planet. Sci. Lett.*, vol. 142, p.289-309.

Houtz, R. and J. Ewing, 1976, Upper crustal structure as a function of plate age. *J. geophys. Res.*, vol. 81, p.2490-2498.

Jenner, G.A., P.A. Cawood, M. Rautenschlein and W.M. White, 1987, Composition of back-arc volcanics, Valu Fa Ridge, Lau Basin: Evidence for slab-derived component in their mantle source. *J. Volc. & Geothermal Res.*, vol. 32, p.209-222.

Kappus, M.E., A.J. Harding and J.A. Orcutt, 1995, A baseline for upper crustal velocity variations along the East Pacific Rise at 13°N. *J. geophys. Res.*, vol. 100, no. B4, p.6143-6161.

Karig, D.E., 1970, Ridges and basins of the Tonga-Kermadec island arc system. *J. geophys. Res.*, vol. 75, no. B2, p.239-354.

Karig, D.E., 1971, Origin and development of marginal basins in the Western Pacific. *J. geophys. Res.*, vol. 76, no. B11, p.2542-2561.

Kent, G.M., A.J. Harding and J.A. Orcutt, 1990, Evidence for a smaller magma chamber beneath the East Pacific Rise at 9° 30′ N. *Nature*, vol. 344, p.650-653.

Kent, G.M., A.J. Harding and J.A. Orcutt, 1993, Distribution of magma beneath the East Pacific Rise near the 9° 03'N deval from forward modelling of common depth point data. *J. geophys. Res.*, vol. 98, no. B8, p.13971-13995.

Kent, G.M., A.J. Harding, J.A. Orcutt, R.S. Detrick, J.C. Mutter and P. Buhl, 1994, Uniform accretion of oceanic crust south of the Garrett transform at 14° 15'S on the East Pacific Rise. *J. geophys. Res.*, vol. 99, no. B5, p.9097-9116.

Kim, I.I. and J.A. Orcutt, 1989, Effects of disrupted axial morphology on the amplitude strength of the crustal magma chamber reflector at the East Pacific Rise. *Eos, Trans. AGU, Fall Meet. Suppl.*, vol. 73, no. 43, p.133.

Kuo, B.-Y. and D.W. Forsyth, 1988, Gravity anomalies of the ridge-transform system in the South Atlantic between 31° and 34.5°S upwelling centres and variations in crustal thickness. *Marine geophys. Res.*, vol. 10, p.205-232.

Langmuir, C.H., J.F. Bender and R. Batiza, 1986, Petrological and tectonic segmentation of the East Pacific Rise 5° 30'N - 14° 30'N. *Nature*, vol. 322, p.422-429.

Lin, J., G.M. Purdy, H. Schouten, J.C. Sempere and C. Zervas, 1990, Evidence from gravity data for focused magmatic accretion along the Mid-Atlantic Ridge. *Nature*, vol. 344, p.627-632.

Livermore, R., A. Cunningham, L. Vanneste and R. Larter, 1997, Subduction influence on magma supply at the East Scotia Ridge. *Earth Planet. Sci. Lett.*, vol. 150, p.261-275.

Lonsdale, P., 1983, Overlapping rift zones at the 5.5° S offset of the East Pacific Rise. *J. geophys. Res.*, vol. 88, no. B11, p.9393-9406.

Lonsdale, P., 1986, Comments on 'East Pacific Rise from Siqueiros to Orinoco FZ: Along strike continuity of axial neovolcanic zone and structure and evolution of overlapping spreading centres.' by K. Macdonald, J. Sempere and P.J. Fox. *J. geophys. Res.*, vol. 91, no. B11, p.10493-10499.

Macdonald, K.C., 1982, Mid-ocean ridges: Fine scale tectonic, volcanic and hydrothermal processes within the plate boundary zone. *Ann. Rev. Earth planet. Sci.*, vol. 10, p.155-190.

Macdonald, K.C., 1989, Anatomy of the magma reservoir. *Nature*, vol. 339, p.178-179.

Macdonald, K.C., J. Sempere and P.J. Fox, 1984, East Pacific Rise from Siqueiros to Orinoco FZ: Along strike continuity of axial neovolcanic zone and structure and evolution of overlapping spreading centres. *J. geophys. Res.*, vol. 87, no. B7, p.6049-6069.

Macdonald, K.C., J. Sempere and P.J. Fox, 1986, The debate concerning overlapping spreading centres and mid-ocean ridge processes. *J. geophys. Res.*, vol. 91, no. B11, p.10501-10511.

Macdonald, K.C., P.J. Fox, L.J. Perram, M.F. Eisen, R.M. Hayman, S.P. Miller, S.M. Carbotte, M.-H. Cormier and A.N. Shor, 1988, A new view of the mid-ocean ridge from the behaviour of ridge-axis discontinuities. *Nature*, vol. 335, p.217-225.

MacGregor, L.M., S. Constable and M.C. Sinha, 1997, Crustal resistivity structure of the Valu Fa Ridge, Lau Basin. *Eos, Trans. AGU, Fall Meet. Suppl.*, vol. 78, no. 46, p.646.

MacGregor, L.M., S. Constable and M.C. Sinha, 1998, The RAMESSES experiment III: Controlled source electromagnetic sounding of the Reykjanes Ridge at 57° 45' N. *Geophys. J. Int.*, in press.

Matthews, P.A., 1993, Crustal structure of the Baltic Shield beneath the Sea of Bothnia: BABEL line 6. unpublished Ph.D. thesis, University of Durham, pp.268.

McDonald, M.A., S.C. Webb, J.A. Hildebrand, B.D. Cornvelle and C.G. Fox, 1994, Seismic structure and anisotropy of the Juan de Fuca Ridge at 45°N. *J. geophys. Res.*, vol. 99, no. B3, p.4857-4873.

MELT Seismic Team, 1998, Imaging the deep seismic structure beneath a mid-ocean ridge: The MELT experiment. *Science*, vol. 280, p.1215-1238.

Moos, D. and D. Marion, 1994, Morphology of extrusive basalts and its relationship to seismic velocities in the shallow oceanic crust. *J. geophys. Res.*, vol. 99, no. B2, p.2985-2994.

Morton, J.L. and N.H. Sleep, 1985, Seismic reflections from a Lau Basin magma chamber. In: *D.W. Scholl and T.L. Vallier (eds.), Geology and offshore resources of Pacific Island Arcs – Tonga region, Earth Sci. Ser.*, vol. 2, Circum-Pacific Council for energy and mineral resources, Houston, Texas, p.441-453.

Morton, J.L., N.H. Sleep, W.R. Normark and D.H. Tompkins, 1987, Structure of the Southern Juan de Fuca Ridge from seismic reflection records. *J. geophys. Res.*, vol. 92, no. B11, p.11315-11326.

Murase, T. and A.R. McBirney, 1973, Properties of some common igneous rocks and their melts at high temperatures. *Geol. Soc. Am. Bull.*, vol. 84, p.3563-3592.

Mutter, J.C., S.M. Carbotte, W.S. Su, L.Q. Xu, P. Buhl, R.S. Detrick, G.M. Kent, J.A. Orcutt and A.J. Harding, 1995, Seismic images of active magma systems beneath the East Pacific Rise between 17° 05' S and 17° 35' S. *Science*, vol. 268, no. 5209, p.391-395.

Nafe, J.E. and C.L. Drake, 1957, Variation with depth in shallow and deep water marine sediment of porosity, density and the velocities of compressional and shear waves. *Geophysics*, vol. 22, p.523-553.

NAUTILAU Group, 1990, Hydrothermal activity in the Lau Basin. *Eos, Trans. AGU*, vol. 71, p.678-679.

Navin, D.A., 1996, Seismic investigation of crustal accretion at the slow-spreading Mid-Atlantic Ridge - The Reykjanes Ridge at 57° 45' N. unpublished Ph.D. thesis, University of Durham, pp.309.

Navin, D.A., C. Peirce and M.C. Sinha, 1998, RAMESSES II - Evidence for accumulated melt beneath a slow spreading ridge from wide-angle refraction and multichannel reflection seismic profiles. *Geophys. J. Int.*, in press.

Northwest Geophysical Associates Inc., 1995, GMSYS users guide. pp.175.

Orcutt, J.A., B.L.N. Kennett, L. Dorman and W. Prothero, 1975, Evidence for a low velocity zone underlying a fast spreading ridge crest. *Nature*, vol. 256, p.475-476.

Parker, R.L., 1972, The rapid calculation of potential anomalies. *Geophys. J. R. astr. Soc.*, vol. 31, p.447-455.

Parson, L.M. and J.W. Hawkins, 1994, Two-stage ridge propagation and the geological history of the Lau back-arc basin. In: *J.W. Hawkins, L.M. Parson and J.F. Allan et al. (eds.), Proc. ODP, Sci. Results*, vol. 135: College Station, TX (Ocean Drilling Program), p.819-828.

Parson, L.M. and I.C. Wright, 1996, The Lau-Havre-Taupo back-arc basin: A southward-propagating, multi-stage evolution from rifting to spreading. *Tectonophysics*, vol. 263, p.1-22.

Parson, L.M., J.A. Pearce, B.J. Murton, R.A. Hodkinson and *RRS Charles Darwin* Scientific Party, 1990, Role of ridge jumps and ridge propagation in the tectonic evolution of the Lau back-arc basin, Southwest Pacific. *Geology*, vol. 18, p.470-473.

Peirce, C., 1990, Crustal structure of the Africa - Eurasian plate boundary. unpublished Ph.D. thesis, University of Cambridge, pp.248.

Peirce, C., M.C. Sinha and S. Constable, 1996, Controlled source electromagnetic and seismic investigation of the Valu Fa Ridge, Lau Basin, SW Pacific. *R/V Maurice Ewing* 9512 Cruise Report, (unpublished), pp.56.

Phipps Morgan, J. and Y.J. Chen, 1993, Dependence of ridge axis morphology on magma supply and spreading rate. *Nature*, vol. 346, p.706-708.

Prince, R.A. and D.W. Forsyth, 1988, Horizontal extent of anomalously thin crust near the Vema fracture zone from the 3-D analysis of gravity anomalies. *J. geophys. Res.*, vol. 93, no. B7, p.8051-8063.

Purdy, G.M. and R.S. Detrick, 1986, Crustal structure of the Mid-Atlantic Ridge at 23°N from seismic refraction studies. *J. geophys. Res.*, vol. 91, p.3739-3762.

Purdy, E.M., L.S.L. Kong, G.L. Christenson and S.C. Solomon, 1992, Relationship between spreading rate and the seismic structure of mid-ocean ridges. *Nature*, vol. 355, p.815-817.

Raitt, R.W., 1963, The crustal rocks. In: *M.N. Hill (ed.), The Sea*, vol. 3, Wiley (Interscience), New York, p.85-102.

Rohr, K., B. Mildreit and C.J. Yorath, 1988, Asymmetric deep crustal structure across the Juan de Fuca Ridge. *Geology*, vol. 16, p.533-537.

Sandwell, D.T. and W.H.F. Smith, 1997, Marine gravity anomaly from Geosat and ERS-1 satellite Altimetry. *J. geophys. Res.*, vol. 102, no. B5, p.10039-10054.

Sempere, J. and K.C. Macdonald, 1987, Marine tectonics: Processes at mid-ocean ridges. *Rev. Geophys.*, vol. 25, p.1313-1347.

Sempere, J., J. Lin, H.S. Brown, H. Schouten and G.M. Purdy, 1993, Segmentation and morphotectonic variations along a slow-spreading centre: The Mid-Atlantic Ridge (24° 00′ N - 30° 40′ N). *Marine geophys. Res.*, vol. 15, p.153-200.

Shipboard Scientific Party, 1973, Site reports. *Initial reports of the Deep Sea Drilling Project*, vol. XXI, p.17-32.

Shipboard Scientific Party, 1992, Site reports. *Proc. Ocean Drill. Program, Initial Rep.*, vol. 135, p.489-570.

Sinha, M.C., 1988, Cruise report: *RRS Charles Darwin* 34, Southern Lau Basin. Internal report, Bullard Laboratories, Cambridge University.

Sinha, M.C., 1995, Segmentation and rift propagation at the Valu Fa Ridge, Lau Basin: Evidence from gravity data. *J. geophys. Res.*, vol. 100, no. B8, p.15025-15043.

Sinha, M.C., S. Constable, C. Peirce, A. White, G. Heinson, L.M. MacGregor and D.A. Navin, 1998, Magmatic processes at slow spreading ridges: Implications of the RAMESSES experiment at 57° 45' N on the Mid-Atlantic Ridge. *Geophys. J. Int.*, in press.

Sinha, M.C., D.A. Navin, L.M. MacGregor, S. Constable, C. Peirce, A. White, G. Heinson and M.A. Inglis, 1997, Evidence for accumulated melt beneath the slow spreading Mid-Atlantic Ridge. *Phil. Trans. R.. Soc. Lond.*, vol. 355, p.233-253.

Sinton, J.M. and R.S. Detrick, 1992, Mid-ocean ridge magma chambers. *J. geophys. Res.*, vol. 97, no. B1, p.197-216.

Sleep, N.H., 1975, Formation of oceanic crust: some thermal constraints. *J. geophys. Res.*, vol. 80, p.4 037-4042.

Smallwood, J.R., R.S. White and T.A. Minshull, 1995, Seafloor spreading in the presence of the Iceland plume: the structure of the Reykjanes Ridge at 61° 40'N. *J. of Geol. Soc. Lond.*, vol. 152, p.1 023-1 029.

Smewing, J.D., 1981, Mixing characteristics and compositional differences in mantle-derived melts beneath spreading axes: Evidence from cyclically layered rocks in the ophiolite of North Oman. *J. geophys. Res.*, vol. 86, p.2645-2659.

Solomon, S.C. and D.R. Toomey, 1992, The structure of mid-ocean ridges. *Ann. Rev. Earth Planet. Sci. Lett.*, vol. 20, p.329-364.

Spudich, P. and J.A. Orcutt, 1980, A new look at the seismic velocity structure of the oceanic crust. *Rev. Geophys. Space Phys.*, vol. 18, no. 3, p.627-645.

Talwani, M. and M. Ewing, 1960, Rapid computation of gravitational effect of three-dimensional bodies of arbitrary shape. *Geophysics*, vol. 25, p.203-225.

Talwani, M., J.C. Worzel and M. Landisman, 1959, Rapid gravity calculations for two-dimensional bodies with application to the Mendocino submarine fracture zone. *J. geophys. Res.*, vol. 64, p.49-59.

Taylor, B., K. Zellmer, F. Martinez and A. Goodliffe, 1996, Seafloor spreading in the Lau back-arc basin. *Earth Planet. Sci. Lett.*, vol. 144, p.35-40.

Teledyne Geotech, 1988, PDAS users guide. pp.193.

Thomson, C.J. and C.H. Chapman, 1986, End-point contributions to synthetic seismograms. *Geophys. J. R. astr. Soc.*, vol. 87, p.285-294.

Toomey, D.R., G.M. Purdy, S.C. Solomon and W.S. Wilcock, 1990, The three-dimensional seismic velocity structure of the East Pacific Rise near latitude 9° 30'N. *Nature*, vol. 347, p.639-645.

Toomey, D.R., S.C. Solomon and G.M. Purdy, 1994, Tomographic imaging of the shallow crustal structure of the East Pacific Rise at 9° 30'N. *J. geophys. Res.*, vol. 99, no. B12, p.24135-24157.

Vallier, T.L., G.A. Jenner, F.A. Frey, J.B. Gill, A.S. Davis, A.M. Volpe, J.W. Hawkins, J.D. Morris, P.A. Cawood, J.L. Morton, D.W. Scholl, M. Rautenschlein, W.M. White, R.W. Williams, A.J. Stevenson and L.D. White, 1991, Subalkaline andesite from Valu Fa Ridge, a back-arc spreading centre in the Southern Lau Basin: petrogenesis, comparative chemistry, and tectonic implications. *Chemical Geology*, vol. 91, p.227-256.

Vera, E.E. and J.B. Diebold, 1994, Seismic imaging of oceanic layer 2A between 9° 30'N and 10°N on the East Pacific Rise from two-ship wide aperture profiles. *J. geophys. Res.*, vol. 99, no. B2, p.3031-3041.

Vera, E.E., J.C. Mutter, P. Buhl, J.A. Orcutt, A.J. Harding, M.E. Kappus, R.S. Detrick and T.M. Brocher, 1990, The structure of 0 to 0.2 Ma. old oceanic crust at 9°N on the East Pacific Rise from expanded spread profiles. *J. geophys. Res.*, vol. 95, no. B10, p.15529-15556.

Vine, F.J., 1966, Spreading of the oceanic floor: New evidence. *Science*, vol. 154, p.1405-1415.

Vine, F.J. and G.C. Smith, 1990, Structure and physical properties of the Troodos crustal section at ICRDG drillholes CY1, 1a and 4. In: *J. Malpas, E.M. Moores, A. Panayiotou and C. Xenophontos (eds.), Ophiolites: Oceanic crustal analogues.* Cyprus Geological Survey Department, p.113-124.

von Stackelberg, U. and the Shipboard Scientific Party, 1988, Active hydrothermalism in the Lau back-arc basin (SW-Pacific): First results from the SONNE 48 Cruise. *Marine Mining*, vol. 7, p.431-442.

Wang, X. and J.R. Cochran, 1993, Gravity anomalies, isostasy and mantle flow at the East Pacific Rise crest. *J. geophys. Res.*, vol. 98, no. B11, p.19505-19531.

Wessel, P. and W.H.F. Smith, 1995, New version of the Generic Mapping Tools released. *EOS Trans. AGU*, vol. 76, p.329.

White, R.S., D.P. McKenzie and R.K. O'Nions, 1992, Oceanic crustal thickness from seismic measurements and rare earth element inversions. *J. geophys. Res.*, vol. 97, no. B13, p.19683-19715.

Wiedicke, M. and J.S. Collier, 1993, Morphology of the Valu Fa spreading ridge in the Southern Lau Basin. *J. geophys. Res.*, vol. 98, no. B7, p.11769-11782.

Wiedicke, M. and W. Habler, 1993, Morphotectonic characteristics of a propagating spreading system in the Northern Lau Basin. *J. geophys. Res.*, vol. 98, no. B7, p.11783-11797.

Wilcock, W.S.D., S.C. Solomon, G.M. Purdy and D.R. Toomey, 1992, Seismic attenuation structure of a fast spreading mid-ocean ridge. *Science*, vol. 258, p.1470-1474.

Wilcock, W.S.D., S.C. Solomon, G.M. Purdy and D.R. Toomey, 1995, Seismic attenuation structure of the East Pacific Rise near 9° 30' N. *J. geophys. Res.*, vol. 100, no. B12, p.24147-24165.

Wilkens, R.H., G.J. Fryer and J. Karsten, 1991, Evolution of porosity and seismic structure of upper oceanic crust: Importance of aspect ratios. *J. geophys. Res.*, vol. 96, no. B11, p.17981-17995.

Wilson, D.S., D.A. Clague, N.H. Sleep and J.L. Morton, 1988, Implications of magma convection for the size and temperature of magma chambers at fast spreading ridges. *J. geophys. Res.*, vol. 93, no. B10, p.11974-11984.

Xu, Y. and D.A. Wiens, 1997, Upper mantle structure of the southwest Pacific from regional waveform inversion. *J. geophys. Res.*, vol. 102, no. B12, p.27439-27451.

Zelt, C.A. and R.B. Smith, 1992, Seismic travel-time inversion for 2-D crustal velocity structure. *Geophys. J. Int.*, vol. 108, p.16-34.

Zhao, D., Y. Xu, D.A. Wiens, L. Dorman, J. Hildebrand and S. Webb, 1997, Depth extent of the Lau back-arc spreading centre and its relation to subduction processes. *Science*, vol. 278, p.254-257.

Appendix A

The wide-angle seismic dataset

The following record sections show the complete 2-D, four-component wide-angle seismic dataset recorded on the DOBSs. Seismograms are plotted at true amplitude with a reduction velocity of 6.0 km s^{-1}. Record sections are filtered using a Hanning window band-pass filter and corner frequencies are detailed below. Note the different time scale used on the horizontal geophone record sections.

(a) Vertical geophone	0-0 — 40-50 Hz.
(b) Hydrophone component	0-0 — 15-20 Hz.
(c) & (d) Horizontal geophones	3-6 — 40-50 Hz.

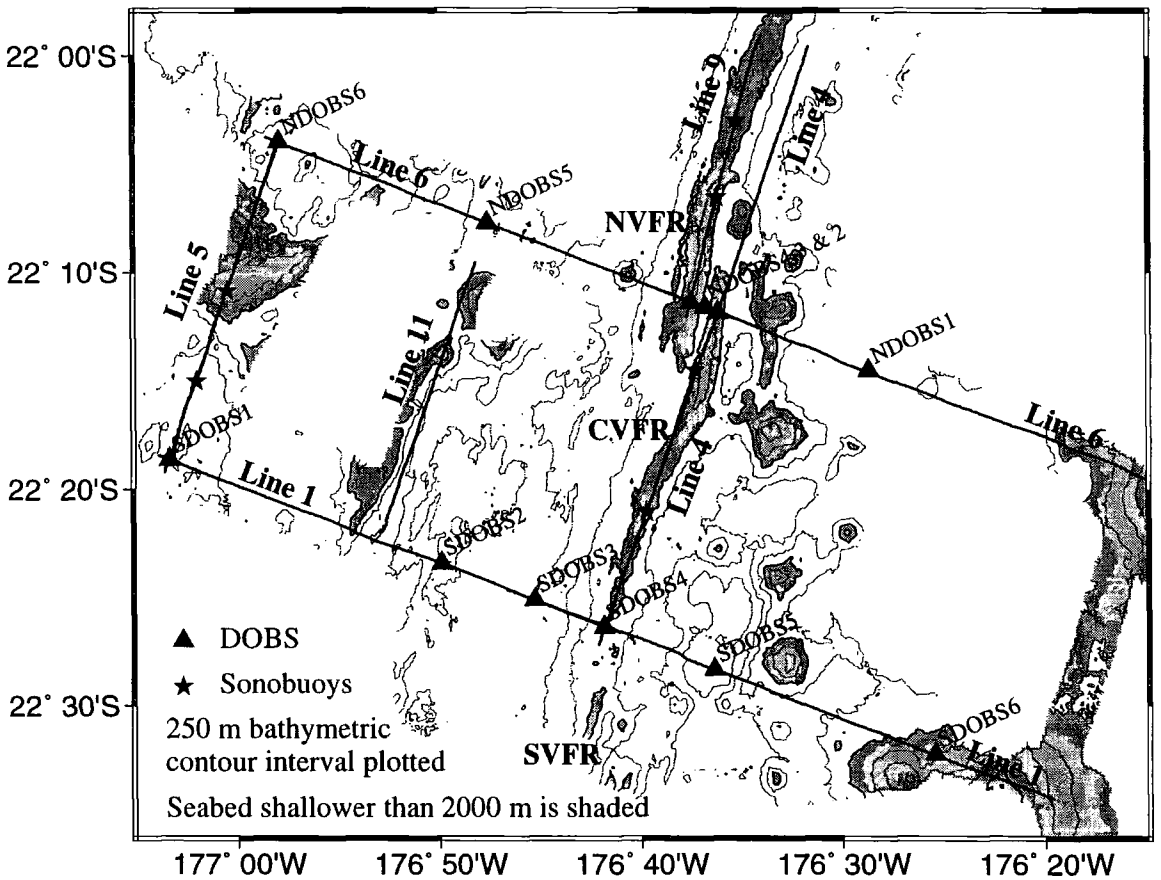

Figure A1: Location map of the main wide-angle seismic lines modelled in this dissertation. DOBS and sonobuoy locations are marked by triangles and stars respectively and bathymetric contours are plotted at the 250 m intervals. Seabed depths shallower than 2000 m have been shaded to show the location of the NVFR, CVFR and SVFR.

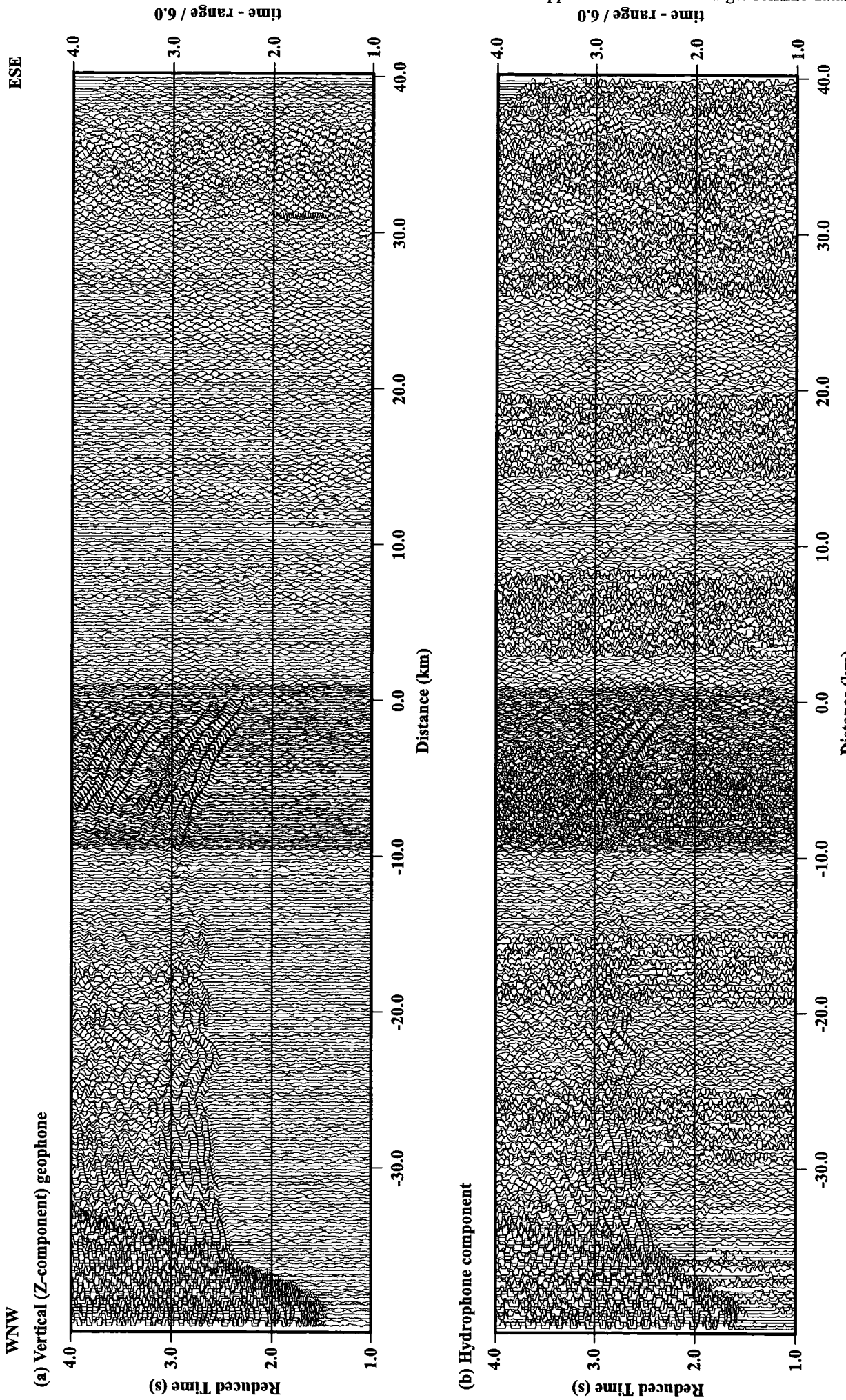

Figure A2: Line 1- SDOBS1

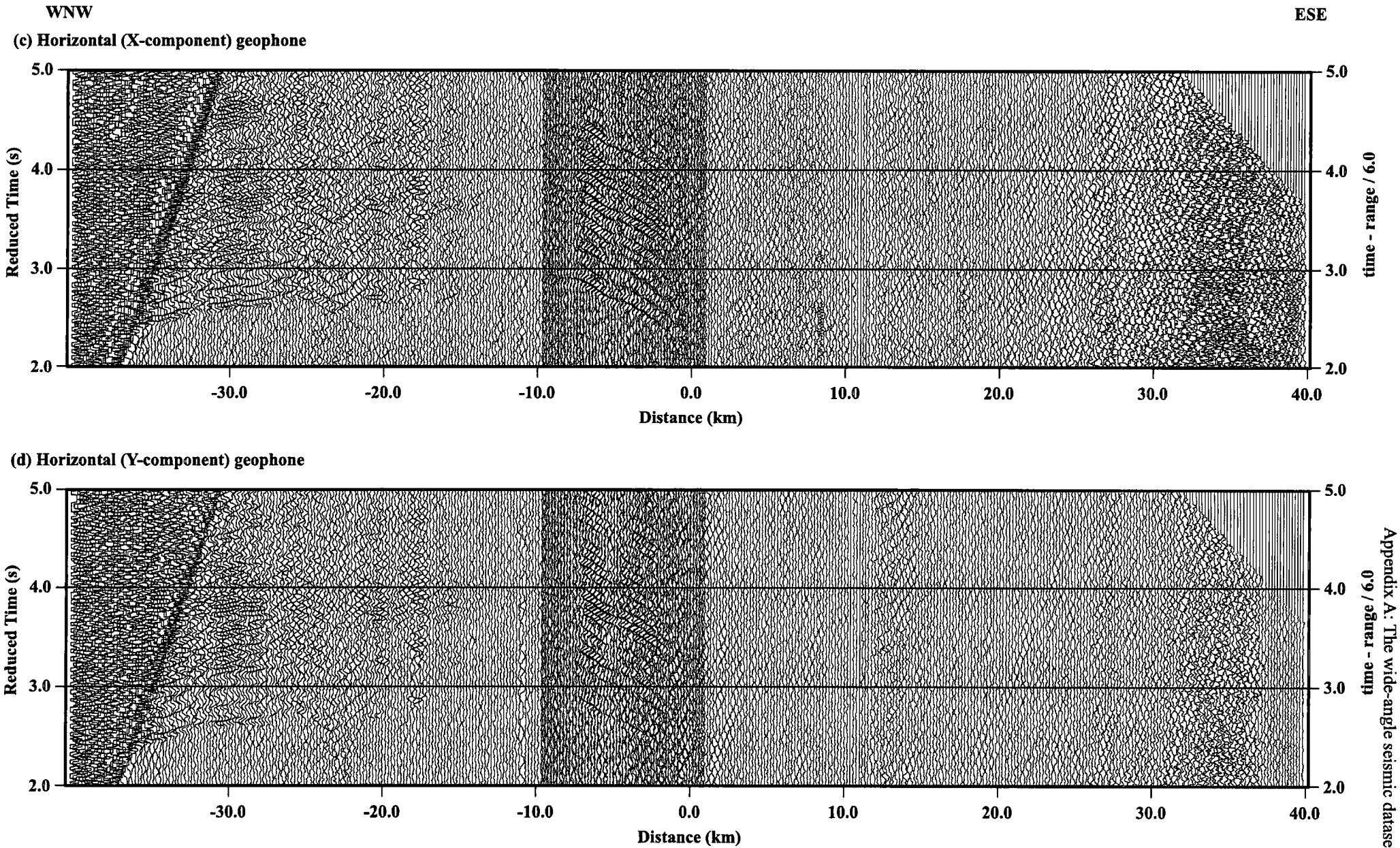

Figure A2 (cont.): Line 1- SDOBS1

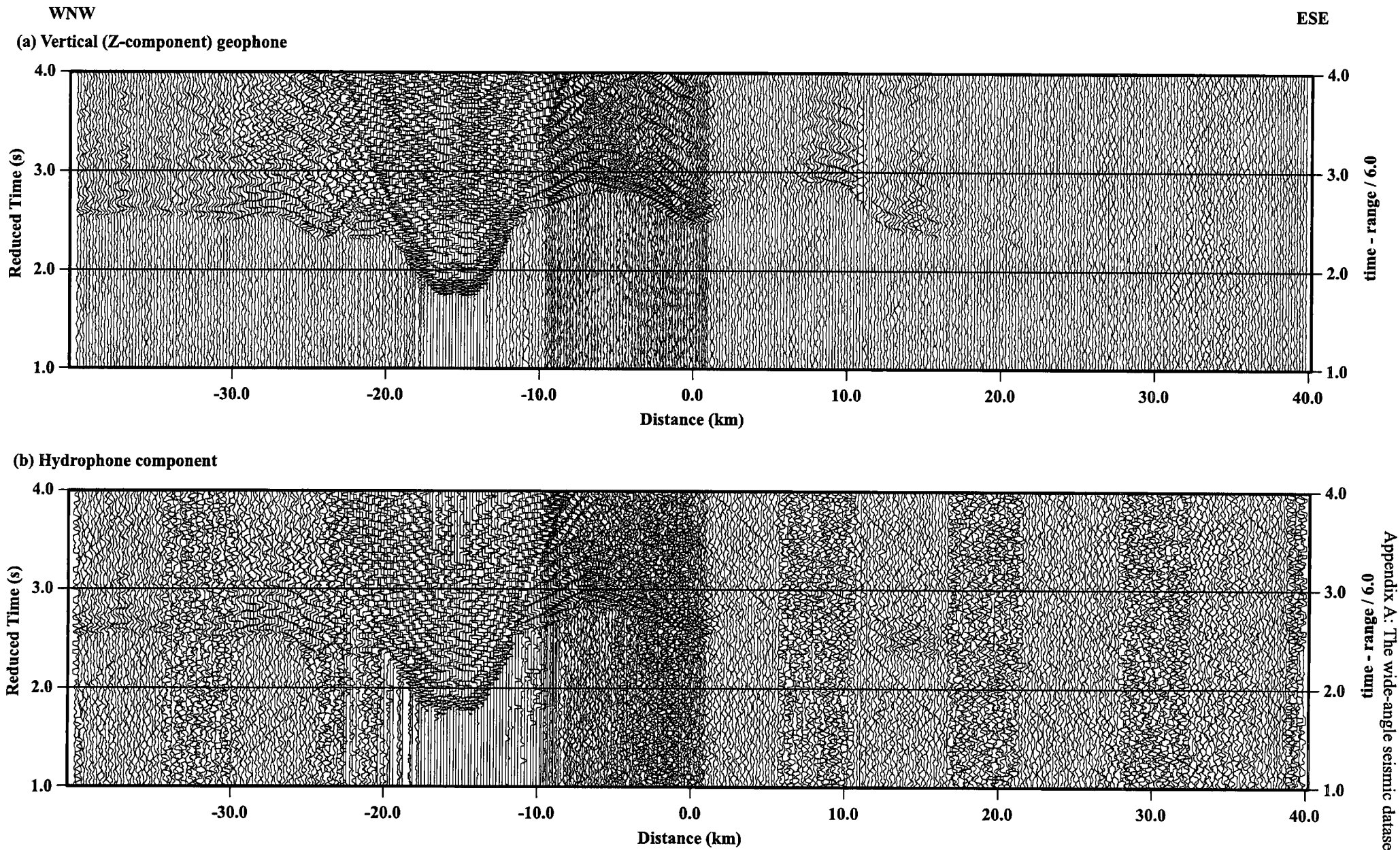

Figure A3: Line 1- SDOBS2

WNW ESE

(c) Horizontal (X-component) geophone

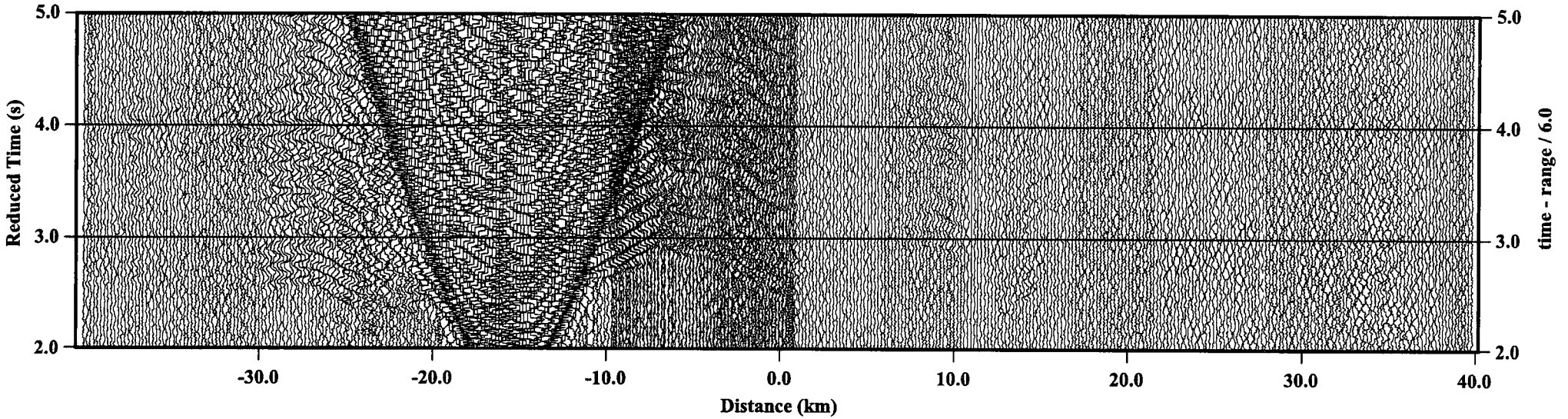

(d) Horizontal (y-component) geophone

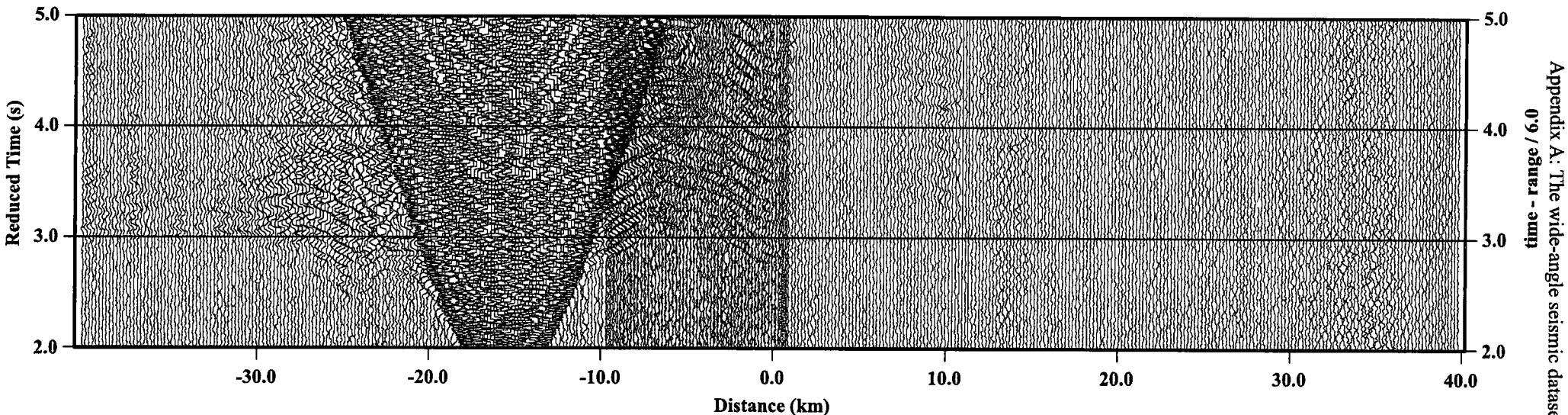

Figure A3 (cont.): Line 1- SDOBS2

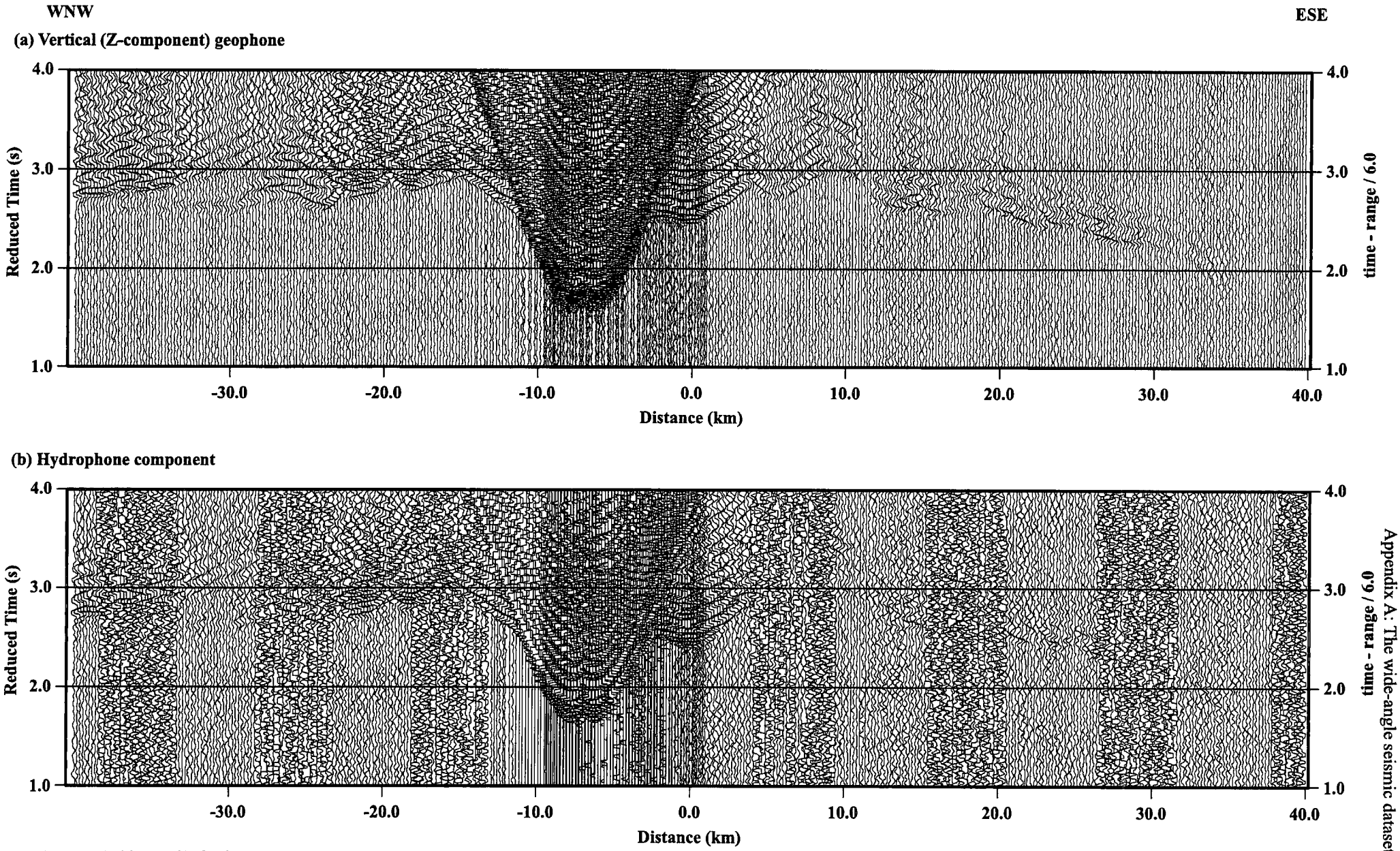

Figure A4: Line 1- SDOBS3

WNW ESE

(c) Horizontal (X-component) geophone

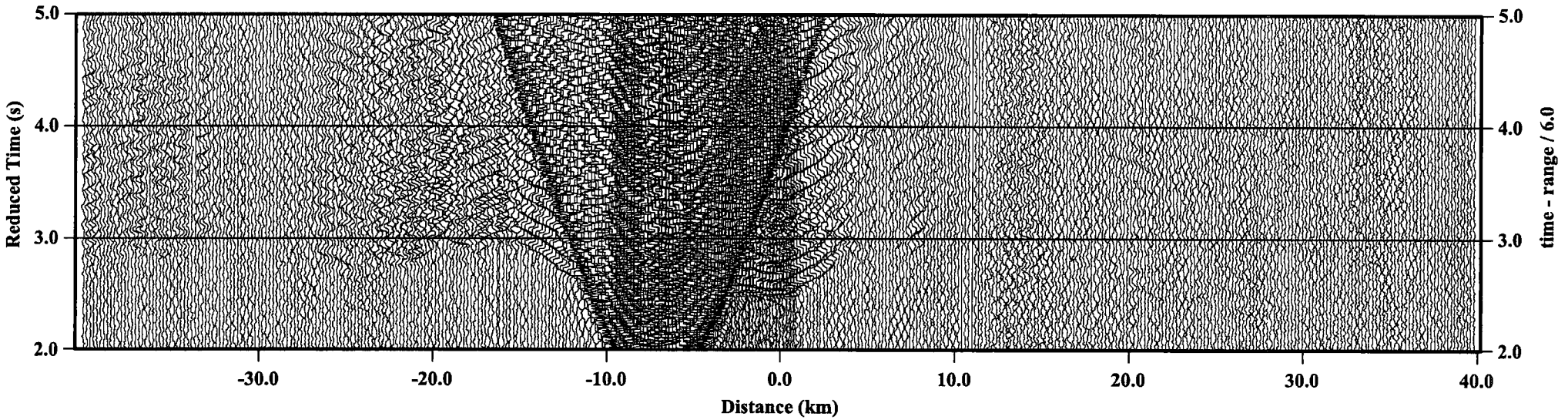

(d) Horizontal (Y-component) geophone

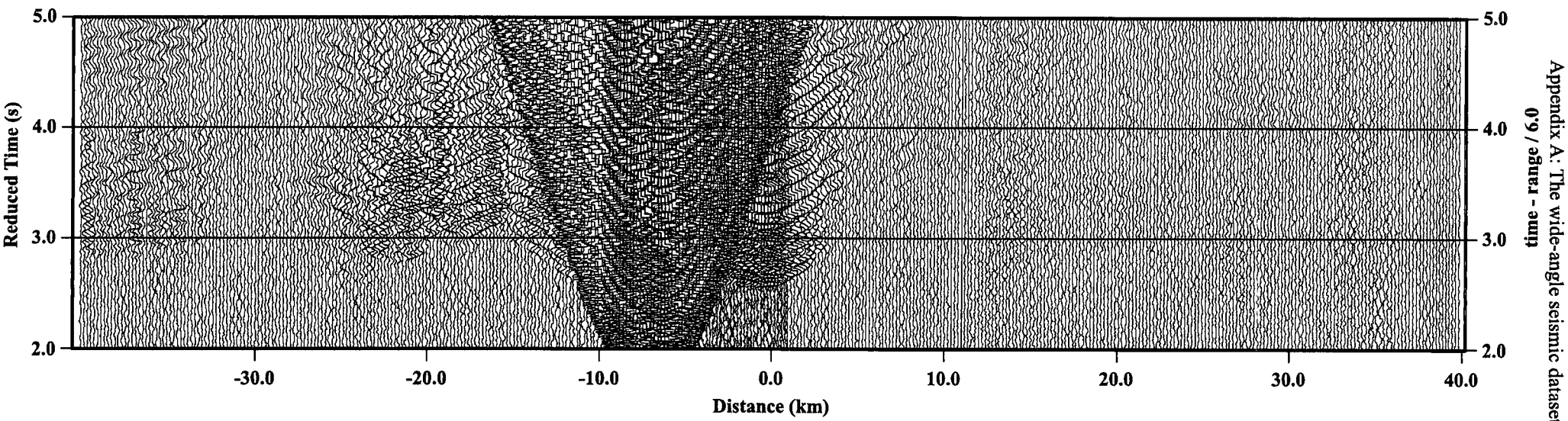

Figure A4 (cont.): Line 1- SDOBS3

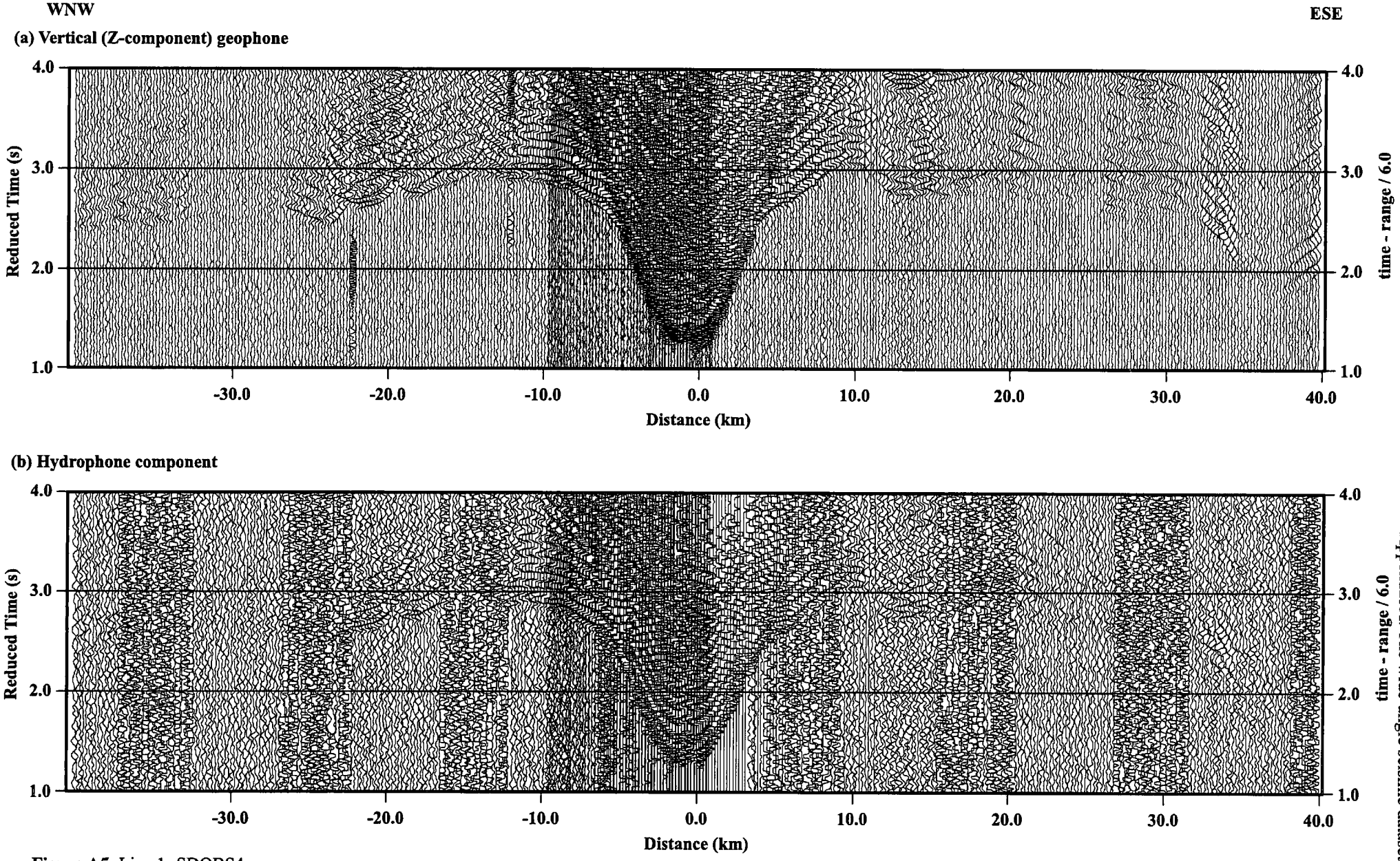

Figure A5: Line 1- SDOBS4

WNW ESE

(c) Horizontal (X-component) geophone

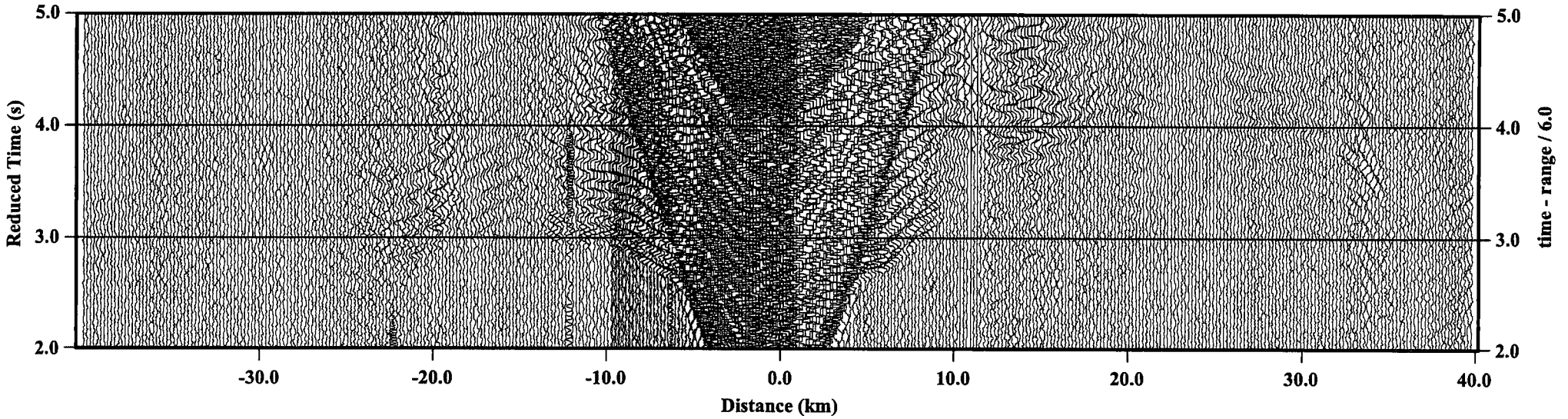

(d) Horizontal (Y-component) geophone

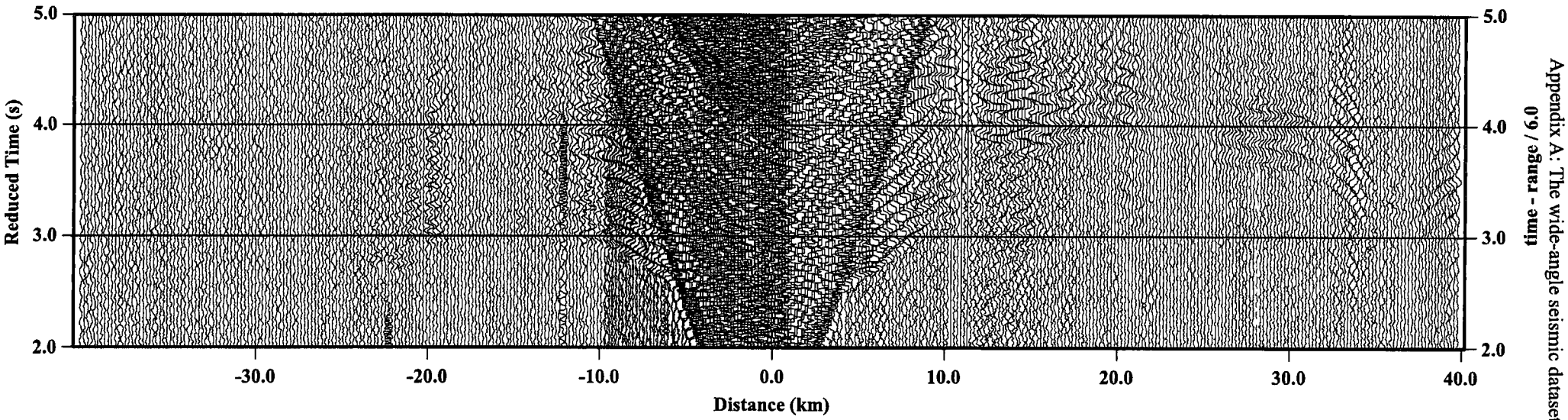

Figure A5 (cont.): Line 1- SDOBS4

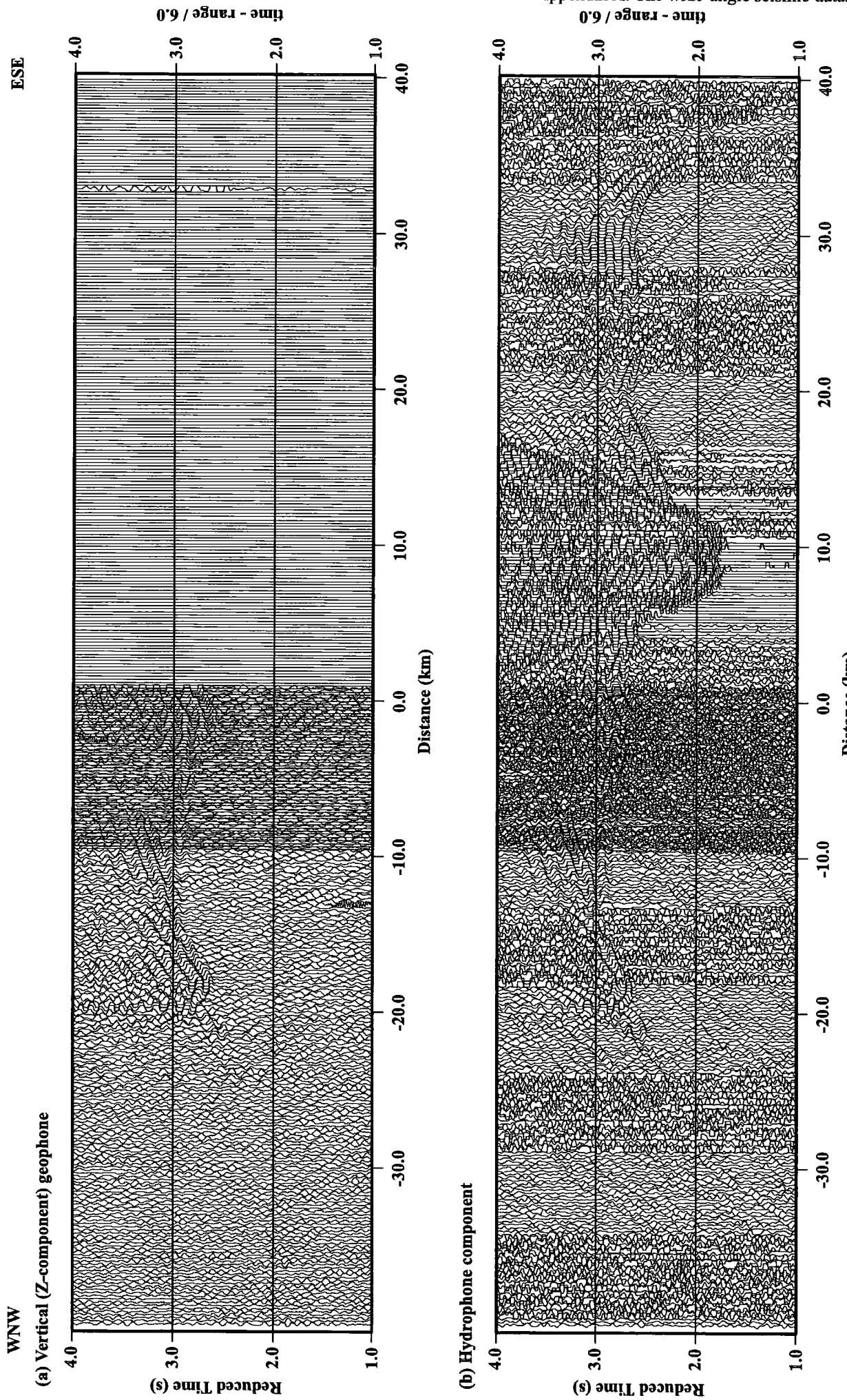

Figure A6: Line 1- SDOBS5

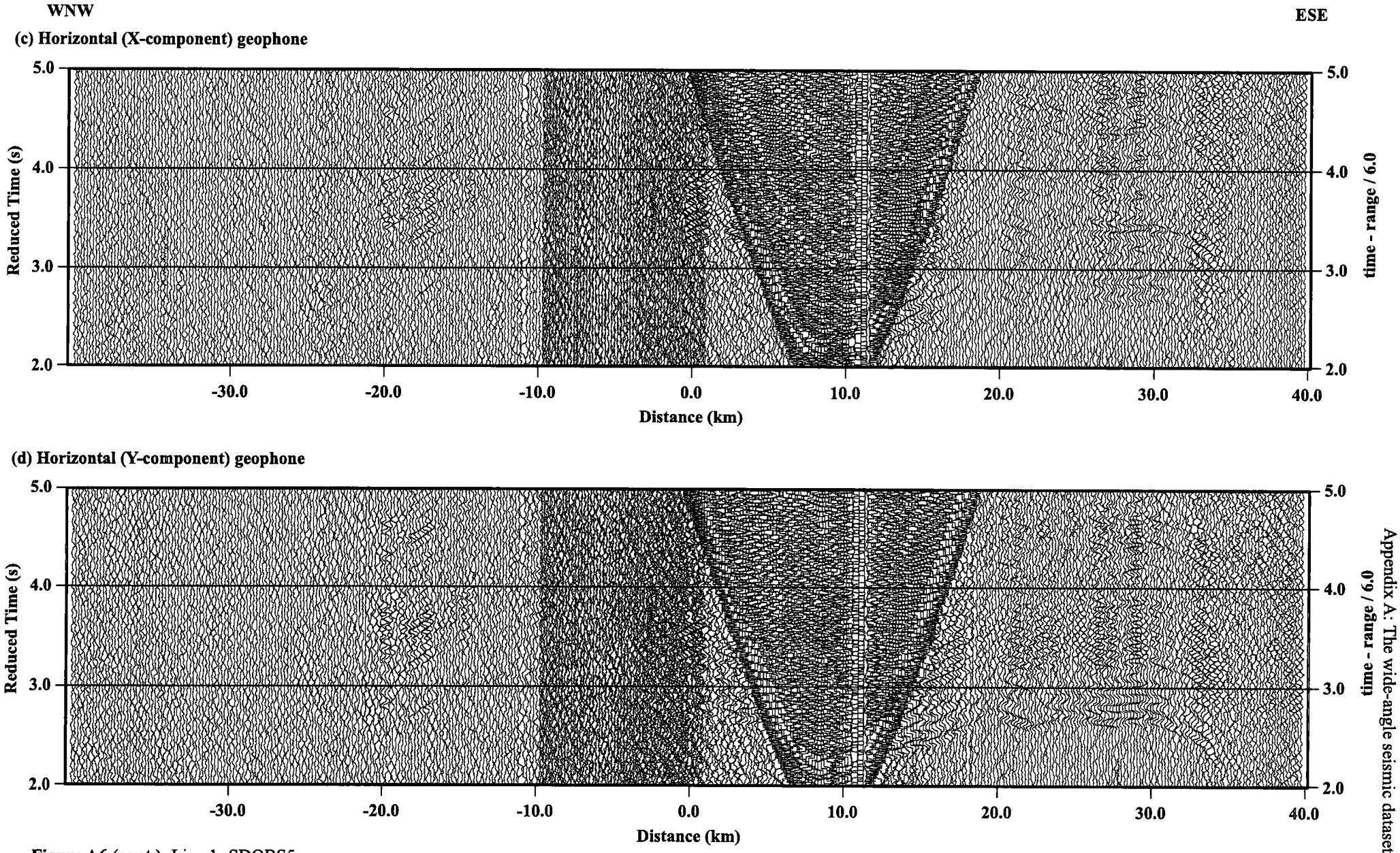

Figure A6 (cont.): Line 1- SDOBS5

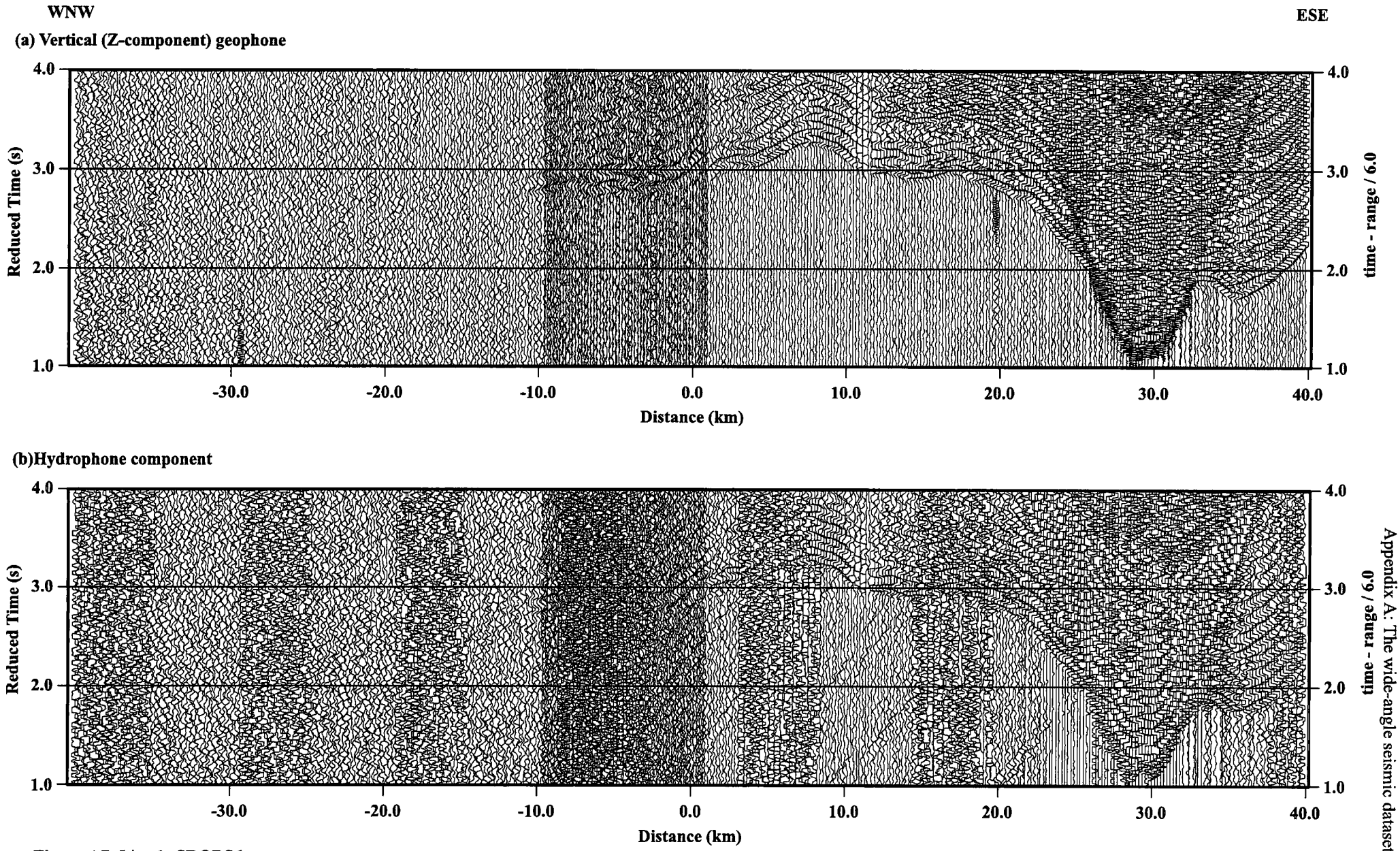

Figure A7: Line 1- SDOBS6

WNW ESE

(c) Horizontal (X-component) geophone

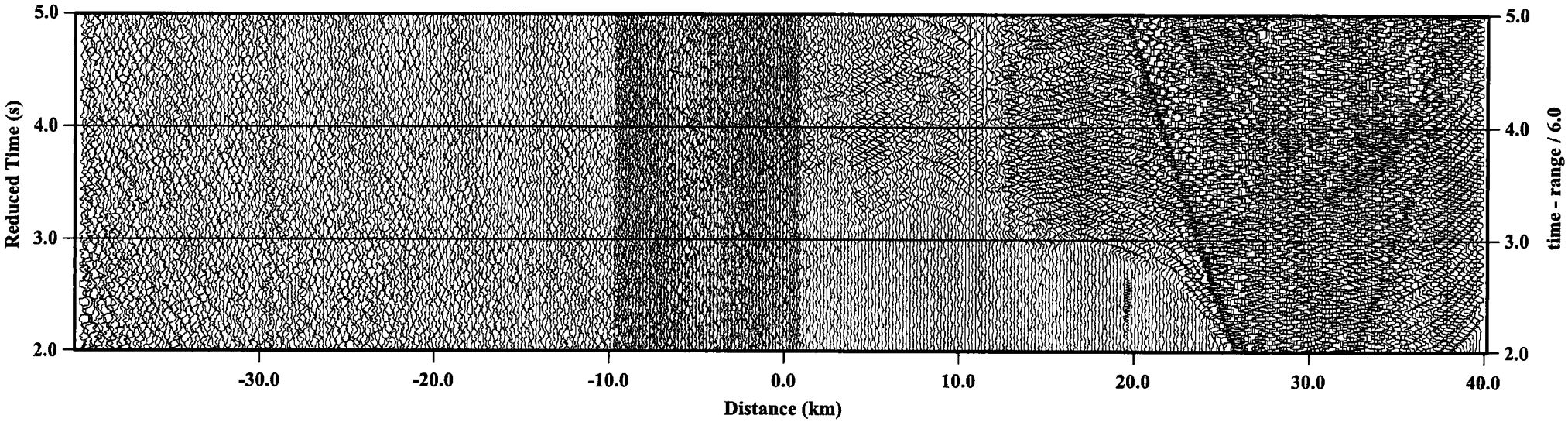

(d) Horizontal (Y-component) geophone

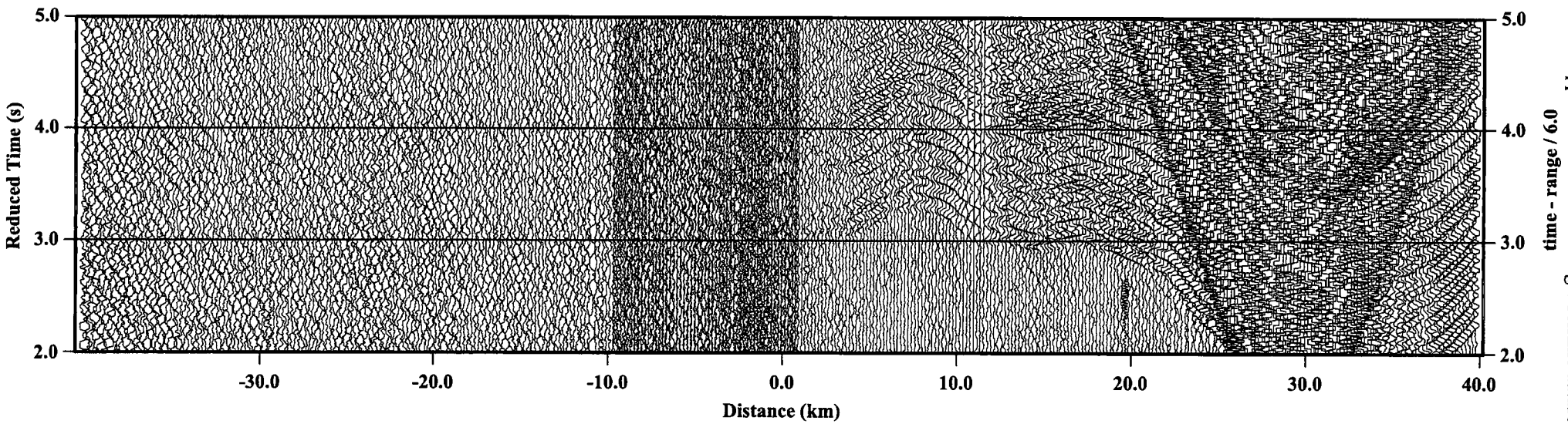

Figure A7 (cont.): Line 1- SDOBS6

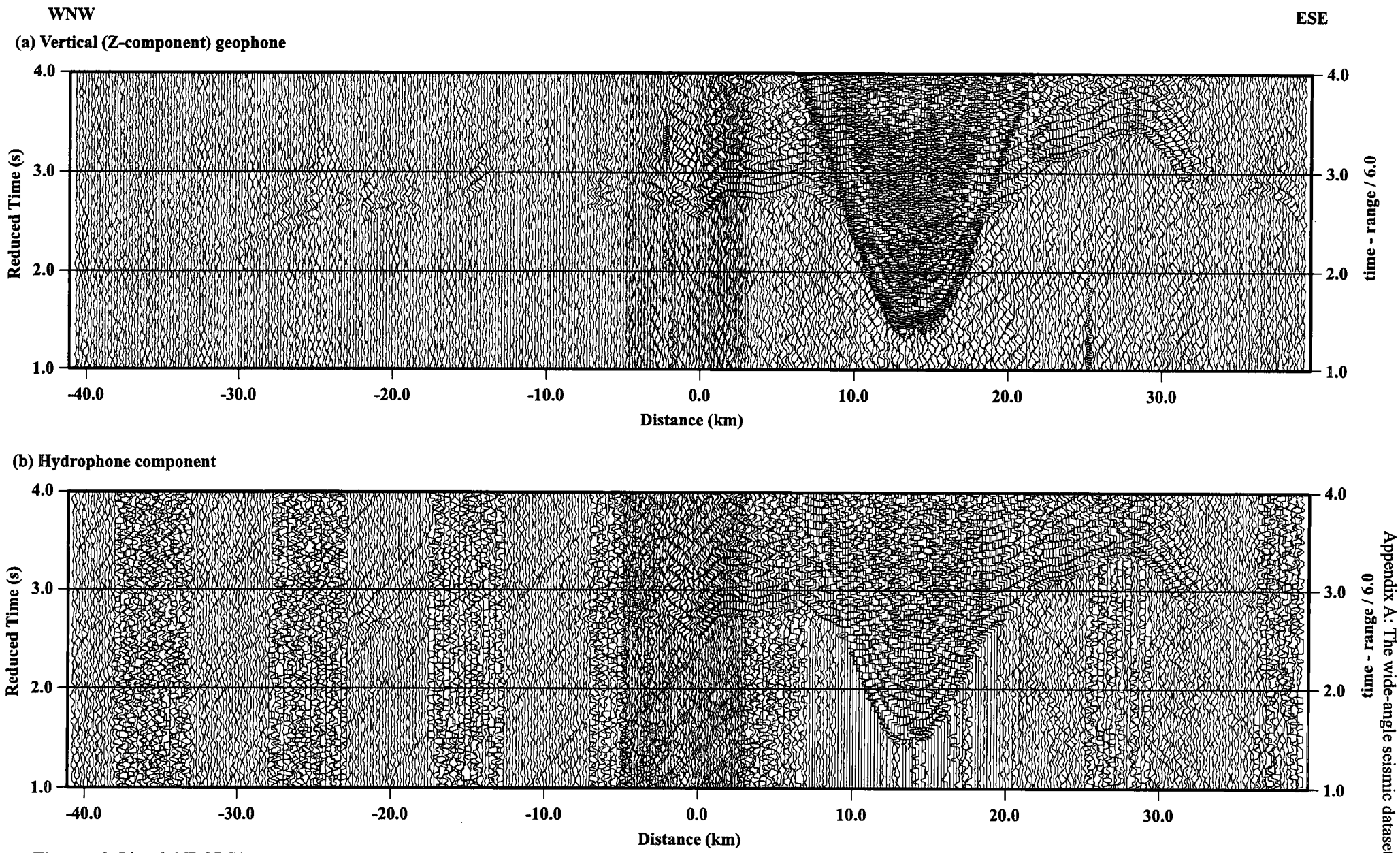

Figure A8: Line 6- NDOBS1

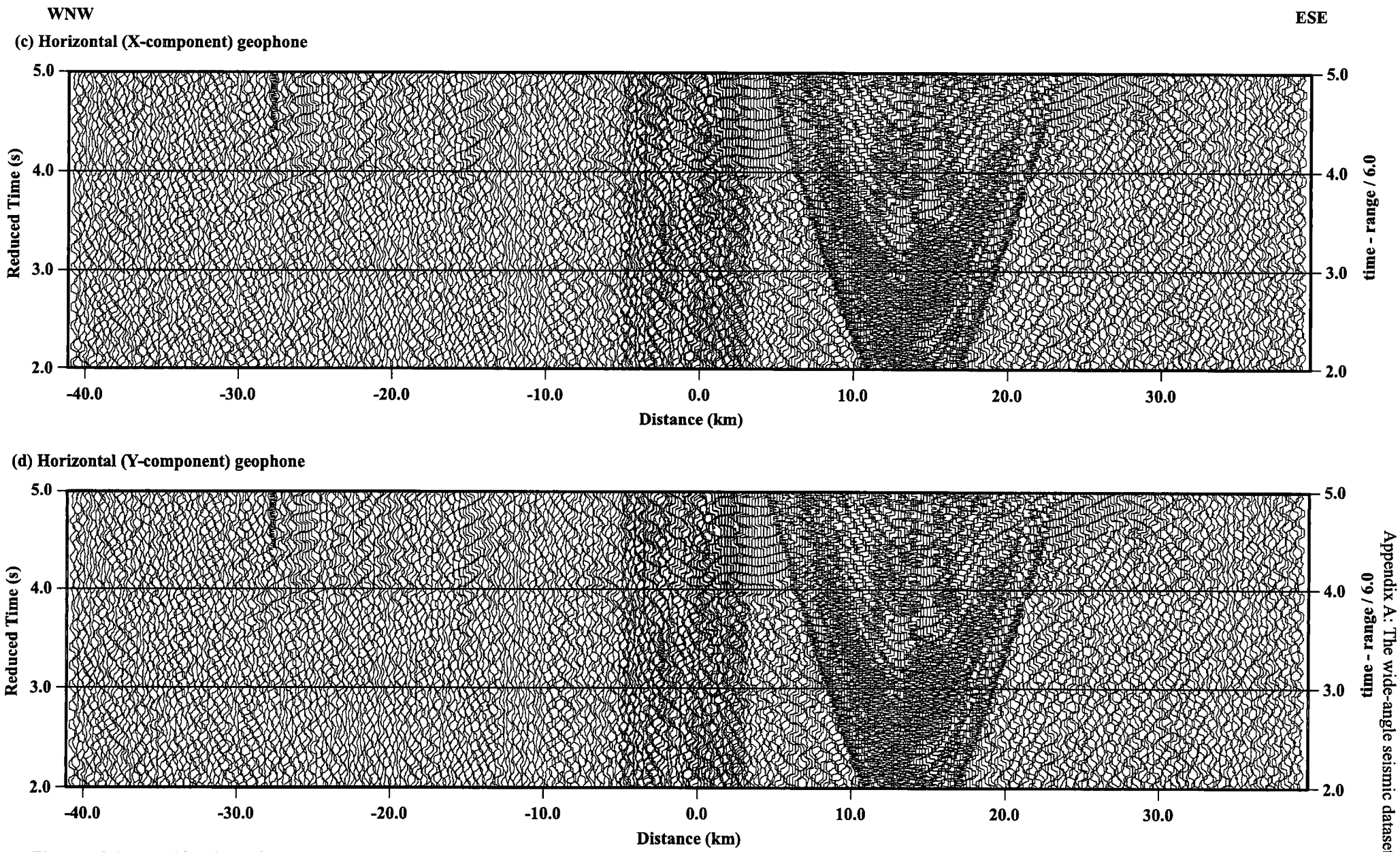

Figure A8 (cont.): Line 6- NDOBS1

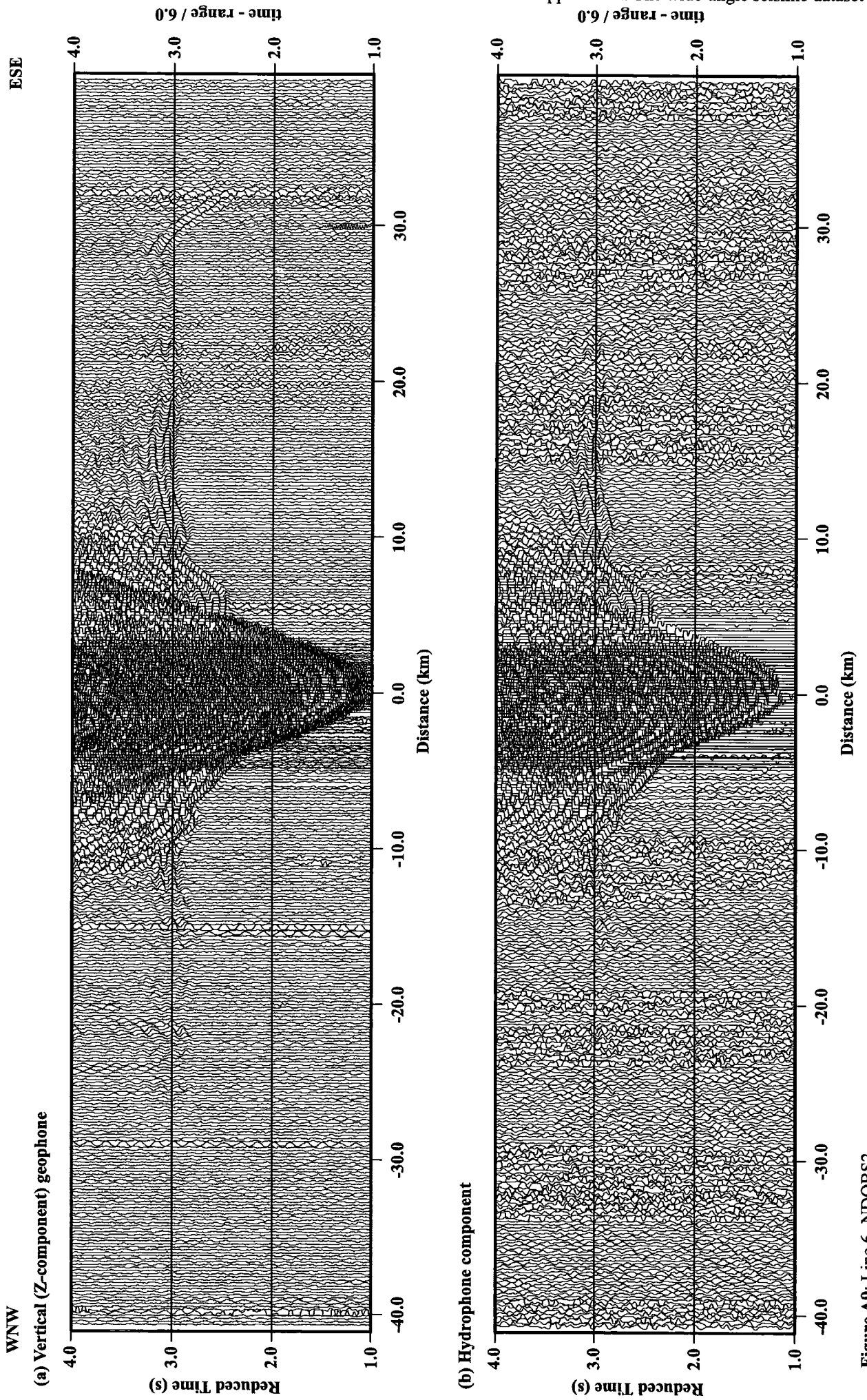

Figure A9: Line 6- NDOBS2

WNW ESE

(c) Horizontal (X-component) geophone

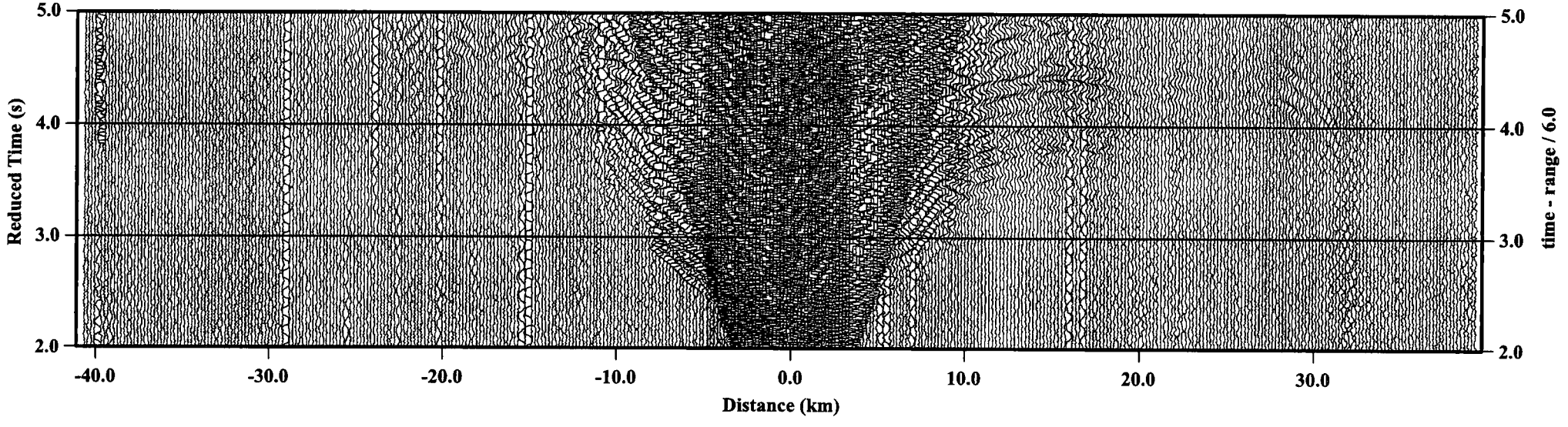

(d) Horizontal (Y-component) geophone

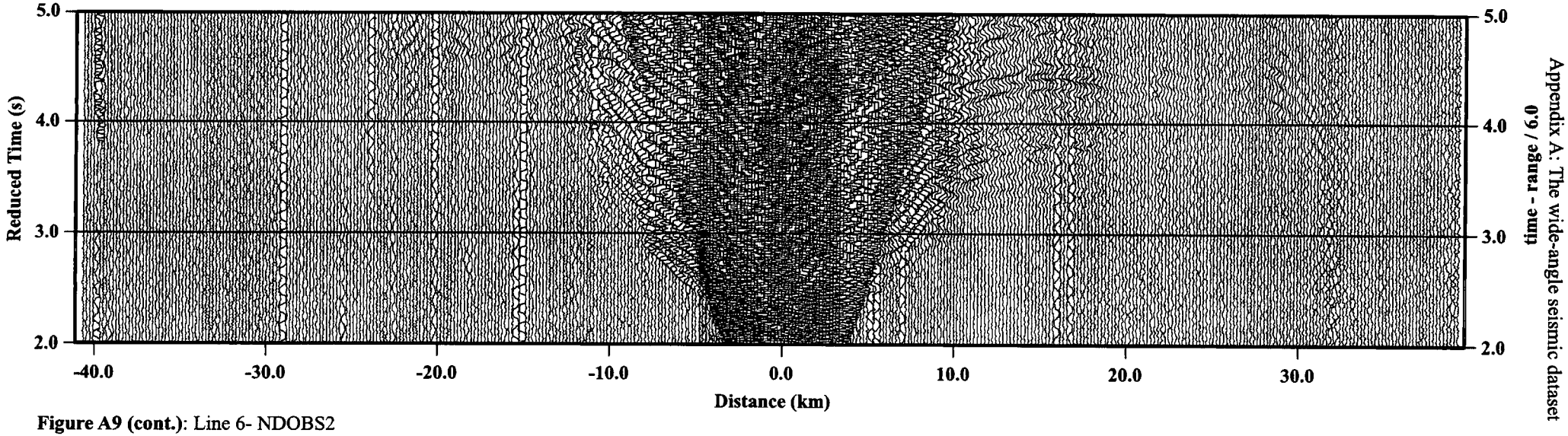

Figure A9 (cont.): Line 6- NDOBS2

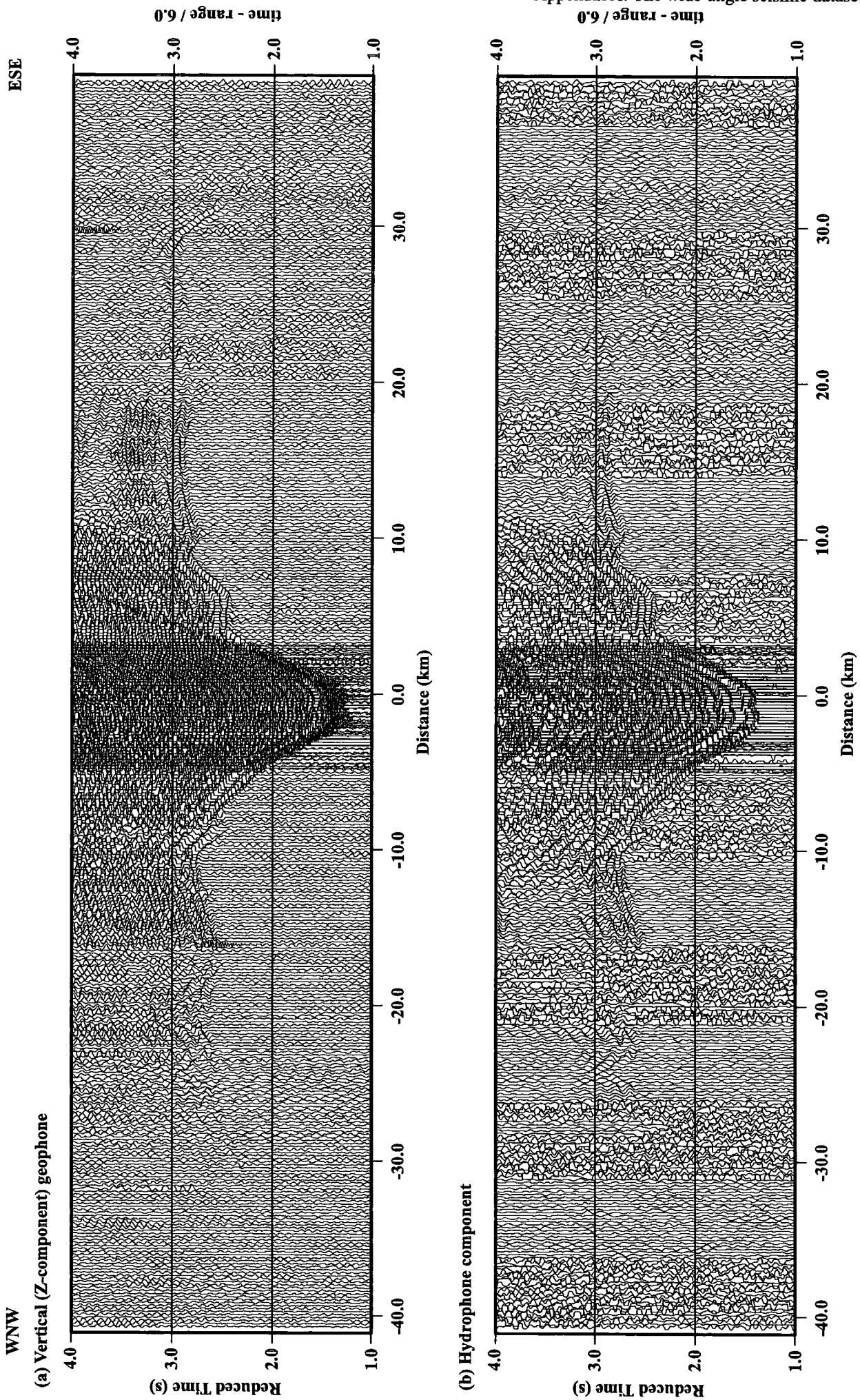

Figure A10: Line 6- NDOBS3

WNW ESE

(c) Horizontal (X-component) geophone

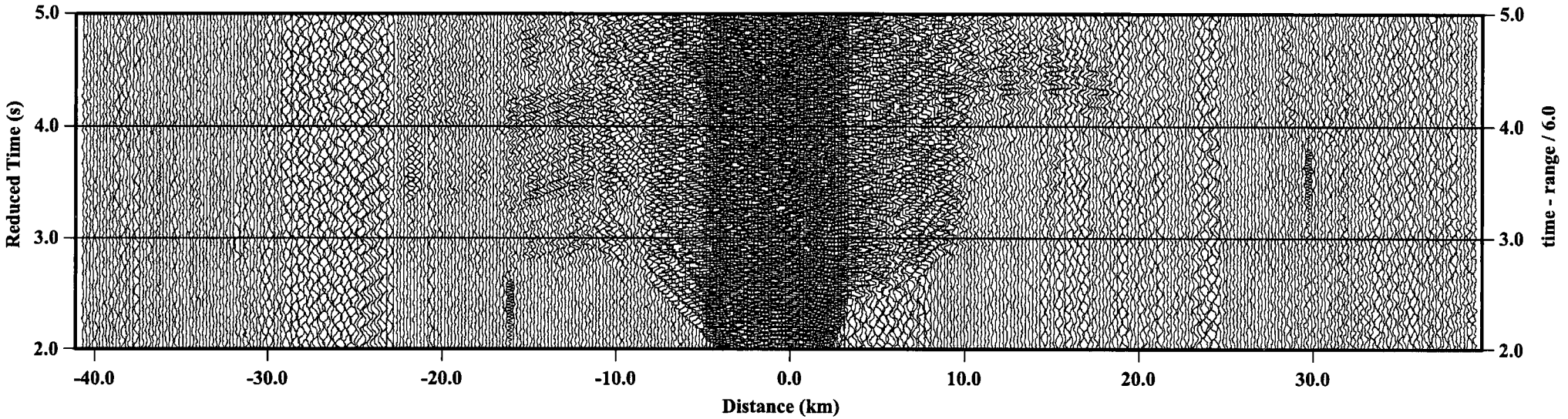

(d) Horizontal (Y-component) geophone

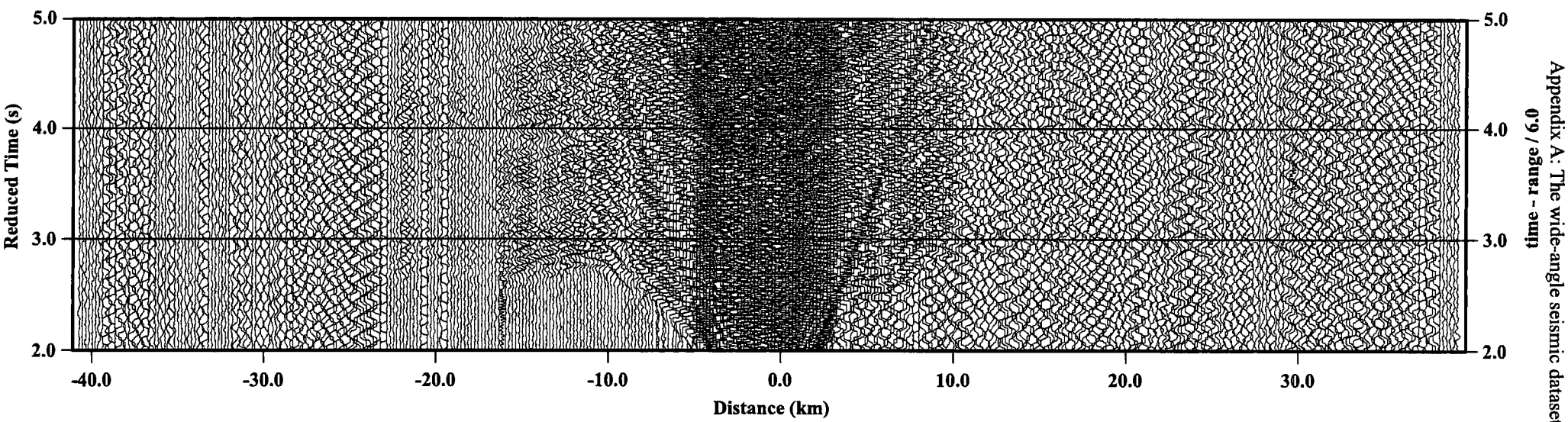

Figure A9 (cont.): Line 6- NDOBS3

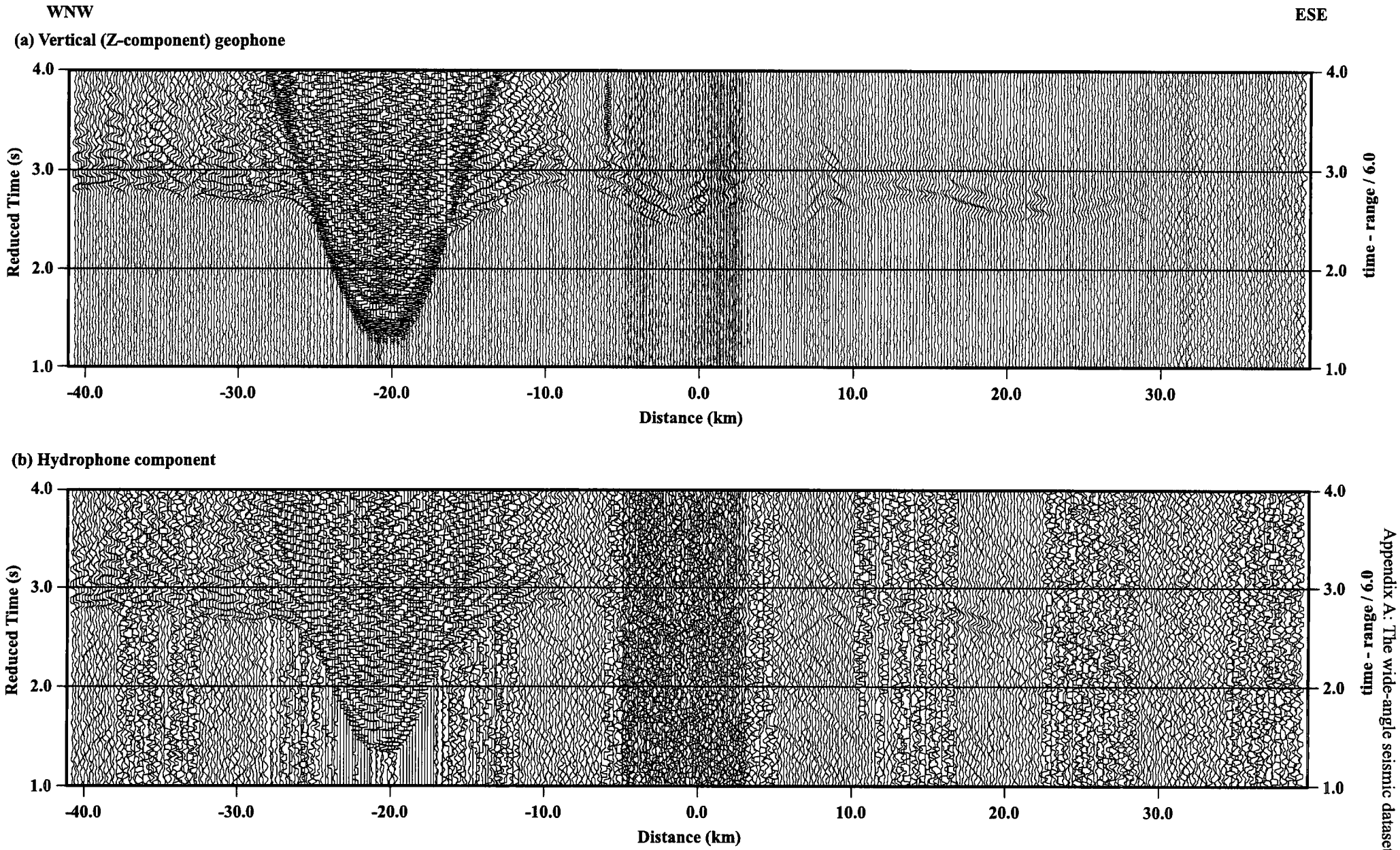

Figure A11: Line 6- NDOBS5

WNW ESE

(c) Horizontal (X-component) geophone

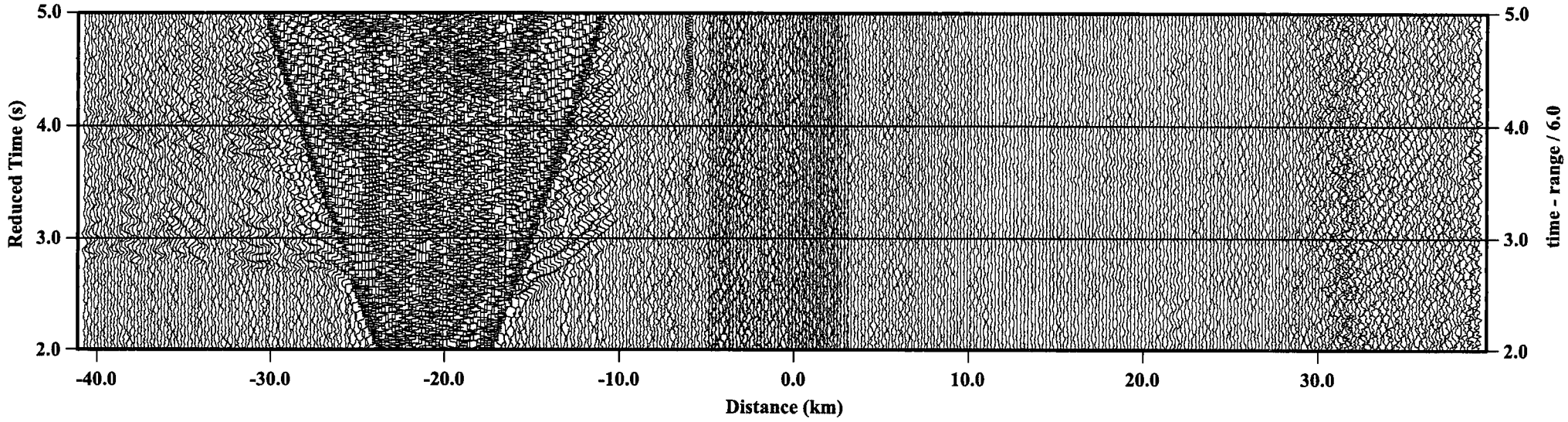

(d) Horizontal (Y-component) geophone

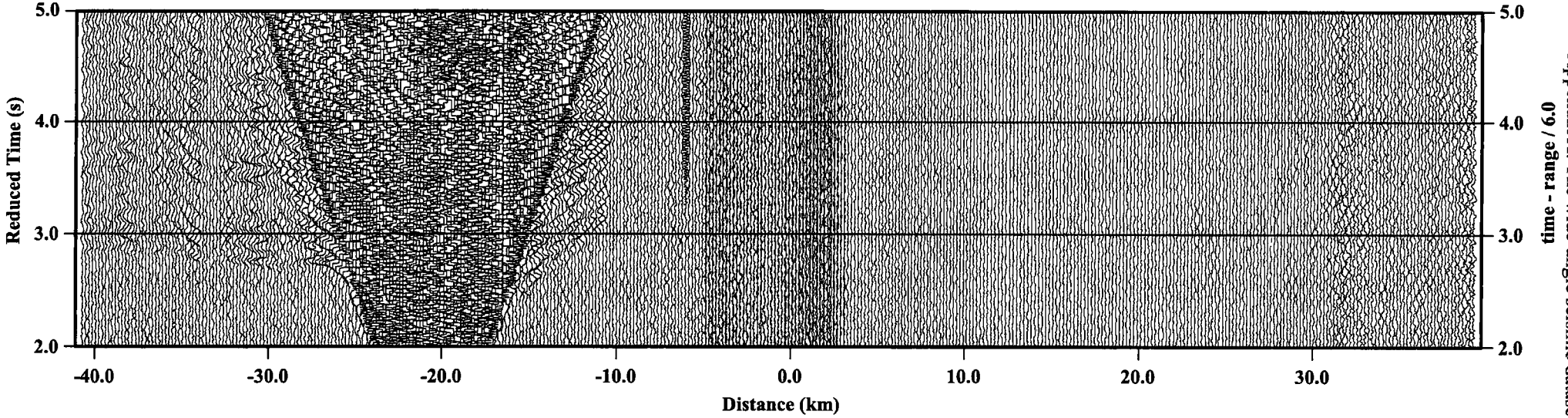

Figure A11 (cont.): Line 6- NDOBS5

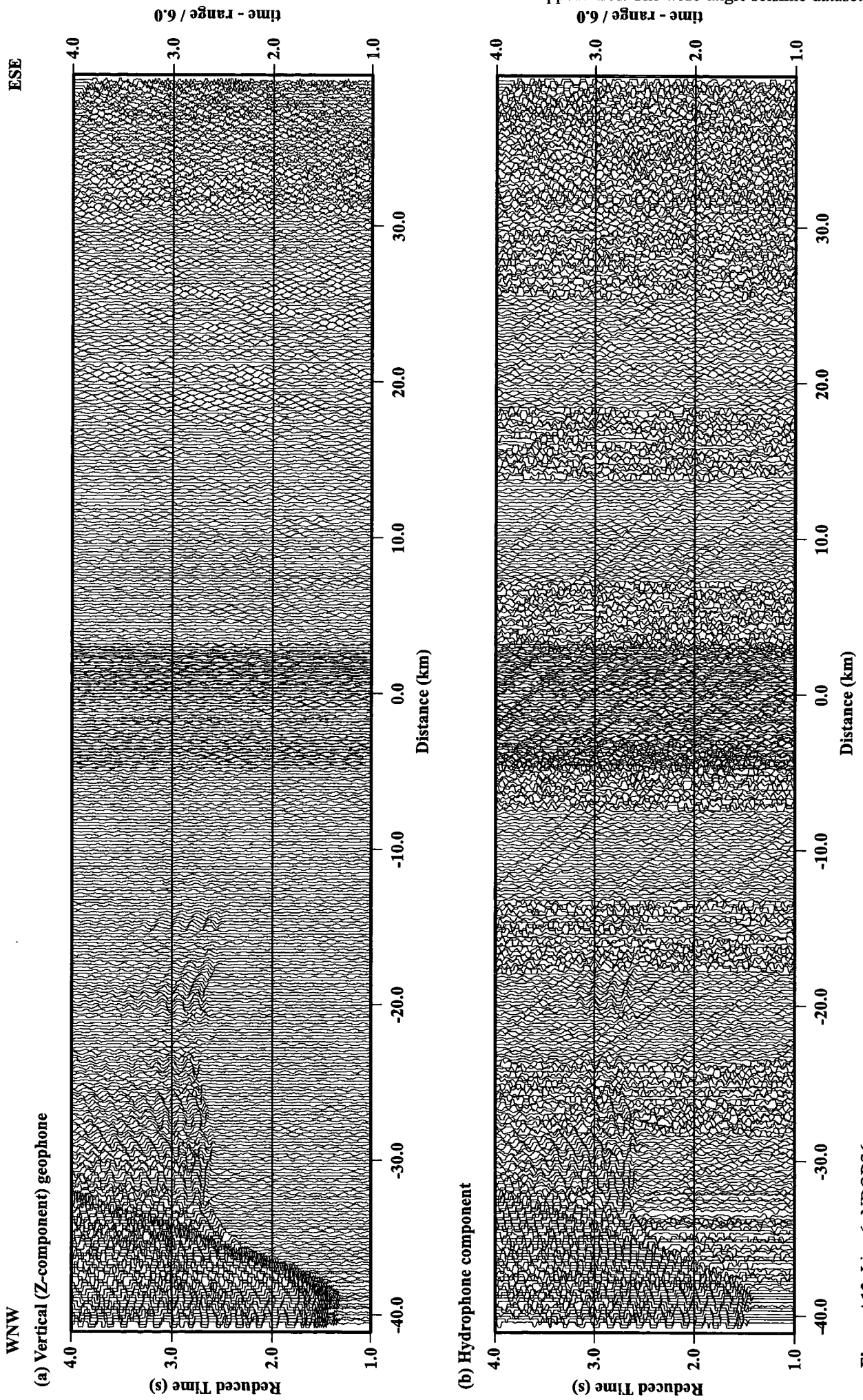

Figure A12: Line 6- NDOBS6

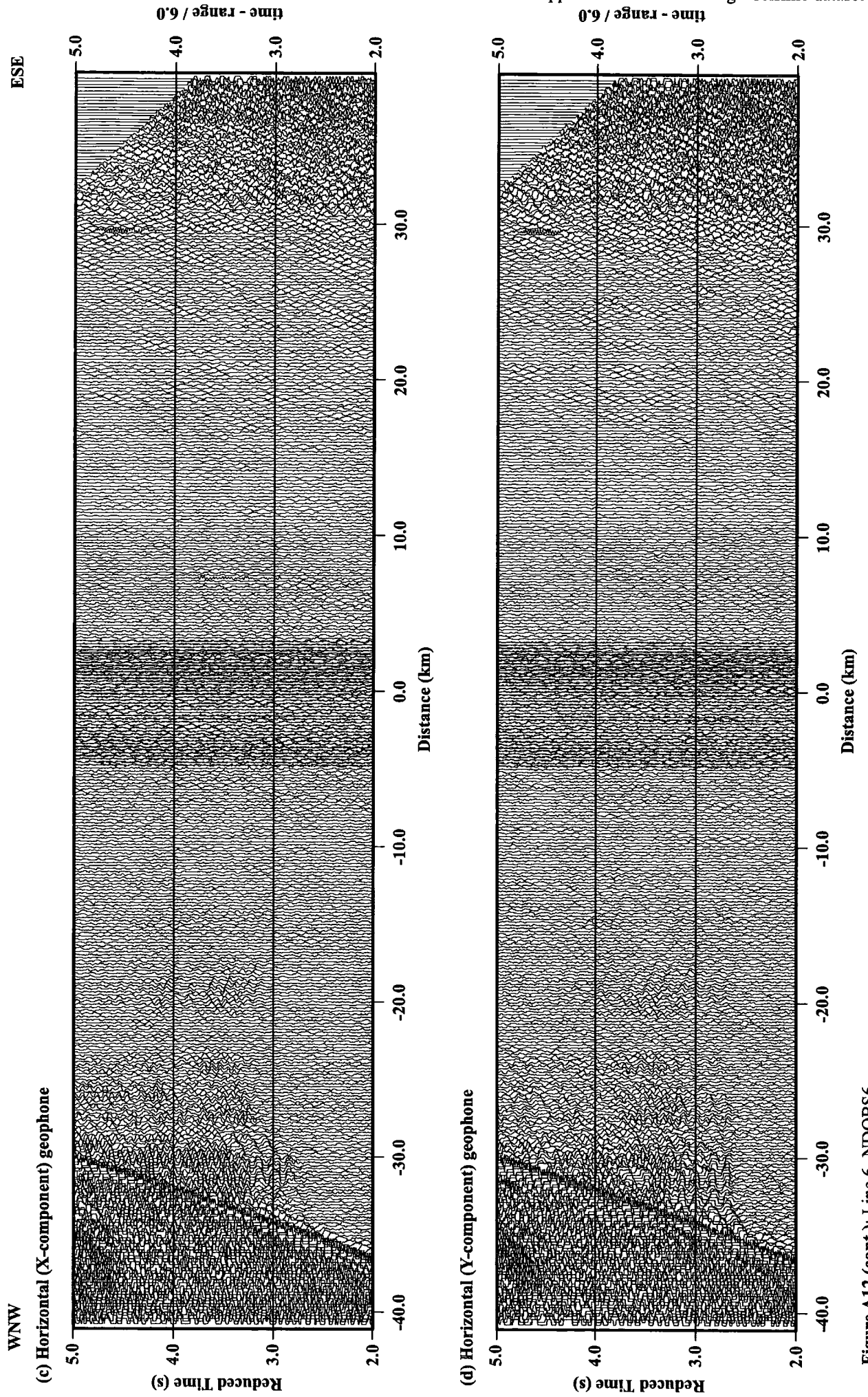

Figure A12 (cont.): Line 6- NDOBS6

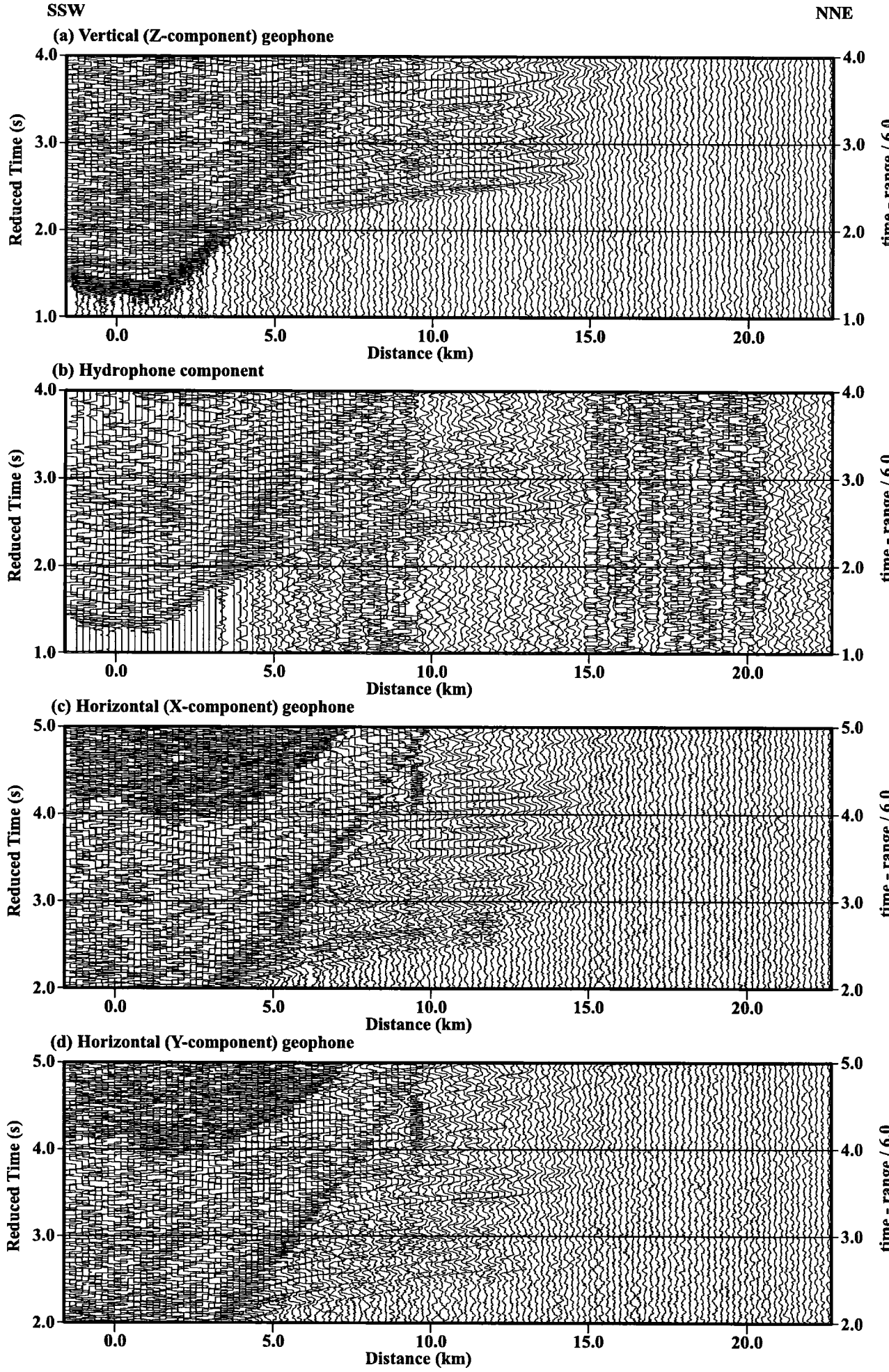

Figure A13: Line 4- SDOBS4

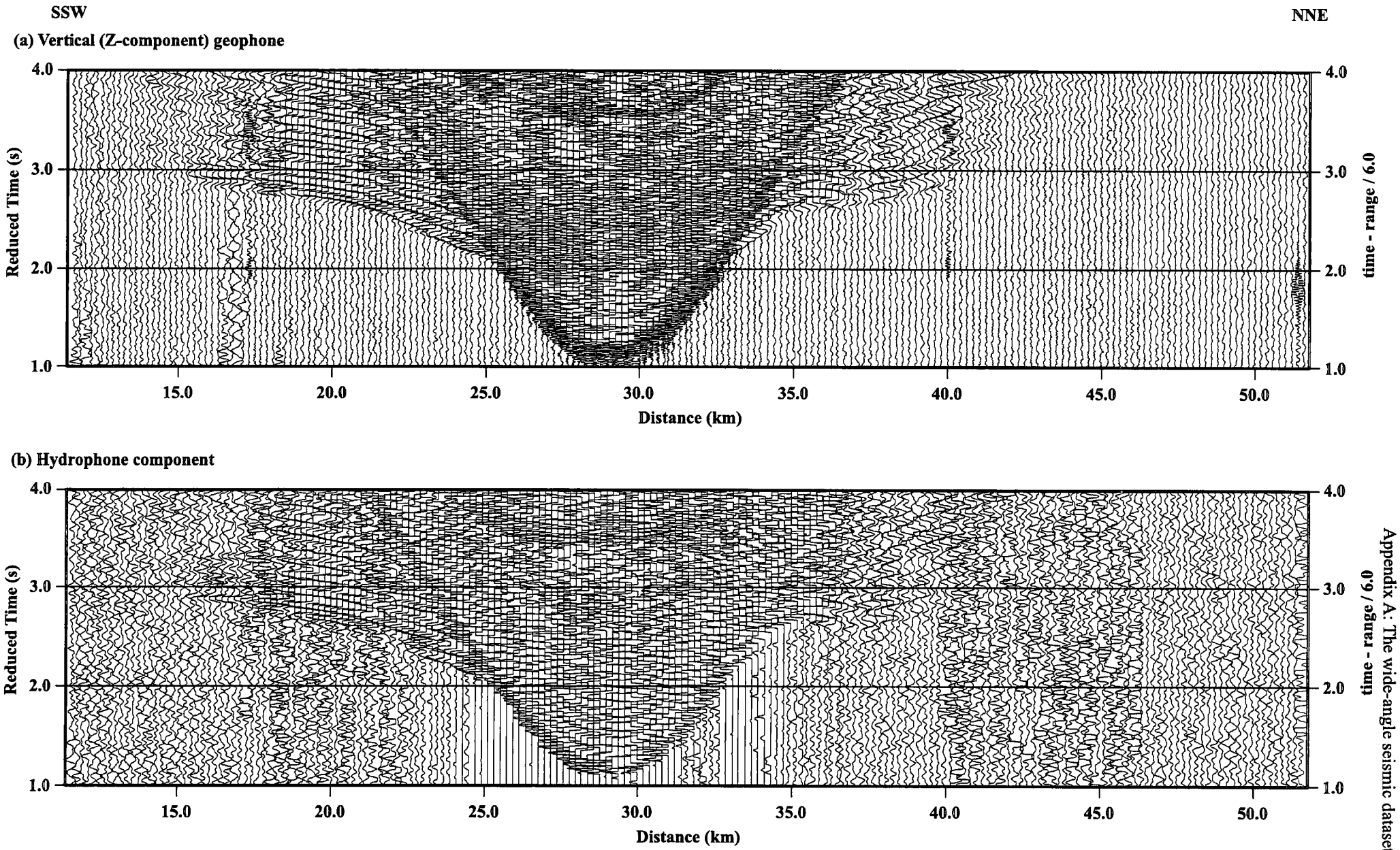

Figure A14: Line 4- NDOBS2

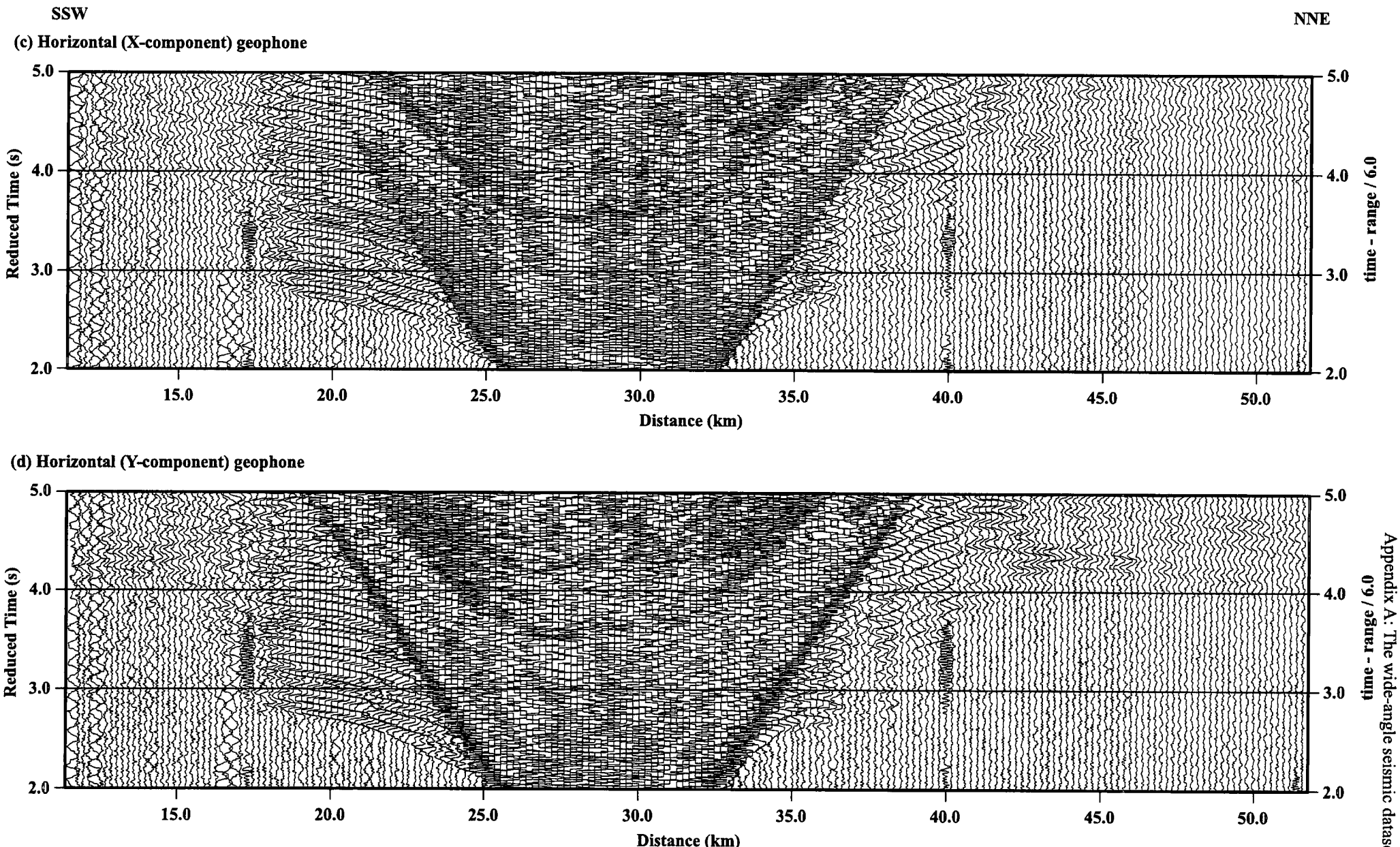

Figure A14 (cont.): Line 4- NDOBS2

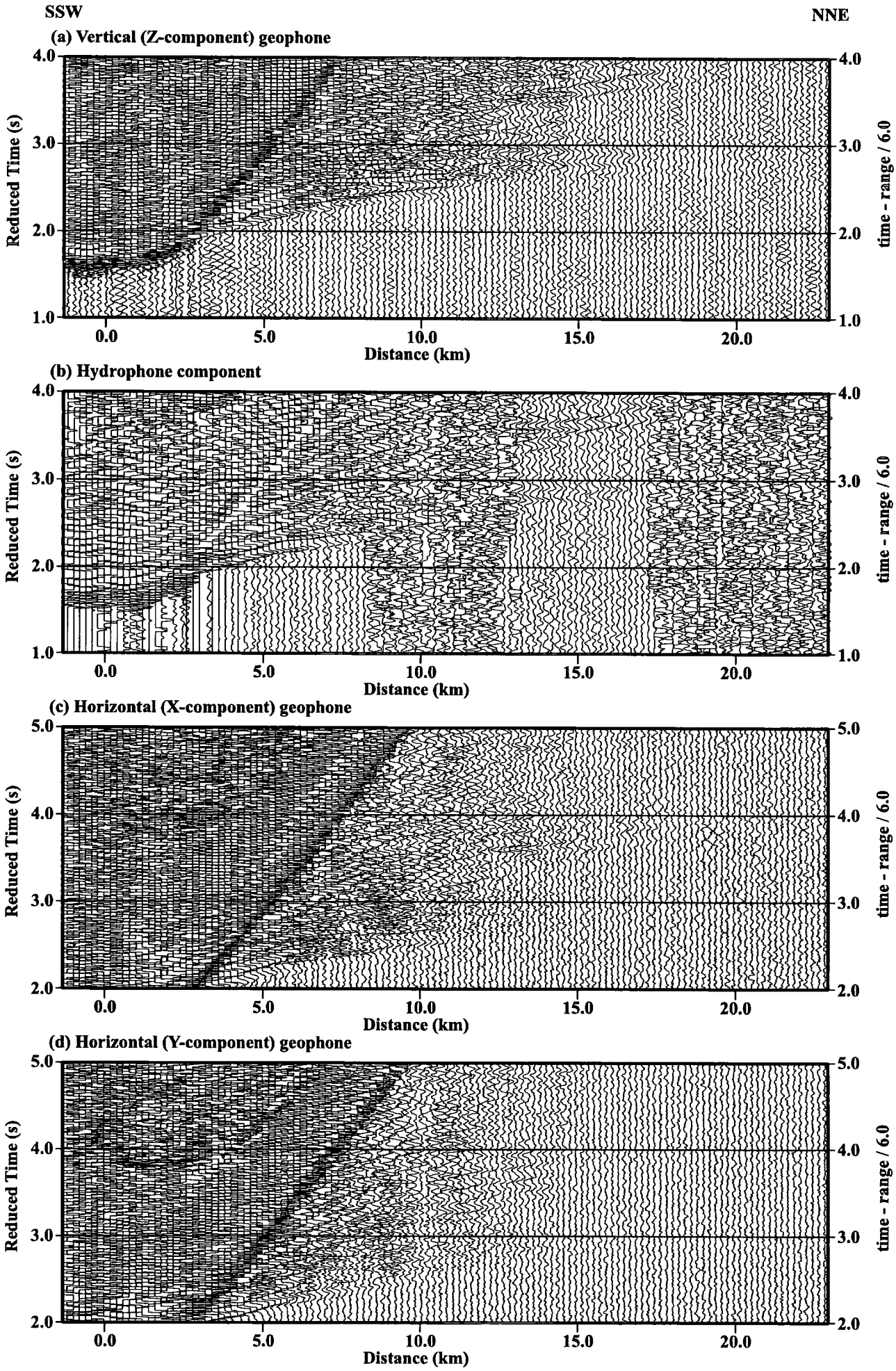

Figure A15: Line 9- SDOBS3

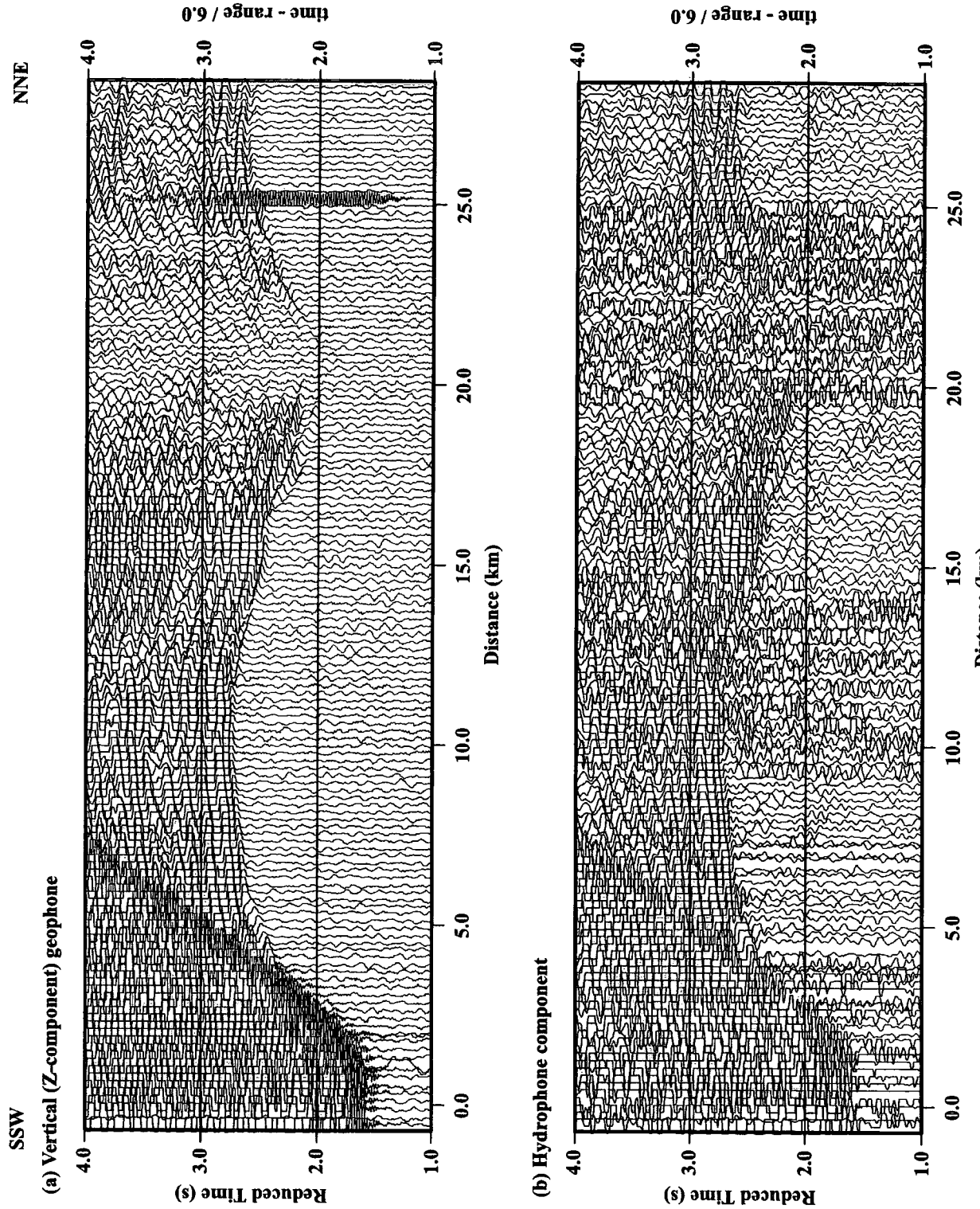

Figure A16: Line 5- SDOBS1

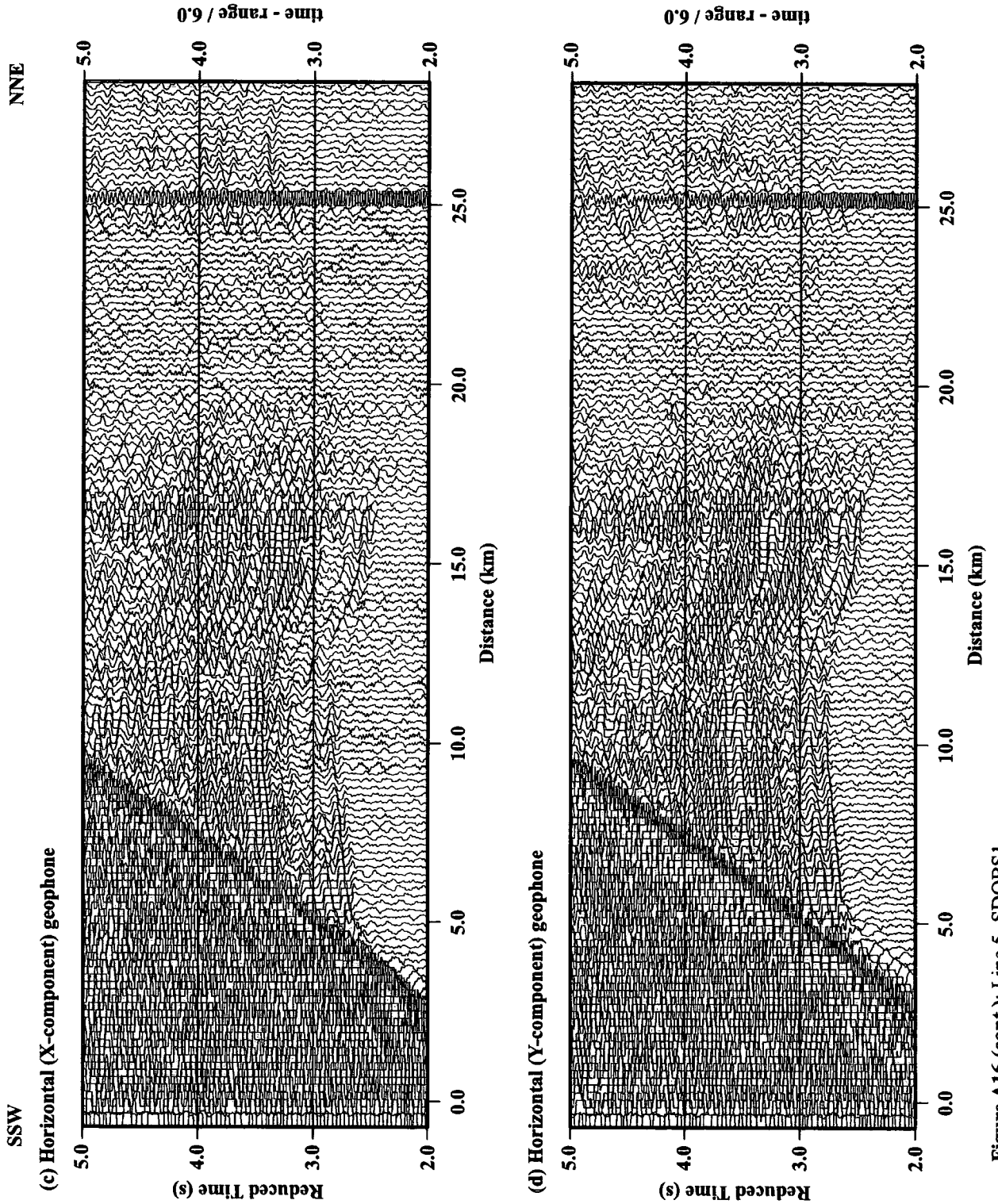

Figure A16 (cont.): Line 5- SDOBS1

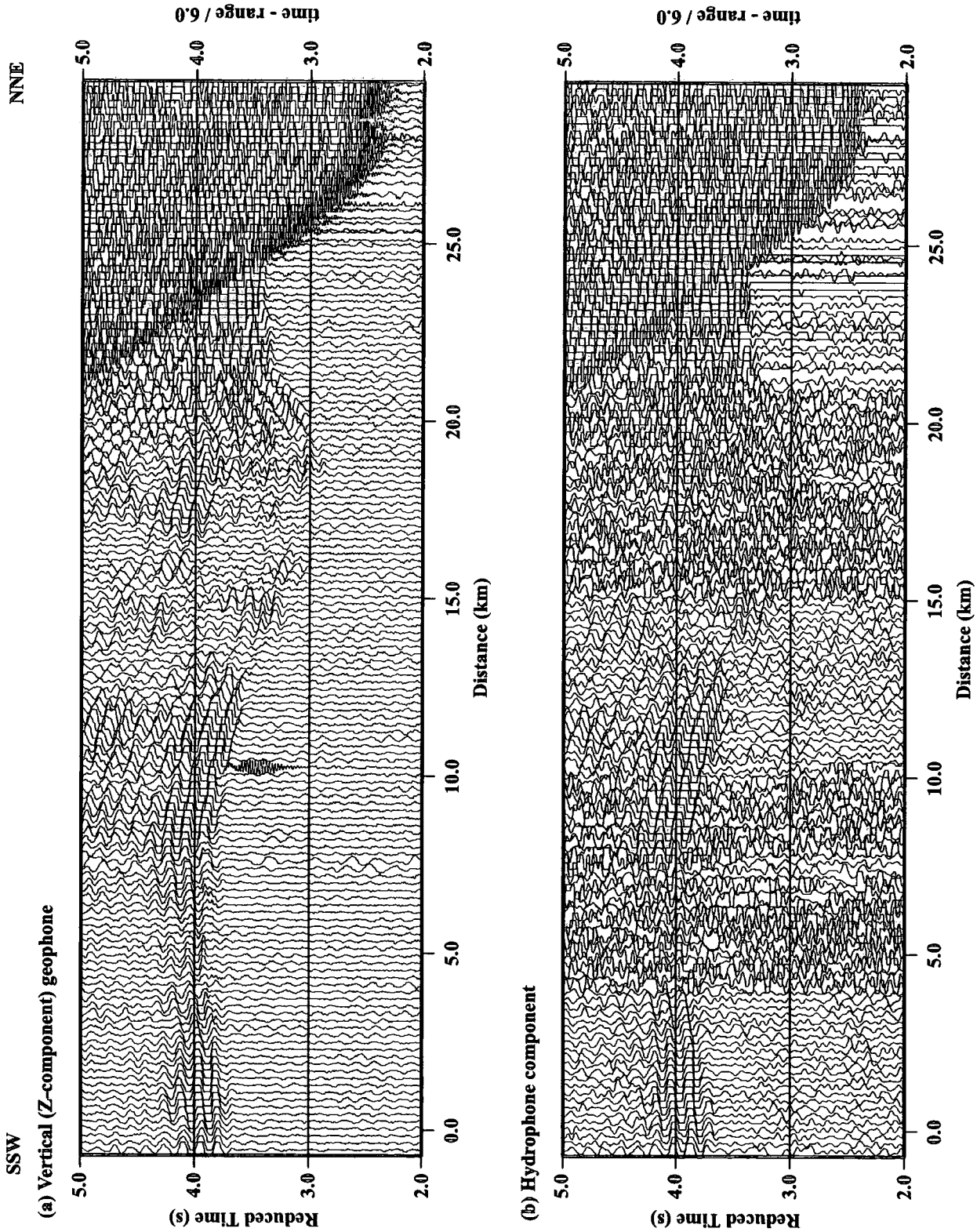

Figure A17: Line 5- NDOBS6

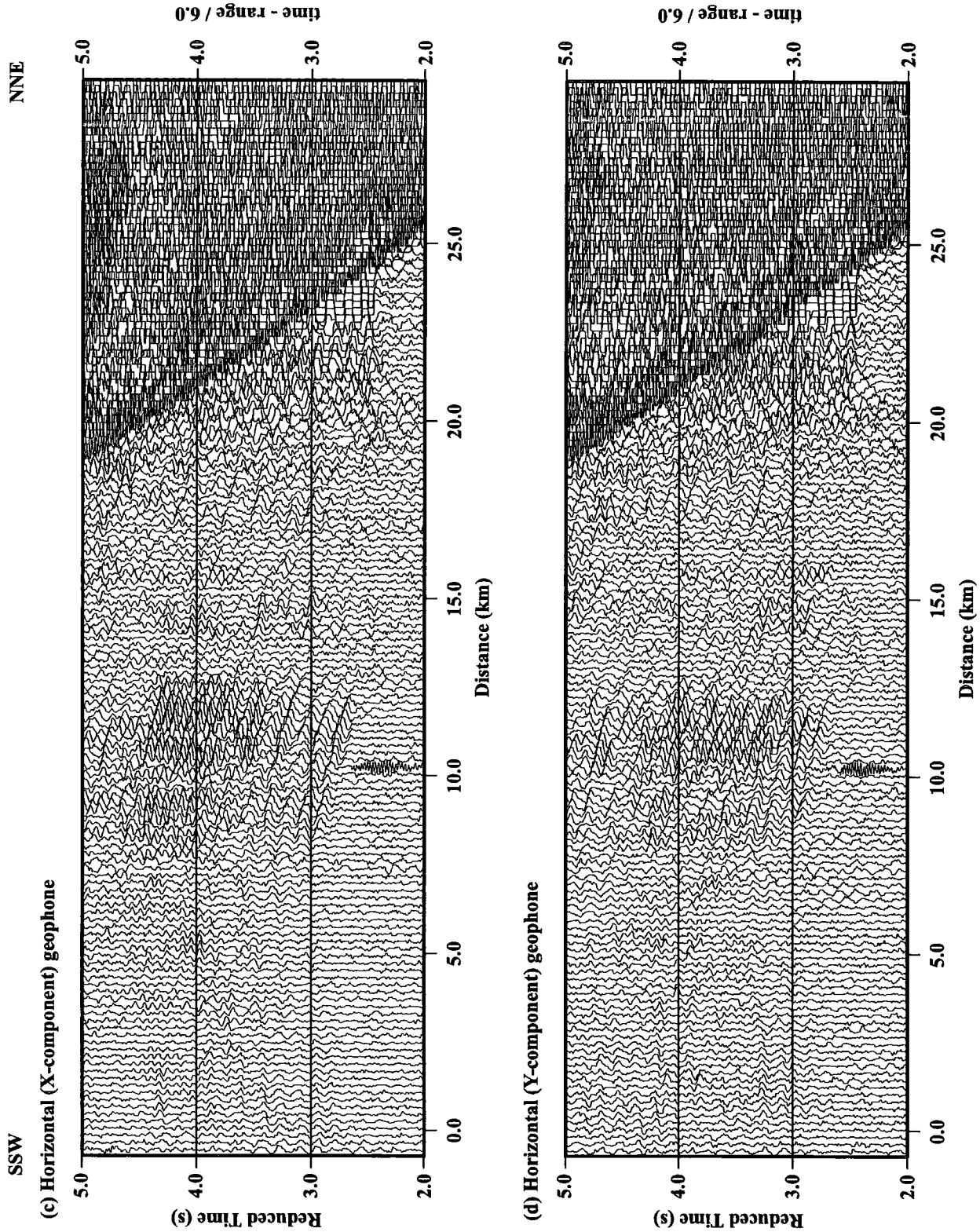

Figure A17 (cont.): Line 5- NDOBS6

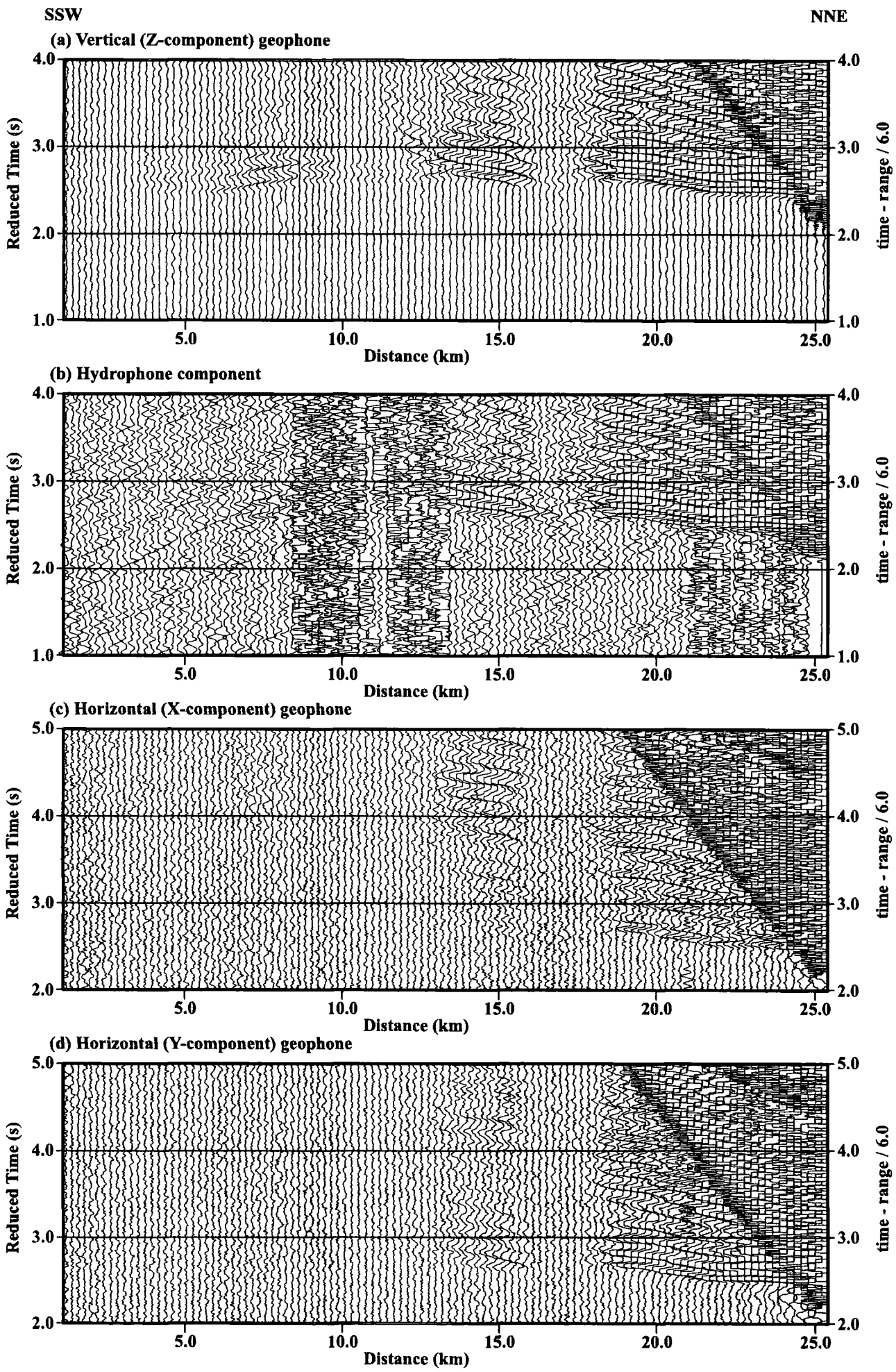

Figure A18: Line 11- SDOBS5

Appendix B

Ray-trace modelling of the final velocity-depth models

A complete set of the final ray-trace modelled sections for each DOBS located on the main 2-D seismic profiles (see figure A1 for instrument and line locations) are shown in Appendix B. Each figure is composed of three parts:

(a) Vertical geophone record section overlain by the travel time picks.

(b) Synthetic seismograms calculated from the final velocity-depth model.

(c) Final velocity-depth model with a subset of the rays used to calculate (b).

To prevent repetitive description of the figures in Appendix B, an extended figure caption applicable to all of the following figures is detailed below.

Figure B?: Ray-trace modelling of the final seismic model for ?DOBS? on Line ? (see figure A1 for instrument and line locations).
(a) Filtered vertical component record section plotted at true amplitude to show the amplitude variations of the first arrivals. Seismograms are plotted with a reduction velocity of 6.0 km s^{-1} and alternate traces are plotted for clarity. The darker band near 0 km model offset shows where the same axial region was crossed over twice (i.e. double the density of traces). Note that the crosses represent travel time picks made on unfiltered data. Inset I displays some of the lower crustal (and upper mantle) phases in greater detail.
(b) Synthetic seismograms calculated from the final model. The geometrical ray-traced solution is shown by a long-dashed line and the direct water waves, Moho reflections (P_mP) and major crustal (P_g) and mantle (P_n) diving rays are annotated. Travel time picks from the observed data are shown by solid dots [cf. crosses in (a)], where the dot size is equivalent to the travel time error.
(c) Final model with, for clarity, a subset of the rays used to calculate the synthetic seismograms shown in (b). Solid lines indicate the location and geometry of the seabed, sediment, layer 2A/2B boundary, layer 2/3 boundary and the seismic Moho. Dotted lines represent the 2.5, 3.0, 3.5, 4.0 (layer 2A/2B boundary), 4.5, 5.0, 5.5, 6.0, 6.25, 6.5, 6.75, 7.0 (Moho) and 8.0 km s^{-1} isovelocity contours.

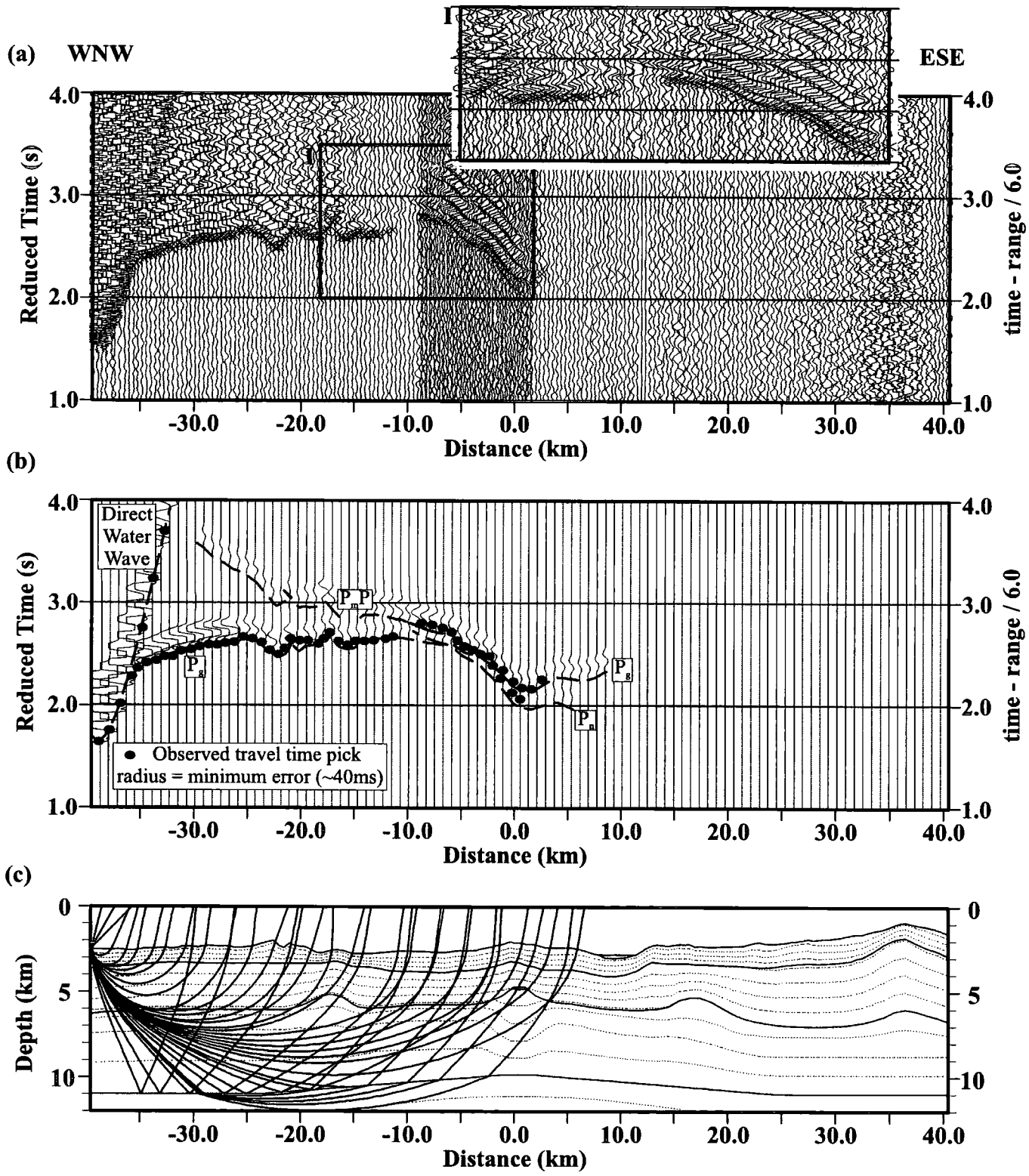

Figure B1: Ray-trace modelling of the final across-axis seismic model for SDOBS1 on Line 1 (see figure A1 for instrument and line locations). Display parameters are described at the start of Appendix B.
(a) Filtered vertical component record section.
(b) Synthetic seismograms calculated from the final velocity-depth model.
(c) Final model with a subset of the rays used to calculate the synthetic seismograms shown in (b).

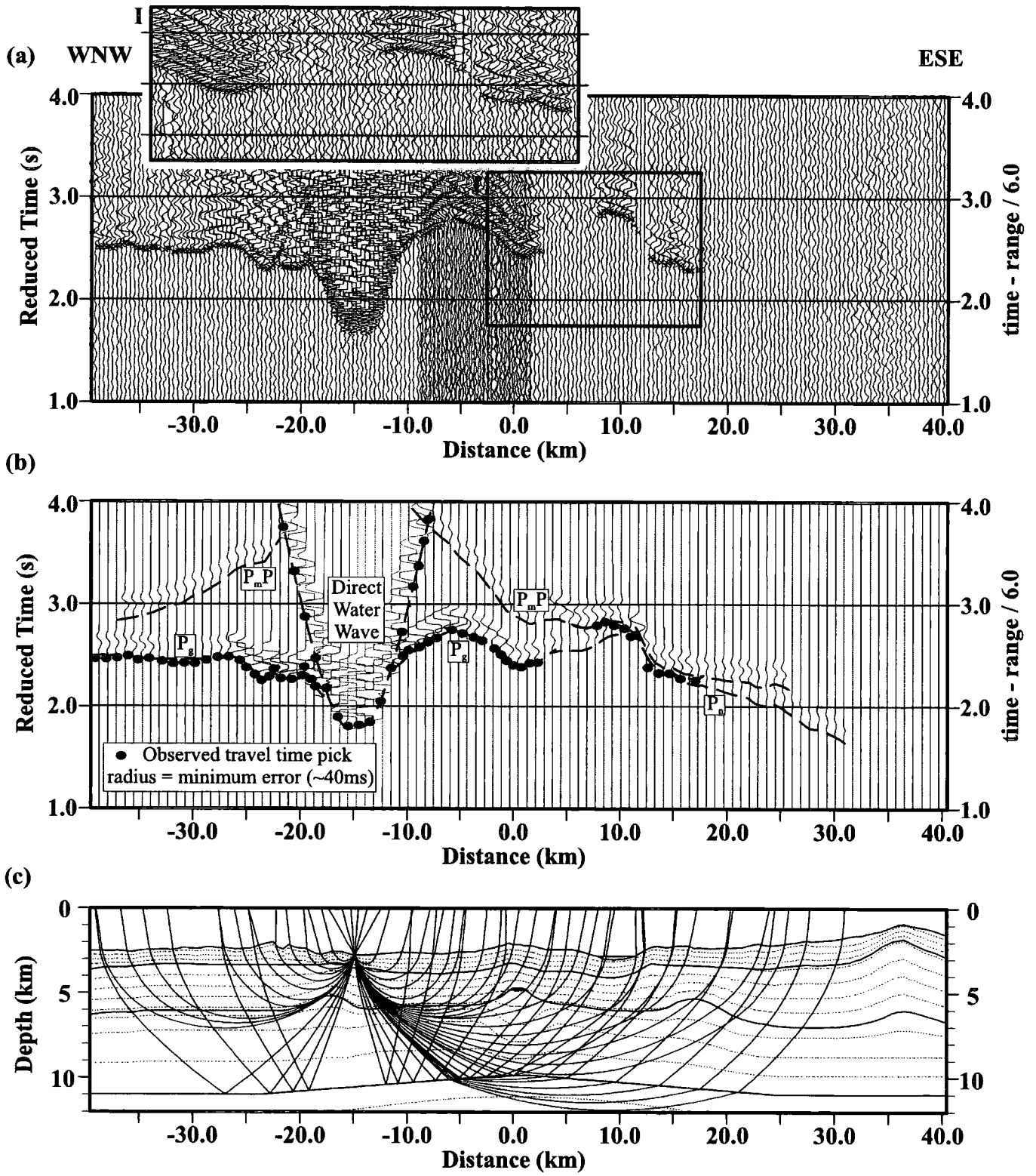

Figure B2: Ray-trace modelling of the final across-axis seismic model for SDOBS2 on Line 1 (see figure A1 for instrument and line locations). Display parameters are described at the start of Appendix B.
(a) Filtered vertical component record section.
(b) Synthetic seismograms calculated from the final velocity-depth model.
(c) Final model with a subset of the rays used to calculate the synthetic seismograms shown in (b).

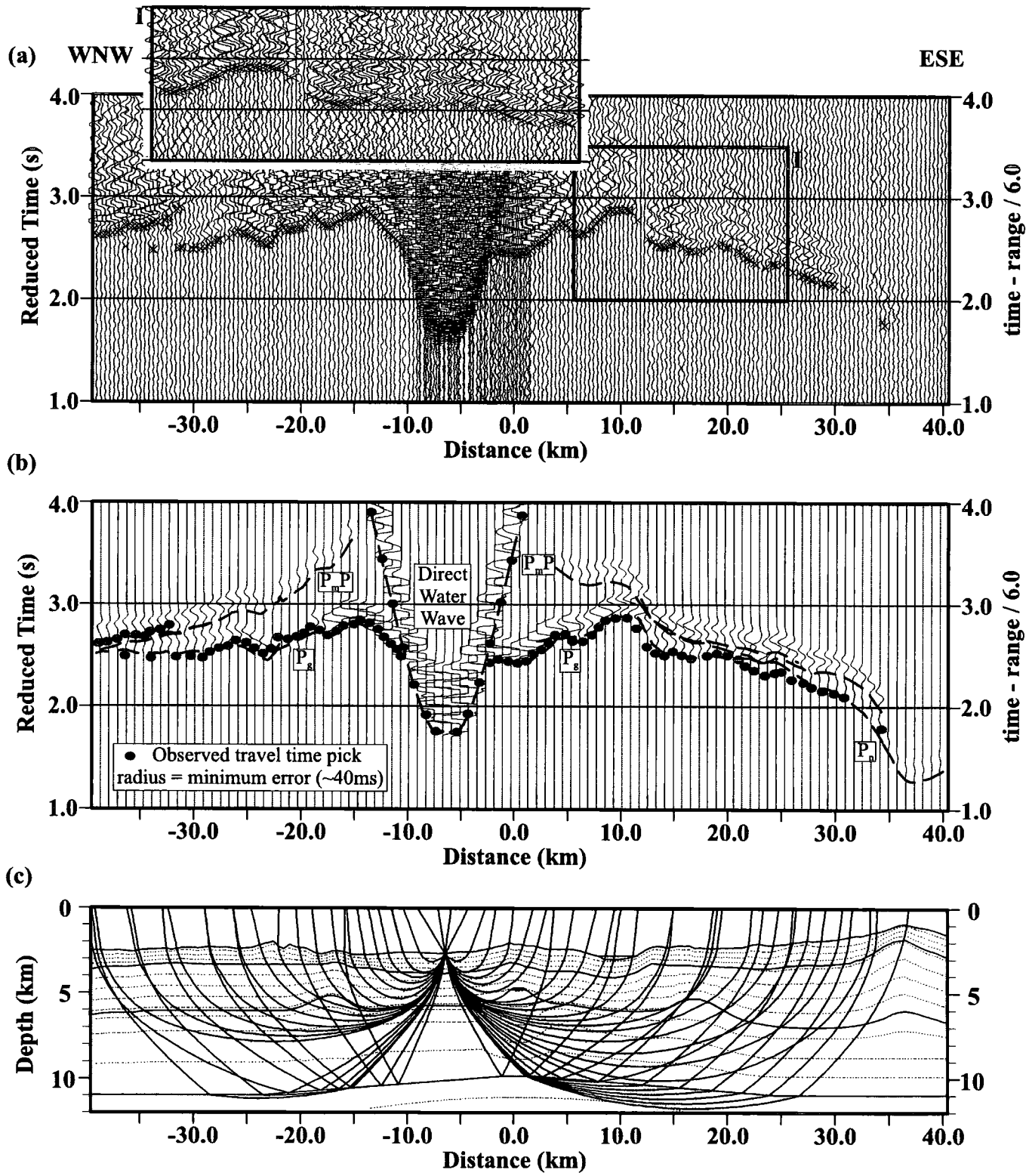

Figure B3: Ray-trace modelling of the final across-axis seismic model for SDOBS3 on Line 1 (see figure A1 for instrument and line locations). Display parameters are described at the start of Appendix B.
(a) Filtered vertical component record section.
(b) Synthetic seismograms calculated from the final velocity-depth model.
(c) Final model with a subset of the rays used to calculate the synthetic seismograms shown in (b).

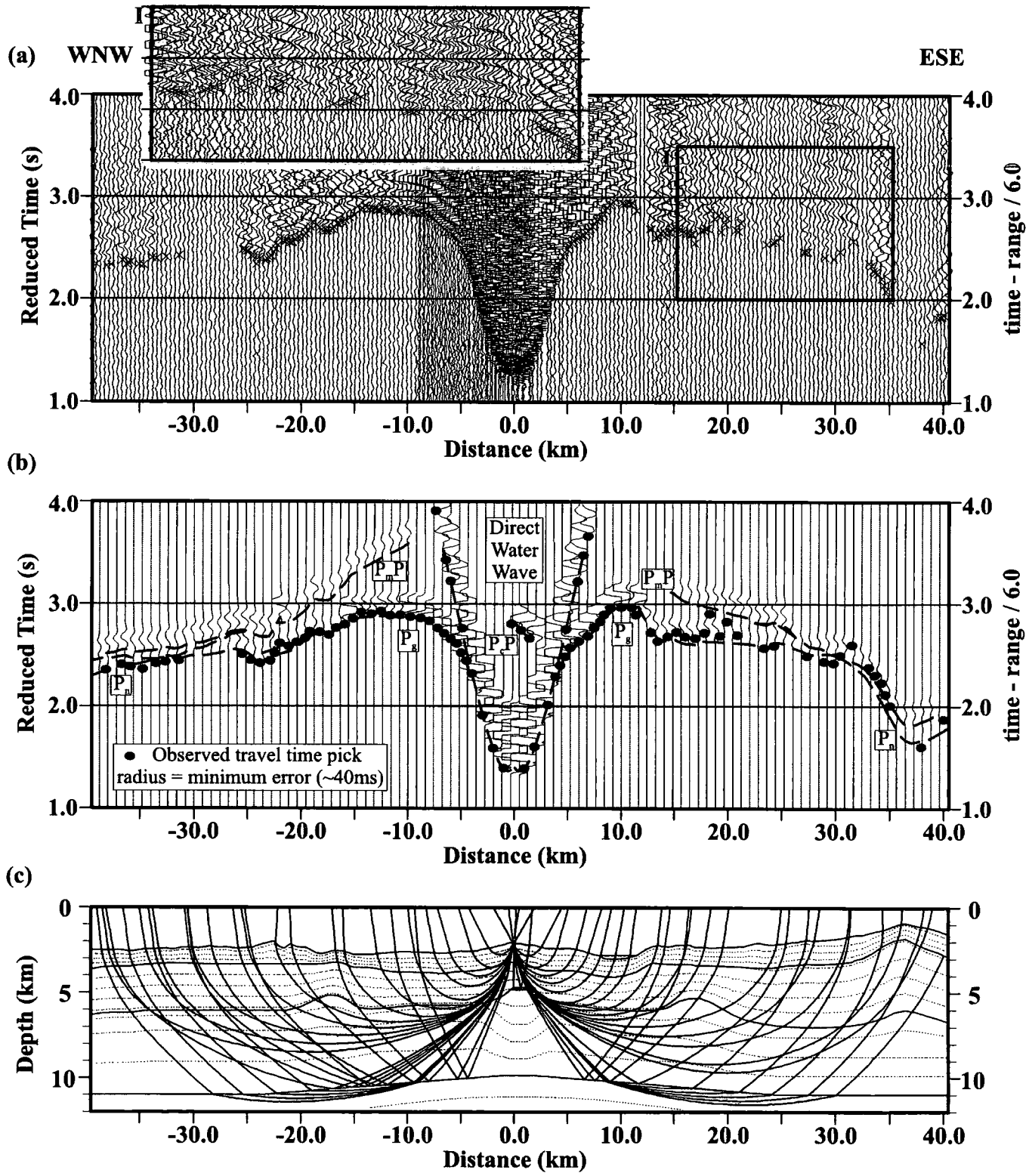

Figure B4: Ray-trace modelling of the final across-axis seismic model for SDOBS4 on Line 1 (see figure A1 for instrument and line locations). Display parameters are described at the start of Appendix B.
(a) Filtered vertical component record section.
(b) Synthetic seismograms calculated from the final velocity-depth model.
(c) Final model with a subset of the rays used to calculate the synthetic seismograms shown in (b).

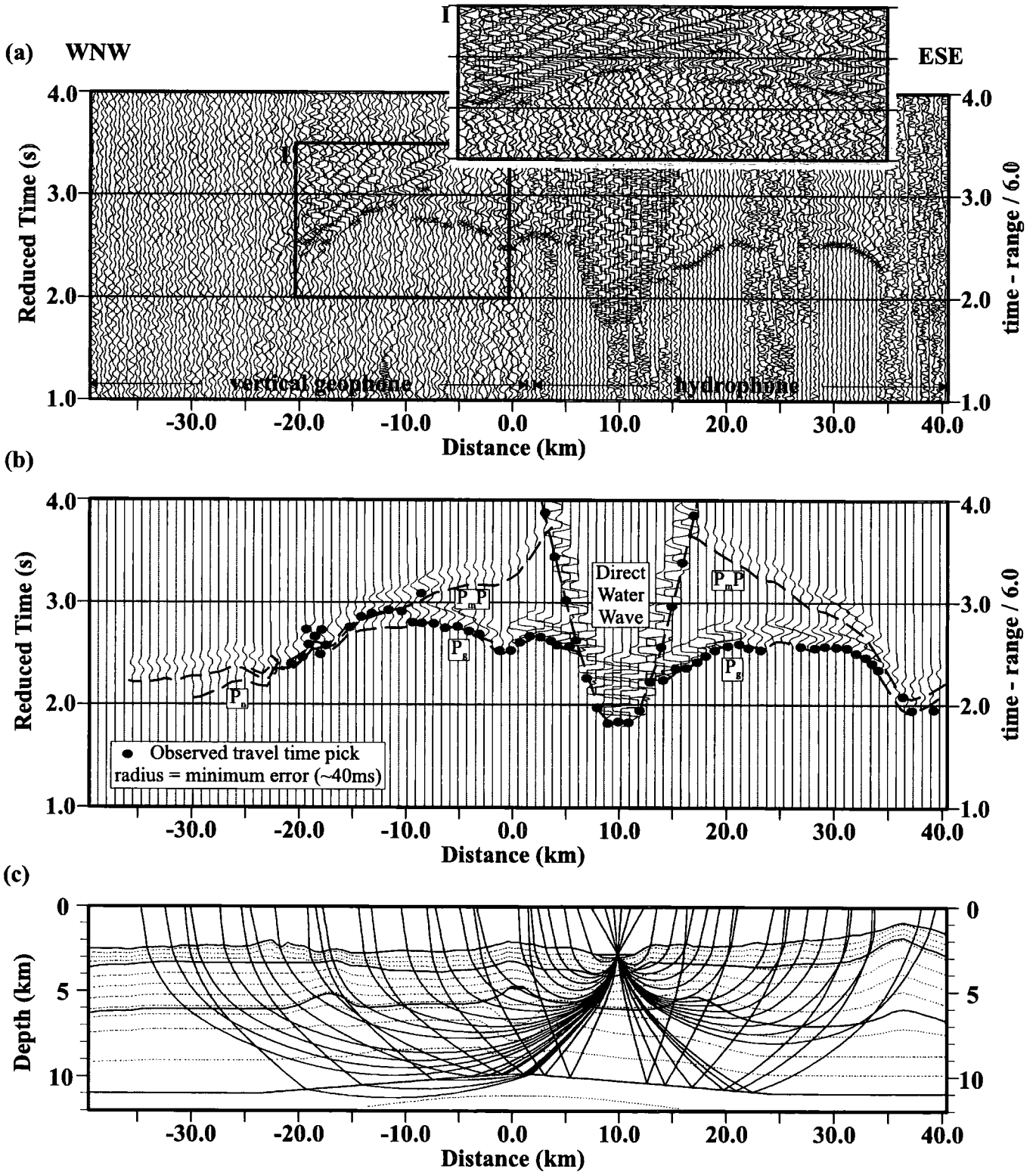

Figure B5: Ray-trace modelling of the final across-axis seismic model for SDOBS5 on Line 1 (see figure A1 for instrument and line locations). Display parameters are described at the start of Appendix B.
(a) Filtered vertical component record section.
(b) Synthetic seismograms calculated from the final velocity-depth model.
(c) Final model with a subset of the rays used to calculate the synthetic seismograms shown in (b).

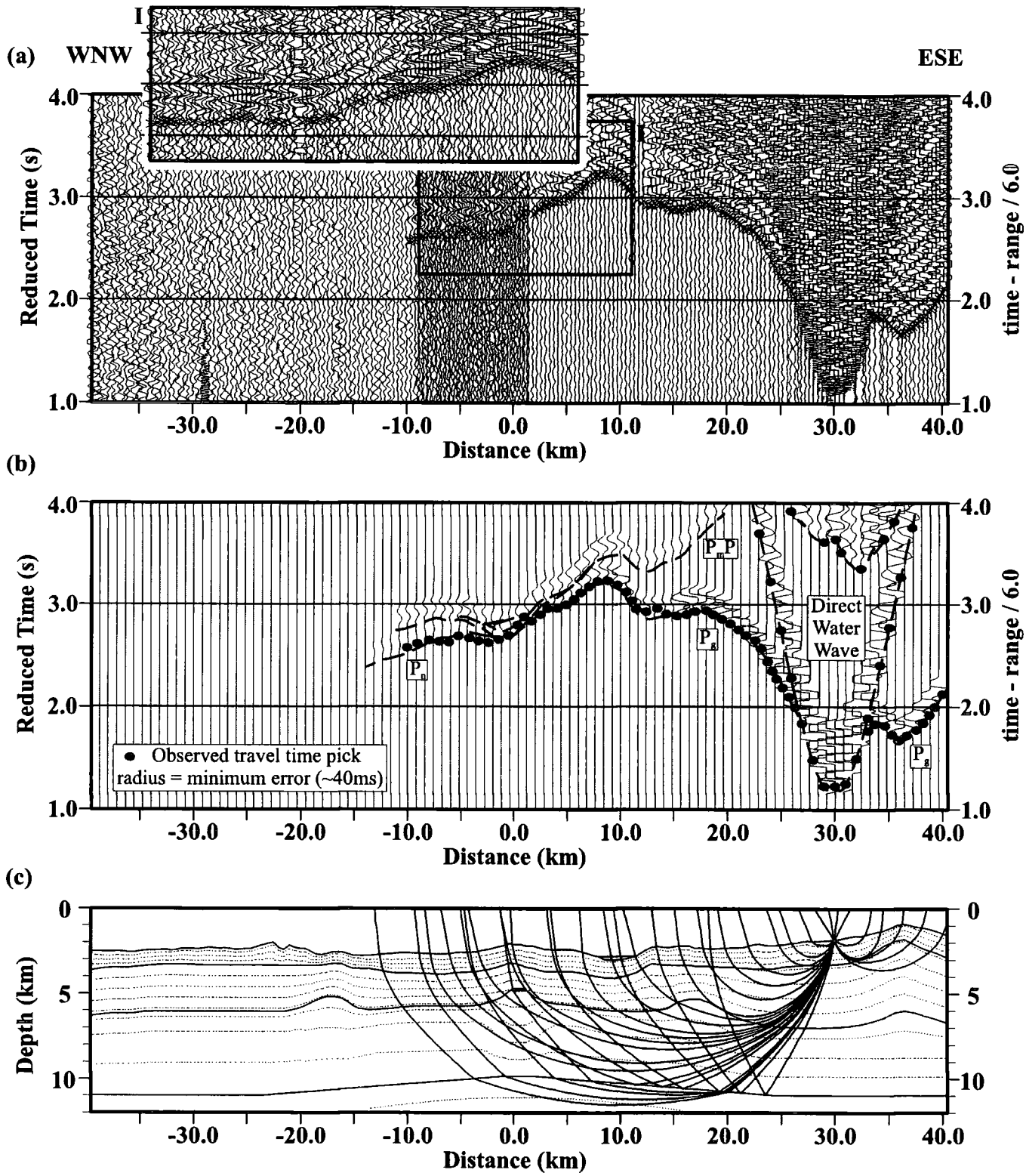

Figure B6: Ray-trace modelling of the final across-axis seismic model for SDOBS6 on Line 1 (see figure A1 for instrument and line locations). Display parameters are described at the start of Appendix B.
(a) Filtered vertical component record section.
(b) Synthetic seismograms calculated from the final velocity-depth model.
(c) Final model with a subset of the rays used to calculate the synthetic seismograms shown in (b).

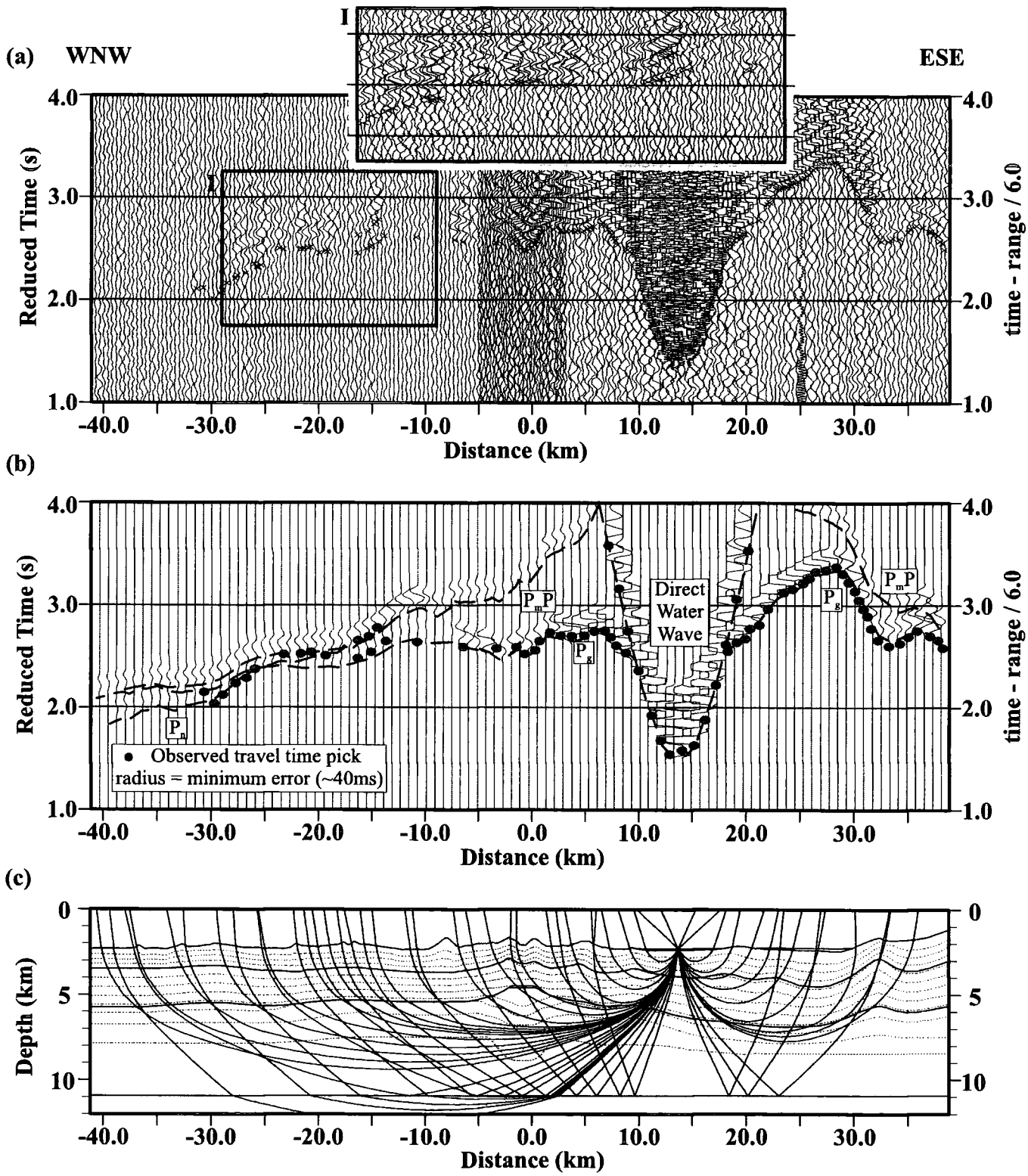

Figure B7: Ray-trace modelling of the final across-axis seismic model for NDOBS1 on Line 6 (see figure A1 for instrument and line locations). Display parameters are described at the start of Appendix B.
(a) Filtered vertical component record section.
(b) Synthetic seismograms calculated from the final velocity-depth model.
(c) Final model with a subset of the rays used to calculate the synthetic seismograms shown in (b).

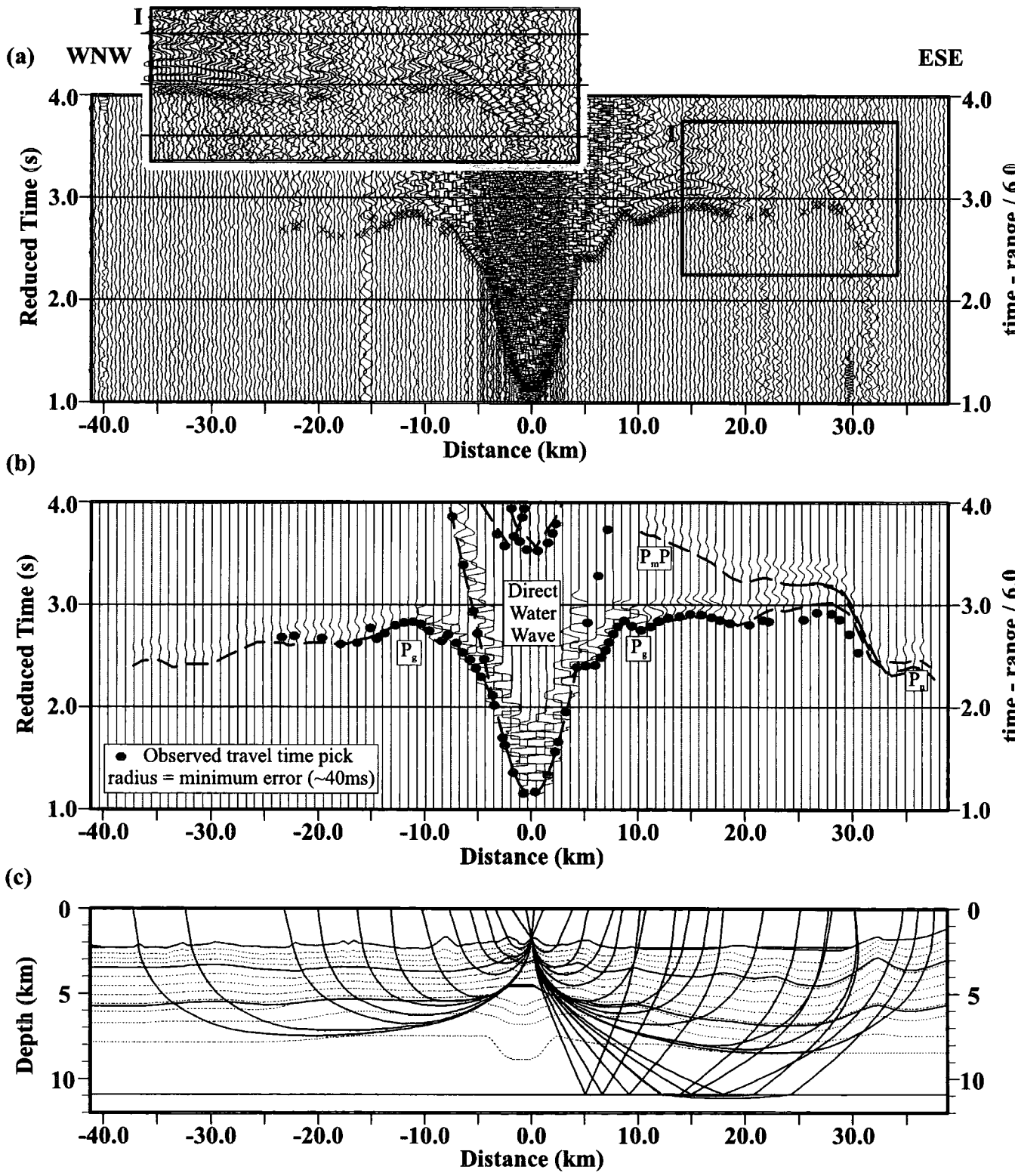

Figure B8: Ray-trace modelling of the final across-axis seismic model for NDOBS2 on Line 6 (see figure A1 for instrument and line locations). Display parameters are described at the start of Appendix B.
(a) Filtered vertical component record section.
(b) Synthetic seismograms calculated from the final velocity-depth model.
(c) Final model with a subset of the rays used to calculate the synthetic seismograms shown in (b).

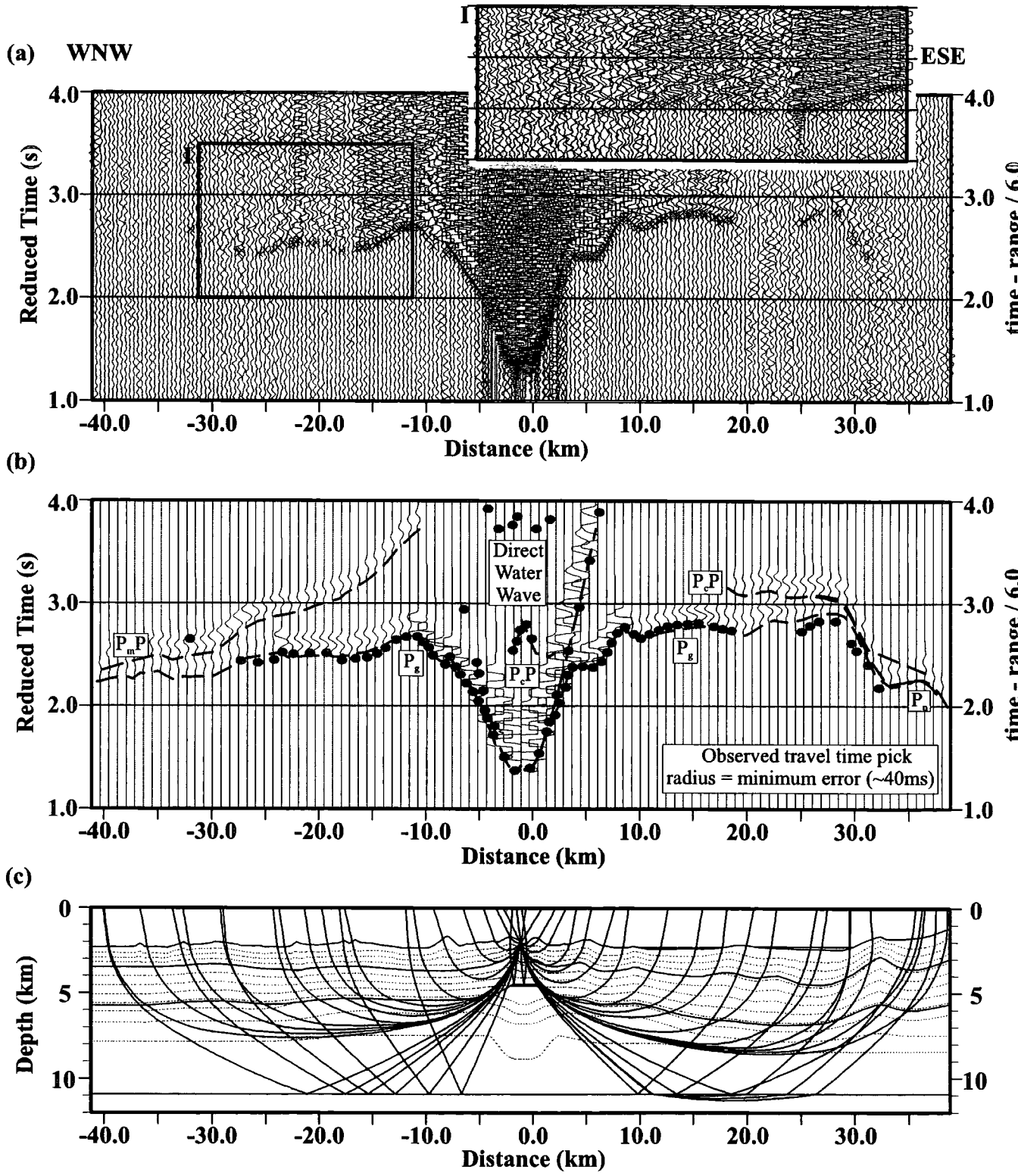

Figure B9: Ray-trace modelling of the final across-axis seismic model for NDOBS3 on Line 6 (see figure A1 for instrument and line locations). Display parameters are described at the start of Appendix B.
(a) Filtered vertical component record section.
(b) Synthetic seismograms calculated from the final velocity-depth model.
(c) Final model with a subset of the rays used to calculate the synthetic seismograms shown in (b).

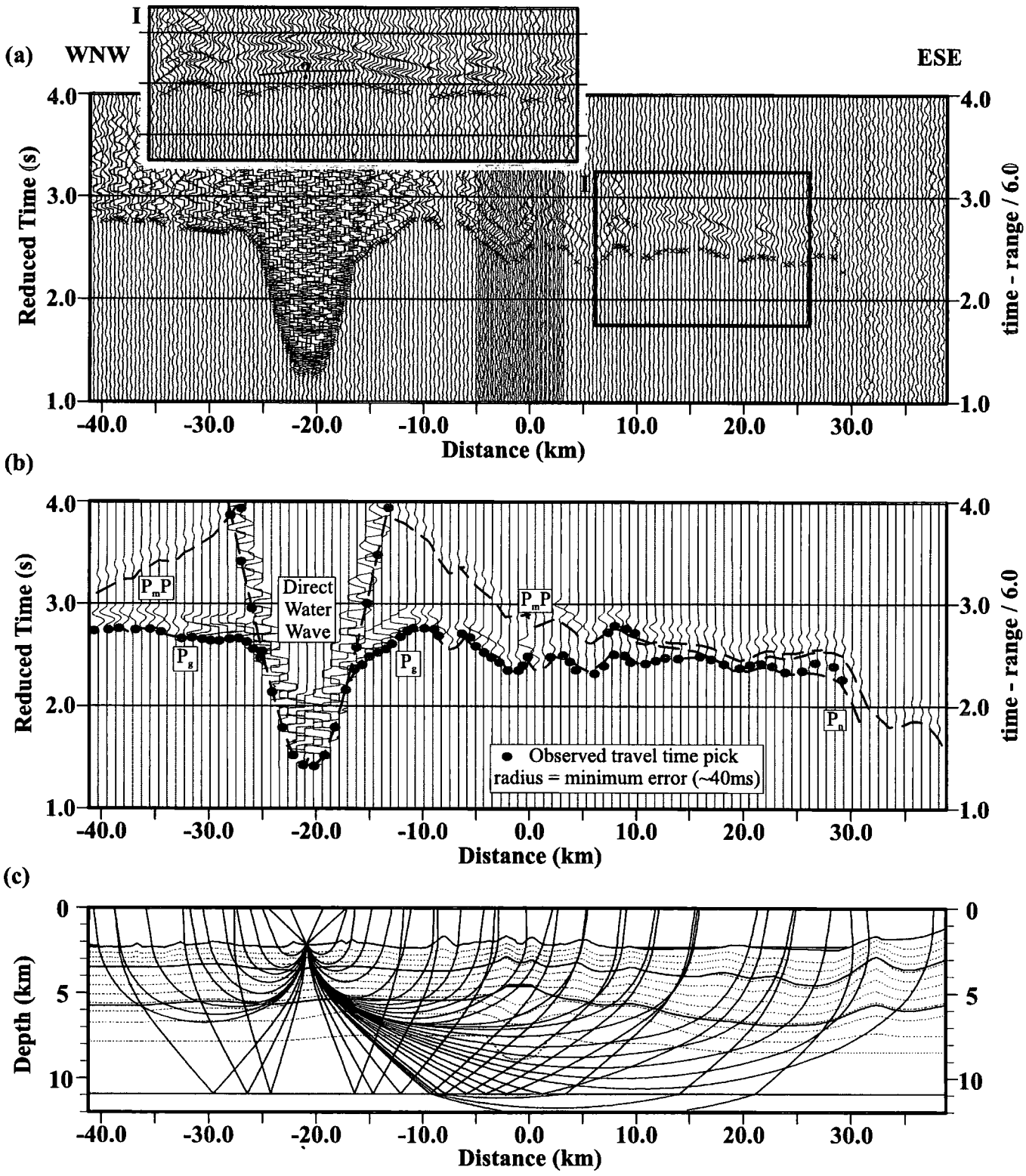

Figure B10: Ray-trace modelling of the final across-axis seismic model for NDOBS5 on Line 6 (see figure A1 for instrument and line locations). Display parameters are described at the start of Appendix B.
(a) Filtered vertical component record section.
(b) Synthetic seismograms calculated from the final velocity-depth model.
(c) Final model with a subset of the rays used to calculate the synthetic seismograms shown in (b).

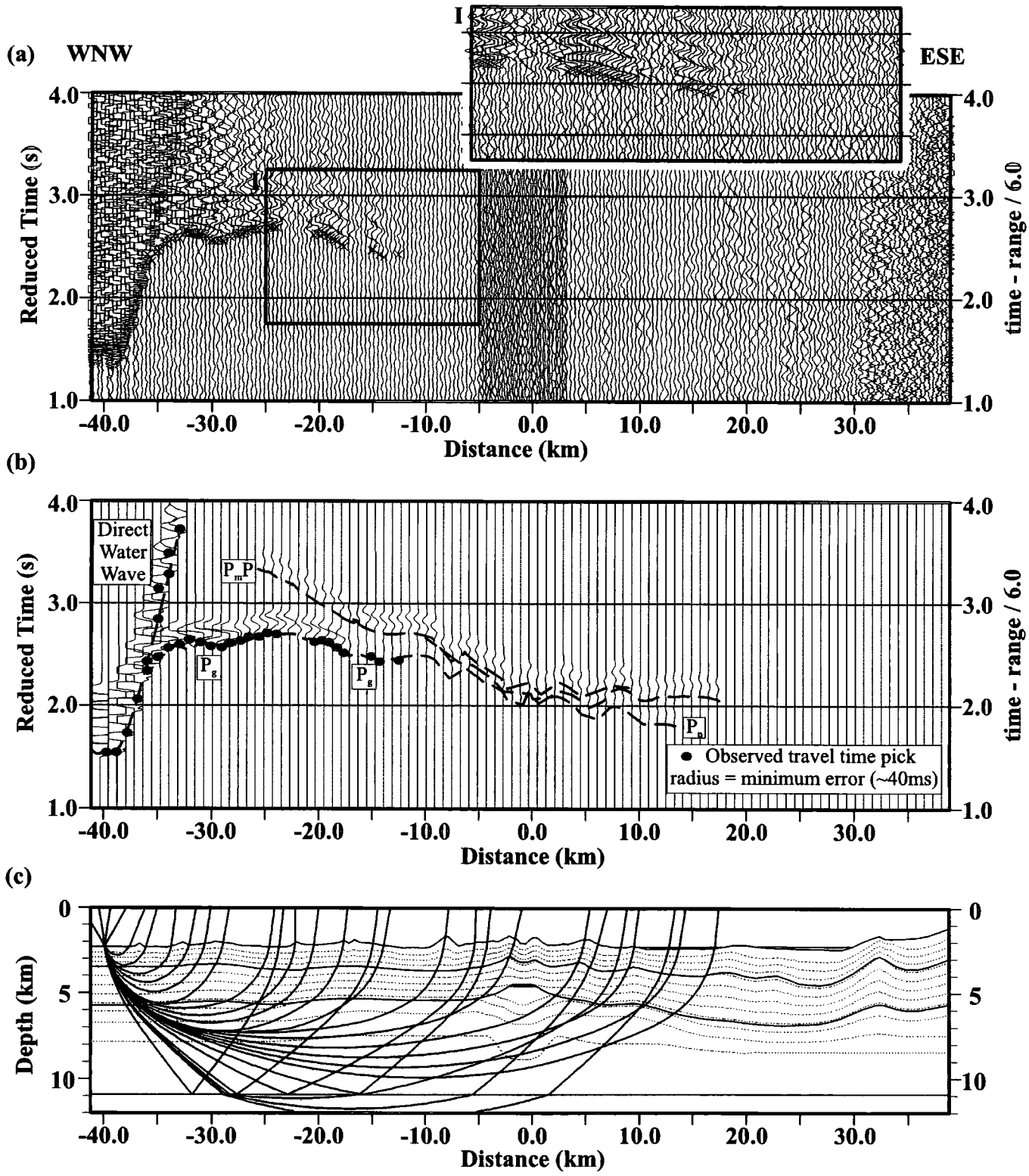

Figure B11: Ray-trace modelling of the final across-axis seismic model for NDOBS6 on Line 6 (see figure A1 for instrument and line locations). Display parameters are described at the start of Appendix B.
(a) Filtered vertical component record section.
(b) Synthetic seismograms calculated from the final velocity-depth model.
(c) Final model with a subset of the rays used to calculate the synthetic seismograms shown in (b).

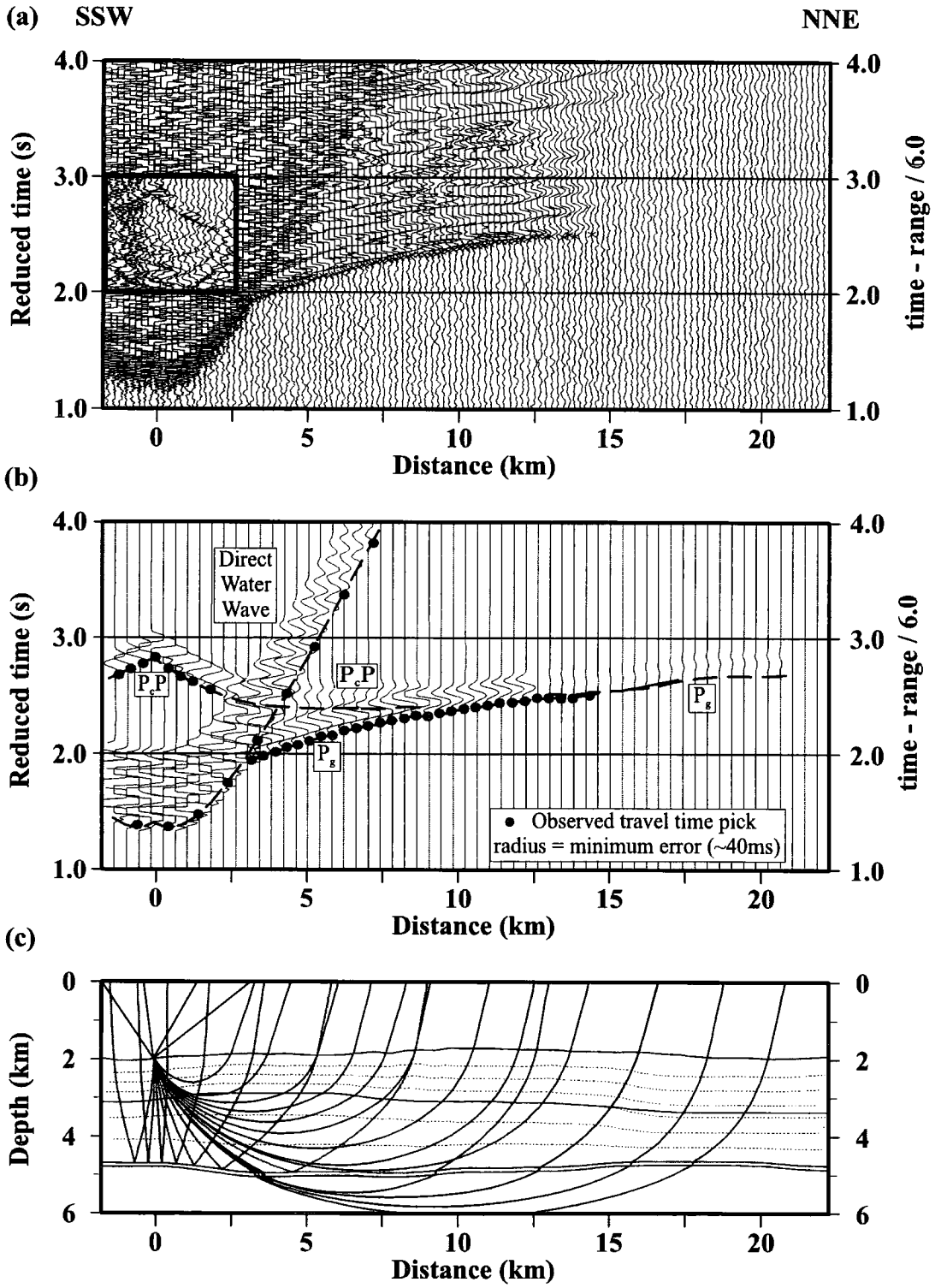

Figure B12: Ray-trace modelling of the final along-axis seismic model for SDOBS4 on Line 4 (see figure A1 for instrument and line locations). Display parameters are described at the start of Appendix B.
(a) Filtered vertical component record section.
(b) Synthetic seismograms calculated from the final velocity-depth model.
(c) Final model with a subset of the rays used to calculate the synthetic seismograms shown in (b).

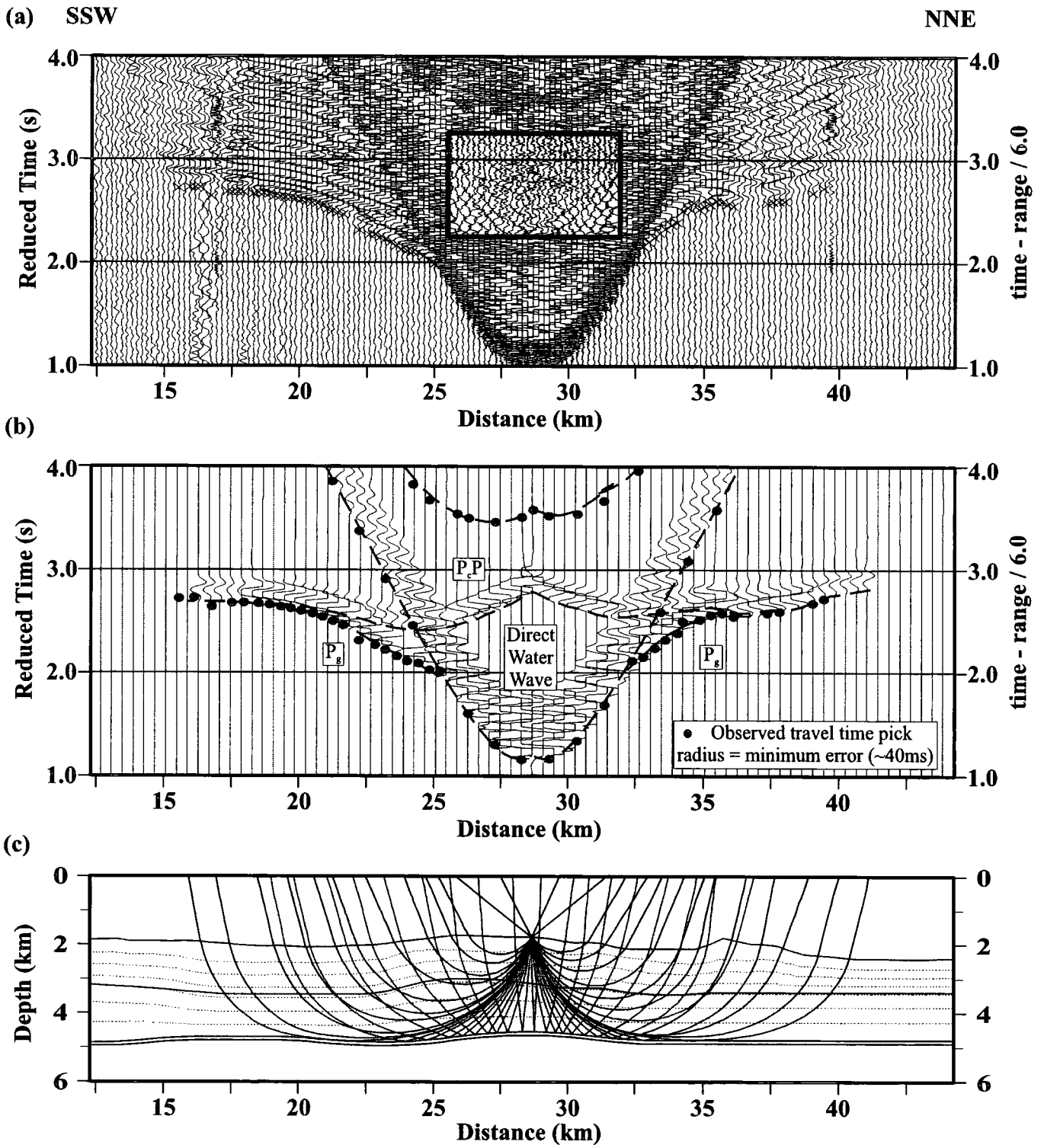

Figure B13: Ray-trace modelling of the final along-axis seismic model for NDOBS2 on Line 4 (see figure A1 for instrument and line locations). Display parameters are described at the start of Appendix B.
(a) Filtered vertical component record section.
(b) Synthetic seismograms calculated from the final velocity-depth model.
(c) Final model with a subset of the rays used to calculate the synthetic seismograms shown in (b).

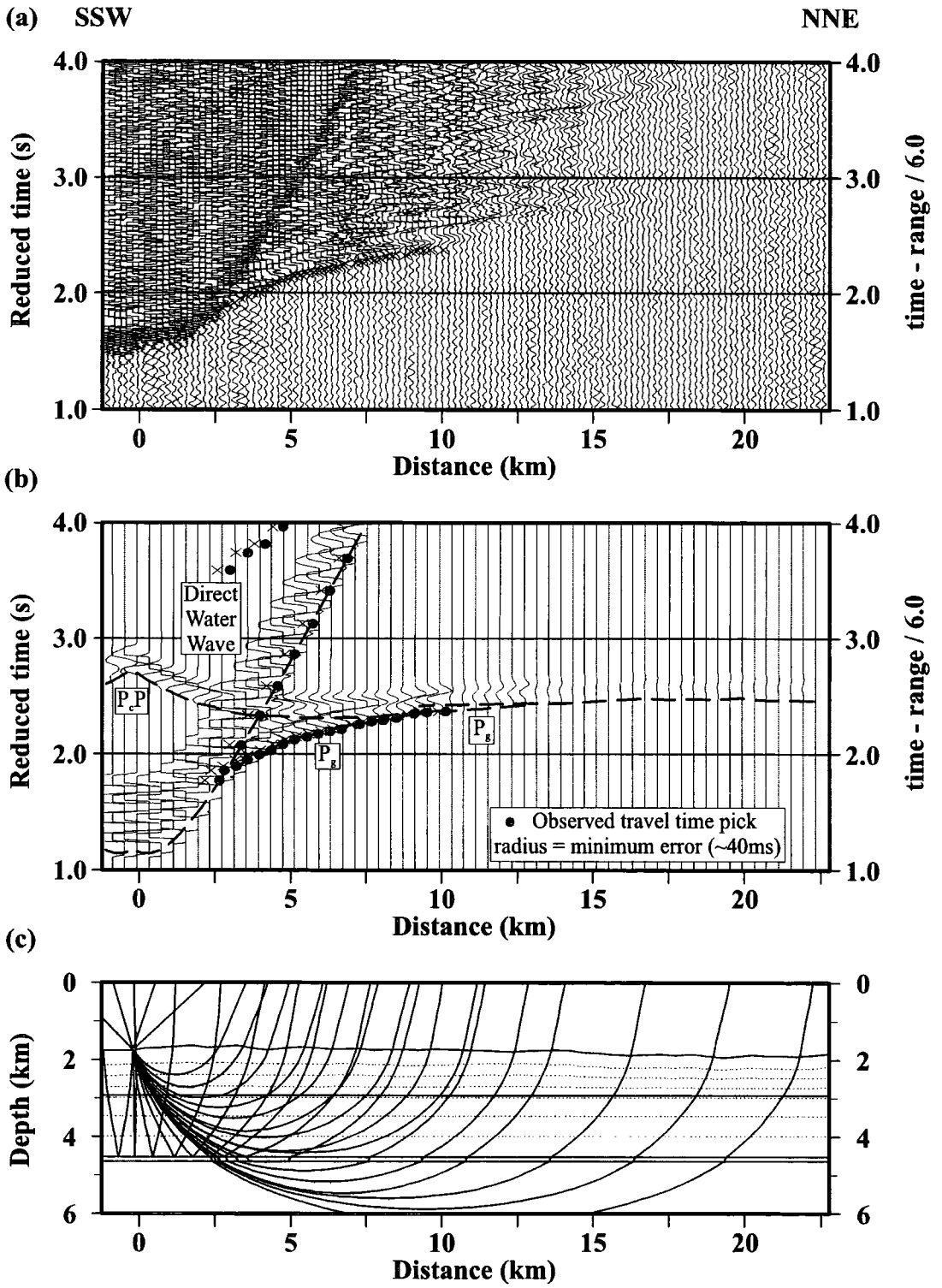

Figure B14: Ray-trace modelling of the final along-axis seismic model for NDOBS3 on Line 9 (see figure A1 for instrument and line locations). Display parameters are described at the start of Appendix B.
(a) Filtered vertical component record section.
(b) Synthetic seismograms calculated from the final velocity-depth model.
(c) Final model with a subset of the rays used to calculate the synthetic seismograms shown in (b).

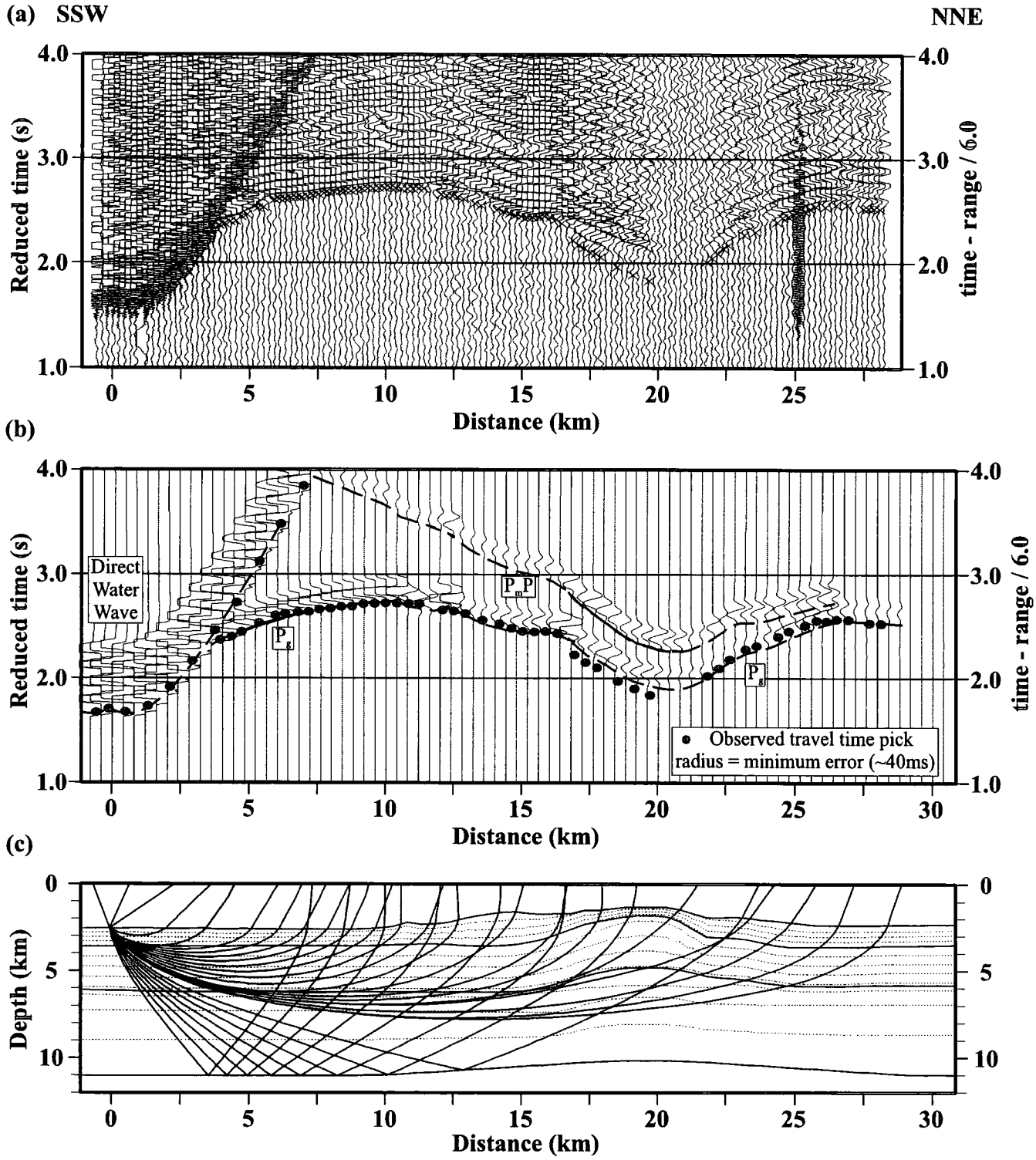

Figure B15: Ray-trace modelling of the final axis-parallel seismic model for SDOBS1 on Line 5 (see figure A1 for instrument and line locations). Display parameters are described at the start of Appendix B.
(a) Filtered vertical component record section.
(b) Synthetic seismograms calculated from the final velocity-depth model.
(c) Final model with a subset of the rays used to calculate the synthetic seismograms shown in (b).

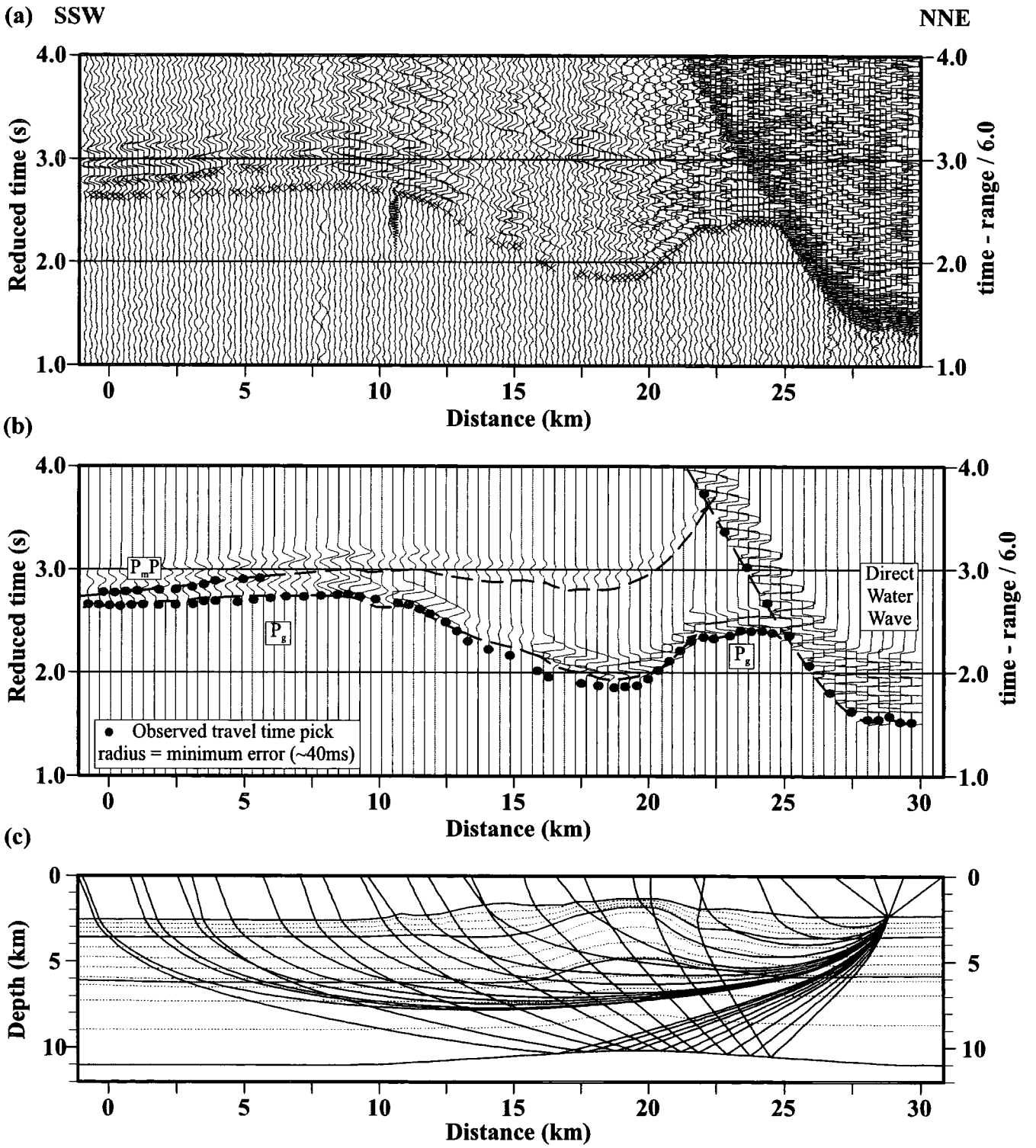

Figure B16: Ray-trace modelling of the final axis-parallel seismic model for NDOBS6 on Line 5 (see figure A1 for instrument and line locations). Display parameters are described at the start of Appendix B.
(a) Filtered vertical component record section.
(b) Synthetic seismograms calculated from the final velocity-depth model.
(c) Final model with a subset of the rays used to calculate the synthetic seismograms shown in (b).

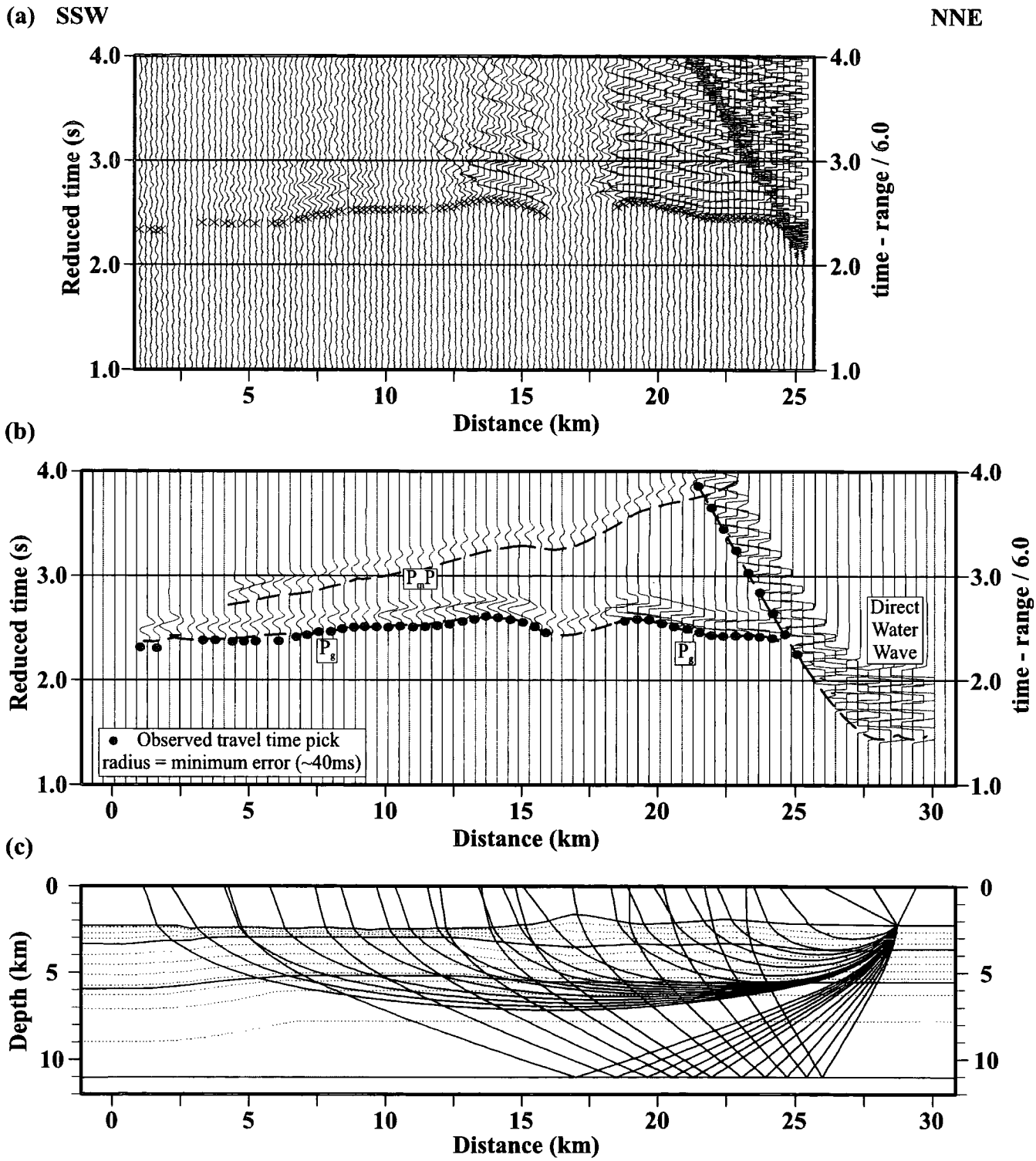

Figure B17: Ray-trace modelling of the final axis-parallel seismic model for NDOBS5 on Line 11 (see figure A1 for instrument and line locations). Display parameters are described at the start of Appendix B.
(a) Filtered vertical component record section.
(b) Synthetic seismograms calculated from the final velocity-depth model.
(c) Final model with a subset of the rays used to calculate the synthetic seismograms shown in (b).

Appendix C

Modelling of the free-air gravity data

The following figures display the results of modelling of the free-air gravity data coincident with the main seismic lines. Modelling was carried out using both *grav2d* (2-D modelling) and *GMSYS* (2¾-D modelling), except for Line 1 (figure C1), where the simple 2-D model provided a very good fit.

To prevent repetitive descriptions of the figures, an extended figure caption applicable to all of the following figures is detailed below.

Figure C?: Final across-axis 2-D/2¾-D free-air gravity model of Line ?, using average P-wave seismic velocities, extracted from the wide-angle seismic model, to estimate initial densities. All layer boundaries remain unchanged from the best-fitting velocity-depth model for this line.
(a) Comparison of the observed (dots) and calculated (solid line) free-air gravity anomalies. Dot size gives an indication of the error bars (±1.5 mGal). *Figure C1*: The calculated gravity anomaly of the initial model (dashed line) consisting of constant layer densities is shown for reference. *Figures C2-C5*: The calculated anomaly from 2-D gravity modelling (dashed line) is included for comparison.
(b) Best fitting density model with layer densities shown in g cm^{-3}. The model extends down to a depth of 15 km and has a semi-infinite half space at either end of the profile. *Figures C2-C5*: 2¾-D input parameters are also shown with densities and minimum and maximum y-lengths shown as subscripts (on-line structures) and superscripts (off-line structures). Stars (-*/*) denote infinite lateral extents.

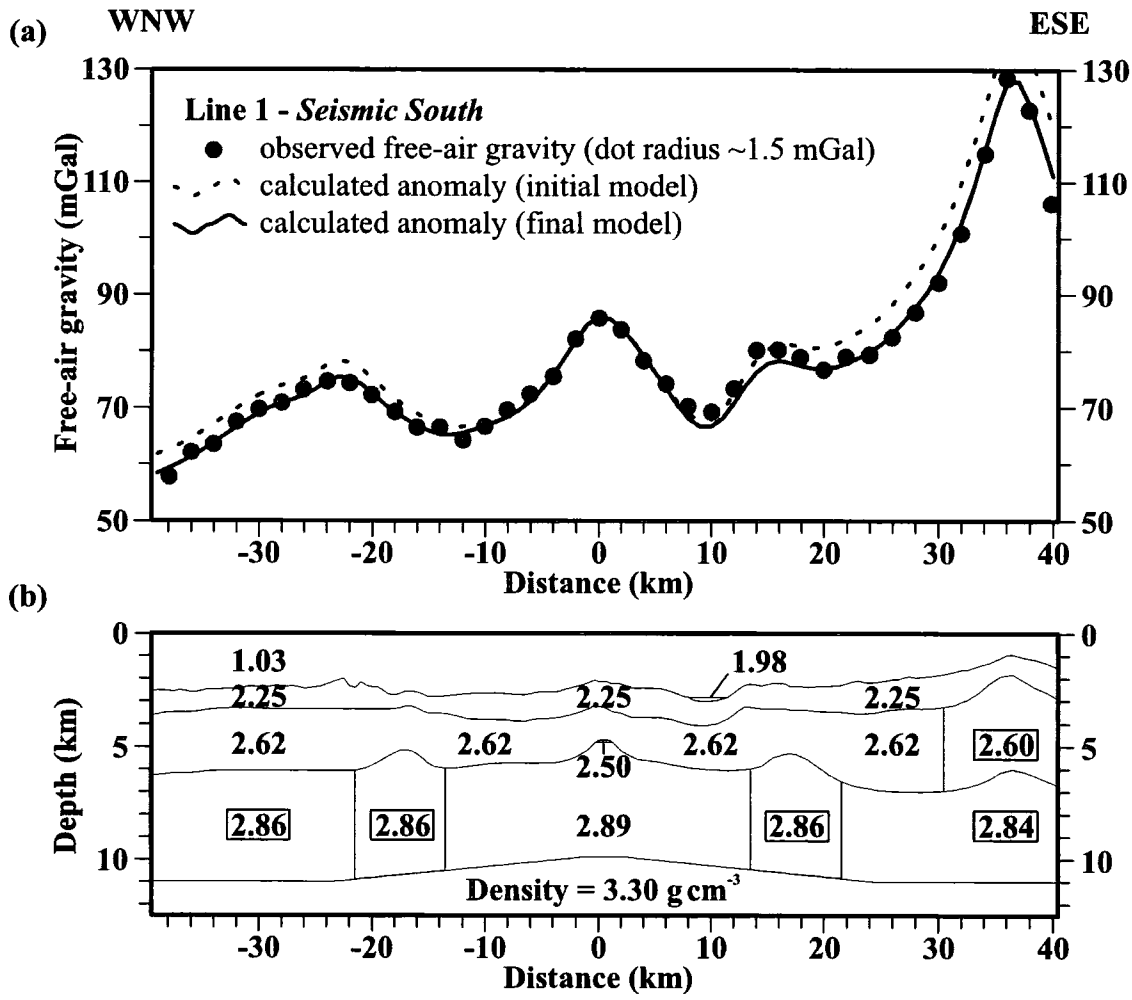

Figure C1: Final across-axis 2-D free-air gravity model of Line 1 (see figure A1 for line location). Display parameters are described at the start of Appendix C.
(a) Comparison of the observed (dots) and calculated (solid line) free-air gravity anomalies.
(b) Best fitting density model with layer densities shown in g cm^{-3}.

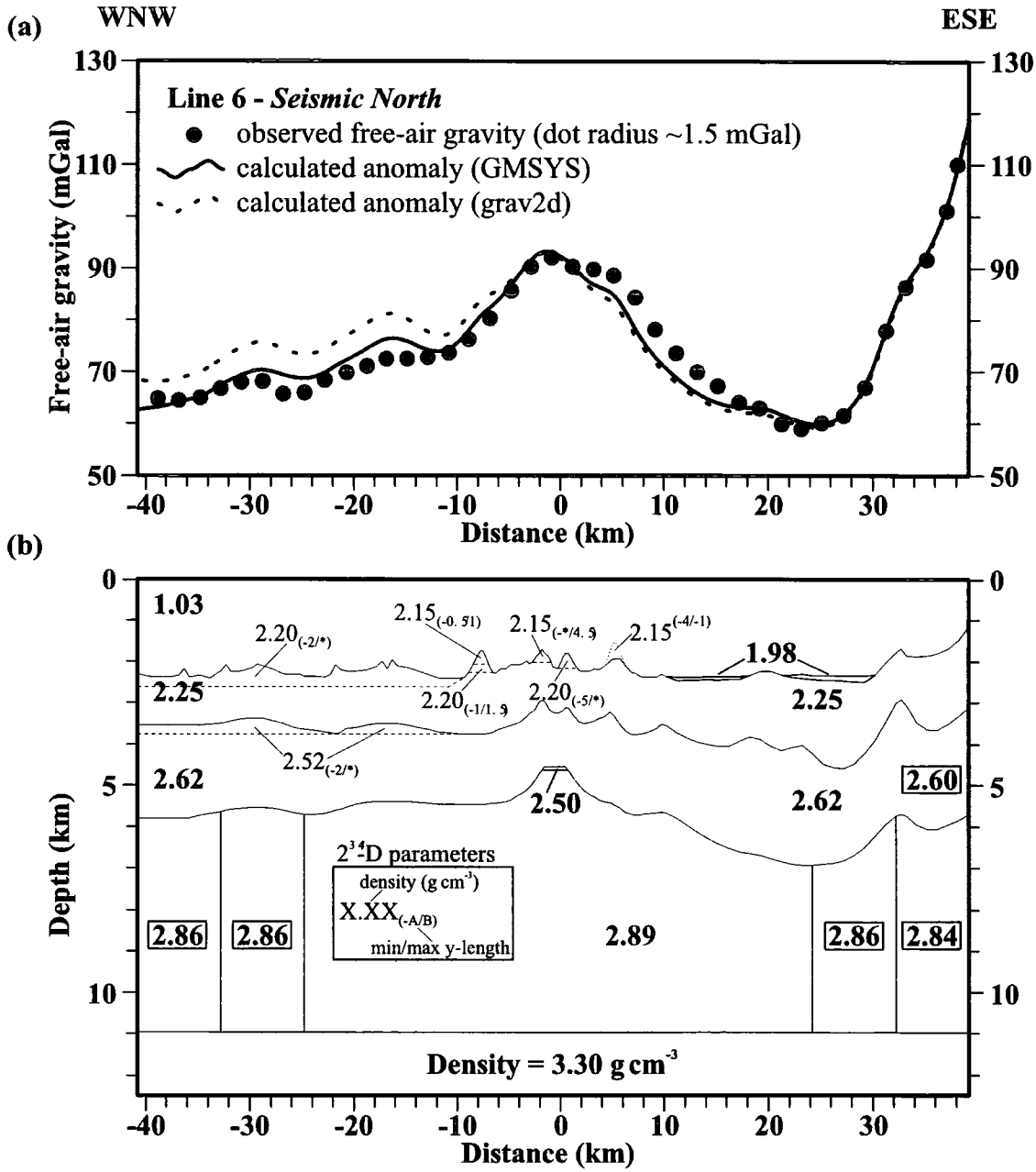

Figure C2: Final across-axis 2¾-D free-air gravity model of Line 6 (see figure A1 for line location). Display parameters are described at the start of Appendix C.

(a) Comparison of the observed (dots) and calculated (solid line) free-air gravity anomalies.The calculated anomaly from *grav2d* gravity modelling (dashed line) is included for comparison.

(b) Best fitting density model with layer densities shown in g cm^{-3}.

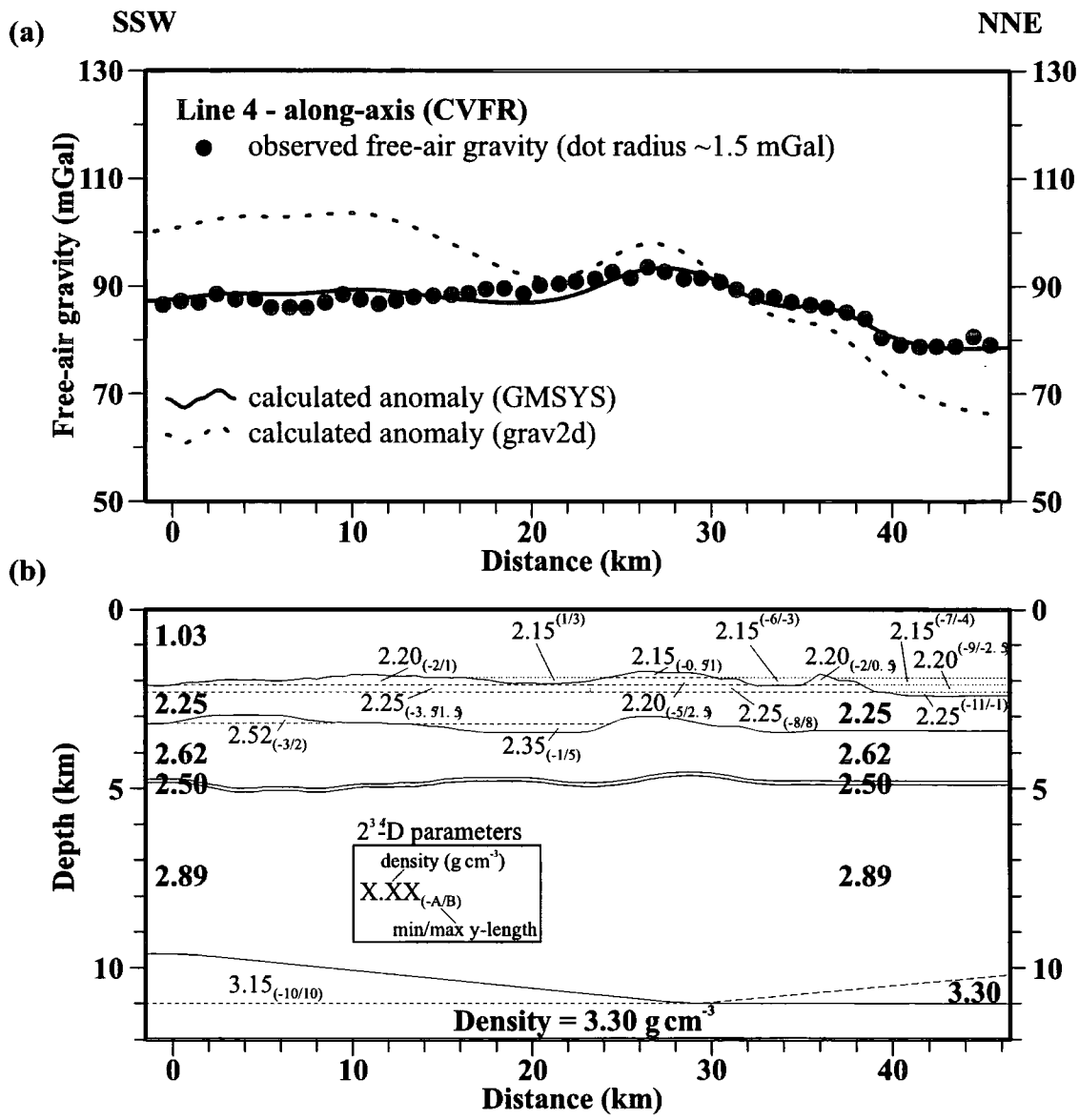

Figure C3: Final across-axis 2¾-D free-air gravity model of Line 4 (see figure A1 for line location). Display parameters are described at the start of Appendix C.
(a) Comparison of the observed (dots) and calculated (solid line) free-air gravity anomalies.The calculated anomaly from *grav2d* gravity modelling (dashed line) is included for comparison.
(b) Best fitting density model with layer densities shown in g cm^{-3}.

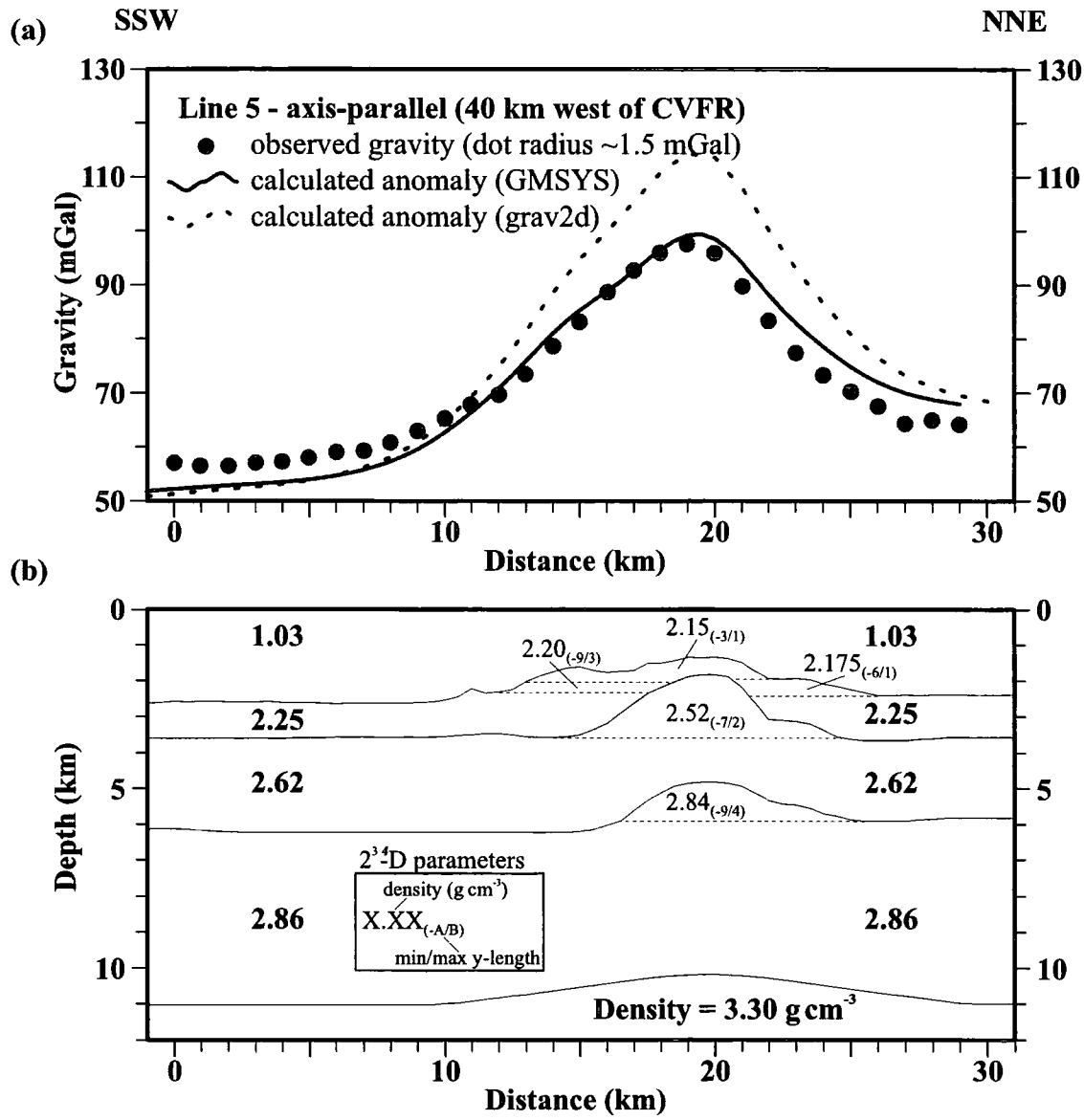

Figure C4: Final across-axis 2¾-D free-air gravity model of Line 5 (see figure A1 for line location). Display parameters are described at the start of Appendix C.
(a) Comparison of the observed (dots) and calculated (solid line) free-air gravity anomalies.The calculated anomaly from *grav2d* gravity modelling (dashed line) is included for comparison.
(b) Best fitting density model with layer densities shown in g cm^{-3}.

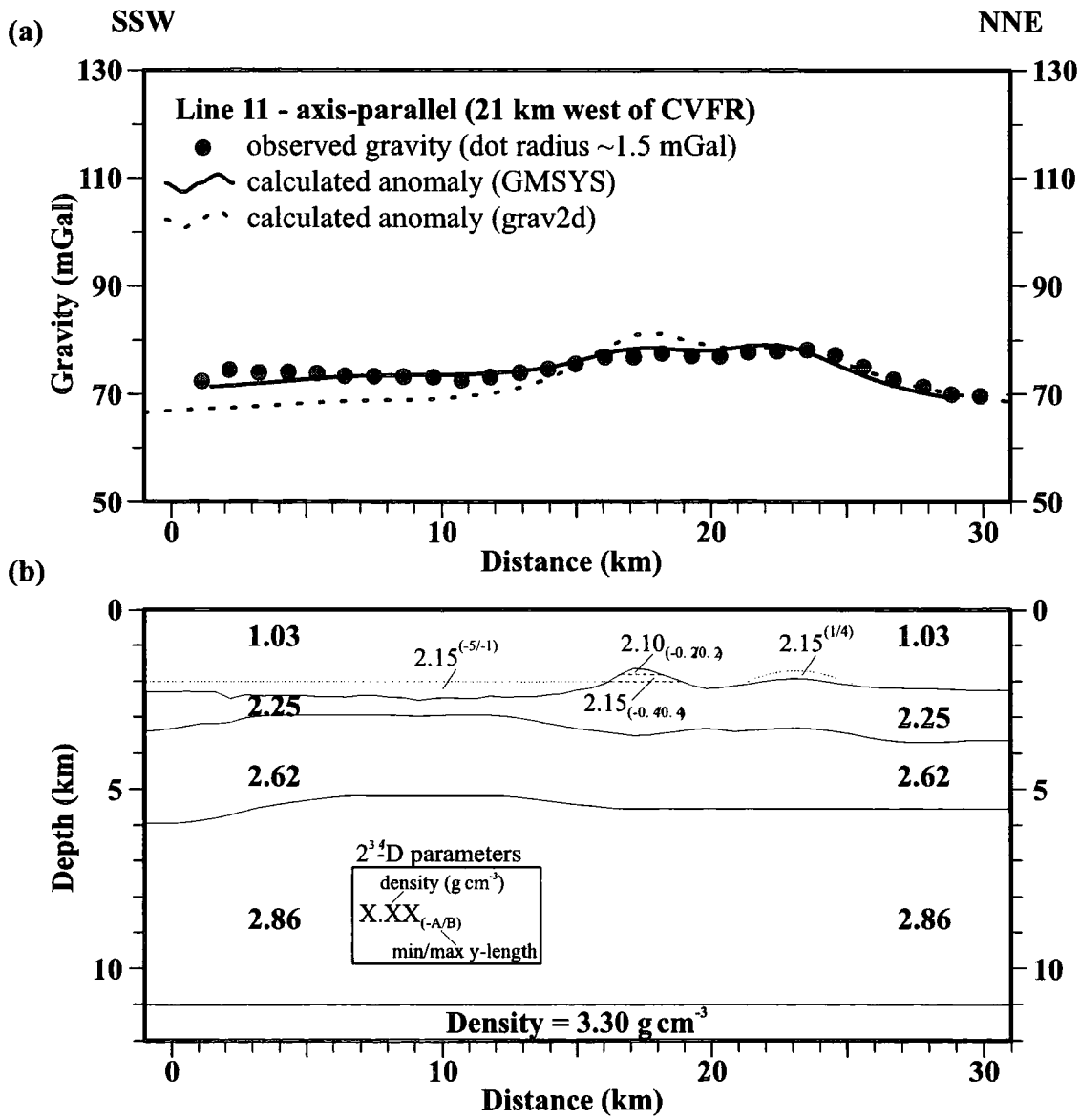

Figure C5: Final across-axis 2¾-D free-air gravity model of Line 11 (see figure A1 for line location). Display parameters are described at the start of Appendix C.
(a) Comparison of the observed (dots) and calculated (solid line) free-air gravity anomalies.The calculated anomaly from *grav2d* gravity modelling (dashed line) is included for comparison.
(b) Best fitting density model with layer densities shown in g cm^{-3}.

Appendix D

Example *GMT* scripts

The following scripts are examples of those used to calculate the residual mantle Bouguer anomaly (see section 5.3.2)

surface

```
#!/bin/sh
#
# fit surface to the data to convert xyz file to a grd file
#
# geographical co-ordinate system
#
blockmean grav95pc.xyz -I0.5m/0.5m -R-176:53/-176:25/-22:35/-21:55 -V >
mean_grav95pc.xyz
surface mean_grav95pc.xyz -Ggrav95pc.grd -I0.125m/0.125m -R-176:53/-176:25/-22:35/-
21:55 -V
#
```

Figure 5.17: Free-air gravity anomaly map calculated from the EW9512 data

```
#
# x,y co-ordinate system
#
blockmean centred_grav95pc.xyz -I1.0/1.0 -R-16/16/-10/54 -V > mean_grav95.xyz
surface mean_grav95.xyz -Ggrav95_rot.grd -I0.25/0.25 -R-16/16/-10/54 -V
```

rotate

```
#!/bin/sh
#
# rotate free-air gravity xyz dataset (grav95pc.xyz) onto an x,y co-ordinate system (units km)
#
mapproject grav95pc.xyz -Joa-176:55/-22:35/111/1:100000 -R-176:55/-176:25/-22:35/-21:55 -
V > rotated_grav95pc.xyz
#
# translate points so origin is located at the southern tip of the CVFR (intersection of Lines 1 & 4)
#
awk '{print($1-19687.622,$2-2601.943,$3)}' rotated_grav95pc.xyz > centred_grav95pc.xyz
#
```

```
run_grav2

#!/bin/sh
#
# grav2 calculates the gravitational attraction of a layered crust of constant thickness and density
#
# must have 256x256 nodes for code
# chosen 48x80 km wide grid (32x64 km grid plus 8 km wide 'buffer zone'
#
# running of grav2 program
#
grav2 << END
bath.z                  bathymetry grid
4                       no. of density interfaces
256                     no. of horizontal nodes
256                     no. of vertical nodes
0.1875                  horizontal node spacing
0.3125                  vertical node spacing
0.                      depth below bathymetry grid of 1st density interface
1250.                   "   "   "   "   2nd   "   "
3000.                   "   "   "   "   3rd   "   "
7500.                   "   "   "   "   4th   "   "
1.22                    density contrast across 1st layer interface
0.37                    "   "   "   2nd layer interface
0.26                    "   "   "   3rd layer interface
0.42                    "   "   "   4th layer interface
seab.out                name of output file
ly2ab.out               "   "   "
ly23.out                "   "   "
moho.out                "   "   "
all.out                 "   "   "
4                       Taylor Series expansion limit (4th order)
END
#
# the output files contain header information, thus the first lines must be removed
#
awk 'NR>2 {print $1}' all.out > xall.out
mv xall.out all.out
#
# combine the gravitational attraction of the crust with the corresponding *.xy data
# The resultant .xyz file is then gridded
#
paste -d' ' bath.xy all.out > gravall.xyz
xyz2grd -R-24/24/-18/62 -I0.1875/0.3125 -F gravall.xyz -V -Ggravall.grd
#
# sample the file of gravitational attraction at the same sample spacing as the free-air gravity
#
grdsample gravall.grd -I0.250 -Gsgravall.grd
#
# plot the 2 grids (16x16 km CVFR grid and 16x64 km axial grid) from the full grid
#
psbasemap -Jx0.4 -P -R-8/8/-10/54 -X7.2 -Y2.0 -B4g4/4g4NESW -K -V > calc_ax.eps
grdcontour sgravall.grd -Jx -P -R-8/8/-10/54 -C1 -A5 -L-100/100 -T -W1.0 -O -K -V >>
calc_ax.eps
#
psbasemap -Jx0.4 -P -R-16/16/-2/30 -X4.0 -Y5.2 -B4g4/4g4NESW -K -V > calc_sq.eps
grdcontour sgravall.grd -Jx -P -R-16/16/-2/30 -C1 -A5 -L-100/100 -T -W1.0 -O -K -V >>
calc_sq.eps
#
```

Figure 5.19: Combined gravitational attraction of a layered crust of constant density/thickness.

```
run_thermal

#!/bin/csh
#
# calculates the gravity anomaly of a simple north-south trending ridge-transform-ridge system
# and assumes passive upwelling
#
echo 'running rtrflow'
run_rtrflow
echo 'running upwsor'
run_upwsor
echo 'running intreg1'
run_intreg1
echo 'running intreg'
run_intreg
echo 'running pratt'
run_pratt
exit(0)
```

```
run_rtrflow
#
rtrflow << END
geom519.parm                    parameter file containing the grid dimensions
                                and location of the ridge-transform-ridge system
rtrflow.out                     output file
END
exit(0)
- - - - - - - - - - - - - - - - - - - - - - - - - - - - - - - - - - - - - - - - - - - -
run_upwsor
#
# determine parameters of the temperature grid
#
upwsor << END
rtrflow.out                     input file
uptemp.out                      output file
0
1
180
1.6
1.6
END
exit(0)
- - - - - - - - - - - - - - - - - - - - - - - - - - - - - - - - - - - - - - - - - - - -
run_intreg1
#
# calculate the variations in the temperature field due to passive upwelling
#
intreg1 << end1
uptemp.out                      input file
ttemp1_2                        output file
0                               no. of layers to skip
end1

intreg1 << end2
uptemp.out
ttemp2_3
1
end2

and so on.....number of temperature layers is defined in the initial parameter file (see run_rtrflow)
```

```
run_intreg
#
# convert temperatures into relative densities and resample onto a regularly spaced grid
#
intreg << end1
ttemp1_2                                    input file
dens1_2                                     output file
deltz1_2                                    output file
end1

intreg << end2
ttemp2_3
dens2_3
deltz2_3
end2

and so on.....number of density layers is defined in the initial parameter file (see run_rtrflow)
- - - - - - - - - - - - - - - - - - - - - - - - - - - - - - - - - - - - - - - - - - - - - - - - - - - -
run_pratt
#
# determine the gravitational signal from layers with density variations
#
pratt << end1
dens1_2                                     input file
n                                           add to another file?
grav1_2                                     output file
n
end1

pratt << end2
y                                           add to another file?
grav1_2                                     original file
grav2_3                                     output file
n
end2

and so on.....number of layers is defined in the initial parameter file (see run_rtrflow)
```

Figure 5.21: Thermal anomaly due to passive upwelling over a ridge-transform-ridge system.